Vincenzo Levizzani
Christopher Kidd · Dalia B. Kirschbaum
Christian D. Kummerow · Kenji Nakamura
F. Joseph Turk   *Editors*

Satellite Precipitation Measurement

Volume 1

Springer

Advances in Global Change Research

Volume 67

Series Editor

Markus Stoffel, Institute of Geological Sciences, University of Geneva, Geneva, Switzerland

Advisory Editors

Wolfgang Cramer, IMEP, Bâtiment Villemin, Europole de l'Arbois,
Aix-en-Provence, France
Urs Luterbacher, University of Geneva, Geneva, Switzerland
F. Toth, International Institute for Applied Systems Analysis (IIASA), Laxanburg,
Austria

More information about this series at http://www.springer.com/series/5588

Vincenzo Levizzani • Christopher Kidd
Dalia B. Kirschbaum • Christian D. Kummerow
Kenji Nakamura • F. Joseph Turk
Editors

Satellite Precipitation Measurement

Volume 1

Springer

Editors
Vincenzo Levizzani
CNR-ISAC
Bologna, Italy

Dalia B. Kirschbaum
Code 617
NASA Goddard Space Flight Center
Greenbelt, MD, USA

Kenji Nakamura
Department of Economics on
Sustainability
Dokkyo University
Saitama, Japan

Christopher Kidd
Earth System Science Interdisciplinary Center
University of Maryland and NASA Goddard
Space Flight Center
Greenbelt, MD, USA

Christian D. Kummerow
Department of Atmospheric Science
Colorado State University
Fort Collins, CO, USA

F. Joseph Turk
Jet Propulsion Laboratory
California Institute of Technology
Pasadena, CA, USA

Sognatore è un uomo con i piedi fortemente appoggiati sulle nuvole[*]

Ennio Flaiano (1910–1972)

[*]*Dreamer is a man with his feet firmly resting on the clouds*

In memory of
Arthur Y. Hou (1947–2013)

Preface

This book is published 13 years after the book *Measuring Precipitation from Space: EURAINSAT and the Future* (V. Levizzani, P. Bauer, and F. J. Turk, Eds., Springer, ISBN 978-1-4020-5835-6), but it is not a revised edition of the previous. It is a new book that aims to construct a quasi-complete picture of the science and applications of satellite-derived precipitation measurements at the present time.

The book comes out at the end of a very exciting era of precipitation measurements from space. The Tropical Rainfall Measuring Mission (TRMM), launched in November 1997, ended its long life in space in April 2015 providing an unprecedented 17-year-long dataset of tropical precipitation and lightning. The Global Precipitation Measurement (GPM) mission, launched in February 2014, is now in space as TRMM's natural successor with a more global perspective that extends precipitation radar observations to the Arctic and Antarctic circles. At the same time, the CloudSat mission, launched in April 2006, is in its 13th year in space and focuses on cloud structure, which is essential for improving precipitation retrievals. These are just a few examples of precipitation-oriented missions that continuously provide data from geostationary and low Earth orbits in a truly cooperative effort worldwide. This effort involves many agencies and a broad range of countries who collaborate in a genuine way to observe global precipitation.

It is by realizing the significance of this historical moment and the need to think about what is important for the future that the community joined in the effort of writing a book with the goal of serving the precipitation community itself, the scholars, the students, the stakeholders, the end users, and all the readers interested in knowing the progress of satellite precipitation studies. The most recent achievements in precipitation monitoring from space drive us into the future of measuring not only heavy rainfall but less intense rainfall, snowfall, and even hailfall. Such a scientific framework would not have even been conceivable 13 years ago and is only possible thanks to the relentless effort of the worldwide space and precipitation communities.

Naturally, we realize that at the time of the printing of this book, the field will already have made advances and thus part of the material may already be a bit

outdated. However, in this era of rapidly evolving technological developments, sensors that take years to design, build, and launch are already considered old. This is particularly true nowadays when the progress in approaching new scientific challenges is particularly fast.

Since 2007, science has made substantial progresses toward transforming satellite rainfall "estimates" into accurate "measurements" and producing operational rainfall products readily available for a wide field of applications ranging from climate research and numerical weather prediction to hydrology, agriculture, health, civil protection, and much more. Satellite-derived precipitation products are now being considered as a valuable tool for a number of applications that benefit society and save lives. This is perhaps the most important achievement of all.

This book represents a significant effort, and each author has provided high-quality material in the topics of current and future mission contributions, observations of precipitation using the suite of precipitation satellites, retrieval techniques, validation, and applications. The result is a book that not only photographs the state of the art of the discipline but also projects it into the future.

Bologna, Italy   Vincenzo Levizzani
Greenbelt, MD, USA   Christopher Kidd
Greenbelt, MD, USA   Dalia B. Kirschbaum
Fort Collins, CO, USA   Christian D. Kummerow
Saitama, Japan   Kenji Nakamura
Pasadena, CA, USA   F. Joseph Turk
9 March 2020

Acknowledgments

The first acknowledgment goes to Springer Nature for asking us to start this project and for being very patient with us for the considerable amount of time it took to put the material together.

All the colleagues who spent their precious time contributing their ideas and results deserve special gratitude. They are all very busy scientists, and this is why their contribution is particularly valuable. We deem the book to be a first-hand image of the achievements of the whole community at this time while also providing an important glimpse into future developments.

Then we feel that we need to thank the readers who have already made the previous 2007 Springer book a success, thus de facto making it possible to start writing the new one. We hope you will get from this new book even more inspiration than you got from its predecessor. While some concepts and details will surely become outdated as time goes by, it is our hope that the material contained herein is sufficiently broad that it will always serve as a springboard to understand and put into context the latest research and findings.

It would be almost impossible to thank all the people and organizations behind this effort. You realize this simple truth by looking at the list of contributors and seeing the very long list of institutes, research organizations, university departments, and operational agencies that allowed their members to spend a substantial amount of time writing and correcting the chapters of the book. We thank, in particular, our home institutions that were very supportive in understanding the importance of our work for the community: CNR, Colorado State University, Dokkyo University, JPL-Caltech, NASA, and University of Maryland.

It is very important to remember all the colleagues who are no longer with us and who worked very hard until the last minute providing an essential contribution. This book is dedicated to the memory of a friend of all of us, Arthur Y. Hou (1947–2013). Arthur was not only the US Project Scientist of the Global Precipitation Measurement (GPM) mission, he was a man of a truly global vision who now is in place with the GPM constellation. More than that, he made great efforts to establish an international science cooperation through his gentle and unique way of approaching

each one of us. Other colleagues left us in recent times, and we want to honor them as well: David (Dave) H. Staelin (1938–2011), David I. F. Grimes (1951–2011), and James (Jim) A. Weinman (1930–2012). They all left us much too soon, and we miss them, but their work is here to testify to their essential contribution to the advancement of science and to meet the needs of mankind.

Two major international organizations gave us the opportunity to work together with a global strategy for the future: the International Precipitation Working Group (IPWG) and the World Meteorological Organization (WMO).

The senior editor (Vincenzo Levizzani) would like to recognize the ceaseless work of his coeditors in effectively putting together the material of their respective sections: F. Joseph (Joe) Turk for Section 1, Christian (Chris) D. Kummerow for Sections 2 and 3, Christopher (Chris) Kidd for Section 4, Kenji Nakamura for Section 5, and Dalia B. Kirschbaum for Section 6. Their commitment and competence largely influenced the quality level of this book.

Finally, our families are part of the project through their understanding and their moral and practical support. Without them, the writing of this book would have never even started.

Bologna, Italy   Vincenzo Levizzani
Greenbelt, MD, USA   Christopher Kidd
Greenbelt, MD, USA   Dalia B. Kirschbaum
Fort Collins, CO, USA   Christian D. Kummerow
Saitama, Japan   Kenji Nakamura
Pasadena, CA, USA   F. Joseph Turk
9 March 2020

Contents of Volume 1

Contents of Volume 2

List of Figures

List of Tables

Contributors

Christophe Accadia European Organization for the Exploitation of Meteorological Satellites (EUMETSAT), Darmstadt, Germany

Robert F. Adler Earth System Science Interdisciplinary Center (ESSIC), University of Maryland, College Park, MD, USA

Kazumasa Aonashi Meteorological Research Institute (MRI), Japan Meteorological Agency (JMA), Tsukuba, Japan

Yoriko Arai Remote Sensing Technology Center of Japan (RESTEC), Tokyo, Japan

Moshe Armon The Fredy & Nadine Herrmann Institute of Earth Sciences, Hebrew University of Jerusalem, Jerusalem, Israel

Kristi Arsenault SAIC, Inc., McLean, VA, and National Aeronautics and Space Administration (NASA), Goddard Space Flight Center (GSFC), Greenbelt, MD, USA

Malarvizhi Arulraj Pratt School of Engineering, Civil & Environmental Engineering, Duke University, Durham, NC, USA

Hamed Ashouri Department of Civil and Environmental Engineering, Center for Hydrometeorology and Remote Sensing (CHRS), University of California, Irvine, CA, USA

Luca Baldini Institute of Atmospheric Sciences and Climate (ISAC), National Research Council (CNR), Roma, Italy

Ana P. Barros Pratt School of Engineering, Civil & Environmental Engineering, Duke University, Durham, NC, USA

Alessandro Battaglia Department of Physics and Astronomy, University of Leicester, Leicester, UK

Hylke E. Beck Department of Civil and Environmental Engineering, Princeton University, Princeton, NJ, USA

Andreas Becker Global Precipitation Climatology Center (GPCC), Deutscher Wetterdienst (DWD), Offenbach, Germany

Ali Behrangi Department of Hydrology and Atmospheric Sciences, University of Arizona, Tucson, AZ, USA

Hugo Bellenger Laboratoire de Météorologie Dynamique/IPSL, CNRS, Sorbonne Université, École Normale Supérieure, École Polytechnique, Paris, France
Japan Agency for Marine-Earth Science and Technology (JAMSTEC), Yokosuka, Japan

Emily Berndt NASA, Marshall Space Flight Center (MSFC), Huntsville, AL, USA

Emily Black Department of Meteorology, University of Reading, Reading, UK

David T. Bolvin Science Systems and Applications, Inc., Lanham, MD, and NASA/GSFC, Greenbelt, MD, USA

Rogerio Bonifacio World Food Programme, Vulnerability Assessment and Mapping Unit, Roma, Italy

Sid-Ahmed Boukabara NOAA/NESDIS/STAR, College Park, MD, USA

Dominique Bouniol Météo France, Centre National de Recherches Météorologiques (CNRM), Groupe de Modélisation et d'Assimilation pour la Prévision (GMAP), OBS, Toulouse, France

Jacqueline Boutin Sorbonne Université, CNRS, Institut de Recherche pour le Développement (IRD), Muséum National d'Histoire Naturelle (MNHN), Laboratoire d'Océanographie et du Climat, Expérimentations et Approches Numériques (LOCEAN), Paris, France

Dan Braithwaite Department of Civil and Environmental Engineering/CHRS, University of California, Irvine, CA, USA

Scott A. Braun NASA/GSFC, Greenbelt, MD, USA

Luca Brocca Research Institute for Geo-Hydrological Protection (IRPI), National Research Council (CNR), Perugia, Italy

Jörg Burdanowitz Institute for Meteorology, University of Hamburg, Hamburg, Germany

Steven J. Burian Department of Civil and Environmental Engineering, University of Utah, Salt Lake City, UT, USA

Stefania Camici CNR/IRPI, Perugia, Italy

Michel Capderou CNRS/LMD, Palaiseau, France

Daniele Casella CNR/ISAC, Roma, Italy

Elsa Cattani CNR/ISAC, Bologna, Italy

Daniel Cecil NASA/MSFC, Huntsville, AL, USA

Philippe Chambon Météo France, CNRM/GMAP/OBS, Toulouse, France

Venkatachalam Chandrasekar Department of Electrical and Computer Engineering, Colorado State University, Ft. Collins, CO, USA

Luca Ciabatta CNR/IRPI, Perugia, Italy

Sophie Cloché CNRS/IPSL, Palaiseau, France

Paolo Colucci EUMETSAT, Darmstadt, Germany

Salvatore D'Addio European Space Agency (ESA), European Space Research and Technology Centre (ESTEC), Noordwijk, The Netherlands

Frank Davenport Climate Hazards Group (CHG), University of California, Santa Barbara, CA, USA

Michel Dejus Centre National d'Études Spatiales (CNES), Toulouse, France

Tufa Dinku International Research Institute for Climate and Society (IRI), The Earth Institute at Columbia University, Palisades, NY, USA

Craig Donlon ESA/ESTEC, Noordwijk, The Netherlands

Mohamed El Saadani Department of Civil Engineering, University of Louisiana Lafayette, Lafayette, LA, USA

Ralph R. Ferraro NOAA/NESDIS/STAR, College Park, MD, USA

Robert D. Field Department of Applied Physics and Applied Mathematics, Columbia University, and NASA Goddard Institute for Space Studies, New York, NY, USA

Paolo Filippucci CNR/IRPI, Perugia, Italy

Thomas Fiolleau CNRS, Laboratoire d'Études en Géophysique et Océanographie Spatiales (LEGOS), Toulouse, France

Efi Foufoula-Georgiu Department of Civil and Environmental Engineering and Department of Earth Science, University of California, Irvine, CA, USA

Kevin Fuell Earth System Science Center (ESSC), University of Alabama in Huntsville, Huntsville, AL, USA

Chris Funk United States Geological Survey (USGS), Earth Resources Observation and Science (EROS) Center, Sioux Falls, SD, and CHG, University of California, Santa Barbara, CA, USA

Kinji Furukawa Japan Aerospace Exploration Agency (JAXA), Tokyo, Japan

Kevin Garrett NOAA/NESDIS/STAR, College Park, MD, USA

Alan Geer European Centre for Medium-range Weather Forecasts (ECMWF), Reading, UK

Radoslaw Goska Iowa Institute of Hydraulic Research (IIHR) – Hydroscience & Engineering, University of Iowa, Iowa City, IA, USA

Marielle Gosset Geoscience Environnement, Toulouse, France

Christopher Grassotti Cooperative Institute for Satellite Earth System Studies (CISESS), ESSIC, University of Maryland, College Park, MD, USA

Helen Greatrex Department of Meteorology, University of Reading, Reading, UK

Mircea Grecu Morgan State University, Baltimore, MD, and NASA/GSFC, Greenbelt, MD, USA

Guojun Gu ESSIC, University of Maryland, College Park, MD, USA

Adrien Guérou CNRS/LEGOS, Toulouse, France

Clément Guilloteau Department of Civil and Environmental Engineering, University of California, Irvine, CA, USA

Ziad S. Haddad Jet Propulsion Laboratory (JPL), California Institute of Technology (Caltech), Pasadena, CA, USA

Sebastian Hahn Department of Geodesy and Geoinformation, Research Group Remote Sensing, TU Wien, Vienna, Austria

Atsushi Hamada Faculty of Sustainable Design, University of Toyama, Toyama, Japan

Laura Harrison CHG, University of California, Santa Barbara, CA, USA

Negin Hayatbini Department of Civil and Environmental Engineering/CHRS, University of California, Irvine, CA, USA

John M. Haynes Cooperative Institute for Research in the Atmosphere (CIRA), Colorado State University, Ft. Collins, CO, USA

Ryan Honeyager UCAR, College Park, MD, USA

Kuo-Lin Hsu Department of Civil and Environmental Engineering/CHRS, University of California, Irvine, CA, USA

George J. Huffman NASA/GSFC, Greenbelt, MD, USA

Toshio Iguchi National Institute of Information and Communications Technology (NICT), Koganei, Japan

Flavio Iturbide-Sanchez NOAA/NESDIS/STAR, College Park, MD, USA

Menglin Jin Department of Atmospheric and Oceanic Science, University of Maryland, College Park, MD, USA

Bradford Johnson Department of Geography, University of Georgia, Athens, GA, USA

Erin Jones NOAA/NESDIS/STAR, College Park, MD, USA

Robert J. Joyce Innovim, Greenbelt, MD, and NOAA, National Weather Service (NWS), Climate Prediction Center (CPC), College Park, MD, USA

Rômulo A. Jucá Oliveira Geoscience Environnement, Toulouse, France

Misako Kachi Earth Observation Research Center (EORC), JAXA, Ibaraki, Japan

Eugenia Kalnay Department of Atmospheric and Oceanic Science, University of Maryland, College Park, MD, USA

Sarah Kapnick NOAA, Geophysical Fluid Dynamics Laboratory (GFDL), Princeton, NJ, USA

Negar Karbalee Department of Civil and Environmental Engineering/CHRS, University of California, Irvine, CA, USA

Nozomi Kawamoto RESTEC, Tokyo, Japan

Masahiro Kazumori JMA, Tokyo, Japan

Christopher Kidd ESSIC, University of Maryland, College Park, MD, and NASA/GSFC, Greenbelt, MD, USA

Dalia B. Kirschbaum NASA/GSFC, Greenbelt, MD, USA

Pierre-Emmanuel Kirstetter School of Meteorology and School of Civil Engineering and Environmental Sciences and Advanced Radar Research Center, University of Oklahoma and NOAA/National Severe Storms Laboratory, Norman, OK, USA

Marian Klein Boulder Environmental Sciences and Technology, Boulder, CO, USA

Ulf Klein ESA/ESTEC, Noordwijk, The Netherlands

Christian Klepp Max Planck Institute for Meteorology, Hamburg, Germany

Stefan Kneifel Institute for Geophysics and Meteorology, University of Cologne, Cologne, Germany

Pavlos Kollias School of Marine and Atmospheric Sciences, Stony Brook University, Stony Brook, NY, USA

Cezar Kongoli University of Maryland, College Park, MD, USA

Shunji Kotsuki RIKEN Center for Computational Science, Kobe, Japan
Center for Environmental Remote Sensing, Chiba University, Chiba, Japan

Witold F. Krajewski IIHR-Hydroscience & Engineering, University of Iowa, Iowa City, IA, USA

Takuji Kubota EORC/JAXA, Ibaraki, Japan

Paul A. Kucera University Corporation for Atmospheric Research (UCAR), Boulder, CO, USA

Mark S. Kulie NOAA/NESDIS/STAR, Advanced Satellite Products Branch, Madison, WI, USA

Christian D. Kummerow Department of Atmospheric Science, Colorado State University, Ft. Collins, CO, USA

Frank Lafontaine Jacobs, Engineering Services and Science Capability Augmentation (ESSCA), NASA/MSFC, Huntsville, AL, USA

Martin Landsfeld CHG, University of California, Santa Barbara, CA, USA

Sante Laviola CNR/ISAC, Bologna, Italy

Minda Le Department of Electrical and Computer Engineering, Colorado State University, Ft. Collins, CO, USA

Matthew D. Lebsock JPL/Caltech, Pasadena, CA, USA

Tristan S. L'Ecuyer Department of Atmospheric and Oceanic Sciences, University of Wisconsin-Madison, Madison, WI, USA

Jussi Leinonen JPL/Caltech, Pasadena, CA, USA

Anita LeRoy ESSC, University of Alabama in Huntsville, Huntsville, AL, USA

Vincenzo Levizzani CNR/ISAC, Bologna, Italy

Guo-Yuan Lien Research and Development Center, Central Weather Bureau, Taipei, Taiwan

Chuntao Liu Texas A&M University, Department of Physical and Environmental Sciences, Corpus Christi, TX, USA

Guosheng Liu Department of Earth, Ocean and Atmospheric Science, Florida State University, Tallahassee, FL, USA

Quanhua Liu NOAA/NESDIS/STAR, College Park, MD, USA

Shuyan Liu CIRA, Colorado State University, Ft. Collins, CO, USA

Eric Maddy NOAA/NESDIS/STAR, College Park, MD, USA

Viviana Maggioni Sid and Reva Dewberry Department of Civil, Environmental, and Infrastructure Engineering, George Mason University, Fairfax, VA, USA

Ross Maidment Department of Meteorology, University of Reading, Reading, UK

Anna Cinzia Marra CNR/ISAC, Roma, Italy

Francesco Marra The Fredy & Nadine Herrmann Institute of Earth Sciences, Hebrew University of Jerusalem, Jerusalem, Israel, and CNR/ISAC, Bologna, Italy

Frank S. Marzano Department of Information Engineering, Electronics and Telecommunications (DIET), Sapienza University of Roma, Roma, Italy

Takeshi Masaki RESTEC, Tokyo, Japan

Bathobile Maseko South African Weather Service, Pretoria, South Africa

Christian Massari CNR/IRPI, Perugia, Italy

Vinia Mattioli EUMETSAT, Darmstadt, Germany

Kevin McGrath Jacobs/ESSCA, NASA/MSFC, Huntsville, AL, USA

Amy McNally ESSIC, University of Maryland, College Park, MD, and NASA/GSFC, Greenbelt, MD, USA

Tomoaki Mega Tokyo Metropolitan University, Tokyo, Japan

Huan Meng NOAA/NESDIS/STAR, College Park, MD, USA

Andrés Merino Department of Chemistry and Applied Physics, University of León, León, Spain

Lisa Milani University of Maryland, College Park, MD, and NASA/GSFC, Greenbelt, MD, USA

Takemasa Miyoshi RIKEN Center for Computational Science, Kobe, Japan

Andrew Molthan NASA/MSFC, Huntsville, AL, USA

Saverio Mori DIET, Sapienza University of Roma, Roma, Italy

Efrat Morin The Fredy & Nadine Herrmann Institute of Earth Sciences, Hebrew University of Jerusalem, Jerusalem, Israel

Kenji Nakamura Dokkyo University, Saitama, Japan

Eric J. Nelkin Science Systems and Applications, Inc., Lanham, MD, and NASA/GSFC, Greenbelt, MD, USA

Brian R. Nelson NOAA/NESDIS, National Centers for Environmental Information (NCEI), Asheville, NC, USA

Phu Nguyen Department of Civil and Environmental Engineering/CHRS, University of California, Irvine, CA, USA

Riko Oki Earth Observation Research Center (EORC)/Japan Aerospace Exploration Agency (JAXA), Ibaraki, Japan

William S. Olson University of Maryland Baltimore County, Baltimore, MD, and NASA/GSFC, Greenbelt, MD, USA

Mohammed Ombadi Department of Civil and Environmental Engineering/CHRS, University of California, Irvine, CA, USA

Davide Ori Institute for Geophysics and Meteorology, University of Cologne, Cologne, Germany

Shigenori Otsuka RIKEN Center for Computational Science, Kobe, Japan

Ming Pan Department of Civil and Environmental Engineering, Princeton University, Princeton, NJ, USA

Giulia Panegrossi CNR/ISAC, Roma, Italy

Florian Pappenberger ECMWF, Shinfield Park, Reading, UK

Salvatore Pascale Department of Earth System Science, Stanford University, Stanford, CA, USA

Diego Pedreros USGS/EROS, Sioux Falls, SD, USA

Walter A. Petersen NASA/MSFC, Huntsville, AL, USA

Pete Peterson CHG, University of California, Santa Barbara, CA, USA

Nazzareno Pierdicca DIET, Sapienza University of Roma, Roma, Italy

Federico Porcù Department of Physics and Astronomy, University of Bologna, Bologna, Italy

Olivier P. Prat Cooperative Institute for Satellite Earth System Studies (CISESS), North Carolina State University, Asheville, NC, USA

Alain Protat Bureau of Meteorology (BoM), Melbourne, VIC, Australia

Felipe Quintero IIHR-Hydroscience & Engineering, University of Iowa, Iowa City, IA, USA

David L. Randel Department of Atmospheric Science, Colorado State University, Ft. Collins, CO, USA

Gilles Reverdin Sorbonne Université, CNRS/IRD/MNHN/LOCEAN, Paris, France

Sarah Ringerud ESSIC, University of Maryland, College Park, MD, and NASA/GSFC, Greenbelt, MD, USA

Rémy Roca CNRS/LEGOS, Toulouse, France

Geun-Hyeok Ryu National Meteorological Satellite Center, Korea Meteorological Administration, Seoul, South Korea

Paolo Sanò CNR/ISAC, Roma, Italy

Mathew R. P. Sapiano Sapiano Statistical Services, Atlanta, GA, USA

Masaki Satoh Atmosphere and Ocean Research Institute (AORI), The University of Tokyo, Chiba, Japan

Peter Schlüssel EUMETSAT, Darmstadt, Germany

Udo Schneider GPCC/DWD, Offenbach, Germany

Marc Schröder DWD, Offenbach, Germany

J. Marshall Shepherd Department of Geography, University of Georgia, Athens, GA, USA

Shoichi Shige Division of Earth and Planetary Sciences, Graduate School of Science, Kyoto University, Kyoto, Japan

Shraddhanand Shukla CHG, University of California, Santa Barbara, CA, USA

Gail M. Skofronick-Jackson NASA, Headquarters, Science Mission Directorate, Washington, DC, USA

Mark A. Smalley JPL/Caltech, Pasadena, CA, USA

Matthew Smith Information Technology and Systems Center, University of Alabama in Huntsville, Huntsville, AL, USA

Byung-Ju Sohn School of Earth and Environmental Sciences, Seoul National University, Seoul, South Korea

Hwan-Jin Song National Institute of Meteorological Sciences, Korea Meteorological Administration, Seoul, South Korea

Soroosh Sorooshian Department of Civil and Environmental Engineering/CHRS, University of California, Irvine, CA, USA

Thomas Stanley Universities Space Research Association (USRA), Columbia, MD, and NASA/GSFC, Greenbelt, MD, USA

Erich F. Stocker NASA/GSFC, Greenbelt, MD, USA

Alexandre Supply Sorbonne Université, CNRS/IRD/MNHN/LOCEAN, Paris, France

Nobuhiro Takahashi Institute for Space-Earth Environmental Research, Nagoya University, Nagoya, Japan

Yukari N. Takayabu Atmosphere and Ocean Research Institute, The University of Tokyo, Tokyo, Japan

Jackson Tan USRA, Columbia, MD, and NASA/GSFC, Greenbelt, MD, USA

Simone Tanelli JPL/Caltech, Pasadena, CA, USA

Wei-Kuo Tao NASA/GSFC, Greenbelt, MD, USA

Francisco J. Tapiador University of Castilla-La Mancha, Toledo, Spain

Elena Tarnavsky Department of Meteorology, University of Reading, Reading, UK

Tomoko Tashima EORC/JAXA, Ibaraki, Japan

Koji Terasaki RIKEN Center for Computational Science, Kobe, Japan

Ali Tokay University of Maryland Baltimore County, Baltimore, MD, and NASA/GSFC, Greenbelt, MD, USA

Hirofumi Tomita RIKEN Center for Computational Science, Kobe, Japan

Frederic Tridon Earth Observation Science, Department of Physics and Astronomy, University of Leicester, Leicester, UK

F. Joseph Turk JPL/Caltech, Pasadena, CA, USA

Jani Tyynelä Finnish Meteorological Institute (FMI), Helsinki, Finland

Tomoo Ushio Tokyo Metropolitan University, Tokyo, Japan

Albert I. J. M. van Dijk Fenner School of Environment & Society, The Australian National University, Canberra, Australia

Jean-Luc Vergely ACRI-st, Guyancourt, France

Noemi Vergopolan Department of Civil and Environmental Engineering, Princeton University, Princeton, NJ, USA

Daniel Vila Instituto Nacional de Pesquisas Espaciais (IPE), Centro de Previsão de Tempo e Estudos Climaticos (CPTEC), Cachoeira Paulista, Brazil

Wolfgang Wagner Department of Geodesy and Geoinformation, Research Group Remote Sensing, TU Wien, Vienna, Austria

Jian-Jian Wang ESSIC, University of Maryland, College Park, MD, USA

Jianxin Wang Science Systems Applications International and NASA/GSFC, Greenbelt, MD, USA

Graham P. Weedon Joint Centre for Hydro-Meteorological Research, Met Office, Wallingford, UK

Tobias Wehr ESA/ESTEC, Noordwijk, The Netherlands

David B. Wolff NASA/GSFC, Wallops Flight Facility, Wallops Island, VA, USA

Eric F. Wood Department of Civil and Environmental Engineering, Princeton University, Princeton, NJ, USA

Norman B. Wood Space Science and Engineering Center (SSEC), University of Wisconsin-Madison, Madison, WI, USA

Pingping Xie NOAA/NWS/CPC, College Park, MD, USA

Moeka Yamaji EORC/JAXA, Ibaraki, Japan

Munehisa K. Yamamoto Division of Earth and Planetary Sciences, Graduate School of Science, Kyoto University, Kyoto, Japan

Hisashi Yashiro Satellite Observation Center, National Institute for Environmental Studies, Tsukuba, Japan

Matthew Young Department of Meteorology, University of Reading, Reading, UK

Bradley Zavodsky NASA/MSFC, Huntsville, AL, USA

Acronyms

ABI	Advanced Baseline Imager (GOES)
ACE	Aerosol-Clouds-Ecosystem Mission (NASA)
AD	Analog-to-Digital converter
ADDA	Amsterdam DDA
AET	Actual Evapotranspiration
AGL	Above Ground Level
AHPS	Advanced Hydrologic Prediction Service (NWS)
AI	Aridity Index
AIP	Algorithm Intercomparison Programme
Air-MSPI	Airborne Multi-angle SpectroPolarimetric Imager (NASA)
AIRS	Atmospheric Infrared Sounder (NASA)
AKDT	Alaska Daylight Time
ALEXI	Atmosphere-Land Exchange Inverse
AMeDAS	Automated Meteorological Data Acquisition System (JMA)
AMIE/DYNAMO	ARM Madden-Julian Oscillation Investigation Experiment/ Dynamics of the Madden-Julian Oscillation
AMIP	Atmospheric Model Intercomparison Project (WCRP)
AMMA	African Monsoon Multidisciplinary Analysis experiment
AMO	Atlantic Meridional Oscillation
AMPR	Advanced Microwave Precipitation Radiometer (NASA)
AMS	Annual Maximum Series (of rainfall)
AMSL	Above Mean Sea Level
AMSR	Advanced Microwave Scanning Radiometer (JAXA)
AMSR-E	AMSR-EOS (NASA)
AMSU	Advanced Microwave Sounding Unit (NOAA and EUMETSAT)
AMW	Active Microwave
APHRODITE	Asian Precipitation—Highly Resolved Observational Data Integration Towards Evaluation of Water Resources (Japan)

APR-3	Airborne Third Generation Precipitation Radar (NASA)
APSIM	Agricultural Production Systems sIMulator
AR	Atmospheric River
ARC (1)	Africa Rainfall Climatology (NOAA)
ARC (2)	Active Radar Calibrator
ARM	Atmospheric Radiation Measurement (DoE)
ARM-SGP	ARM Southern Great Plains (DoE)
ARMAR	Airborne Rain-Mapping Radar (NASA and JPL)
ASCAT	Advanced SCATterometer (ESA)
ASCII	American Standard Code for Information Interchange
ASI	Italian Space Agency
ASL	Above Sea Level (a.s.l.)
ASTRAIA	Analyse Stereoscopique par Radar Aeroporte (CNRS)
ATBD	Algorithm Theoretical Basis Document
ATMS	Advanced Technology Microwave Sounder (NASA/NOAA)
AWARE	ARM West Antarctic Radiation Experiment
AWIPS	Advanced Weather Interactive Processing System (NWS and UNIDATA)
BAECC	Biogenic Aerosols-Effects on Clouds and Climate Experiment (ARM)
BB	Bright Band
BC	British Columbia
BCS	Bias Correction Scheme
BMKG	Badan Meteorologi, Klimatologi, dan Geofisika (Indonesia)
BoM	Bureau of Meteorology (Australia)
BRAIN	Bayesian Rain Algorithm Including Neural Networks (Megha-Tropiques)
BSA	Backscatter Alignment
BUFR	Binary Universal Form for the Representation of Meteorological Data
BUI	Buildup Index (FWI)
CAPE	Convective Available Potential Energy
CAPRICORN	Clouds, Aerosols, Precipitation, Radiation, and Atmospheric Composition over the Southern Ocean
CARE	Centre for Atmospheric Research Experiments (Environment Canada)
CATDS	Centre Aval de Traitement des Données SMOS
CC	Correlation Coefficient
CCD	Cold Cloud Duration
CCDF	Complementary Cumulative Distribution Function
CCI	Climate Change Initiative (ESA)
CCl	Commission for Climatology (WMO)
CCP (1)	Clouds, Convection, and Precipitation
CCP (2)	Cloud and Precipitation Process Mission

CCZ	Continent-Climate Zone
CDD	Consecutive Dry Days Index (ETCCDI)
CDF	Cumulative Density Function
CDR	Climate Data Record
CDRD	Cloud Dynamics and Radiation Database
CEMADEN	Centro Nacional de Monitoramento e Alertas de Desastres Naturais (Brazil)
CEOS	Committee on Earth Observation Satellites
CERES	Clouds and the Earth's Radiant Energy System (NASA)
CESM	Community Earth System Model
CFAD	Contoured Frequency by Altitude Diagram
CG	Cloud-to-Ground Lightning
CGMS	Coordination Group for Meteorological Satellites
CHC	Climate Hazards Center (University of California, Santa Barbara)
CHIRPS	Climate Hazards center InfraRed Precipitation with Stations
CHPcli	Climate Hazards Group's Precipitation Climatology
CIMR	Copernicus Imaging Microwave Radiometer Mission (EU)
CIndO	Central Equatorial Indian Ocean index
CIRA	Cooperative Institute for Research in the Atmosphere (CSU)
CLC	Corine Land Cover
CLIVAR	Climate Variability and Predictability (WMO)
CLW	Cloud Liquid Water
CLWC	Cloud Liquid Water Content
CMA	China Meteorological Administration
CMAP	CPC Merged Analysis of Precipitation
CMIP	Coupled Model Intercomparison Project (WCRP)
CMIP-5	CMIP Phase 5
CMORPH	CPC MORPHing algorithm
CMORPH-CRT	CMORPH Bias Corrected
CMORPH-KF	CMORPH-Kalman Filter
CM-SAF	Climate Monitoring-SAF (EUMETSAT)
CNES	Centre National D'Études Spatiales (France)
CNRM/GAME	Centre National de Recherches Météorologiques—Groupe d'études de l'Atmosphère Météorologique (Météo France)
CNR	Consiglio Nazionale delle Ricerche (Italy)
CNR-IRPI	CNR-Istituto di Ricerca per la Protezione Idrogeologica
CNR-ISAC	CNR-Istituto di Scienze dell'Atmosfera e del Clima
CNRS	Centre National de la Recherche Scientifique (France)
CNTL	Control Run
COADS	Comprehensive Ocean Atmosphere Data Set
ConQ	Moisture Flux Convergence
CONUS	Conterminous US
CORRA	Combined Radar-Radiometer Product (GPM)

CoSMIR	Conical Scanning Millimeter-wave Imaging Radiometer (NASA)
CPC	Climate Prediction Center (NOAA)
CPI	Convective Percent Index
CPL	Cloud Physics Lidar (NASA)
CPR	Cloud Profiling Radar (NASA)
CRS	Cloud Remote Sensing Radar (NASA)
CrIS	Cross-Track Infrared Sounder (NASA)
CRM	Cloud-Resolving Model
CRS	Cloud Radar System (NASA)
CRTM	Community Radiative Transfer Model
CRU	Climate Research Unit (Univ. of East Anglia)
CSA	Climate Service for Agriculture (Rwanda)
CSH	Convective and Stratiform Heating
CSI	Critical Success Index
CSK	COSMO-SkyMed (ASI)
CSP	Climate Services Partnership
CSU	Colorado State University
CSPP	Community Satellite Processing Package
CT	Cloud Thickness
CTH	Cloud Top Height
CWD	Consecutive Wet Days (ETCCDI)
CWV	Columnar Water Vapor
CYGNSS	Cyclone Global Navigation Satellite System (NASA)
DA	Data Assimilation
DAR	Differential Absorption Radar
DB	Dark Band
DBNet	Direct Broadcast Network
DC	Drought Code (FWI)
DD	Downward Decreasing
DDA	Discrete Dipole Approximation
DDSCAT	Discrete Dipole Scattering
DEM	Digital Elevation Model
DFR	Dual-Frequency Ratio
DI	Downward Increasing
DJF	December-January-February
DKRZ	Deutsches Klimarechenzentrum (Germany)
DLR	Deutschen Zentrums für Luft- und Raumfahrt (Germany)
DMC	Duff Moisture Code (FWI)
DMIP2	Distributed Hydrologic Model Intercomparison Project–Phase 2 (NWS)
DMSP	Defense Meteorological Satellite Program (US Navy)
DNN	Deep Neural Network

DoE	Department of Energy
DO-Op	Daylight Only Operations (CloudSat)
DoW	Doppler on Wheels (Center for Severe Weather Research)
DP	Dual Polarimetric Radar
DPC (1)	Data Processing Center (CloudSat)
DPC (2)	Department of Civil Protection of Italy
DPCA	Displaced Phase Center Antenna
DPR	Dual-frequency Precipitation Radar (GPM)
DRC	Democratic Republic of the Congo
DryMOD	Dryland hydrological MODel (University of Reading)
DSD	Drop Size Distribution
DSI	Drought Severity Index
DSSAT	Decision Support System for Agrotechnology Transfer
DWR	Dual-Wavelength Ratio
DYNAMO	Dynamics of the MJO experiment
D3R	Dual-Frequency Dual-Polarized Doppler Radar (NASA)
EA	East Africa
EAF	East Africa
EarthCARE	Earth Clouds, Aerosols, and Radiation Explorer (ESA-JAXA)
EASE	Equal-Area Scalable Earth
EBCM	Extended Boundary Condition Method
EC	European Commission
ECCC	Environment and Climate Change Canada
ECDI	Enhanced Combined Drought Index
ECMWF	European Centre for Medium-Range Weather Forecasts
EDF	Environmental Data Fusion
EDOP	ER-2 Doppler Radar
EDR	Environmental Data Record
EEA	Eastern East Africa
EIA	Earth Incident Angle
ELDORA	Electra Doppler Radar (NCAR)
EM	Electromagnetic
EMA	Effective Medium Approximations
eMAs	extended MODIS Airborne Simulator (NASA)
EMSR	Electronically Scanning Microwave Radiometer (NOAA)
ENACTS	Enhancing National Climate Services
ENSO	El Niño Southern Oscillation
EOF	Empirical Orthogonal Function
EOS	Earth Observing System (NASA)
EPD2	Extreme Precipitation Day > 2 in day^{-1}
EPD4	Extreme Precipitation Day > 4 in day^{-1}
EPS	EUMETSAT Polar System
EPSAT-SG	Estimation of Precipitation by Satellite Second Generation (CNRS-LMD)

EPS-SG	EPS Second Generation
ERA	ECMWF Reanalysis
ESA	European Space Agency
ESA-CCI	ESA Climate Change Initiative
ESMR	Electronically Scanned Microwave Radiometer (NOAA)
ESPC	Environmental Satellite Processing Center (NESDIS)
ESSIC	Earth System Science Interdisciplinary Center
ET	Evapotranspiration
ETCCDI	Expert Team on Climate Change Detection and Indices
EU	European Union
EUMETCast	EUMETSAT's Multicast Distribution System
EUMETSAT	European Organization for the Exploitation of Meteorological Satellites
EVI-3	Earth Venture Instrument-3 program (NASA)
EVT	Extreme Value Theory
EWFN	Energy-Water-Food Nexus
EWS	Early Warning System
EXRAD	ER-2 X-band Radar (NASA)
FAO	Food and Agriculture Organization (UN)
FAR	False Alarm Rate
FAS	Foreign Agricultural Service (USDA)
FB	Frequency Bias
FCDR	Fundamental Climate Data Record
FD	Frost Days
FDRS	Fire Danger Rating Systems
FEWS NET	Famine Early Warning Systems Network
FFMC	Fine Fuel Moisture Code (FWI)
FL	Freezing Level
FLDAS	FEWS NET Land Data Assimilation System
FLOR	Forecast-oriented Low Ocean Resolution model (GFDL)
FMI	Finnish Meteorological Institute
FNMOC	Fleet Numerical Meteorology and Oceanography Center (US Navy)
FoV	Field of View
FP	Forward Processing (GMAO)
FRMSE	Fractional RMSE
FSOI	Forecast Sensitivity Observation Impact
FWI	Fire Weather Index
GAGES	Geospatial Attributes of Gages for Evaluating Streamflow (USGS)
GANAL	Global Analysis (JMA)
GATE	Global Atmospheric Research Program Atlantic Tropical Experiment
GC	Ground Clutter

GCEM	Goddard Cumulus Ensemble Model (NASA)
GCM	General Circulation Model
GCOM	Global Change Observation Mission (JAXA)
GCOM-W	GCOM-Water
GCOS	Global Climate Observing System (WMO)
GCPEx	GPM Cold Season Precipitation Experiment
GDAP	GEWEX Data and Assessment Panel
GDAS/GFS	Global Data Assimilation System/Global Forecast System (NOAA)
GEC	Geocoded Ellipsoid Corrected
GEO (1)	Geostationary orbit
GEO (2)	Group on Earth Observations
GEOGLAM	GEO Global Agricultural Monitoring
GEOS	Goddard Earth Observing System (NASA)
GEOS FP	Global Earth Observing System Forward Processing
GEOSS	Group on Earth Observation System of Systems
GeoSTAR	Geostationary Synthetic Thinned Aperture Radiometer (NASA)
GES DISC	Goddard Earth Sciences Data and Information Services Center
GEV	Generalized Extreme Value Distribution
GEWEX	Global Energy and Water Exchanges (WCRP)
GFCS	Global Framework for Climate Services (WMO)
GFDL	Geophysical Fluid Dynamics Laboratory (NOAA and Princeton University)
GFS	Global Forecast System (NCEP)
GFWED	Global Fire Weather Database (NASA GISS)
GHA	Greater Horn of Africa
GHCN-D	Global Historical Climatology Network-Daily (NOAA)
GHM	Global Hydrological Model
GHRC	Global Hydrology Resource Center (NASA)
GIRAFE	Global Interpolated RAinFall Estimation
GIS	Geographic Information System
GISS	Goddard Institute for Space Studies (NASA)
GLC	Global Landslide Catalog (NASA)
GMa	Gulf of Mexico area
GMAO	Global Modeling and Assimilation Office (NASA)
GMI	GPM Microwave Imager
GMM	Generalized Multiparticle Mie-solution
GoAMAZON	Green Ocean Amazon Experiment
GOES	Geostationary Operational Environmental Satellite (NOAA)
GOSAT-3	Greenhouse Gases Observing Satellite (JAXA)
GOTM	General Ocean Turbulence Model
GPC	Global Precipitation Climatology Center (DWD)
GPCP	Global Precipitation Climatology Project (GEWEX)

GPI	GOES Precipitation Index
GPM	Global Precipitation Measurement mission (NASA and JAXA)
GPM-CO	GPM Core Observatory
GPP	Gross Primary Production
GPROF	Goddard Profiling Algorithm (NASA)
GPS	Global Positioning System
GRACE	Gravity Recovery and Climate Experiment (NASA and DLR)
GRACE-FO	GRACE Follow-On
GRDC	Global Runoff Data Centre
Grid-Sat	Gridded Satellite Data (NOAA)
GRIP	Genesis and Rapid Intensification Processes (NASA)
GRISO	Rainfall Generator of Spatial Interpolation from Observation
GS	Grain Size
GSFC	Goddard Space Flight Center (NASA)
GSI	Gridpoint Statistical Interpolation
GSM	Global Spectral Model
GSMaP	Global Satellite Mapping of Precipitation (Japan)
GSMaP-MVK	GSMaP Motion Vector Kalman
GSMaP-NRT	GSMaP Near Real Time
GSOD	Global Surface Summary of the Day (NOAA)
GT	Gaussian Transformation
GTC	Geocoded Terrain Corrected
GTS	Global Telecommunication System
GV	Ground Validation
GW	Global Warming
GWIS	Global Wildfire Information System
GWP	Graupel Water Path
G5NR	GEOS-5 Nature Run (NASA)
HADS	Hydrometeorological Automated Data System (NWS)
HAMSR	High-Altitude MMIC Sounding Radiometer (JPL)
HDF	Hierarchical Data Format
HEMT	High Electron Mobility Transistor
HEPEX	Hydrological Ensemble Prediction Experiment
HID	Hydrometeor Identification algorithms
HIRS	High-Resolution Infrared Radiation Sounder (NOAA)
HISA	Hurricane Intensity and Structure Algorithm
HIWRAP	High-Altitude Imaging Wind and Rain Airborne Profiler (NASA)
HLM	Hillslope-Link Model
HMA	High Mountain Asia
HOAPS	Hamburg Ocean Atmosphere Parameters and Fluxes from Satellite Data (University of Hamburg)
HQPrecip	High-Quality Precipitation (GPM)

HR	Hit Rate
HRPP	High-Resolution Precipitation Product
HRWS	High-Resolution Wide Swath
H-SAF	Support to Operational Hydrology and Water Management (EUMETSAT)
HSS	Heidke Skill Score
HyMeX	Hydrological Cycle in Mediterranean Experiment
IC	Intra-cloud Lightning
ICDC	Integrated Climate Data Center (University of Hamburg)
ICE-POP	International Collaborative Experiment for the PyeongChang Olympics and Paralympics Experiment 2018
ICHARM	International Centre for Water Hazard and Risk Management
ICI	Ice Cloud Imager (EUMETSAT)
ICO-LETKF	Icosahedral LETKF
IDF	Intensity-Duration-Frequency Curve
IDW	Inverse Distance Weighting
IFAS	Integrated Flood Analysis System
IFM	Index Flood Method
IMERG	Integrated Multi-satellitE Retrievals for GPM
IMERG_E	IMERG Early Run (near real time with a latency of 6 h)
IMERG_F	IMERG Final Run (gauged-adjusted with a latency of 4 months)
IMERG_L	IMERG Late Run (reprocessed near real time with a latency of 18 h)
IOD	Indian Ocean Dipole
IPHEx	Integrated Precipitation and Hydrology Experiment (GPM)
IPS	Institut Pierre Simon Laplace (CNRS)
IPWG	International Precipitation Working Group (CGMS)
IR	Infrared
IRI	International Research Institute for Climate and Society (Columbia University)
IRP	Infrared Precipitation Estimate
ISI	Initial Spread Index (FWI)
ISRO	Indian Space Research Organisation
ISS	International Space Station
ITCZ	Intertropical Convergence Zone
IWP	Ice Water Path
I&Q	In-Phase and Quadrature Signal
JAXA	Japan Aerospace Exploration Agency
JCOMM	Joint Technical Commission for Oceanography and Marine Meteorology (WMO)
JCSDA	Joint Center for Satellite Data Assimilation (NOAA)
JERD	JPSS NESDIS ESPC Requirements Document
JF	January-February

JJA	June-July-August
JJAS	June-July-August-September
JMA	Japan Meteorological Agency
JPL	Jet Propulsion Laboratory
JPSS	Joint Polar Satellite System
JRA55	Japanese 55-year Reanalysis
JRC	Joint Research Centre (EC)
KGE	Kling-Gupta Efficiency
KMA	Korea Meteorological Administration
KWAJEX	Kwajalein Experiment
LACA&D	Latin American Climate Assessment & Dataset
LDM	Local Data Manager (UNIDATA)
LDR	Linear Depolarization Ratio
LEGOS	Laboratoire d'Études en Géophysique et Océanographie Spatiales
LEO	Low Earth Orbit
LETKF	Local Ensemble Transform Kalman Filter (RIKEN)
LFM	Local Forecast Model
LH	Latent Heating
LHASA	Landslide Hazard Assessment for Situational Awareness (NASA)
LIA	Local Incidence Angle
LLCF	Low-Level Clouds and Fog
LL-LETKF	Latitude-Longitude LETKF
LMD	Laboratoire de Météorologie Dynamique (CNRS)
LMODEL	Lagrangian Model (UC Irvine and University of Hull)
LPVEx	Light Precipitation Validation Experiment (GPM)
LR	Logistic Regression
LST	Land Surface Temperature
LUT	Lookup Table
LWP	Liquid Water Path
LZA	Local Zenith Angle
L1SR	Level 1 Science Requirements (GPM)
MADRAS	Microwave Analysis and Detection of Rain and Atmospheric Structures (Megha-Tropiques)
MAE	Mean Absolute Error
MAFF	Ministry of Agriculture, Forestry and Fisheries (Japan)
MAM	March-April-May
MARSOP	Monitoring Agricultural ResourceS Operational (JRC)
MBE	Mean Bias Error
MCS	Mesoscale Convective System
MCTA	Merged CloudSat, TRMM, and AMSR product
MC3E	Mid-latitude Continental Convective Clouds Experiment
ME	Mean Error

Medicane	Mediterranean hurricane
MERRA	Modern-Era Retrospective analysis for Research and Applications (NASA)
MGD	Multilook Ground Detected
MGDSST	Merged Satellite and In Situ Data Global Daily SST (JMA)
MHEMT	Metamorphic HEMT
MHOPrEx	Monsoon Himalaya Orographic Precipitation Experiment
MHS	Microwave Humidity Sounder (EUMETSAT)
MicroMAS-2	Micro-sized Microwave Atmospheric Satellite-2
MIIDAPS	Multi-instrument Inversion and Data Assimilation Preprocessing System (NOAA)
MIR	Middle IR
MIRA	Microwave/Infrared Rainfall Algorithm
MIRAS	Microwave Imaging Radiometer using Aperture Synthesis
MiRS	Microwave Integrated Retrieval System (NOAA)
MISDc	Modello Idrologico Semi-Distribuito in continuo (CNR-IRPI)
MLP	Melting Level Precipitation
MLS	Microwave Limb Sounder (EOS)
MMIC	Millimeter-Wave Monolithic Integrated Circuits
MODIS	Moderate Resolution Imaging Spectroradiometer (NASA)
MPE	Multisensor Precipitation Estimator
MP-M	Max-Planck-Institut für Meteorologie (Germany)
MRR	Micro Rain Radar
MREA	Modified Regression Empirical Algorithm
MRMS	Multi-Radar/Multisensor Precipitation Data
MREA	Modified Regression Empirical Algorithm
MRMS	Multi-Radar Multisensor system (NOAA)
MS	Multiple Scattering
MSG	Meteosat Second Generation (EUMETSAT)
MSG-CPP	MSG Cloud Physical Properties (EUMETSAT)
MSLP	Mean Sea-Level Pressure
MSPPS	Microwave Surface and Precipitation Products System (NOAA)
MSU	Microwave Sounding Unit (NOAA)
MSWEP	Multisource Weighted-Ensemble Precipitation
MTSAT	Multifunctional Transport Satellites (JMA)
MW	Microwave
MWCC	Microwave Cloud Classification
MWCOMB	Combined MW Rainfall Retrieval (CPC)
MWHS-2	Microwave Humidity Sounder-2 (CMA)
MWI	Microwave Imager (EUMETSAT)
MWR (1)	Microwave Radiometer
MWR (2)	Moving Window Regression

MWS	Microwave Sounder
NAa	North Atlantic Area
NAMMA	NASA African Monsoon Multidisciplinary Analyses
NAS	National Academies of Sciences (US)
NASA	National Aeronautics and Space Administration
NCA	North and Central America
NCAR	National Center for Atmospheric Research
NCE	National Centers for Environmental Information (NOAA)
NCEI	National Centers for Environmental Information
NCEP	National Centers for Environmental Prediction (NOAA)
NCEP-CFSR	Climate Forecast System Reanalysis
NCL	NCAR Command Language
NDVI	Normalized Difference Vegetation Index
NESDIS	National Environmental Satellite, Data, and Information Service (NOAA)
netCDF	Network Common Data Form
NEWS	NASA Energy and Water Cycle Study
NEXRAD	Next-Generation Weather Doppler Radar (NOAA/NWS)
NH	Northern Hemisphere
NHM	National Hydrometeorological Service
NICAM	Nonhydrostatic Icosahedral Atmospheric Model (RIKEN)
NIR	Near IR
NM	National Meteorology Agency
NMAE	Normalized Mean Absolute Error
NMHS	National Meteorological and Hydrological Service
NMQ	National Mosaic Quantitative Precipitation Estimation (NOAA/NSSL)
NU-WRF	NASA-Unified WRF
NPP	Net Primary Production
NRCS	Normalized Radar Cross Section
NOAA	National Oceanic and Atmospheric Administration
NOP	Numerical Ocean Prediction
NPOL	NASA S-Band Dual Polarimetric
NRL	Naval Research Laboratory (US Navy)
NRMSE	Normalized Root Mean Square Error
NRT	Near Real Time
NSE	Nash-Sutcliffe Efficiency
NSMC	National Satellite Meteorological Center (CMA)
NSSL	National Severe Storms Laboratory (NOAA)
NTPa	North Tropical Pacific Area
NUBF	Nonuniform Beam Filling
NU-WRF	NASA-Unified Weather Research and Forecasting
NWP	Numerical Weather Prediction
NWS	National Weather Service (NOAA)

OBCT	On-Board Calibration Target
OCE	Oceania
OceanRain	Ocean Rainfall And Ice-Phase Precipitation Measurement Network
OE	Optimal Estimation
OI	Optimal Interpolation
OLYMPEX	Olympic Mountains Experiment
OM	Observatoire Midi-Pyrénées
OND	October-November-December
OSCAR	Observing Systems Capability Analysis and Review (WMO)
OSPO	Office of Satellite and Product Operations (NOAA)
OSSE	Observing Systems Simulation Experiment
OZA	Observation Zenith Angle
PAW	Percentage Available Water
PCT	Polarization Corrected Temperature
PDF (1)	Probability Density Function
PDF (2)	Particle Distribution Function
PDO	Pacific Decadal Oscillation
PDSI	Palmer Drought Severity Index
PERHPP	Program for the Evaluation of High-Resolution Precipitation Products
PERSIANN	Precipitation Estimation from Remotely Sensed Information using Artificial Neural Networks (UC Irvine)
PERSIANN-CCS	PERSIANN-Cloud Classification System
PERSIANN-CDR	PERSIANN-Climate Data Records
PERSIANN-MSA	PERSIANN-Multispectral Analysis
PF	Precipitation Feature
PHEMT	Pseudomorphic HEMT
PHIVOLCS	Philippine Institute of Volcanology and Seismology
PIA	Path-Integrated Attenuation
PICSA	Participatory Integrated Climate Services
PIP	Precipitation Imaging Package
PMA	Probability Matching Algorithm
PMI	Polarimetric Microwave Imager (CMA)
PMM (1)	Precipitation Measurement Mission (NASA)
PMM (2)	Probability Matching Method
PMP	Probable Maximum Precipitation
PMW	Passive Microwave
PNPR	Passive Microwave Neural Network Precipitation Retrieval (CNR-ISAC)
POD	Probability of Detection
POES	Polar Operational Environmental Satellites (NOAA)
POFD	Probability of False Detection
PoP	Probability of Precipitation

POS	Probability of Snowfall
PPI	Plan Position Indicator
PPP	Precipitation Per Person
PPS	Precipitation Processing System (IMERG)
PQPE	Probabilistic Quantitative Precipitation Estimation
PR	Precipitation Radar (TRMM)
PRCPTOT	Total Rainfall Amount (ETCCDI)
PRISM	Parameter-Elevation Regressions on Independent Slopes Model (Oregon State University)
PRPS	Precipitation Retrieval and Profiling Scheme
PSD	Particle Size Distribution
PSS	Practical Salinity Scale
PTH	Precipitation Top Height
PUSH	Precipitation Uncertainties for Satellite Hydrology
PV	Physical Validation (GPM)
PW	Precipitable Water
PWC	Precipitable Water Content
QA	Quality Assurance
QC	Quality Control
QCLCD	Quality Controlled Local Climatological Data
QI	Quality Index
QPE	Quantitative Precipitation Estimation
RADAP	Radar Data Processor (NOAA)
RADAR	Radio Detection and Ranging
RADEX	Radar Definition Experiment (OLYMPEX)
RCM	Regional Climate Model
RCS	Radar Cross Section
REA	Regressive Empirical Algorithm
REFAME	Rain Estimation Using Forward Adjusted-Advection of Microwave Estimates (UC Irvine)
RFC	River Forecast Center (NWS)
RFE	Rainfall Estimate (FAO)
RFI	Radio Frequency Interference
RGA	Rayleigh-Gans Approximation
RGB	Red Green Blue
RH	Relative Humidity
RHI	Range Height Indicator
RICO	Rain in Cumulus over the Ocean
RIM	Rain Impact Model (salinity)
RMS	Root Mean Square
RMSD	RMS Deviation
RMSE	RMS Error
RoF	Rain on Fog
RoFCC	RoF and Cap Clouds

ROI	Region of Interest
RoLLC	Rain on Low-Level Clouds
ROSA	Radio Occultation Sensor for Atmosphere
RQI	Radar Quality Index
RR	Rain Rate
RRFA-S	Regional Rainfall Frequency Analysis using Satellite Precipitation
RSS	Remote Sensing Systems Inc.
RTH	Rain Top Height
RTM	Radiative Transfer Model
RTTOV	Radiative Transfer for TOVS
RV (or (R/V)	Research Vessel
RWH	Rainwater Harvesting
RW	Rainwater Path
R2O/O2	Research-to-Operations/Operations-to-Research paradigm (SPoRT)
SAa	South Atlantic Area
SAF	Satellite Application Facility (EUMETSAT)
SAM (1)	System for Atmospheric Modeling
SAM (2)	Southern Appalachian Mountains
SAPHIR	Sondeur Atmosphérique du Profile d'Humidité Intertropicale par Radiométrie (Megha-Tropiques)
SAR	Synthetic Aperture Radar
SARRA-H	Systéme d'Analyse Régional des Risques Agroclimatiques-Habillé
SBA	Split-Based Approach
SCA	Scatterometer (ESA)
SCaMPR	Self-Calibrating Multivariate Precipitation Retrieval (NESDIS)
ScaRaB	Scanner for Radiation Budget (Megha-Tropiques)
scPDSI	Self-Calibrated PDSI
SCS	Single-Look Complex Slant Products
SCSMEX	South China Sea Monsoon Experiment
SCSMEX/NESA	SCSMEX Northern Enhanced Sounding Array
SCSMEX/SESA	SCSMEX Southern Enhanced Sounding Array
SD (1)	Snowfall Detection
SD (2)	Standard Deviation
SDCI	Scaled Drought Condition Index
SDG	Sustainable Development Goal
SDII	Simple Daily Intensity Index (ETCCDI)
SEA	Southeast and East Asia
SEAK	Southeast Alaska
SEM	Semiempirical Model

SEVIRI	Spinning Enhanced Visible and Infrared Imager (EUMETSAT)
SFI	Seeder-Feeder Interactions
SFR	Snowfall Rate (NOAA)
SH	Southern Hemisphere
SI	Snow Index
SIA	Sea Ice Age
SIC	Sea Ice Concentration
SID	Sea Ice Drift
SIDOC	SAR Images Dark Object Classifier
SIT	Sea Ice Thickness
SLH	Spectral Latent Heating
SM	Soil Moisture
SMA	Soil Moisture Anomaly
SMAP	Soil Moisture Active Passive (NASA)
SMMR	Scanning Multichannel Microwave Radiometer (NOAA)
SMOS	Soil Moisture and Ocean Salinity (ESA)
SM2RAIN	Soil Moisture to Rain Algorithm (CNR-IRPI)
S-NPP	Suomi National Polar-Orbiting Partnership (NASA/NOAA)
SNR	Signal-to-Noise Ratio
SON	September-October-November
SOS	Start of Season
SPA	Specific Power Attenuation
SPCZ	South Pacific Convergence Zone
SPEI	Standardized Precipitation Evapotranspiration Index
SPI	Standardized Precipitation Index
SPICE	Solid Precipitation Intercomparison Experiment (WMO)
SPoRT	Short-term Prediction Research and Transition Center (NASA)
SPP (1)	Satellite Precipitation Product
SPP (2)	Seasonal Performance Probability
SPS	Special Weather Statement (NWS)
SPURS	Salinity Processes in the Upper Ocean Regional Study
SR	Success Ratio
SRE	Satellite-Based Rainfall Estimate
SREM2D	Two-Dimensional Satellite Rainfall Error Model
SRI	Surface Rainfall Intensity
SRT	Surface Reference Technique
SSA (1)	Space Situational Awareness
SSA (2)	Sub-Saharan Africa
SSN	Spatial Stream Network
SSM/I	Special Sensor Microwave/Imager (DMSP)
SSMIS	Special Sensor Microwave Imager Sounder (DMSP)
SSM/T	Special Sensor Microwave Temperature (DMSP)
SSP	Surface Salinity Profiler

SSRGA	Self-Similar Rayleigh-Gans Approximation
SSS	Sea Surface Salinity
SST	Sea Surface Temperature
SSU	Stratospheric Sounding Unit (NOAA)
SSW	Sea Surface Wind
STAR	Center for Satellite Applications and Research (NOAA-NESDIS)
STDV	Standard Deviation
STH	Storm-Top Height
STIa	South Tropical Indian Area
STPa	South Tropical Pacific Area
SWA	South and West Asia
SWB	Soil Water Balance
SWE	Snow Water Equivalent
SWER	Snow Water Equivalent Rate
SYNOP	Surface Synoptic Observation (WMO)
TAMSAT	Tropical Applications of Meteorology Using Satellite and Ground-Based Observations
TAPEER	Tropical Amount of Precipitation with an Estimate of Errors
TARCAT	TAMSAT African Rainfall Climatology and Time Series
TB	Brightness Temperature
TC	Tropical Cyclone
TCA	Triple Collocation Analysis
TCC	TRMM Composite Climatology
TC4	Tropical Composition, Cloud and Climate Coupling Experiment
TDTS	Time-Dependent Two-Stream Method
TEMPEST	Temporal Experiment for Storms and Tropical Systems
TEMPEST-D	TEMPEST Technology Demonstration
TIR	Thermal Infrared
TLC	Tropical-Like Cyclone
TMD	Thai Meteorological Department (Thailand)
TMI	TRMM Microwave Imager
TMPA	TRMM Multisatellite Precipitation Analysis (NASA)
TOOCAN	Tracking Of Organized Convection Algorithm through a 3-D segmentatioN
TOGA-COARE	Tropical Ocean Global Atmosphere Coupled Ocean-Atmosphere Response Experiment
TOVS	TIROS Operational Vertical Sounder
TPW	Total Precipitable Water
TQV	Total Precipitable Water Vapor
TRMM	Tropical Rainfall Measuring Mission
TROPICS	Time-Resolved Observations of Precipitation structure and storm Intensity with a Constellation of Smallsats (NASA)

TSX	TerraSAR-X (DLR)
TVA	Tennessee Valley Authority
TWP-ICE	Tropical Warm Pool – International Cloud Experiment
TWSA	Terrestrial Water Storage Anomaly
T2M	Two-Meter Temperature
UCA	Urban Climate Archipelago
UCLM	Universidad de Castilla-La Mancha
UH	University of Helsinki
UHI	Urban Heat Island
UMORA	Unified Microwave Ocean Retrieval Algorithm
UN	United Nations
UNEP	United Nations Environment Programme (UN)
UNESCO	United Nations Educational, Scientific and Cultural Organization (UN)
US	United States of America
USCRN	US Climate Reference Network
USDA	US Department of Agriculture
USDM	US Drought Monitor
USGS	US Geological Survey
UTC	Universal Time Coordinated
UWSI	Urban Water Stress Index per Individual
VAM	Vulnerability Assessment and Mapping (WFP)
VarBC	Variable Bias Correction
VI	Vegetation Index
VMI	Vertical Maximum Intensity
VN	Validation Network (GPM)
WATCH	Water and Global Change (EU)
WCOM	Water Cycle Observation Mission (CMA)
WCRP	World Climate Research Programme (WMO)
WDCC	World Data Center for Climate (DKRZ)
WDM6	WRF Double-Moment 6-Class
WEA	Western East Africa
WFF	Wallops Flight Facility (NASA)
WFO	Weather Forecast Office (NWS)
WFP	World Food Programme
WFDEI-CRU	WATCH Forcing Data ERA Interim-CRU
WII	Weather Index-Based Insurance
WMMD	Wet Millimeter Days
WMO	World Meteorological Organization (UN)
WR	Weather Radar
WRF	Weather Research and Forecasting Model
WRF-ARW	WRF-Advanced Research WRF
WRSI	Water Requirements Satisfaction Index
WS	Wind Speed

WSR-57	Weather Surveillance Radar 1957 (NWS)
WV	Water Vapor
XCAL	Intersatellite Calibration Working Group (GPM)
ZAR	Zones À Risque model
2DVD	2D Video Disdrometer

Part I
Status of Observations and Satellite Programs

Chapter 1
The Global Precipitation Measurement (GPM) Mission

Christopher Kidd, Yukari N. Takayabu, Gail M. Skofronick-Jackson, George J. Huffman, Scott A. Braun, Takuji Kubota, and F. Joseph Turk

Abstract Water is a fundamental component of the Earth's water and energy cycles and is essential to our economic and social wellbeing. Since precipitation is the primary input into these cycles and affects the availability of water resources over land areas, the measurement of precipitation across the globe is of critical importance. The Global Precipitation Measurement (GPM) Core Observatory (CO), a joint US and Japan mission launched in 2014, extends and enhances the legacy of the Tropical Rainfall Measuring Mission (TRMM). The GPM-CO carries high-quality passive and active microwave instruments designed to observe the structure and intensity of falling rainfall and snowfall. The high standard of accuracy of these sensors also provides a reference standard for other precipitation sensors in the GPM constellation which comprises of a suite of satellites from international organisations, enabling global sampling from passive microwave (PMW) sensors at a 3-hourly interval better than 90% of the time. Together with geostationary (GEO) infrared (IR) observations, these data enable global 30-min, $0.1° \times 0.1°$ precipitation products to be computed and posted in near real-time. Precipitation products are

C. Kidd (✉)
Earth System Science Interdisciplinary Center, University of Maryland, College Park, MD, USA

NASA, Goddard Space Flight Center, Greenbelt, MD, USA
e-mail: chris.kidd@nasa.gov

Y. N. Takayabu
Atmosphere and Ocean Research Institute, The University of Tokyo, Chiba, Japan

G. M. Skofronick-Jackson
NASA Headquarters, Washington, DC, USA

G. J. Huffman · S. A. Braun
NASA, Goddard Space Flight Center, Greenbelt, MD, USA

T. Kubota
JAXA, Earth Observation Research Center, Tokyo, Japan

F. J. Turk
Jet Propulsion Laboratory, California Institute of Technology, Pasadena, CA, USA

made available to, and utilized by, user communities ranging from numerical weather prediction (NWP) organisations to water resources services.

1.1 Introduction

The role of water is key to the Earth's water and energy cycles and essential for life on Earth. The availability of fresh water is driven largely by precipitation in the form of rainfall or snowfall, governing the water resources and the environment around us. The variability of precipitation across all scales, from short-duration storms to climate-scale variations, and from local to global spatial scales, affects not only our lives, but also the physical nature of the climate upon which we depend. The World Climate Research Programme (WCRP) identified four water-related challenges: clouds, circulation, and climate sensitivity; weather and climate extremes; water for the food baskets of the world; and near-term climate prediction WCRP (2019). The questions associated with these challenges are how the availability of fresh water will change, how the frequency and intensity of the extremes of precipitation (droughts and storms) will change, and what are the convection-cloud feedbacks. Key to answering these questions is the better measurement of precipitation, rainfall and snowfall across all scales, together with improving our understanding of the microphysics of precipitation that underpin the formation of precipitation and associated feedbacks.

The Global Precipitation Measurement (GPM) mission is an international satellite mission to advance our knowledge and understanding of global precipitation. The GPM Core Observatory (CO), a collaboration between NASA and the Japan Aerospace Exploration Agency (JAXA), was launched on 28 February 2014 by an H-IIA #23 rocket from the Tanegashima launch site in Japan, into a 65° inclination, 407 km altitude orbit. The main goal of the GPM mission is to improve precipitation measurements through understanding the physics and space-time variability of precipitation across the Earth. The GPM-CO carries the most advanced precipitation instrumentation currently in orbit: a Dual-frequency Precipitation Radar (DPR; Chap. 11) and the GPM Microwave Imager (GMI; Draper et al. 2015b) (see Fig. 1.1). The DPR is comprised of Ku and Ka-band radars that measure the 3-dimensional structure of precipitation through the atmosphere to the surface. The GMI provides well-calibrated, multi-frequency, wide-swath observations across 13 channels. The two instruments on the GPM-CO are designed to measure rainfall from 0.2-111.0 mm h^{-1} (Hou et al. 2014), to detect moderate to intense snowfall events and to serve as a precipitation physics laboratory. Furthermore, due to the accuracy of the instruments, the GPM-CO acts as a calibration reference standard for unifying the observations from other satellite sensors (as listed in Table 1.1)
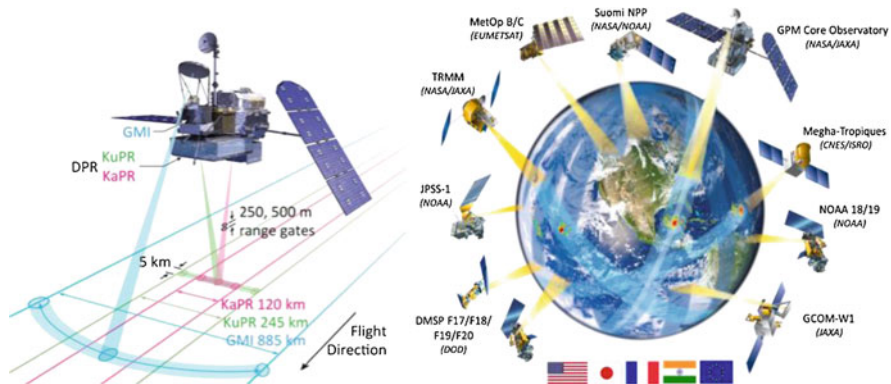
Fig. 1.1 Schematic of the Global Precipitation Measurement (GPM) mission Core Observatory (CO; left) and the GPM international partner constellation (right). Note that as of 21 May 2018 the KaPR swath width has been increased to 245 km to match that of the KuPR. (Note that the GPM-CO alternates flight directions to keep the canted solar panel towards the Sun: half the time the flight direction is 180° from that shown)

provided by international partner organisations that form the GPM precipitation constellation (Skofronick-Jackson et al. 2017).

The GPM mission follows the very successful Tropical Rainfall Measuring Mission (TRMM; Kummerow et al. 1998, 2000). TRMM was placed in a non-sun synchronous Low Earth Orbit (LEO) and was equipped with the first space-borne Precipitation Radar (PR), the TRMM multi-channel Microwave Imager (TMI), and three other cloud-system-related instruments. TRMM provided observations from November 1997 to April 2015, including a precious one-year overlap of observations with GPM, enabling the inter-calibration of GPM and TRMM observations. While the latitudinal range of TRMM observations was from 35°N to 35°S, GPM expanded coverage to 65°N to 65°S to cover 91% of the globe. In order to increase the capability of measuring frozen and light precipitation that is abundant in higher latitudes, the GPM DPR consists of a 13.6 GHz Ku-band radar similar to the TRMM PR and a new 35.5 GHz Ka-band radar, while the GMI consists of a 13-channel microwave imager (which is the TMI complement) plus two additional high frequency bands at 165.5 GHz and 183.31 GHz. Since frequent sampling of precipitation at the global scale, a primary objective of GPM, cannot be achieved by the single GPM-CO, an international constellation of space-borne passive microwave (PMW) partner sensors is utilised. The non-sun synchronous nature of the GPM-CO orbit allows the observations of these constellation sensors to be cross-calibrated with the GPM-CO. By combining the observations from the GPM constellation, aided by infrared (IR) observations from geostationary satellites, two representative high temporal and spatial resolution mapped precipitation products, the Integrated Multi-satellitE Retrievals for GPM (IMERG) and Global Satellite Mapping of Precipitation (GSMaP) from the US and Japan, respectively, are publically available for various applications.

Table 1.1 Satellites and sensors contributing to the GPM constellation

Satellite	DMSP-F16, F17, F18, F19[a]	GCOMW1	TRMM[b]	GPM	NOAA-18[c],-19, MetOp-A, -B	Megha-Tropiques	SNPP NOAA-20
Sensor	SSMIS	AMSR2	TMI[b]	GMI	MHS	SAPHIR	ATMS
Type	Conical	Conical	Conical	Conical	Cross-track	Cross-track	Cross-track
Frequencies	–	6.925/7.3VH	–	–	–	–	–
		10.65VH	10.65VH	10.65VH	–	–	–
	19.35VH	18.70VH	18.70VH	18.70VH	–	–	–
	22.235V	23.80 VH	23.80 VH	23.80V	–	–	23.8
	37.0VH	36.5VH	36.5VH	36.5VH	–	–	31.4
	50.3-63.3VH	–	–	–	–	–	50-3-57.3
	91.65VH	89.0VH	89.0VH	89.0VH	89V	–	87-91
	150H	–	–	165.5VH	157V	–	164-167
	183.31H	–	–	183.31V(2)	183.31H (2)	183.31H(6)	183.31(5)
	–	–	–	–	190.31V	–	–
Sampling resolution[d] km²	12.8 × 12.6	4.7 × 4.3	4.7 × 13.1	5.1 × 13.2	16.9 × 17.6	6.7 × 9.9	16.1 × 17.7
Retrieval resolution km²	50 × 40	19 × 11	26 × 21	16 × 10	16 × 16[e]	10 × 10[e]	16 × 16[e]

[a]Until 11 February 2016
[b]Until 8 April 2015
[c]Until 5 October 2018
[d]Sampling resolutions across-track × along-track
[e]Resolution at nadir

1.2 Satellite Sensors and Characteristics

The major roles for the GPM-CO are to provide observations of both rainfall and snowfall, and to act as a calibrator for the other precipitation sensors in the constellation. The higher inclination orbit with coverage from 65°N to 65°S extends the latitudinal range of coincident PMW/active microwave (AMW) measurements to cover more regions dominated by mid-latitude precipitation systems, including snowfall. Like TRMM, it provides observations throughout the diurnal cycle, as well as intersecting the orbital paths of the other GPM constellation satellites, which allows co-temporal, co-located observations to take place.

The DPR instrument is the first dual-frequency precipitation radar to be flown in space, and expands the capability of the TRMM PR. The Ku radar is an improved version of the TRMM PR, increasing the sensitivity from 18 to 12 dBZ for the GPM DPR, while the Ka radar provides observations at 35.5 GHz, providing greater sensitivity to light precipitation. The DPR Ku-band radar provides a swath of 245 km with 250 m vertical resolution. At launch, the Ka-band radar provided a narrower swath of 120 km and a combined Ku/Ka swath also of 120 km. More recently, after 21 May 2018, the Ka-band radar was reconfigured operationally to provide a broader 245 km swath that is coincident with the Ku swath.

As a result of the improved sensitivity, shallow and relatively light convective precipitation may be observed, as shown in Fig. 1.2; here, lake effect precipitation over the Japan Sea is clearly captured. The effect of the difference in the sensitivity can be seen in Fig. 37.2 (Chap. 37 of volume 2) through comparison of the sensitivity thresholds to the same organized systems in the Tropics; notice that in addition to the improved detectability of very shallow precipitation found in the centre, a large volume of anvil precipitation, above the melting level, is detected with

Fig. 1.2 An infrared image from Himawari 8 of the "lake effect" clouds over the Japan Sea (top), and three-dimensional snapshot of shallow precipitation from those clouds observed by the effective radar reflectivity at Ku band of the GPM/DPR at 0955 UTC 2 December 2014 (bottom)
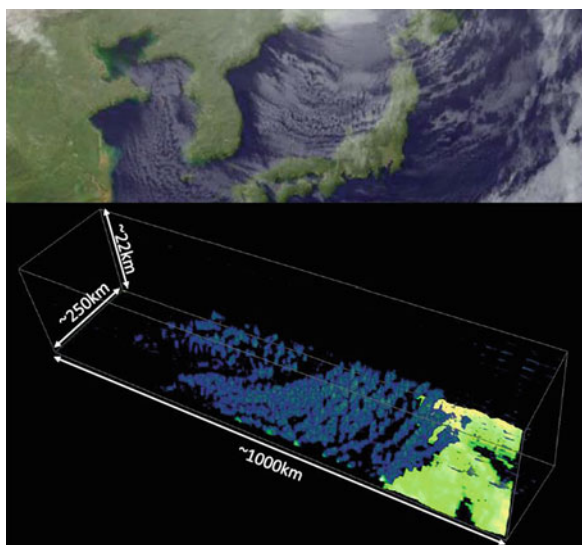
the improved sensitivity. The resultant enhancement of precipitation detection between 40°N and 40°S compared to the PR, is 21.1% and 1.9%, in occurrence and amount, respectively (Hamada and Takayabu 2016).

The use of dual-frequency radar data enables more physics-based rainfall retrieval possibilities. Recently, various science studies have started to detail the precipitation microphysics based on the dual-frequency radar observations. For example, utilizing the difference in attenuation characteristics between Ku- and Ka-band radars. Iguchi et al. (2018) successfully determined heavy ice precipitation from the Dual Frequency Ratio method (*DFRm = Zm(Ku)-Zm(Ka)*) as shown in Fig. 1.3.

The one-year overlap of the GPM DPR and the TRMM PR allowed comparison and cross-calibration between the two instruments. Although the orbits of the DPR and PR are different, limiting the number of precipitation cases for simultaneous observations, the observed rain structure and estimated rain intensity matched well with one another. From such comparisons, the accuracy of the DPR performance was confirmed, with some deficiencies revealed in the TRMM PR data; this was the first time that multiple space-borne precipitation radars had been assessed. During the comparison, engineering calibration methods were improved, and a vicarious calibration using the sea-surface signature has also been developed, along with a comparison of rain totals. As an end-to-end calibration, DPR rain estimates were compared with ground-based rain data (see Chap. 27 of volume 2), where data from operational agencies, such as JMA and NOAA, were utilized.

The Ka-band radar on the DPR is a new space-borne instrument, requiring additional initial investigations, not least since the scattering characteristics of precipitation particles at Ka-band are different from those for Ku-band. The scattering is complicated, particularly, for melting particles. Because one of the DPR objectives is to measure precipitation rates including solid particles, understanding of the scattering characteristics is essential for the full utilization of the Ka-band
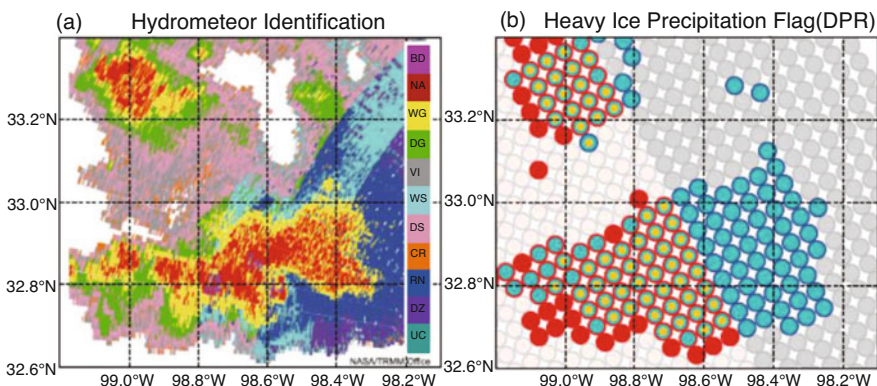
Fig. 1.3 Hail detection in the thunderstorm near Fort Worth, Texas, on 26 May 2015. (**a**) Hydrometeor identification by a ground-based polarimetric radar and (**b**) the output from the "flagHeavyIcePrecip" from the DPR product. (Adapted from Iguchi et al. 2018; see the reference for details)

radar. JAXA has developed a ground-based dual Ka-band radar system for observation of precipitation on the ground. The system consists of two identical radars, and they observe the same precipitation systems. From the difference of the range profiles, scattering and attenuation can be estimated. From the observation, the scattering tables used in DPR rain retrieval algorithms are found to be reasonable (see Chap. 27 of volume 2).

The GMI instrument provides observations at the commonly used passive microwave frequencies of 10.65, 18.7, 23.8, 36.5 and 89.0 GHz with dual polarization, except at 23.8 GHz (see Table 1.1). In addition, GMI adds four high-frequency channels at 165.5 (vertical and horizontal polarizations) and 183.31 $\pm$ 3.0, $\pm$7.0 GHz (vertical polarization). The high-frequency PMW channels (together with the Ka radar) were specifically added to enable the observation and measurement of frozen and light precipitation. It should also be noted that the resolution of the GMI instrument is significantly better than most other passive microwave instruments, with the highest frequency channels providing observations at 6×4 km^2.

The GMI was designed to be an accurate reference standard for other PMW radiometers, consequently a number of design features were included to eliminate solar intrusions, minimize antenna emissivity issues, and improve calibration of the window channels (Draper et al. 2013). The performance of the GMI instrument is described in (Draper et al. 2015a, b), with subsequent work (Wentz and Draper 2016) noting a Tb accuracy for all channels to within 0.4 K and stability to within 0.2 K.

1.3 Products

Within the GPM mission, the NASA Precipitation Processing System (PPS) captures, processes, archives and distributes data from the GPM-CO and constellation members. Ancillary data such as the GEO-IR and model data are also ingested to provide inputs to the precipitation retrieval schemes. Incoming data are processed to ensure consistency between the satellite data sets, including information content, orbital data structure, common file name conventions and, most importantly, the inter-calibration of the observed brightness temperatures. The GPM Intersatellite Calibration Working Group (XCAL) is dedicated to the inter-calibration of the GPM-CO and constellation observations to ensure consistency across the satellite sensors (e.g., Kroodsma et al. 2017; Berg et al. 2016). The incoming GPM-CO data at Level 1A are processed to standard Level 1B files containing brightness temperatures (Tb), and then to the Level 1C inter-calibrated brightness temperatures (Tc); all constellation data are processed to Level 1C. Consistency between the different international partner PMW sensors is achieved through the use of the GMI as a calibration reference. Pre-screening of the individual sensor Tbs is performed in order to identify and correct for calibration biases both along scans and between scans. The XCAL uses a number of techniques (to lessen the flaws or limitations in

any single technique) to adjust the calibration of the partner radiometers to ensure consistency with GMI (Berg et al. 2016). Below 92 GHz, differences between the radiometers were typically less than 2-3 K, while above 150 GHz, differences were found to be about 2 K except for the SSMIS on the F19 satellite which showed differences up to 11 K colder than GMI. Cross-track, or sounding, sensors exhibited differences generally within 0.5 K for the Sondeur Atmospherique du Profil d'Humidite Intertropicale par Radiometrie (SAPHIR) and the Microwave Humidity Sounder (MHS) sensors, and within 1 K for the Advanced Technology Microwave Sounder (ATMS). The coordination of data files of all the precipitation-capable observations greatly simplifies the generation of multi-sensor precipitation retrievals for the user community.

The precipitation products are generated in near real-time (and again after real-time) by the NASA PPS. These Level 2 products provide the instantaneous precipitation retrievals and the retrieval resolution for each sensor on a swath basis for each satellite orbit. Data from the microwave radiometers use the GPROF scheme (see Kummerow et al. 2001, 2015; Chap. 8), the DPR product uses a scheme developed by Masaki et al. (2015) and Seto et al. (2015), and the Combined Radar-Radiometer Algorithm (CORRA) follows a scheme described in Grecu et al. (2016) and in Chap. 14. Products from the GMI instrument are available within 1 h of the observation time, while the DPR and CORRA products are available within 3 h most of the time. The post real-time products are intended to provide research-quality retrievals.

Mapped precipitation products are available as Level 3 data. The Level 2 products, together with GEO IR data, are used as input to the US GPM Science Team's IMERG scheme (see Chap. 19), which provides precipitation products at $0.1° \times 0.1°$, 30 min resolution. All of the microwave retrievals developed above, based upon GPROF, are inter-calibrated to the CORRA estimate while the IR-based estimates are calibrated to these microwave retrievals. Three IMERG products are available at different latencies: an Early Run that includes all available data within 4 h, a Late Run that includes all available data within 14 h, and a Final Run that uses all satellite data that is available and a global monthly gauge analysis, and is generated 3 months later. The last product is considered to be the research-grade product. In addition to the precipitation rate, each product contains information on the provenance of the data, its quality, and the precipitation phase (liquid/solid) determined diagnostically from numerical assimilation/forecast information.

Mapped precipitation datasets in high spatial and temporal resolution based on satellite observations, using PMW sensors on multiple LEO satellites and GEO-IR observations, as well as the GPM DPR, are also developed in Japan, namely the GSMaP (Aonashi et al. 2009; Ushio et al. 2009; Chap. 20). The original GSMaP algorithm was developed in the TRMM era, with PMW on LEO satellites, and TMI and TRMM PR (Okamoto et al. 2005; Kubota et al. 2007). There are seven products in GSMaP which are elaborated later in this book (see Kubota et al. 2007 and Chap. 20). All products have spatial and temporal resolutions of $0.1° \times 0.1°$ and hourly, respectively. The standard products are GSMaP_MVK and GSMaP_Gauge with 3 days latency, while GSMaP_NOW is a product with the shortest latency,

available in real time. GSMaP is characterized by its careful treatment of precipitation types in its algorithm, fully utilizing the TRMM/PR, GPM/DPR, TMI and GMI observations. For example, GSMaP employs precipitation-regime classifications and precipitation-profile information constructed from the TRMM/PR, GPM/DPR, and ancillary meteorological data, in order to derive adequate LUTs for precipitation retrievals in the PMW algorithm. Careful classification of land/coast/ocean surface types and utilization of land surface emissivity obtained from TRMM data are included. In addition, severe underestimation of orographic precipitation in the original product is mitigated by incorporating an orographic rainfall scheme (Yamamoto and Shige 2015). A recent improvement is an implementation of a snowfall estimation scheme that significantly extended the estimated data availability to higher latitudes. Details for the algorithm can be found in Chap. 20.

1.4   Validation

As part of the US GPM program, NASA includes a ground validation (GV) component aimed at not only verifying and validating the precipitation products generated from the GPM observations, but also gaining a greater insight into the precipitation processes that the GPM sensors observe. The GPM GV work can be broken down into three main areas:

(i) *Direct validation* of the precipitation products through comparison of the satellite estimates with routinely collected, large-scale precipitation measurements as provided by national and international ground-based networks such as the Multi-Sensor/Multi-Source radar data (see Zhang et al. 2011, 2016). Examples of this type of validation include Kidd et al. (2018), who validated the Level-2 GPROF precipitation products over Europe and the US using surface radar and gauge data, Tan et al. (2017a), who validated the Level-3 IMERG precipitation product over different spatial and temporal scales, and Tan et al. (2017b), who compared the DPR and GPROF products against dense gauge networks. The International Precipitation Working Group (IPWG) also provides ongoing direct validation of satellite precipitation products over a number of regions across the globe (see Chap. 25 of volume 2).

(ii) *Physical validation* through concerted field campaigns during which surface, airborne, and spaceborne measurements are coordinated to provide multi-tiered observations of precipitation systems. The GPM GV team has organised a number of intensive GV campaigns covering a range of meteorological and climatological regimes. These have included the Light Precipitation Validation Experiment (LPVEx) centred on Helsinki, Finland (Iguchi et al. 2014; Huang et al. 2015); the GPM Cold Precipitation Experiment (GCPEx) centred on the Environment Canada Center for Atmospheric Research Experiments (CARE) site at Egbert, north of Toronto (see Skofronick-Jackson et al. 2015; Colle et al. 2017); the Mid-latitude Continental Convective Clouds Experiment (MC3E) in

Oklahoma (Tao et al. 2013; Jensen et al. 2016); and the Olympic Mountain Experiment (OLYMPEX) over the NW US (Petersen et al. 2016; Houze et al. 2017).

(iii) *An integrated approach* whereby the precipitation products are related to particular applications to ascertain the errors and uncertainties associated with such products, particularly across multiple spatial and temporal scales. Examples include the estimation and measurement of the drop-size distribution (DSD) by different sensors and trying to reconcile the differences, both from the physical understanding of the precipitation and associated processes, and from the differences in the observation techniques (e.g., Bringi et al. 2015; Liao et al. 2014), and through identifying and reducing errors and uncertainties in hydrological modelling using satellite-derived precipitation data products (see Chap. 32 of volume 2).

The GV activities span a range of spatial and temporal scales, to assess a range of different parameters, such as occurrence, accumulation, and phase (e.g., You et al. 2016; Chase et al. 2018). Further studies have concentrated upon the derivation of DSDs from satellite and ground measurements to enable better radar-precipitation measurements to be made, together with providing global maps of DSDs (e.g., Williams et al. 2014; Thurai et al. 2017). More detail on GV can be found in Chap. 26 of volume 2. Validation over the oceans remains a significant problem. Current efforts, such as the OceanRAIN data set (Chap. 34 of volume 2), provide ship-based disdrometer measurements that are useful for research into DSDs as well as the occurrence and accumulation of precipitation across a range of climatological regimes.

In addition, the GV program was tasked with evaluating the performance of the GPM-CO against the pre-launch science requirements (see Skofronick-Jackson et al. 2017). As such, the validation of the GPM products shows that the mission requirements have been met, with excellent (low) bias and uncertainty for instantaneous rain rates (Skofronick-Jackson et al. 2017), typically less than 50% at 1 mm h^{-1} and less than 25% at 10 mm h^{-1}. The validation of snowfall retrievals is currently being evaluated. Because the physical measurement of snowfall at the surface is difficult, obtaining definitive and accurate surface data is crucial in establishing the accuracy of satellite snowfall retrievals. At present, comparisons between the IMERG product and surface radar data show agreement in the identification of snowfall.

1.5 Advancing Precipitation Science

The improved features of the GPM-CO together with the constellation partner sensors and the GPM GV program have enhanced observations of precipitation across the Earth's surface and through its atmosphere. The greater extent of the GPM-CO coverage over TRMM now means that different meteorological and climatological regimes are observed by combined PMW/AMW observations.

These regimes present new challenges and opportunities to advance precipitation research; the inclusions of these regimes have led to new research leading to a greater understanding of precipitation and its role in the Earth's water and energy cycles.

1.5.1 Snowfall and Cold-Season Precipitation

While the Tropics are dominated by convective precipitation, the mid- and high-latitudes tend to be dominated by stratiform precipitation, often light, shallow and of mixed phase. This fact poses a number of problems for both the PMW and AMW observations. Signals associated with light and shallow precipitation are often subtle, and differentiating between precipitation and no-precipitation is difficult. The addition of high-frequency PMW channels helps due to their higher sensitivity to small precipitation particles, while the increased sensitivity of the DPR allows lighter precipitation to be observed and measured.

The estimation of snowfall (falling snow) has always been somewhat equivocal due to the sensitivity of the observations coupled with inadequate relationships between the observations and surface precipitation in snowfall situations. Although improved multi-channel observations can improve the identification of snowfall, advances have also been necessary in the modelling of the scattering signal associated with the ice particles of snowfall-related hydrometeors (see Chap. 15). Improved modelling of scattering due to non-spherical hydrometeors at high frequencies has enabled better retrievals of snowfall to be made, and opened up new research opportunities (see Chaps. 17 and 36 of volume 2). GPM data have revealed insights into the intensity and microphysical composition of cold-season precipitation, and regions of predominantly light mixed-phase precipitation rates (see von Lerber et al. 2018).

Very light precipitation remains challenging even for the GPM DPR instrument. Some improvements to light precipitation incorporated in GPM observations have combined DPR with W-band radar CloudSat Cloud Profiling Radar (CPR) observations (Panegrossi et al. 2015). However, despite the advances in the above measurements, one significant drawback at present is the limitation of the AMW measurements for both the DPR and CPR due to surface clutter that limits the lowest altitude at which the radar can provide useful observations; at nadir this is about 1 km, so precipitation below 1 km may not be faithfully captured by any existing AMW sensor.

1.5.2 Drop Size Distributions (DSDs)

Improving our knowledge and understanding of hydrometeor DSDs within precipitating systems is key for the estimation of precipitation using radar, through the use of an appropriate Z–R relationship, together with understanding of the processes

associated with the formation and evolution of precipitation within weather systems. Current radar and combined (radar + radiometer) precipitation retrieval algorithms for GPM are designed around the assumption of a gamma-shaped raindrop size distribution, representing the number of raindrops per diameter interval per unit volume. This DSD is described by three mathematical parameters relating to the scale (i.e., number concentration), shape, and slope of the DSD. The DPR provides two independent measurements to inform the GPM algorithms on these three parameters. Using ground-based data, Williams et al. (2014) described efforts to identify inter-relationships between these DSD parameters, to constrain all three parameters in a manner consistent with independent ground validation gauges and video disdrometers, while uncertainties within the GPM DPR rain estimates caused by DSD parameterizations in the retrieval schemes are presented in Liao et al. (2014). These relationships are central to the GPM algorithms to specify the DSD in a physical way in precipitation retrievals, and central to ground validation programs such as OLYMPEX (Houze et al. 2017). Many of these efforts contribute to the mapping of DSDs and their variability, such as the work of Bringi et al. (2015), who investigate the spatial relationships between the DSDs and rain rates.

1.5.3   Latent Heating Products

Global estimates of convective latent heating profiles based on satellite observations have been a major goal among tropical meteorologists since the design phase of TRMM (Simpson et al. 1988). The capability of observing the three-dimensional structure of precipitation from space by TRMM and GPM realized this dream.

There are two standard convective latent heating products utilizing TRMM and GPM observations. One is the Spectral Latent Heating (SLH) product from Japan (Shige et al. 2004, 2007, 2008, 2009), and the other is the Convective Stratiform Heating (CSH) product from the US (Tao et al. 2001, 2006, 2010, 2016). Both algorithms utilize the outputs from cloud system-resolving model simulations to generate appropriate look-up tables (LUTs).

The SLH algorithm uses LUTs to obtain latent heating profiles from precipitation profile data obtained from space-borne radar observations. These LUTs are constructed in a spectral manner, in terms of either precipitation top heights or cloud-base level precipitation intensity, depending on precipitation types. The SLH algorithm was first developed for tropical precipitation in the TRMM era with the aid of Goddard Cumulus Ensemble Model (GCEM) simulations for the Tropics. In order to apply this algorithm to the high-latitude precipitation observed by GPM, a mid-latitude scheme was added in the latest V05 and V06 versions, with the aid of Local Forecast Model simulations by the Japanese Meteorological Agency. The CSH algorithm was originally based on the convective-stratiform precipitation ratio estimated from TRMM observations. The GPM version of the CSH algorithm utilizes the GCE model to generate LUTs for various tropical

regions, and the NASA Unified Weather Research and Forecasting (NU-WRF) model to generate LUTs for high-latitude regions.

The latest versions of SLH and CSH are distributed as GPM SLH V06 and GPM CSH V06, respectively. For further details, see Chap. 46 of volume 2.

1.6 Applications and Outreach

The increasing time span of TRMM and GPM precipitation data, together with improved (reduced) data latency and online distribution methods, have made precipitation datasets quickly and easily available for use in various cross-discipline investigations and Earth science-related applications (Kucera et al. 2013; Kirschbaum et al. 2017; Levizzani et al. 2018). With its grater latitudinal coverage relative to the predecessor TRMM satellite, the increased GPM over-land coverage expands or opens up additional land-related applications (Skofronick-Jackson et al. 2017). A review of these and many additional applications of GPM precipitation data products is provided in Kirschbaum et al. (2017), as well as in Part VI of volume 2.

1.6.1 Precipitation Extremes, Food Security, and Health

One key role for satellite-derived precipitation products is the ability of observe, monitor and measure precipitation on a (quasi-)global basis in near real-time. Applications range from the assimilation of satellite observations into numerical weather prediction (NWP) models (see Chaps. 48 and 49 of volume 2), to the use of GPM data for monitoring tropical cyclone locations, to the use of precipitation products to generate maps of accumulated rainfall from tropical cyclones to aid disaster relief efforts (Skofronick-Jackson et al. 2018).

The hydrological community utilises many of the satellite-derived precipitation products for hydrological modelling. Over poorly gauged or large river basins, satellite-based precipitation datasets are often the only low-latency precipitation data to allow flow predictions for downstream interests with sufficient lead time to initiate response (Maggioni and Massari 2018). One of the great challenges is the complexity of the hydrological system and relating the satellite surface rainfall measurements to final river flow (see Chap. 32 of volume 2). Extremes of precipitation are discussed in Chaps. 40 and 55 of volume 2, with the detection of hail presented in Chap. 44 of volume 2. Flooding is not the only consequence of heavy precipitation events; periods of sustained rain often trigger landslides and debris flows. Near real-time GPM precipitation data are routinely used for initializing the Landslide Hazard Assessment for Situational Awareness (LHASA) model (Kirschbaum and Stanley 2018). JAXA has collaborated with the International Centre for Water Hazard and Risk Management (ICHARM) since 2005. The

GSMaP near-real-time data are used in a flood forecasting system by the ICHARM Integrated Flood Analysis System (IFAS) in Asian regions such as Pakistan. JAXA has also collaborated with the Philippine Institute of Volcanology and Seismology (PHIVOLCS) as a "Sentinel Asia Success Story in the Philippines" project since 2009, studying the use of GSMaP for landslide warnings.

At the other extreme, the lack of precipitation causes drought, impacting food security. Changing weather patterns and variability in precipitation under conditions such as the El Niño Southern Oscillation (ENSO) affects many food-producing areas of Africa and Central and South America. Over the past decade, the change of rainfall patterns and weather over Africa has been extensively studied with TRMM satellite precipitation products (Maidment et al. 2015). The Famine Early Warning System Network (FEWS Net; Funk and Verdin 2010) utilises precipitation information to help with determining the start of the growing season and drought metrics (Kirschbaum et al. 2017). Shepherd et al. (2016) used GPM data to compare global precipitation with population density to derive a metric of water stress. The role of satellite observations in drought risk management is explored in Chap. 52 of volume 2. A consequence of drought is reduced food security; Chap. 56 of volume 2 provides an overview of the use of satellite-derived precipitation products for agriculture and food security. Because of the key role that water plays in the transmission of disease, GPM precipitation data provide a vital element in addressing societal issues such as outbreaks of malaria and cholera (Moore et al. 2017).

More recently the use of satellite precipitation data sets has been used to assess the lack of precipitation in fire-prone regions, particularly along the Western seaboard of the US and western Canada. Here, the lack of snowfall during the winter season can have serious impacts on water availability during the following summer when dry conditions can enhance the likelihood of forest fires (see Chap. 57 of volume 2).

In Japan, JAXA provides agro-met data including the GSMaP to the Ministry of Agriculture, Forestry and Fisheries in Japan (MAFF) for monitoring crop status around the entire world. Through MAFF, Japan operationally utilizes this agro-met information in their practical work.

1.6.2 Assimilation and Numerical Modelling

With recent assimilation techniques, GPM data are utilized in operational numerical weather forecast routines. The Japan Meteorological Agency (JMA) started GPM DPR assimilation in the meso-NWP system on 24 March 2016 (Ikuta 2016). This is the world's first operational assimilation of space-borne radar data in the NWP system of meteorological agencies. Improvements in moisture analysis have resulted in significant improvements in rainfall forecasts. Furthermore, improvements in tropical cyclone position errors were verified by assimilation and forecast experiments using GPM DPR and GMI data for Typhoon Halong (Okamoto et al. 2016).

The NASA Global Modeling and Assimilation Office (GMAO) began assimilating all-sky GMI radiances into their Forward Processing (FP) System in real time on 11 July 2018. The addition of GMI radiances produced the largest impact per observation of all radiance-type observations in the Tropics, significantly improving the specific humidity in short term (0–72 h) forecasts, with similar improvements in tropical middle and lower tropospheric temperature and winds. In particular, the total impact of GMI is comparable to a single Microwave Humidity Sounder instrument. Preliminary results demonstrate that assimilating microwave radiance data from GPM and several MHS sounders adjusts precipitating snow during the winter storms and makes Goddard Earth Observing System (GEOS) analyses closer to the observations. Other atmospheric parameters like water vapour and surface pressure are also adjusted in a physically-consistent manner (Kim et al. 2016).

1.6.3 Outreach Activities

In addition to the important role of GPM in providing precipitation data to the user community and the public, GPM also provides educational material through outreach activities. The number of users registered in the home page "JAXA Global Rainfall Watch", which visualizes and provides GSMaP data, has been expanding, and there were 4261 independent users from 114 countries as of the end of October 2018. JAXA held a public GPM symposium in November 2017 in Tokyo, Japan. A total of 160 participants attended the symposium, with active discussions among the participants including students and company persons (e.g., civil engineering, agriculture, etc.). JAXA also held GPM Asia Workshops, to promote satellite precipitation data utilization in Asia. The 6th Workshop was held in the Thai Meteorological Department (TMD) in January 2017, and the 7th Workshop was held in Badan Meteorologi, Klimatologi, dan Geofisika (BMKG), Jakarta, Indonesia, in January 2018.

The NASA PPS provides centralised access to all the GPM data sets for many users. For example, in October 2018, it served over 700 unique users with more than eight million files totalling more than 60 TB of data. In addition, GPM has a social media presence, attracting more than 25,000 followers on Twitter and more than 52,000 on Facebook. The top Twitter post in October 2018 was an animation of a GPM fly-over of Typhoon Yutu as it made landfall in the Northern Mariana Islands, while the top Facebook post in October was a fly-through of Hurricane Maria (https://www.facebook.com/NASARain/videos/2134322840143432/, last accessed 15 Dec. 2018). The use of Twitter and Facebook engages the general public in the GPM mission. In addition, the GPM educational outreach team provide links between the mission scientists, school-aged children, and the public in general (see https://pmm.nasa.gov/education/, last accessed 15 Dec. 2018).

1.7   Beyond GPM

In January 2018, the US National Academies of Sciences published the 2017-2027 Decadal Survey for Earth Science and Applications from Space (NAS 2018). The purpose of this study was to help shape science priorities and to guide agency investments into the next decade. Two Targeted Observables, "Clouds, Convection, and Precipitation (CCP)" and "Aerosols" are directly relevant to precipitation studies. The cloud and precipitation science communities and aerosol science community are currently working towards defining new mission architectures in response to this study, with an emphasis on coupled aerosol-cloud-precipitation processes. Future cloud-precipitation observing systems are being designed to better understanding cloud and precipitation processes and potentially coupling them to aerosols and to atmospheric dynamics through vertical motions.

In addition to a core research-science mission, the mapping of global precipitation will require an on-going suite of sensors. At present, the current constellation of precipitation sensors is comprised of a number of PMW and AMW sensors in LEO, with IR observations provided by GEO satellites. Many of the LEO sensors are more than 10 years old, with the majority of the PMW sensors now comprised of sounding instruments, not specifically designed for precipitation retrievals (see Huffman et al. 2016). Nevertheless, schemes have been devised to extract precipitation from these different sensors, and to ensure that there is long-term continuity and consistency between them. It should be noted that the most direct measurements of precipitation from space are from the DPR, although the limited coverage severely limits its usefulness. The combination of multi-satellite, multi-sensor observations through schemes like IMERG and GSMaP, therefore continues to be of great importance.

Development of new satellite systems is also looking towards new technologies, such as the use of small-sats or cubesats, which by necessity operate with limited PMW frequencies. Cubesats in LEO, such as the Time-Resolved Observations of Precipitation structure and storm Intensity with a Constellation of Smallsats (TRO-PICS, Blackwell et al. 2018) are currently, or will soon be, in operation and have the potential to contribute to the precipitation constellation. The development of Geo-stationary Synthetic Thinned Aperture Radiometer (GeoSTAR; Tanner et al. 2007) is also being evaluated, although multiple GeoSTAR instruments in conjunction with LEO sensors would be required for global measurements. Further discussion on the future of precipitation sensors may be found in Chap. 6).

References

Aonashi, K., Awaka, J., Hirose, M., Kozu, T., Kubota, T., Liu, G., Shige, S., Kida, S., Seto, S., Takahashi, N., & Takayabu, Y. N. (2009). GSMaP passive, microwave precipitation retrieval algorithm: Algorithm description and validation. *Journal of the Meteorological Society of Japan, 87A*, 119–136. https://doi.org/10.2151/jmsj.87A.119.

Berg, W., Bilanow, S., Chen, R. Y., Datta, S., Draper, D., Ebrahimi, H., Farrar, S., Jones, W. L., Kroodsma, R., McKague, D., Payne, V., Wang, J., Wilheit, T., & Yang, J. X. (2016). Intercalibration of the GPM microwave radiometer constellation. *Journal of Atmospheric and Oceanic Technology, 33*, 2639–2654. https://doi.org/10.1175/JTECH-D-16-0100.1.

Blackwell, W. J., Braun, S., Bennartz, R., Velden, C., DeMaria, M., Atlas, R., Dunion, J., Marks, F., Rogers, R., Annane, B., & Leslie, R. V. (2018). An overview of the TROPICS NASA Earth venture mission. *Quarterly Journal of the Royal Meteorological Society, 114*(S1), 16–26. https://doi.org/10.1002/qj.3290.

Bringi, V. N., Thurai, M., Tolstoy, L., & Petersen, W. A. (2015). Estimation of spatial correlation of rain drop size distribution parameters and rain rate using NASA's S-band polarimetric radar and 2D-video disdrometer network: Two case studies from MC3E. *Journal of Hydrometeorology, 16*, 1207–1221. https://doi.org/10.1175/JHM-D-14-0204.1.

Chase, R. J., Finlon, J. A., Borque, P., McFarquhar, G. M., Nesbitt, S. W., Tanelli, S., Sy, O. O., Durden, S. L., & Poellot, M. R. (2018). Evaluation of triple-frequency radar retrieval of snowfall properties using coincident airborne in-situ observations during OLYMPEX. *Geophysical Research Letters, 45*, 5752–5760. https://doi.org/10.1029/2018GL077997.

Colle, B. A., Naeger, A. R., & Molthan, A. (2017). Structure and evolution of a warm frontal precipitation band during the GPM Cold Season Precipitation Experiment (GCPEx). *Monthly Weather Review, 145*, 473–493. https://doi.org/10.1175/MWR-D-16-0072.1.

Draper, D. W., Newell, D. A., Teusch, D. A., & Yoho, P. K. (2013). Global precipitation measurement microwave imager hot load calibration. *IEEE Transactions on Geoscience and Remote Sensing, 51*, 4731–4742. https://doi.org/10.1109/TGRS.2013.2239300.

Draper, D. W., Newell, D. A., McKague, D., & Piepmeier, J. (2015a). Assessing calibration stability using the Global Precipitation Measurement (GPM) Microwave Imager (GMI) noise diodes. *IEEE Journal of Selected Topics in Applied Earth Observations and Remote Sensing, 8*, 4239–4247. https://doi.org/10.1109/JSTARS.2015.2406661.

Draper, D. W., Newell, D. A., Wentz, F. J., Krimchansky, S., & Skofronick-Jackson, G. (2015b). The Global Precipitation Measurement (GPM) Microwave Imager (GMI): Instrument overview and early on-orbit performance. *IEEE Journal of Selected Topics in Applied Earth Observations and Remote Sensing, 8*, 3452–3462. https://doi.org/10.1109/JSTARS.2015.2403303.

Funk, C., & Verdin, J. (2010). Real-time decision support systems: The famine early warning system network. In M. Gebremichael & F. Hossain (Eds.), *Satellite rainfall applications for surface hydrology* (pp. 3–22). Dordrecht: Springer, ISBN:978-90-481-2914-0.

Grecu, M., Olson, W. S., Munchak, S. J., Ringerud, S., Liao, L., Haddad, Z. S., Kelley, B. L., & McLaughlin, S. F. (2016). The GPM combined algorithm. *Journal of Atmospheric and Oceanic Technology, 33*, 2225–2245. https://doi.org/10.1175/JTECH-D-16-0019.1.

Hamada, A., & Takayabu, Y. N. (2016). Improvements in detection of light precipitation with the Global Precipitation Measurement dual-frequency precipitation radar (GPM/DPR). *Journal of Atmospheric and Oceanic Technology, 33*, 653–667. https://doi.org/10.1175/JTECH-D-15-0097.1.

Hou, A. Y., Kakar, R. K., Neeck, S. A., Azarbarzin, A., Kummerow, C. D., Kojima, M., Oki, R., Nakamura, K., & Iguchi, T. (2014). The global precipitation measurement mission. *Bulletin of the American Meteorological Society, 95*, 701–722. https://doi.org/10.1175/BAMS-D-13-00164.1.

Houze, R. A., Jr., McMurdie, L. A., Petersen, W. A., Schwaller, M. R., Baccus, W., Lundquist, J. D., Mass, C. F., Nijssen, B., Rutledge, S. A., Hudak, D. R., Tanelli, S., Mace, G. G., Poellot, M. R., Lettenmaier, D. P., Zagrodnik, J. P., Rowe, A. K., DeHart, J. C., Madaus, L. E., Barnes,

H. C., & Chandrasekar, V. (2017). The Olympic Mountains experiment (OLYMPEX). *Bulletin of the American Meteorological Society, 98*, 2167–2188. https://doi.org/10.1175/BAMS-D-16-0182.1.

Huang, G., Bringi, V. N., Moisseev, D., Petersen, W. A., Bliven, L., & Hudak, D. (2015). Use of 2D-video disdrometer to derive mean density-size and Ze-SR relations: Four snow cases from the light precipitation validation experiment. *Atmospheric Research, 153*, 34–48. https://doi.org/10.1016/j.atmosres.2014.07.013.

Huffman, G. J., Ferraro, R. R., Kidd, C., Levizzani, V., & Turk, F. J. (2016, April 11–14). Requirements for a robust precipitation constellation. In *Proceedings of MicroRad 2016* (pp. 37–41). Espoo: IEEE. https://doi.org/10.1109/MICRORAD.2016.7530500.

Iguchi, T., Matsui, T., Tao, W.-K., Khain, A. P., Phillips, V. T. J., Kidd, C., L'Ecuyer, T., Braun, S. A., & Hou, A. Y. (2014). WRF–SBM simulations of melting-layer structure in mixed-phase: Precipitation events observed during LPVEx. *Journal of Applied Meteorology and Climatology, 53*, 2710–2731. https://doi.org/10.1175/JAMC-D-13-0334.1.

Iguchi, T., Kawamoto, N., & Oki, R. (2018). Detection of intense ice precipitation with GPM/DPR. *Journal of Atmospheric and Oceanic Technology, 35*, 491–502. https://doi.org/10.1175/JTECH-D-17-0120.1.

Ikuta, Y. (2016). Data assimilation using GPM/DPR at JMA. CAS/JSC WGNE. *Research Activities in Atmospheric and Oceanic Modeling*, 1.11–1.13.

Jensen, M. P., Petersen, W. A., Bansemer, A., Bharadwaj, N., Carey, L. D., Cecil, D. J., Collis, S. M., Del Genio, A. D., Dolan, B., Gerlach, J., Giangrande, S. E., Heymsfield, A., Heymsfield, G., Kollias, P., Lang, T. J., Nesbitt, S. W., Neumann, A., Poellot, M., Rutledge, S. A., Schwaller, M., Tokay, A., Williams, C. R., Wolff, D. B., Xie, S., & Zipser, E. J. (2016). The mid-latitude continental convective clouds experiment (MC3E). *Bulletin of the American Meteorological Society, 97*, 1667–1686. https://doi.org/10.1175/BAMS-D-14-00228.1.

Kidd, C., Tan, J., Kirstetter, P., & Petersen, W. (2018). Validation of the version 05 precipitation products from the GPM core observatory and constellation satellite sensors. *Quarterly Journal of the Royal Meteorological Society, 144*(S1), 313–328. https://doi.org/10.1002/qj.3175.

Kim, M. J., Jin, J., McCarty, W., Todling, R., Gelaro, R., & Gu, W. (2016). All-sky microwave radiance data assimilation in NASA GEOS-5 system: developments, impacts, and future plans. In *20th Conference on integrated observing assimilation systems for the atmosphere, oceans, and landsurface*, AMS 2016, New Orleans, LA. Available at https://ams.confex.com/ams/. Last accessed 16 Dec 2018.

Kirschbaum, D., & Stanley, T. (2018). Satellite-based assessment of rainfall-triggered landslide hazard for situational awareness. *Earth's Future, 6*, 505–523. https://doi.org/10.1002/2017EF000715.

Kirschbaum, D. B., Huffman, G. J., Adler, R. F., Braun, S., Garrett, K., Jones, E., McNally, A., Skofronick-Jackson, G., Stocker, E. F., Wu, H., & Zaitchik, B. F. (2017). NASA's remotely sensed precipitation: A reservoir for applications users. *Bulletin of the American Meteorological Society, 98*, 1169–1184. https://doi.org/10.1175/BAMS-D-15-00296.1.

Kroodsma, R. A., McKague, D. S., & Ruf, C. S. (2017). Vicarious cold calibration for conical scanning microwave imagers. *IEEE Transactions on Geoscience and Remote Sensing, 55*, 816–827. https://doi.org/10.1109/TGRS.2016.2615552.

Kubota, T., Shige, S., Hashizume, H., Aonashi, K., Takahashi, N., Seto, S., Hirose, M., Takayabu, Y. N., Ushio, T., Nakagawa, K., Iwanami, K., Kachi, M., & Okamoto, K. (2007). Global precipitation map using satellite borne microwave radiometers by the GSMaP project: Production and validation. *IEEE Transactions on Geoscience and Remote Sensing, 45*, 2259–2275. https://doi.org/10.1109/TGRS.2007.895337.

Kucera, P. A., Ebert, E. E., Turk, F. J., Levizzani, V., Kirschbaum, D., Tapiador, F. J., Loew, A., & Borsche, M. (2013). Precipitation from space: Advancing Earth system science. *Bulletin of the American Meteorological Society, 94*, 365–375. https://doi.org/10.1175/BAMS-D-11-00171.1.

Kummerow, C. D., Barnes, W., Kozu, T., Shiue, J., & Simpson, J. (1998). The tropical rainfall measuring Mission (TRMM) sensor package. *Journal of Atmospheric and Oceanic Technology, 15*, 809–817. https://doi.org/10.1175/1520-0426(1998)015<0809:TTRMMT>2.0.CO;2.

Kummerow, C. D., Simpson, J., Thiele, O., Barnes, W., Chang, A. T. C., Stocker, E., Adler, R. F., Hou, A., Kakar, R., Wentz, F., Ashcroft, P., Kozu, T., Hong, Y., Okamoto, K., Iguchi, T., Kuroiwa, H., Im, E., Haddad, Z., Huffman, G., Ferrier, B., Olson, W. S., Zipser, E., Smith, E. A., Wilheit, T. T., North, G., Krishnamurti, T., & Nakamura, K. (2000). The status of the Tropical Rainfall Measuring Mission (TRMM) after two years in orbit. *Journal of Applied Meteorology, 39*, 1965–1982. https://doi.org/10.1175/1520-0450(2001)040<1965:TSOTTR>2. 0.CO;2.

Kummerow, C. D., Hong, Y., Olson, W. S., Yang, S., Adler, R. F., McCollum, J., Ferraro, R., Petty, G., Shin, D.-B., & Wilheit, T. T. (2001). The evolution of the Goddard Profiling Algorithm (GPROF) for rainfall estimation from passive microwave sensors. *Journal of Applied Meteorology, 40*, 1801–1820. https://doi.org/10.1175/1520-0450(2001)040<1801:TEOTGP>2.0. CO;2.

Kummerow, C., Randel, D. L., Kulie, M., Wang, N.-Y., Ferraro, R., Munchak, S. J., & Petkovic, V. (2015). The evolution of the Goddard profiling algorithm to a fully parametric scheme. *Journal of Atmospheric and Oceanic Technology, 32*, 2265–2280. https://doi.org/10.1175/ JTECH-D-15-0039.1.

Levizzani, V., Kidd, C., Aonashi, K., Bennartz, R., Ferraro, R., Huffman, G., Roca, R., Joseph, T. F., & Wang, N.-Y. (2018). The activities of the international precipitation working group. *Quarterly Journal of the Royal Meteorological Society, 144*, 3–15. https://doi.org/10.1002/qj. 3214.

Liao, L., Meneghini, R., & Tokay, A. (2014). Uncertainties of GPM DPR rain estimates caused by DSD parameterizations. *Journal of Applied Meteorology and Climatology, 53*, 2524–2537. https://doi.org/10.1175/JAMC-D-14-0003.1.

Maggioni, V., & Massari, C. (2018). On the performance of satellite precipitation products in riverine flood modeling: A review. *Journal of Hydrology, 558*, 214–224, ISSN 0022-1694. https://doi.org/10.1016/j.jhydrol.2018.01.039.

Maidment, R. I., Allan, R. P., & Black, E. (2015). Recent observed and simulated changes in precipitation over Africa. *Geophysical Research Letters, 42*, 8155–8164. https://doi.org/10. 1002/2015GL065765.

Masaki, T., Kubota, T., Oki, R., Furukawa, K., Kojima, M., Miura, T., Iguchi, T., Hanado, H., Kai, H., Yoshida, N., & Higashiuwatoko, T. (2015). Current status of GPM/DPR level 1 algorithm development and DPR calibration. In *Proceedings IEEE International Conference Geoscience Remote Sensing Symposium 2015*, Milan, pp. 2615–2618. https://doi.org/10.1109/IGARSS. 2015.7326348.

Moore, S. M., Azman, A., Zaitchik, B. F., Mintz, E. D., Brunkard, J., Legros, D., Hill, A., Mckay, H., Luquero, F. J., Olson, D., & Lessler, J. (2017). El Niño and the shifting geography of cholera in Africa. *PNAS, 114*(17), 4436–4441. https://doi.org/10.1073/pnas.1617218114.

NAS. (2018). *Thriving on our changing planet: A decadal strategy for Earth observation from space*. Washington, DC: The National Academies Press. https://doi.org/10.17226/24938.

Okamoto, K., Iguchi, T., Takahashi, N., Iwanami, K., & Ushio, T. (2005). The global satellite mapping of precipitation (GSMaP) project. In *Proceedings of IGARSS 2005*, Seoul, pp. 3414–3416. https://doi.org/10.1109/IGARSS.2005.1526575.

Okamoto, K., Aonashi, K., Kubota, T., & Tashima, T. (2016). Experimental assimilation of the GPM-Core DPR reflectivity profiles for Typhoon Halong. *Monthly Weather Review, 144*, 2307–2326. https://doi.org/10.1175/MWR-D-15-0399.1.

Panegrossi, G., Rysman, J.-F., Casella, D., Marra, A. C., Sanò, P., & Kulie, M. S. (2015). CloudSat-based assessment of GPM microwave imager snowfall observation capabilities. *Remote Sensing, 9*, 1263. https://doi.org/10.3390/rs9121263.

Petersen, W. A., Houze, R. A., McMurdie, L., Zagrodnik, J., Tanelli, S., Lundquist, J., & Wurman, J. (2016). The Olympic Mountains Experiment (OLYMPEX): From ocean to summit. *Meteorological Technology International, 2016*, 22–26.

Seto, S., Iguchi, T., Shimozuma, T., & Hayashi, S. (2015). NUBF correction methods for the GPM/DPR level-2 algorithms. *International geoscience and remote sensing symposium*, IEEE, Milan, pp. 2612–2614. https://doi.org/10.1109/IGARSS.2015.7326347.

Shepherd, J. M., Burian, S., Lui, C., & Bernardes, S. (2016). Satellite precipitation metrics to study the Energy-Water-Food Nexus within the backdrop of an urbanized globe. *Earthzine*. Available at https://earthzine.org/satellite-precipitation-metrics-to-study-the-energy-water-food-nexus-within-the-backdrop-of-an-urbanized-globe/. Last accessed 7 Dec 2018.

Shige, S., Takayabu, Y. N., Tao, W.-K., & Johnson, D. E. (2004). Spectral retrieval of latent heating profiles from TRMM PR data. Part I: Development of a model-based algorithm. *Journal of Applied Meteorology, 43*, 1095–1113. https://doi.org/10.1175/1520-0450(2004)043<1095:SROLHP>2.0.CO;2.

Shige, S., Takayabu, Y. N., Tao, W.-K., & Shie, C.-L. (2007). Spectral retrieval of latent heating profiles from TRMM PR data. Part II: Algorithm improvement and heating estimates over tropical ocean regions. *Journal of Applied Meteorology and Climatology, 46*, 1098–1124. https://doi.org/10.1175/JAM2510.1.

Shige, S., Takayabu, Y. N., & Tao, W.-K. (2008). Spectral retrieval of latent heating profiles from TRMM PR data. Part III: Estimating apparent moisture sink profiles over tropical oceans. *Journal of Applied Meteorology and Climatology, 47*, 620–640. https://doi.org/10.1175/2007JAMC1738.1.

Shige, S., Takayabu, Y. N., Kida, S., Tao, W.-K., Zeng, X., Yokoyama, C., & L'Ecuyer, T. (2009). Spectral retrieval of latent heating profiles from TRMM PR data. Part IV: Comparisons of lookup tables from two- and three-dimensional cloud-resolving model simulations. *Journal of Climate, 22*, 5577–5594. https://doi.org/10.1175/2009JCLI2919.1.

Simpson, J., Adler, R. F., & North, G. R. (1988). A proposed Tropical Rainfall Measuring Mission (TRMM) satellite. *Bulletin of the American Meteorological Society, 69*, 278–295. https://doi.org/10.1175/1520-0477(1988)069<0278:APTRMM>2.0.CO;2.

Skofronick-Jackson, G., Hudak, D., Petersen, W. A., Nesbitt, S. W., Chandrasekar, V., Durden, S., Gleicher, K. J., Huang, G.-J., Joe, P., Kollias, P., Reed, K. A., Schwaller, M., Stewart, R., Tanelli, S., Tokay, A., Wang, J. R., & Wolde, M. (2015). Global Precipitation Measurement Cold Season Precipitation Experiment (GCPEx): For measurement sake let it snow. *Bulletin of the American Meteorological Society, 96*, 1719–1741. https://doi.org/10.1175/BAMS-D-13-00262.1.

Skofronick-Jackson, G., Petersen, W. A., Berg, W., Kidd, C., Stocker, E. F., Kirschbaum, D. B., Kakar, R., Braun, S. A., Huffman, G. J., Iguchi, T., Kirstetter, P. E., Kummerow, C., Meneghini, R., Oki, R., Olson, W. S., Takayabu, Y. N., Furukawa, K., & Wilheit, T. (2017). The Global Precipitation Measurement (GPM) mission for science and society. *Bulletin of the American Meteorological Society, 98*, 1679–1695. https://doi.org/10.1175/BAMS-D-15-00306.1.

Skofronick-Jackson, G., Kirschbaum, D., Petersen, W. A., Huffman, G. J., Kidd, C., Stocker, E. F., & Kakar, R. (2018). The Global Precipitation Measurement (GPM) mission's scientific achievements and societal contributions: Reviewing four years of advanced rain and snow observations. *Quarterly Journal of the Royal Meteorological Society, 144*(S1), 27–48. https://doi.org/10.1002/qj.3313.

Tan, B.-Z., Petersen, W. A., Kirstetter, P., & Tian, Y. (2017a). Performance of IMERG as a function of spatiotemporal scale. *Journal of Hydrometeorology, 18*, 307–319. https://doi.org/10.1175/JHM-D-16-0174.1.

Tan, B.-Z., Petersen, W. A., Kirchengast, G., Goodrich, D. C., & Wolff, D. B. (2017b). Evaluation of global precipitation measurement rainfall estimates against three dense gauge networks. *Journal of Hydrometeorology, 19*, 517–532. https://doi.org/10.1175/JHM-D-17-0174.1.

Tanner, A. B., Wilson, W. J., Lambrigtsen, B. H., Dinardo, S. J., Brown, S. T., Kangaslahti, P. P., Gaier, T. C., Ruf, C. S., Gross, S. M., Lim, B. H., Musko, S. B., Rogacki, S., & Piepmeier, J. R. (2007). Initial results of the geostationary synthetic thinned array radiometer. *IEEE Transactions on Geoscience and Remote Sensing, 45*. https://doi.org/10.1109/TGRS.2007.894060.

Tao, W.-K., Lang, S., Olson, W. S., Yang, S., Meneghini, R., Simpson, J., Kummerow, C., Smith, E. A., & Halverson, J. (2001). Retrieved vertical profiles of latent heating release using TRMM rainfall products for February 1998. *Journal of Applied Meteorology, 40*, 957–982. https://doi.org/10.1175/1520-0450(2001)040<0957:RVPOLH>2.0.CO;2.

Tao, W.-K., Smith, E. A., Adler, R. F., Haddad, Z. S., Hou, A. Y., Iguchi, T., Kakar, R., Krishnamurti, T. N., Kummerow, C. D., Lang, S., Meneghini, R., Nakamura, K., Nakazawa,

T., Okamoto, K., Olson, W. S., Satoh, S., Shige, S., Simpson, J., Takayabu, Y., Tripoli, G. J., & Yang, S. (2006). Retrieval of latent heating from TRMM measurements. *Bulletin of the American Meteorological Society, 87*, 1555–1572. https://doi.org/10.1175/BAMS-87-11-1555.

Tao, W.-K., Lang, S., Zeng, X., Shige, S., & Takayabu, Y. (2010). Relating convective and stratiform rain to latent heating. *Journal of Climate, 23*, 1874–1893. https://doi.org/10.1175/2009JCLI3278.1.

Tao, W.-K., Wu, D., Matsui, T., Peters-Lidard, C., Lang, S., Hou, A., Reinecker, M., & Petersen, W. A. (2013). The diurnal variation of precipitation during MC3E: A modeling study. *Journal of Geophysical Research, 118*, 7199–7218. https://doi.org/10.1002/jgrd.50410/asset/jgrd50410.

Tao, W.-K., Takayabu, Y. N, Lang, S., Olson, W., Shige, S., Hou, A, Jiang, X., Lau, W., Krishnamurti, T., Waliser, D., Zhang, C., Johnson, R., Houze, R., Ciesielski, P., Grecu, M., Hagos, S., Kakar, R., Nakamura, N., Braun, S., & Bhardwaj, A. (2016). TRMM latent heating retrieval and comparison with field campaigns and large-scale analyses, *American meteorological society meteorological monographs – Multi-scale convection-coupled systems in the tropics*, Chapter 2. https://doi.org/10.1175/AMSMONOGRAPHS-D-15-0013.1.

Thurai, M., Gatlin, P. N., Bringi, V. N., Petersen, W., Kennedy, P., Notaros, B., & Carey, L. D. (2017). Towards completing the rain drop size spectrum: Case studies involving 2D-video disdrometer, droplet spectrometer, and polarimetric radar measurements. *Journal of Applied Meteorology and Climatology, 56*, 877–896. https://doi.org/10.1175/JAMC-D-16-0304.1.

Ushio, T., Kubota, T., Shige, S., Okamoto, K., Aonashi, K., Inoue, T., Takahashi, N., Iguchi, T., Kachi, M., Oki, R., Morimoto, T., & Kawasaki, Z. (2009). A Kalman filter approach to the Global Satellite Mapping of Precipitation (GSMaP) from combined passive microwave and infrared radiometric data. *Journal of the Meteorological Society of Japan, 87A*, 137–151. https://doi.org/10.2151/jmsj.87A.137.

von Lerber, A., Moisseev, D., Marks, D. A., Petersen, W. A., Harri, A., & Chandrasekar, V. (2018). Validation of GMI snowfall observations by using a combination of weather radar and surface measurements. *Journal of Applied Meteorology and Climatology, 57*, 797–820. https://doi.org/10.1175/JAMC-D-17-0176.1.

WCRP. (2019). *WCRP grand challenges*. Available at https://www.wcrp-climate.org/grand-challenges/grand-challenges-overview. Last accessed 3 Dec 2018.

Wentz, F. J., & Draper, D. (2016). On-orbit absolute calibration of the global precipitation measurement microwave imager. *Journal of Atmospheric and Oceanic Technology, 33*, 1393–1412. https://doi.org/10.1175/JTECH-D-15-0212.1.

Williams, C. R., Bringi, V. N., Carey, L. D., Chandrasekar, V., Gatlin, P. N., Haddad, Z. S., Meneghini, R., Munchak, S. J., Nesbitt, S. W., Petersen, W. A., Tanelli, S., Tokay, A., Wilson, A., & Wolff, D. B. (2014). Describing the shape of raindrop size distributions using uncorrelated raindrop mass spectrum parameters. *Journal of Applied Meteorology and Climatology, 53*, 1282–1296. https://doi.org/10.1175/JAMC-D-13-076.1.

Yamamoto, M. K., & Shige, S. (2015). Implementation of an orographic/nonorographic rainfall classification scheme in the GSMaP algorithm for microwave radiometers. *Atmospheric Research, 163*, 36–47. https://doi.org/10.1016/j.atmosres.2014.07.024.

You, Y., Wang, N.-Y., Ferraro, R., & Rudlosky, S. (2016). Quantifying the snowfall detection performance of the global precipitation measurement (GPM) microwave imager channels over land. *Journal of Hydrometeorology, 17*, 1101–1117. https://doi.org/10.1175/JHM-D-16-0190.1.

Zhang, J., Howard, K., Langston, C., Vasiloff, S., Kaney, B., Arthur, A., Van Cooten, S., Kelleher, K., Kitzmiller, D., Ding, F., Seo, D. J., Wells, E., & Dempsey, C. (2011). National Mosaic and multi-sensor QPE (NMQ) system: Description, results, and future plans. *Bulletin of the American Meteorological Society, 92*, 1321–1338. https://doi.org/10.1175/2011BAMS-D-11-00047.1.

Zhang, J., Howard, K., Langston, C., Kaney, B., Qi, Y. C., Tang, L., Grams, H., Wang, Y. D., Cocks, S., Martinaitis, S., Arthur, A., Cooper, K., Brogden, J., & Kitzmiller, D. (2016). Multi-Radar Multi-Sensor (MRMS) quantitative precipitation estimation: Initial operating capabilities. *Bulletin of the American Meteorological Society, 97*, 621–638. https://doi.org/10.1175/BAMS-D-14-00174.1.

Chapter 2
Status of the CloudSat Mission

**Matthew D. Lebsock, Tristan S. L'Ecuyer, Norman B. Wood,
John M. Haynes, and Mark A. Smalley**

Abstract This chapter provides an overview of the CloudSat mission as it relates to precipitation remote sensing. We describe how the Cloud Profiling Radar (CPR) contributes to the global observing system through precise precipitation detection, quantification of snowfall rate, quantification of light rain fall, and stratiform/convective delineation. We provide an overview of the mission operations, which have changed at several points throughout the mission history, introducing sampling artifacts in the diurnal cycle that need to be accounted for when using the data. Finally, we describe the three operational precipitation products produced by the CloudSat data system.

Keywords Precipitation · Rainfall · Light rainfall · Snowfall · Stratiform · Convective · Satellite · CloudSat · CALIPSO · Cloud radar · CPR

2.1 CloudSat Instrument and Measurements

CloudSat carries the Cloud Profiling Radar (CPR), the first ever spaceborne W-band (94 GHz) radar. The satellite flies in a sun-synchronous orbit in the A-Train at an altitude of 705 km with a fixed equator crossing time of 0130 AM/PM. Because the primary mission science objective was determining the radiative effects of clouds,

M. D. Lebsock (✉) · M. A. Smalley
Jet Propulsion Laboratory, California Institute of Technology, Pasadena, CA, USA
e-mail: matthew.d.lebsock@jpl.nasa.gov

T. S. L'Ecuyer
University of Wisconsin-Madison, Madison, WI, USA

N. B. Wood
Space Science and Engineering Center, University of Wisconsin-Madison, Madison, WI, USA

J. M. Haynes
Cooperative Institute for Research in the Atmosphere, Colorado State University, Ft. Collins, CO, USA

the CPR is overdesigned for the detection of precipitation. At launch the radar sensitivity was ~ −30 dBZ and has degraded over time to ~ −27 dBZ, which is sufficiently capable to detect even the lightest drizzle (Kollias et al. 2011). The calibration accuracy is better than 1 dBZ (Tanelli et al. 2008) and the precision for large reflectivity values associated with precipitation is ~0.16 dBZ.

The CPR operates in a nadir only sampling mode acquiring 2 dimensional curtains of the radar reflectivity profile. The ground footprint is 1.4 km across track and 1.7 km along track. The CPR range resolution is 480 m, which is oversampled by a factor of 2 resulting in 240 m range bins throughout the troposphere. A well-known limitation of the CPR measurements is the contamination of reflectivity near the Earth surface by ground clutter leaking into bins adjacent to the surface (Marchand et al. 2008). A correction is made to reduce the clutter effect, which is more effective over water surfaces than over irregular topography (Tanelli et al. 2008). Because of this fact, over ocean surfaces precipitation signals can generally be detected in the third bin above the surface (~720 m), while over land and ice surfaces the fourth or fifth bin is used (~960–1200 m).

The CPR operating frequency of 94 GHz is much higher than those typically used for precipitation remote sensing. With the high frequency comes the benefit of high sensitivity but also several notable complications including the saturation of the radar reflectivity signal due to Mie scattering and significant attenuation (Lhermitte 1990), and also non-negligible multiple scattering (Battaglia et al. 2008). These limiting factors complicate the typical approach of using relatively simple reflectivity-to-rate relationships to derive precipitation; they also make simple detection of precipitation more complicated since the signal may be completely attenuated before reaching the near surface layers. On the other hand, while the attenuation signal complicates the interpretation of the reflectivity, it provides powerful and unique information to quantify moderate rain rates and classify convective and stratiform precipitation. Specifically, the Path Integrated Attenuation (PIA) at W-band is very sensitive to the integrated precipitation water path. Our exploitation of this signal in the operational algorithms is outlined below in Sect. 2.4. Figure 2.1 highlights some of these important signatures in the radar reflectivity profile through a tropical deep convective complex.

2.2 Limitations and Benefits of CloudSat for Precipitation Sensing

CloudSat was not designed with precipitation remote sensing in mind. It lacks several characteristics generally desired by the precipitation remote sensing community including (1) scanning, (2) diurnal-cycle sampling, and most notably (3) the ability to quantify heavy rainfall. The lack of scanning capability is not an issue in terms of long-term averages. For example, annual means and the seasonal cycle can be calculated on the regional scale. However, sampling does become problematic at
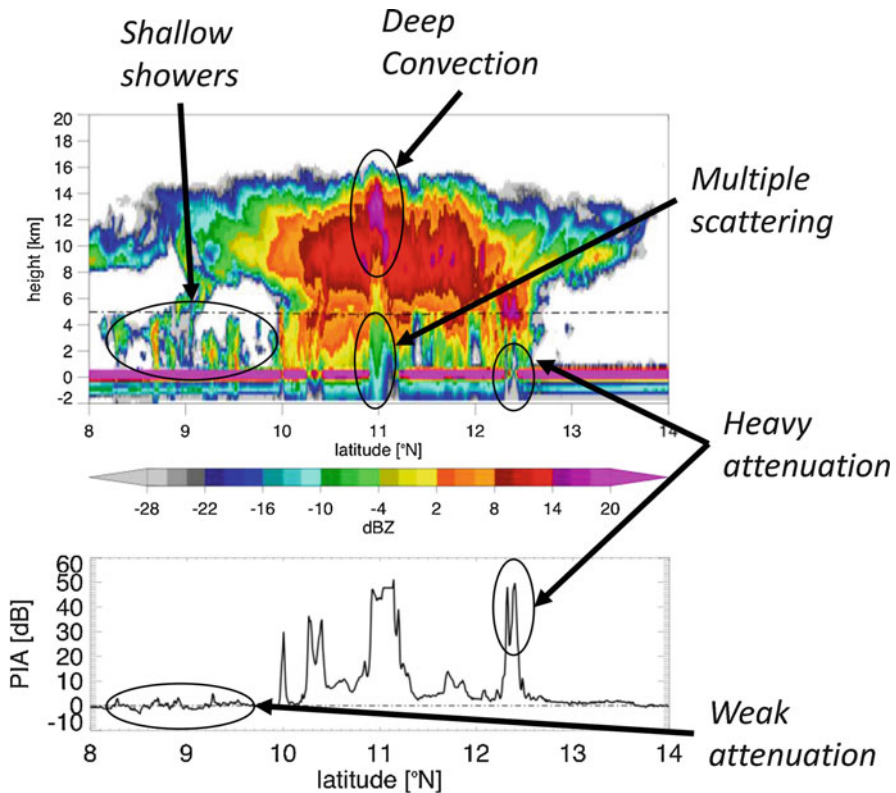
Fig. 2.1 Highlights several of the unique features of the CloudSat data. The image shows an example of a tropical deep convective system with obvious heavy attenuation and multiple scattering effects. Attenuation can be so heavy at times that the surface reflection is not observed. The convective core area is identifiable through the lack of a radar bright band and elevated reflectivity maximum. Also notice the frequent detection of shallow isolated light showers with reflectivity generally <8 dBZ

temporal resolution finer than seasonal. The fixed diurnal sampling time on the other hand does significantly bias the precipitation statistics from CloudSat. Figure 2.2 demonstrates the influence of both of these effects on the observed Probability of Precipitation (PoP) using data from the CPC Morphing algorithm (CMORPH) dataset (Joyce et al. 2004) between 2007 and 2010. CMORPH offers a complete gridded space-time coverage of precipitation occurrence and rate. By subsampling the CMORPH to the CloudSat sampling mode we may estimate the influence of the diurnal and scanning effects on the PoP. Panel (a) shows the difference between the full CMORPH PoP and CMORPH sampled at the CloudSat diurnal sampling time (0130 AM/PM). Panel (b) shows the difference between the CMORPH dataset at the CloudSat sample times and a randomly selected nadir-only track at random longitude emulating the CloudSat non-scanning sampling. Diurnal differences in PoP (a) can be as large as 6%, whereas the non-scanning effect is an order of magnitude
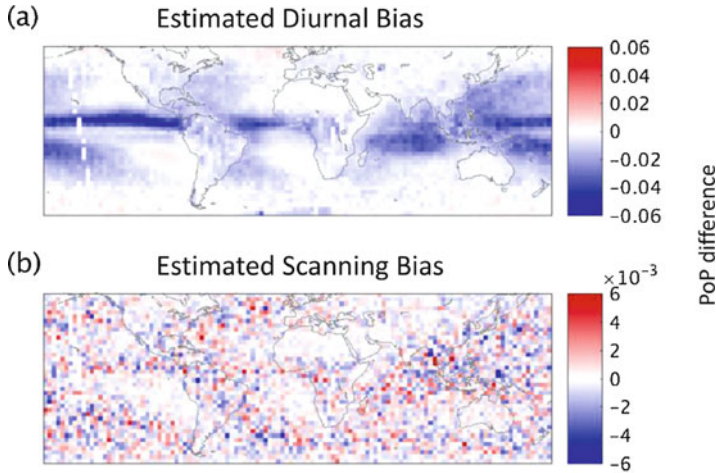
Fig. 2.2 Panel (**a**) shows an estimate of effect of CloudSat fixed diurnal sampling on the annual mean Probability of Precipitation (PoP). The map shows the difference of the full CMORPH dataset from 2007 to 2010 from the CMORPH dataset subsampled at the CloudSat ground track. In most regions the effect causes an underestimate of the PoP that can be as large as 6%. Panel (**b**) shows an estimate of the effect of non-scanning sampling on the PoP again using CMORPH. The CMORPH data is restricted to the CloudSat sampling times at each latitude and compared to that calculated from a single cross section at a random longitude
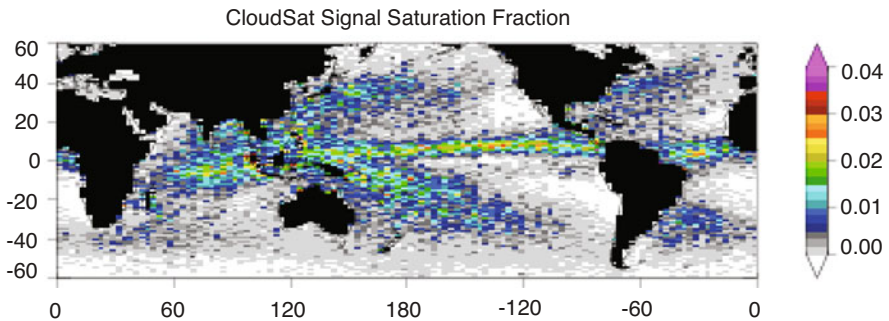
Fig. 2.3 The fraction of total (rain & no-rain) pixels in which the surface signal is saturated by heavy attenuation

smaller and randomly distributed geographically as might be expected. It is important to remember that these results are sensitive to scale. Here an annual mean from 2007 to 2010 is considered at regional scales. The finer the scale in either space or time the larger the biases may become.

Because of the inability to quantify heavy rainfall CloudSat data should not generally be used for rainfall accumulations. The only exception to this rule is in regions where the only rain that falls is extremely light such as the subtropical stratocumulus regimes. Figure 2.3 shows a map of the occurrence of signal

saturation, defined as a loss of the surface reflection due to heavy attenuation. Unsurprisingly this map looks like a map of rainfall rate. The highest occurrence of saturation occurs in the tropical convergent regions with frequent heavy rains. Note that saturation rarely occurs in the extratropics where the freezing level is shallower and thus the column integrated liquid condensate path tends to be smaller than in the tropics.

Despite its limitations, CloudSat data provide a valuable complement to data from dedicated precipitation radars such as the GPM DPR. There are four areas where CloudSat has made a significant contribution to the remote sensing of precipitation from space.

- **Precipitation detection:** CloudSat provides the most accurate detection of precipitation of any phase over all surface types at very high spatial resolution. On a global scale the fraction of CloudSat pixels containing surface rain is 5.9% and surface snow is 2% (Stephens et al. 2018). An additional 1.3% of pixels, which primarily occur over the midlatitude oceans have precipitation identified as mixed phase, but which for all intents and purposes have uncertain phase. Figure 2.4 shows the PoP averaged annually using the 2007–2010 time period. These data have allowed for precise quantification of the detection capabilities of other sensors and algorithms. For example, the CloudSat data have demonstrated that over land no more than 50% of the precipitation occurrence equatorward of 40° and 20% poleward of 40° is identified by other precipitation measuring sensors (Behrangi et al. 2014a). CloudSat has further been used to identify gaps in the detection of precipitation by ground-based radar over the United States, which has limited capability to detect snowfall in mountainous regions due to beam blockages Smalley et al. (2014).
- **Snowfall quantification:** Studies using CloudSat snowfall data have improved understanding of the role of different cloud types in global snowfall, examined snowfall's role in Antarctic ice sheet mass balance, and diagnosed observational biases in ground-based radar estimates of snowfall at high latitudes. Using 2C-Snow-Profile and 2B-CldClass (Sassen and Wang 2008), Kulie et al. (2016)

Fig. 2.4 The frequency of occurrence of surface precipitation of any phase. Occurrence is estimated using the certain precipitation flag in the 2C-Precip-Column product described below using data from 2007 to 2010
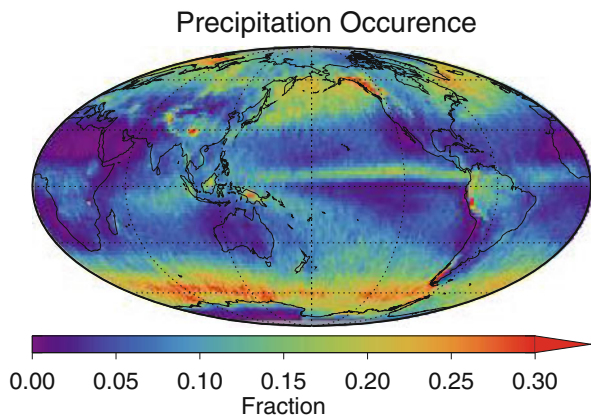
identified significant contributions by shallow cumuliform cloud systems (typically associated with lake effect snow, but also with oceanic and other water bodies and with orographic influence) to global snowfall occurrence and precipitation amounts. For CloudSat's near-global observations, these shallow events comprise about 36% of snowfall occurrence and 18% of the global snowfall amount based on rates. Palerme et al. (2014) employed CloudSat snowfall estimates to generate the first multi-year, model-independent climatology of Antarctic precipitation and subsequently used these data to assess the performance of climate models (Palerme et al. 2017a) and reanalyses (Palerme et al. 2017b) for quantifying Antarctic snowfall. By comparing CloudSat snowfall estimates against matched observations by the Swedish national radar network, Norin et al. (2015) identified ground-based radar biases that result due to the decrease in sensitivity and overshooting with increasing range of shallow, snow-producing cloud systems common at high northern latitudes.

- **Light rainfall over oceans:** CloudSat has been used to estimate how much rainfall over oceans falls beneath the sensitivity threshold of other spaceborne precipitation radars. A few papers have attempted to combine CloudSat observations of light precipitation to the heavier precipitation estimates from other sensors in a statistical manner. The first study to do this by Berg et al. (2010) estimated that the Precipitation Radar (PR) missed about 10% of the accumulation over oceans within the tropical/subtropical sampling region of the Tropical Rainfall Measurement Mission (TRMM). More recently Behrangi et al. (2014b) estimate that the oceanic mean rain rate between $80°N$ and $80°S$ is 2.94 mm day^{-1}, which is 8% higher than that of Climate Prediction Center (CPC) Merged Analysis of Precipitation (CMAP) and 4% higher than that of the Global Precipitation Climatology Project (GPCP).

- **Stratiform/convective classification**: As already discussed, the PIA signal in CPR observations is a powerful indicator of rainfall and drizzle presence. Aside from depressed surface returns, the characteristic decay of reflectivity with decreasing height owing to attenuation provides a unique method for identifying convective cores in CloudSat observations. This is the premise behind a unique convective core detection algorithm that is part of the 2C-Precip-Column product (described below). The method can be thought of as a W-band analogue to identifying bright band signatures in more traditional precipitation radar observations (e.g., Steiner et al. 1995) but, in this case, the characteristic feature of interest is the inflection point in the reflectivity profile caused by attenuation from significant quantities of liquid precipitation. An example of such a signature was highlighted in Fig. 2.1. The level where attenuation becomes evident in the column is identified as '*rain top height*' (RTH) and forms the basis for identifying the presence of convective updrafts at the 1.4×1.7 km^2 CPR resolution. Strong convective updrafts can loft raindrops to high altitudes causing RTH to exceed the Freezing Level (FL) by several km and inducing large along-track reflectivity gradients. Stratiform precipitation is characterized by RTH near or slightly below the freezing level and often exhibits a bright band-like feature although its origins are primarily rooted in attenuation as opposed to enhanced reflectivity from large

melting ice particles (Sassen et al. 2007). Raining pixels with cloud and RTH below the FL constitute warm rain. CloudSat's rain type classification qualitatively agrees with bright band and convective features in TRMM PR reflectivity profiles. While the associated strong attenuation generally prohibits accurate rainfall intensity estimates in identified convective cores, the high resolution, high sensitivity CPR allow cores to be identified at a resolution comparable to ground-based radar providing a more precise depiction of updraft regions within storms than coarser resolution radar or passive sensors. As a result, the fractional area of convective cores identified by the CloudSat CPR is substantially lower than convection maps produced using sensors with coarser fields of view that may be only partially filled by convection (Fig. 2.5).
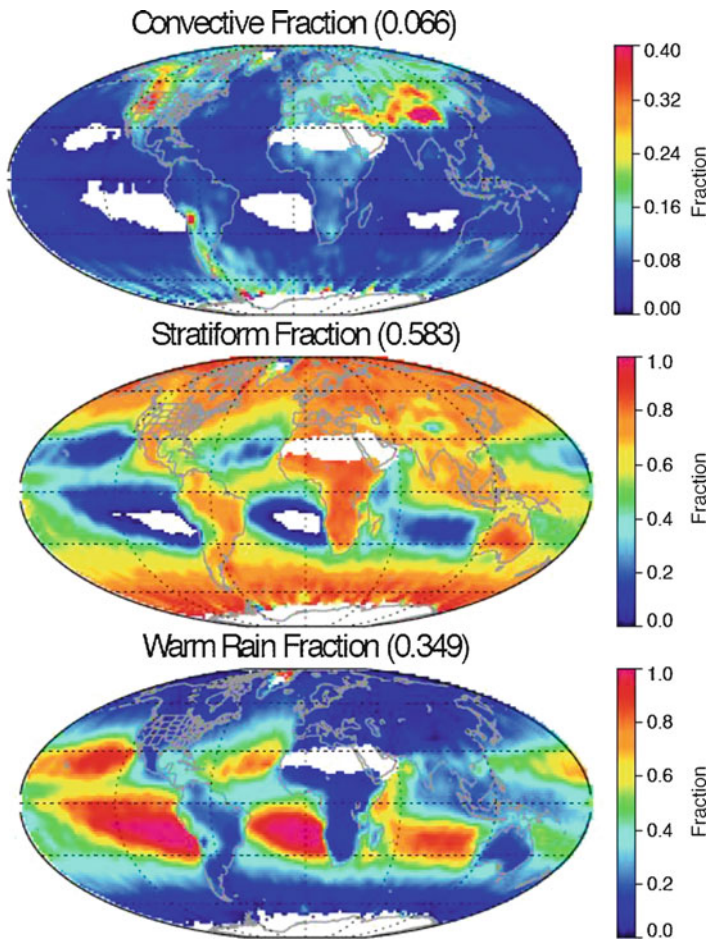
Fig. 2.5 The global frequency of occurrence of convective cores identified in CloudSat's 2C-Precip-Column product using data from 2007 to 2010

2.3 CloudSat Mission Operations History

CloudSat was launched into the A-Train on 28 April 2006, beginning operations shortly thereafter on 2 June. Operations proceeded relatively smoothly for approximately 5 years with only minor adjustments to the CPR pointing during the first few months of operations. A minor $1.7°$ pointing error was corrected on 2 July 2006. However, nadir pointing was found to increase specular reflection of the surface increasing ground clutter and the CPR was pointed $0.16°$ in the forward direction on 15 August. In practice these changes have very minor effects on the precipitation sensing capabilities of CloudSat.

In December 2009 a battery anomaly occurred that resulted in a prolonged period of halted radar operations into early 2010. Continued declines in the health of the battery led to small changes in the CPR pulse rate and reduced sensitivity in early 2010 and 2011, however the adjustments were far below the sensitivity required for precipitation detection. However, on 17 April 2011 a serious battery anomaly caused the CPR to power down and CloudSat to exit the A-Train. The compromised battery was no longer able to operate through umbra so a new Daylight Only Operations (DO-Op) had to be developed. The CPR was not turned back on in this DO-OP mode until November 2011 at which point it was well outside of the A-Train and no longer in a sun-synchronous orbit. A lengthy series of orbit maneuvers were begun to return CloudSat to the A-Train, which it rejoined on 15 May 2012. An intricacy of DO-Op is that it takes a finite amount of time for the spacecraft to require the sun and stabilize pointing before it can begin acquiring data on each orbit. This results in a gap in the sampling in the very high latitude southern hemisphere even during daylit hours (Skofronick-Jackson et al. 2018).

DO-OP mode continued successfully until a failure of a reaction wheel on 4 June 2017. As a result of this failure, it was decided that CloudSat should exit the A-Train to ensure the safety of the other constellation members. Very little science data was taken between the failure and the eventual exit. DO-OP resumed on 8 May 2018. The new CloudSat orbit is only slightly below the A-Train at 696 km altitude and maintains the 0130 AM/PM equator crossing time for the time being. In the near future CloudSat plans to begin to drift eastward (later in the day) to maintain coincidence with its companion satellite CALIPSO, which will soon run out of propellant.

The complicated operation history of CloudSat has little impact on the precipitation algorithms and data products described below. However, there are significant effects on the sampling in both the diurnal and annual cycle, which must be considered carefully. Four main sampling artifacts are noted: (1) the loss of the nocturnal sampling after 2011; (2) sampling outside of the 0130 AM/PM sun-synchronous orbit during late 2011 and early 2012; (3) uneven distribution of sampling across the annual cycle due to prolonged instrument down-time; and (4) during DO-Op disproportionate sampling of the northern high-latitudes as compared to the southern high latitudes through all seasons. Because of these sampling issues we provide the following guidance for using CloudSat data.

- Climatologies are best constructed using data from 2007 to 2010.
- Because there is a significant data loss during some winter months, annual averages should be constructed from monthly mean climatologies.
- Data during the period when CloudSat was not in formation with the A-Train (late 2011-mid 2012) should be used only for case studies.
- Time series should examine only ascending (daylit) data. Care should be taken at high-latitudes to ensure even sampling rates from month to month.

2.4   CloudSat Data Products

The CloudSat project produces three precipitation data products. The first is a precipitation identification and classification algorithm called 2C-Precip-Column, the second is a rain profiling algorithm called 2C-Rain-Profile, and the third is a snow profiling algorithm called 2C-Snow-Profile. The most recent version of the products is release 05, which is available as of June 2018. The data and associated Algorithm Theoretical Basis Documents (ATBD) for each algorithm can be accessed at the CloudSat data processing center (http://www.cloudsat.cira.colostate.edu/, last accessed 17 Nov. 2018). Summaries of each algorithm are provided below.

2.4.1   Precipitation Identification and Classification

The 2C-Precip-Column product is the original CloudSat precipitation product, and the theoretical basis is outlined in Haynes et al. (2009). The algorithm utilizes surface backscatter returns to derive the PIA in the atmospheric column, and in turn relates this PIA to the precipitation rate. Precipitation rate is assumed to be constant with height in this retrieval, a restriction which is removed in the 2C-Rain-Profile algorithm that will be described below. 2C-Precip-Column is run alongside 2C-Rain-Profile in today's suite of CloudSat algorithms. While the former is now used primarily for PIA estimation, precipitation flagging, and precipitation classification, the latter is recommended for quantitative precipitation rate estimates.

At the heart of the algorithm is the estimation of PIA. As the CPR radar beam intersects the ground, a great deal of energy is scattered back to the radar. The strength of this surface return is given by σ_0, which is the backscatter cross section of the Earth's surface normalized by the area of the radar footprint. Over land, σ_0 varies with surface type, roughness, and wetness; over ocean it is primarily a function of the wind speed and, to a lesser extent, surface temperature (e.g., Li et al. 2005, Freilich and Vanhoff 2003). Given a radar measurement of σ_0, including any intervening clouds, precipitation, and atmosphere; and a prediction of what that backscatter would be without the presence of said clouds and precipitation (σ_{clr}), it is possible to derive the PIA as

$$PIA = \sigma_{clr} - (\sigma_0 + G), \qquad (2.1)$$

where G is the gaseous attenuation, primarily from water vapor in the atmospheric column.

The key to retrieving PIA, therefore, is knowledge of the clear-sky surface backscatter. In 2C-Precip-Column this is obtained in one of two ways. The first is from the type of wind speed and sea-surface temperature relationships mentioned above, and illustrated in Fig. 2.6. The figure shows the relationship between derived surface wind speeds from the AMSR-E instrument (Advanced Microwave Scanning Radiometer – Earth Observing System), and collocated surface backscatter for oceanic scenes that the radar determined were clear of clouds. Note that the relationship is most useful for moderate wind speeds, as at low wind speeds the variability in σ_{clr} can be quite large. The second method of determining PIA in a cloudy scene is to interpolate the value of σ_{clr} from a set of nearby profiles that are known to be clear (if available), using a distance-based weighting function (Lebsock et al. 2011). Over ocean, 2C-Precip-Column uses this latter method when possible, as the resulting PIA uncertainties are generally smaller; in practice, however, the radar oftentimes observes large swaths of unbroken cloudiness, and in these cases the wind speed method must be used. The determination of PIA over land is considered experimental, as σ_0 can vary greatly between surface types.

2C-Precip-Column only attempts to quantify precipitation rate over ocean. Having determined the PIA, a series of predetermined lookup tables are used to relate the observed PIA to rain rate within the column. The appropriate lookup table is selected based on whether the profile is determined to be stratiform or convective/shallow, and on various cloud height and reflectivity-based thresholds as described below. Since multiple scattering can be significant when precipitation rates exceed more than a few millimeters per hour (Battaglia et al. 2008), these lookup tables are based on a forward model that simulates these effects (Hogan and Battaglia 2008).

Fig. 2.6 Variation of clear-sky surface backscatter with wind speed as derived from matched AMSR-E and CloudSat wind observations over the ocean, for a multi-month period and a fixed sea surface temperature range of 15 to 25 °C. Colors indicate normalized frequency of occurrence; the red line is the mean, and the dashed black lines are one standard deviation either side of the mean
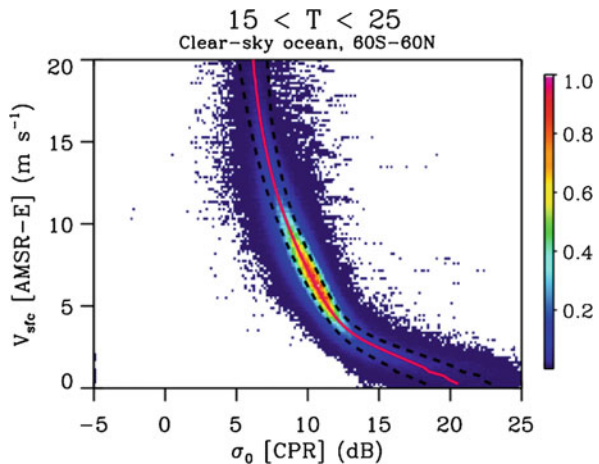
For stratiform modes, a melting layer model is incorporated to better represent the transition from snow to rain and the attenuation characteristics of melting snowflakes. Liquid or mixed precipitation layers are allowed to extend up to the height of the lowest continuous cloud layer (not exceeding the height of the freezing level). Attenuation due to purely frozen hydrometeors is neglected unless a significant reflectivity core of 10 dBZ or greater extends above the freezing level. In the absence of such a core, melting is considered to start at the freezing level. Surface precipitation type is determined simply from the proximity to the freezing level and by using an approximated lapse rate in the melting layer model.

For convective/shallow modes, precipitation is considered to be all liquid below the freezing level. Above the freezing level, a core that includes supercooled liquid is allowed to exist up to a height called the rain-top height (determined using reflectivity gradients); ice is also mixed in linearly with the liquid between the freezing level and the rain-top height. Above this level, up to the height of the 10 dBZ echo level, precipitation is considering to be all snow. Although this treatment neglects the preferential growth of ice particles dictated by the Bergeron-Findeisen process, it is probably a considerably better approximation of attenuation due to convective processes than the gradual melting of ice particles considered by the stratiform portion of the retrieval.

The occurrence of precipitation over ocean is determined by evaluating the unattenuated reflectivity, Z_u (i.e. the reflectivity that would be observed if there were no attenuation due to clouds and water vapor), at a height of several range gates above the Earth's surface. The reason a near-surface range gate is used is that there is considerably noise in the lowest several range gates above the surface. Given an observation of the attenuated near-surface reflectivity Z_{ns}, Z_u is given by

$$Z_u = Z_{ns} + PIA \cdot \chi + G, \tag{2.2}$$

where χ is a rain-rate dependent factor that removes attenuation affects in the radar column below the height of the near-surface range gate. Precipitation type-dependent reflectivity thresholds are used to translate Z_u into a precipitation mask. For example, for rain, values of Z_u between -15 and -7.5 dBZ indicate "rain possible", values between -7.5 and 0 dBZ indicate "rain probable", and larger values indicate "rain certain". Over land, where PIA cannot easily be determined, reflectivity thresholds at the near-surface are used to determine precipitation occurrence. The atmospheric column is also checked for large reflectivity values that may indicate that total attenuation has occurred, as in this case small values of reflectivity at the near-surface are also indicative of precipitation.

2.4.2 Quantifying Snowfall

The CloudSat product 2C-Snow-Profile (2CSP; Wood and L'Ecuyer 2018) estimates vertical profiles of snow water content along with snow size distribution parameters

and snowfall rate for radar reflectivity profiles observed by the CPR which, based on an evaluation of the profile and ancillary data, appear to coincide with snow aloft producing precipitation (snow, mixed-phase, or rain) at the surface. If the surface precipitation type appears to be dry snow or snow with only a small melted fraction as assessed by 2C-Precip-Column, the product also estimates the snowfall rate at the surface. The key features of the product are that it:

- provides vertically-resolved information about snowfall and snow properties extending to 82°N and 82°S latitudes,
- provides explicit estimates of uncertainties in retrieved and derived quantities, and
- treats complications due to radar attenuation and multiple scattering that can be significant in heavier snowfall, including allowing for increased retrieval uncertainty.

As is true for lower-frequency precipitation radars, radar backscattering at 94 GHz is sensitive to particle size distribution (PSD) and particle masses; however, at this higher frequency, backscattering by precipitation-sized particles is also strongly sensitive to particle shape. With even simple models for the PSD, the particle masses, and the particle shapes, reflectivity observations alone at 94 GHz are insufficient to constrain the models sufficiently to determine snow properties. As a result, the retrieval method used by 2CSP employs significant and explicit a priori information about PSD, mass, shape, and scattering properties and their uncertainties (Wood et al. 2013, 2014, 2015).

The retrieval uses an optimal estimation method (Rodgers 2000). The method minimizes a cost function which represents differences between simulated and observed reflectivity profiles and also differences between estimated and a priori values for the snow microphysical properties. The retrieval is applied to individual profiles of CPR reflectivity observations. For each profile, each of which contains a vertically-resolved vector of radar reflectivities, the retrieval estimates a vertically-resolved array of size distribution parameters for assumed exponential size distributions. These estimated parameters are then used along with the a priori assumptions about snow microphysical properties to derive vertical profiles of properties such as snow water content and snowfall rate.

In heavier snowfall, radar beam propagation at 94 GHz may be influenced by both attenuation by hydrometeors and multiple scattering. In 2CSP, propagation is modeled to include the effects of both attenuation and multiple scattering using a parameterization derived from Matrosov and Battaglia (2009). In this parameterization, the modeled multiply-scattered radar reflectivity and its uncertainty is estimated as a simple function of the modeled singly-scattered attenuated and unattenuated reflectivities.

The optimal estimation treatment allows the various sources of the retrieval uncertainties to be propagated explicitly into estimates of uncertainties in retrieval products such as snowfall rate. The snowfall retrieval represents retrieved quantities as Gaussian probability density functions (PDFs). These PDFs incorporate estimates of the uncertainties in the a priori information, in the model used to simulate the radar observations (the forward model), and in the observations. These PDFs define the

expected values and uncertainties for the retrieved quantities. When these expected values are then used to derive quantities such as snowfall rate and snow water content, the uncertainties are propagated as well. In this way, the retrieval provides explicit estimates for the uncertainties in the instantaneous retrieved and derived variables.

Aside from uncertainties related to a priori snow properties and radar forward model assumptions, a number of other issues may influence the accuracy of products like 2CSP developed from satellite-borne radar observations. First, determining the phase of precipitation particles both aloft and at the surface generally requires coincident information about atmospheric temperatures. 2CSP uses temperature profiles from European Centre for Medium-range Weather Forecasts medium-range forecasts collocated to the CPR radar profiles from the CloudSat ECMWF-AUX product. Due to the narrow temperature range of about 0–4 °C over which the transition from solid to liquid occurs (Liu 2008), small variations in temperature could lead to pronounced changes in precipitation phase classification and the associated precipitation.

Second, due to near-surface ground clutter mentioned earlier, snowfall rates at the surface have to be estimated based on retrieval results just above the clutter-affected radar range bins. For the CPR, this gap between the height of the retrieval results in the near-surface uncluttered bin and the actual surface ranges from about 700 to 1300 m, depending on the surface characteristics. This gap has two effects. First, microphysical and advective processes may cause the surface snowfall properties to vary in uncertain ways from those in the near-surface uncluttered bin. This is especially significant for snowfall, where particle fall speeds are generally about 1 m s^{-1} or smaller. Second, shallow snowfall events may be completely obscured by the ground clutter and go undetected.

Finally, in 2CSP snowfall rates at the surface and aloft are determined using estimated fall speeds for snow particles. These snowfall rates represent mass fluxes that transport water in and remove it from the atmosphere. 2CSP uses a parameterization for particle terminal velocities (Mitchell and Heymsfield 2005), and fall speeds are assumed to equal terminal velocities; however, clearly this assumption is accurate only for environments with no vertical air motion.

These issues represent opportunities for ongoing work and improvements in both retrieval approaches and in satellite-borne radar observational capabilities. Fall speed constraints from Doppler measurements, enhanced radar spatial resolution to reduce clutter, and increased employment of model-based atmospheric state information in retrievals may allow these limitations to be overcome to a greater degree than now possible.

2.4.3 Quantifying Rainfall

The 2C-Rain-Profile product produces profiles of rain water content and surface rain rate over ocean surfaces. The theoretical basis for the algorithm has been outlined in L'Ecuyer and Stephens (2002), Mitrescu et al. (2010) and Lebsock and L'Ecuyer

(2011). The algorithm uses the observed reflectivity profile and a measure of the Path Integrated Attenuation (PIA) to derive the rain water profiles using an optimal estimation framework. The PIA is derived in the 2C-Precip-Column algorithm described above. The utility of the PIA lies in the fact that it is primarily sensitive to the integrated rain water path through the column, and therefore provides a strong integral constraint on the rain profile retrievals.

The algorithm uses the optimal estimation approach to derive profiles of the rain water content. The true utility of the optimal estimation retrieval framework lies in careful error characterization, the details of which are buried in the process of defining the elements of the measurement and a priori error covariance matrices. A detailed description of the error characterization is provided in Lebsock and L'Ecuyer (2011) and the ATBD. There are two key aspects to the error covariances. First, the a priori error covariance is used not to constrain the estimated value of the rain water content but instead to impose rather tight correlations in the vertical from bin to bin so that the a priori acts as a smoothing constraint. Second the retrieval is strongly influenced by and exploits the attenuation signal. To account for attenuation in the measurement error the measurement error covariance matrix includes cumulative contributions from uncertainty within each bin along with uncertainty in the attenuation from all of the bins above it. A central focus of this process was to ensure a tight constraint on the retrieval from the integrate PIA relative to the reflectivity profile. This was done through inflating the reflectivity errors and introducing the correlations each of which decreases the contribution of the N reflectivity observations overwhelming a single PIA observation.

Both attenuation and multiple scattering must be accounted for in the radar forward model. Simulated radar reflectivities PIA are both corrected for the multiple scattering effects. Multiple scattering is modeled using the fast Time-Dependent Two-Stream (TDTS) method of Hogan and Battaglia (2008). The TDTS model has been shown to compare favorably with benchmark Monte Carlo simulations while being significantly more computationally efficient. The TDTS model is used to correct both the reflectivities and the observed PIA for multiple scattering effects. Multiple scattering always increases the apparent reflectivity therefore these corrections always reduce the single scattering reflectivity values while increasing the PIA estimate.

The problem of estimating the rain rate from the observations is incompletely defined as posed and requires a number of simplifying assumptions. These assumptions take the form of simple physical models that are imposed upon the problem to make the necessary radiative calculations possible. These models include: (1) a model to distribute cloud water in the vertical and determine the cloud DSD; (2) a model of evaporation of rain below cloud base; (3) a model of the precipitation DSD; and (4) a description of the thermodynamic phase of the hydrometeors in each radar bin. These models are described in this sub-section.

Cloud water must be modeled not because of its influence on the reflectivities themselves but rather due to its influence on the PIA. As a result, the location of the cloud water within the vertical profile is of second order importance. It is assumed within the algorithm that the cloud water content is uniform with height below the

freezing level and the cloud water path is given by a parameterization based on Lebsock and L'Ecuyer (2011).

A model of evaporation of rain water from cloud base to the surface is taken from Comstock et al. (2004). The evaporation fraction is based on the distance below cloud base and the mean radius of the drop size distribution. Based on a large sample of in-situ data in marine stratocumulus and cumulus Kalmus and Lebsock (2017) have reformulated the parameters in the original formulation to be representative of a diverse set of shallow precipitating regimes. This modified parameterization tends to increase evaporation in shallow cumulus and eliminates bias relative to in-situ observations.

We implement a single moment parameterization of the DSD as a function of the rain liquid water content taken from Abel and Boutle (2012) that was originally developed to improve model simulations of rainfall intensity but has much broader applicability. Through an analysis of a large amount of aircraft data they define this parameterization which provides the best fit to a diversity of rain types from heavy deep convective rain to stratocumulus drizzle. The parameterization assumes an exponential size distribution with a power law relationship between the slope and intercept parameters.

The vertical structure of thermodynamic phase is based on the stratiform/convective flag input from 2C-Precip-Column. For convective clouds liquid is assumed from the surface to the freezing level at which point there is a linear mixing of liquid and ice up to the rain top height, above which the profile is entirely ice. Stratiform profiles are ice from the top down to the freezing level at which point there is a linear ramp between ice and liquid (to represent the melting layer) below which the profile is assumed to be entirely liquid. Cloud liquid water is distributed uniformly throughout the liquid portion of the profile.

The optical properties of the liquid region are modeled assuming spherical drops and Mie theory. The optical properties of the mixed phase regions are modeled again assuming spherical drops as a mixture of liquid and ice using a Maxwell-Garnett mixing formulation (Meneghini and Liao 1996). The ice particle scattering properties are from the dataset of Leinonen and Szyrmer (2015). The properties are calculated using the discrete dipole approximation (DDA) for three-dimensional models of unrimed snowflake aggregates consisting of dendrite ice crystals. Due to the limited range of snowflake diameters available in the dataset, the cross sections for the smallest particles are instead derived with the T-matrix method. This is applied to oblate spheroids with the aspect ratio and the mass-dimension relation equivalent to the snowflakes in the dataset.

In the heaviest precipitation, the surface return may be completely saturated making an estimate of the surface cross section impossible. In this situation, only an estimate of the lower bound on the PIA may be made and the retrieval will be biased low. Figure 2.3 shows a map of the frequency of occurrence of this condition. Because these pixels likely have the heaviest rain rates that contribute disproportionately to rainfall accumulations, this scenario causes a rather severe bias in the data product. The results of this bias are seen clearly in Fig. 2.7, which compares the CPR accumulated rainfall over oceans with the DPR Ku band accumulations. Those
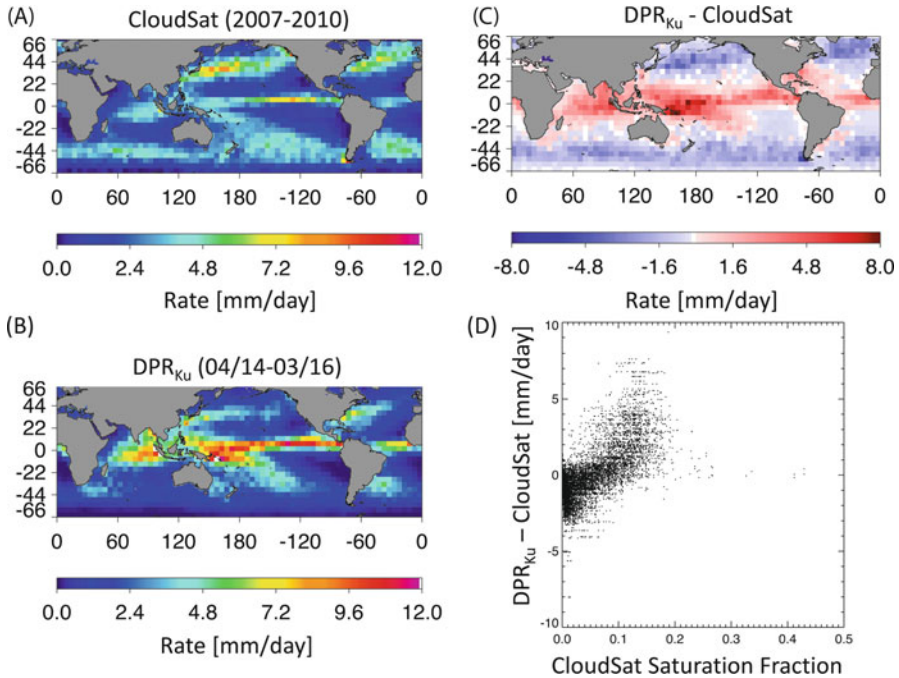
Fig. 2.7 (panel a) the accumulate rainfall from the CloudSat 2C-Rain Profile product for the years 2007–2010; (panel b) the same from the DRP Ku band algorithm for a 2-year period from 2014 to 2016; (panel c) the difference between panels a and b; (panel d) the scatter plot of the rate difference shown in panel c with the saturation occurrence fraction from CloudSat

differences are quite clearly associated with the occurrence of saturated CPR pixels, in which case the CPR underestimates the DPR. Note that different time periods are used for the two products and the figure is not meant as a comprehensive comparison between the two products.

References

Abel, S. J., & Boutle, I. A. (2012). An improved representation of the raindrop size distribution for single-moment microphysics schemes. *Quarterly Journal of the Royal Meteorological Society, 138*, 2151–2162. https://doi.org/10.1002/qj.1949.

Battaglia, A., Haynes, J. M., L'Ecuyer, T., & Simmer, C. (2008). Identifying multiple-scattering-affected profiles in CloudSat observations over the oceans. *Journal of Geophysical Research, 113*, D00A17. https://doi.org/10.1029/2008JD009960.

Behrangi, A., Tian, Y., Lambrigtsen, B. H., & Stephens, G. L. (2014a). What does CloudSat reveal about global land precipitation detection by other spaceborne sensors? *Water Resources Research, 50*, 4893–4905. https://doi.org/10.1002/2013WR014566.

Behrangi, A., Stephens, G. L., Adler, R. F., Huffman, G. J., Lambrigtsen, B., & Lebsock, M. D. (2014b). An update on the oceanic precipitation rate and its zonal distribution in light of advanced observations from space. *Journal of Climate, 27*, 3957–3965. https://doi.org/10.1175/JCLI-D-13-00679.1.

Berg, W., L'Ecuyer, T. S., & Haynes, J. M. (2010). The distribution of rainfall over oceans from spaceborne radars. *Journal of Applied Meteorology and Climatology, 49*, 535–543. https://doi.org/10.1175/2009JAMC2330.1.

Comstock, K. K., Wood, R., Yuter, S. E., & Bretherton, C. S. (2004). Reflectivity and rain rate in and below drizzling stratocumulus. *Quarterly Journal of the Royal Meteorological Society, 130*, 2891–2918. https://doi.org/10.1256/qj.03.187.

Freilich, M. H., & Vanhoff, B. A. (2003). The relationship between winds, surface roughness, and radar backscatter at low incidence angles from TRMM precipitation radar measurements. *Journal of Atmospheric and Oceanic Technology, 20*, 549–562. https://doi.org/10.1175/1520-0426(2003)20<549:TRBWSR>2.0.CO;2.

Haynes, J. M., L'Ecuyer, T. S., Stephens, G. L., Miller, S. D., Mitrescu, C., Wood, N. B., & Tanelli, S. (2009). Rainfall retrieval over the ocean with spaceborne W-band radar. *Journal of Geophysical Research, 114*, D00A22. https://doi.org/10.1029/2008JD009973.

Hogan, R. J., & Battaglia, A. (2008). Fast lidar and radar multiple-scattering models. Part II: Wide-angle scattering using the time-dependent two-stream approximation. *Journal of the Atmospheric Sciences, 65*, 3636–3651. https://doi.org/10.1175/2008JAS2643.1.

Joyce, R. J., Janowiak, J. E., Arkin, P. A., & Xie, P. (2004). CMORPH: A method that produces global precipitation estimates from passive microwave and infrared data at high spatial and temporal resolution. *Journal of Hydrometeorology, 5*, 487–503. https://doi.org/10.1175/1525-7541(2004)005<0487:CAMTPG>2.0.CO;2.

Kalmus, P., & Lebsock, M. D. (2017). Correcting biased evaporation in CloudSat warm rain. *IEEE Transactions on Geoscience and Remote Sensing*, 1–11. https://doi.org/10.1109/TGRS.2017.2722469.

Kollias, P., Rémillard, J., Luke, E., & Szyrmer, W. (2011). Cloud radar Doppler spectra in drizzling stratiform clouds: 1. Forward modeling and remote sensing applications. *Journal of Geophysical Research, 116*, D13201. https://doi.org/10.1029/2010JD015237.

Kulie, M. S., Milani, L., Wood, N. B., Tushaus, S. A., & Bennartz, R. (2016). A shallow cumuliform snowfall census using spaceborne radar. *Journal of Hydrometeorology, 17*, 1261–1279. https://doi.org/10.1175/JHM-D-0123.1.

Lebsock, M. D., & L'Ecuyer, T. S. (2011). The retrieval of warm rain from CloudSat. *Journal of Geophysical Research, 116*, D20209. https://doi.org/10.1029/2011JD016076.

Lebsock, M. D., L'Ecuyer, T. S., & Stephens, G. L. (2011). Detecting the ratio of rain and cloud water in low-latitude shallow marine clouds. *Journal of Applied Meteorology and Climatology, 50*, 419–432. https://doi.org/10.1175/2010JAMC2494.1.

L'Ecuyer, T. S., & Stephens, G. L. (2002). An estimation-based precipitation retrieval algorithm for attenuating radars. *Journal of Applied Meteorology, 41*, 272–285. https://doi.org/10.1175/1520-0450(2002)041<0272:AEBPRA>2.0.CO;2.

Leinonen, J., & Szyrmer, W. (2015). Radar signatures of snowflake riming: A modeling study. *Earth and Space Science, 2*, 346–358. https://doi.org/10.1002/2015EA000102.

Lhermitte, R. (1990). Attenuation and scattering of millimeter wavelength radiation by clouds and precipitation. *Journal of Atmospheric and Oceanic Technology, 7*, 464–479. https://doi.org/10.1175/1520-0426(1990)007<0464:AASOMW>2.0.CO;2.

Li, L. H., Heymsfield, G. M., Tian, L., & Racette, P. E. (2005). Measurements of ocean surface backscattering using an airborne 94-GHz cloud radar - implication for calibration of airborne and spaceborne W-band radars. *Journal of Atmospheric and Oceanic Technology, 22*, 1033–1045. https://doi.org/10.1175/JTECH1722.1.

Liu, G. (2008). Deriving snow cloud characteristics from CloudSat observations. *Journal of Geophysical Research, 113*, D00A09. https://doi.org/10.1029/2007JD009766.

Marchand, R., Mace, G. G., Ackerman, T., & Stephens, G. L. (2008). Hydrometeor detection using CloudSat—an Earth-orbiting 94-GHz cloud radar. *Journal of Atmospheric and Oceanic Technology, 25*, 519–533. https://doi.org/10.1175/2007JTECHA1006.1.

Matrosov, S. Y., & Battaglia, A. (2009). Influence of multiple scattering on CloudSat measurements in snow: A model study. *Geophysical Research Letters, 36*, L12806. https://doi.org/10.1029/2009GL038704.

Meneghini, R., & Liao, L. (1996). Comparisons of cross sections for melting hydrometeors as derived from dielectric mixing formulas and a numerical method. *Journal of Applied Meteorology, 35*, 1658–1670. https://doi.org/10.1175/1520-0450(1996)035<1658:COCSFM>2.0.CO;2.

Mitchell, D. L., & Heymsfield, A. J. (2005). Refinements in the treatment of ice particle terminal velocities, highlighting aggregates. *Journal of the Atmospheric Sciences, 62*, 1637–1644. https://doi.org/10.1175/JAS3413.1.

Mitrescu, C., L'Ecuyer, T. S., Haynes, J. M., Miller, S., & Turk, F. J. (2010). CloudSat precipitation profiling algorithm—model description. *Journal of Applied Meteorology and Climatology, 49*, 991–1003. https://doi.org/10.1175/2009JAMC2181.1.

Norin, L., Devasthale, A., L'Ecuyer, T. S., Wood, N. B., & Smalley, M. (2015). Intercomparison of snowfall estimates derived from the CloudSat cloud profiling radar and the ground-based weather radar network over Sweden. *Atmospheric Measurement Techniques, 8*, 5009–5021. https://doi.org/10.5194/amt-8-5009-2015.

Palerme, C., Kay, J. E., Genthon, C., L'Ecuyer, T. S., Wood, N. B., & Claud, C. (2014). How much snow falls on the Antarctic ice sheet? *The Cryosphere, 8*, 1577–1587. https://doi.org/10.5194/tc-8-1577-2014.

Palerme, C., Genthon, C., Claud, C., Kay, J. E., Wood, N. B., & L'Ecuyer, T. S. (2017a). Evaluation of current and projected Antarctic precipitation in CMIP5 models. *Climate Dynamics, 48*, 225–239. https://doi.org/10.1007/s00382-016-3071-1.

Palerme, C., Claud, C., Dufour, A., Genthon, C., Wood, N. B., & L'Ecuyer, T. S. (2017b). Evaluation of Antarctic snowfall in global meteorological reanalyses. *Atmospheric Research, 190*, 104–112. https://doi.org/10.1016/jatmos.res.2017.02.015.

Rodgers, C. D. (2000). *Inverse methods for atmospheric sounding: Theory and practice*. Singapore: World Scientific, 240 pp.

Sassen, K., & Wang, Z. (2008). Classifying clouds around the globe with the CloudSat radar: 1 year of results. *Geophysical Research Letters, 35*, L04805. https://doi.org/10.1029/2007GL032591.

Sassen, K., Matrosov, S., & Campbell, J. (2007). CloudSat spaceborne 94 GHz radar bright bands in the melting layer: An attenuation-driven upside-down lidar analog. *Geophysical Research Letters, 34*, L16818. https://doi.org/10.1029/2007GL030291.

Skofronick-Jackson, G., Kulie, M. S., Milani, L., Munchak, J., Wood, N. B., & Levizzani, V. (2018). Satellite estimation of falling snow: A global precipitation measurement (GPM) Core Observatory perspective. *Journal of Applied Meteorology and Climatology*, *58*, 1429–1448. https://doi.org/10.1175/JAMC-D-18-0124.1.

Smalley, M., L'Ecuyer, T. S., Lebsock, M. D., & Haynes, J. M. (2014). A comparison of precipitation occurrence from the NCEP stage IV QPE product and the CloudSat cloud profiling radar. *Journal of Hydrometeorology, 15*, 444–458. https://doi.org/10.1175/JHM-D-13-048.1.

Steiner, M., Houze, R. A., & Yuter, S. E. (1995). Climatological characterization of three-dimensional storm structure from operational radar and rain gauge data. *Journal of Applied Meteorology, 34*, 1978–2007. https://doi.org/10.1175/1520-0450(1995)034<1978:CCOTDS>2.0.CO;2.

Stephens, G. L., Winker, D., Pelon, J., Trepte, C., Vane, D., Yuhas, C., L'Ecuyer, T. S., & Lebsock, M. D. (2018). CloudSat and CALIPSO within the A-train: Ten years of actively observing the Earth system. *Bulletin of the American Meteorological Society, 99*, 569–581. https://doi.org/10.1175/BAMS-D-16-0324.1.

Tanelli, S., Durden, S. L., Im, E., Pak, K. S., Reinke, D. G., Partain, P., Haynes, J. M., & Marchand, R. T. (2008). CloudSat's cloud profiling radar after two years in orbit: Performance, calibration, and processing. *IEEE Transactions on Geoscience and Remote Sensing, 46*, 3560–3573. https://doi.org/10.1109/TGRS.2008.2002030.

Wood, N. B., & L'Ecuyer, T. S. (2018). Level 2C snow profile process description and interface control document, Product Version P1_R05, NASA JPL CloudSat project document revision 0, 26 pp. Available from http://www.cloudsat.cira.colostate.edu/sites/default/files/products/files/2C-SNOW-PROFILE_PDICD.P1_R05.rev0_.pdf, last accessed 5 Oct 2018.

Wood, N. B., L'Ecuyer, T. S., Bliven, F. L., & Stephens, G. L. (2013). Characterization of video disdrometer uncertainties and impacts on estimates of snowfall rate and radar reflectivity. *Atmospheric Measurement Techniques, 6*, 3635–3648. https://doi.org/10.5194/amt-6-3635-2013.

Wood, N. B., L'Ecuyer, T. S., Heymsfield, A. J., Stephens, G. L., Hudak, D. R., & Rodriguez, P. (2014). Estimating snow microphysical properties using collocated multisensor observations. *Journal of Geophysical Research, 119*, 8941–8961. https://doi.org/10.1002/2013JD021303.

Wood, N. B., L'Ecuyer, T. S., Heymsfield, A. J., & Stephens, G. L. (2015). Microphysical constraints on millimeter-wavelength scattering properties of snow particles. *Journal of Applied Meteorology and Climatology, 54*, 909–931. https://doi.org/10.1175/JAMC-D-14-0137.1.

Chapter 3
The Megha-Tropiques Mission After Seven Years in Space

Rémy Roca, Michel Dejus, Philippe Chambon, Sophie Cloché, and Michel Capderou

Abstract The Megha-Tropiques mission is operating since 12 October, 2011 and serves research and operational objectives related to the tropical water and energy cycle. The satellite is on a low inclination orbit that enhances the sampling over the intertropical belt. The original payloads were dedicated to the estimation of the radiation budget at the top of the atmosphere, the water vapor profiles and the instantaneous precipitation rate. The original suite of geophysical products that was developed permitted to demonstrate the proof of concept of the mission in the early part of its operation. Following an unfortunately expedited exploitation of the conically scanning multispectral radiometer (16 months), efforts have been geared to mitigate the loss by extending the use of the 183 GHz sounder towards the precipitation objectives. This induced some delays in the setting of the current set of products that are now being used for research investigations. Despite not being an operational meteorological satellite, the real time capability of the mission has shown its usefulness with a large and growing set of Numerical Weather Prediction centers assimilating the Megha-Tropiques data, in clear and total skies. After 7 years in space, the satellite and operating instruments are in excellent shape and sustain their very good initial performances. The mission has acquired a large and unique set of observations of the tropical water and energy cycle which is only at the beginning of its exploitation.

R. Roca (✉)
CNRS/LEGOS, Toulouse, France
e-mail: remy.roca@legos.obs-mip.fr

M. Dejus
CNES, Toulouse, France

P. Chambon
Météo France, CNRM/GMAP/OBS, Toulouse, France

S. Cloché
CNRS/IPSL, Palaiseau, France

M. Capderou
CNRS/LMD, Palaiseau, France

3.1 Introduction

The water and energy cycle is central to the functioning of the Earth system. The strong coupling between water and energy is at the core of the process that regulates the temperature of the planet (Stephens and Ellis 2008; Roca et al. 2010). The water and energy climatic feedbacks are the dominant source of warming associated with the anthropogenic increase greenhouse gas concentration (Ramanathan 1981). In the tropics, the tight link between the hydrological cycle and the large-scale dynamics further complicates the understanding of these feedbacks and the estimation of their magnitude (Ma et al. 2018; Stephens et al. 2018). At the heart of the complexity is the deep convection process that has been under investigation for over a century and is still not fully understood (Houze 2018). The convective systems that influence both the radiation and the hydrological cycle are ubiquitous in the tropics and happen at the meso- and sub-daily scale making their observations a challenge (see Chap. 38 of volume 2). In complement to the existing space-based effort to monitor precipitation (Hou et al. 2014) and the radiation budget (Loeb et al. 2018), an enhanced sampling of the tropical region in line with the underlying tropical phenomenon is needed.

Megha stands for clouds in Sanskrit and Tropiques for tropics in French. The Megha-Tropiques mission is an Indo-French mission dedicated to the surveillance of the atmospheric water and energy cycle of the intertropical belt. Within the large questions mentioned above, the specific scientific objectives of the mission are:

- The monitoring of the water and energy budget of the intertropical belt.
- The understanding of the life cycle of tropical convective systems.
- The functioning of tropical surface hydrometeorology.
- The improvements of tropical weather forecasts.

The three first objectives are related to research questions and the fourth one is associated with operational numerical weather prediction.

The mission has been built and operated jointly by the Indian Space Research Organization (ISRO) and the Centre National d'Etudes Spatiales (CNES). The satellite was successfully launched in October 2011 from the ISRO pad in Sriharicota using a PSLV rocket. The mission is characterized by a unique orbit with a low inclination on the equator that permits a high repetition of the measurements (up to 6 times a day). A suite of complementary payloads is carried on board: a scanning broad band radiometer for Earth radiation budget measurements: SCARAB (Viollier and Raberanto 2010; Chomette et al. 2012), a radio-occultation GPS receiver (ROSA, Radio Occultation Sensor for Atmosphere, Karouche and Raju 2010) and of more importance to the present paper, a conical scanning multispectral microwave imager MADRAS (Microwave Analysis and Detection of Rain and

Atmospheric Structures) and a cross scanning microwave sounder, SAPHIR that stands for Sondeur Atmosphérique du Profile d'Humidité Intertropicale par Radiométrie (Eymard et al. 2002).

A number of publications are describing the Megha-Tropiques mission (Desbois et al. 2003). Desbois et al. (2007) provides a historical account on the genesis of the mission, Roca et al. (2010) elaborates on the scientific objectives of the mission while Roca et al. (2015) report the status of the mission after 3 years in operation. The Handbook of the mission is also a useful resource (CNES 2015). Here we focus on the salient features of the mission and on the incremental new information since this last status publication with emphasis on the two latter instruments that contributes to the rainfall related objectives.

3.2 The Status of the Mission

3.2.1 Orbital Aspects

The originality of the MT orbit lies in the sampling. The orbit of the mission is a quasi-circular orbit with a flight altitude of 865.5 km and a low inclination on the Equator (Capderou 2009). This unique orbit was selected after various discussions during the development phase and also to avoid the 1-day phasing trap that would otherwise occur at the ~820 km initially selected altitude. Under such orbital configuration, the tropical regions are seen, by on-board instruments, about 6 times a day. Near the tropics, the passages are made in a single pack of 6 consecutive overpasses (each overpass being separated by a time equivalent to the satellite period of 100 min). Near the equator, they are made in two disjointed packs, of 2 passages each, separated by half a day (Roca et al. 2015).

Another consequence of this orbit is that the cycle in relation to the Sun is 53 days. This means that when the satellite overpasses at a given time at a given location, it will be 53 days before it returns to the same time. In other words, the satellite's overpass to the equator is made each day with an advance of (1440 min/ 53) or 27 min. This advance is therefore roughly half an hour a day. In addition, this cycle requires the position of the satellite's solar panels to be adapted with the direction of the Sun rays. It must be carried out several times a year, a so-called "flip" maneuver: the satellite makes a U-turn on itself (the front passes to the back). Figure 3.1 shows an illustration of the change in the satellite-sun geometry over a 2-year period. The 53 days' precession cycle is also clearly seen in using this metric.

While strict maintenance at this altitude was not specified by the scientists, since October 2011, the MT altitude has been remarkably well maintained by ISRO between 865.37 and 865.57 km, an amplitude of 100 m relative to the nominal mean value, which is the standard for satellites like Aqua, Terra and remote sensing satellites like Pleiades or Landsat (Vijayasree et al. 2014). All the checks have shown that the flight segment (satellite and instrument) is in good health and fully within the specifications. Despite that, the satellite control center decided not to control the yaw
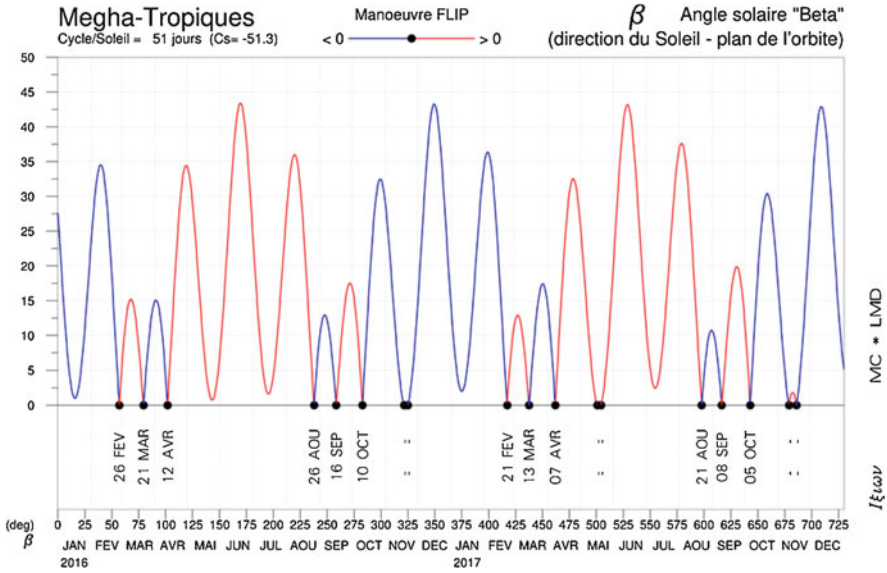
Fig. 3.1 Two-years times series of the flip maneuver schedule based on the beta solar angle (the angle between the sun direction and the orbital plan; see Capderou 2014 for details)
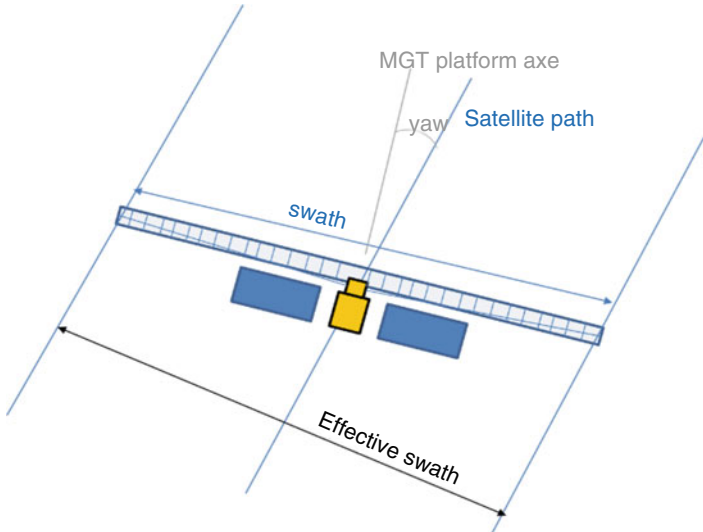
Fig. 3.2 Schematic of the effect of the relaxed control of the yaw

of the satellite in the future in the same exact way as it was done till now. The yaw angle can change in the window $\pm 10°$ (Fig. 3.2). An analysis based on that assumption shows that the effect is minor. This does not affect the localization of

the product because the restitution of this parameter will still lie within the specification. Moreover, the quality of the products will not degrade as the swath will rotate of the same value as the yaw does and the revisit time will thus change only negligibly.

3.2.2 The MADRAS Radiometer

The MADRAS radiometer is a five-frequency, nine-channel conical scanning passive microwave imager. The radiometer observes the Earth with a 53.5° angle in both horizontal and vertical polarizations. The radiometer is presented at length in various earlier publications (Desbois et al. 2003; Karouche and Raju 2010; Karouche et al. 2012; Raju 2013; Roca et al. 2015) and here we only present its salient features. Table 3.1 summarize the channel frequency and performances.

After a few months in operation the MADRAS data showed signs of electric perturbations that altered the multiplexing of the multispectral observations preventing any scientific use of the data flow. This early contamination was termed the "glitch" effect and was a sign of early aging of the instrument and eventually MADRAS stopped data acquisition on 26 January, 2013 after a little less than 1.5 years of data acquisition. Wendt et al. (2016) further investigated the consequence of the glitch and proposed a very efficient patch to recover the channel multiplexing errors and allowing the scientific exploitation of the dataset to be pursued. CNES and ISRO eventually made 16 months of corrected data available to the public in November 2015.

3.2.3 The SAPHIR Sounder

The SAPHIR sounders consists in a 6-channel microwave sounder operating near the absorption band of water vapor at 183 GHz (Eymard et al. 2002). The nadir pixel dimension is 10×10 km^2 along and across track and varies respectively up to 23 km and 16 km at the end of the scan. The swath is close to 1700 km across.

Investigators from the NASA GPM science team (Personal communication) pointed out a shift in the geometry of the instrument on the ground. Indeed, it was confirmed by CNES that the nadir pixel is not at the center of the swath of the scan but the true nadir is shifted. This shift is illustrated in Fig. 3.3 that shows the maximum latitude of the scan as a function of time. The figure reveals a very

Table 3.1 MADRAS channel frequency and noise levels

Frequency	18.6	18.6	23.8	36.5	36.5	89.0	89.0	157.0	157.0
Polarization	H	V	V	H	V	H	V	H	V
NEΔT	0.57	0.7	0.67	0.58	0.67	0.93	0.89	2.07	2.16

Adapted from Karouche et al. (2012) and Goldstein and Karouche (2013)
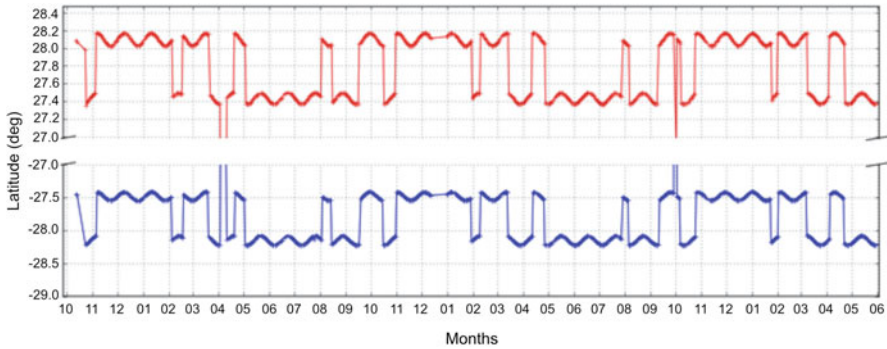
Fig. 3.3 Time series of maximum (red) and minimum (blue) latitude of the scan of the SAPHIR instrument

Table 3.2 Noise and difference with simulations in K for each SAPHIR channels

Channel #	Frequency(GHz)	NEΔT specifications	NEΔT In flight	RS-data(K)
1	183 ± 0.2	2.4	1.4	+0.2
2	183 ± 1.1	1.8	1.0	+0.7
3	183 ± 2.8	1.8	0.9	+1.3
4	183 ± 4.2	1.5	0.8	+1.6
5	183 ± 6.6	1.5	0.6	+1.5
6	183 ± 11	1.2	0.5	+2.3

Adapted from Karouche et al. (2012) and Clain et al. (2015)

weak random variation (~0.01°) which was confirmed by the instrument commissioning as well as a sinusoidal 33 days' variation (~0.2°) due to the slight departure from circular orbit (e = 0.00102). The larger changes are related to the flip-flop maneuver and provide an estimate of the shift to ~1 pixel (0.1° on Earth). SAPHIR dissymmetry is explained by the accommodation done on the platform.

While it is an important aspect of the geometry of scan, it should be noted that the actual location of each individual pixel in level 1 data are not affected by the shift and that the dissymmetry is taken in account in ground segment parameters and guaranty the perfect location of the products well within the specifications (<5 km).

The absolute accuracy of the calibration of the radiometer has been investigated in details. The post-launch estimation of the calibration sustained a better behavior than the specifications (Table 3.2) in lines with intercomparisons with other similar radiometers (Moradi et al. 2015). Independent evaluation of the calibration using high quality radiosondes confirmed the good accuracy of the sounder and revealed a 2 K warm anomaly on the 183±11 GHz channel (Clain et al. 2015). This was further shown to likely be attributable to the lack of representation of the water vapor continuum in the radiation simulations (Brogniez et al. 2016) although this is still under investigation and debate (Bobryshev et al. 2018).

The stability of the radiometer, both mechanically and radiometrically, is monitored by CNES using a suite of automated diagnostics. More than 150 parameters are surveyed daily. The instrument has reached more than 136 million rotations (as of
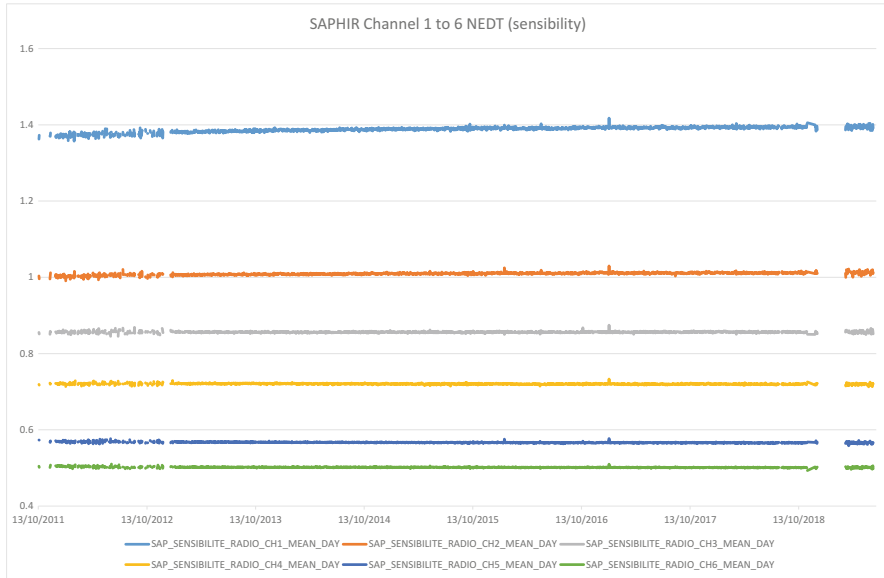
Fig. 3.4 Time series of the noise (NEΔT) for each channel of the SAPHIR sounder

14 June 2018) and no sign of aging on the mechanics is found. An example of such monitoring is shown in Fig. 3.4 where the time series of the noise of the channels is plotted against time. The monitoring shows the flat steady behavior of the radiometer. The data availability is close to 99.99% over the course of the last 7 years. The few missing observations and orbits are due to Space Situational Awareness (SSA) and technical issues at ground segment and some links cut that occurred only before 2016 and the implementation of backup link for the stations.

This overall good behavior has prompted many users to make benefit of the SAPHIR data, including its use as a calibration reference for the sounders of the GPM constellation (Berg et al. 2016) and various research and applications illustrated in the next sections.

3.3 Addressing the Scientific Objectives

3.3.1 Precipitation Related Remote Sensing Products from MT Payloads

A suite of operational geophysical products has been developed in support of the scientific objectives and are discussed in Gohil et al. (2013), Kidd et al. (2013) and Roca et al. (2015). These operational products concern the instantaneous rainfall estimation from MADRAS and a large spectrum of non-scattering skies water vapor

Fig. 3.5 Zonal mean of the fraction of time for which the baseline product and the No-meghatropiques products differs by more than 50% of the daily accumulation. Summer 2012 conditions are considered. (Adapted from Roca et al. 2018)
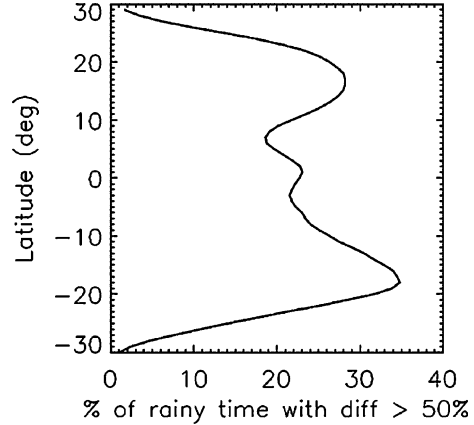
profiles retrievals. Research efforts have also yield to experimental products ranging from land emissivity estimation (Raju et al. 2013) to ice water content (Piyush et al. 2017). More recently, the SAPHIR data are being used for instantaneous rainfall detection and estimation (Balaji et al. 2014; Goyal et al. 2014; Varma et al. 2016) allowing for a mitigation of the loss of MADRAS to the scientific objectives of the mission. Efforts to adapt the sounder retrievals designed for MHS and AMSU-B (Kidd et al. 2016) to SAPHIR is also underway (Chap. 24; merging IR and MW datasets). The Megha-Tropiques data are not used in a standalone approach but also merged with the GPM constellation data (Hou et al. 2014) to estimate the accumulated precipitation at the $1° \times 1°$ daily scale (Chambon et al. 2012). The SAPHIR detection capability are used to bring in the constellation based the tropical enhanced sampling of the mission as discussed in Chap. 24 on the Merging of IR data with MW observations. The evaluation of this product is shown to outperform the currently existing product over West Africa (Gosset et al. 2018).

This is by large attributable to the enhanced sampling of the mission as detailed in Roca et al. (2018). Figure 3.5 shows the number of days for which including the SAPHIR sampling in the constellation do alter by more than 50% the estimated daily accumulation. It is a convolution of the sampling pattern of SAPHIR with the actual rain distribution. During summer over the 10–15° latitude band, the impact can reach up to 30%.

3.3.2   Tropical Science

Following the demise of MADRAS and the shift to using SAPHIR towards precipitation related objectives to mitigate the loss of the conical radiometer, the commissioning of the geophysical operational product was substantially delayed from the original plan. Yet tropical science studies based on the suite of geophysical products are now emerging along the different research objectives.

3.3.2.1 Hydrometeorology

Tropical hydrometeorology investigations strongly rely on satellite derived precipitation estimate owing to the scarcity of the conventional observation networks over tropical land. The potential for the use of the GPM/Megha-Tropiques accumulation product was demonstrated over the Niger basin and shown to fulfill the accuracy expectation for flood forecasts there (Casse et al. 2015) allowing more hydrometeorological investigations (see Chap. 24). The information content of the satellite products is also shown to be scale dependent, with low to null correlation between the ground-based radar observations and various satellite products detection at scale lower than 50 km/3 h (Guilloteau et al. 2016) prompting the need to build upon downscaling approaches to provide precipitation estimation at these fine hydrological sensitive scales (Guilloteau et al. 2016). The consequence of these recent analysis on the development of the next generation of precipitation products is discussed in Chap. 24.

3.3.2.2 Deep Convection

Deep convective clouds observations by MADRAS have been used, in particular the 157 GHz polarized channels to explore the microphysics of the storms and the crystal orientation that is found to be mainly horizontal (Defer et al. 2014). AMSU-B 3 channel deep convection identification method has been extended to the 6 channels of SAPHIR revealing the exceedance occurrence of very deep convective clouds (overshooting) in the northern most part of the Bay of Bengal compared to the very active environment all through the Bay (Mathew et al. 2016). Intra-seasonal variability of precipitation in the ITCZ over Eastern Pacific is shown to be impacted by the organization of mesoscale convective systems and not only by the variability of their occurrence (Berthet et al. 2017).

Efforts to revisit the conceptual model of the life cycle of tropical MCS are also on going where IR observations are merged with microwave observations to explore the scaling of deep convective regions to the fuller extent of the anvil clouds of the systems along its life cycle (Fiolleau and Roca 2013; Bouniol et al. 2016; Roca et al. 2017).

3.4 Addressing the Operational Objective

SAPHIR was proven useful for operational Numerical Weather Predictions by several weather services across the globe. In particular, four-dimensional data assimilation systems like 4D-Var are well adapted tools to benefit from Megha-Tropiques low-inclined orbit. Figure 3.6 illustrates its high temporal sampling of the
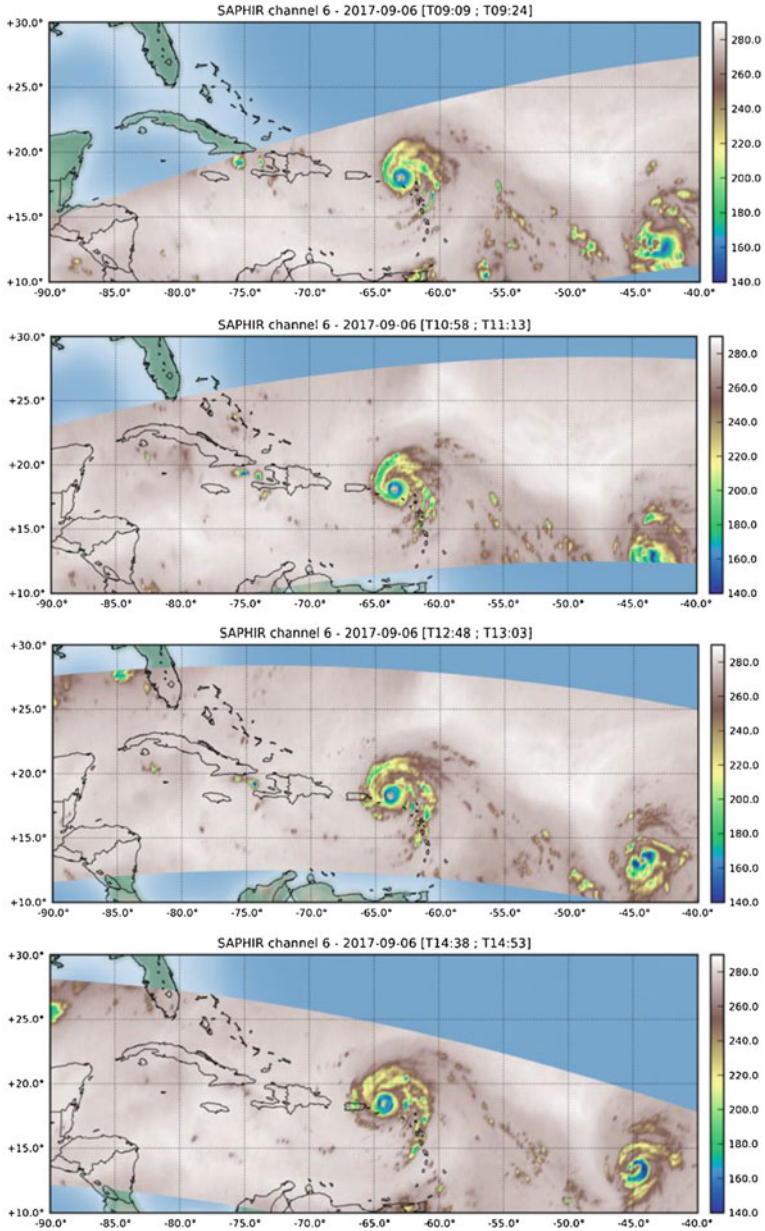
Fig. 3.6 Brightness temperatures from SAPHIR channel 6 over the Tropical Atlantic on 6 September, 2017. The four scans correspond to consecutive orbits and show the developments of the two hurricanes IRMA and JOSE. These two hurricanes were observed within the same orbit, illustrating the unique feature of this observing system

same meteorological scene, like hurricanes Irma and Jose in September 2017 and caused major losses and damages on several of the Caribbean Islands.

3.4.1 Upstream Investigations

A number of SAPHIR data assimilation studies have been performed in the past years, either in operational centers or in research laboratories. They focused both on global (e.g., Chambon et al. 2015; Prasad and Singh 2016; Krishnamoorthy and Balaji 2016; Chambon and Geer 2017; Jones et al. 2017; Singh and Prasad 2017; Dhanya and Chandrasekar 2018; Doherty et al. 2018; Kumar et al. 2018) and regional models (e.g., Singh et al. 2013; Chandramouli and Balaji 2018) with a particular focus on tropical cyclone forecasting (e.g., Dhanya et al. 2016; Guerbette et al. 2016; Dhanya and Chandrasekar 2018).

All the studies mentioned above have been investigating the impact of clear sky SAPHIR observations onto NWP analyses and forecasts. Within these clear-sky frameworks, positive impacts have been demonstrated onto forecasts of tropical winds and humidity up to several days ahead, as well as a positive synergy with the rest of the observing system. In particular, an improvement of the innovation statistics (observations – model first guess) of infrared geostationary satellites as well as humidity channels of hyperspectral infrared instruments was shown in these different numerical weather prediction systems.

Another move forward toward the usage of SAPHIR observations was the investigation conducted at the European Center for Medium-range Weather Forecast (ECMWF) with the so-called all-sky system which take benefit from both clear and cloudy observations of SAPHIR (Chambon and Geer 2017). The all-sky assimilation experiments of SAPHIR observations was made possible thanks to the recent improvements of the radiative transfer model RTTOV-SCATT, using non-spherical particle shapes for the radiative properties of snowfall (Geer and Baordo 2014) of particular importance at the SAPHIR frequencies. These studies performed by Chambon and Geer (2017) showed that assimilating SAPHIR data have a similar impact than assimilating the data from 2 to 3 MHS sounders within the Tropics.

At Météo-France, developments are also ongoing for assimilating SAPHIR observations in cloudy and rainy areas to complement the clear-sky assimilation with an original Bayesian framework (Wattrelot et al. 2014). A feasibility study was first performed by Guerbette et al. (2016), then a full assimilation framework was implemented in the Météo-France system to perform assimilation tests of SAPHIR observations in a context close to the operational framework (Duruisseau et al. 2017). The impacts onto tropical winds and temperature forecasts, obtained by only adding the cloudy and rainy observations of SAPHIR within the Météo-France global model are very encouraging and may lead to the operational implementation of this framework in a few years from now.

Some of the upstream investigations mentioned above led to the operational assimilation of SAPHIR observations in several numerical weather predictions centers which are listed in the next section.

3.4.2 Operational Applications

The Megha-Tropiques ground component is complex and extensive. It consists of a ground component aggregate having also other functions. Roles are shared between France and India, mainly CNES and ISRO. ISRO is in charge of the mission center, located in Bangalore, which manages the satellite and processes the raw data to Level 1 based on CNES specifications. The data are collected by a network of three stations: Bangalore (ISRO), Kourou (CNES) and Hartbeesthoek (CNES). SAPHIR NRT data (L1 DUMP) are produced and sent to EUMETSAT for further dissemination via EUMETCAST to meteorological agencies, all in less than 3 h. Thanks to this broadcasting system users can have access to the SAPHIR Level 1 data, into both HDF and BUFR formats, with a latency compatible with NWP applications. Indeed, a large fraction of the data arrives in less than 4 h after acquisition. Figure 3.7 below shows an example of the fraction of the SAPHIR dataset than have been used for the period June 2015 to June 2018 within the Météo-France global data assimilation system which is characterized by a 4-h cutoff for its 6-h assimilation cycle. Apart from two "outliers" in these statistics (May and December 2017), this averaged fraction reaches 66% which is a high fraction for a satellite mission which was not originally designed to fulfill NWP operational requirements.

Météo-France and the Japan Meteorological Agency started assimilating SAPHIR observations operationally in 2015 (e.g., Chambon et al. 2015). The positive impacts demonstrated on tropical forecasts with their clear sky assimilation frameworks were confirmed by the Met Office which started assimilating SAPHIR data in 2016 (Doherty et al. 2018) as well as by the Joint Center for Satellite Data Assimilation (JCSDA) which extended the National Oceanic and Atmospheric Administration (NOAA) Global Data Assimilation System/Global Forecast System (GDAS/GFS) to assimilate SAPHIR brightness temperatures (Jones et al. 2017). This latter work performed by JCSDA led to the operational assimilation of SAPHIR data within
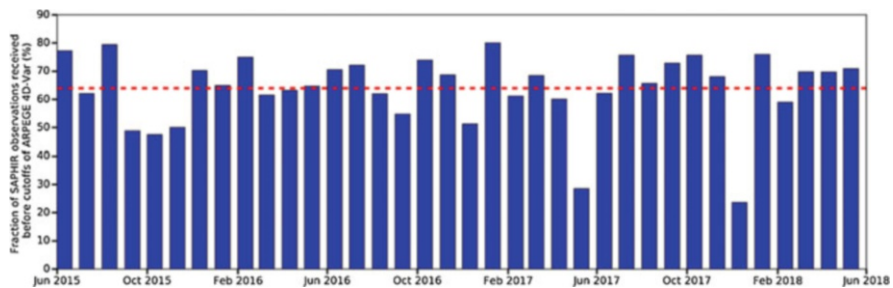
Fig. 3.7 Fraction of SAPHIR observations per month which have been received and used a Météo-France before the cutoff times of the Météo-France global data assimilation system (4–5 h depending on the assimilation cycle) (Courtesy of Hervé Benichou, Météo-France DIROP/COM-PAS/COM). The period starts in June 2015, which corresponds to the beginning of the operational assimilation of Megha-Tropiques data at Météo-France. The dashed red line refers to the averaged fraction over this 4-year period

Table 3.3 List of weather prediction agencies which are assimilating SAPHIR observations within an operational framework

Numerical Weather Prediction Center	Assimilation method for SAPHIR	References
European Centre for Medium-range Weather Forecasts (ECMWF)	All-sky	Chambon and Geer (2017)
Fleet Numerical Meteorology and Oceanography Center (FNMOC) – US Navy	Clear-sky	Jones et al. (2017) and Karpowicz et al. (2017)
Japan Meteorological Agency (JMA)	Clear-sky	
Joint Center for Satellite Data Assimilation (JCSDA)	Clear-sky	Jones et al. (2017)
Korea Meteorological Administration (KMA)	Clear-sky	
Météo France	Clear-sky	Chambon et al. (2015)
National Center for Environmental Predictions (NCEP)	Clear-sky	Jones et al. (2017)
UK Met Office	Clear-sky	Doherty et al. (2018)

the 2018 parallel suite of the National Centers for Environmental Prediction (NCEP) global model at NOAA as well as Fleet Numerical Meteorology and Oceanography Center (FNMOC) of the United States Navy (Karpowicz et al. 2017).

Table 3.3 summarizes the agencies which are, to the knowledge of the authors, assimilating SAPHIR observations operationally.

These efforts of the international community to bring SAPHIR data within their operational system showcase, if needed, the proof of concept of a low inclination orbit mission and its high added value to the operational observing system. It is also a good indicator for future satellite missions onto tropical orbits providing enhanced sampling of these regions, like the TROPICS mission (Blackwell et al. 2018) which will provide microwave observations at a frequency close to geostationary satellite.

The various research and operational use of the SAPHIR instruments by different numerical weather prediction systems confirming, if needed, the proof of concept of a low inclination orbit mission and its high added value to the operational observing system.

3.5   Conclusions and Outlook

After a long commissioning phase, the Megha-Tropiques observations and products have been made widely available for both research investigations and operational use. The demise of the MADRAS instrument required an enhanced effort to mitigate the loss using the sounder instead, to address the precipitation related objective of the mission. The proof of concept of a water and energy tropical mission has been demonstrated. In the era of GPM, the tropical precipitation estimation as well as the tropical weather forecasts both benefit significantly from the sampling of the

mission. The excellent performances of the two sensors SAPHIR (and SCARAB) after 7 years in space grants further success for the mission. The legacy of the Megha-Tropiques mission, instrument or orbit wise, is already at play in upcoming missions like MetOP-SG/MWI and TROPICS, or emerging mission concept like D-TRAIN (Haddad et al. 2018).

References

Balaji, C., Krishnamoorthy, C., & Chandrasekar, R. (2014). On the possibility of retrieving near surface rain rate from the microwave sounder SAPHIR of the Megha-Tropiques mission. *Current Science*, *106*, 587–593. Available at https://www.jstor.org/stable/24100066, last accessed 7 Dec 2018.

Berg, W., Bilanow, S., Chen, R., Datta, S., Draper, D., Ebrahimi, H., Farrar, S., Jones, W. L., Kroodsma, R., McKague, D., Payne, V., Wang, J., Wilheit, T., & Yang, J. X. (2016). Intercalibration of the GPM microwave radiometer constellation. *Journal of Atmospheric and Oceanic Technology, 33*, 2639–2654. https://doi.org/10.1175/JTECH-D-16-0100.1.

Berthet, S., Roca, R., Duvel, J. P., & Fiolleau, T. (2017). Subseasonal variability of mesoscale convective systems over the tropical northeastern Pacific. *Quarterly Journal of the Royal Meteorological Society, 143*, 1086–1094. https://doi.org/10.1002/qj.2992.

Blackwell, W. J., Braun, S., Bennartz, R., Velden, C., DeMaria, M., Atlas, R., Dunion, J., Marks, F., Rogers, R., Annane, B., & Leslie, R. V. (2018). An overview of the TROPICS NASA earth venture Mission. *Quarterly Journal of the Royal Meteorological Society, 144*, 16–26. https://doi.org/10.1002/qj.3290.

Bobryshev, O., Buehler, S. A., John, V. O., Brath, M., & Brogniez, H. (2018). Is there really a closure gap between 183.31-GHz satellite passive microwave and in situ radiosonde water vapor measurements? *IEEE Transactions on Geoscience and Remote Sensing, 56*, 2904–2910. https://doi.org/10.1109/TGRS.2017.2786548.

Bouniol, D., Roca, R., Fiolleau, T., & Poan, D. E. (2016). Macrophysical, microphysical, and radiative properties of tropical mesoscale convective systems over their life cycle. *Journal of Climate, 29*, 3353–3371. https://doi.org/10.1175/jcli-d-15-0551.1.

Brogniez, H., English, S., Mahfouf, J.-F., Behrendt, A., Berg, W., Boukabara, S., Buehler, S. A., Chambon, P., Gambacorta, A., Geer, A., Ingram, W., Kursinski, E. R., Matricardi, M., Odintsova, T. A., Payne, V. H., Thorne, P. W., Tretyakov, M. Y., & Wang, J. (2016). A review of sources of systematic errors and uncertainties in observations and simulations at 183 GHz. *Atmospheric Measurement Techniques, 9*, 2207–2221. https://doi.org/10.5194/amt-9-2207-2016.

Capderou, M. (2009). Sampling comparison with other meteorological satellites. Megha-Tropiques Technical Memorandum, 1, 49 pp. Available at http://meghatropiques.ipsl.polytechnique.fr/megha-tropiques-technical-memorandum/, last accessed 7 Dec 2018.

Casse, C., Gosset, M., Peugeot, C., Pedinotti, V., Boone, A., Tanimoun, B. A., & Decharme, B. (2015). Potential of satellite rainfall products to predict Niger River flood events in Niamey. *Atmospheric Research, 163*, 162–176. https://doi.org/10.1016/j.atmosres.2015.01.010.

Chambon, P., & Geer, A. (2017). All-sky assimilation of Megha-Tropiques/SAPHIR radiances in the ECMWF numerical weather prediction system. *ECMWF Research Department Memorandum*, 802, 45 pp. Available at https://www.ecmwf.int/en/elibrary/17253-all-sky-assimilation-megha-tropiques-saphir-radiances-ecmwf-numerical-weather, last accessed 7 Dec 2018.

Chambon, P., Jobard, I., Roca, R., & Viltard, N. (2012). An investigation of the error budget of tropical rainfall accumulation derived from merged passive microwave and infrared satellite measurements. *Quarterly Journal of the Royal Meteorological Society, 139*, 879–893. https://doi.org/10.1002/qj.1907.

Chambon, P., Meunier, L.-F., Guillaume, F., Piriou, J.-M., Roca, R., & Mahfouf, J.-F. (2015). Investigating the impact of the water-vapour sounding observations from SAPHIR on board Megha-Tropiques for the ARPEGE global model. *Quarterly Journal of the Royal Meteorological Society, 141*, 1769–1779. https://doi.org/10.1002/qj.2478.

Chandramouli, K., & Balaji, C. (2018). Ingesting microwave sounder radiances for improvement in track forecast of cyclone Vardah. *Journal of Applied Remote Sensing, 12*.

Chomette, O., Kandel, R., Raberanto, P., Roca, R., & Viollier, M. (2012). The European experiment ScaRaB (scanner for radiation budget). In: *GEWEX-RFA Report,* WCRP report no. 19/2012, E. Raschke, Kinne, S., & Stackhouse, P. W., (Eds.), (pp. 75–80). Available at https://www.wcrp-climate.org/documents/GEWEX%20RFA-Volume%202-appendices.pdf, last accessed 5 Oct 2018.

Clain, G., Brogniez, H., Payne, V. H., John, V. O., & Luo, M. (2015). An assessment of SAPHIR calibration using quality tropical soundings. *Journal of Atmospheric and Oceanic Technology, 32*, 61–78. https://doi.org/10.1175/jtech-d-14-00054.1.

CNES. (2015). *The MEGHA-TROPIQUES Level 1 products handbook*. Available at http://www.icare.univ-lille1.fr/projects_data/mt/docs/megha-tropiques_handbook_final_09_2015.pdf, last accessed 5 Oct 2018.

Defer, E., Galligani, V. S., Prigent, C., & Jimenez, C. (2014). First observations of polarized scattering over ice clouds at close-to-millimeter wavelengths (157 GHz) with MADRAS on board the Megha-Tropiques mission. *Journal of Geophysical Research, 119*, 12301–12316. https://doi.org/10.1002/2014JD022353.

Desbois, M., Roca, R., Eymard, L., Viltard, N., Viollier, M., Srinivasan, J., & Narayanan, S. (2003). The Megha-Tropiques mission. *SPIE, Atmospheric and Oceanic Processes, Dynamics, and Climate Change*. https://doi.org/10.1117/12.466703.

Desbois, M., Capderou, M., Eymard, L., Roca, R., Viltard, N., Viollier, M., & Karouche, N. (2007). Megha-Tropiques: Un satellite hydrométéorologique franco-indien. *La Météorologie, 8*, 19. https://doi.org/10.4267/2042/18185.

Dhanya, M., & Chandrasekar, A. (2018). Multivariate background error covariances in the assimilation of SAPHIR radiances in the simulation of three tropical cyclones over the Bay of Bengal using the WRF model. *International Journal of Remote Sensing, 39*, 191–209. https://doi.org/10.1080/01431161.2017.1381350.

Dhanya, M., Gopalakrishnan, D., Chandrasekar, A., Singh, S. K., & Prasad, V. S. (2016). The impact of assimilating Megha-Tropiques SAPHIR radiances in the simulation of tropical cyclones over the Bay of Bengal using the WRF model. *International Journal of Remote Sensing, 37*, 3086–3103. https://doi.org/10.1080/01431161.2016.1194542.

Doherty, A., Rani, S. I., Newman, S., & Bell, W. (2018). Benefits of assimilating SAPHIR observations on analysis and forecasts of tropical fields in the Met Office global model. *Quarterly Journal of the Royal Meteorological Society, 144*(S1), 405–418. https://doi.org/10.1002/qj.3258.

Duruisseau, F., Chambon, P., Guedj, S., Guidard, V., Fourrié, N., Taillefer, F., Brousseau, P., Mahfouf, J.-F., & Roca, R. (2017). Investigating the potential benefit to a mesoscale NWP model of a microwave sounder on board a geostationary satellite. *Quarterly Journal of the Royal Meteorological Society, 143*, 2104–2115. https://doi.org/10.1002/qj.3070.

Eymard, L., & Coauthors. (2002). The SAPHIR humidity sounder. *MEGHATROPIQUES 2nd scientific workshop*, 2–6 July 2001, Paris, France.

Fiolleau, T., & Roca, R. (2013). Composite life cycle of tropical mesoscale convective systems from geostationary and low earth orbit satellite observations: Method and sampling considerations. *Quarterly Journal of the Royal Meteorological Society, 139*, 941–953. https://doi.org/10.1002/qj.2174.

Geer, A. J., & Baordo, F. (2014). Improved scattering radiative transfer for frozen hydrometeors at microwave frequencies. *Atmospheric Measurement Techniques, 7*, 1839–1860. https://doi.org/10.5194/amt-7-1839-2014.

Gohil, B. S., Gairola, R. M., Mathur, A. K., Varma, A. K., Mahesh, C., Gangwar, R. K., & Pal, P. K. (2013). Algorithms for retrieving geophysical parameters from the MADRAS and SAPHIR sensors of the Megha-Tropiques satellite: Indian scenario. *Quarterly Journal of the Royal Meteorological Society, 139*, 954–963. https://doi.org/10.1002/qj.2041.

Goldstein, C., & Karouche, N. (2013). CAL/VAL MADRAS radiometric sensitivity. Rep. MAD_RAD_02 TRO-NT-32-NT-2817-CNES, 8. Available at https://megha-tropiques.cnes.fr/sites/default/files/migration/smsc/megha-tropiques/PDF/MADRASRadiometricSensitivity.pdf, last accessed 5 Oct 2018.

Gosset, M., Alcoba, M., Roca, R., Cloché, S., & Urbani, G. (2018). Evaluation of TAPEER daily estimates and other GPM era products against dense gauge networks in West Africa, analyzing ground reference uncertainty. *Quarterly Journal of the Royal Meteorological Society, 144*(S1), 255–269. https://doi.org/10.1002/qj.3335.

Goyal, J. M., Srinivasan, J., & Satheesh, S. K. (2014). Can SAPHIR instrument onboard MEGHATROPIQUES retrieve hydrometeors and rainfall characteristics? AGU fall meeting abstracts.

Guerbette, J., Mahfouf, J.-F., & Plu, M. (2016). Towards the assimilation of all-sky microwave radiances from the SAPHIR humidity sounder in a limited area NWP model over tropical regions. *Tellus A, 68*. https://doi.org/10.3402/tellusa.v68.28620.

Guilloteau, C., Roca, R., & Gosset, M. (2016). A multiscale evaluation of the detection capabilities of high-resolution satellite precipitation products in West Africa. *Journal of Hydrometeorology, 17*, 2041–2059. https://doi.org/10.1175/jhm-d-15-0148.1.

Haddad, Z. S., & Coauthors. (2018). Distributed satellite microwave observation strategies for cloud and precipitation dynamics. *Current Science*, submitted.

Hou, A. Y., Kakar, R. K., Neeck, S., Azarbarzin, A. A., Kummerow, C. D., Kojima, M., Oki, R., Nakamura, K., & Iguchi, T. (2014). The Global Precipitation Measurement (GPM) mission. *Bulletin of the American Meteorological Society, 95*, 711–722. https://doi.org/10.1175/BAMS-D-13-00164.1.

Houze, R. A., Jr. (2018). 100 years of research on MCS. In *A Century of progress in atmospheric and related sciences: celebrating the American Meteorological Society centennial* (American meteorological society monograph) (Vol. 17, pp. 1–17.54). https://doi.org/10.1175/AMSMONOGRAPHS-D-18-0001.1.

Jones, E. E., Garrett, K., & Boukabara, S. A. (2017). Assimilation of Megha-Tropiques SAPHIR observations in the NOAA global model. *Monthly Weather Review, 145*, 3725–3744. https://doi.org/10.1175/MWR-D-16-0148.1.

Karouche, N., & Raju, G. (2010). Megha-Tropiques satellite mission: Sensors performances. *Sensors, Systems, and Next-Generation Satellites, XIV*. https://doi.org/10.1117/12.868048.

Karouche, N., Goldstein, C., Rosak, A., Malassingne, C., & Raju, G. (2012). Megha-Tropiques satellite mission: In flight performances results. *IEEE Geoscience and Remote Sensing Symposium (IGARSS)*, 4684–4687. https://doi.org/10.1109/IGARSS.2012.6350420.

Karpowicz, B., Ruston, B., & Swadley, S. (2017). *Microwave radiance assimilation at NRL: Advanced techniques, developments and future sensorts*. 21st International TOVS study conference, Darmstadt, Germany, 29 November–5 December. Available at http://cimss.ssec.wisc.edu/itwg/itsc/itsc21/program/posters/4p.05_karpowicz.pdf, last accessed 4 Oct 2018.

Kidd, C., Srinivasan, J., & Roca, R. (2013). The Megha-Tropiques mission: Day 1 algorithms. *Quarterly Journal of the Royal Meteorological Society, 139*, 841. https://doi.org/10.1002/qj.2201.

Kidd, C., Matsui, T., Chern, J., Mohr, K., Kummerow, C., & Randel, D. (2016). Global precipitation estimates from cross-track passive microwave observations using a physically based retrieval scheme. *Journal of Hydrometeorology, 17*, 383–400. https://doi.org/10.1175/JHM-D-15-0051.1.

Krishnamoorthy, C., & Balaji, C. (2016). Impact of horizontal and vertical localization scales on microwave sounder SAPHIR radiance assimilation. *SPIE-APRS, Remote Sensing of the Atmosphere, Clouds, and Precipitation VI, 9876*, New Delhi, 4–7 April.

Kumar, S., Rani, S. I., George, J. P., & Rajagopal, E. N. (2018). Megha-Tropiques SAPHIR radiances in a hybrid 4D-Var data assimilation system: Study of forecast impact. *Quarterly Journal of the Royal Meteorological Society, 144*, 792–805. https://doi.org/10.1002/qj.3251.

Loeb, N. G., Doelling, D. R., Wang, H., Su, W., Nguyen, C., Corbett, J. G., Liang, L., Mitrescu, C., Rose, F. G., & Kato, S. (2018). Clouds and the Earth's Radiant Energy System (CERES) Energy Balanced and Filled (EBAF) Top-of-Atmosphere (TOA) Edition-4.0 data product. *Journal of Climate, 31*, 895–918. https://doi.org/10.1175/JCLI-D-17-0208.1.

Ma, J., Chadwick, R., Seo, K.-H., Dong, C., Huang, G., Foltz, G. R., & Jiang, J. H. (2018). Responses of the tropical atmospheric circulation to climate change and connection to the hydrological cycle. *Annual Review of Earth and Planetary Sciences, 46*, 549–580. https://doi.org/10.1146/annurevearth-082517-010102.

Mathew, N., Raju, C. S., Renju, R., & Antony, T. (2016). Distribution of tropical deep convective clouds from Megha-Tropiques SAPHIR data. *IEEE Transactions on Geoscience and Remote Sensing, 54*, 6409–6414. https://doi.org/10.1109/TGRS.2016.2584540.

Moradi, I., Ferraro, R. R., Eriksson, P., & Weng, F. (2015). Intercalibration and validation of observations from ATMS and SAPHIR microwave sounders. *IEEE Transactions on Geoscience and Remote Sensing, 53*, 5915–5925. https://doi.org/10.1109/TGRS.2015.2427165.

Piyush, D. N., Goyal, J., & Srinivasan, J. (2017). Retrieval of cloud ice water path using SAPHIR on board Megha-Tropiques over the tropical ocean. *Advances in Space Research, 59*, 1895–1906. https://doi.org/10.1016/J.ASR.2017.01.022.

Prasad, V. S., & Singh, S. K. (2016). Efforts in assimilating Indian satellite data in the NGFS and monitoring of their quality. *Proceedings SPIE 9882, Remote Sensing and Modeling of the Atmosphere, Oceans, and Interactions VI, 98821E*. https://doi.org/10.1117/12.2223550.

Raju, G. (2013). Engineering challenges in the Megha-Tropiques satellite. *Current Science, 104*, 1662–1670.

Raju, C. S., Antony, Y., Mathew, N., Uma, K. N., & Krishna Moorthy, K. (2013). MT-MADRAS brightness temperature analysis for terrain characterization and land surface microwave emissivity estimation. *Current Science, 104*, 1643–1649.

Ramanathan, V. (1981). The role of ocean-atmosphere interactions in the CO_2 climate problem. *Journal of the Atmospheric Sciences, 38*, 918–930. https://doi.org/10.1175/1520-0469(1981)038<0918:TROOAI>2.0.CO;2.

Roca, R., Bergès, J.-C., Brogniez, H., Capderou, M., Chambon, P., Chomette, O., Cloché, S., Fiolleau, T., Jobard, I., Lémond, J., Ly, M., Picon, L., Raberanto, P., Szantai, A., & Viollier, M. (2010). On the water and energy cycles in the tropics. *Comptes Rendus Geoscience, 342*, 390–402. https://doi.org/10.1016/j.crte.2010.01.003.

Roca, R., Brogniez, H., Chambon, P., Chomette, O., Cloché, S., Gosset, M. E., Mahfouf, J.-F., Raberanto, P., & Viltard, N. (2015). The Megha-Tropiques mission: A review after three years in orbit. *Frontiers in Earth Science, 3*. https://doi.org/10.3389/feart.2015.00017.

Roca, R., Fiolleau, T., & Bouniol, D. (2017). A simple model of the life cycle of mesoscale convective systems cloud shield in the tropics. *Journal of Climate, 30*, 4283–4298. https://doi.org/10.1175/JCLID-16-0556.1.

Roca, R., Taburet, N., Lorant, E., Chambon, P., Alcoba, M., Brogniez, H., Cloché, S., Dufour, C., Gosset, M., & Guilloteau, C. (2018). Quantifying the contribution of the Megha-Tropiques mission to the estimation of daily accumulated rainfall in the tropics. *Quarterly Journal of the Royal Meteorological Society, 144*(S1), 49–63. https://doi.org/10.1002/qj.3327.

Singh, S. K., & Prasad, V. S. (2017). Impact of Megha-Tropiques SAPHIR radiances in T574L64 global data assimilation and forecasting system at NCMRWF. *International Journal of Remote Sensing, 38*(16), 4587–4610. https://doi.org/10.1080/01431161.2017.1323279.

Singh, R., Ojha, S. P., Kishtawal, C. M., & Pal, P. K. (2013). Quality assessment and assimilation of Megha-Tropiques SAPHIR radiances into WRF assimilation system. *Journal of Geophysical Research, 118*(13), 6957–6969. https://doi.org/10.1002/jgrd.50502.

Stephens, G. L., & Ellis, T. D. (2008). Controls of global-mean precipitation increases in global warming GCM experiments. *Journal of Climate, 21*, 6141–6155. https://doi.org/10.1175/2008jcli2144.1.

Stephens, G. L., Hakuba, M. Z., Webb, M. J., Lebsock, M. D., Yue, Q., Kahn, B. H., Hristova-Veleva, S., Rapp, A. D., Stubenrauch, C. J., Elsaesser, G. S., & Slingo, J. (2018). Regional intensification of the tropical hydrological cycle during ENSO. *Geophysical Research Letters, 45*, 4361–4370. https://doi.org/10.1029/2018GL077598.

Varma, A. K., Piyush, D. N., Gohil, B. S., Pal, P. K., & Srinivasan, J. (2016). Rain detection and measurement from Megha-Tropiques microwave sounder-SAPHIR. *Journal of Geophysical Research, 121*, 9191–9207. https://doi.org/10.1002/2016JD024907.

Vijayasree, P., Kumar, N., Karidhal, R., Harendranath, K., Kesava Raju, V., & Shivakumar, S. K. (2014). Megha-Tropiques: Mission planning, analysis, and operations. *International Journal of Remote Sensing, 35*, 5370–5383. https://doi.org/10.1080/01431161.2014.926412.

Viollier, M., & Raberanto, P. (2010). Radiometric and spectral characteristics of the ScaRaB-3 instrument on Megha-Tropiques: Comparisons with ERBE, CERES, and GERB. *Journal of Atmospheric and Oceanic Technology, 27*, 428–442. https://doi.org/10.1175/2009jtecha1307.1.

Wattrelot, E., Caumont, O., & Mahfouf, J.-F. (2014). Operational implementation of the 1D+ 3D-Var assimilation method of radar reflectivity data in the AROME model. *Monthly Weather Review, 142*(5), 1852–1873. https://doi.org/10.1175/MWR-D-13-00230.1.

Wendt, H., Dobigeon, N., Tourneret, J.-Y., Albinet, M., Goldstein, C., & Karouche, N. (2016). Detection and correction of glitches in a multiplexed multichannel data stream application to the MADRAS instrument. *IEEE Transactions on Geoscience and Remote Sensing, 54*, 2803–2811. https://doi.org/10.1109/TGRS.2015.2505902.

Chapter 4
Microwave Sensors, Imagers and Sounders

Kazumasa Aonashi and Ralph R. Ferraro

Abstract Passive microwave sensors flown on low Earth orbiting satellites are the cornerstones to precipitation retrieval because of their strong connection to the physical processes related to rain and snow. They penetrate through cirrus clouds and respond to both liquid and frozen hydrometeors which are highly correlated to surface precipitation rates. Despite their rather coarse spatial resolution and less frequent temporal sampling as compared to geostationary based visible and infrared measurements, the evolution of the microwave sensors through both research and operational missions have led to their important role in global precipitation retrieval. This chapter summarizes the primary microwave sensors and their attributes for the past 40 years.

Keywords Precipitation · Rainfall · Snowfall · Satellite · Microwave · Radiometers · Imagers · Sounders · Polarization · Cross-track scan · Conical scan · Precipitable water · Cloud liquid water

4.1 Introduction

Passive microwave sensors have flown on both research and operational missions for over 40 years. They have evolved from research missions in their early stages, to operational missions that supported weather forecasting. Over time, newer technology was developed, tested and advanced through a number of international research missions focusing on Earth science applications, with a growing emphasis on instrument stability for tracking climate variability and change.

K. Aonashi (✉)
Meteorological Research Institute, Japan Meteorological Agency, Tsukuba, Japan
e-mail: aonashi@mri-jma.go.jp

R. R. Ferraro
NOAA/NESDIS/STAR, College Park, MD, USA

Because of antenna size constraints, to date, all passive microwave sensors have been flown on low-Earth orbiting satellites. This then provides the best spatial resolution opportunities as opposed to flying it on a geostationary platform, although this option is being discussed by several agencies through the use of synthetic aperture antennas and will someday become a reality. As a general rule, the operational sensors are placed on satellites that are in a sun-synchronous orbit whereas several of the research satellites are orbited in different inclination planes to provide for a much broader sampling of the diurnal cycle.

Figure 4.1 provides a time sequence of the super-typhoon NANGKA images from 0540 to 1731 UTC 12 July 2015, observed by various microwave sensors around 89 GHz, except 36 GHz for WindSat. Note the general similarity in the features related to the storm, however, sensor resolution differences can be seen, where the AMSR2 and GMI show more detailed structure whereas AMSU-B shows less because of its coarser spatial resolution. Each of these sensors will be described in more detail in the sections that follow.
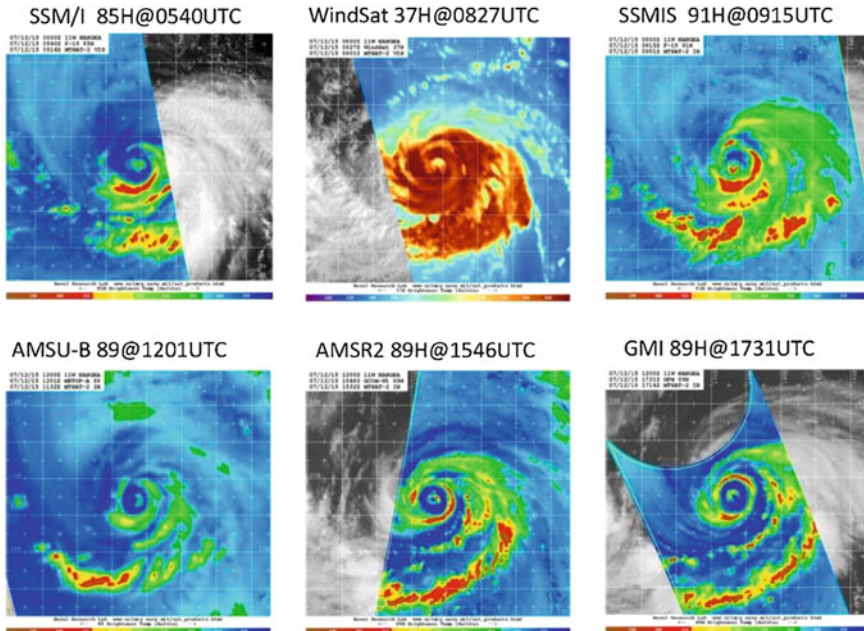
Fig. 4.1 A time sequence of the microwave images of the super-typhoon NANGKA from 0540 to 1731 UTC 12 July 2015, superimposed on MTSAT IR images. (From NRL Tropical Cyclone page – https://www.nrlmry.navy.mil/TC.html, last accessed 21 Oct 2018)

4.2   Characteristics of Microwave Imagers

Microwave Imagers (MWIs) observe brightness temperatures (TBs) mainly in microwave window regions to monitor atmospheric water subsistence, surface variables over ocean and land. Some MWIs also have channels near the weak H_2O absorption band (22.3 GHz) to see Precipitable Water Content (PWC). Table 4.1 shows typical satellite MWI channels used for the retrieval of the physical variables. PWC and Cloud Liquid Water Content (CLWC) retrievals over sea mainly employ 23 and 37 GHz. 10–19 GHz provide valuable information about rain over ocean, while 89 GHz and higher frequencies are sensitive to frozen precipitation. Low frequency channels ($\leq$10 GHz) are necessary for Sea Surface Temperature (SST) and over-land soil moisture retrievals. 37 GHz channels are mainly used for Sea Surface Wind (SSW) retrievals. Sea ice and over-land snow depth are retrieved based on the sensitivity differences between 19 GHz and higher frequencies. Surface reflectivity in the microwave spectrum greatly varies in terms of the incident angle and polarization. Hence, most MWIs except for earliest sensors scanned conically to observe TBs at constant surface incident angles and polarizations (horizontal and vertical).

Early MWIs adopted Dicke radiometer design which switched the receiver input between the antenna and reference load in order to calibrate TBs. The Special Sensor Microwave Imager (SSM/I) demonstrated a new design, combination of total-power radiometer and rotary-scanning for direct calibration of the whole system including its feed horn. The success of the SSM/I has made this design the standard for later MWIs.

Recent MWIs have installed large antenna in order to alleviate lower spatial resolution compared with infrared or visible radiometers. The following sections introduce the major satellite MWI's data from the 1970's to the present (see Table 4.2).

Table 4.1 Typical MWI channels used for the retrieval of the physical variables ◉ and ○ denotes necessary and important channels, respectively. S and L denotes over-sea and over-land retrievals, respectively

	7 GHz	10 GHz	19 GHz	23 GHz	37 GHz	89 GHz	183 GHz
PWC (S)			○	◉	○		
CLWC (S)			○	○	◉		
Rain (S)		○	◉		○		
Frozen precipitation (S/L)					○	◉	○
SST (S)	◉	◉	○	○			
Sea surface wind (S)	○	○	○		◉		
Sea ice (S)		○	◉		◉	○	
Snow (L)			◉		◉	○	
Soil moisture (L)	◉	◉	○				

Table 4.2 Major satellite MWIs from the 1970s to the present

Satellite/Launch year	Sensor	Frequencies (GHz)	Swath width (km)	Highest horizontal resolution (km)
Nimbus5/1972	ESMR	19.35	3000	25 × 25
Nimbus6/1975	ESMR	37	1300	20 × 40
Nimbus7/1978	SMMR	6.6, 10.69, 18, 21, 37	800	18 × 27
SEASAT/1978	SMMR	6.6, 10.69, 18, 21, 37	600	14 × 21
DMSP5D2/1987	SSM/I	19.35, 22.235, 37, 85.5	1394	13 × 15
TRMM/1997	TMI	10.65, 19.35, 21.3, 37, 85.5	759	5 × 7
Coriolis/2003	WindSat	6.8, 10.7, 18.7, 23.8	950	8 × 13
Aqua/2003	AMSR-E	6.925, 10.65,18.7, 23.8, 36.5, 89	1445	4 × 6
GCOMW1/2012	AMSR2	6.925, 7.3, 10.65, 18.7, 23.8, 36.5, 89	1450	3 × 5
GPM/2014	GMI	10.65, 18.7, 23.8, 36.5, 89, 165.5, 183 ± 3, 183 ± 7	885	4 × 6

4.2.1   The Electrically Scanning Microwave Radiometers (ESMRs)

The first ESMR was on Nimbus-5 launched in 1972. This sensor was an electrically cross-tracked Dicke radiometer which observed linearly polarized TBs at 19.35 GHz (Wilheit 1972). The second ESMR was flown aboard Nimbus-6 in 1975. This electrically scanning Dicke radiometer was designed to observe dual polarized, 37 GHz TBs at a nearly constant surface incident angle (~50°) (Wilheit 1975). Tables 4.3 and 4.4 illustrate radiometric performance characteristics of the ESMRs. Studies using the ESMR TBs (Wilheit et al. 1977, Weinman and Guetter 1977) indicated that the TBs were valuable for rain retrieval over sea.

4.2.2   The Scanning Multichannel Microwave Radiometer (SMMR)

The SMMR was on Nimbus-7 and SEASAT launched in 1978. The Nimbus-7 sensor operated for many years while the SMMR on SEASAT failed after a few years of operation. The SMMR sensor was a Dicke radiometer which observed dual-polarized TBs at 5 frequencies from 6.6 to 37 GHz. The SMMR scanned conically with surface incident angle of 50° for Nimbus-7, and 49° for SEASAT (Gloersen and Barath 1977) . Table 4.5 provides the radiometric performance characteristics of the SMMR (Gloersen and Hardis 1978). Studies using SMMR multi-frequency TBs (e.g., Wilheit and Chang 1980) proposed retrieval algorithms for various atmospheric and surface variables.

Table 4.3 Radiometric performance characteristics of ESMR on NIMBUS-5

Central frequency (GHz)	RF band width (MHz)	Polarization	Antenna beam width	IFOV (km)	Sensitivity (K)
19.35	300	Linear	1.4° × 1.4°~ 2.4° × 1.4°	25 × 25 ~ 45 × 160	1.5

Table 4.4 Radiometric performance characteristics of ESMR on NIMBUS-6

Central frequency (GHz)	RF band width (MHz)	Polarization	Antenna beam width	IFOV (km)	Sensitivity (K)
19.35	300	Linear	1.4° × 1.4°~ 2.4° × 1.4°	25 × 25 ~ 45 × 160	1.5

Table 4.5 Radiometric performance characteristics of SMMR on NIMBUS-7, SEASAT

Central frequency (GHz)	RF band width (MHz)	Polarization	Antenna beam width	IFOV (km) Nimbus7(N) SEASAT(S)	Sensitivity (K)
6.6	220	H&V	4.2°	148 × 95 (N) 121 × 79 (S)	0.9
10.69	220	H&V	2.6°	91 × 59 (N) 74 × 49 (S)	0.9
18	220	H&V	1.6°	55 × 41 (N) 44 × 29 (S)	1.2
21	220	H&V	1.4°	46 × 30 (N) 38 × 25 (S)	1.5
37	220	H&V	0.8°	27 × 18 (N) 21 × 14 (S)	1.5

4.2.3   The Special Sensor Microwave Imager (SSM/I)

The SSM/I was aboard the Defense Meteorological Satellite Program (DMSP) 5D satellites. Since the first SSM/I launch in 1987, six sensors have become operational. The SSM/I was a 4-frequency 7-channel MWI which observed vertical TBs at 22.235 GHz and dual polarized TBs at other 3 frequencies (19.35, 37.0, and 85.5 GHz). The SSM/I scanned conically with a surface incident angle of 53.2° (see Fig. 4.2). The SSM/I was a rotary-scanning total power radiometer which directly calibrated the whole system by measuring hot and cold reference loads with its feed horn. This design achieved high sensitivities and absolute accuracy. Table 4.6 illustrates radiometric performance characteristics of the SSM/I (Hollinger et al. 1990). The success of the SSM/I boosted new precipitation retrieval algorithms, in particular, using TBs at 85.5 GHz over land (Spencer et al. 1989).
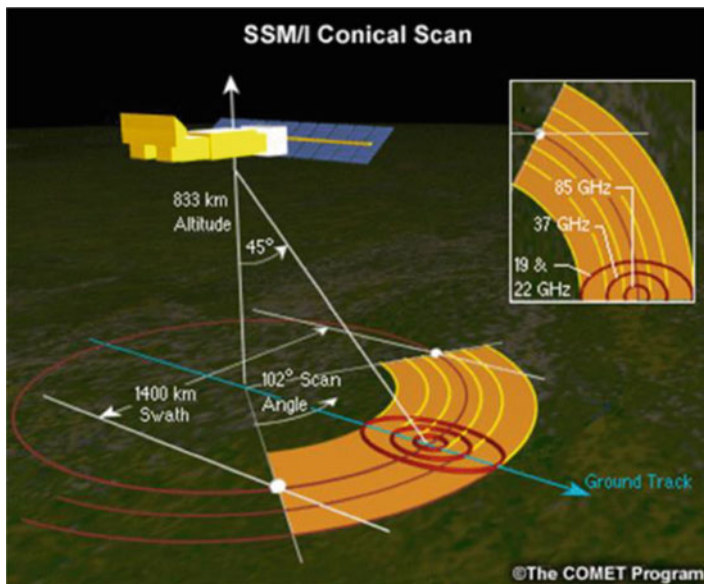
Fig. 4.2 Scan geometries of the SSM/I sensors. (The COMET Program – https://www.meted.ucar.edu/index.php, last accessed 21 Oct. 2018)

Table 4.6 Radiometric performance characteristics of SSM/I on DMSP 5D satellites

Central frequency (GHz)	RF band width (MHz)	Polarization	Antenna beam width	IFOV (km)	Sensitivity (K)
19.35	500	H&V	1.87°	43 × 69	0.42(H) 0.45(V)
22.235	500	V	1.65°	50 × 40	0.74
37	2000	H&V	1.10°	28 × 37	0.37(H) 0.38(V)
85.5	3000	H&V	0.43°	13 × 15	0.73(H) 0.69(V)

4.2.4 The TRMM Microwave Imager (TMI)

The TMI was on the Tropical Rainfall Measuring Mission (TRMM) satellite launched in 1997. The TMI was a 5-frequency 9-channel MWI which observed vertical TBs at 21.3 GHz and dual polarized TBs at other 4 frequencies (10.65, 19.35, 37.0, and 85.5 GHz). The TMI scanned conically with a surface incident angle of 52.88°. The TMI was a rotary-scanning total power radiometer which adopted the "SSM/I design". Table 4.7 illustrates radiometric performance characteristics of the TMI (Kummerow et al. 1998).

Figure 4.3 displays scan geometries of the TRMM precipitation radar (PR), TMI, and infrared imager (IR) (Kummerow et al. 1998). The TRMM enabled the global validation of MWI and IR retrievals by the radar, and encouraged projects for near-real-time global precipitation data sets.

Table 4.7 Radiometric performance characteristics of TMI on TRMM

Central frequency (GHz)	RF band width (MHz)	Polarization	Antenna beam width	IFOV (km)	Sensitivity (K)
10.65	100	H&V	3.7°(H) 3.8°(V)	63 × 37	0.63(H) 0.54(V)
19.35	500	H&V	1.9°	30 × 18	0.50(H) 0.47(V)
21.3	200	V	1.7°	23 × 18	0.71
37	2000	H&V	1.0°	16 × 9	0.36(H) 0.31(V)
85.5	3000	H&V	0.42°(H) 0.43°(V)	7 × 5	0.52(H) 0.93(V)
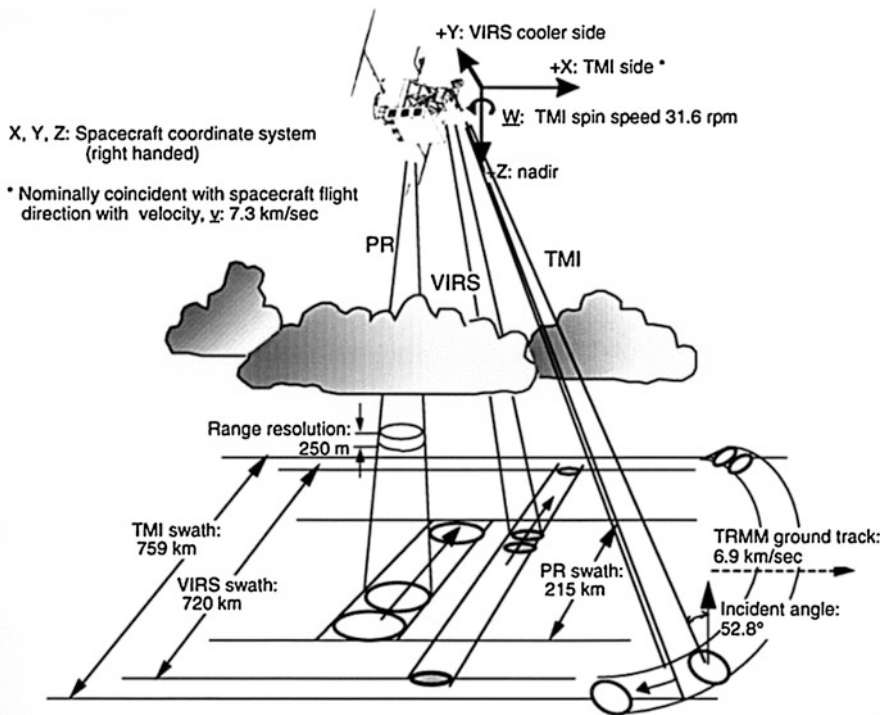
Fig. 4.3 Scan geometries of the TRMM PR, TMI and VIRS. (Adapted from Kummerow et al. 1998)

4.2.5 WindSat

WindSat was launched on Coriolis satellite in 2003, designed to measure sea surface wind vectors. WindSat was a 5-frequency polarimetric MWI which had horizontal and vertical polarizations for all frequencies, and +45, −45, left-hand circular, and right-hand circular polarizations for 10.7, 18.7 and 37.0 GHz (Gaiser et al. 2004). While WindSat is a conical scanning radiometer, the surface incident angles were not the same for different frequencies. Table 4.8 illustrates radiometric performance characteristics of the WindSat.

Table 4.8 Radiometric performance characteristics of WindSat on Coriolis

Central frequency (GHz) /Surface incident angle	RF band width (MHz)	Polarization	Antenna beam width	IFOV (km)	Sensitivity (K)
6.8/53.5°	125	H&V	1.78°	60 × 40	0.48
10.7/49.9°	300	H&V ±45, L, R	1.13°	38 × 25	0.37
18.7/55.4°	750	H&V ±45, L, R	0.65°	27 × 16	0.39
23.8/53.0°	500	H&V	0.54°	20 × 12	0.55
37.0/53.0°	2000	H&V ±45, L, R	0.33°	13 × 8	0.45

4.2.6 Advanced Microwave Scanning Radiometer (AMSR) Series

The AMSR-E was on the Aqua satellite launched in 2002. The AMSR-E was an "SSM/I design" MWI which observed dual polarized TBs at 6 frequencies (6.9–89.0 GHz). The AMSR2 is aboard the Global Change Observation Mission-Water 1 (GCOM-W 1) launched in 2012. The AMSR2 is a "SSM/I design" MWI which observes dual polarized TBs at 7.3 GHz in addition to the AMSR-E channels in order to address radiofrequency interference over land. The AMSR-E and the AMSR2 scan conically with a surface incident angle of 55°, except 54.5° for 89 GHz B channels. The AMSRs improved horizontal resolution of their FOVs by installing large antennas (1.6 m for AMSR-E, 2.0 m for AMSR2). Tables 4.9 and 4.10 illustrate radiometric performance characteristics of the AMSR-E and the AMSR2 (Imaoka et al. 2010).

4.2.7 GPM Microwave Imager (GMI)

The GMI is on the Global Precipitation Measuring mission (GPM) satellite launched in 2014. The GMI is an 8-frequency 13-channel "SSM/I design" MWI which observed vertical TBs at 21.3, 183 ± 3, and 183 ± 7 GHz and dual polarized TBs at other 5 frequencies (10.65, 19.35, 37.0, 85.5, and 165.5 GHz). The GMI scanned conically with a surface incident angle of 52.88°, with its 1.2 m antenna. Table 4.11 illustrates radiometric performance characteristics of the GMI. The addition of the higher-frequency channels (>165.5 GHz) improves the detection capability of frozen precipitation over land.

Table 4.9 Radiometric performance characteristics of AMSR-E on Aqua

Central frequency (GHz)	RF Band width (MHz)	Polarization	Antenna beam width	IFOV (km)	Sensitivity (K)
6.925	350	H&V	2.2°	74 × 43	0.34
10.65	100	H&V	1.5°	51 × 29	0.7
18.7	200	H&V	0.8°	27 × 16	0.7
23.8	400	H&V	0.92°	32 × 18	0.6
36.5	1000	H&V	0.42°	14 × 8	0.7
89.0A	3000	H&V	0.19°	6 × 4	1.2
89.0B	3000	H&V	0.19°	6 × 4	1.2

Table 4.10 Radiometric performance characteristics of AMSR2 on GCOMW1

Central frequency (GHz)	RF Band width (MHz)	Polarization	Antenna beam width	IFOV (km)	Sensitivity (K)
6.925	350	H&V	1.8°	62 × 35	0.34
7.3	350	H&V	1.7°	62 × 35	0.43
10.65	100	H&V	1.2°	42 × 24	0.70
18.7	200	H&V	0.65°	22 × 14	0.70
23.8	400	H&V	0.75°	26 × 15	0.60
36.5	1000	H&V	0.35°	12 × 7	0.70
89.0A	3000	H&V	0.15°	5 × 3	1.2
89.0B	3000	H&V	0.15°	5 × 3	1.4

Table 4.11 Radiometric performance characteristics of GMI on GPM

Central frequency (GHz)	RF band width (MHz)	Polarization	Antenna beam width	IFOV (km)	Sensitivity (K)
10.65	100	H&V	1.73°	32 × 19	0.96
18.7	200	H&V	0.98°	18 × 11	0.82
23.8	400	V	0.86°	16 × 10	0.82
36.5	1000	H&V	0.84°	16 × 9	0.56
89.0	6000	H&V	0.39°	7 × 4	0.40
165.5	4000	H&V	0.40°	6 × 4	0.81
183 ± 3	2000	V	0.36°	6 × 4	0.87
183 ± 7	2000	V	0.36°	6 × 4	0.81

4.3   Characteristics of Microwave Sounders

Microwave Sounder (MWSs) are designed primarily to measure and infer the vertical distribution of temperature and water vapor across the globe. Their TB's are widely used by all of the major Numerical Weather Prediction (NWP) centers in the world, as this data complements the much sparser radiosonde network. As such, the majority of channels that are on MWSs are in the 50–60 GHz O_2 and 183 GHz

H_2O absorption bands. The earlier built sensors generally made observations in the O_2 bands; however, more recent sensors focus on the H_2O bands. Additionally, because atmospheric contamination by clouds and precipitation can affect the vertical profiles of temperature and humidity, the current class of MWSs generally contains some window channels to edit out precipitation. These channels provide valuable information on the surface emissivity which can vastly improve the temperature and moisture information over land. Because of these additional channel compliments, the MWSs have shown to be useful in retrieving several physical variables similar to their MWI counterparts (Table 4.1), but with some limitations described shortly. The addition of the high frequency channels, above 89 GHz, has shown great utility in improving precipitation over land and also snowfall (Ferraro et al. 2005, Skofronick-Jackson et al. 2004). Many of the current MWSs are incorporated within the GPM precipitation constellation.

In terms of typical design features, MWSs are usually cross-track scanning sensors (i.e., they have a variable Earth incidence angle, usually ranging from 50° either side of nadir) which leads to a wider swath width than MWI's. But this geometry leads to varying FOV sizes across the scan and varying incidence angle, posing retrieval problems with surface and atmospheric affects. Table 4.12 provides a list of the primary MWSs flown to date.

Table 4.12 Major MWS satellite and instruments from the 1970's to present

First satellite/ Launch year	Sensor	Frequencies	Swath width (km)	Highest horizontal resolution (km)
TIROS-N/1978 and NOAA-6/ 1979	MSU	50.3, 53.74, 54.96, 57.95	2000	110
DMSP-F4/1979	SSM/T1	50.5, 53.2, 54.35, 54.9, 58.4, 58.83, 59.4	1500	200
DMSP-F11/ 1992	SSM/T2	91.7, 150.0, 183.3 (3 channels)	1500	48
DMSP-F16/ 2003	SSMIS	19.35, 22.235, 37, 50.3, 52.8, 53.6, 54.4, 55.5, 57.3, 59.4, 60.793 (5 channels), 91.65, 150.0, 183.3 (3 channels)	1700	12
NOAA-15/1998	AMSU-A	23.8, 31.4, 50.3, 52.8, 53.6, 54.4, 54.9, 57.29 (6 channels), 89.0	2200	48
NOAA-15/1998	AMSU-B	89.0, 150.0, 183.3 (3 channels)	2200	16
NOAA-18/2005 and MetOp-A/ 2006	MHS	89.0, 157.0, 183.3 (two channels), 190.3	2200	16
Megha-Tropiques/2011	SAPHIR	183.3 (6 channels)	1700	10
S-NPP/2011 and NOAA-20/2017	ATMS	23.8, 31.4, 50.3, 51.8, 52.8, 53.6, 54.4, 54.9, 55.5, 57.29 (6 channels), 89.5, 165.5, 183.3 (5 channels)	2200	16

4.3.1   Microwave Sounding Unit (MSU)

The Microwave Sounding Unit (MSU) was the first operational microwave sensor and was designed for temperature profiling in the atmosphere (Mo 1995). It was part of a package of sensors known as the TOVS – Tiros Operational Vertical Sounder – and was comprised of two additional sensors – the High Spectral Infrared Radiation Sounder (HIRS) and the Stratospheric Sounding Unit (SSU). These were infrared (IR) sensors. MSU was to aid in the profile retrievals under cloudy conditions.

The MSU was first launched aboard the TIROS-N satellite in late 1978 and provided global coverage (from Pole to Pole). It is 4-channel Dicke microwave radiometer, operating between 50 and 60 GHz. Spatial resolution varies from approximately 110 km at nadir to about 250 km at the edge of the scan at +47.5°. There were 9 different MSUs launched; the most recent one on NOAA-14. They provided measurements of the temperature of the troposphere and lower stratosphere until 1998, when the first Advanced Microwave Sounding Unit (AMSU) was deployed. AMSU provides many more channels and finer resolution (about 50 km). Table 4.13 provides more details on the MSU sensor.

It should be noted that although the MSU was designed for weather forecasting applications, the length of record has led to several studies using the time series to explore temporal and spatial variations in the Earth tropospheric temperature (Christy et al. 1998; Zou et al. 2006). Special care is needed to intercalibrate the data across all nine satellites.

4.3.2   Special Sensor Microwave Temperature and Temperature-2 (SSM/T and SSM/T2)

Beginning with DMSP-F07 in 1983, the first SSM/T was placed into operation, and the SSM/T continued through the DMSP-F15 satellite (launched in 1999). The SSM/T has similar heritage to the MSU in terms of its channel range and cross track scan geometry, however, it has seven channels as opposed to four on MSU (Grody et al. 1985). Details are provided in Table 4.14.

To compliment the temperature sounding capability of the SSM/T, the SSM/T-2 sensor was deployed starting on DMSP F-14 (launched in 1997); this sensor was flown to retrieve water vapor profiles. The SSM/T2 is a five-channel radiometer,

Table 4.13   Radiometric performance of the MSU sensor on NOAA satellites

Central frequency (GHz)	RF band width (MHz)	Polarization	Antenna beam width (Deg)	IFOV at nadir (km)	NEDT (K)
50.30	220	V	7.5	105	0.3
53.74	220	V	7.5	105	0.3
54.96	220	V	7.5	105	0.3
57.95	220	V	7.5	105	0.3

Table 4.14 Radiometric performance of the SSM/T sensor on DMSP satellites

Central frequency (GHz)	RF band width (MHz)	Polarization	Antenna beam width (Deg)	IFOV at nadir (km)	NEDT (K)
50.50	400	H	14.5	175	0.6
53.20	400	H	14.5	175	0.4
54.35	400	H	14.5	175	0.4
54.90	400	H	14.5	175	0.4
58.40	115	H	14.5	175	0.5
58.825	400	H	14.5	175	0.4
59.40	250	H	14.5	175	0.4

Table 4.15 Radiometric performance of the SSMT/2 sensor on DMSP satellites

Central frequency (GHz)	RF band width (MHz)	Polarization	Antenna beam width (Deg)	IFOV at nadir (km)	NEDT (K)
91.65	3000	H	6.0	84	0.6
150.0	1500	H	3.7	54	0.6
183.31 ± 7	500	H	3.3	48	0.6
183.31 ± 3	1000	H	3.3	48	0.6
183.31 ± 1	1500	H	3.3	48	0.8

with two window channels at 91 and 150 GHz, and three channels at 183 GHz (Falcone et al. 1992). Details are provided in Table 4.15.

4.3.3 Special Sensor Microwave Imager Sounder (SSMIS)

The Special Sensor Microwave Imager/Sounder (SSMIS) continues the legacy of passive microwave instruments carried aboard the DMSP satellites (Kunkee et al. 2008). Beginning with the launch of the DMSP F-16 satellite on 18 October 2003, the SSMIS marked the beginning of a new series of passive microwave conically scanning imagers and sounders planned for operation for approximately 20 years (Sun and Weng 2008). SSMIS improves upon the surface and atmospheric retrievals of the SSM/I, and upon the atmospheric temperature and water vapor sounding capabilities of both the SSM/T and SSM/T2. Furthermore, the SSMIS imaging and sounding sensors share the same viewing geometry, thereby allowing surface parameters to be retrieved simultaneously (Yan and Weng 2009).

The SSMIS operates at frequencies between 19 GHz and 183 GHz with a swath width of 1700 km. (details in Table 4.16). It has flown on four DMSP satellites: F-16 (October 2003); F-17 (November 2006); F-18 (October 2009) and F-19 (April 2014). The planned launch of DMSP F-20 was canceled and the SSMIS on F-19 stopped operating in February 2016. There are no immediate plans to develop a

Table 4.16 Radiometric performance of the SSMIS sensor on the DMSP satellites

Central frequency (GHz)	RF band width (MHz)	Polarization	IFOV (km)	NEDT (K)
19.35	356	V, H	42×70	0.34
22.235	407	V	42×70	0.45
37.0	1580	V, H	28×44	0.24
50.3	380	H	18×26	0.21
52.8	389	H	18×26	0.20
53.60	380	H	18×26	0.21
54.4	382	H	18×26	0.20
55.5	391	H	18×26	0.22
57.29	330	RC	18×26	0.26
59.40	239	RC	18×26	0.25
$60.793 \pm 0.3579 \pm 0.050$	106	RC	18×26	0.38
$60.793 \pm 0.3579 \pm 0.016$	29	RC	18×26	0.37
$60.793 \pm 0.3579 \pm 0.006$	10	RC	18×26	0.58
$60.793 \pm 0.3579 \pm 0.002$	5	RC	18×26	0.86
60.793 ± 0.3579	3	RC	18×26	1.18
63.283 ± 0.2853	3	RC	18×26	1.23
91.65	2829	V,H	13×14	0.19
150.0	3284	H	13×14	0.53
183.31 ± 6.6	1025	H	13×14	0.56
183.31 ± 3	2038	H	13×14	0.39
183.31 ± 1	3052	H	13×14	0.38

Note it is a conical sounder

RC denotes right-hand circular polarization

continuity mission, thus, once the current sensors cease operation, there will be no replacement.

4.3.4 Advanced Microwave Sounding Unit–A and –B (AMSU-A and AMSU-B) and the Microwave Humidity Sounder (MHS)

The AMSU-A sensor is designed to enhance the vertical profiling of temperature to support NOAA's operational mission. In this manner, it is used in conjunction with the AMSU-B (later on Microwave Humidity Sounder, MHS) and HIRS/4 sensor as part of the ATOVS system; this is substantial upgrades to their predecessors, the HIRS, MSU and SSU sensors. The first AMSU-A was flown on the NOAA-15 satellite in July 1998; subsequent sensors have been flown on NOAA-16 (September 2000), -17 (June 2002), -18 (May 2005) and -19 (February 2009) satellites, as well as

the MetOp-A (October 2006) and MetOp-B (September 2012) satellites. Several are still in operation today. AMSU-A also was flown on the EOS Aqua satellite (May 2002) to work synergistically with the AIRS sensor. The final AMSU-A and MHS will be flown on the MetOp-C satellite, scheduled for the fall of 2018.

In addition to the legacy TOVS products and MSU climate time series which primarily utilize "sounding" channels in the oxygen (50–60 GHz) and water vapor (183 GHz) absorption bands, NOAA began to use the AMSU-A and -B window channels (initially included for surface and precipitation screening) generating "Hydrological Products" (e.g., rain rate, snow cover, sea-ice concentration, etc.) from NOAA-15 through the Microwave Surface and Precipitation Products System (MSPPS; Ferraro et al. 2005) and the Microwave Integrated Retrieval System (MiRS) (Boukabara et al. 2011). These products have gained increasing popularity in both the operational weather and climate communities, thus, the motivation for this project.

AMSU-A, AMSU-B and MHS are cross-track scanning sensors that scan to approximately 50° of nadir. Nadir spatial resolution is 48 km for AMSU-A and 16 km for AMSU-B/MHS (see Fig. 4.4). Twenty microwave channels are combined there as opposed to five of the MSU. Tables 4.17, 4.18 and 4.19 provide details on each of these sensors.
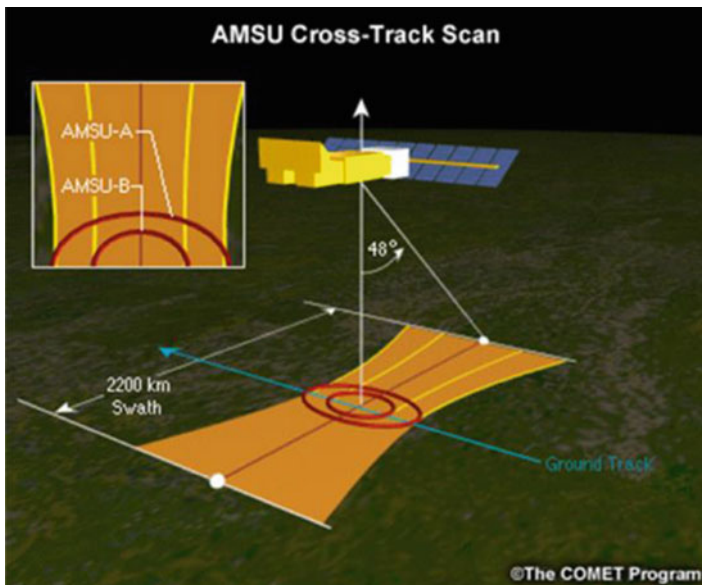
Fig. 4.4 Scan geometries of the AMSU-A and AMSU-B sensors. (The COMET Program – https://www.meted.ucar.edu/index.php, last accessed 21 Oct 2018)

Table 4.17 Radiometric performance of the SAPHIR sensor on the M-T Satellite

Central frequency (GHz)	RF band width (MHz)	Polarization	IFOV at nadir (km)	NEDT (K)
183.31 ± 0.2	200	H	10	2.0
183.31 ± 1.1	350	H	10	1.5
183.31 ± 2.7	500	H	10	1.5
183.31 ± 4.2	700	H	10	1.3
183.31 ± 6.6	1200	H	10	1.3
183.31 ± 11	2000	H	10	1.0

Table 4.18 Radiometric performance of the AMSU-A sensor on NOAA and MetOp satellites

Central frequency (GHz)	RF band width (MHz)	Polarization	Antenna beam width (Deg)	IFOV at nadir (km)	NEDT (K)
23.8	270	V	3.3	48	0.30
31.4	180	V	3.3	48	0.30
50.3	180	V	3.3	48	0.40
52.8	400	V	3.3	48	0.25
53.60	170	H	3.3	48	0.25
54.4	400	H	3.3	48	0.25
54.94	400	V	3.3	48	0.25
55.50	330	H	3.3	48	0.25
$F0 = 57.290$	330	H	3.3	48	0.25
$F0 \pm 0.217$	78	H	3.3	48	0.40
$F0 \pm 0.3222 \pm 0.048$	36	H	3.3	48	0.40
$F0 \pm 0.3222 \pm 0.022$	16	H	3.3	48	0.60
$F0 \pm 0.3222 \pm 0.010$	8	H	3.3	48	0.80
$F0 \pm 0.3222 \pm 0.00045$	3	H	3.3	48	1.20
89.0	6000	V	3.3	48	0.50

Table 4.19 Radiometric performance of the AMSU-B sensor on NOAA satellites

Central frequency (GHz)	RF band width (MHz)	Polarization	Antenna beam width (Deg)	IFOV at nadir (km)	NEDT (K)
89.0	1000	V	1.1	16	0.37
150.0	1000	V	1.1	16	0.84
183.31 ± 7	2000	V	1.1	16	0.60
183.31 ± 3	1000	V	1.1	16	0.70
183.31 ± 1	500	V	1.1	16	1.00

4.3.5 Sondeur Atmosphérique du Profil d'Humidité Intertropicale par Radiométrie (SAPHIR)

Megha-Tropiques (M-T), launched in Nov 2011, is a low-inclination satellite that observes the tropical band between 30°S and 30°N, was designed to study the tropical water cycle (Raju and Shivakumar 2012) with two MW instruments: MADRAS (Microwave Analysis and Detection of Rain and Atmospheric Systems), and Sondeur Atmosphérique du Profil d'Humidité Intertropicale par Radiométrie (SAPHIR). MADRAS (MWI), designed primarily to measure atmospheric temperature, surface properties, and precipitation, experienced several malfunctions and ceased to function after ∼1 year of sporadic operation. So, the SAPHIR is currently the only MW instrument onboard M-T.

The characteristics of SAPHIR channels are shown in Table 4.20. They all have horizontal polarization, swath width 1700 km, and resolution 10 km at nadir. The SAPHIR and ATMS channels operate at slightly different frequencies and SAPHIR also has a few additional water vapor channels.

ATMS is a cross-track MW sounder with 22 channels operating at frequencies from 23.8 to 190.31 GHz (Weng et al. 2013; see Table 4.21). It continues the legacy of the AMSU-A/MHS sensors, combining all channels into a single sensor optimizing size, weight and operation efficiency. It is designed to work synergistically with the Crosstrack Infrared Sounder (CrIS). Measurements from ATMS can be used to extend the long-standing time series of O_2 bands that started from MSU.

4.3.6 Advanced Technology Atmospheric Sounder (ATMS)

As was the case with AMSU and MHS, it also has several window channels that can be utilized for hydrological parameters. Additional bands at 183 GHz provide additional capability for precipitation retrieval, including snowfall (Ferraro et al. 2018). ATMS is currently flying on S-NPP (October 2011) and NOAA-20 (November 2017) satellites. It will also be flown in the NOAA-21 satellite, scheduled for launch around 2020.

Table 4.20 Radiometric performance of the MHS sensor on NOAA satellites

Central frequency (GHz)	RF band width (MHz)	Polarization	Antenna beam width (Deg)	IFOV at nadir (km)	NEDT (K)
89.0	2800	V	1.11	16	0.22
157.0	2800	V	1.11	16	0.38
183.31 ± 3	2000	H	1.11	16	0.42
183.31 ± 1	1000	H	1.11	16	0.57
190.311	2000	V	1.11	16	0.45

Table 4.21 Radiometric performance of the ATMS sensor on the S-NPP and NOAA-20 satellites

Central frequency (GHz)	RF band width (MHz)	Polarization	Antenna beam width (Deg)	IFOV at nadir (km)	NEDT (K)
23.8	270	V	5.35	75	0.90
31.4	180	V	5.35	75	0.90
50.3	180	H	2.20	32	1.20
51.76	400	H	2.20	32	0.75
52.8	400	H	2.20	32	0.75
53.6	170	H	2.20	32	0.75
54.4	400	H	2.20	32	0.75
54.94	400	H	2.20	32	0.75
55.5	330	H	2.20	32	0.75
F0 = 57.29	330	H	2.20	32	0.75
F0 $\pm$ 0.217	78	H	2.20	32	1.2
F0 $\pm$ 0.3222 $\pm$ 0.048	36	H	2.20	32	1.2
F0 $\pm$ 0.3222 $\pm$ 0.022	16	H	2.20	32	1.5
F0 $\pm$ 0.3222 $\pm$ 0.010	8	H	2.20	32	2.4
F0 $\pm$ 0.3222 $\pm$ 0.00045	3	H	2.20	32	3.6
88.2	5000	V	2.05	16	0.5
165.5	3000	H	1.16	16	0.60
183.31 $\pm$ 7	2000	H	1.10	16	0.80
183.31 $\pm$ 4.5	2000	H	1.10	16	0.80
183.31 $\pm$ 3	1000	H	1.10	16	0.80
183.31 $\pm$ 1.8	1000	H	1.10	16	0.80
183.31 $\pm$ 1	500	H	1.10	16	0.90

4.4 Summary and Future

This chapter has described the primary passive microwave sensors (MWIs and MWSs) and their attributes for the past 40 years. These sensors are the cornerstones to global precipitation retrievals, in particular, over oceans where other observations are rare. This is because they penetrate through clouds and respond to both liquid and frozen precipitation.

It is critical to maintain the constellation of passive microwave sensors in order to ensure quality satellite precipitation products for weather, climate, and hydrological applications. Maintaining a sufficient number of satellites that are properly spaced around the diurnal cycle is extremely important. However, in the near term, there may be a gap in coverage of the MWIs because of the end of the DMSP and potentially, the GCOM mission. However, there are other sensors (not described in this section) that could be considered if the data were freely available in real-time, such as missions operated by China and Russia. In addition, new missions are anticipated, such as the Meteosat second generation, that will contain both MWI and MWS. Additionally, Korea is planning its own polar satellite program, that will

operate a MWS and potentially, a MWI. It is also hopeful that there will be a GCOM W1 follow on mission.

References

Boukabara, A., Garrett, K., Chen, W., Iturbide-Sanchez, F., Grassotti, C., Kongoli, C., Chen, R., Liu, Q., Yan, B., Weng, F., Ferraro, R. R., Kleespies, T., & Meng, H. (2011). MiRS: An all-weather 1DVAR satellite data assimilation and retrieval system. *IEEE Transactions on Geoscience and Remote Sensing, 49*, 3249–3272. https://doi.org/10.1109/TGRS.2011.2158438.

Christy, J. R., Spencer, R. W., & Lobl, E. S. (1998). Analysis of the merging procedure for the MSU daily temperature time series. *Journal of Climate, 11*, 2016–2041. https://doi.org/10.1175/1520-0442-11.8.2016.

Falcone, V. J., Griffin, M. K., Isaacs, R. G., Pickle, J. D., Morrissey, J. F., Jackson, A. J., Bussey, A., Kakar, R., Wang, J., Racette, P., Boucher, D. J., Thomas, B. H., & Kishi, A. M. (1992). DMSP F11 SSM/T-2 calibration and validation. *Environmental Research Papers 1111*, PL-TR-92-2293. [Available from Philips Laboratory, Hanscom Air Force Base, MA 01731-5000]

Ferraro, R. R., Weng, F., Grody, N., Zhao, L., Meng, H., Kongoli, C., Pellegrino, P., Qiu, S., & Dean, C. (2005). NOAA operational hydrological products derived from the AMSU. *IEEE Transactions on Geoscience and Remote Sensing, 43*, 1036–1049. https://doi.org/10.1109/TGRS.2004.843249.

Ferraro, R. R., Meng, H., Zavodsky, B., Kusselson, S., Kann, D., Guyer, B., Jacobs, A., Perfater, S., Folmer, M., Dong, J., Kongoli, C., Yan, B., Wang, N.-Y., & Zhao, L. (2018). Snowfall rates from satellite data help weather forecasters. *Eos, 99*. https://doi.org/10.1029/2018EO096715.

Gaiser, P. W., St Germain, K. M., Twarog, E. M., Poe, G. A., Purdy, W., Richardson, D., Grossman, W., Jones, W. L., Spencer, D., Golba, G., Cleveland, J., Choy, L., Bevilacqua, R. M., & Chang, P. S. (2004). The WindSat spaceborne polarimetric microwave radiometer: Sensor description and early orbit performance. *IEEE Transactions on Geoscience and Remote Sensing, 42*, 2347–2361. https://doi.org/10.1109/TGRS.2004.836867.

Gloersen, P., & Barath, F. T. (1977). A scanning multichannel microwave radiometer for Nimbus-G and SeaSat-A. *IEEE Journal of Oceanic Engineering, 2*, 172–178. https://doi.org/10.1109/JOE.1977.1145331.

Gloersen, P., & Hardis, L. (1978). The scanning multichannel microwave radiometer (SMMR) experiment. In C. R. Madrid (Ed.), *The Nimbus 7 Users' Guide*. Greenbelt: NASA/Goddard Space Flight Center.

Grody, N. C., Gray, D. G., Novak, C. S., Prasad, J. S., Piepgrass, M., & Dean, C. A. (1985). In H. Fleming & M. Chahine (Eds.), *Advances in remote sensing retrieval methods* (pp. 249–266). Hampton: Deepak Publ.

Hollinger, J. P., Pierce, J. L., & Poe, G. A. (1990). SSM/I instrument evaluation. *IEEE Transactions on Geoscience and Remote Sensing, 28*, 781–790. https://doi.org/10.1109/36.58964.

Imaoka, K., Kachi, M., Kasahara, M., Ito, N., Nakagawa, K., & Oki, T. (2010). Instrument performance and calibration of AMSR-E and AMSR2. *The International Archives of the Photogrammetry, Remote Sensing and Spatial Information Sciences, 38*(8), 13–16.

Kummerow, C. D., Barnes, W., Kozu, T., Shiue, J., & Simpson, J. (1998). The Tropical Rainfall Measuring Mission (TRMM) sensor package. *Journal of Atmospheric and Oceanic Technology, 15*, 809–817. https://doi.org/10.1175/1520-0426(1998)015<0809:TTRMMT>2.0.CO;2.

Kunkee, D. B., Poe, G. A., Boucher, D. J., Swadley, S. D., Hong, Y., Wessel, J. E., & Uliana, E. A. (2008). Design and evaluation of the first special sensor microwave imager/sounder. *IEEE Transactions on Geoscience and Remote Sensing, 46*, 863–883. https://doi.org/10.1109/TGRS.2008.917980.

Mo, T. (1995). A study of the microwave sounding unit on the NOAA-12 satellite. *IEEE Transactions on Geoscience and Remote Sensing, 33*, 1141–1152. https://doi.org/10.1109/36.469478.

Raju, G., & Shivakumar S. K. (2012). Megha-Tropiques mission for climate and atmospheric applications. *IEEE Geoscience and Remote Sensing Newsletter*, 33–37. Available at http://www.grss-ieee.org/wp-content/uploads/2010/03/ngrs_NL_Dec_web.pdf. Last accessed 5 Oct 2018.

Skofronick-Jackson, G. M., Kim, M.-J., Weinman, J. A., & Chang, D.-E. (2004). A physical model to determine snowfall over land by microwave radiometry. *IEEE Transactions on Geoscience and Remote Sensing, 42*, 1047–1058. https://doi.org/10.1109/TGRS.2004.825585.

Spencer, R. W., Goodman, H. M., & Hood, R. E. (1989). Precipitation retrieval over land and ocean with the SSM/I: Identification and characteristics of the scattering signal. *Journal of Atmospheric and Oceanic Technology, 6*, 254–273. https://doi.org/10.1175/1520-0426(1989)006<0254:PROLAO>2.0.CO;2.

Sun, N., & Weng, F. (2008). Evaluation of special sensor microwave imager/sounder (SSMIS) environmental data records. *IEEE Transactions on Geoscience and Remote Sensing, 46*, 1006–1016. https://doi.org/10.1109/TGRS.2008.917368.

Weinman, J. A., & Guetter, P. J. (1977). Determination of rainfall distributions from microwave radiation measured by the Nimbus 6 ESMR. *Journal of Applied Meteorology, 16*, 437–442. https://doi.org/10.1175/1520-0450(1977)016<0437:DORDFM>2.0.CO;2.

Weng, F., Zou, X., Sun, N., Yang, H., Tian, M., Blackwell, W. J., Wang, X., Lin, L., & Anderson, K. (2013). Calibration of Suomi National Polar-Orbiting Partnership (NPP) Advanced Technology Microwave Sounder (ATMS). *Journal of Geophysical Research-Atmospheres, 118*, 11187–11200. https://doi.org/10.1002/jgrd.50840.

Wilheit, T. T. (1972). The electrically scanning microwave radiometer (ESMR) experiment. In R. R. Sabatini (Ed.), *The Nimbus 5 User's Guide* (pp. 59–105). Greenbelt: NASA/Goddard Space Flight Center.

Wilheit, T. T. (1975). The electrically scanning microwave radiometer (ESMR) experiment. In J. E. Sissala (Ed.), *The Nimbus 6 User's Guide* (pp. 87–108). Greenbelt: NASA/Goddard Space Flight Center.

Wilheit, T. T., & Chang, A. T. C. (1980). An algorithm for retrieval of ocean surface and atmospheric parameters from the observations of the scanning multichannel microwave radiometer. *Radio Science, 15*, 525–544. https://doi.org/10.1029/RS015i003p00525.

Wilheit, T. T., Chang, A. T. C., Rao, M. S. V., Rodgers, E. B., & Theon, J. S. (1977). A satellite technique for quantitatively mapping rainfall rates over the ocean. *Journal of Applied Meteorology, 16*, 551–560. https://doi.org/10.1175/1520-0450(1977)016<0551:ASTFQM>2.0.CO;2.

Yan, B., & Weng, F. (2009). Assessments of F16 special sensor microwave imager and sounder antenna temperatures at lower atmospheric sounding channels. *Advances in Meteorology*, 420985. https://doi.org/10.1155/2009/420985.

Zou, C., Goldberg, M. D., Cheng, Z., Grody, N. C., Sullivan, J. T., Cao, C., & Tarpley, D. (2006). Recalibration of microwave sounding unit for climate studies using simultaneous nadir overpasses. *Journal of Geophysical Research, 111*, D19114. https://doi.org/10.1029/2005JD006798.

Chapter 5
Microwave and Sub-mm Wave Sensors: A European Perspective

Christophe Accadia, Vinia Mattioli, Paolo Colucci, Peter Schlüssel, Salvatore D'Addio, Ulf Klein, Tobias Wehr, and Craig Donlon

Abstract The EUMETSAT Polar System (EPS) will be followed by a second generation system, EPS-SG, in the 2020–2040 timeframe and is the European contribution to the Joint Polar System being jointly set up with the National Oceanic and Atmospheric Administration (NOAA) of the United States. Among the various missions which are part of EPS-SG, there are the Microwave Imager (MWI) and the Ice Cloud Imager (ICI). The MWI frequencies are from 18 up to 183 GHz. All MWI channels up to 89 GHz measure both V and H polarizations. The primary objective of the MWI mission is to support Numerical Weather Prediction at regional and global scales, and to support the retrieval of precipitation and provide information on surface characteristics. The ICI has channels from 183 up to 664 GHz. The ICI's primary objectives are to support climate monitoring and validation of ice cloud models and the parameterization of ice clouds in weather and climate models through the provision of ice cloud products. The Copernicus Imaging Microwave Radiometry (CIMR) Mission is also described, which is currently being studied at Phase A/B1 as a candidate for the future Copernicus High Priority Candidate Mission expansion missions. This has a focus on high-latitude regions in support of European Union (EU) Integrated Arctic Policy. Benefits from synergy with MWI and ICI in support to characterization of hydrometeors are briefly discussed.

C. Accadia (✉) · V. Mattioli · P. Colucci · P. Schlüssel
European Organization for the Exploitation of Meteorological Satellites (EUMETSAT), Darmstadt, Germany
e-mail: christophe.accadia@eumetsat.int

S. D'Addio · U. Klein · T. Wehr · C. Donlon
European Space Agency (ESA), European Space Research and Technology Centre (ESTEC), Noordwijk, The Netherlands

5.1 Introduction

The EUMETSAT Polar System – Second Generation (EPS-SG) will provide operational continuity and service enhancements to missions carried by the Metop satellites of the current EUMETSAT Polar System (EPS). This development is the result of the long and successful collaboration and partnership between EUMETSAT and the European Space Agency (ESA). The EPS-SG satellites will further enhance the services provided by the EPS as a consequence of the new missions embarked, such as the Ice Cloud Imaging (ICI) and the Microwave Imaging (MWI) missions (see Fig. 5.1). The EPS-SG system is planned for operation in the 2020–2040 timeframe and will contribute to the Joint Polar System being jointly set up with NOAA. The satellites will fly, like Metop, in a sun synchronous, low Earth orbit at around 830 km altitude with an equator crossing time at 09:30 in descending node. Two different EPS-SG satellites (A and B) are planned and will carry the instruments presented in Table 5.1. Table 5.1 also shows the instrument payload currently carried by Metop.

The MWI and ICI missions will be described in the following sections of this chapter, illustrating the most relevant mission requirements, the expected impact on the relevant applications and the mission implementation.

The Copernicus Imaging Microwave Radiometry (CIMR) Mission is also described, which is currently being studied at Phase B2 as one of the future High Priority Copernicus expansion missions. CIMR has a focus on high-latitude regions in support of European Union (EU) Integrated Arctic Policy. Benefits from complementarity and synergy with MWI and ICI in support to characterization of hydrometeors and surface geophysical parameters are briefly discussed.

Fig. 5.1 MWI and ICI accommodation on Metop-SG

Table 5.1 Payload complement of EPS and EPS-SG satellites

Metop payload	Metop-SG payload	Metop-SG satellite
Infrared atmospheric sounding interferometer (IASI)	Infrared atmospheric sounding interferometer – New generation (IASI-NG)	A
Advanced very high resolution radiometer (AVHRR)	Visible-infrared imager (METimage)	A
Advanced microwave sounding unit A (AMSU-A1/A2), micro-wave humidity sounder (MHS)	Micro-wave sounder (MWS)	A
Global ozone monitoring experiment 2 (GOME-2)	UV-VIS-NIR-SWIR sounder (Sentinel-5)	A
Advanced scatterometer (ASCAT)	Scatterometer (SCA)	B
Global navigation satellite system receiver for atmospheric sounding (GRAS)	Radio occultation (RO)	A and B
–	Micro-wave imager (MWI)	B
–	Sub-mm wave ice cloud imager (ICI)	B
–	Multi-viewing, -channel, -polarisation Imager (3MI)	A

5.1.1 EPS-SG Microwave Imaging (MWI) Mission

The MWI mission is implemented as a conically scanning imaging radiometer with distinct spectral bands in the microwave region of the electromagnetic spectrum. The MWI has a direct heritage from instruments including the Special Sensor Microwave/Imager (SSM/I) on the Defence Meteorological Satellite Program (DMSP), its successor, the Special Sensor Microwave Imager Sounder (SSMIS), the Tropical Rainfall Measuring Mission (TRMM) Microwave Imager (TMI), the Advanced Microwave Scanning Radiometer-EOS (AMSR-E) and the Global Precipitation Mission – GPM – Microwave imager (GMI). All of these missions have provided, or provide global microwave imaging data useful to retrieve information on precipitating and non-precipitating liquid and frozen hydrometeors, information on water vapour content and relevant surface characteristics (e.g., wind speed over ocean and sea-ice coverage).

The MWI spectral bands are presented in Table 5.2, together with other relevant requirements.

MWI-1 to MWI-3 and MWI-8 can be considered as SSM/I legacy channels. These channels provide information on total column water vapour, liquid and frozen hydrometeors, sea ice and snow coverage, windspeed information over ocean, land surface emissivity. Channels in the oxygen absorption complexes near 50–60 GHz and 118 GHz are also included (MWI-4 to MWI-7, MWI-9 to MWI-12). These channels are one of the innovative features of MWI, enabling the retrieval of information on weak precipitation and snowfall, typically affecting the weather at

Table 5.2 Required MWI performance

Channel	Frequency (GHz)	Bandwidth (MHz)	NEΔT (K)	Bias (K)	Polarisation	Footprint Size at 3 dB (km)
MWI-1	18.7	200	0.8	1.0	V, H	50
MWI-2	23.8	400	0.7	1.0	V, H	50
MWI-3	31.4	200	0.9	1.0	V, H	30
MWI-4	50.3	180	1.1	1.0	V, H	30
MWI-5	52.7	180	1.1	1.0	V, H	30
MWI-6	53.24	400	1.1	1.0	V, H	30
MWI-7	53.750	400	1.1	1.0	V, H	30
MWI-8	89.0	4000	1.1	1.0	V, H	10
MWI-9	118.7503 ± 3.20	2×500	1.3	1.0	V	10
MWI-10	118.7503 ± 2.10	2×400	1.3	1.0	V	10
MWI-11	118.7503 ± 1.40	2×400	1.3	1.0	V	10
MWI-12	118.7503 ± 1.20	2×400	1.3	1.0	V	10
MWI-13	165.5 ± 0.75	2×1350	1.2	1.0	V	10
MWI-14	183.31 ± 7.0	2×2000	1.3	1.0	V	10
MWI-15	183.31 ± 6.1	2×1500	1.2	1.0	V	10
MWI-16	183.31 ± 4.9	2×1500	1.2	1.0	V	10
MWI-17	183.31 ± 3.4	2×1500	1.2	1.0	V	10
MWI-18	183.31 ± 2.0	2×1500	1.3	1.0	V	10

high latitudes (Gasiewski et al. 1990; Bauer and Mugnai 2003; Bauer et al. 2005). Channels MWI-13 to MWI-18 can provide information on water vapour profiles and precipitation (Laviola and Levizzani 2011).

The instrument collects radiation emitted from the Earth by means of a rotating antenna assembly, composed of an offset parabolic reflector antenna and feed-horn cluster rotating together. The rotation of the offset antenna rotation results in a conical scan having a wide swath and constant observation zenith angle. The same observation geometry is applicable to ICI. However, ICI is counter-rotating with respect to MWI.

The offset angle of the offset parabolic antenna is adjusted in order to have the antenna mechanical boresight pointing in a direction providing an observation zenith angle (OZA) close to $53° \pm 2°$ (also known as incidence angle). Assuming the nominal EPS-SG orbit altitude of 830 km, the offset angle θ is $44.817°$. It must be noted however that the OZA will be different for the various channels because channel feedhorns are necessarily located in different positions on the focal plane.

The observations are acquired within an angle of $\pm 65°$ in azimuth in the flight direction, equivalent to a swath of about 1700 km from the altitude of the nominal orbit. The baseline scan rate is 45 rpm, implying an along-track footprint overlap of at least 20%. Every rotation, two other angular sectors are used to calibrate the receivers. In the initial part of the calibration cycle the horns look at a fixed calibration reflector, collecting the energy coming from the cold sky, and then at a fixed microwave hot calibration target providing the receivers with a known input noise power.

Noise diodes are implemented as part of the calibration system for channels MWI-1, MWI-2 and MWI-3. These control the calibration stability and correct transfer function non-linearity. An additional advantage is that it provides a backup calibration method in case of anomalies on the hot calibration target. Noise diodes will be active every two scan cycles. Hence two consecutive calibration cycles will be needed to perform a continuous computation of the non-linearity for these channels in flight. Additionally, it would be possible to perform a calibration cycle considering the hot and cold calibration targets together with noise diodes.

The MWI-1 channel at 18.7 GHz also includes a radio frequency interference (RFI) resistant receiver to mitigate observed RFI in this spectral region (Draper 2016, 2018). MWI will downlink the corrected and uncorrected measurements. RFI is a growing problem that is best addressed using on-board hardware solutions because a spectral decomposition of the signal in the time domain is required to identify and remove RFI contaminated samples. This requires high data sampling rates resulting in data volumes that could not be sent to ground if no on-board capability is provided.

5.1.2 EPS-SG Ice Cloud Imaging (ICI) Mission

The EPS-SG Ice Cloud Imager (ICI) mission is implemented as a sub-millimetre (sub-mm) wave conical imager.

The use of sub-mm frequencies for observation of cloud ice properties was initially investigated and proposed by Evans and Stephens (1995a, b), and Evans et al. (1998), while Buehler et al. (2007, 2012) and Jiménez et al. (2007) provided a broad overview and justification for a similar concept proposed as potential ESA Earth Explorer mission. Sub-millimetre channels have also been proposed for water vapour and temperature profiling (Klein and Gasiewski 2000) and the retrieval of precipitation (Staelin et al. 1998; Bizzarri et al. 2007).

The sub-millimetre frequency range offers unique capability for the observation of ice clouds. This because, in the sub-mm, the interaction of radiation with cloud ice particles is significantly stronger than in the mm-wave range, and it is dominated by scattering mechanisms. As the atmospheric opacity increases because of the water vapour absorption, the information from channels above roughly 1 THz becomes limited.

Current existing satellite submillimetre instruments for Earth observation, e.g. the Earth Observing System (EOS) Microwave Limb Sounder (MLS) on the Aura satellite (Waters et al. 2006) and the Odin submillimetre radiometer (Murtagh et al. 2002) have provided valuable information for cloud ice retrieval (Eriksson et al. 2007; Wu et al. 2008), but are primarily intended for measuring atmospheric composition and channels were not specifically selected for ice cloud. The limb-sounding viewing, combined with high gaseous absorption, also results in having poor horizontal resolution and limits the measurements to the upper troposphere and above with only relatively high clouds detectable.

The potential of compact CubeSat radiometers for validating sub-mm-wave technology has been also demonstrated with missions as NASA IceCube (Wu et al. 2015), and it is expected that miniaturized radiometer constellations operating at high microwave frequency channels will become available. In this respect, having a reference instrument against which measurements are compared is of high relevance.

ICI is the first radiometer of this type designed with the objective of remote sensing of cloud ice. It will perform observations over a wide range of sub-mm wavelengths with 11 channels from 183.31 up to 664 GHz, providing good cloud penetration capability and sensitivity to a significant portion of particle size range that not covered either in the optical/thermal IR or in the mm-wave range (Evans et al. 1998; Eriksson et al. 2007; Buehler et al. 2007, 2012).

The ICI spectral bands are presented in Table 5.3 together with other relevant requirements. The instrument has several channels selected in three different absorption lines of water vapour (around 183, 325 and 448 GHz) and are in V polarization. Two window channels (243 and 664 GHz) provide measurement at both V and H polarization. ICI has a 16-km on-ground footprint at all frequencies.

Channels ICI-1 to ICI-3 around 183.3 GHz also provide information on water vapour profiles. They supply information on the upwelling atmospheric emission background, useful to retrieve the cloud properties (e.g., Evans et al. 2002, 2012; Rydberg et al. 2007). The use of a combination of sounding channels measurements along the various water vapour lines sensed by ICI allows sampling of clouds at different heights and with different particle sizes. The availability of channels measuring radiances with both horizontal and vertical polarisation (ICI-4 and ICI-11) provides information on different ice crystal characteristics, with polarisation effects increasing with frequency (Evans et al. 2002).

ICI collects radiation emitted from the Earth by means of a rotating antenna assembly, composed of an offset parabolic reflector antenna and feed-horn cluster rotating together. The rotation of the offset antenna rotation results in a conical scan

Table 5.3 Required ICI performance

Channel	Frequency (GHz)	Bandwidth (MHz)	NEΔT (K)	Bias (K)	Polarisation	Footprint size 3 dB (km)
ICI-1	183.31 ± 7.0	2×2000	0.8	1.0	V	16
ICI-2	183.31 ± 3.4	2×1500	0.8	1.0	V	16
ICI-3	183.31 ± 2.0	2×1500	0.8	1.0	V	16
ICI-4	243.2 ± 2.5	2×3000	0.7	1.5	V, H	16
ICI-5	325.15 ± 9.5	2×3000	1.2	1.5	V	16
ICI-6	325.15 ± 3.5	2×2400	1.3	1.5	V	16
ICI-7	325.15 ± 1.5	2×1600	1.5	1.5	V	16
ICI-8	448 ± 7.2	2×3000	1.4	1.5	V	16
ICI-9	448 ± 3.0	2×2000	1.6	1.5	V	16
ICI-10	448 ± 1.4	2×1200	2	1.5	V	16
ICI-11	664 ± 4.2	2×5000	1.6	1.5	V, H	16

having a wide swath and constant observation zenith angle. ICI scans in clockwise rotation when viewed from the nadir side of the platform, where it is located.

As for MWI, the observations are acquired within an angle of $\pm 65°$ in azimuth for the fore view (flight direction), equivalent to a swath of about 1700 km at nominal orbit altitude. Every rotation, two other angular sectors are used to calibrate the receivers. In the initial part of the calibration cycle the horns look at a fixed calibration reflector, collecting the energy coming from the cold sky, and then at a fixed microwave hot On Board Calibration Target (OBCT) providing the receivers with a known input noise power.

The basic ICI observation cycle includes the direct observation of the OBCT providing the receivers with a known input noise power, observation of the cold space through the space view reflector and observation of the Earth view. The baseline scan rate is 45 rpm, implying an along-track footprint overlap of at least 40%.

The offset angle of the offset parabolic antenna is adjusted in order to have the antenna mechanical boresight pointing in a direction providing an OZA close to $53° \pm 2°$. Assuming the nominal EPS-SG orbit altitude of 830 km, the offset angle θ is $44.767°$. Also for ICI the OZA will be different for the various channels due to the different feedhorn positions on the focal plane.

5.2 MWI and ICI Data Processing and Products

The sensor Level 1B products obtained from the processing of raw data from MWI and ICI will be calibrated, geo-located, and quality-controlled Earth-view spectral radiances.

Various geophysical products can be derived from MWI L1B data: cloud and precipitation products including bulk microphysical variables, total column water vapour over ocean, water vapour and temperature gross profiles. Furthermore, MWI can provide all weather surface imagery including: sea ice coverage (and type), snow coverage and water equivalent, sea surface wind speed (complementary and eventually in synergy with the scatterometer SCA on the same platform).

The core geophysical products of ICI will be data characterising the bulk mass of ice particles and their size. These can be retrieved as global columns, or as vertical profiles, albeit with a limited vertical resolution. ICI will also provide observations related to snowfall detection, precipitation content (frozen; total column and gross profile), snowfall rate near the surface, and water vapour profiles.

Considering MWI and ICI, the following products will be produced at the EUMETSAT Central Facilities and delivered in Near Real Time:

- Level 1B: Spectral radiances from MWI and ICI;
- Level 2: Liquid Water Path (LWP) from MWI and Ice Water Path (IWP) mean ice particle size by mass and mean mass height from ICI.

5.3   Applications

MWI has to be viewed as the European contribution to an international partnership supporting global precipitation observations, like the Global Precipitation Mission (GPM), providing adequate sampling of precipitation over the oceans from a variety of orbits (Neeck et al. 2010). Considering the orbit of the EPS-SG platforms, both MWI and ICI will support the observations of the polar regions where information from geostationary imagers is generally unavailable. This is particularly relevant in the case of polar lows, for example.

The 54–118 GHz sounding channel pairs carry information on light rain and precipitating snow over land. This is particularly relevant at mid- to high-latitudes, where frontal and stratiform precipitation systems are a significant source of light precipitation (Mugnai et al. 2007). Information on the solid or liquid phase precipitation is the primary input to any system aimed to hydrological applications.

MWI can support the retrieval of important surface variables, such as sea surface wind speed, sea ice extent, concentration, type, and motion as well as snow cover, snow water equivalent, and wet/dry-status. These surface parameters are used by NWP systems as important boundary conditions, which cannot be obtained from measurements other than micro-wave imagery.

ICI will provide global information on ice clouds, with continuous coverage and good horizontal resolution, comparable to current numerical weather prediction (NWP) and high-resolution climate models, with continuous delivery for long-term data record and climate model evaluation.

Numerical weather and climate models are not yet fully able to represent the radiative and thermodynamic effects of ice clouds, which is especially problematic because these effects couple to the circulation in various ways that are still poorly understood. Clouds and their interaction with the circulation therefore are one of the biggest sources of uncertainty in climate predictions. But it is not only model understanding that is lacking, there is also a lack of ice cloud data with global coverage. Thus, a particularly important aim of ICI is the provision of such global measurements related to ice clouds, including bulk microphysical variables, in order to improve the representation of ice clouds in NWP and climate models.

Being on the same platform, the MWI and ICI radiometers will provide an unprecedented set of microwave passive measurements from 18.7 up to 664 GHz. Synergy of use of MWI and ICI observations will surely provide an improved description of precipitating and non-precipitating systems (e.g., Wang et al. 2017; Brath et al. 2018).

5.3.1   Numerical Weather Prediction

Assimilation of all-weather information from microwave imagers like MWI has demonstrated its beneficial impact in the most advanced NWP systems (Bauer

et al. 2010; Geer et al. 2010), being complementary to clear air temperature and humidity soundings to support quantitative precipitation forecasting. Information related to the integrated total column water vapor as well as near-surface wind speed derived from MWI data is considered critical in operational NWP analyses, and is not adequately covered by infra-red or microwave sounder observations alone.

Considering its novelty, it is expected that ICI data will be initially monitored by NWP centres after launch. It is expected however that after a physiological development, ICI data will be considered for assimilation, since ICI observations will provide information on non-precipitating ice, which is neither accessible in the micro-wave region nor in the infrared domain (Buehler et al. 2007, 2012). In addition, ICI will provide information on vertical humidity profiles and vertical profiles of hydrometeors. Furthermore, the inclusion of vertical and horizontal polarization measurements at 243 and 664 GHz will provide information on particle habit and intensity of convection.

Availability of data from the ICI mission will allow NWP model developers to improve descriptions of diabatic forcing in forecast models, particularly latent heat release and radiative forcing. This is particularly critical at high latitudes where small energetic polar lows develop and evolve within short time periods. ICI data will provide information on three-dimensional cloud fields, with particular focus on ice clouds. Different altitudes of clouds can be retrieved, that can be used to estimate ice mass and mean particle size within the non-precipitating clouds. Ice-cloud microphysics will need data for validation and model initialization, and will benefit from ICI data.

5.3.2 Climate Monitoring

MWI will ensure long term continuity and consistency of measurements in key microwave imager channels, with three planned instruments over a time range of more than 20 years, considering observation of sea ice concentration or precipitation detection, for example. MWI will also be important for intercalibration and comparison with other instruments (e.g., GMI), including microwave radiometers on cubesats.

An important aspect to underline is that EPS-SG platforms will be on controlled orbits over all their operational life, greatly reducing the risk of introducing artificial geophysical trends in long time data series due to orbital drift or decay.

Precipitation retrievals from MWI (and ICI) data will continue to support projects as the Global Precipitation Climatology Project (GPCP, Huffman et al. 1997) as part of the WMO/WCRP GEWEX (World Climate Research Programme/Global Energy and Water EXchanges) project.

The main aim of GPCP is the quantification of the long-term distribution of precipitation around the globe. Microwave observations are a fundamental source of information since they provide data mainly over oceans where no in situ or ground-based radar observations are available.

MWI provides significant enhancements over SSM/I and SSMIS in terms of spatial resolution and inclusion of sounding and high frequency channels above 89 GHz. High frequency channels will be relevant to characterize frozen precipitation at high latitudes (GPM Microwave Imager – GMI, reaches about 60° latitude), with further benefit from synergy with ICI. Observations of cloud ice will also benefit climate modelling as ice clouds play an important role in cloud radiative forcing and the prediction of climate change. Climate models could capitalise upon the experience matured in the NWP framework.

In this respect, the primary objective of the ICI mission is to support climate monitoring providing information on IWP on a global scale. IWP is an essential climate variable that is currently known with highly uncertainty. Availability of accurate observations to derive global IWP estimates will support the development of advanced cloud schemes better representing the radiative and dynamic effects of ice clouds in climate models (Buehler et al. 2012). This is very relevant to better estimate the impact of ice clouds on the Earth's radiative balance, and can further benefit hydrological applications, especially at high latitudes. The high resolution of MWI and ICI measurements will support provision of small-scale information in cloudy and precipitating situations. This will be in line with the anticipated increase in spatial resolution of numerical forecast and climate models and the expected advances of cloud schemes able to better represent the fast components of the hydrological cycle, i.e. cloud formation and precipitation.

5.3.3   Nowcasting

The frequent overpasses of the EPS-SG platforms provide further support to nowcasting services at high latitudes, where few conventional observations are available. The availability of high-quality information from MWI and ICI related to cloud and precipitation will contribute to fulfil key requirements common to nowcasting and very short-range forecasting at regional scales of relevant phenomena like heavy snow or polar lows.

5.4   Copernicus Imaging Microwave Radiometry (CIMR) Mission

The frequent observations of sea-ice extent and other sea ice variables in Arctic and Antarctic Oceans are only possible via microwave imaging instruments, as polar nights and persistent cloud cover prevent complete coverage by optical imagers. Other observations of sea ice (airborne, naval) are scarce. These measurements are crucial to describe the seasonal and long-term variation of the polar sea ice caps. The

long-term decline of sea ice has been monitored and quantified by satellite micro-wave radiometer measurements over the past 30 years.

While MWI and ICI provide a world-class capability for microwave imaging of the Earth, access to measurements in frequencies from 1.4 to 10.65 GHz is not possible due to the need for a large antenna system. The sensitivity of low-frequency channels to parameters of great importance in a changing Arctic environment for example:

- Sea Ice Concentration (SIC) can be retrieved using 6–7 GHz channels where the separation of open water and sea ice is readily derived from polarisation differences.
- Sea Surface Temperature (SST) – in all weather conditions except precipitation – can be derived from 6 to 10 GHz channels.
- Thin Sea Ice Thickness (SIT) can be derived from channels in the 1.4 to 7 GHz regime up to SIT depths of ~0.5 m providing important information for tactical navigation.
- Sea Ice Drift (SID) can be derived from a combination of channels where low-frequency measurements are used as a background field.
- Estimates of snow depth on sea ice can be derived using a combination of channels.
- Sea surface salinity (SSS) can be measured using L-band (~1.4 GHz) measure-ments, dominates ocean circulation at high latitudes and is a fundamental prop-erly of sea ice evolution.
- Extreme winds (including hurricane force, also typical of polar lows) can be derived from L-band measurements.

However, the challenge is to provide such measurements at high spatial resolu-tion and with high radiometric fidelity to serve modern operational sea ice, Numer-ical Ocean Prediction (NOP) and NWP systems. The need for these measurements was recognised by Stammer et al. (2007) as part of the requirements setting process for ocean observations relevant to EPS-SG activities. This important aspect has been considered in the Integrated European Union (EU) Arctic Policy that is served by Copernicus, the largest European Earth Observation system in the world, which is now in place. Of particular concern is the future loss of L-band capability provided by ESA Soil Moisture Ocean Salinity (SMOS) and NASA Soil Moisture Active Passive (SMAP) missions that have no follow-on mission. The successor research mission to the JAXA GCOM-W AMSR/2 provides a large (32 km x 64 km) footprint C-band capability serving gridded 25 km resolution SST products to the global community.

Recognising these issues, a Copernicus Imaging Microwave Radiometry (CIMR) mission is currently being studied at Phase B2, led by ESA, as a High Priority Copernicus Mission. These missions are responding to the urgent and immediate need to expand the Copernicus satellite fleet driven by user needs (in this case monitoring of the rapidly changing Arctic environment and providing evidence to underpin the European Union (EU) Integrated Arctic Policy). The mission concept is based on a multi-frequency conically-scanning imaging microwave radiometer. The

Table 5.4 CIMR channels complement and required performance according to current requirements (2019). See https://cimr.eu/documents

Channel	Frequency (GHz)	Bandwidth (MHz)	NEΔT (K)	Bias (K)	Polarisation	Footprint size 3 dB (km)
CIMR-1	1.4135	27	≤0.3	≤0.5	V, H	≤60
CIMR-2	6.925	825	≤0.2	≤0.5	V, H	≤15
CIMR-3	10.65	100	≤0.3	≤0.5	V, H	≤15
CIMR-4	18.7	200	≤0.4	≤0.6	V, H	≤5.5
CIMR-5	36.5	1000	≤0.7	≤0.8	V, H	≤5

baseline flight configuration considers to fly CIMR in a dawn-dusk orbit. The mission design includes a large rotating reflector (about 8 m) with a swath larger than 1900 km providing ~95% global coverage every day with a single satellite. The dawn-dusk orbit will insure synergy with the EPS-SG missions so that in the polar regions (latitude greater than 65°N and S) collocated measurements between CIMR and MWI/ICI and SCA measurements would be available within ±10 min. Moreover, it must be noted that the orbit phasing of AMSR/3 (13:30 Local Time of Ascending Node – LTAN) and CIMR (06:00 LTAN) are very complementary, allowing CIMR to retrieve an estimate of the pre-dawn sea surface foundation temperature for the first time complemented by AMSR/3 that will measure close to the peak of diurnal warming. Sub-daily coverage of the polar regions (with no hole at the pole) is required to serve the EU Integrated Arctic policy and is achieved in the concept. Measurements are made at an observation zenith angle of 55° in both H and V polarisation at high spatial resolution (compared to other sensors carrying these channels) and high radiometric fidelity. Its main objective is to provide improved continuity of sea ice variables (concentration, extent, drift, thin sea ice thickness at a spatial resolution of ~4–5 km and SST at ~15 km) with a sub-daily temporal resolution in the Arctic. An L band (1.4135 GHz) channel (CIMR-1, see Table 5.4) will be implemented for measurement of thin SIT, SSS and an additional capability to determine soil moisture. Measurements of the geophysical parameters of interest to the CIMR mission can be improved considering a strong synergy with MWI and SCA on board of EPS-SGB platform. SCA scatterometer data are extremely valuable to independently estimate the ocean surface roughness (inputs to emissivity estimates for SST and SSS algorithms) and for sea ice type.

Synergistic use of CIMR, MWI, SCA, and eventually ICI, has an enormous potential to improve the capability to retrieve precipitation, surface and cloud information at high spatial resolution and over an unprecedented spectral range from L band up to the sub-mm wave range. MWI and CIMR measurements would provide observations of a wide range of meteorological situations including heavy precipitation in tropical storms and in mid-latitude cyclones over ocean with improved horizontal resolution and higher linearity, while ICI is providing information on ice cloud. Synergy between SCA and CIMR (beyond surface roughness characterisation) will provide an extension of wind speed measurements up to and including hurricane force. The synergy among MWI, ICI, SCA and CIMR would

benefit NOP, NWP and nowcasting services through observation of some of the most important and difficult to predict meteorological variables serving the Copernicus services, National Meteorological and Oceanographic Services and Sea Ice Services.

5.5 Summary

The EPS-SG MWI and ICI missions will continue and enhance important measurements of cloud and precipitation, which need frequent observations that can only be obtained by a constellation system like GPM. These missions will contribute to long term projects and provide new observations of precipitating and non-precipitating hydrometeors in liquid and solid phase in the 2020–2040 time frame. Combined use of MWI and ICI observations will lead to improved retrieval of cloud parameters. Further complementarity with observations from the CIMR mission would significantly enhance the capability to observe and retrieve heavy precipitation in tropical and mid-latitude cyclones. Most importantly, in the rapidly changing Arctic, the CIMR and Metop-SG missions will provide unique synergistic measurements to monitor the impact of European Policies, provide essential information to better predict weather systems in European countries and monitor planetary climate change.

References

Bauer, P., & Mugnai, A. (2003). Precipitation profile retrievals using temperature-sounding microwave observations. *Journal of Geophysical Research, 108*, 4730. https://doi.org/10.1029/2003JD003572.

Bauer, P., Moreau, E., & Di Michele, S. (2005). Hydrometeor retrieval accuracy using microwave window and sounding channel observations. *Journal of Applied Meteorology, 44*, 1016–1032. https://doi.org/10.1175/JAM2257.1.

Bauer, P., Geer, A. J., Lopez, P., & Salmond, D. (2010). Direct 4D-Var assimilation of all-sky radiances. Part I: Implementation. *Quarterly Journal of the Royal Meteorological Society, 136*, 1868–1885. https://doi.org/10.1002/qj.659.

Bizzarri, B., Gasiewski, A. J., & Staelin, D. (2007). Ch. 50: Observing rain by millimetre — Submillimetre wave sounding from geostationary orbit. In *Series on Advances in Global Change Research* (pp. 675–692). New York: Springer.

Brath, M., Fox, S., Eriksson, P., Harlow, R. C., Burgdorf, M., & Buehler, S. A. (2018). Retrieval of an ice water path over the ocean from ISMAR and MARSS millimeter and submillimeter brightness temperatures. *Atmospheric Measurement Techniques, 11*, 611–632. https://doi.org/10.5194/amt-11-611-2018.

Buehler, S. A., Jimenez, C., Evans, K. F., Eriksson, P., Rydberg, B., Heymsfield, A. J., Stubenrauch, C. J., Lohmann, U., Emde, C., John, V. O., Sreerekha, T. R., & Davis, C. P. (2007). A concept for a satellite mission to measure cloud ice water path, ice particle size, and cloud altitude. *Quarterly Journal of the Royal Meteorological Society, 133*, 109–128. https://doi.org/10.1002/qj.143.

Buehler, S. A., Defer, E., Evans, F., Eliasson, S., Mendrok, J., Eriksson, P., Lee, C., Jimenez, C., Prigent, C., Crewell, S., Kasai, Y., Bennartz, R., & Gasiewski, A. J. (2012). Observing ice clouds in the submillimeter spectral range: The CloudIce mission proposal for ESA's Earth Explorer 8. *Atmospheric Measurement Techniques, 5*, 1529–1549. https://doi.org/10.5194/amt-5-1529-2012.

Draper, D. W. (2016). *Terrestrial and space-based RFI observed by the GPM microwave imager (GMI) within NTIA semi-protected passive earth exploration bands at 10.65 and 18.7 GHz* (pp. 26–30). Socorro: 2016 Radio Frequency Interference (RFI).

Draper, D. W. (2018). Radio frequency environment for Earth-observing passive microwave imagers. *IEEE Journal Selected Topics in Applied Earth Observations and Remote Sensing, 11*, 1913–1922. https://doi.org/10.1109/JSTARS.2018.2801019.

Eriksson, P., Ekstrom, M., Rydberg, B., & Murtagh, D. P. (2007). First Odin sub-mm retrievals in the tropical upper troposphere: Ice cloud properties. *Atmospheric Chemistry and Physics, 7*, 471–483. https://doi.org/10.5194/acp-7-471-2007.

Evans, K. F., & Stephens, G. L. (1995a). Microwave radiative transfer through clouds composed of realistically shaped ice crystals. Part I: Single scattering properties. *Journal of the Atmospheric Sciences, 52*, 2041–2057. https://doi.org/10.1175/1520-0469(1995)052<2041:MRTTCC>2.0.CO;2.

Evans, K. F., & Stephens, G. L. (1995b). Microwave radiative transfer through clouds composed of realistically shaped ice crystals. Part II: Remote sensing of ice clouds. *Journal of the Atmospheric Sciences, 52*, 2058–2072. https://doi.org/10.1175/1520-0469(1995)052<2058:MRTTCC>2.0.CO;2.

Evans, K. F., Walter, S. J., Heymsfield, A. J., & Deeter, M. N. (1998). Modeling of submillimeter passive remote sensing of cirrus clouds. *Journal of Applied Meteorology, 37*, 184–205. https://doi.org/10.1175/1520-0450(1998)037<0184:MOSPRS>2.0.CO;2.

Evans, K. F., Walter, S. J., Heymsfield, A. J., & McFarquhar, G. M. (2002). Submillimeter-wave cloud ice radiometer: Simulations of retrieval algorithm performance. *Journal of Geophysical Research, 107*, 2.1–2.21. https://doi.org/10.1029/2001JD000709.

Evans, K. F., Wang, J. R., O'C Starr, D., Heymsfield, G., Li, L., Tian, L., Lawson, R. P., Heymsfield, A. J., & Bansemer, A. (2012). Ice hydrometeor profile retrieval algorithm for high-frequency microwave radiometers: Application to the CoSSIR instrument during TC4. *Atmospheric Measurement Techniques, 5*, 2277–2306. https://doi.org/10.5194/amt-5-2277-2012.

Gasiewski, A. J., Barrett, J. W., Bonanni, P. G., & Staelin, D. H. (1990). Aircraft-based radiometric imaging of tropospheric temperature and precipitation using the 118.75-GHz oxygen resonance. *Journal of Applied Meteorology, 29*, 620–632. https://doi.org/10.1175/1520-0450(1990)029<0620:ABRIOT>2.0.CO;2.

Geer, A. J., Bauer, P., & Lopez, P. (2010). Direct 4D-Var assimilation of all-sky radiances. Part II: Assessment. *Quarterly Journal of the Royal Meteorological Society, 136*, 1886–1905. https://doi.org/10.1002/qj.681.

Huffman, G. J., Adler, R. F., Arkin, P., Chang, A., Ferraro, R. R., Gruber, A., Janowiak, J., McNab, A., Rudolf, B., & Schneider, U. (1997). The Global Precipitation Climatology Project (GPCP) combined precipitation dataset. *Bulletin of the American Meteorological Society, 78*, 5–20. https://doi.org/10.1175/1520-0477(1997)078<0005:TGPCPG>2.0.CO;2.

Jiménez, C., Buehler, S. A., Rydberg, B., Eriksson, P., & Evans, K. F. (2007). Performance simulations for a submillimetre wave cloud ice satellite instrument. *Quarterly Journal of the Royal Meteorological Society, 133*(S2), 129–149. https://doi.org/10.1002/qj.134.

Klein, M., & Gasiewski, A. J. (2000). Nadir sensitivity of passive millimeter and submillimeter wave channels to clear air temperature and water vapor variations. *Journal of Geophysical Research, 105*, 17481–17511. https://doi.org/10.1029/2000JD900089.

Laviola, S., & Levizzani, V. (2011). The 183-WSL fast rain rate retrieval algorithm. Part I: Retrieval design. *Atmospheric Research, 99*, 443–461. https://doi.org/10.1016/j.atmosres.2010.11.013.

Mugnai, A., Di Michele, S., Smith, E. A., Baordo, F., Bauer, P., Bizzarri, B., Joe, P., Kidd, C., Marzano, F. S., Tassa, A., Testud, J., & Tripoli, G. J. (2007). Snowfall measurements by proposed European GPM mission. In V. Levizzani, P. Bauer, & F. J. Turk (Eds.), *Measuring*

precipitation from space: EURAINSAT and the future (pp. 655–674). Dordrecht: Springer. ISBN:978-1-4020-5835-6.

Murtagh, D., Frisk, U., Merino, F., Ridal, M., Jonsson, A., Stegman, J., Witt, G., Eriksson, P., Jiménez, C., Megie, G., de la Noë, J., Ricaud, P., Baron, P., Pardo, J. R., Hauchcorne, A., Llewellyn, E. J., Degenstein, D. A., Gattinger, R. L., Lloyd, N. D., Evans, W. F., McDade, I. C., Haley, C. S., Sioris, C., von Savigny, C., Solheim, B. H., McConnell, J. C., Strong, K., Richardson, E. H., Leppelmeier, G. W., Kyrölä, E., Auvinen, H., & Oikarinen, L. (2002). An overview of the Odin atmospheric mission. *Canadian Journal of Physics, 80*, 309–319. https://doi.org/10.1139/p01-157.

Neeck, S. P., Kakar, R. K., Azarbarzin, A. A., & Hou, A. Y. (2010). Global Precipitation Measurement (GPM) implementation. In R. Meynart, S. P. Neeck, & H. Shimoda (Eds.), *Sensors, systems and next-generation satellites XIV*. Proceedings of SPIE, 78260X. https://doi.org/10.1117/12.868537.

Rydberg, B., Eriksson, P., & Buehler, S. A. (2007). Prediction of cloud ice signatures in submillimetre emission spectra by means of ground-based radar and in situ microphysical data. *Quarterly Journal of the Royal Meteorological Society, 133*, 151–162. https://doi.org/10.1002/qj.151.

Staelin, D. H., Gasiewski, A. J., Kerekes, J. P., Shields, M. W., & Solman III, F. J. (1998). *Concept proposal for a Geostationary Microwave (GEM) observatory. Prepared for the NASA/NOAA Advanced Geostationary Sensor (AGS) Program* (p. 23). Lexington: MIT Lincoln Laboratory.

Stammer, D., Johanessen, J., LeTraon, P., Minnett, P., Roquet, H., & Srokosz, M. (2007). Position paper: *Requirements for ocean observations relevant to post-EPS*. AEG Ocean Topography and Ocean Imaging, 10 January 2007, Version 3.

Wang, D., Prigent, C., Aires, F., & Jimenez, C. (2017). A statistical retrieval of cloud parameters for the millimeter wave ice cloud imager on board MetOp-SG. *IEEE Access, 5*, 4057–4076. https://doi.org/10.1109/ACCESS.2016.2625742.

Waters, J. W., Froidevaux, L., Harwood, R. S., Jarnot, R. F., Pickett, H. M., Read, W. G., Siegel, P. H., Cofield, R. E., Filipiak, M. J., Flower, D. A., Holden, J. R., Lau, G. K., Livesey, N. J., Manney, G. L., Pumphrey, H. C., Santee, M. L., Wu, D. L., Cuddy, D. T., Lay, R. R., Loo, M. S., Perun, V. S., Schwartz, M. J., Stek, P. C., Thurstans, R. P., Boyles, M. A., Chandra, K. M., Chavez, M. C., Chen, G.-S., Chudasama, B. V., Dodge, R., Fuller, R. A., Girard, M. A., Jiang, J. H., Jiang, Y., Knosp, B. W., LaBelle, R. C., Lam, J. C., Lee, K. A., Miller, D., Oswald, J. E., Patel, N. C., Pukala, D. M., Quintero, O., Scaff, D. M., Snyder, W. V., Tope, M. C., Wagner, P. A., & Walch, M. J. (2006). The Earth observing system microwave limb sounder (EOS MLS) on the aura satellite. *IEEE Transactions on Geoscience and Remote Sensing, 44*, 1075–1092. https://doi.org/10.1109/TGRS.2006.873771.

Wu, D. L., Jiang, J. H., Read, W. G., Austin, R. T., Davis, C. P., Lambert, A., Stephens, G. L., Vane, D. G., & Waters, J. W. (2008). Validation of the Aura MLS cloud ice water content measurements. *Journal of Geophysical Research, 113*, D15S10. https://doi.org/10.1029/2007JD008931.

Wu, D., Esper, J., Ehsan, N., Johnson, T., Mast, W., Piepmeier, J. R., & Racette, P. E. (2015). IceCube: CubeSat 883-GHz radiometry for future ice cloud remote sensing. *NASA Report 20150021071*. [Available at: https://ntrs.nasa.gov/search.jsp?R=20150021071. Last accessed 5 Oct 2018]

Chapter 6
Plans for Future Missions

**Christian D. Kummerow, Simone Tanelli, Nobuhiro Takahashi,
Kinji Furukawa, Marian Klein, and Vincenzo Levizzani**

Abstract This chapter speculates on the future, and as such, is highly uncertain given the fluid nature with which specific satellite missions are selected and deselected as budgets fluctuate and priorities are modified to suit political expediencies. To reduce some of this uncertainty, the chapter focuses instead on the evolving needs from an application as well as climate understanding perspective. While it is difficult to associate such needs or requirements with individual missions, it nonetheless point in the direction that the field must evolve towards. The other determinant for future missions that cannot be ignored are the expected technical advances to improve both instruments, satellites, and associated technology. Only then do we discuss future missions which are also divided into the immediate future, for which missions and sensors have already been defined, followed by a review of ongoing discussion to define the next generation of missions designed to address some the needs tied to improved weather and climate forecasts, as well as "process understanding" discussed in the first section.

C. D. Kummerow (✉)
Department of Atmospheric Science, Colorado State University, Ft. Collins, CO, USA
e-mail: christian.kummerow@colostate.edu

S. Tanelli
Jet Propulsion Laboratory (JPL), California Institute of Technology, Pasadena, CA, USA

N. Takahashi
Institute for Space-Earth Environmental Research, Nagoya University, Nagoya, Japan

K. Furukawa
JAXA, Tokyo, Japan

M. Klein
Boulder Environmental Sciences and Technology, Boulder, CO, USA

V. Levizzani
National Research Council, Institute of Atmospheric Sciences and Climate (CNR-ISAC),
Bologna, Italy

Climate · Hydrology · Meteorology · Water cycle · Numerical weather prediction ·
Water vapor · Clouds · GCOS · CEOS · Smallsats · CubeSats · TROPICS ·
TEMPEST-D · RainCube · WCOM · EarthCARE

6.1 Requirements of Future Global Precipitation Measurement

Irrespective of missions, there are continuing needs and challenges to better under-
stand and predict precipitation changes in weather, hydrology, and the climate
system. While all interconnected, they differ in their need for the frequency of
observations, their timeliness, their resolution and their uncertainty. As such, it is
best to examine these needs separately with the notion that they may be combined
when specific missions are designed.

Weather monitoring and forecasting is a complex task that does not easily reduce
to a unique set of requirements, as there is great dependence on the application area:
global numerical weather prediction (NWP), high-resolution NWP, nowcasting,
agricultural meteorology, and ocean state forecasts. The World Meteorological
Organization (WMO) Observing Systems Capability Analysis and Review
(OSCAR, https://www.wmo-sat.info/oscar/observingrequirements) is the reference
for the requirements that are expressed in terms of six criteria: uncertainty, horizontal
resolution, vertical resolution, observing cycle, timeliness and stability. For each
criterion three values are indicated: threshold (minimum value to be met for the data
to be useful), breakthrough (intermediate level representing a significant improve-
ment for the targeted application), and goal (requirement above which no further
improvements are necessary). If one examines the OSCAR tables for surface
precipitation intensity (liquid or solid), the values associated with "goal" capabilities
vary in the following way: horizontal resolution (from 0.25 km of agricultural
meteorology to 5 km of global NWP), observing cycle (from 5 min for nowcasting
and ocean to 60 min of global NWP), timeliness (from 5 min of nowcasting and
ocean to 15 min of high resolution NWP), uncertainty (0.1 mm h^{-1} for all applica-
tions). The confidence level for liquid precipitation in all these cases is between firm
(result of impact studies on actual data used in actual applications) and reasonable
(not firm, but based on a strong heritage of experiments with similar data). In the case
of solid precipitation intensity at the surface, the confidence level for high resolution
NWP is only tentative (positive impact expected but not yet validated due to lack of
suitable data). From this analysis, it is clear that the improvement of future precip-
itation missions with regard to observing cycle, resolution, timeliness and uncer-
tainty level are deemed necessary. Because requirements focus on parameters rather
than on individual missions, the overarching goals in the case of precipitation tend to
focus both on high quality individual products as well as merged products as
discussed in Parts II and III. The International Precipitation Working Group
(IPWG; Levizzani et al. 2018) is helping WMO and the Coordination Group for

Meteorological Satellites (CGMS) to meet these goals in the near future with the clear notion of making available operational products for specific user needs. Note that robustness of the constellation of passive and active sensors in orbit is a key issue for ensuring the necessary continuity of products (Huffman et al. 2016).

Hydrologic predictions try to meet the fundamental societal need for water, which remains insecure in large portions of the Earth. Needs vary from monitoring and predicting water availability in water-scarce areas (especially developing countries) to ensuring an efficient use of water where it is often used without adequate plans (most of the industrialized countries). Accurate observations are thus a key element of hydrologic predictions (e.g., Lettenmaier 2017). The US Decadal Survey (2017) underlines the importance of monitoring and modeling the water cycle "…from the accurate quantification of water and energy fluxes at the river basin scale, to accurate snow water equivalent measurements for water supply forecasting, to improved drought monitoring, to flash flooding hazard prediction, to changes in land use and water quality in highly coupled human-natural systems". And it stretches from recommendations to extend ongoing measurements, to new endeavors in detecting the phase (rain or snow) of precipitation, to measuring snow water equivalent and evapotranspiration, to new fields for application of remotely sensed data, such as water quality, groundwater recharge, effects of urbanization, water-modulated bio-geochemical cycling, and prediction of hazard chains. Improvements in our observing capabilities from space relate not only to precipitation (rainfall and snowfall), but snow water equivalent (still quite elusive especially in mountain areas in spite of our ability to estimate snow cover), evapotranspiration, snow and ice melt, and recharge and withdrawal of groundwater. Advances are planned in the areas of precipitation, river discharge, evapotranspiration, total storage estimates, soil moisture, and surface water storage (lakes, wetlands and reservoirs) (Lettenmaier et al. 2015), while the US Decadal Survey (2017) further highlights the need for snow water equivalent measurements. It is thus very relevant to conceive new precipitation missions along a future refinement of other present key hydrology-related missions such as the Gravity Recovery and Climate Experiment (GRACE), and the Soil Moisture and Ocean Salinity (SMOS) and Soil Moisture Active Passive (SMAP), or even the Snow Water Equivalent mission that is possible from the Decadal Survey recommendations. This will allow for a much more integrated view of precipitation in the Earth System, as well as monitoring of extreme precipitation in the context of its causes and consequences.

A better understanding of the climate system is critical for long term decision making. To that end, the World Climate Research Program (WCRP) Grand Challenges have identified seven challenges in climate science (https://www.wcrp-climate.org/grand-challenges/grand-challenges-overview, last accessed 8 Feb. 2019), including three that are directly related to observations of precipitation. These include "understanding and predicting the extreme weather", "clouds, circulation and climate sensitivity" and "water for the food baskets of the world". Each of these challenges, in turn, can be addressed in three steps: monitoring the Earth, understanding the process, and improving predictions (Weatherhead et al. 2017). For the first two of them, the contribution of satellite observations is expected to be

paramount, while further combination of observation and numerical model research is important for the third step. These scientific/societal demands are broken down into specific science questions, such as: How does climate change affect precipitation, i.e. "is the total rainfall amount increasing?" or "is the extreme rainfall event increasing?" Another question is: "how climate change affects the global water cycle?" To answer these questions, a deeper understanding of each element of the atmospheric water budget (e.g., water vapor, clouds and precipitation), hydrological processes (e.g., runoff, floods and droughts, and biogeoscience aspects such as vegetation and forest), must be combined into a unified view. In particular, it will become necessary to better understand cloud-precipitation processes, which will, in turn, require observations of the process of changes clouds to precipitation, as well as coincident three-dimensional kinematic observation of convective processes. At the same time future observations will need to address fundamental questions that are still not completely answered on: frequency of rain and snow episodes (e.g., Trenberth and Zhang 2018); intensity and phase (e.g., Trenberth et al. 2003); frequency and distribution of extremes (see Chap. 40 of volume 2). Naturally, not all global precipitation products are suitable for each of the tasks described above. Guidance is needed by the satellite precipitation community on the use of such data sets in data assimilation, model validation and verification and for improving physical parameterizations (e.g., Tapiador et al. 2017, 2019).

One key aspect that underlies all aspects of climate and climate change is the need for long-term precipitation records that have been collected for more than 20 years by the Tropical Rainfall Measuring Mission-Global Precipitation Measurement mission (TRMM-GPM). To extract changes in precipitation due to climate change by observation, accurate long-term (more than 30 years) data are necessary to reduce the effect of long-term variation of the earth (El Niño Southern Oscillation-ENSO, solar cycle, Arctic oscillation, etc.). Given the time series that is available today, a significant requirement is thus to maintain and extend this time series of high-quality precipitation observations. The plan for the proposed implementation of a global observing system for climate was devised by the Global Climate Observing System (GCOS 2016) guiding the development of such a system and setting out what is needed to meet increasing and more diverse needs for data and information, including for improved management of the impacts and consequences of climate variability and current and future climate change.

In recent years it has become increasingly clear that direct contributions to societal needs other than meteorology, hydrology and climate are also required (e.g., Kucera et al. 2013; Kirschbaum et al. 2017; Skofronick-Jackson et al. 2017) as the mission of the Earth observation satellite, and construction of a data system for precipitation information on a real time basis is also required for the future mission. At the same time, the development plan should fit the 2030 Agenda for Sustainable Development and the Sustainable Development Goals (SDGs) set up by the Committee on Earth Observation Satellites (CEOS) towards a sustainable society (Paganini et al. 2018). Each goal includes a set of targets that countries are working to achieve by 2030. Each target in turn includes a set of indicators that define the quantitative measurement for the targets. Satellites, small satellites in particular,

contribute to reaching the goals and to monitor the progress towards the targets (Wood and Stober 2018; Madry et al. 2018). In order to significantly help reaching the goals of sustainable development satellite data need to become even more accessible without barriers. In the case of precipitation this is already a reality and datasets are freely available thus meeting the concept of "open access" satellite observations (Wulder and Coops 2014). The problem still remains for the observation of other variables and thus more work towards reaching an international agreement of data availability is ahead of us.

Outstanding examples of societal needs met by precipitation products are detailed in Part VI. Among them, we will mention landslide potential, fire monitoring, high-resolution estimates of terrestrial surface heat and moisture, pests and disease control (vector- and water-borne), agriculture and food production (fight against famine), influence on ocean salinity, and atmospheric aerosol scavenging.

6.2   Technical Developments

Current satellite estimates of global precipitation, as captured in Parts II and III, rely fundamentally on a hierarchy of sensors from spaceborne radars – the most capable but with currently the least sampling density, to microwave (MW) radiometers with lower information content but larger numbers and swaths due to their use in numerical weather forecasts, to geostationary infrared (IR) observations which are available continuously for weather applications but provide only limited information about precipitation. Imminent and potential advances in each of these is addressed separately.

6.2.1   Radar

Future needs, and the perhaps limited information content inherent in passive MW and infra-red sensors points to a future in which precipitation radars will play a greater role. They will likely have any combination of higher sensitivity, wider swath, higher spatial resolution and reduced surface clutter extent than the current systems to meet the evolving requirements described above. The need for identifying more particle types and cloud processes also points to the desirability of simultaneous multi-frequency, polarization and Doppler velocity measurement.

High sensitivity is essential for understanding the cloud-precipitation processes and observation of snowfall at high latitudes. Although the introduction of cloud radars is indispensable to detect drizzle and light precipitation, it is important to overlap the sensitivity ranges of radars to obtain more independent pieces of information, which are needed to better constrain largely underconstrained retrievals of cloud and precipitation properties. For very small drops, this may even require higher frequencies than are used today in order avoid having all radars observed

drops in the Rayleigh regime. The technologies necessary to enable such radars are being developed and demonstrated (e.g., Battaglia et al. 2014; Roy et al. 2018). As drizzle intensifies, however, W-band cloud radars such CloudSat (Stephens et al. 2002; Tanelli et al. 2008) have more than enough sensitivity and begin to operate in the Mie scattering regime. A lower frequency such as Ka-band with enough sensitivity to detect light drizzle is therefore warranted. The GPM Dual Frequency Precipitation radar Ka band channel has a minimum detectable signal of 12 dBZ in its High Sensitivity mode (range resolution of 500 m) which is insufficient for drizzle. Nonetheless, currently available technology has enabled the development of spaceborne radar concepts with Ka-band channels capable of achieving sensitivities around -10 dBZ, and electronic scanning radars operating at Ku-, Ka- and W-band (e.g., ACE 2016; Tanelli et al. 2018 and references cited therein). This will allow multiple frequency radars such as the airborne Airborne Third Generation Precipitation Radar (APR-3; Ku-, Ka- and W-band) flown in the OLYMPEX Campaign (e.g., Chase et al. 2018; Houze et al. 2017), to be available on space platforms.

Wide swath observation is an effective means of simply increasing the observation area by radar to meet some of the sampling requirements laid out in the previous section. The feasibility of achieving a wider swath using current designs from GPM's DPR is partly confirmed by the TRMM end-of-mission experiment (Takahashi et al. 2016; Takahashi 2017). This experiment was conducted during the period when the TRMM satellite descended below the nominal observation altitude. Three kinds of experiments were conducted: wide swath observation, 90° yaw observation (rotating the satellite yaw angle by 90°), and 3- and 4-times dense sampling observations. In the wide swath width experiment, scan angle was set up to 32° (usually 17° for observation). This experiment increased the swath width from 220 to 400 km which is nearly twice as wide as normal observations. For wide-angle observations, the clutter height range is of concern. From the experimental results, it was confirmed that the clutter altitude linearly increased with the incident angle as expected. Smaller FOV would mitigate this issue. A drawback of wide-swath pencil beam scanning radars is that the dwell time available for each footprint is reduced linearly with the number of cross-track beams: this in turn reduces the number of independent samples and consequently not only the radar sensitivity but also its precision. Methods to mitigate such drawback exist (e.g., frequency diversity, orthogonal waveforms) but in general they result in either increased power demands, increased data rates, increased system complexity or a combination of the above. As such the design of a scanning radar and the definition of its data acquisition configuration must carefully balance specific performance requirements with size, power, mass and data rate demands.

Alternative approaches to increase the global sampling of clouds and precipitation by spaceborne radars include the deployment of multiple compact radars on small platforms (e.g., Peral et al. 2019; Muraki 2017). The Ka-band nadir-pointing radar on the RainCube 6U CubeSat (Peral et al. 2019) demonstrated in August 2018 that state-of-the-art technology, careful design of high-performance pulse compression approaches, and innovative architectural solutions can provide precipitation detection and profiling capabilities previously achievable only by a much larger class

of radars with a fraction of the resources. Such a simplification and reduction in cost allows to one to conceive launching multiple copies either on different orbits (to provide effective and rapid global sampling of the diurnal cycle of precipitation) or in a train formation (similar to the A-Train) where the same storm is observed within minutes by multiple sensors in order to provide measurements of the evolution of the storm itself (e.g., Haddad et al. 2017; Sy et al. 2017). The same architecture can be applied to other wavelengths.

Combinations of these two approaches (i.e., one or few very capable radars vs. many simple radars) are currently being considered not only to increase global sampling and mapping, but also to provide three dimensional datasets at the meso-gamma scale, necessary to properly interpret the observed vertical profiles.

For both increased sampling, as well as physical insight into clouds and convection, it is necessary to increase the spatial resolution of the radar both in both the horizontal and vertical dimension. The high horizontal resolution is important so that individual cloud and convective processes occurring at cloud-scale can be properly resolved. While for specific investigations horizontal resolutions as small as a few tens of meters are necessary, such level of performance is currently considered only for airborne and ground-based instruments, while the key contributions by spaceborne radars are expected to address processes occurring at scales between a few hundred meters and a couple of kilometers. For example, the Cloud Profiling Radar (CPR) onboard the Earth Cloud Aerosol and Radiation Explorer (EarthCARE) satellite (Illingworth et al. 2016), which is supposed to launch in 2021, is designed to provide a horizontal resolution of ~700 m. For scanning real-aperture radar solutions, a small beamwidth is also necessary to prevent the FOV from interacting with the surface at off-nadir angles and therefore elevating the region affected by surface clutter (which masks the echo from precipitation) in the Planetary Boundary Layer. These needs however push either towards larger antenna sizes, which typically result in more onerous accommodation and development requirements, or lower orbital altitudes (which impose additional requirements on the platform to achieve equal mission duration). Therefore, larger deployable antennas are being developed and may well have a role in the future. The first spaceborne deployable antenna was launched with RainCube in 2018 (Chahat et al. 2016), but other designs are currently in development. With large enough antennas, even geostationary radars as proposed by Im et al. (2004) may someday be feasible.

For Doppler velocity measurements (e.g., Amayenc et al. 1993; Meneghini and Kozu 1990; Tanelli et al. 2008), the CPR onboard the EarthCARE satellite has Doppler velocity measurement functions. EarthCARE/CPR is a nadir pointing radar with a frequency of 94 GHz. The largest factor deteriorating the Doppler velocity measurement accuracy is degradation of the coherence between the pulses because of the movement of the satellite. The movement of the platform (7 km s^{-1}) combined with the finite size of the single antenna directly degrades the coherence. For example, the EarthCARE/CPR will use a 2.6 m diameter antenna with a wavelength of about 3 mm to achieve a Doppler velocity error of about 1.0 m s^{-1} at -19 dBZ in most cloud scenarios (e.g., Kollias et al. 2014). Additional issues regarding the Doppler velocity measurement are: effect of non-uniform beam filling and pointing

uncertainty (e.g., Sy et al. 2014; Tanelli et al. 2005 and references cited therein). In general, for single antenna radar systems in Low Earth Orbit (LEO), the larger the antenna size (in the along-track direction) the higher the quality of Doppler measurements: therefore, the most stringent horizontal resolution requirements result intrinsically in better Doppler accuracies (all other parameters being the same), while coarser horizontal resolutions can be achieved by radars that would produce essentially uncorrelated pulses with the classical configurations. To mitigate the decorrelating effect of the high platform velocity without having to adopt a very large antenna, several techniques that have been developed and demonstrated on airborne platforms in the last decades are viable to achieve accurate Doppler measurements (e.g., polarization diversity techniques such as in Pazmany et al. 1999 and Battaglia et al. 2018; or Displaced Phase Center Antenna – DPCA approaches as in Durden et al. 2007 and Tanelli et al. 2016). Doppler measurements have also been proposed for systems operating at angles significantly off-nadir to provide measurements of the horizontal wind components in clouds and precipitation (e.g., Amayenc et al. 1993; Illingworth et al. 2018).

In recent years, mm-wave technology advances have enabled the development and demonstration of instruments in the G-band. Within this broad band, two specific frequency ranges have been investigated: the flanks of the 183 GHz water vapor absorption line where multiple frequencies can be used to implement differential absorption techniques to profile the water vapor content in cloud (e.g., Cooper et al. 2018; Battaglia and Kollias 2019; Roy et al. 2018), and the window region around 239 GHz to further extend the differential backscattering approaches to size particles down to a 200 µm (Battaglia et al. 2014). Inclusion of such capabilities in future radar systems that also operate at W-band (or lower) would allow measurement relative humidity and particle size in ice clouds and thus provide essential information for determining ice crystal growth processes and rates.

In addition to the advances needed to address ongoing requirements, significant effort has been paid to ensure the continuity of data between TRMM/PR and GPM/DPR. The most important point is the radar calibration. External calibration using active radar calibrator (ARC) is introduced for the overall calibration of TRMM/PR and GPM/DPR as well as the receiver calibration. Careful treatment is needed to guarantee the continuity of radar performance such as the calibration of ARC itself including temperature monitoring, power monitor procedure as well as the radar characteristics such as pulse shape and antenna pattern. Since it is difficult to perform the external calibration frequently, the normalized radar cross section (NRCS) of the sea surface has been utilized for routine monitoring (e.g., Tanelli et al. 2008; Furukawa et al. 2015). For future missions, it is necessary to establish the traceability of the calibration method based on these experiences.

An additional point is the use of radar as a radiometer to obtain overlapped fields of view (FOV) between the two instruments on one side and also to make use of the potential of the radar in radiometry mode as a method for constantly monitoring the performance of the radar receiver system (e.g., Fabry 2001). Moreover, this kind of technique enables the application of combined radar-radiometer approaches with the additional advantage provided by the fact that the two measurements share the

observing geometry (hence reducing the impact of the different footprint sizes and orientation typically affecting the same approaches when a near-nadir radar measurement is combined with a conically scanning radiometer). This approach has been demonstrated by early uses of the CloudSat brightness temperature product (e.g., Mace et al. 2016).

6.2.2 Microwave Radiometer

A number of radiometer advances have occurred or are occurring. Chief among these is the miniaturization of radiometer receivers. In particular, Millimeter-wave Monolithic Integrated Circuits (MMIC) (e.g., Marsh 2006; Robertson and Lucyszyn 2001) allow for MW mixing, power amplification, low-noise amplification, and high-frequency switching, all down to dimensions from 1 to 10 mm^2. Jet Propulsion Laboratory's (JPL) High-Altitude MMIC Sounding Radiometer (HAMSR, Brown et al. 2011), a 25-channel cross-track scanning MW sounder with channels near the 60- and 118-GHz oxygen lines and the 183-GHz water-vapor line is an example of this technology.

This kind of circuit also makes it feasible to build very small radiometers suitable for launch as small satellite constellations. Coupled with generally available CubeSats, this has led to a number of spaceborne MW radiometers to be flown recently as well as manifested for the near future. Such small satellites can be launched and separated to form constellations that can increase sampling significantly at a reasonable cost. Yet, the requirement that the satellite remains small also points to small antenna system and thus limited spatial resolution.

The recent development of High Electron Mobility Transistors (HEMT) promise an economical hardware solution for radiometers operating within the MW and millimeter wave spectrum (Ajayan and Nirmal 2015; Deal et al. 2011; Leong et al. 2017; Samoska 2011; Liu et al. 2011). Deal et al. (2016) describe a direct detection radiometer operating at 670 GHz with a 9.6 dB noise figure. Such MW chips and radiometer receivers are extremely expensive now, but the technology is, in principle, well suited for mass production. Very promising technology for MW radiometry is metamorphic HEMT (MHEMT) developed by, for example, BAE Systems, (Smith et al. 2016), see Fig. 6.1. The plot illustrates continuous development of low noise amplifiers with low noise figures operating at increasingly higher frequencies. An advantage of the MHEMT technology for radiometry is its gain temperature stability with temperature. The MHEMT gain variations are 0.0031 dB/K/stage, about a half of the PHEMT (pseudomorphic) low noise amplifier (Smith et al. 2016).

Microwave sensors spatial resolution is a function of frequency of operation, orbit altitude, and antenna aperture size. The largest antenna currently deployed is used by AMSR2 with 2 m diameter. The solid parabolic reflector antennas are very large, heavy, and very expensive to launch to orbit. Deployable antennas for small satellites, e.g. CubeSats, are under development (Hohmann et al. 2019). An antenna concept is shown in Fig. 6.2. Such antenna, together with integrated MW electronics
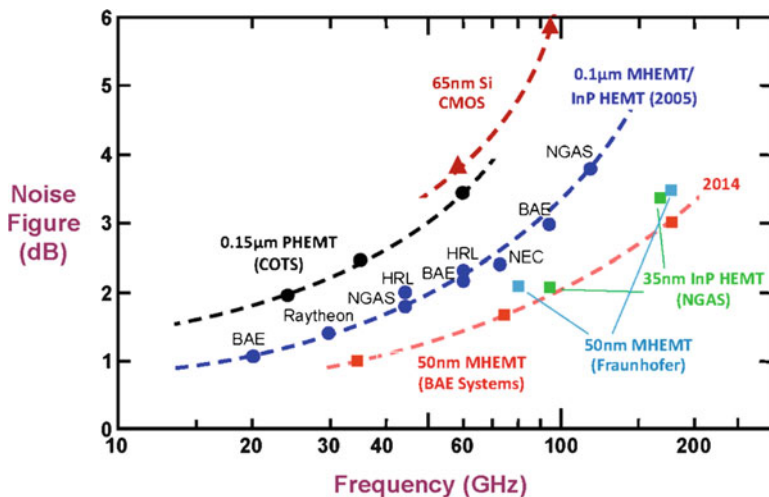
Fig. 6.1 State-of-the-art microwave monolithic integrated circuits low noise amplifiers' noise figure
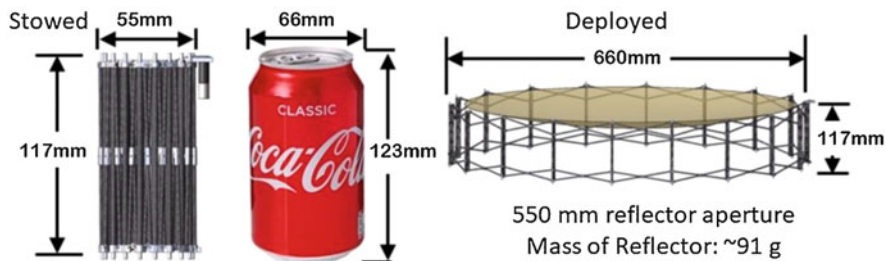
Fig. 6.2 A deployable reflector antenna concept for the small satellites. The antenna reflector surface can fit to less than 1.5 U volume and it is designed to operate up to ~100 GHz

could significantly reduce the size and mass of future satellite active (radar) and passive (MW radiometer) sensors. Using the same technology, a reflector with 2 m aperture and ~500 g mass could be stowed into a 102 mm diameter cylinder 323 mm long, thus fitting into a 3U volume of a CubeSat.

A final requirement that is evident from Sect. 6.1 is the need for calibration stability and either absolute knowledge or lacking that, methods to more easily intercalibrate existing satellites for use in long term trend analyses. These advances too, are coming, so that in the future it may be possible to have large fleets of CubeSat-based radiometers with stable calibration and high spatial resolution meeting most of the high spatial and temporal resolution requirements that today require geostationary IR sensors to achieve.

The first CubeSat to provide cross-track scanning MW observations relevant to precipitation sensing is the Micro-sized Microwave Atmospheric Satellite

(MicroMAS-2) launched in Jan 2018 (Blackwell et al. 2012). MicroMAS-2 has provided excellent on-orbit temperature and moisture profiling measurements in 10 channels spanning 90–205 GHz, and data of this type is expected to provide improved weather forecasts (Li et al. 2019).

6.2.3 Infrared Radiometer

Many advances are occurring in the field of hyperspectral IR sensing (e.g., Bernard et al. 2017) with foreseen substantial impacts on NWP (e.g., Andrey-Andrés et al. 2018) while sensors are subject to the same miniaturization as is ongoing for MW radiometers. However, the IR information content for precipitation retrieval is limited and probably well served by the latest generation of Geostationary Imagers. With 2 km resolution and 15 min global refresh rates, these sensors, together with existing polar orbiting systems, are likely to constitute the bulk of the high frequency observations needed for precipitation estimation. The one unknown in this scheme may be the ability to construct precipitation products directly from rapid changes in cloud cover, perhaps even constrained by dynamical models, and how these may be used for quantitative rainfall estimation.

6.3 Proposed Mission Concepts

6.3.1 Missions and Sensors Moving Ahead

The European Organization for the Exploitation of Meteorological Satellites (EUMETSAT) is currently finalizing its EUMETSAT Polar System-Second Generation (EPS-SG), which represents the European contribution to meteorological observations from polar orbit in the 2022–2043 time frame. Three cloud and precipitation-related MW instruments will be launched (see Chap. 5 for details): the Microwave Sounder (MWS), the Microwave Imager (MWI) and the Ice Cloud Imager (ICI). MWS and MWI are conventional heritage instruments for sounding and imaging (Kangas et al. 2012). MWS is a cross-track scanning instrument conceived for atmospheric temperature and humidity profiling and for the total liquid water column, with 24 channels between 23 and 230 GHz. MWI is a conically scanning imager for precipitation and water vapor, with 18 channels between 18 and 183 GHz. The ICI is a millimeter and sub-millimeter wave conically scanning radiometer, with 13 channels between 183 and 664 GHz (Buehler et al. 2012; Kangas et al. 2014). While these frequencies have been flown on aircraft missions, this set of frequencies has not previously been observed from space. The three sensors represent a unique opportunity to observe clouds using conventional MW sensors (conically and cross-tracking scanning) with the unprecedented addition of

the very-high-frequency ICI data that will play a relevant role in ice cloud structure characterization via retrieval of ice hydrometeor profiles (e.g., Liu et al. 2018).

The National Oceanic and Atmospheric Administration (NOAA) has manifested its Advanced Technology Microwave Sounder (ATMS) sensor on its Suomi National Polar-orbiting Partnership (S-NPP, launched 2011), NOAA-20 (launched 2017) and Joint Polar Satellite System-2 (JPSS-2) through JPSS-4 spacecraft for operations through 2038. ATMS is a conventional MW cross-track sounding radiometer with 22 channels from 23 to 183 GHz. While not as concrete as the above plans, the Japanese Space Exploration Agency (JAXA) continues with plans to launch an Advanced Microwave Scanning Radiometer (AMSR2) follow-on (AMSR3) mission aboard its Greenhouse gases Observing SATellite (GOSAT-3) platform as part of its commitment to continue monitoring the global water cycle.

The Chinese meteorological Agency (CMA) has concrete plans to continue flying the MW sounder (MWHS-2) which is a conventional cross-track sounding radiometer operating from 50 to 183 GHz. In addition, it will fly the conically scanning MWRI radiometer with 5 frequencies (10.65–89 GHz), at horizontal and vertical polarization on its FY-3 series of satellites through 2022.

While more "traditional" missions will continue to contribute essential observations for global precipitation retrievals, the design of small satellite constellations for precipitation monitoring is subject to rapid development. These new missions are based on the technology of CubeSats (U-class spacecrafts), miniaturized satellites made up of multiples of 10 cm × 10 cm × 10 cm units with a mass around 1.33 kg per unit. The CubeSats are normally deployed in orbit either from the International Space Station (ISS) or launched as secondary payloads on a launch vehicle. These characteristics contribute to substantial cost reduction by using commercial off-the-shelf components and thus increasing the feasibility of new constellations.

One of the missions in advanced planning stages is the Time-Resolved Observations of Precipitation structure and storm Intensity with a Constellation of Smallsats (TROPICS) mission selected by NASA as part of the Earth Venture-Instrument (EVI-3) program (Blackwell et al. 2018). TROPICS aims at providing observations of 3-D temperature and humidity, as well as cloud ice and precipitation horizontal structure, at high temporal resolution for investigating tropical cyclones. The median refresh rate of the measurements will be better than 60 min for the baseline mission; this will allow to observe the thermodynamics of the troposphere and precipitation structure for storm systems at the mesoscale and synoptic scale over the entire storm life cycle. TROPICS comprises six CubeSats in three LEO planes. Each constellation member will host a high-performance radiometer to provide temperature profiles using a total of 12 channels: seven channels near the 118.75 GHz oxygen absorption line, water vapor profiles using three channels near the 183 GHz water vapor absorption line, imagery in a single channel near 90 GHz for precipitation measurements (when combined with higher-resolution water vapor channels), and a single channel near 205 GHz more sensitive to precipitation-sized ice particles. The launch is currently foreseen for no earlier than 2020 at the time of writing. A single technology demonstration satellite for the Temporal Experiment for Storms and Tropical Systems (TEMPEST) constellation was successfully launched in 2018

(Reising et al. 2018b) and was operating well in its first year in orbit. It successfully demonstrates the calibration characteristics of this new class of radiometers for use in the TEMPEST mission consisting of a constellation of eight identical 6U-Class Cubesats observing at 5 millimeter-wave frequencies with three-minute temporal sampling to observe the time evolution of clouds and their transition to precipitation (Reising et al. 2017, 2018a).

A novel concept is also the Radar in a CubeSat (RainCube), a technology demonstration mission designed to enable Ka-band precipitation radar technologies on a low-cost 6U CubeSat platform (Peral et al. 2017, 2018, 2019). Like TEMPEST D, it was launched in May 2018 through a resupply mission launched by NASA's Wallops Flight Facility. A novel architecture compatible with the 6U class (or larger) has been developed at the Jet Propulsion Laboratory (JPL) through a simplification and miniaturization of the radar subsystems to reduce power consumption and the design of a new deployable small size antenna. The RainCube architecture reduces the number of components, power consumption and mass by over one order of magnitude with respect to the existing spaceborne radars. The RainCube radar is a fixed nadir-pointing profiler at Ka-band with a minimum detectable reflectivity factor better than +20 dBZ at 250 m range resolution. The footprint size, determined by the antenna size, at a nominal orbital altitude of 400 km is approximately 8.5 km.

A final mission worth noting here is the Chinese Meteorological Administration (CMA) Water Cycle Observation Mission (WCOM) currently scheduled for flight around 2020. Built around its key science question of understanding the spatial-temporal distribution characteristics of water cycle components and processes, and whether these are accelerating, the mission nominally consist of a fully polarized interferometric radiometer at L, S and C bands for soil moisture and salinity; a dual frequency polarized scatterometer at X and Ku band for snow water equivalent and monitoring of the freeze/thaw cycle; and a Polarimetric Microwave Imager (PMI) with frequencies between 6.8 and 89 GHz for temperature, water vapor and precipitation.

6.3.2   Missions in Planning Stages

JAXA is examining a proposed mission named DPR-2, which is a precipitation radar mission to satisfy the need for Doppler velocity in addition to higher sensitivity, wider swath and higher resolution than the current DPR instrument on the GPM satellite. DPR-2 follows the basic technology of DPR, but introduces the latest technology to greatly improve the radar performance. The basic design of DPR-2 is the same as DPR, but the sensitivity is improved by about 10–20 dB, and the swath width is doubled. Higher spatial resolution is achieved by oversampling with the footprint interval being less than half the FOV. Doppler velocity measurement is a new challenge for DPR technology.

Other than DPR-2, inexpensive and compact radar constellation satellites applying the technology cultivated in TRMM/PR and GPM/DPR are another option of future mission. Radar constellations will make it possible to dramatically improve the accuracy of the precipitation map such as the ones from the Integrated Multi-satelliE Retrievals for GPM (IMERG) and from GSMaP.

The planning of precipitation-related missions at the geostationary orbit (GEO) need to be mentioned as well, since it would ensure unprecedented coverage for a vast number of applications. However, technological obstacles are still not completely overcome. Several advancements were made since the first proposed efforts for a GEO MW imager (e.g., Savage et al. 1995), to include an interferometric antenna design described by Tanner et al. (2007). The interferometric array antenna concept has made it possible to build sensors whose antenna aperture is in excess of 2 m (e.g., Gaier et al. 2016). Several investigations were carried out at JPL and the European Space Agency (ESA), but the proposed missions have not been approved at the time of writing. The GEO MW mission project that currently appears closer to launch is the one of the CMA National Satellite Meteorological Center (NSMC) planned for 2021 onboard the FY-4M satellite. The Chinese mission is oriented towards tropical storm monitoring and for nowcasting of severe weather in general.

The ultimate goal for spaceborne observations of precipitation is probably a radar constellation operating from GEO orbit (Fig. 6.3). It would lead to great advances in studying severe precipitation system such as typhoon/hurricane and mesoscale convective system especially over the ocean by the continuous observation and Doppler velocity observations (which are relatively easier than from LEO orbiting satellites). The biggest problem of radar observation from GEO is the footprint size (i.e., antenna diameter). Current technology can achieve the footprint size of about 30 km, which may not be enough for practical use. Further investigation is needed to realize the radar observation from GEO (e.g., Okazaki et al. 2019).

Alternative designs are being studied by the National Aeronautics and Space Administration (NASA) for the Cloud and Precipitation Process (CPP) mission which focuses, as its name implies, on processes needed to elucidate cloud responses to climate forcing. It will therefore likely focus more on detailed measurements of
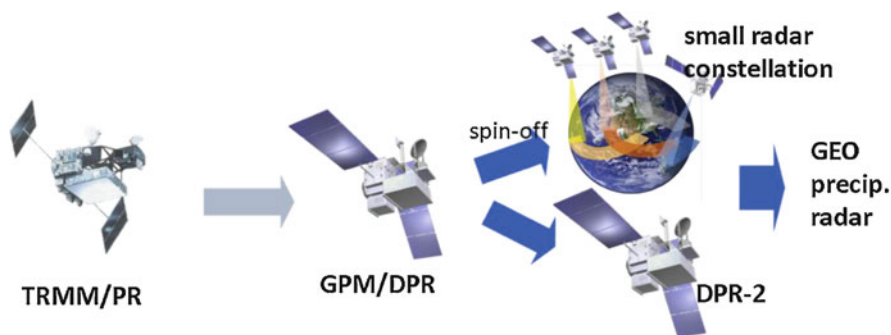
Fig. 6.3 Roadmap of spaceborne precipitation radar

clouds while leaving sampling to more weather-oriented endeavors led by the National Weather agencies, or potentially even the private sector as smaller and cheaper satellites become available.

Stephens and Kummerow (2007) articulated the need for a better definition of the atmospheric state and the vertical structure of clouds and precipitation to improve the information extracted from satellite observations. This has been the overarching reason for combining multiple frequency active and passive measurements that offers some hope for constraining the atmospheric states needed to derive unique rain and snow rate signals. Radar improvements and the launch of constellations of high-quality radiometers for an adequate space-time sampling are likely to provide the observations needed for a substantial step forward in the quality of the retrieval algorithms.

This framework will surely evolve from the above concepts to meet JAXA's needs, NASA's Decadal Survey (2017) needs, as well as the WCRP research needs, and the World Meteorological Organization (WMO) constellation of sensors. While the missions may not be fully mature (or at least not mature enough to have a timeline associated with them), the goals are well defined, and the community is moving forward from the scientific and technological points of view.

References

ACE. (2016). ACE 2011–2015 Progress report and future outlook. *NASA Earth Science. Decadal Survey Studies*, GSFC, 154 pp. [Available at https://acemission.gsfc.nasa.gov/documents/ACE_5YWP-FINAL_Redacted.pdf. Last accessed 11 Mar 2019]

Ajayan, J., & Nirmal, D. (2015). A review of InP/InAlAs/InGaAs based transistors for high frequency applications. *Superlattices and Microstructures, 86*, 1–19. https://doi.org/10.1016/j.spmi.2015.06.048.

Amayenc, P., Testud, J., & Marzoug, M. (1993). Proposal for a spaceborne dual-beam rain radar with Doppler capability. *Journal of Atmospheric and Oceanic Technology, 10*, 262–276. https://doi.org/10.1175/1520-0426(1993)010<0262:PFASDB>2.0.CO;2.

Andrey-Andrés, J., Fourrié, N., Guidard, V., Armante, R., Brunel, P., Crevoisier, C., & Tournier, B. (2018). A simulated observation database to assess the impact of the IASI-NG hyperspectral infrared sounder. *Atmospheric Measurement Techniques, 11*, 803–818. https://doi.org/10.5194/amt-11-803-2018.

Battaglia, A., & Kollias, P. (2019). Evaluation of differential absorption radars in the 183 GHz band for profiling water vapour in ice clouds. *Atmospheric Measurement Techniques, 12*, 3335–3349. https://doi.org/10.5194/amt-12-3335-2019.

Battaglia, A., Westbrook, C. D., Kneifel, S., Kollias, P., Humpage, N., Löhnert, U., Tyynelä, J., & Petty, G. W. (2014). G band atmospheric radars: New frontiers in cloud physics. *Atmospheric Measurement Techniques, 7*, 1527–1546. https://doi.org/10.5194/amt-7-1527-2014.

Battaglia, A., Dhillon, R., & Illingworth, A. (2018). Doppler W-band polarization diversity space-borne radar simulator for wind studies. *Atmospheric Measurement Techniques, 11*, 5965–5979. https://doi.org/10.5194/amt-11-5965-2018.

Bernard, F., Calvel, B., Pasternak, F., Davancens, R., Buil, C., Baldit, E., Luitot, C., & Penquer, A. (2017). Overview of IASI-NG the new generation of infrared atmospheric sounder. *Proceedings of SPIE*, 10563. https://doi.org/10.1117/12.2304101.

Blackwell, W., Allen, G., Galbraith, C., Hancock, T., Leslie, R., Osaretin, I., Retherford, L., Scarito, M., Semisch, C., Shields, M., Silver, M., Toher, D., Wight, K., Miller, D., Cahoy, K., & Erickson, N. (2012). Nanosatellites for earth environmental monitoring: The MicroMAS project. *Proceedings of IEEE Specialist Meeting on Microwave Radiometry and Remote Sensing of the Environment (MicroRad)*, Roma, 5–9 Mar., https://doi.org/10.1109/MicroRad.2012. 6185263.

Blackwell, W. J., Braun, S., Bennartz, R., Velden, C., DeMaria, M., Atlas, R., Dunion, J., Marks, F., Rogers, R., Annane, B., & Leslie, R. V. (2018). An overview of the TROPICS NASA Earth Venture Mission. *The Quarterly Journal of the Royal Meteorological Society, 144*(S1), 16–26. https://doi.org/10.1002/qj.3290.

Brown, S. T., Lambrigtsen, B., Denning, R. F., Gaier, T., Kangaslahti, P., Lim, B. H., Tanabe, J. M., & Tanner, A. B. (2011). The high-altitude MMIC sounding radiometer for the Global Hawk unmanned aerial vehicle: Instrument description and performance. *IEEE Transactions on Geoscience and Remote Sensing, 49*, 3291–3301. https://doi.org/10.1109/TGRS.2011.2125973.

Buehler, S. A., Defer, E., Evans, F., Eliasson, S., Mendrok, J., Eriksson, P., Lee, C., Jiménez, C., Prigent, C., Crewell, S., Kasai, Y., Bennartz, R., & Gasiewski, A. J. (2012). Observing ice clouds in the submillimeter spectral range: The CloudIce mission proposal for ESA's Earth Explorer 8. *Atmospheric Measurement Techniques, 5*, 1529–1549. https://doi.org/10.5194/amt-5-1529-2012.

Chahat, N., Hodges, R., Sauder, J., Thomson, M., Peral, E., & Rahmat-Samii, Y. (2016). CubeSat deployable Ka-band mesh reflector antenna development for Earth science missions. *IEEE Transactions on Antennas and Propagation, 64*, 2083–2093. https://doi.org/10.1109/TAP. 2016.2546306.

Chase, R. J., Finlon, J. A., Borque, P., McFarquhar, G. M., Nesbitt, S. W., Tanelli, S., Sy, O. O., Durden, S. L., & Poellot, M. R. (2018). Evaluation of triple-frequency radar retrieval of snowfall properties using coincident airborne in situ observations during OLYMPEX. *Geophysical Research Letters, 45*, 5752–5760. https://doi.org/10.1029/2018GL077997.

Cooper, K. B., Rodriguez Monje, R., Millán, L., Lebsock, M., Tanelli, S., Siles, J. V., Lee, C., & Brown, A. (2018). Atmospheric humidity sounding using differential absorption radar near 183 GHz. *IEEE Geoscience and Remote Sensing Letters, 15*, 163–167. https://doi.org/10.1109/LGRS.2017.2776078.

Deal, W. R., Leong, K., Radisic, V., Sarkozy, S., Gorospe, B., Lee, J., Liu, P. H., Yoshida, W., Zhou, J., Lange, M., Lai, R., & Mei, X. B. (2011). Low noise amplification at 0.67 THz using 30 nm InP HEMTs. *IEEE Microwave and Wireless Components Letters, 21*, 368–370. https://doi.org/10.1109/LMWC.2011.2143701.

Deal, W. R., Kangaslahti, P., Zamora, A., Schlecht, E., Leong, K., Mei, G., Shih, S., & Reising, S. C. (2016). 25 nm InP HEMT LNAs and receiver technology for the TWICE instrument. *NASA Earth Science Technology Forum*, Annapolis, 14–16 Jun. [Abstract available at https:// esto.nasa.gov/forum/estf2016/abstracts/Deal_Reising.htm. Last accessed 19 Mar. 2019]

Decadal Survey (Ed.). (2017). *Thriving on our changing planet: A decadal strategy for Earth observation from space* (p. 716). Washington, DC: The National Academies Press. https://doi. org/10.17226/24938.

Durden, S. L., Siqueira, P. R., & Tanelli, S. (2007). On the use of multiantenna radars for spaceborne Doppler precipitation measurements. *IEEE Geoscience and Remote Sensing Letters, 4*, 181–183. https://doi.org/10.1109/LGRS.2006.887136.

Fabry, F. (2001). Using radars as radiometers: Promises and pitfalls. *Prepr. 30th International Conference on Radar Meteorology*, Munich, Germany, American Meteorological Society, 197–198. [Available at https://ams.confex.com/ams/30radar/webprogram/Paper21576.html. Last accessed 12 Feb 2019]

Furukawa, K., Yamamoto, K., Kubota, T., Oki, R., & Iguchi, T. (2015). Current status of the dual-frequency precipitation radar on the Global Precipitation Measurement core spacecraft and scan pattern change test operations results. *Proceedings of SPIE Remote Sensing of the Atmosphere, Clouds, and Precipitation VII*, 107762. https://doi.org/10.1117/12.2323964.

Gaier, T., Kangaslahti, P., Lambrigtsen, B., Ramos-Perez, I., Tanner, A., McKague, D., Ruf, C., Flynn, M., Zhang, Z., Backhus, R., & Austerberry, D. (2016). A 180 GHz prototype for a geostationary microwave imager/sounder-GEOSTAR-III. *IGARSS 2016*, Beijing, 10–15 July, 2021–2023. https://doi.org/10.1109/IGARSS.2016.7729521.

GCOS. (2016). The global observing system for climate: Implementation needs. WMO, GCOS-200, 315 pp. [Available at https://gcos.wmo.int/en/gcos-implementation-plan. Last accessed 8 Feb 2019]

Haddad, Z. S., Sy, O. O., Hristova-Veleva, S., & Stephens, G. L. (2017). Derived observations from frequently sampled microwave measurements of precipitation. Part I: Relations to atmospheric thermodynamics. *IEEE Transactions on Geoscience and Remote Sensing, 55*, 3441–3453. https://doi.org/10.1109/TGRS.2017.2671598.

Hohmann, T., Fay, J., Dunlap, C., & Klein, M. (2019). Deployable W-band antennas for CubeSats, NanoSats, and SmallSats. *99th AMS Annual Meeting*, Phoenix, 6–10 Jan. [Available at https://ams.confex.com/ams/2019Annual/meetingapp.cgi/Paper/350574. Last accessed 19 Mar 2019]

Houze, R. A., McMurdie, L. A., Petersen, W. A., Schwaller, M. R., Baccus, W., Lundquist, J. D., Mass, C. F., Nijssen, B., Rutledge, S. A., Hudak, D. R., Tanelli, S., Mace, G. G., Poellot, M. R., Lettenmaier, D. P., Zagrodnik, J. P., Rowe, A. K., DeHart, J. C., Madaus, L. E., Barnes, H. C., & Chandrasekar, V. (2017). The Olympic Mountains Experiment (OLYMPEX). *Bulletin of the American Meteorological Society, 98*, 2167–2188. https://doi.org/10.1175/BAMS-D-16-0182.1.

Huffman, G. J., Ferraro, R., Kidd, C., Levizzani, V., & Turk, F. J. (2016). Requirements for a robust precipitation constellation. *14th Specialist Meeting on Microwave Radiometry and Remote Sensing of the Environment, MicroRad*, Espoo, Finland, 11–14 Apr. https://doi.org/10.1109/MICRORAD.2016.7530500.

Illingworth, A. J., Barker, H. W., Beljaars, A., Ceccaldi, M., Chepfer, H., Clerbaux, N., Cole, J., Delanoë, J., Domenech, C., Donovan, D. P., Fukuda, S., Hirakata, M., Hogan, R. J., Huenerbein, A., Kollias, P., Kubota, T., Nakajima, T., Nakajima, T. Y., Nishizawa, T., Ohno, Y., Okamoto, H., Oki, R., Sato, K., Satoh, M., Shephard, M. W., Velázquez-Blázquez, A., Wandinger, U., Wehr, T., & van Zadelhoff, G.-J. (2016). The EarthCARE satellite: The next step forward in global measurements of clouds, aerosols, precipitation, and radiation. *Bulletin of the American Meteorological Society, 96*, 1311–1332. https://doi.org/10.1175/BAMS-D-12-00227.1.

Illingworth, A. J., Battaglia, A., Bradford, J., Forsythe, M., Joe, P., Kollias, P., Lean, K., Lori, M., Mahfouf, J.-F., Melo, S., Midthassel, R., Munro, Y., Nicol, J., Potthast, R., Rennie, M., Stein, T. H. M., Tanelli, S., Tridon, F., Walden, C. J., & Wolde, M. (2018). WIVERN: A new satellite concept to provide global in-cloud winds, precipitation, and cloud properties. *Bulletin of the American Meteorological Society, 99*, 1669–1687. https://doi.org/10.1175/BAMS-D-16-0047.1.

Im, E., Durden, S. L., Rahrnat-Sarnii, Y., Fang, H., Cable, V., Lou, M., & Huang, J. (2004). Advanced geostationary radar for hurricane monitoring and studies. *Proceedings 2004 IEEE Radar Conference (IEEE Cat. No.04CH37509)*, Philadelphia, PA, 307–311. https://doi.org/10.1109/NRC.2004.1316440.

Kangas, V., D'Addio, S., Betto, M., Barre, H., Loiselet, M., & Mason, G. (2012). Metop second generation microwave sounding and microwave imaging missions. *Proceedings 2012 EUMETSAT Meteor. Satellite Conference*, Sopot, Poland, Sept. 3–7. [Available at https://www.eumetsat.int/website/wcm/idc/idcplg?IdcService=GET_FILE&dDocName=PDF_CONF_P61_S1_09_KANGAS_V&RevisionSelectionMethod=LatestReleased&Rendition=Web. Last accessed 14 Feb 2019]

Kangas, V., D'Addio, S., Klein, U., Loiselet, M., Mason, G., Orlhac, J.-C., Gonzalez, R., Bergada, M., Brandt, M., & Thomas, B. (2014). Ice cloud imager instrument for MetOp second generation. *13th Specialist Meeting on Microwave Radiometry and Remote Sensing*, *MicroRad*, Pasadena, CA, 24–27 Mar, 228–231. https://doi.org/10.1109/MicroRad.2014.6878946.

Kirschbaum, D. B., Huffman, G. J., Adler, R. F., Braun, S., Garrett, K., Jones, E., McNally, A., Skofronick-Jackson, G., Stocker, E., Wu, H., & Zaitchik, B. F. (2017). NASA's remotely sensed precipitation: A reservoir for applications users. *Bulletin of the American Meteorological Society, 98*, 1169–1198. https://doi.org/10.1175/BAMS-D-15-00296.1.

Kollias, P., Bharadwaj, N., Widener, K., Jo, I., & Johnson, K. (2014). Scanning ARM cloud radars. Part I: Operational sampling strategies. *The Journal of Atmospheric and Oceanic Technology, 31*, 569–582. https://doi.org/10.1175/JTECH-D-13-00044.1.

Kucera, P. A., Ebert, E. E., Turk, F. J., Levizzani, V., Kirschbaum, D. B., Tapiador, F. J., Loew, A., & Borsche, M. (2013). Precipitation from space: Advancing Earth system science. *Bulletin of the American Meteorological Society, 94*, 365–375. https://doi.org/10.1175/BAMS-D-11-00171.1.

Leong, K. M. K. H., Mei, X., Yoshida, W. H., Zamora, A., Padilla, J. G., Gorospe, B. S., Nguyen, K., & Deal, W. R. (2017). 850 GHz receiver and transmitter front-ends using InP HEMT. *IEEE Transactions on Terahertz Science and Technology, 7*, 466–475. https://doi.org/10.1109/TTHZ.2017.2710632.

Lettenmaier, D. P. (2017). Observational breakthroughs lead the way to improved hydrological predictions. *Water Resources Research, 53*, 2591–2597. https://doi.org/10.1002/2017WR020896.

Lettenmaier, D. P., Alsdorf, D., Dozier, J., Huffman, G. J., Pan, M., & Wood, E. F. (2015). Inroads of remote sensing into hydrologic science during the WRR era. *Water Resources Research, 51*, 7309–7342. https://doi.org/10.1002/2015WR017616.

Levizzani, V., Kidd, C., Aonashi, K., Bennartz, R., Ferraro, R. R., Huffman, G. J., Roca, R., Turk, F. J., & Wang, N.-Y. (2018). The activities of the International Precipitation Working Group. *Quarterly Journal of the Royal Meteorological Society, 144*(S1), 3–15. https://doi.org/10.1002/qj.3214.

Li, Z., Li, J., Schmit, T. J., Wang, P., Lim, A., Li, J., Nagle, F. W., Bai, W., Otkin, J. A., Atlas, R., Hoffman, R. N., Boukabara, S.-A., Zhu, T., Blackwell, W. J., & Pagano, T. S. (2019). The alternative of CubeSat-based advanced infrared and microwave sounders for high impact weather forecasting. *Atmospheric and Oceanic Science Letters, 12*, 80–90. https://doi.org/10.1080/16742834.2019.1568816.

Liu, L., Alt, A. R., Benedickter, H., & Bolognesi, C. R. (2011). InP/GaInAs pHEMT ultralow-power consumption MMICs. *IEEE Compound Semiconductor Integrated Circuit Symp. (CSICS)*, Waikoloa, Hawaii, 16–19 Nov., https://doi.org/10.1109/CSICS.2011.6062493.

Liu, Y., Buehler, S. A., Brath, M., Liu, H., & Dong, X. (2018). Ensemble optimization retrieval algorithm of hydrometeor profiles for the Ice Cloud Imager submillimeter-wave radiometer. *Journal of Geophysical Research, 123*, 4594–4612. https://doi.org/10.1002/2017JD027892.

Mace, G. G., Avey, S., Cooper, S., Lebsock, M., Tanelli, S., & Dobrowalski, G. (2016). Retrieving co-occurring cloud and precipitation properties of warm marine boundary layer clouds with A-Train data. *Journal of Geophysical Research, 121*, 4008–4033. https://doi.org/10.1002/2015JD023681.

Madry, S., Martinez, P., & Laufer, R. (2018). Small satellites and the U. N. sustainable development goals. In *Innovative design, manufacturing and testing of small satellites* (pp. 65–79). Cham: Springer Praxis Books. https://doi.org/10.1007/978-3-319-75094-1_5.

Marsh, S. (2006). *Practical MMIC design* (p. 356). Norwood: Artech House. ISBN-10: 1-59693-036-5.

Meneghini, R., & Kozu, T. (1990). *Spaceborne weather radar* (p. 199). Boston: Artech House Publ. ISBN: 0890063826.

Muraki, Y. (2017). Concept of Asian small precipitation radar constellation. *68th International Astronautical Congress*, Paper ID. 37216. [Available at https://iafastro.directory/iac/paper/id/37216/abstract-pdf/IAC-17,B1,1,7,x37216.brief.pdf?2017-04-03.15:45:03. Last accessed 10 Mar 2019]

Okazaki, A., Honda, T., Kotsuki, S., Yamaji, M., Kubota, T., Oki, R., Iguchi, T., & Miyoshi, T. (2019). Simulating precipitation radar observations from a geostationary satellite. *Atmospheric Measurement Techniques*, 12, 3985–3996. https://doi.org/10.5194/amt-12-3985-2019.

Paganini, M., Petiteville, I., Ward, S., Dyke, G., Steventon, M., Harry, J., & Kerblat, F., (Eds.) (2018). Satellite Earth observations in support of the sustainable development goals. CEOS, ESA-EOGB, 107 pp. [Available at http://eohandbook.com/sdg/files/CEOS_EOHB_2018_SDG.pdf. Last accessed 11 Feb 2019]

Pazmany, A. L., Galloway, J. C., Mead, J. B., Popstefanija, I., McIntosh, R. E., & Bluestein, H. W. (1999). Polarization diversity pulse-pair technique for millimeter-wave Doppler radar measurements of severe storm features. *Journal of Atmospheric and Oceanic Technology, 16*, 1900–1911. https://doi.org/10.1175/1520-0426(1999)016<1900:PDPPTF>2.0.CO;2.

Peral, E., Imken, T., Sauder, J., Statham, S., Tanelli, S., Price, D., Chahat, N., & Williams, A. (2017). RainCube, a Ka-band precipitation radar in a 6U CubeSat. *31st Annual AIAA/USU Conference on Small Satellites*, Logan, UT, Aug 31–3 Sept., SSC17-III-03. [Available at https://digitalcommons.usu.edu/cgi/viewcontent.cgi?article=3611&context=smallsat. Last accessed 13 Feb 2019]

Peral, E., Im, E., Wye, L., Lee, S., Tanelli, S., Rahmat-Samii, Y., Horst, S., Hoffman, J., Yun, S.-H., Imken, T., & Hawkins, D. (2018). Radar technologies for Earth remote sensing from CubeSat platforms. *Proceedings of the IEEE, 106*, 404–418. https://doi.org/10.1109/JPROC.2018.2793179.

Peral, E., Tanelli, S., Statham, S., Joshi, S., Imken, T., Price, D., Sauder, J., Chahat, N., & Williams, A. (2019). RainCube – The first ever radar measurements from a CubeSat in space. *The Journal of Applied Remote Sensing, 13*(3), 032504.

Reising, S. C., Gaier, T. C., Kummerow, C. D., Padmanabhan, S., Lim, B. H., Heneghan, C., Berg, W. K., Chandrasekar, V., Olson, J. P., Brown, S. T., Carvo, J., & Pallas, M. (2017). Global measurement of temporal signatures of precipitation: Development of the temporal experiment for storms and tropical systems technology demonstration mission. *IGARSS 2017*, Ft. Worth, TX, 23–28 July, 5931–5933. https://doi.org/10.1109/IGARSS.2017.8128359.

Reising, S. C., Gaier T. C., Padmanabhan S., Lim B. H., Heneghan C., Kummerow C. D., Berg W. K., Chandrasekar V., Radhakrishnan C., Brown S. T., Carvo J., & Pallas M. (2018a). An Earth Venture in-space technology demonstration mission for Temporal Experiment for Storms and Tropical Systems (Tempest). *IGARSS* 2018, Valencia, 22–27 July, 6301–6303. https://doi.org/10.1109/IGARSS.2018.8517330.

Reising, S. C., Gaier, T., Brown, S. T., Padmanabhan, S., Kummerow, C. D., Chandrasekar, V., Heneghan, C., Lim, B., Berg, W. K., Schulte, R., Radhakrishnan, C., & Pallas, M. (2018b). Temporal Experiment for Storms and Tropical Systems Technology Demonstration (TEMPEST-D) mission: Early results and potential science capabilities. AGU: AG-A44G-05, Washington, DC, 10–14 Dec.

Robertson, I. D., & Lucyszyn, S. (Eds.). (2001). *RFIC and MMIC design and technology* (p. 582). Herts: IET. https://doi.org/10.1049/PBCS013E.

Roy, R. J., Lebsock, M., Millán, L., Dengler, R., Rodriguez Monje, R., Siles, J. V., & Cooper, K. B. (2018). Boundary-layer water vapor profiling using differential absorption radar. *Atmospheric Measurement Techniques, 11*, 6511–6523. https://doi.org/10.5194/amt-11-6511-2018.

Samoska, L. A. (2011). An overview of solid-state integrated circuit amplifiers in the submillimeter-wave and THz regime. *IEEE Transactions on Terahertz Science and Technology, 1*, 9–24. https://doi.org/10.1109/TTHZ.2011.2159558.

Savage, R. C., Smith, E. A., & Mugnai, A. (1995). Concepts for a geostationary microwave imaging sounder (GeoMIS). *IGARSS 1995*, Firenze, 10–14 July, 652–654. https://doi.org/10.1109/IGARSS.1995.520483.

Skofronick-Jackson, G., Petersen, W. A., Berg, W., Kidd, C., Stocker, E. F., Kirschbaum, D. B., Kakar, R., Braun, S. A., Huffman, G. J., Iguchi, T., Kirstetter, P. E., Kummerow, C. D., Meneghini, R., Oki, R., Olson, W. S., Takayabu, Y. N., Furukawa, K., & Wilheit, T. (2017). The Global Precipitation Measurement (GPM) mission for science and society. *Bulletin of the*

American Meteorological Society, 98, 1679–1695. https://doi.org/10.1175/BAMS-D-15-00306.1.

Smith, P. M., Xu D., Ashman M., Yang X., Chao P. C., Chu K., Duh K. H. G., & Nichols K. (2016). 50nm MHEMT technology for ultra-sensitive low noise amplifiers. *2016 Electronics Design Innovation Conference, EDI-CON 2016*, Boston, 19–21 Apr.

Stephens, G. L., & Kummerow, C. D. (2007). The remote sensing of clouds and precipitation from space: A review. *Journal of the Atmospheric Sciences, 64*, 3742–3765. https://doi.org/10.1175/2006JAS2375.1.

Stephens, G. L., Vane, D. G., Boain, R. J., Mace, G. G., Sassen, K., Wang, Z., Illingworth, A. J., O'Connor, E. J., Rossow, W. B., Durden, S. L., Miller, S. D., Austin, R. T., Benedetti, A., Mitrescu, C., & the CloudSat Science Team. (2002). The CloudSat mission and the A-train: A new dimension of space-based observations of clouds and precipitation. *Bulletin of the American Meteorological Society, 83*, 1771–1790. https://doi.org/10.1175/BAMS-83-12-1771.

Sy, O. O., Tanelli, S., Takahashi, N., Ohno, Y., Horie, H., & Kollias, P. (2014). Simulation of EarthCARE spaceborne Doppler radar products using ground-based and airborne data: Effects of aliasing and nonuniform beam-filling. *IEEE Transactions on Geoscience and Remote Sensing, 52*, 1463–1479. https://doi.org/10.1109/TGRS.2013.2251639.

Sy, O. O., Haddad, Z. S., Stephens, G. L., & Hristova-Veleva, S. (2017). Derived observations from frequently sampled microwave measurements of precipitation. Part II: Sensitivity to atmospheric variables and instrument parameters. *IEEE Transactions on Geoscience and Remote Sensing, 55*, 2898–2912. https://doi.org/10.1109/TGRS.2017.2656061.

Takahashi, N. (2017). Surface echo characteristics derived from the wide swath experiment of the precipitation radar onboard TRMM satellite during its end-of-mission operation. *IEEE Transactions on Geoscience and Remote Sensing, 55*, 1988–1993. https://doi.org/10.1109/TGRS.2016.2633971.

Takahashi, N., Hanado, H., Nakamura, K., Kanemaru, K., Nakagawa, K., Iguchi, T., Nio, T., Kubota, T., Oki, R., & Yoshida, N. (2016). Overview of the end-of-mission observation experiments of precipitation radar onboard the tropical rainfall measuring mission satellite. *IEEE Transactions on Geoscience and Remote Sensing, 54*, 3450–3459. https://doi.org/10.1109/TGRS.2016.2518221.

Tanelli, S., Im, E., Kobayashi, S., Mascelloni, R., & Facheris, L. (2005). Spaceborne Doppler radar measurements of rainfall: Correction of errors induced by pointing uncertainties. *Journal of Atmospheric and Oceanic Technology, 22*, 1676–1690. https://doi.org/10.1175/JTECH1797.1.

Tanelli, S., Durden, S. L., Im, E., Pak, K., Reinke, D. G., Partain, P., Haynes, J. M., & Marchand, R. T. (2008). Cloudsat's cloud profiling radar after 2 years in orbit: Performance, calibration and processing. *IEEE Transactions on Geoscience and Remote Sensing, 46*, 3560–3573. https://doi.org/10.1109/TGRS.2008.2002030.

Tanelli, S., Durden, S. L., & Johnson, M. P. (2016). Airborne demonstration of DPCA for velocity measurements of distributed targets. *IEEE Geoscience and Remote Sensing Letters, 13*, 1415–1419. https://doi.org/10.1109/LGRS.2016.2581174.

Tanelli, S., Haddad, Z. S., Im, E., Durden, S. L., Sy, O. O., Sadowy, G. A., & Sanchez-Barbetty, M. (2018). Radar concepts for the next generation of spaceborne observations of cloud and precipitation processes. *IEEE Radar Conference (RadarConf18)*, Oklahoma City, OK, 1245–1249.

Tanner, A. B., Wilson, W. J., Lambrigtsen, B. H., Dinardo, S. J., Brown, S. T., Kangaslahti, P. P., Gaier, T. C., Ruf, C. S., Gross, S. M., Lim, B. H., Musko, S. B., Rogacki, S. A., & Piepmeier, J. R. (2007). Initial results of the Geostationary Synthetic Thinned Array Radiometer (GeoSTAR) demonstrator instrument. *IEEE Transactions on Geoscience and Remote Sensing, 45*, 1947–1957. https://doi.org/10.1109/TGRS.2007.894060.

Tapiador, F. J., Navarro, A., Levizzani, V., García-Ortega, E., Huffman, G. J., Kidd, C., Kucera, P. A., Kummerow, C. D., Masunaga, H., Petersen, W. A., Roca, R., Sánchez, J.-L., Tao, W.-K., & Turk, F. J. (2017). Global precipitation measurements for validating climate models. *Atmospheric Research, 197*, 1–20. https://doi.org/10.1016/j.atmosres.2017.06.021.

Tapiador, F. J., Roca, R., Del Genio, A., Dewitte, B., Petersen, W., & Zhang, F. (2019). Is precipitation a good metrics for model performance? *Bulletin of the American Meteorological Society, 100*, 223–233. https://doi.org/10.1175/BAMS-D-17-0218.1.

Trenberth, K. E., & Zhang, Y. (2018). How often does it rain? *Bulletin of the American Meteorological Society, 99*, 289–298. https://doi.org/10.1175/BAMS-D-17-0107.1.

Trenberth, K. E., Dai, A., Rasmussen, R. M., & Parsons, D. B. (2003). The changing character of precipitation. *Bulletin of the American Meteorological Society, 84*, 1205–1218. https://doi.org/10.1175/BAMS-84-9-1205.

Weatherhead, E. C., Wielicki, B. A., Ramaswamy, V., Abbott, M., Ackerman, T. P., Atlas, R., Brasseur, G., Bruhwiler, L., Busalacchi, A. J., Butler, J. H., Clack, C. T. M., Cooke, R., Cucurull, L., Davis, S. M., English, J. M., Fahey, D. W., Fine, S. S., Lazo, J. K., Liang, S., Loeb, N. G., Rignot, E., Soden, B., Stanitski, D., Stephens, G., Tapley, B. D., Thompson, A. M., Trenberth, K. E., & Wuebbles, D. (2017). Designing the climate observing system of the future. *Earth's Future, 6*, 80–102. https://doi.org/10.1002/2017EF000627.

Wood, D., & Stober K. J. (2018). Small satellites contribute to the United Nation's sustainable development goals. *Proceedings of 32nd Annual AIAA/USU Conference on Small Satellites*, Logan UT, 4-9 Aug., SSC18-WKVIII-08. [Available at https://digitalcommons.usu.edu/smallsat/2018/all2018/437/. Last accessed 19 Mar 2019]

Wulder, M. A., & Coops, N. C. (2014). Satellites: Make Earth observations open access. *Nature, 513*, 30–31. https://doi.org/10.1038/513030a.

Part II
Retrieval Techniques, Algorithms and Sensors

Chapter 7
Introduction to Passive Microwave Retrieval Methods

Christian D. Kummerow

Abstract This chapter introduces the reader to the basic concepts behind the remote sensing of precipitation from passive microwave radiation. Distinctions are drawn between emission-based frameworks that work well over radiometrically cold oceans, scattering methods that work better over land, and the newer optimal estimation methods that incorporate both of these concepts as well as principles adopted from the atmospheric sounding community. The reader is introduced simultaneously to the basic spaceborne sensors, and their evolution, to show how sensors and algorithms have evolved over time, leading to the current GPM satellite concept. This chapter is not a comprehensive review of all the algorithms that have been developed. Instead, it highlights individual algorithms that represent the spectrum of algorithm being employed.

7.1 Theory

The Earth emits and absorbs microwave radiation according to the Planck formula given by

C. D. Kummerow (✉)
Department of Atmospheric Science, Colorado State University, Ft. Collins, CO, USA
e-mail: christian.kummerow@colostate.edu

$$I_\nu(T) = \frac{2h\nu^3}{c^2(e^{h\nu/kT} - 1)} \quad \left[Wm^{-2}sr^{-1}Hz^{-1}\right] \tag{7.1}$$

where ν is the frequency, T is the temperature of the emitting body, h is the Planck constant, c is the speed of light and k is Boltzmann's constant. In the microwave regime, the relatively low frequencies between 1 and 300 GHz result in $h\nu$ being much smaller than kT for terrestrial temperatures. This allows Eq. (7.1) to be simplified as

$$I_\nu(T) = \frac{2k\nu^2}{c^2}T \quad \left[Wm^{-2}sr^{-1}Hz^{-1}\right] \tag{7.2}$$

Thus, in microwave remote sensing at a given wavelength, the radiance of a black body is directly proportional to the physical temperature of the object in question. The only caveat to this equation is that the Earth itself has a wavelength dependent emissivity, which changes the emitted radiation according to:

$$I_{\nu,obs}(T) = \varepsilon_\nu \frac{2k\nu^2}{c^2}T_{Sfc} \quad \left[Wm^{-2}sr^{-1}Hz^{-1}\right] \tag{7.3}$$

where ε_ν is the Earths' emissivity at the specified frequency, ν, and T_{Sfc} the surface skin temperature. The brightness temperature, or physical radiating temperature of a black body ($\varepsilon = 1$), is thus linearly related to the radiance itself. The emissivity, in turn, depends primarily on the dielectric properties of the material and the roughness of the surface. Dielectric properties for water, ice as well as wet and dry soil can be found in numerous publications, including Ulaby et al. (1986). To first order, one sees very large distinctions between ocean, land, and ice/snow covered surfaces. In particular, oceans have relatively low emissivities across the microwave spectrum (typically around 0.5) while land is considerably higher (closer to unity) but sensitive to soil moisture, particularly at lower frequencies (i.e., <10 GHz). Snow- and ice-covered surface can vary significantly based on the snow and ice properties.

Emission and scattering by gases and hydrometeors in the atmosphere occur when the incident radiation interacts with the dipoles in the material. While emission and scattering are distinct manifestations of the same interaction, it is convenient here to treat them as separate phenomena given that scattering by individual water vapor molecules in the microwave regime is so small as to be entirely negligible. That leaves only absorption by gases that are shown in Fig. 7.1. There is a weak water vapor absorption line at 22.235 GHz, followed by a strongly absorbing complex of oxygen lines between 54 and 60 GHz, another oxygen line at 118 GHz and a second, stronger water vapor absorption line at 183 GHz.

Water vapor sounders focus on the stronger 183 GHz line while temperature sounders, relying on well mixed oxygen, have historically employed the 54–60 GHz complex. Some sensors are planned to exploit the 118 GHz line in the near future. In addition to the lines noted above, there is some continuum absorption but it is modest for frequencies below 100 GHz.
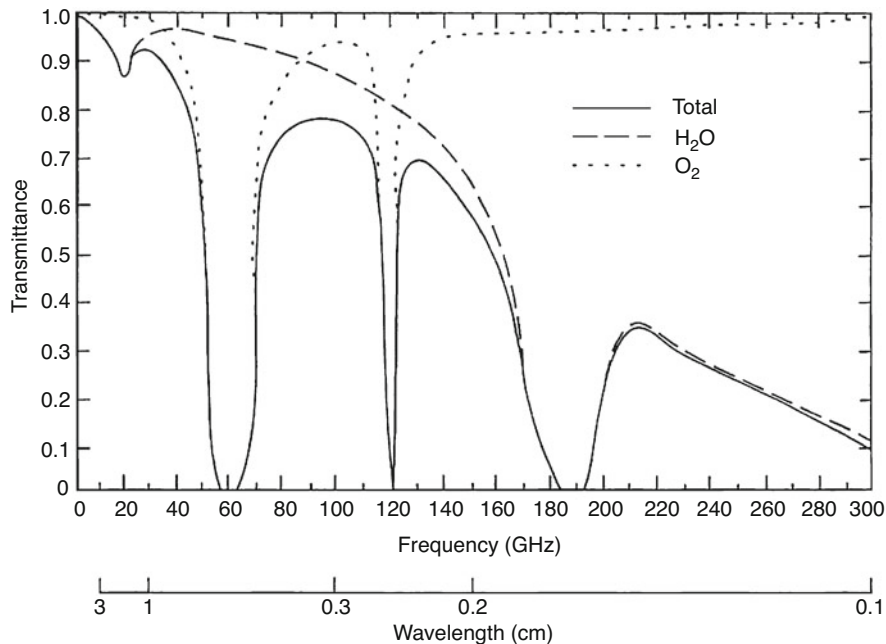
Fig. 7.1 Demonstrative atmospheric transmittances (total, H_2O and O_2) as a function of frequency and wavelength in the microwave region. (Adapted from Liou 2002, p. 415)

For water drops, the dielectric properties of liquid water are responsible for very broad absorption across the microwave frequency range due to Debye relaxation, with absorption increasing with frequency. Ice, on the other hand, responds quite different as the ice crystal lattice structure is not easily able to resonate with the incoming frequency. Ice thus exhibits relatively little absorption, particularly at the lower end of the commonly used frequencies (typically <10 GHz).

As long as water droplets are small compared to the wavelength (generally true for cloud drops in the microwave regime), Rayleigh absorption and scattering apply and the absorption and scattering cross section of droplets, σ_{abs}, and σ_{sca}, respectively, can be expressed as:

$$\sigma_{abs,\nu} = \frac{8\pi^2 a^3 \nu}{c} \text{Im}\left\{\frac{\tilde{n}^2 - 1}{\tilde{n}^2 + 2}\right\} \tag{7.4}$$

$$\sigma_{sca,\nu} = \frac{128\pi^5 a^6 \nu^4}{c^4} \left|\frac{\tilde{n}^2 - 1}{\tilde{n}^2 + 2}\right|^2 \tag{7.5}$$

where a is the particle radius, ν is the frequency of the radiation and $\tilde{n}$ is the complex refractive index of water at the specified wavelength. Noteworthy in Eq. 7.4, is that the absorption is related the third moment of the drop diameter. This implies that

absorption is directly proportional to the liquid water content of the cloud with no sensitivity to drop sizes. While this makes the retrieval of cloud liquid water content over radiometrically cold oceans relatively straightforward, it also implies that it is difficult to separate small non-precipitating drops from larger precipitating ones. Scattering is sensitive to the cloud drop sizes but is relatively small for cloud- and rain-drops at frequencies below 30 GHz. Higher frequencies are needed before the scattering signal can be differentiated from instrument or surface noise. The background noise makes it difficult to distinguish different drop sizes from their scattering signal even if the equation indicates some sensitivity. For ice particles, the imaginary component of the refractive index is quite small and absorption is negligible. The scattering behavior is similar to that of water which implies little scattering below 30 GHz but increased effects as the frequency increases.

Once particles get larger, they enter into the Mie (1908) regime. Here, the absorption and scattering relations become more complex. Details of the particle shape also become important. For spheres, many public sites offer codes to compute scattering parameters using the Lorentz-Mie formulation. For larger drops that become flattened as they fall through the atmosphere, many applications use oblate spheroids that can be dealt with using a T-Matrix (Mischenko et al. 1996). For ice particles, not only the size, but shape and variations in the density become important. A number of approaches have been used to compute absorption and scattering parameters for ice particles. Liu (2004) provides tabulated scattering parameters from a Discrete Dipole Approximation (DDA) for bullet rosettes, sector snowflakes, and dendrite snowflakes for frequencies between of 85 and 220 GHz. Kuo et al. (2016) also relies on a DDA method but uses a 3D growth model to simulate pristine ice crystals, which are aggregated using a collection algorithm to create larger, multicrystal particles. Kuo et al. (2016), in particular, make it clear that the proportion of forward scattering at 89 GHz and higher microwave frequencies is generally overestimated if complex particles are replaced by their spherical equivalent. Much more detail on ice particle scattering is provided in Chap. 15, while Bohren and Huffmann (2010) is useful as the book covers the broad subject of single particle scattering.

7.2 Sensors and Algorithms

7.2.1 The ESMR Era

The earliest attempts to retrieve precipitation from passive microwave sensors in space can be traced back to the Electronically Scanning Microwave Sensor (ESMR, Wilheit 1972) aboard the Nimbus-5 Satellite launched in 1972. This ESMR operated at 19.35 GHz. At this frequency, the ocean appears quite cold, and, as described in Sect. 7.1, water vapor, clouds, and precipitation all act to increase the observed radiances, or warm the brightness temperatures. Water vapor, which has a weak absorption line at 22.235 GHz, still has a fairly moderate effect on this frequency.

Fig. 7.2 Example of brightness temperatures as a function of column averaged rain rate at 19 GHz used to illustrate the "beamfilling" or non-homogeneous rain distribution effect
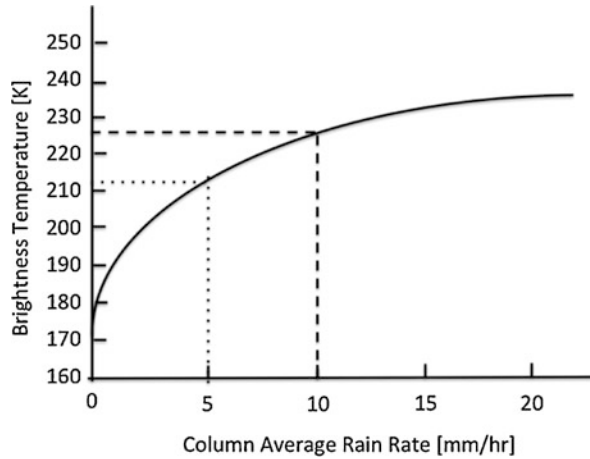
A number of groups, including Savage and Weinman (1975) began demonstrating that brightness temperatures could be reliably calculated using radiative transfer methods for a broad range of atmospheric constituents, including cloud and precipitation water content. The calculations hinted that quantitative approaches were possible over oceans. With a single channel, however, it is next to impossible to determine the relative contribution of cloud- and rain-water, let alone the other parameters, such as sea surface temperature and roughness, as well as water vapor, that all affect the brightness temperature. Nonetheless, when rainfall gets sufficiently intense, it tends to overwhelm cloud water and the other parameters and thus can be estimated with some success. The theoretical basis for estimating rainfall from the ESMR emission signal was laid out by Wilheit et al. (1977). Theoretically derived brightness temperatures as a function of rainfall rate and freezing level height were simply matched to observations in that work. Results compared very favorably to independently obtained rainfall rates from a WSR-57 radar over coastal Florida.

Because of the increased focus on quantitative rainfall rates over oceans, the issue of non-homogeneous beamfilling also became important. A schematic of the problem is presented in Fig. 7.2. The figure illustrates the typical shape of 19 GHz brightness temperatures for a 4 km tall, horizontally homogeneous rain cloud as a function of the mean column rain rate. The figure illustrates quite clearly that a homogeneous rain cloud with 5 mm h^{-1} rain and a Tb of 212 K is significantly warmer than an inhomogeneous cloud consisting of 50% no rain and 50% at 10 mm h^{-1}. The footprint averaged temperature in the latter case would be roughly 200 K which corresponds to only a 2 mm h^{-1} under a homogeneous FOV assumption. A number of different approaches to overcome this issue are discussed later in this chapter as well as in the literature of that period.

While the Nimbus-5 ESMR work did not focus very much on trying to estimate precipitation over land (due to its already warm background), encouraging results over ocean facilitated the launch of a new ESMR with a slightly higher frequency on Nimbus-6.

ESMR on Nimbus-6 was launched in 1975 (Wilheit 1975), and operated at 37 GHz. At this frequency, Eqs. (7.4) and (7.5) suggest that absorption is linearly larger than at 19.35 GHz due to the shorter wavelength. More importantly, however, scattering increases by ν^4 and can become significant. Thus, while work continued to improve the emission-based methods cited above, observations of ice scattering seen in airborne radiometers operating at 19.35, 92 and frequencies around 183 GHz (Wilheit et al. 1982), led Rodgers and Siddalingaiah (1983) to search for, and find scattering signals in the 37 GHz ESMR data as well. These scattering signals were fairly evident in the data but it was difficult to quantitatively separate ice scattering from wet surfaces that also lowered the observed brightness temperatures. Work was thus confined primarily to identifying precipitating areas.

7.2.2 The SMMR Era

The next milestone in the development of rainfall algorithms came with the launch of the Scanning Multichannel Microwave Radiometer (SMMR) on Nimbus-7 (Gloerson and Hardis 1978). SMMR was a 5-channel instrument, with frequencies at 6.6, 10.7, 19.35, 23 and 37 GHz, measuring both horizontal and vertical polarizations at a constant incidence angle of approximately 49° from nadir. Multiple channels on SMMR made it possible to simultaneously retrieve a number of geophysical parameters. The addition of polarization, in particular, made it feasible to retrieve the ocean surface wind speed as the surface roughness affects the emissivity quite differently in the horizontal and vertical polarizations. With a better surface characterization, and water vapor information from the 23 GHz channel, more physically based retrievals of clouds and precipitation were now possible over oceans.

With multiple channels and polarizations, Chang and Milman (1982) showed that it was possible to retrieve sea surface temperature, wind speed, and rain rate from SMMR. They constructed a large number of models of microwave emission over the ocean for different rain rates, freezing levels, surface wind speeds, ocean temperature and non-precipitating cloud water. Other parameters, like the water vapor and atmospheric lapse rate, were held fixed. They then utilized a simple liner regression

$$p_i = \sum_j a_{i,j} Tb_j \qquad (7.6)$$

were the three parameters p_i (sea surface temperature, wind speed, and rain rate) are fitted to the SMMR Tb vector via coefficients $a_{i,j}$. The study made explicit mention of the impacts of non-homogeneous rain, particularly at the large FOV of SMMR at 10.7 GHz (156 km). Their solution at this point in time was to use locally liner regressions partitioned by 6 mm h^{-1} intervals below 24 mm h^{-1} and 12 mm h^{-1} intervals above the 24 mm h^{-1} threshold. The algorithm was then allowed to iterate to the correct interval. The method was quite robust and applicable to oceanic rain in general.

Table 7.1 Channel combinations and correlations against radar reflectivity (dBZ) (Alishouse et al. 1990)

Regression equation	Correlation coefficients	A	B	C
$dBZ = A \cdot T_H + B$	0.71	0.2222	−27.4222	
$dBZ = A \cdot T_V + B$	0.69	0.4522	−89.3542	
$dBZ = A \cdot T_V + A \cdot T_H + C$	0.72	−0.4309	0.4252	33.5698
$dBZ = A \cdot T_C + B$	0.71	0.2995	−48.1846	
$dBZ = A \cdot T_C + B \cdot T_C^2 + C$	0.71	1.1123	−0.0018	−138.6212

$T_C = 0.5 \cdot T_V + 0.5 \cdot T_H$

In an attempt to focus on rainfall retrievals in tropical cyclones, Alishouse et al. (1990) used a more empirical approach in which they used data from three hurricanes in addition to convective storms around the Tampa Bay, Florida, area to regress brightness temperatures against ground-based radar reflectivities obtained from NOAA's RADAP-II project (Green et al. 1983). They then correlated 37 GHz observed brightness temperatures and polarization differences to radar data at 18 km scales and computed liner regression against a number of channel combinations. Channel combinations, and their correlation against the radar-observed reflectivity (in dBZ) are summarized in Table 7.1.

Using the same channels, they also regressed the brightness temperatures against the fraction of the FOV filled with rain. This produced higher correlations (approx. 0.88) but they speculated and then confirmed that the mean reflectivity and fractional area of the FOV covered by rain are highly correlated. In general, they found that while the correlations were quite high, there was a general overestimation of light rain rates and an underestimation of the heavier ones.

From the scattering perspective, Rodgers and Siddalingaiah (1983) used the 37 GHz channels together with theoretical computations performed earlier by Savage and Weinman (1975) to develop a rain classification algorithm over land. It used the polarization difference over land which is large for wet or water covered surfaces, while being small or zero when the emission is due to rain drops. While not a quantitative rainfall algorithm, they did successfully classify 77% of raining cases over land, while also correctly identifying 94% as dry land and 79% as wet land cases.

Spencer (1986) correctly noted that the 37 GHz of SMMR had a non-unique relationship with precipitation – increasing first as cloud water and light precipitation filled the field of view, and then decreasing again as more and more ice scattering associated with convection filled the field of view. The polarization difference, however, continued to decrease as the rainfall increased. A liner transformation to variables that contained the sum and difference of the two channels, however, could be shown to linearize the problem. It was also independent of any non-homogeneous rainfall issues that plagued the emission methods. Based upon comparisons with ground-based radar data from different parts of the world, Spencer (1986) derived the equation for rainfall given by:

$$R = a(b \cdot Tb_{37H} - Tb_{37V} + c) \tag{7.7}$$

with a value of $a \approx 2.9$, $b \approx 0.5$, and $c \approx 138$. While this is perhaps a bit reminiscent of the liner equations derived by Alishouse (1990) discussed above, that work used only the sum of the channels, and thus did not make explicit use of the scattering signal dealt with here.

Starting with the SMMR era, more physical algorithms were also being developed to fully match observed Tb to theoretically derived ones. Olson (1989) used the parameters that had the greatest impact upon SMMR radiances (rainfall, the horizontal and vertical dimension of the rain cell, the height of the rain to ice transition and the surface wind speed), together with the SMMR antenna response function, to build a physical model that could be directly inverted. As with Chang and Milman (1982), the remaining geophysical parameters were held fixed. Unlike the Chang and Milman (1982) approach, however, a solution was sought that minimized the cost function ζ,

$$\zeta = \min \sum_{i=1}^{Nchannels} \left[e_i(p_1, p_2, \ldots, p_m)^2 \right] \tag{7.8}$$

where $N_{channels}$ for SMMR was set to 10, e_i is the difference in Tb space between the observed and simulated Tb for the m parameters being retrieved. The steepest descent method, or the conjugate gradient procedure utilized in the Olson (1989) study, was used to find the minimum with reasonable computational efficiency. Much of this early work focused its effort on representing cloud and precipitation morphology as realistically as possible, as well as dealing with microphysical parameters needed in the radiative transfer computations.

7.2.3   The SSM/I Era

Following SMMR, the US Department of Defense launched the Special Sensor Microwave/Imager (SSM/I) in 1987 (Hollinger et al. 1987). SSM/I was a conically scanning radiometer with channels at 19.35, 22.235, 37.0 and 85.5 GHz. All channels, except 22.235 GHz, measured both the horizontal and vertical polarizations. Only the vertical polarization was measured at the 22.235 GHz water vapor absorption line. The SSM/I instrument generated great interest because of its relative calibration stability, and broad access to the data provided by NOAA. On the precipitation side, the various algorithms developed for SMMR were refined and adapted to SSM/I. Newer approaches were developed not only to exploit the higher frequency channels, but also the stability of the instrument that allowed for more quantitative approaches. Several studies were dedicated to demonstrate SSM/I's potential for quantitative precipitation estimates (e.g., Mugnai et al. 1990; Smith et al. 1992; Wilheit et al. 1994). The SSM/I ushered in the modern era of the

microwave remote sensing of precipitation to a great degree because of its long, and stable time series over the next 20 years. Instead of reviewing all algorithms that were developed in this era, only a few select examples are presented here that represent the different types of algorithms that were developed. They are largely chosen because they were in operational use for significant periods of time or served as a basis for operational algorithms.

Algorithms using only emission suffered from a great deal of uncertainty due to inhomogeneous rainfall in satellite FOVs, unknown water vapor, as well as uncertainties in the heights of the liquid to ice transition. The latter was necessary to convert the total liquid water into a rainfall rate. Wilheit et al. (1991) partially solved the problem by focusing on histograms of brightness temperatures in $5° \times 5°$ cells at monthly time scales instead of individual pixels. Histograms were constructed of Tb19 V, Tb22 V, and $(2 \times \text{Tb19 V} - \text{Tb22 V})$. Because the difference in the Tb19 V and Tb22 V channels is related to the total water vapor, and water vapor is in turn closely coupled to the atmospheric temperature structure, this technique was statistically quite robust in raining conditions. The rain rate itself was obtained by plotting a probability density function of the $(2 \times \text{Tb19 V} - \text{Tb22 V})$. This channel combination showed a well-defined peak corresponding to non-raining conditions, followed by a more or less linear portion (in log space) corresponding to precipitating pixels. The rainfall retrieval itself, was accomplished by computing a PDF of brightness temperatures for a given log-normal distribution for rainfall and adjusting the log-normal distribution parameters until a good fit between theoretical and observed Tb histograms was achieved. While the technique only worked over oceans where the emission signal was evident, it required data aggregated at monthly, $5° \times 5°$, scale to ensure robust pdfs of rain and brightness temperatures. Versions of this algorithm formed the basis for the Global Precipitation Climatology Project (Adler et al. 2003) for the entire lifecycle of the SSM/I and future SSMIS instrument series, as well as early TRMM and AMSR-E products.

Early scattering-based methods tested on ESMR on Nimbus-6 and SMMR grew significantly in the SSM/I era due to the addition of the 85 GHz channels that exhibit much greater scattering signals. Ice scattering processes at 85 GHz in deep convection cause brightness temperatures to fall below 100 K and even below 50 K on rare occasions. To exploit this scattering signal, Spencer (1989) defined the Polarization Corrected Temperature (PCT) that remains broadly in use today. PCT is defined as:

$$PCT = \frac{(\beta \cdot Tb_{85H} - Tb_{85V})}{\beta - 1} \tag{7.9}$$

where $\beta = (Tb_{c,V} - Tb_{0,V})/(Tb_{c,H} - Tb_{0,H})$, and Tb_V is the vertically polarized brightness temperature of the precipitating scene at 85 GHz, $Tb_{c,V}$ is the 85 GHz brightness temperature of a nearby clear scene, and $Tb_{0,V}$ is the 85 GHz predicted temperature emanating from the surface without an overlying atmosphere. He then found that a value of $\beta = 0.45$ worked well to produce PCT values between 275 and 290 K for non-raining atmospheres. With that value of β, the PCT reduces to the value that is commonly used:

$$PCT = 1.818 Tb_V - 0.818 Tb_H \tag{7.10}$$

The relationship between rain rate and PCT was left for the community to adjust, and a series of algorithms quickly emerged (e.g., Ferraro et al. 1996; Kidd 1998; Conner and Petty 1998). Instead of using the single channel, Grody (1991) had derived a scattering index to accomplish the same objective of discriminating cold brightness temperatures due to land features from those due to ice scattering. That approach used the 19 and 22 GHz channels of SSM/I over land to predict the 85 GHz brightness temperatures for non-raining conditions. By comparing that to the observed 85 GHz channel, the ice scattering signal from precipitating ice could be extracted. Ferraro et al. (1994, 1998) used this technique to derive a scattering index defined by

$$SI_{85V} = a + b \cdot Tb_{19V} + c \cdot Tb_{22V} + d \cdot Tb_{22V}^2 - Tb_{85V} \tag{7.11}$$

While these algorithms all tend to use more than one channel to discriminate raining scenes or to provide additional information about the background state, the rainfall determination remained largely a function of the 85 GHz channel.

Another category of algorithms were the physically based retrieval approaches such as used by Wentz and Spencer (1998). The algorithm simultaneously retrieves near-surface wind speed, column water vapor, column integrated cloud water, and rain rate over water. It does so by relying on the fact that the brightness temperature is directly related to the transmittance of water in the atmosphere. The first step in the retrieval is thus to simultaneously retrieve this atmospheric transmittance, along with the water vapor, and surface properties - wind speed, and effective radiating temperature. This is possible as each of the individual parameters has a unique radiometric signature in the 19- through 37-GHz range. Once this is accomplished, the difference between 19- and 37-GHz channels is used to determine the beamfilling, or inhomogeneous rain effect. A correction is applied for the total attenuation due to liquid. The formulation then used Mie theory and an assumed relationship between cloud- and rain-water to derive a column rain water and, together with an assumed rain column height based upon the SST, a surface rainfall rate.

The simultaneous inversion work that was started by Olson (1987) continued into the SSM/I era, but the minimum variance solution was more or less supplanted by Bayesian schemes. The overarching difficulty with the minimum variance schemes was ultimately the severely under-constrained nature of the retrieval (Stephens and Kummerow 2007). There are simply far too many variables in a precipitating cloud related to the hydrometeor types and their vertical distribution, than can be uniquely retrieved with radiometers carrying a limited number of frequencies. This led more investigators to adopt Bayesian schemes (e.g., Kummerow and Giglio 1994; Evans et al. 1995; Marzano et al. 1999). In Bayes' formulation, the probability of a observing a particular hydrometeor profile, R, given an observed Tb vector, Pr(R| Tb), can be written as:

$$\Pr(R|Tb) = \Pr(R) \cdot \Pr(Tb|R) \tag{7.12}$$

where R is the rainfall profile, $\Pr(R)$ is the probability that a given profile, R, is observed, and $\Pr(Tb|R)$ is the probability of observing the brightness temperature vector, Tb, given the rainfall profile R. The greatest challenge to implementing the Bayesian scheme was a way to find the correct distribution of observed rainfall rates. Absent any global observations, this generation of Bayesian schemes all relied on various cloud resolving model (CRM) outputs to represent hydrometeor profiles that would be observed in nature. CRM model-based approaches had to tackle the critical issue of being representative of actual observations and to ensure that Bayesian schemes accounted for uncertainties in both the modeled microphysical profiles and the radiative transfer modeling used to simulate multi-channel brightness temperatures (Panegrossi et al. 1998). However, since cloud resolving models of that era were regional and typically simulated only individual precipitating cloud systems, the Bayesian scheme needed to first screen non-raining pixels so that these would not be included in the statistics. Much of the early work was thus focused on producing realistic cloud model simulations and screening of non-raining pixels, particularly over complex coasts and topography. Once the profiles were identified, however, radiative transfer could be used to compute $\Pr(Tb|R)$. Uncertainties had to be estimated as they include many of the assumptions in the cloud resolving models and radiative transfer computations and remain an area of research 20 years after the first Bayesian schemes were introduced. These early radiative transfer computations formed the basis for most of today's "satellite simulators" in the microwave regime (e.g., Matsui et al. 2013) that simulate observable radiances from cloud resolving model output.

7.2.4 The TRMM and GPM Era

The TRMM era continued to see emission-based algorithm such as Wilheit et al. (1991) be used for monthly rain estimates. Given that TMI was quite similar to the SSM/I, the algorithms could be adapted rather easily not only to TRMM's TMI, but also the SSMIS instrument that succeeded the SSM/I in late 2005. In effect, because there was no longer simply an SSM/I, but new instruments such as TMI, launched in 1997, the Advanced Microwave Sounding Radiometers on EOS (AMSR-E), and the SSMIS series, the focus turned more on the physical algorithms such as Wilheit et al. (1991) that could produce uniform results across the entire constellation of passive microwave sensors.

Remote Sensing Systems (RSS) also continued developing the over-ocean rainfall retrieval algorithm from Wentz and Spencer (1998), later re-named the Unified Microwave Ocean Retrieval Algorithm (UMORA) (Hilburn and Wentz 2008). The algorithm uses the 19 and 37 GHz observations common to a wide variety of microwave sensors (AMSR, GMI, SSM/I, SSMIS, TMI, and WindSat). The small

differences in frequency and incidence angle present between these sensors are removed using the RSS radiative transfer model (Meissner and Wentz 2012; Wentz and Meissner 2016). As before, atmospheric transmittance is estimated from the difference between the vertically and horizontally polarized brightness temperatures (Tbs), while beamfilling effects are corrected for by using the ratio of 19 and 37 GHz to infer the sub-pixel variance of absorption. Improvements (Hilburn and Wentz 2008) also incorporated the effects of footprint size, in order to remove systematic biases among rain retrievals from the various sensors. The resulting estimate of absorption is directly related to the total amount of liquid water path (LWP) in the footprint, but is indirectly related to the surface rain rate (RR). To estimate the RR, the contribution of cloud water to the LWP is removed using a global relationship between rain and cloud water. Then the algorithm estimates RR from the rain water by assuming that the liquid is distributed uniformly between the surface and the freezing layer estimated from the sea surface temperature.

JAXA's microwave algorithm developed for their GSMAP algorithm (Aonashi et al. 2009) made direct use of TRMM's precipitation radar data to deal with some of the non-uniqueness problems in passive microwave inversions. In their case, mean rainfall profiles were constructed from TRMM's precipitation radar observations and radiative transfer calculations were used to predict observed radiances not only for TRMM's TMI but for all other orbiting radiometers as well. The inversion then tried to find the closest match to the observations but more details of that method can be found in Chap. 20.

The Bayesian approaches that relied heavily on cloud resolving models to provide a-priori information on cloud structures also began using the cloud hydrometeor profiles provided by TRMM's radar. The Goddard profiling algorithm, GPROF (Kummerow et al. 2015), in particular, was adapted for the TRMM and later the GPM imagers and constellation satellites. The a-priori database needed to describe Pr(R) came directly from the radar retrievals (Kummerow et al. 2010). Because the TRMM radar observed raining and non-raining pixels in the correct proportions, the GPROF scheme no longer needed to screen pixels for rainfall before applying the Bayesian scheme. While the early versions of GPROF developed for TRMM and AMSR-E (Kummerow et al. 2001) still used scattering algorithms over land, that aspect was eventually replaced by a fully parametric Bayesian scheme in the GPM era. The fully parametric approach can also be coupled, as was done by Casella et al. (2013, 2017) to more fully exploit meteorological data to help minimize the non-uniqueness of solutions, particularly over land areas.

The above schemes all share the property that they are physically based and thus capable of being adapted very quickly to different sensors with no need to recalibrate or tune the algorithm to account for channel differences, footprint sizes or other instrument differences. The main advantage of the approaches is that they can be used across sensors to construct long time series needed to study climate and climate variability. Together with the algorithms being constructed for sounding radiometers, they are also very useful for weather applications which require consistent rainfall retrievals with the highest possible sampling rate.

7.2.5 The NOAA AMSU/ATMS Sensor Era

While the approaches discussed in the previous sections where generally motivated and developed for microwave imagers, there is a long history of microwave sounders that also contain information about precipitation. Operational sounders have typically operated in the 50–60 GHz oxygen complex, and the 183 GHz water vapor absorption line to retrieve temperature and water vapor profiles. They often also carried lower frequency channels to correct for surface radiation.

An early algorithm is due to Spencer (1993) who used relative warming in the histograms of channels 1 & 2 (50.3 and 53.74 GHz) of the Microwave Sounding Unit (MSU) to infer the total cloud and rain water content of clouds at 2.5° grid scales – the approximate footprint size of those channels. The background temperature fluctuations from the air mass itself were corrected for by channel 3 (54.96 GHz) that is sensitive to the temperature itself. By using a series of seven satellites, he was able to produce a climatology of oceanic precipitation from 1978–1991.

With the advent of the Advance Microwave Sounding Unit (AMSU), much higher spatial resolutions were available than with its predecessor. This made scattering approaches feasible. Ferraro et al. (2000) used NOAA-15's AMSU instrument to detect the scattering signal from precipitation sized particles at the 89 and 150 GHz channels. This algorithm used the scattering indices that have been described earlier but separated convective from stratiform rainfall in order to account for the difference in the vertical hydrometeor structures of these two types systems. Scattering indices were converted to surface precipitation by matching the index to ground based observations over the United States.

Other approaches were developed to exploit channels around 183.31 GHz, originally designed to retrieve water vapor profiles, but showing great potential for precipitating cloud characterization (Hong et al. 2005) and for precipitation retrieval (Laviola and Levizzani 2011). Among these, approaches based on artificial neural networks, successfully applied to microwave sounders (Surussavadee and Staelin 2008), are also used for NRT applications within European operational programs (Sanò et al. 2015, 2016).

Both emission and scattering algorithms were refined over time but the more physical approaches being developed for the microwave imagers were slower to develop in the sounding community because the information content pertaining to precipitation was more limited in sounders – particularly over oceans where imagers had good information from the emission channels The GPROF algorithm (Kummerow et al. 2015) mentioned above, and described more fully in the next chapter, was nonetheless able to adapt the Bayesian methodology to sounders as well. An alternative approach that was developed for use with imagers, sounders, or their combination, is MIRS algorithm (Boukabara et al. 2011). MiRS, more fully described in Chap. 9, is a 1-D Optimal Estimation (OE) solution that inverts the radiative transfer equation by finding radiometrically appropriate profiles of temperature, moisture, liquid cloud, and hydrometeors, as well as the surface emissivity

spectrum and skin temperature. Like earlier minimum variance solutions, the OE approach minimizes the difference between observed and simulated brightness temperatures but includes an a-priori term that prevents the solution from deviating too far from expected values. The formal solution is given by:

$$\Phi = [y - f(x,b)]^T S_y^{-1}[y - f(x,b)] + (x - x_a)S_a^{-1}(x - x_a) \qquad (7.13)$$

where x are the geophysical parameters being retrieved, y is the brightness temperature vector, b are assumed parameters needed for the radiative transfer simulations, and x_a are the a-priori values of the geophysical parameters. While optimal estimation procedures, particularly if clouds and precipitation are included, usually suffer from insufficient constraints on the solution as described earlier, MiRS's approach to tackle this problem is to constrain the inversion problem by using Eigenvalue decomposition and employing a limited number of eigenvectors that is consistent with the information content present in the observations. It also has the option to use a forecast model to provide good a-priori information, instead of the default climatology background. Because of the variable reduction approach, MiRS is highly flexible, and it could be used as a retrieval tool, independent of numerical weather prediction. The MiRS system was implemented operationally at the US National Oceanic and Atmospheric Administration (NOAA) in 2007 for the NOAA-18 satellite. Since then, it has been extended to the microwave sensors onboard Metop-A and B (AMSU/MHS), DMSP (SSMIS), S-NPP and JPSS (ATMS), as well as to research missions such as Megha-Tropiques (SAPHIR).

References

Adler, R. F., Huffman, G. J., Chang, A., Ferraro, R., Xie, P., Janowiak, J., Rudolf, B., Schneider, U., Curtis, S., Bolvin, D., Gruber, A., Susskind, J., Arkin, P., & Nelkin, E. (2003). The version 2 Global Precipitation Climatology Project (GPCP) monthly precipitation analysis (1979–present). *Journal of Hydrometeorology, 4*(6), 1147–1167. https://doi.org/10.1175/1525-7541 (2003)004<1147:TVGPCP>2.0.CO;2.

Alishouse, J. C., Ferraro, R. R., & Fiore, J. V. (1990). Inference of oceanic rainfall properties from the Nimbus 7 SMMR. *Journal of Applied Meteorology, 29*, 551–560. https://doi.org/10.1175/ 1520-0450(1990)029<0551:IOORPF>2.0.CO;2.

Aonashi, K., Awaka, J., Hirose, M., Kozu, T., Kubota, T., Liu, G., Shige, S., Kida, S., Seto, S., Takahashi, N., & Takayabu, Y. (2009). GSMaP passive microwave precipitation retrieval algorithm: Algorithm description and validation. *Journal of the Meteorological Society of Japan, 87A*, 119–136. https://doi.org/10.2151/jmsj.87A.119.

Bohren, C. F., & Huffmann, D. R. (2010). *Absorption and scattering of light by small particles*. New York: Wiley-Interscience. ISBN:3-527-40664-6.

Boukabara, S. A., Garrett, K., Chen, W. C., Iturbide-Sanchez, F., Grassotti, C., Kongoli, C., Chen, R. Y., Liu, Q. H., Yan, B. H., Weng, F. Z., Ferraro, R. R., Kleespies, T. J., & Meng, H. (2011). MiRS: An all-weather 1DVAR satellite data assimilation and retrieval system. *IEEE Transactions on Geoscience and Remote Sensing, 49*(9), 3249–3272. https://doi.org/10.1109/TGRS. 2011.2158438.

Casella, D., Panegrossi, G., Sanò, P., Dietrich, S., Mugnai, A., Smith, E. A., Tripoli, G. J., Formenton, M., Di Paola, F., Leung, W. H., & Mehta, A. V. (2013). Transitioning from CRD to CDRD in Bayesian retrieval of rainfall from satellite passive microwave measurements. Part 2: Overcoming database profile selection ambiguity by consideration of meteorological control on microphysics. *IEEE Transactions on Geoscience and Remote Sensing, 51*, 4650–4671. https://doi.org/10.1109/TGRS.2013.2258161.

Casella, D., Amaral, L. M., Dietrich, S., Marra, A. C., Sanò, P., & Panegrossi, G. (2017). The cloud dynamics and radiation database algorithm for AMSR2: Exploitation of the GPM observational dataset for operational applications. *IEEE Journal of Selected Topics in Applied Earth Observations and Remote Sensing, 10*, 3985–4001. https://doi.org/10.1109/JSTARS.2017.2713485.

Chang, A. T. C., & Milman, A. S. (1982). Retrieval of ocean surface and atmospheric parameters from multichannel microwave radiometric measurements. *IEEE Transactions on Geoscience and Remote Sensing, GE-20*, 217–224. https://doi.org/10.1109/TGRS.1982.350402.

Conner, M. D., & Petty, G. W. (1998). Validation and intercomparison of SSM/I rain-rate retrieval methods over the continental United States. *Journal of Applied Meteorology, 37*, 679–700. https://doi.org/10.1175/1520-0450(1998)037<0679:VAIOSI>2.0.CO;2.

Evans, K. F., Turk, F. J., Wong, T., & Stephens, G. L. (1995). A Bayesian approach to microwave precipitation profile retrieval. *Journal of Applied Meteorology, 34*, 260–279. https://doi.org/10.1175/1520-0450-34.1.260.

Ferraro, R. R., Grody, N. C., & Marks, G. F. (1994). Effects of surface conditions on rain identification using the SSM/I. *Remote Sensing Reviews, 11*, 195–209. https://doi.org/10.1080/02757259409532265.

Ferraro, R. R., Weng, F., Grody, N. C., & Basist, A. (1996). An eight-year (1987–1994) time series of rainfall, clouds, water vapor, snow cover, and sea ice derived from SSM/I measurements. *Bulletin of the American Meteorological Society, 77*, 891–906. https://doi.org/10.1175/1520-0477(1996)077<0891:AEYTSO>2.0.CO;2.

Ferraro, R. R., Smith, E. A., Berg, W., & Huffman, G. J. (1998). A screening methodology for passive microwave precipitation retrieval algorithms. *Journal of the Atmospheric Sciences, 55*, 1583–1600. https://doi.org/10.1175/1520-0469(1998)055<1583:ASMFPM>2.0.CO;2.

Ferraro, R. R., Weng, F., Grody, N. C., & Zhao, L. (2000). Precipitation characteristics over land from the NOAA-15 AMSU sensor. *Geophysical Research Letters, 27*, 2669–2672. https://doi.org/10.1029/2000GL011665.

Gloerson, P., & Hardis L. (1978). *The Scanning Multichannel Microwave Radiometer (SMMR) experiment*. Nimbus-7 User's Guide. NASA Goddard Space Flight Center, 213–245.

Green, D. R., Nilsen J. D., Saffle R. E., Holmes D. W., Hudlow M. D., & Ahnert P. R. (1983). RADAP-II, an interim radar data processor. *Preprints 21st Conference Radar Meteorology*. American Meteorological Society, 404–408.

Grody, N. C. (1991). Classification of snow cover and precipitation using the special sensor microwave/imager (SSM/I). *Journal of Geophysical Research, 96*, 7423–7435. https://doi.org/10.1029/91JD00045.

Hilburn, K. A., & Wentz, F. J. (2008). Intercalibrated passive microwave rain products from the unified microwave ocean retrieval algorithm (UMORA). *The Journal of Applied Meteorology and Climatology, 47*, 778–794. https://doi.org/10.1175/2007JAMC1635.1.

Hollinger, J., Lo R., & Poe G. (1987). Special Sensor Microwave/Imager user's guide, Naval Research Laboratory, Washington, DC, Sep. 14.

Hong, G., Heygster, G., Miao, J., & Kunzi, K. (2005). Detection of tropical deep convective clouds from AMSU-B water vapor channels measurements. *Journal of Geophysical Research, 110*, D05205. https://doi.org/10.1029/2004JD004949.

Kidd, C. (1998). On rainfall retrieval using polarization-corrected temperatures. *International Journal of Remote Sensing, 19*, 981–996. https://doi.org/10.1080/014311698215829.

Kummerow, C., & Giglio, L. (1994). A passive microwave technique for estimating rainfall and vertical structure information from space. Part I: Algorithm description. *Journal of Applied Meteorology, 33*, 3–18. https://doi.org/10.1175/1520-0450(1994)033<0003:APMTFE>2.0.CO;2.

Kummerow, C., Hong, Y., Olson, W. S., Yang, S., Adler, R. F., McCollum, J., Ferraro, R. R., Petty, G., Shin, D., & Wilheit, T. T. (2001). The evolution of the Goddard profiling algorithm (GPROF) for rainfall estimation from passive microwave sensors. *Journal of Applied Meteorology, 40*, 1801–1820. https://doi.org/10.1175/1520-0450(2001)040<1801:TEOTGP>2.0.CO;2.

Kummerow, C. D., Ringerud, S., Crook, J., Randel, D., & Berg, W. (2010). An observationally generated a-priori database for microwave rainfall retrievals. *Journal of Atmospheric and Oceanic Technology, 28*, 113–130. https://doi.org/10.1175/2010JTECHA1468.1.

Kummerow, C. D., Randel, D. L., Kulie, M. S., Wang, N.-Y., Ferraro, R. R., Munchak, S. J., & Petkovic, V. (2015). The evolution of the Goddard profiling algorithm to a fully parametric scheme. *Journal of Atmospheric and Oceanic Technology, 32*, 2265–2280. https://doi.org/10.1175/JTECH-D-15-0039.1.

Kuo, K., Olson, W. S., Johnson, B. T., Grecu, M., Tian, L., Clune, T. L., van Aartsen, B. H., Heymsfield, A. J., Liao, L., & Meneghini, R. (2016). The microwave radiative properties of falling snow derived from nonspherical ice particle models. Part I: An extensive database of simulated pristine crystals and aggregate particles, and their scattering properties. *Journal of Applied Meteorology and Climatology, 55*, 691–708. https://doi.org/10.1175/JAMC-D-15-0130.1.

Laviola, S., & Levizzani, V. (2011). The 183-WSL fast rain rate retrieval algorithm. Part I: Retrieval design. *Atmospheric Research, 99*, 443–461. https://doi.org/10.1016/j.atmosres.2010.11.013.

Liou, K. N. (2002). *An introduction to atmospheric radiation* (2nd ed., p. 583). New York: Academic Press. ISBN: 9780124514515.

Liu, G. (2004). Approximation of single scattering properties of ice and snow particles for high microwave frequencies. *Journal of the Atmospheric Sciences, 61*, 2441–2456. https://doi.org/10.1175/1520-0469(2004)061<2441:AOSSPO>2.0.CO;2.

Marzano, F. S., Mugnai, A., Panegrossi, G., Perdicca, N., Smith, E. A., & Turk, F. J. (1999). Bayesian estimation of precipitating cloud parameters from combined measurements of space-borne microwave radiometer and radar. *IEEE Transactions on Geoscience and Remote Sensing, 37*, 593–613. https://doi.org/10.1109/36.739124.

Matsui, T., Iguchi, T., Li, X., Han, M., Tao, W., Petersen, W., L'Ecuyer, T., Meneghini, R., Olson, W., Kummerow, C. D., Hou, A. Y., Schwaller, M. R., Stocker, E. F., & Kwiatkowski, J. (2013). GPM satellite simulator over ground validation sites. *Bulletin of the American Meteorological Society, 94*, 1653–1660. https://doi.org/10.1175/BAMS-D-12-00160.1.

Meissner, T., & Wentz, F. J. (2012). The emissivity of the ocean surface between 6 – 90 GHz over a large range of wind speeds and earth incidence angles. *IEEE Transactions on Geoscience and Remote Sensing, 50*(8), 3004–3026. https://doi.org/10.1109/TGRS.2011.2179662.

Mie, G. (1908). Beiträge zur Optik trüber Medien, speziell kolloidaler Metallösungen. *Annalen der Physik, 330*(3), 377–445.

Mishchenko, M. I., Travis, L. D., & Mackowski, D. W. (1996). T-matrix computations of light scattering by nonspherical particles: A review. *Journal of Quantitative Spectroscopy & Radiative Transfer, 55*, 535–575. https://doi.org/10.1016/0022-4073(96)00002-7.

Mugnai, A., Cooper, H. J., Smith, E. A., & Tripoli, G. J. (1990). Simulation of microwave brightness temperatures of an evolving hailstorm at SSM/I frequencies. *Bulletin of the American Meteorological Society, 71*, 2–13. https://doi.org/10.1109/36.739124.

Olson, W. S. (1987). *Estimation of rainfall rates in tropical cyclones by passive microwave radiometry*. Ph.D. Thesis, University of Wisconsin, 282 pp.

Olson, W. S. (1989). Physical retrieval of rainfall rates over the ocean by multispectral microwave radiometry: Application to tropical cyclones. *Journal of Geophysical Research, 94*, 2267–2280. https://doi.org/10.1029/JD094iD02p02267.

Panegrossi, G., Dietrich, S., Marzano, F. S., Mugnai, A., Smith, E. A., Xiang, X., Tripoli, G. J., Wang, P. K., & Poiares Baptista, J. P. V. (1998). Use of cloud model microphysics for passive microwave-based precipitation retrieval: Significance of consistency between model and measurement manifolds. *Journal of the Atmospheric Sciences, 55*, 1644–1673. https://doi.org/10.1175/1520-0469(1998)055<1644:UOCMMF>2.0.CO;2.

Rodgers, E., & Siddalingaiah, H. (1983). The utilization of Nimbus-7 SMMR measurements to delineate rainfall over land. *Journal of Climate and Applied Meteorology, 22*, 1753–1763. https://doi.org/10.1175/1520-0450(1983)022<1753:TUONSM>2.0.CO;2.

Sanò, P., Panegrossi, G., Casella, D., Di Paola, F., Milani, L., Mugnai, A., Petracca, M., & Dietrich, S. (2015). The Passive microwave Neural network Precipitation Retrieval (PNPR) algorithm for AMSU/MHS observations: Description and application to European case studies. *Atmospheric Measurement Techniques, 8*, 837–857. https://doi.org/10.5194/amt-8-837-2015.

Sanò, P., Panegrossi, G., Casella, D., Marra, A. C., Di Paola, F., & Dietrich, S. (2016). The new Passive microwave Neural network Precipitation Retrieval (PNPR) algorithm for the cross-track scanning ATMS radiometer: Description and verification study over Europe and Africa using GPM and TRMM spaceborne radars. *Atmospheric Measurement Techniques, 9*, 5441–5460. https://doi.org/10.5194/amt-9-5441-2016.

Savage, R. C., & Weinman, J. A. (1975). Preliminary calculations of the upwelling radiance from rain clouds at 37.0 and 19.35 GHz. *Bulletin of the American Meteorological Society, 56*, 1272–1274.

Smith, E. A., Cooper, H. J., Xiang, X., Mugnai, A., & Tripoli, G. J. (1992). Foundations for statistical-physical precipitation retrieval from passive microwave satellite measurements. Part I: Brightness-temperature properties of a time-dependent cloud-radiation model. *Journal of Applied Meteorology, 31*, 506–531. https://doi.org/10.1175/1520-0450(1992)031<0506:FFSPPR>2.0.CO;2.

Spencer, R. W. (1986). A satellite passive 37-GHz scattering based method for measuring oceanic rain rates. *Journal of Climate and Applied Meteorology, 25*, 754–766. https://doi.org/10.1175/1520-0450(1986)025<0754:ASPGSB>2.0.CO;2.

Spencer, R. W. (1993). Global oceanic precipitation from the MSU during 1979—91 and comparisons to other climatologies. *Journal of Climate, 6*, 1301–1326. https://doi.org/10.1175/1520-0442(1993)006<1301:GOPFTM>2.0.CO;2.

Spencer, R. W., Goodman, H. M., & Hood, R. E. (1989). Precipitation retrieval over land and ocean with the SSM/I: Identification and characteristics of the scattering signal. *Journal of Atmospheric and Oceanic Technology, 6*, 254–273. https://doi.org/10.1175/1520-0426(1989)006<0254:PROLAO>2.0.CO;2.

Stephens, G. L., & Kummerow, C. D. (2007). The remote sensing of clouds and precipitation from space: A review. *Journal of the Atmospheric Sciences, 64*, 3742–3765. https://doi.org/10.1175/2006JAS2375.1.

Surussavadee, C., & Staelin, D. H. (2008). Global millimeter-wave precipitation retrievals trained with a cloud-resolving numerical weather prediction model. Part I: Retrieval design. *IEEE Transactions on Geoscience and Remote Sensing, 46*, 99–108. https://doi.org/10.1109/TGRS.2007.908302.

Ulaby, F. T., Moore, R. K., & Fung, A. K. (1986). *Microwave remote sensing: Radar remote sensing and surface scattering and emission theory* (1064 pp). Norwood: Artech House, Inc. ISBN:0890061912.

Wentz, F. J., & Meissner, T. (2016). Atmospheric absorption model for dry air and water vapor at microwave frequencies below 100 GHz derived from spaceborne radiometer observations. *Radio Science, 51*, 381–391. https://doi.org/10.1002/2015RS005858.

Wentz, F. J., & Spencer, R. W. (1998). SSM/I rain retrievals within a unified all-weather ocean algorithm. *Journal of the Atmospheric Sciences, 55*, 1613–1627. https://doi.org/10.1175/1520-0469(1998)055<1613:SIRRWA>2.0.CO;2.

Wilheit, T. (1972). *The Electrically Scanning Microwave Radiometer (ESMR) experiment*. Nimbus-5 user's guide, NASA/Goddard Space Flight Center, Greenbelt, 59–105.

Wilheit, T. (1975). *The Electrically Scanning Microwave Radiometer (ESMR) experiment*. Nimbus-6 user's guide, NASA/Goddard Space Flight Center, Greenbelt, 87–108.

Wilheit, T. T., Chang, A. T. C., Rao, M. S. V., Rodgers, E. B., & Theon, J. S. (1977). A satellite technique for quantitatively mapping rainfall rates over the ocean. *Journal of Applied Meteorology, 16*, 551–560. https://doi.org/10.1175/1520-0450(1977)016<0551:ASTFQM>2.0.CO;2.

Wilheit, T. T., Chang, A. T. C., King, J. L., Rodgers, E. B., Nieman, R. A., Krupp, B. M., Milman, A. S., Stratigos, J. S., & Siddalingaiah, H. (1982). Microwave radiometric observations near

19.45, 92, and 183 GHz of precipitation in tropical storm Cora. *Journal of Applied Meteorology, 21*, 1137–1145. https://doi.org/10.1175/1520-0450(1982)021<1137:MRONAG>2.0.CO;2.

Wilheit, T. T., Chang, A. T., & Chiu, L. S. (1991). Retrieval of monthly rainfall indices from microwave radiometric measurements using probability distribution functions. *Journal of Atmospheric and Oceanic Technology, 8*, 118–136. https://doi.org/10.1175/1520-0426(1991)008<0118:ROMRIF>2.0.CO;2.

Wilheit, T. T., Adler, R. F., Avery, S., Barrett, E., Bauer, P., Berg, W., Chang, A. T., Ferriday, J., Grody, N. C., Goodman, S., Kidd, C., Kniveton, D., Kummerow, C. D., Mugnai, A., Olson, W. S., Petty, G., Shibata, A., & Smith, E. A. (1994). Algorithms for the retrieval of rainfall from passive microwave measurements. *Remote Sensing Reviews, 11*, 163–194. https://doi.org/10.1080/02757259409532264.

Chapter 8
The Goddard Profiling (GPROF) Precipitation Retrieval Algorithm

David L. Randel, Christian D. Kummerow, and Sarah Ringerud

Abstract Early in the 1990s, the Goddard Profiling Algorithm (GPROF) was created to retrieve both surface rainfall and hydrometeor vertical profiles from satellite passive microwave sensors. Over the last 25 years it has been the primary algorithm for the TRMM Microwave Imager (TMI) and the follow-on sensor – the Global Precipitation Measurement (GPM) Microwave Imager (GMI). To meet the objectives of these missions, GPROF has been designed not just for single sensors, but to consistently retrieve rainfall from the full suite of passive sensors in the GPM constellation. These include Advanced Microwave Scanning Radiometer-2 (AMSR2), Special Sensor Microwave Imager/Sounder (SSMIS), Microwave Humidity Sounder (MHS), Advanced Technology Microwave Sounder (ATMS), and the historical sensors, Special Sensor Microwave Imager (SSM/I), and the Advanced Technology Microwave Sounder (AMSR-E).

8.1 Introduction

The GPROF algorithm in founded in Bayes' theorem. In Bayes' formulation, the probability of a particular hydrometeor profile **R**, given an observed **Tb** vector, can be written as:

D. L. Randel (✉) · C. D. Kummerow
Department of Atmospheric Science, Colorado State University, Ft. Collins, CO, USA
e-mail: drandel@atmos.colostate.edu

S. Ringerud
ESSIC, University of Maryland, College Park, MD, and NASA/GSFC, Greenbelt, MD, USA

$$Pr(\boldsymbol{R} \mid \boldsymbol{Tb}) = Pr(\boldsymbol{R}) \times Pr(\boldsymbol{Tb} \mid \boldsymbol{R}) \tag{8.1}$$

where $Pr(\boldsymbol{R})$ is the probability that a the profile $\boldsymbol{R}$ will be observed and $Pr(\boldsymbol{Tb} \mid \boldsymbol{R})$ is the probability of observing the brightness temperature vector, $\boldsymbol{Tb}$, given a particular rain profile $\boldsymbol{R}$. The probability that a certain profile $\boldsymbol{R}$ will be observed can be derived directly from the GPM core satellite, while the Tb corresponding to that profile, R, can be observed directly for GMI and computed for other sensors based upon the observed hydrometeor profiles.

The expected value of R, $\hat{E}(R)$ of each model profile, R, in the Bayesian formulation is given by:

$$\widehat{E}(R) = \sum_j R_j \frac{exp\left\{-0.5\left(Tb_0 - Tb_s\left(R_j\right)\right)^T (O+S)^{-1}\left(Tb_0 - Tb_{s\left(R_j\right)}\right)\right\}}{\widehat{A}} \tag{8.2}$$

Here, R_j is a vector of model profile values, Tb_o is the set of observed brightness temperatures, $Tb_s(R_j)$ is the corresponding set of brightness temperatures computed from profiles. The variables O and S are the observational and model error covariance matrices, respectively, and $\hat{A}$ is a normalization factor. The distribution of profiles R_j, has evolved over time, but in the latest version it is supplied by the GPM Combined radar/radiometer algorithm. The computed brightness temperatures, Tb_s correspond to the hydrometeor profiles from the Combined algorithm. This defines the *a priori* cloud structure database. The formal solution to the above problem is presented in detail in Kummerow et al. (2015). In summary, the Bayesian retrieval procedure can be said to create a new hydrometeor profile (with surface precipitation) by taking the weighted sum of structures in the *a priori* database that are radiometrically consistent, Pr(Tb,R), with the observations.

The current version of GPROF has evolved from a pseudo-parametric algorithm used for TRMM to a fully parametric approach used operationally in the GPM era (Kummerow et al. 2015). The fully parametric approach now uses the above Bayesian inversion scheme for all Earth surface types. The algorithm thus abandons previous rainfall screening procedures used in all early implementations, and instead uses the full brightness temperature vector to obtain the most likely precipitation.

Using this approach, where we rely on $\boldsymbol{R}$ from the Combined radar/radiometer algorithm, and radiative transfer computations to obtain $\boldsymbol{Tb}(\boldsymbol{R})$, the GPROF algorithm can be applied equally to all sensors in the GPM constellation. Results show that GPROF retrievals are quite consistent among different GPM sensors with agreement over ocean usually within 1–2%. Over vegetated land surfaces, the inter-sensor consistency is also quite good after one accounts for the diurnal precipitation variability. However, the total precipitation retrieved over snow-covered surfaces, for monthly global estimates, exhibit differences of up to 25% between sensors which is traceable to the availability of high-frequency (166–183 GHz) channels (see Fig. 8.4).
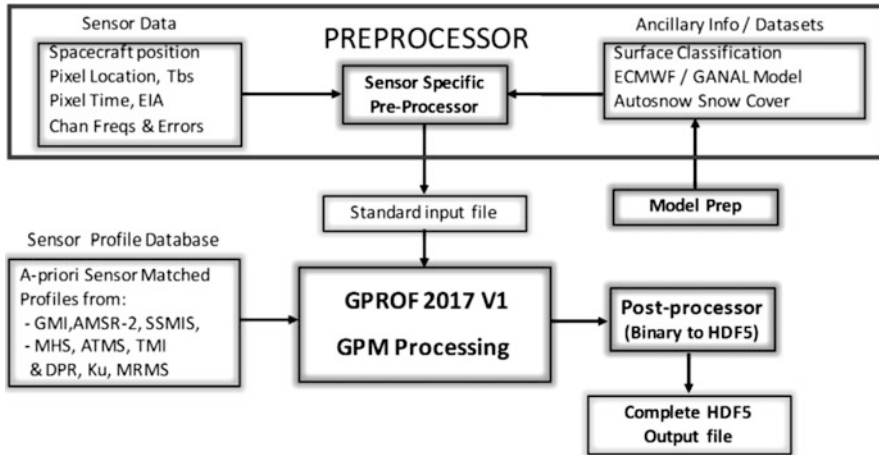
Fig. 8.1 Schematic for the GPROF Processing Algorithm. The three main components are the Sensor Profile Database, the Preprocessor, and the GPROF 2017 Processing Engine

For computational efficiency, the GPROF retrieval algorithm does not examine every a priori database pixel for each observation as implied by Eq. (8.1). Instead, during the formation of the database, profiles are categorized in three dimensions: 14 surface types, total precipitable water (TPW) in 1 mm increments and two-meter temperature (T2 m) in 1 K increments. Bayesian weighted averaging occurs only within database pixels that match these three parameters to those assigned to the observed satellite pixel. A more thorough description of the database construction is provided in Sect. 8.2. Figure 8.1 highlights the operational GPROF process scheme, including the "Preprocessor" which does the dimensional assignment, and whose description is provided in Sect. 8.3.

The GPROF GPM processing engine produces the surface rainfall amounts of both freezing and liquid states, and the vertical profiles of hydrometeors. The full description of this component is described in Sect. 8.4.

8.2   GPROF *a priori* Database

8.2.1   *Hydrometeor Profiles and Surface Precipitation*

The GPROF a priori databases constructed for each of the constellation radiometers are based on precipitation data from two sources. First and primary, are retrievals from the GPM Combined radar/radiometer algorithm. The Combined algorithm, described in Grecu et al. (2016), retrieves hydrometeor profiles optimized to be consistent with observations from both GPM radar frequencies (Ku and Ka) as well as GMI observed Tbs, making this an ideal basis for a Bayesian approach.

From the Combined algorithm, hydrometeor profiles, and surface precipitation are utilized. Additional data, supplied with the Combined retrievals, include those parameters necessary to perform the forward model calculations for all GPM instrument channel sets. These include GANAL model profiles of temperature, vapor density, air pressure, cloud liquid water and surface temperature. Furthermore, the Combined product effective emissivity, calculated directly from observations, is utilized. Additionally, information is also required in non-precipitating areas. These come from the CSU 1Dvar (Duncan and Kummerow 2016) and include integrated liquid water path (for the cloud water profile), TPW, and surface winds. The GPROF databases are constructed using 1 year of Combined data, totaling approximately 400 million profiles. In order to create the databases for other sensors in the GPM constellation, a forward radiative transfer model is implemented which uses all geophysical and profile information to derive the Tbs for each sensor's set of channel frequencies, footprint sizes and view angles.

The second source of precipitation in the a priori database was added due to the lack of sensitivity of the GPM core radars (minimum detectable signal is approx. 12 dBZ) to light and moderate snowfall events. The solution implemented was to supplement the combined retrievals with precipitation derived from the Multi-Radar Multi-Sensor (MRMS) dataset (Kirstetter et al. 2012) over snow covered surfaces. This version of MRMS included only surface precipitation amounts, and did not include the hydrometeor profile information, therefore no profile information is available over these snow-covered surfaces. Two years of hourly MRMS precipitation are matched with coincident overpasses from GMI and each GPM constellation sensor to create observational databases of surface precipitation and associated sensor Tbs.

A second issue related to the sensitivity of the DPR radar, was the deficit of precipitation in high latitude ocean areas where drizzle is known to occur frequently. This was addressed in the a priori database by setting a threshold in the 1Dvar cloud liquid water retrieval from GMI (done before the DPR or Combined rainfall was inserted into the scene), so as to match light rainfall observed by CloudSat (Haynes et al. 2009). There is a reasonable assumption here that high cloud liquid water amounts are the most likely pixels to be raining. Cloud water beyond the CloudSat determined threshold was partitioned between cloud water and rain water similar to the procedure used by Hilburn and Wentz (2008). Though slightly increasing precipitation in drizzle areas, the retrievals continue to be low relative to other estimates and more work is needed to assess high latitude drizzle from different sources.

In the first 3 years post-launch as well as throughout the TRMM era, ice particles in the GPM Combined retrieval and constellation databases were represented in the radiative transfer as "fluffy spheres", with single scattering parameters calculated using Mie theory. Resulting simulated Tbs agreed reasonably well at frequencies up to 89 GHz (TRMM's highest frequency), but showed significant biases compared with observed Tb at higher frequencies. The large differences between observed and computed Tbs implied large error covariances, S, in Eq. (8.2) which led to the higher frequency channels receiving little of no weight. In an effort to improve database

accuracy in these higher frequency channels, an ensemble of non-spherical ice particles was substituted for the "fluffy spheres". For radiometric consistency, ice water content profiles from the GPM Combined Retrieval optimizing the full suite of active and passive core satellite observations are used as a first guess, and adjusted iteratively for optimal radiometric agreement with observed 166 GHz H-pol Tbs. This channel was chosen for its sensitivity to ice scattering. The ice particle database of Liu (2008) was used with single scattering properties calculated via the discrete dipole method. Resulting Tbs showed significantly decreased bias and increased correlations compared to observed values at the higher frequency channels. There were also corresponding improvements in final retrievals, particularly over land surfaces (Ringerud et al. 2019).

The constellation retrieval database was assembled combining liquid hydrometeors with the iteratively adjusted ice profiles. Radiative transfer simulations, using the Eddington approximation and slant path geometry appropriate to each instrument, were then performed to calculate each database Tb. Tb were convolved to the native footprint size of each individual constellation sensor. Light precipitation below the sensitivity of the GPM radar was added as well in non-raining pixels when retrieved cloud water path exceeded a local threshold as determined by drizzle onset observed by the NASA CloudSat cloud profiling radar. The result of this process was a set of databases relating Tb to geophysical parameters, representative of 1 year of observed precipitation, with appropriate Tb associated with the observations calculated for each GPM constellation sensor in a parametric retrieval scheme.

8.2.2 Ancillary Datasets

While the mechanics of Bayesian inversions are fairly well understood (Kummerow et al. 2015), creating an algorithm to run operationally, in a timely manner, creates a variety of problems which necessitates creative solutions. An example is the use of ancillary data such as surface temperature and total precipitable water (TPW) to search only appropriate portions of the a priori database. Previous studies such as Berg et al. (2006) have shown that searching only over the appropriate SST and TPW over oceans constrains the solution in a significant and positive manner. An important step is, therefore, to select the appropriate a priori profiles for the Bayesian inversion. In the current version of the algorithm, which retrieves over all surface types, the SST was replaced by model derived 2-meter temperature (T2m). The T2m showed much less variability between different model re-analyses and is therefore more robust.

GPM surface types are defined by using monthly averaged self-similar emissivities originally classified by Aires et al. (2011). Daily sea ice and land cover snow maps from NOAA's Auto Snow dataset (Romanov et al. 2000) are added to the monthly databases, and a coastline surface class is assigned which is dependent on each sensor footprint resolution. Finally, the two-meter temperature and TPW, are

added to each profile from two global analyses products: Japanese Global Analysis (GANAL) and ECMWF Interim or ERA-5 datasets. Using other global analyses is possible as versions using MERRA/GEOS5 have been also successfully created.

The profile quantity and their distribution for three surface types are shown in Fig. 8.2. One year of profiles over oceans has as many as 500,000 profiles in a single category, while over land the numbers are an order of magnitude less. The number of profiles is simply too large to operationally run GPROF, but it's critical to have an entire year of profiles in order to sample all areas geographically and seasonally. Therefore, for operational GPROF processing, a k-means clustering routine was implemented to decrease the number of profiles in each T2 m/TPW/Surface Type grouping. A maximum of 800 profiles were kept along with a frequency of precipitation occurrence of the profiles within a given cluster. The clustering algorithm also does a broadening of the TPW range up to ±4 mm. This has the intended effect of smoothing the profiles in each clustered bin, and also increasing the total number of profiles in each bin. The TPW broadening happens gradually until a maximum of 300,000 profiles is included in each of the 800 profile clusters within the bin. The clustering results in 14 individual sensor GPROF databases, made up of 14 files – one for each surface type. GPROF uses these 14 files to run the final the Bayesian rainfall retrieval, one surface type at a time.

The process for creating the databases for the cross-track sounding instruments, MHS, AMSU-B, and ATMS is very similar to the above description of the conical databases, however there are some significant differences. The conical imagers have a constant Earth Incident Angle (EIA) – defined as the angle between nadir and the instrument view angle at the Earth's surface. Therefore, when running the forward model radiative transfer, only a single EIA needs to be included for the path through the atmosphere. The cross-track instruments have a variable EIA for each of the 90 (MHS and AMSU-B), or 96 (ATMS) scan positions. To most accurately calculate the top of the atmosphere Tbs, the forward model would need to run using the EIA of each of the scan positions.
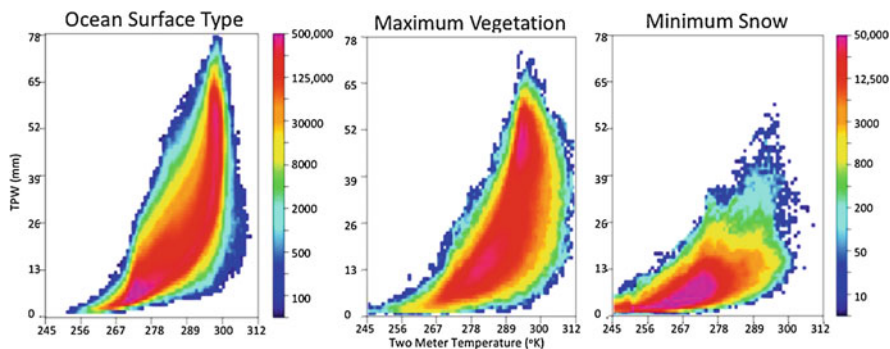
Fig. 8.2 GPROF database distribution of Total Precipitable Water (TPW) and Two-Meter Temperature (T2M) profiles included in the a priori database year. These represent the number of database profiles in each TPW/T2 m and Surface Type category

This is computational expensive and not necessary for the operational GPROF retrieval. Instead the forward model was run at 10 scan angles and these were used as tie-points for interpolating the other scan position Tbs. At very high scan angles (generally the last 5 scan positions on each side), the errors in the radiative transfer become large, and the error covariances become correspondingly larger. This causes the retrieved rain rates to be less reliable and therefore the Tbs at these scan positions are set to missing and no rainfall retrieval is performed.

8.3 Satellite Sensor Pixel Preparation: GPROF Preprocessor

The GPROF retrieval is a simple Bayesian engine that compares the satellite observed brightness temperatures (Tbs) against Tbs in the a priori databases. In order to prepare the satellite pixels, additional data is added as described above. This is the function of the GPROF Preprocessor. While the GPROF databases are static and created from 1 year of DPR/GMI observations, the preprocessor routine takes the real-time satellite observations and adds the most current and also forecast (for real-time retrievals) ancillary data fields available. Often these are model analysis fields both of surface and profile data. For the first 5 years of GPM, the near-real time retrievals use JMA model analyses and forecast fields. A more accurate version of the retrieval is run 1–2 days after real-time using the GANAL products. Two to three months after real-time, the Climatology version of GPROF is created using the ECMWF Interim or ERA-5 model products. This last processing using the ECMWF data enables a stable product set for historical or multi-year retrieval datasets. From each of the input model analyses, the TPW, T2 m, and surface moisture are attached to each satellite pixel. An additional ancillary parameter, the surface wet bulb temperature is added for use within GPROF to discriminate between the phase of the precipitation (snow vs. rain).

Finally, the daily GPROF surface type map is created and used to assign one of the 14 surface types to the satellite pixel. Once again, this will be used in the GPROF algorithm to limit the a -priori database pixels within the Bayesian averaging.

8.4 The GPROF Bayesian Retrieval Algorithm

The GPROF algorithm begins by ingesting a standard input file produced from the each of the unique sensor preprocessors. This includes all the ancillary data needed to match the T2 m/TPW/Surface Type in the profile databases. This 3-dimensional

matching is used to subset the entire set of database profiles for the Bayesian precipitation and profile retrieval. The width of the search in T2 m/TPW space is variable in TPW space in the database creation depending on the number of binned profiles, in the retrieval ± 1 K is used in the T2 m bin space. All the conical imager sensors use identical GPROF code.

If vertical profile retrieval of the hydrometeor species is implemented, then the Bayesian averaging is executed for all the layers in each of the hydrometeor profiles. This approximately triples the run time. After the Bayesian profile is computed they are matched to the closest profile from a database of 960 representative profiles for each hydrometeor species. These were created from a clustering process of 1 year of full profile GPROF retrievals. This step greatly reduces the data volume of the output files while adding little additional error. The cross-track sensors have a different executable for GPROF 2017 to account for the changing incident angle in the observations and the database.

As part of the Bayesian formulation the uncertainty for each sensor's channels must be defined. Uncertainties in physical inversions come from a combination of sensor noise and forward assumptions and errors. As described in Stephens and Kummerow (2007), channel uncertainties tend to be dominated by the forward model assumptions. That is the case here as well, and is particularly true when surface characteristics are not well known. In the GPROF 2017 retrieval, the uncertainty is determined from the fit between the observed dataset and the computed forward model Tbs that ultimately make the a priori database. Because errors are simplistically assumed uncorrelated, larger FOV have smaller error characteristics. An additional and very important source of error comes from the incompleteness of the database. This is particularly evident if only a few thousand profiles are used to characterize rainfall as seen from 13 different channels, as is the cases with GMI. An example here might be that in the 1 year of profiles from the Combined product, there are very few overpasses of the narrow DPR directly over tropical storms. Whenever GPROF attempts to retrieve rain rates around tropical storms, there are an inadequate number of profiles in the a priori database to describe the variability of rain rates with similar Tbs. This problem was explored with a separate hurricane version of the retrieval (Brown et al. 2016) where 10 years of TRMM PR profiles, only over tropical storms, were used to construct the a priori databases. This "Hurricane GPROF" algorithm, showed less bias for both high and low rain rates and less overall RMS when directly comparing the TMI retrieval to the TRMM PR. An example of the retrieval is shown in Fig. 8.3.

Petty and Li (2013) have presented a channel reduction procedure to define the importance and uniqueness of each sensors frequencies to the rain rate retrieval. The goals, as they stated were to, "decorrelate geophysical background noise while retaining the majority of radiometric information concerning precipitation". This effectively reduced the error introduced by sparsely populating the 13-channel dimensional space. A full solution to this problem, applicable to GMI and all the constellation sensors has not been implemented.
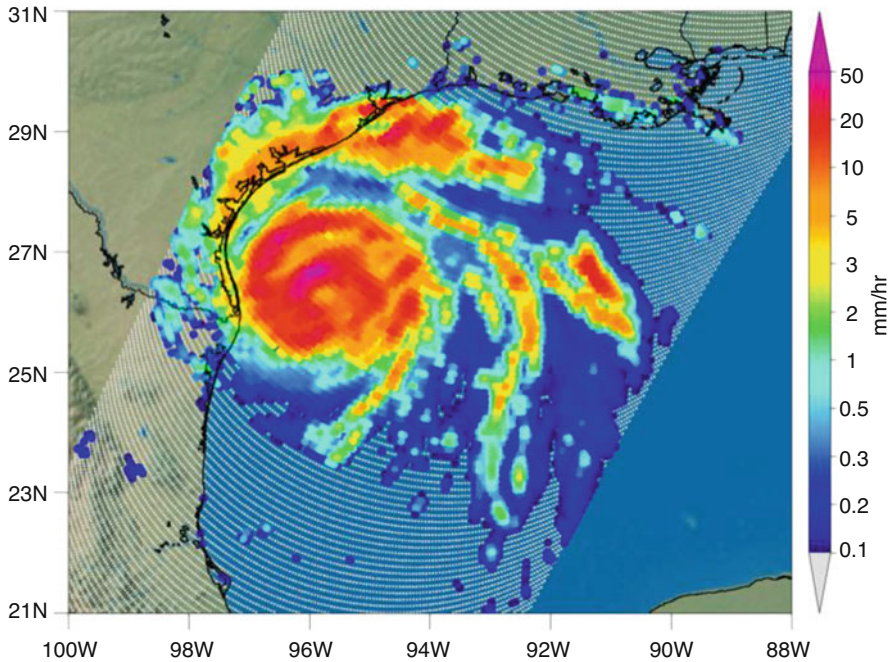
Fig. 8.3 GPROF GMI retrieval of surface rain for hurricane Harvey, 25 August 2017 shortly before making landfall on the Texas coast. Over 60 inches (1500 mm) of precipitation was recorded near Houston over the next 5 days

The current version of GPROF applies a probability of precipitation (PoP) directly to the retrieved precipitation values. The PoP thresholds for rain/no-rain are calculated for each sensor, are bin (T2m/TPW/Surface class) dependent. The process as it's currently implemented, is described as follows. For each of the bins in the database, the number of raining and non-raining profiles, as well as the rain fraction was calculated. An example is that in warm/moist bins the rain/(rain + no-rain) ratio is near 70% while in cooler dryer climates it might be 5%. One year of GPROF rain retrieval was created without any probability thresholds applied. The frequency of rain was collated, and a histogram of PoP for each bin was made. Next, the required POP threshold was calculated that matched the database rain frequency, and this sets a POP threshold for that bin. Finally, the fraction of rain is computed that was removed using this PoP threshold. The PoP threshold, and the fractional rain that is removed by the threshold was output and saved in a file that is read into the GPROF retrieval.

During the GPROF retrieval process, precipitation with probability below the threshold is set to 0.0. Retrieved Precipitation about the threshold is increased by the fraction of removed precipitation. This method conserves the total precipitation of the retrieval, an important step in the Bayesian statistical scheme.
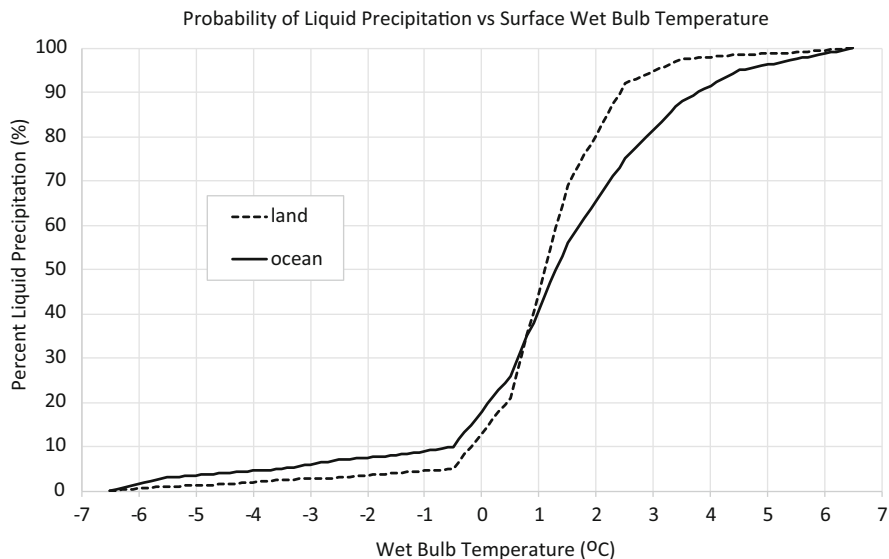
Fig. 8.4 Solid (Snow) vs. Liquid Precipitation and Wet Bulb for both ocean and land locations. (Adapted from Sims and Liu 2015)

The GPROF 2017 algorithm retrieves the total surface precipitation, not its phase. In order to make this rain/snow separation, an additional piece of information is needed, the surface dew point temperature. From Sims and Liu (2015) a lookup table was used of the fractional precipitation that is liquid/solid at certain dew point temperatures. As noted earlier, the surface dew point temperature was attached to each satellite pixel in the GPROF preprocessor. At -6.5 °C and below, 100% of the precipitation is frozen, while above 6.5 °C the precipitation is all liquid. Between these extremes, the precipitation is mixed and each type is output in the GPROF output file. There are two different lookup tables, one for ocean and one for land. The lookup tables which use the surface wet bulb temperature and used in GPROF are graphically described in Fig. 8.4.

The GPROF algorithm is run on all the sensors of the GPM constellation. Zonal averages of the results are shown in Fig. 8.5 for total annual averaged surface precipitation (left) and for frozen precipitation in the Northern Hemisphere winter season (right). The average and spread of values are for five the sensors: GMI, SSMIS, AMSR2, MHS and ATMS. Results show that the total precipitation can be retrieved with great agreement between the sensors – striking considering the different frequencies in the channel set for each sensor. However, the greater variance in the frozen precipitation is most likely caused by the lack of some sensor frequencies above 89 GHz (AMSR2) which greatly affect the snow retrieval.
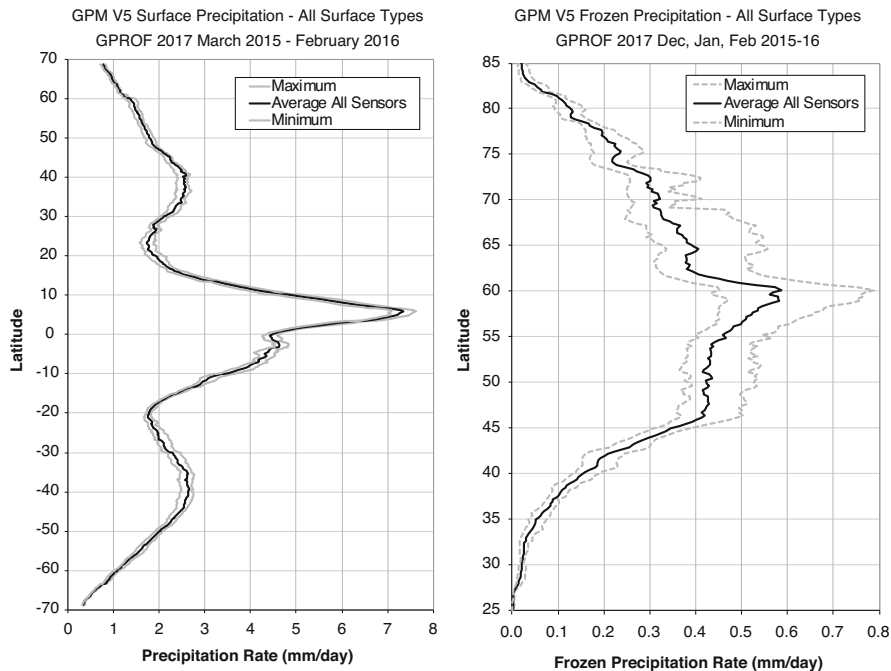
Fig. 8.5 GPROF zonal averaged precipitation retrieval for Total (left) and Frozen precipitation (right) for five GPM constellation sensors

8.5 Conclusions

GPROF 2017 represents the most recent iteration of a parametric retrieval scheme for precipitation from space borne passive microwave radiometers. By utilizing a physically-based a priori database created from the GPM Combined radar/radiometer retrievals, coupled with full column radiative transfer and a Bayesian retrieval, the algorithm is consistently applied for sensors of varying frequency, observing angle, and footprint size. The result is global, consistent precipitation retrievals across a diversity of sensors for real-time analysis. The nature of the scheme also allows for the ability to process retrospectively for consistent climatological-scale retrievals from the global constellation.

Future development of GPROF will occur as GPM's Combined algorithm improves, ancillary data becomes more consistent, and uncertainty estimates in the forward model, a difficult parameter to estimate from first principles, improves over time. In addition, there are still situations, such as high latitude drizzle, and orographic precipitation, where the brightness temperatures and current ancillary data may not be sufficient to retrieve an unambiguous rain signal. Here, it is likely that the algorithm may use additional ancillary data to help constrain the potential solution space.

References

Aires, F., Prigent, C., Bernardo, F., Jiménez, C., Saunders, R., & Brunel, P. (2011). A tool to estimate land-surface emissivities at microwave frequencies (TELSEM) for use in numerical weather prediction. *Quarterly Journal of the Royal Meteorological Society, 137*, 690–699. https://doi.org/10.1002/qj.803.

Berg, W., L'Ecuyer, T., & Kummerow, C. D. (2006). Rainfall climate regimes: The relationship of regional TRMM rainfall biases to the environment. *Journal of Applied Meteorology and Climatology, 45*, 434–454. https://doi.org/10.1175/JAM2331.1.

Brown, P. J., Kummerow, C. D., & Randel, D. L. (2016). Hurricane GPROF: An optimized ocean microwave rainfall retrieval for tropical cyclones. *Journal of Atmospheric and Oceanic Technology, 33*, 1539–1556. https://doi.org/10.1175/JTECH-D-15-0234.1.

Duncan, D. I., & Kummerow, C. D. (2016). A 1DVAR retrieval applied to GMI: Algorithm description, validation, and sensitivities. *Journal of Geophysical Research, 121*, 7415–7429. https://doi.org/10.1002/2016JD024808.

Grecu, M., Olson, W. S., Munchak, S. J., Ringerud, S., Liao, L., Haddad, Z. S., Kelley, B. L., & McLaughlin, S. F. (2016). The GPM combined algorithm. *Journal of Atmospheric and Oceanic Technology, 33*, 2225–2245. https://doi.org/10.1175/JAM2331.1.

Haynes, J. M., L'Ecuyer, T. S., Stephens, G. L., Miller, S. D., Mitrescu, C., Wood, N. B., & Tanelli, S. (2009). Rainfall retrieval over the ocean with spaceborne W-band radar. *Journal of Geophysical Research, 114*, D00A22. https://doi.org/10.1029/2008JD009973.

Hilburn, K. A., & Wentz, F. J. (2008). Intercalibrate passive microwave rain products from the Unified Microwave Ocean Retrieval Algorithm (UMORA). *Journal of Applied Meteorology and Climatology, 47*, 778–794. https://doi.org/10.1175/2007JAMC1635.1.

Kirstetter, P. E., Hong, Y., Gourley, J. J., Chen, S., Flamig, Z., Zhang, J., Schwaller, M., Petersen, W., & Amitai, E. (2012). Toward a framework for systematic error modeling of spaceborne precipitation radar with NOAA/NSSL ground radar-based national mosaic QPE. *Journal of Hydrometeorology, 13*, 1285–1300. https://doi.org/10.1175/JHM-D-11-0139.1.

Kummerow, C. D., Randel, D. L., Kulie, M., Wang, N., Ferraro, R., Joseph Munchak, S., & Petković, V. (2015). The evolution of the Goddard profiling algorithm to a fully parametric scheme. *Journal of Atmospheric and Oceanic Technology, 32*, 2265–2280. https://doi.org/10.1175/JTECH-D-15-0039.1.

Liu, G. (2008). A database of microwave single-scattering properties for nonspherical ice particles. *Bulletin of the American Meteorological Society, 89*, 1563–1570. https://doi.org/10.1175/2008BAMS2486.1.

Petty, G. W., & Li, K. (2013). Improved passive microwave retrievals of rain rate over land and ocean. Part I: Algorithm description. *Journal of Atmospheric and Oceanic Technology, 30*, 2493–2508. https://doi.org/10.1175/JTECH-D-12-00144.1.

Ringerud, S., Kulie, M. S., Randel, D. L., Skofronick-Jackson, G. S., & Kummerow, C. D. (2019). Effects of ice particle representation on passive microwave precipitation retrieval in a Bayesian scheme. *IEEE Transactions on Geoscience and Remote Sensing, 57*, 3619–3632. https://doi.org/10.1109/TGRS.2018.2886063.

Romanov, P., Gutman, G., & Csiszar, I. (2000). Automated monitoring of snow cover over North America with multispectral satellite data. *Journal of Applied Meteorology, 39*, 1866–1880. https://doi.org/10.1175/1520-0450(2000)039<1866:AMOSCO>2.0.CO;2.

Sims, E. M., & Liu, G. (2015). A parameterization of the probability of snow–rain transition. *Journal of Hydrometeorology, 16*, 1466–1477. https://doi.org/10.1175/JHM-D-14-0211.1.

Stephens, G. L., & Kummerow, C. D. (2007). The remote sensing of clouds and precipitation from space: A review. *Journal of the Atmospheric Sciences, 64*, 3742–3765. https://doi.org/10.1175/2006JAS2375.1.

Chapter 9
Precipitation Estimation from the Microwave Integrated Retrieval System (MiRS)

Christopher Grassotti, Shuyan Liu, Quanhua Liu, Sid-Ahmed Boukabara, Kevin Garrett, Flavio Iturbide-Sanchez, and Ryan Honeyager

Abstract The Microwave Integrated Retrieval System (MiRS) has been the NOAA official operational microwave retrieval algorithm since 2007 and is run operationally on multiple microwave satellite/sensor systems. The algorithm is based on a 1-dimensional variational (1-DVAR) methodology, in which the fundamental physical attributes affecting the microwave observations are retrieved physically, including the profile of atmospheric temperature, water vapor, hydrometeors, as well as surface emissivity and temperature. A description of the mathematical basis and algorithm components are presented here, followed by examples of retrieved hydrometeorological parameters. Examples presented show that global estimates of surface rain rate from different satellites are generally consistent, and that the explicit treatment of both surface (e.g., emissivity) and atmospheric parameters in the forward radiative transfer model allows for accurate and consistent estimates over a variety of surfaces (e.g., ocean, land with different vegetation types, coastal regions). Validation and performance metrics using independent reference data indicate that the rainfall rates meet most NOAA operational requirements. Suggested avenues for future development and enhancements are also presented including an example of one planned operational enhancement that has led to improved light rain detection over land.

C. Grassotti (✉)
Cooperative Institute for Satellite Earth System Studies (CISESS), ESSIC, University of Maryland, College Park, MD, USA
e-mail: christopher.grassotti@noaa.gov

S. Liu
CIRA, Colorado State University, Ft. Collins, CO, USA

Q. Liu · S.-A. Boukabara · K. Garrett · F. Iturbide-Sanchez
NOAA/NESDIS/STAR, College Park, MD, USA

R. Honeyager
UCAR, College Park, MD, USA

9.1 Background

The Microwave Integrated Retrieval System (MiRS, https://www.star.nesdis.noaa.gov/mirs, last accessed 31 Oct. 2018) has been the NOAA official operational microwave retrieval algorithm since 2007 (Boukabara et al. 2011) and has been or is currently run operationally on microwave data from NOAA (-18, -19), Metop ($-$A, -B)/AMSUA-MHS, DMSP (F-16, F-17, F-18)/SSMIS, Suomi-NPP polar orbiting satellites, and on data from Megha-Tropiques/SAPHIR. In addition, MiRS also processes operationally GPM/GMI data (Liu et al. 2017). In 2018 MiRS began processing at NOAA/NESDIS/STAR ATMS data from NOAA-20 (launched in November 2017); following calibration and validation activities MiRS NOAA-20/ATMS capability was delivered to NOAA operations in 2019. It has also been run experimentally on data from TRMM/TMI, Aqua/AMSR-E, and GCOM-W1/AMSR2. Extension of MiRS to data from Metop-C (launched in late 2018) was also completed in 2019.

   The inversion within MiRS follows a 1-dimensional variational (1DVAR) methodology, in which the fundamental physical attributes affecting the microwave observations are retrieved physically, including the profile of atmospheric temperature, water vapor, hydrometeors, as well as surface emissivity (Boukabara et al. 2018) and temperature. The Community Radiative Transfer Model (CRTM) is used as the forward and Jacobian operator to simulate the radiances at each iteration prior to fitting the measurements to within the combined instrument and forward model noise level. The retrieved surface properties are then used to determine surface physical characteristics, including, when appropriate, cryospheric parameters such as sea ice concentration, ice age, and snow water amount, and snow grain size, using pre-determined relationships that link emissivity and effective skin temperature to these parameters. These links are based, in part, on physical modeling of snow and ice radiative properties. In the case of the surface precipitation rate the determination is sensor-independent in that the same relationships (determined off-line using numerical weather prediction model simulations) between the surface precipitation rate and the core retrieved vertical hydrometeor profiles are used. MiRS has also been integrated into the Community Satellite Processing Package (CSPP), developed at the University of Wisconsin/Space Science and Engineering Center for users in the Direct Broadcast/Readout community. The MiRS software package is available publicly for download, and more than 30 institutions and/or individuals have installed and run MiRS locally. MiRS retrieval products are used routinely in operational weather analyses and forecasts, and also serve as inputs to downstream applications that are also used in operations. For example, MiRS water vapor profiles, and total precipitable water (TPW) are used to generate the multi-satellite

blended layer precipitable water, and blended TPW products (Forsythe et al. 2015). MiRS profiles of temperature and water vapor are also used as inputs to the tropical cyclone (TC) intensity estimation algorithm (HISA) developed at CIRA (Chirokova et al. 2015) and is used operationally at the National Hurricane Center. Finally, MiRS precipitation rates are used as one of several satellite-based precipitation inputs to the NOAA Climate Prediction Center (CPC) Morphing Technique Algorithm (CMORPH) (Joyce and Xie 2011; Joyce et al. 2004).

9.2 Algorithm Description

A schematic of the MiRS algorithm processing components and data flow is shown in Fig. 9.1. The 1DVAR algorithm used by MiRS (Rodgers 2000; Liu and Weng 2005) is an iterative approach finding the optimal solution that fits the observed satellite radiance, subject to other constraints. The cost function to be minimized is:

$$J(X) = \left[\frac{1}{2} (X - X_0)^{\mathrm{T}} \times B^{-1} \times (X - X_0) \right]$$
$$+ \left[\frac{1}{2} (Y^m - Y(X))^{\mathrm{T}} \times E^{-1} \times (Y^m - Y(X)) \right] \tag{9.1}$$

where X is the retrieved state vector. The first term on the right represents the penalty for departing from background X_0 weighted by the background error covariance
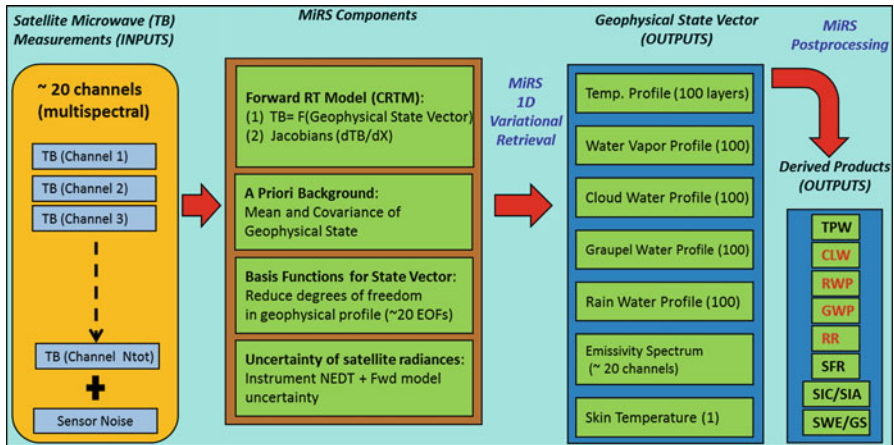
Fig. 9.1 Schematic of MiRS processing components and data flow showing MiRS core retrieval and post-processing components. Core products are retrieved simultaneously as part of the state vector. Post-processing products are derived through vertical integration (water vapor, hydrometeors), catalogs (SIC, SWE), or fast regressions (rain rate). Post-processed hydrometeor retrieval products are indicated in red: Rain Rate, Graupel Water Path, Rain Water Path and Cloud Liquid Water

matrix B. The second term represents the penalty for the simulated radiances Y departing from the observed radiances Y^m, weighted by instrument and modeling error E.

Assuming local linearity,

$$y(x) = y(x_0) + K[x - x_0] \tag{9.2}$$

leads to an iterative solution,

$$\Delta X_{n+1} = \left\{ BK_n^{\mathrm{T}} \left[K_n BK_n^{\mathrm{T}} + E \right]^{-1} \right\} \left\{ [Y^m - Y(X_n)] + K_n \Delta X_n \right\} \tag{9.3}$$

where ΔX is the increment of the state vector iteration $n + 1$, and K is the matrix of Jacobians which contains the sensitivity of the radiances to changes in X (parameters to retrieve).

The departure from measured radiances normalized by the noise level and the specification of uncertainty in the forward modeling make it possible to use the signal of a particular channel when the geophysical signature is stronger than the noise. Conversely, at other times it may be possible to de-weight the information from same channel when the signal in question is within the noise level. The departure from the background scaled by the uncertainty assigned to the background result in retrievals closer to an a priori background estimate if it is assumed accurate. MiRS currently uses a "dynamic background" as an a priori constraint, for temperature, water vapor, and skin temperature, which varies with latitude, longitude, season and time of day. Empirical orthogonal functions (EOFs) are used as basis functions to further reduce the degrees of freedom in the solution and stabilize the retrieval. The criterion for convergence is satisfied when the fit over all channels of simulated to observed brightness temperatures (normalized by the combined instrument and forward model uncertainty) is less than 1.

CRTM (Weng et al. 2005; Han et al. 2006) produces radiances and the corresponding Jacobians under clear, cloudy, and precipitating conditions. MiRS currently uses CRTM version 2.1.1. The model has been validated against various satellite measurements (Chen et al. 2008; Ding et al. 2011). MiRS uses CRTM as the forward operator to perform retrievals under all sky conditions. Given a set of radiances, and an a priori (background) estimate of the geophysical mean and its associated covariance matrix, and assuming the hypotheses for its mathematical basis are satisfied, MiRS produces a set of self-consistent parameters that are also consistent with the measured parameters. When processing satellite sensor data with a full complement of temperature, water vapor and surface-sensitive channels, the official MiRS products generally include temperature (T) and water vapor (WV) vertical profiles, cloud and precipitation vertical profiles (non-precipitating cloud amount, rain, and graupel, pCLW, pRWP, pGWP, respectively) all defined on 100 pressure layers, skin temperature (Tskin), and the surface emissivity spectrum (Em). Post-processing of elements within the retrieved state vector yield additional retrieval products such as rain rate, total precipitable water (TPW), sea ice

concentration and age (SIC, SIA), snow water equivalent (SWE) and grain size (GS). In the case of TPW, simple vertical integration of the retrieved water vapor profile is done.

Post-processing to determine a surface precipitation rate (RR) is done by first vertically integrating each of the cloud, as well as the precipitation-related profiles of rain water and graupel water to obtain total cloud liquid water (CLW), rain water (RWP), and graupel water (GWP) path, respectively. Off-line relationships between surface RR and RWP, GWP, and CLW were developed from mesoscale forecast model simulations. The precipitation rate is then computed from the following equations

$$RR(CLW, RWP, GWP) = RR_{CLW} + 3.879 \times (RWP + GWP)^{1.103} \qquad (9.4)$$

where

$$RR_{CLW} = 2.339 \times (CLW)^{1.156} \qquad (9.5)$$

The same equation is applied for all operational satellites, and over all surface types, with the exception that over land the CLW-based term is set to zero, since it had been previously determined that the CLW microwave signal over land was low relative to variations in the higher background surface emissivity. However, recent testing indicates that CLW can be retrieved with sufficient accuracy so that use of CLW can improve light rain detection and estimation over land (see Sect. 9.7).

Finally, for sea ice and snow water, external catalogs that relate the surface emissivity spectrum to ice and snow amounts are used. In the case of snow water, a single-layer physical snow model developed at NOAA is used to build the catalogs. An important feature of MiRS is that, as currently configured, retrievals do not require real-time ancillary data such as those coming from numerical weather prediction model forecasts. MiRS products based on various satellite/sensors have been examined, including precipitation, for example (Boukabara et al. 2013; Iturbide-Sanchez et al. 2011).

9.3 Algorithm Components

As noted, the MiRS algorithm has been running in operations for over 10 years and has been extensively validated using a variety of reference data sets. Additionally, several updates to the algorithm have been delivered to operations which have led to improved performance. The current version of MiRS is v11.4 which has been running operationally since July 2019. Global performance characteristics generally meet NOAA operational requirements, for example as specified in the JPSS NESDIS ESPC Requirements Document (JERD) (NOAA 2015). Key features of the operational MiRS are:

- Use of a "dynamic" climatology for the a priori background and first guess T, WV, T_{skin}, and CLW profiles that is stratified by latitude, longitude, time of year, and time of day. This climatology was derived from 1 year of ECMWF analyses.
- A priori background covariances of T, WV, CLW, and all hydrometeor profiles derived from a global set of atmospheric profiles chosen to span a large range of climate regimes.
- Empirical Orthogonal Function basis functions for all elements of the retrieved state vector (T, WV, CLW, hydrometeors, surface emissivity), which, with the exception of emissivity are computed from the previously mentioned covariances.
- Use of all available microwave channels, which generally consist of temperature, and water vapor sounding channels, in addition to surface sensitive channels.
- Use of the CRTM fast forward radiative transfer model which, given an estimate of the atmospheric and surface state, will compute both satellite-observed radiances, and their sensitivities with respect to each of the atmospheric/surface state variables (i.e., Jacobians).
- Post-processing modules that convert the elements of the core retrieved state vector to derived quantities such as surface rain rate, snow water equivalent, and sea ice concentration.

9.4   Treatment of Hydrometeors

Hydrometeor representation in MiRS is largely driven by corresponding representation in the CRTM forward model which contains a total of five cloud types (i.e., non-scattering cloud droplets, and larger particles for rain, ice, graupel, and snow). The MiRS state vector contains three types of hydrometeors: non-scattering cloud droplets, and larger precipitation-sized scattering particles of rain water and graupel water. In the retrieval system, the particle size effective radius is assumed fixed at 30 microns for cloud droplets, and 500 microns for both rain and graupel water. Pre-computed scattering coefficient tables are generated off-line for CRTM and assume all particles are spherical in shape for rain droplets and cloud droplets of small particle sizes. Non-spherical particles are used for solid clouds: ice, snow, graupel and hail. (Liu and Lu 2016) The distinction between non-scattering and scattering particles leads to a retrieval approach within MiRS that consists of two attempts: (1) In the first attempt only non-scattering droplets are contained within the atmospheric state vector. If the retrieval successfully converges (i.e., simulated brightness temperatures fit observed measurements to within the assumed combined noise plus forward model uncertainty) then the retrieval is completed and the associated atmospheric profile is the final retrieval (a minimum threshold of 0.275 mm is used to identify a retrieved scene as containing rain); (2) If the retrieval does not converge, then a second attempt is made in which rain and graupel water are added to the atmospheric state vector, and cloud droplets are removed. Since the scattering simulations in CRTM are computationally costly, the partitioning of

attempts into non-scattering and scattering has the advantage of limiting CRTM scattering calculations to only those scenes in which scattering is likely.

A retrieval example from a single scene (field of view) of data from NOAA-18 AMSUA-MHS is shown in Fig. 9.2 to highlight the evolution by iteration of retrieved rain and graupel water and associated Jacobians. The figure shows (1) non-linear behavior in that Jacobian profile changes with hydrometeor amount, and (2) the final retrieved profile can have a different shape than an a priori
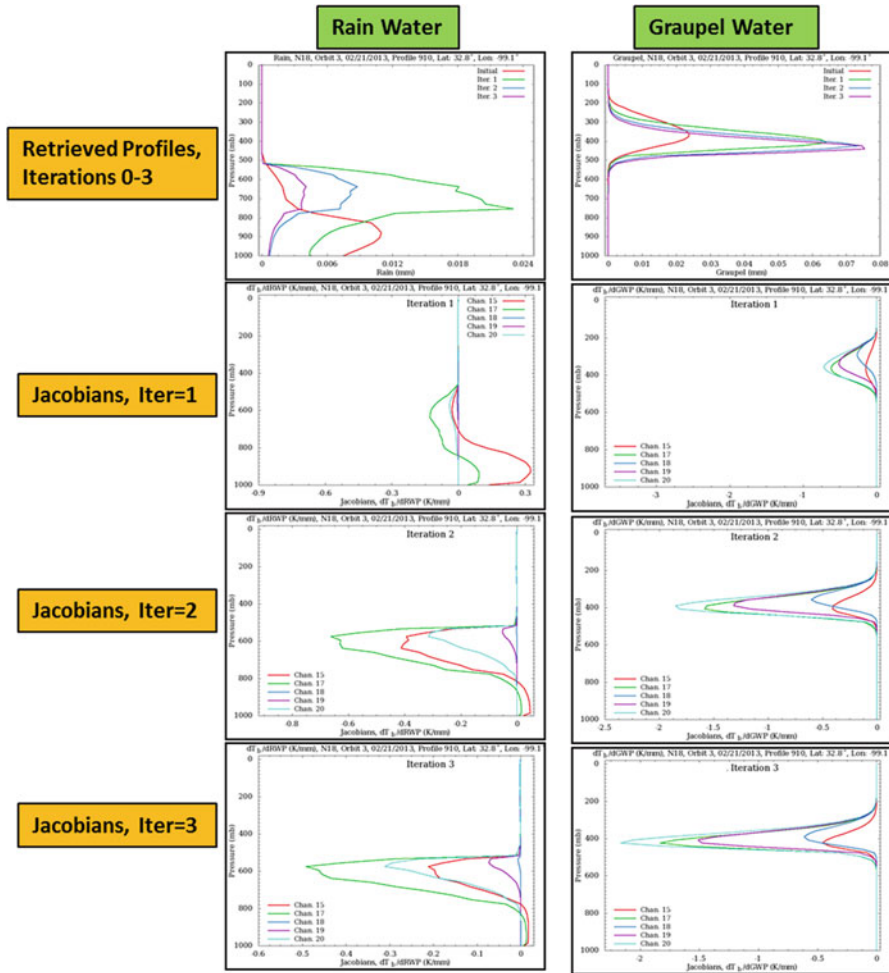
Fig. 9.2 Example of rain water (left) and graupel water (right) retrieval evolution for a single vertical profile based on NOAA-18 AMSU-MHS measurements. Top panels show rain and graupel water profile retrieval as function of iteration (3 iterations total). The remaining panels show the CRTM Jacobians with respect to rain and graupel at channels 15, 17, 18, 19, 20 (89, 157, 183 ± 1, 183 ± 3, and 190 GHz), for each iteration. In this case, the retrieval converged in 3 iterations. Rain and graupel particle effective radii were assumed to be 500 microns

background/first guess. Generally speaking, retrievals of the total integrated amounts of rain and graupel will have lower uncertainty, while the vertical structure or distribution will have larger associated uncertainty. Additionally, assumptions built into the scattering simulations related to effective particle size, size distribution and orientation, and particle shape will all impact the final retrieved amounts. As currently configured, these parameters that describe the scattering particles are fixed and not part of the retrieval state vector. However, results shown in Chap. 48 indicate that there may be a benefit in explicitly accounting for these parameters. For example, several of their experiments show clear sensitivity of simulated brightness temperatures to both hydrometeor (rain and graupel) size and total amount and that this sensitivity is frequency dependent.

9.5   Retrieval Examples

As noted, the MiRS algorithm is run on passive microwave data generated by a number of different operational satellite systems. Figure 9.3 shows an example of MiRS global retrieved rain rates from the GPM/GMI and S-NPP/ATMS instruments on 21 June 2016. Although the temporal and spatial coverage of the two satellite data sets are different, the location and intensity of the primary precipitation systems are captured in both retrieval sets. This is noteworthy since the estimates are from two different passive microwave instruments (i.e., ATMS: cross-track scanning, with changing zenith angle across each scan, and mixed horizontal/vertical polarizations that change with scan angle; GMI: conical scanning, with fixed zenith angle across each scan, and separate horizontal/vertical polarizations). Consistency in the retrieved rainfall between the two satellites is due, in part, to the explicit accounting
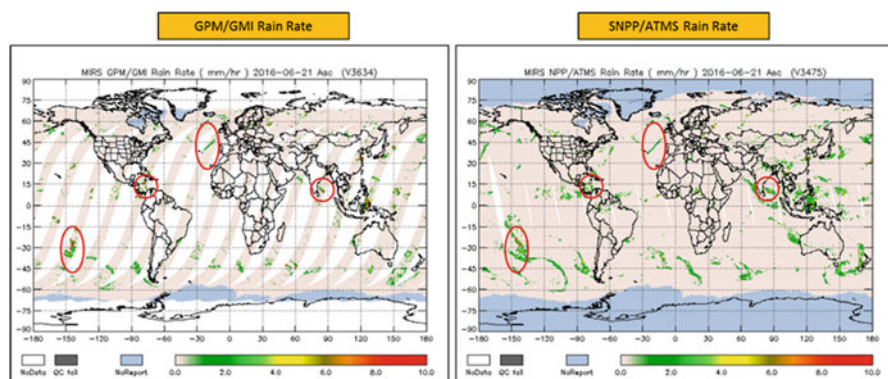
Fig. 9.3 Comparison of global rain rate maps on 21 June 2016 from MiRS when applied to GPM/GMI (left) and SNPP/ATMS measurements (right). Examples of weather systems detected by both satellites are circled
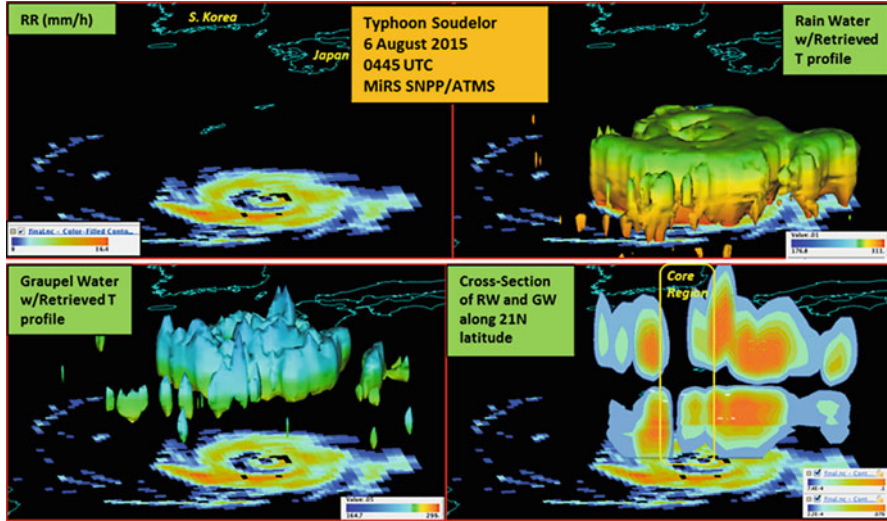
Fig. 9.4 MiRS retrievals of hydrometeor and temperature structure around Typhoon Soudelor from Suomi-NPP/ATMS valid 0445 UTC on 6 August 2015. Panels show surface rain rate (top left), rain water 0.01 mm isosurface with temperature profile superimposed (top right), graupel water 0.05 mm isosurface with temperature profile superimposed (bottom left), and a vertical cross-section along 21°N of both rain and graupel water (bottom right)

for angular dependence of surface emissivity, and atmospheric attenuation/scattering.

One of the features of MiRS is that it simultaneously retrieves the atmospheric profiles of temperature and water vapor, rain water, graupel and cloud, making it possible to reconstruct the 3-dimensional structure of tropical storms and severe weather systems. Figure 9.4 shows an example of S-NPP/ATMS retrievals in the environment of Typhoon Soudelor which struck both Taiwan and the mainland of China in August 2015 causing significant damage and loss of life due to high winds, heavy rainfall and flooding (Guardian 2015). Results show that the structure of atmospheric rain and ice, as well as the surface rain rate are realistically retrieved, with maximum rain rates of 16 mm h^{-1}, and the storm core feature present in both rain and graupel fields.

9.6   Validation Results

Quantitative assessment and validation of the MiRS precipitation is done through comparisons with other standard reference data sets. Most commonly, validation is done using the operational National Weather Service (NWS) Stage IV hourly blended radar-rain gauge analyses which are produced at a resolution of 4 km over the conterminous US (CONUS) (Baldwin and Mitchell 1998; Lin and Mitchell
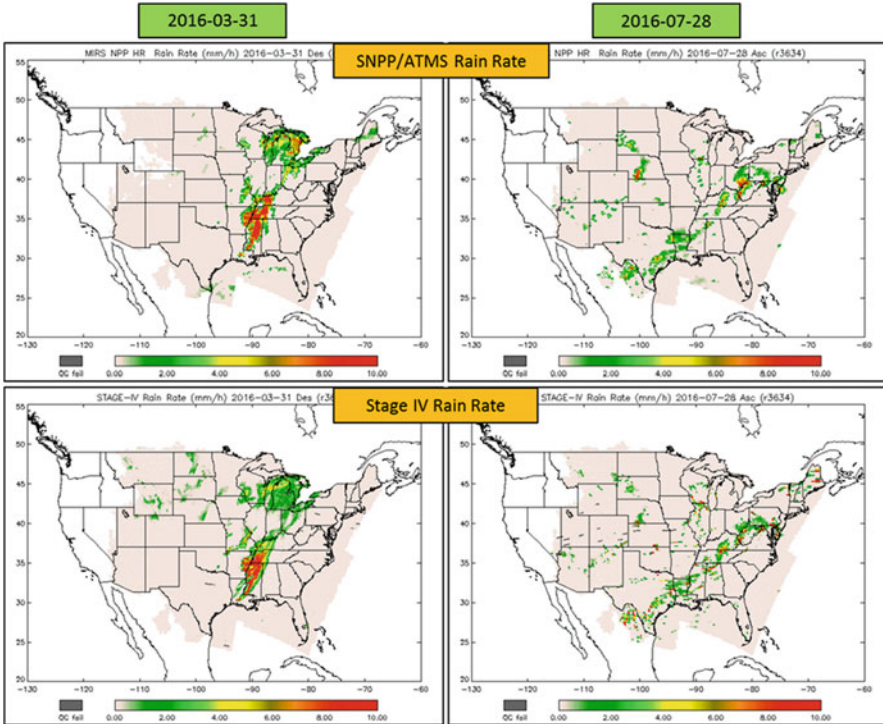
Fig. 9.5 Comparison of MiRS SNPP/ATMS instantaneous rain rate (mm/h) (top) with operational NWS Stage IV rain rate (bottom) over the conterminous US for two different dates, 16 March 2016 (left), and 28 July 2016 (right)

2005). The Stage IV data are based on the Multisensor Precipitation Estimator (MPE) analyses known as Stage III which use multi-sensor data (WSR-88D radar and gauges) and are specified on 4-km polar-stereographic grids produced by the 12 NWS River Forecast Centers.

Figure 9.5 shows an example of MiRS and Stage IV rain rates on two different dates, 31 March 2016 and 28 July 2016, indicating good agreement between the MiRS and Stage IV estimates. Closer inspection of the results shows that while the overall agreement is high with the Stage IV estimates, the agreement is not uniform. In particular, there is higher agreement in areas with heavier rainfall, especially convective systems. This is because these rain systems contain larger amounts of rain water, and most likely ice crystals which enhance the scattering signal over the higher and variable land emissivity background. Generally, direct accounting of the surface emissivity spectrum and land surface temperature (via information present in lower frequency channel measurements less affected by clouds and rain) allows the retrieval system to accommodate natural variations in these parameters and tends to reduce the occurrence of precipitation false alarms. Conversely, areas of lighter – possibly stratiform – rain, for example as seen over the Northern Plains and Upper

Midwest (descending pass, left hand panels), are underdetected and underestimated. In these cases, there is a much weaker hydrometeor signal, which is difficult to separate from variations in either surface emissivity or water vapor. Nevertheless, as shown in Sect. 9.7 planned operational enhancements of MiRS should lead to better detection and estimation of lighter rainfall over land.

Validation statistics using Stage IV have also been computed for longer term periods. Tables 9.1 and 9.2 contain summary performance statistics for March and July 2016, respectively, and stratified into land and ocean (i.e., coastal) points. These statistics are based on the daily collocations of MiRS instantaneous rainfall with the Stage IV estimates. The statistics shown in the tables are the bias (MiRS – Stage IV) and standard deviation (STDV, mm h^{-1}), along with the categorical scores Probability of Detection (POD), Probability of False Detection (POFD), and the Heidke

Table 9.1 Summary of MiRS precipitation rate performance relative to Stage IV measurements over the CONUS for the period 1–30 March 2016

Sfc	Performance parameter	MiRS	JPSS requirement
Sea	Bias (mm h^{-1})	**0.07**	0.10
	STDV (mm h^{-1})	**0.92**	1.0
	Probability of detection (%)	**80**	50
	Prob. of false detection (%)	**4.0**	5.0
	Heidke skill score	**0.53**	0.30
Land	Bias (mm h^{-1})	**−0.01**	0.05
	STDV (mm h^{-1})	**0.58**	1.5
	Probability of detection (%)	**46**	50
	Prob. of false detection (%)	**1.0**	6.0
	Heidke skill score	**0.51**	0.30

For reference, the JPSS program environmental data record (EDR) performance requirements are also shown

Table 9.2 Summary of MiRS precipitation rate performance relative to Stage IV measurements over the CONUS for the period 1–31 July 2016

Sfc	Performance parameter	MiRS	JPSS requirement
Sea	Bias (mm h^{-1})	**0.00**	0.10
	STDV (mm h^{-1})	**0.78**	1.0
	Probability of detection (%)	**69**	50
	Prob. of false detection (%)	**2.6**	5.0
	Heidke skill score	**0.55**	0.30
Land	Bias (mm h^{-1})	**0.02**	0.05
	STDV (mm h^{-1})	**0.95**	1.5
	Probability of detection (%)	**62**	50
	Prob. of false detection (%)	**2.6**	6.0
	Heidke skill score	**0.51**	0.30

For reference, the JPSS program Environmental Data Record (EDR) performance requirements are also shown

Skill Score (HSS). Description and definition of these and other categorical scores
are presented in Doswell et al. (1990). For comparison, the JPSS program Environ-
mental Data Record (EDR) product requirements are also shown, and indicate that
the retrieval performance exceeds the threshold requirements in both months.

9.7 Planned Operational Improvements

As discussed in Sect. 9.2 above, retrieval of non-scattering liquid water clouds
(represented as cloud droplets of 30 micron effective radius) over land was consid-
ered to have much larger errors than over ocean surfaces, due in part to the difficulty
of distinguishing the signal of such clouds over the more emissive and variable land
surface (Jones and Vonder Haar 1990; Aires et al. 2001). However, recent tests have
indicated that, while displaying higher noise levels, the signal of light rain in the
microwave satellite measurements and in the corresponding CLW retrievals is
sufficient to detect and estimate lighter rain amounts.

Figure 9.6 shows an example from 1 May 2016. Panels (d) and (e) show the
MiRS retrieved cloud plus rain water, and the coincident GOES visible imagery
valid at the same time, indicating fairly close agreement in terms of cloud cover.
Panels (a) and (b) show the baseline operational (v11.3) rain rate and the experi-
mental rain rate that exclude and include CLW, respectively, within the rain rate
estimation equation. Comparison with the MRMS operational gauge adjusted
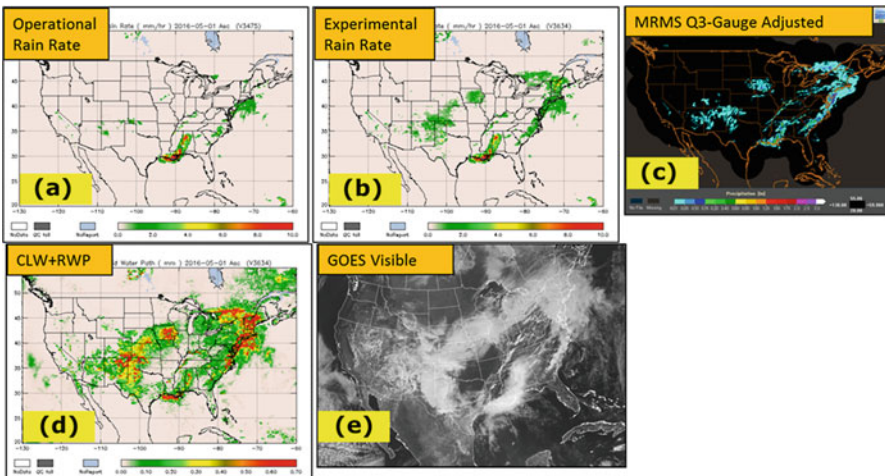
Fig. 9.6 Example of impact of using retrieved CLW over land in the land precipitation estimation
from SNPP/ATMS on 01 May 2016. Shown are (**a**) MiRS operational v11.3 rain rate (mm/h), (**b**)
MiRS rain rate using CLW, (**c**) MRMS Q3 radar-gauge analysis valid at 1900 UTC (units in
inches), (**d**) MiRS Liquid Water Path (LWP = RWP + CLW, mm), and (**e**) visible satellite image
from GOES-East valid at 1915 UTC

analysis (panel c) shows that the experimental rain rates have much better agreement than the operational estimates, due mainly to improved detection of the lighter rain rates. The incorporation of CLW into the S-NPP/ATMS rain rate estimate clearly improves the detection and estimation of light rainfall over land in this case.

Further quantitative analysis also supports this conclusion. MiRS operational and experimental rain rate retrievals for a 3-month period, September–November 2016, were collocated with operational Stage IV analyses over the US. Figure 9.7 shows the probability distribution functions of MiRS and Stage IV rainfall during this period, and indicate that the experimental rain rates more closely match the Stage IV analyses, at nearly all rain rate intensities. In addition, when considering all points where Stage IV rain rates were greater than zero, the mean rain rate for the experimental retrievals (1.24 mm h^{-1}) is in better agreement with the mean Stage IV rain rate (1.34 mm h^{-1}) than the operational value (0.99 mm h^{-1}).

Additional analyses of this time period is shown in Tables 9.3 and 9.4 which contain the categorical scores POD, POFD and HSS, corresponding to two different
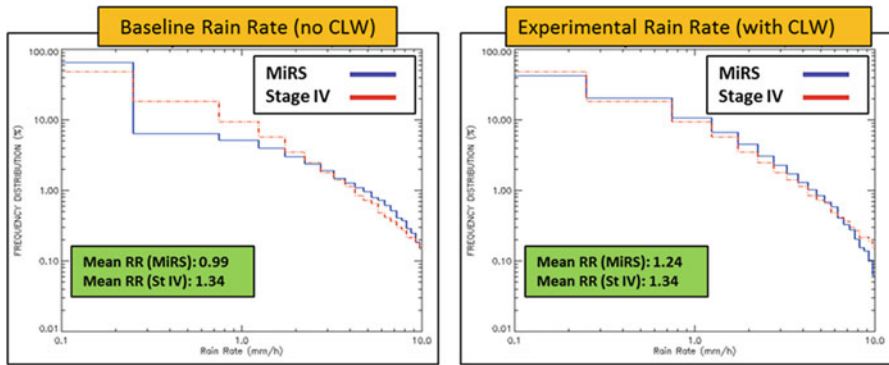
Fig. 9.7 Probability distribution functions of MIRS ATMS vs. Stage IV baseline (operational v11.3, no CLW included in rain rate estimation) and experimental rain rate (CLW included) over land during September–November 2016. Note improved frequency distribution and agreement with Stage IV in experimental rain rate. Distributions are for all points with Stage IV rain rate greater than 0 mm h^{-1}

Table 9.3 Categorical scores (Probability of Detection (%), Probability of False Detection (%), and Heidke Skill Score) of MiRS ATMS (Oper: operational version v11.3; Test: experimental test version) rain rates relative to Stage IV for a rain rate threshold of 0.5 mm h^{-1}

Time period	POD (0.5)		POFD (0.5)		HSS (0.5)		
	Oper	Test	Oper	Test	Oper	Test	Npts
Sept 2016	56.0	79.5	2.1	4.0	0.510	0.536	28,329
Oct 2016	44.6	72.3	1.1	2.8	0.448	0.458	21,344
Nov 2016	38.4	66.1	0.8	2.2	0.411	0.431	11,190

Performance for individual months of September, October, and November 2016 is shown. Total number of samples (Npts) is also indicated

Table 9.4 Categorical scores (Probability of Detection (%), Probability of False Detection (%), and Heidke Skill Score) of MiRS ATMS (Oper: operational version v11.3; Test: experimental test version) rain rates relative to Stage IV for a rain rate threshold of 3.0 mm h^{-1}

Time period	POD (3.0)		POFD (3.0)		HSS (3.0)		
	Oper	Test	Oper	Test	Oper	Test	Npts
Sept 2016	48.7	49.9	0.7	0.5	0.451	0.491	8010
Oct 2016	45.5	46.0	0.3	0.3	0.372	0.405	3423
Nov 2016	36.8	34.3	0.1	0.1	0.382	0.377	1579

Performance for individual months of September, October, and November 2016 is shown. Total number of samples (Npts) is also indicated

rain rate thresholds, 0.5 and 3.0 mm h^{-1}. For both operational and experimental rain rates, categorical scores generally show best performance in September, when higher rain rates associated with warm season convection are better detected and estimated. For both rain rate thresholds, categorical scores for experimental (test) rain rates are better than the operational rain rates. Larger improvements in POD and HSS are seen for a threshold of 0.5 mm h^{-1}, consistent with the fact that most of the improvement in the experimental retrievals is for very light – probably stratiform – rainfall. Further testing has shown this improvement is also seen in other seasons, and consequently this enhancement was included in version v11.4 of MiRS.

9.8 Conclusions and Future Work

MiRS is a robust, flexible satellite retrieval system designed for rapid, physically-based atmospheric and surface property retrievals from passive microwave measurements. The MiRS algorithm has been running operationally at NOAA since 2007 and routinely distributing satellite derived products through the NOAA Office of Satellite and Product Operations (OSPO). Assessment and validation of the hydrometeor products, and in particular the precipitation rate, are done routinely via comparison with ground-based as well as other satellite-based references. One of the strengths of the MiRS system is the capability to retrieve simultaneously not just precipitation rates, but associated atmospheric profiles of temperature, water vapor, as well as liquid and frozen hydrometeors in a manner consistent with satellite measurements, a physically-based radiative transfer model (i.e., CRTM), and assumed a priori constraints. This provides an opportunity for potential improvements. Several avenues are listed here: (1) evaluating the impact of assumed radiometric uncertainty (instrument plus forward model) in each channel, (2) assessing the influence of assumed a priori hydrometeor background constraints, (3) possible implementation of an a priori temperature and water vapor error covariance matrix specific to rainy conditions, (4) exploring methods to distinguish convective and stratiform (or mixed) precipitation types using, when available, signal differences between measurements in vertical and horizontal polarization, (5) direct or indirect incorporation of assumed effective hydrometeor particle size in the retrieval state vector, (6) evaluating the impact of updated scattering tables (to be

available in upcoming versions of CRTM) that account for the effects of non-spherical particles, and (7) extension to use of infrared sensor measurements which, when combined with microwave measurements, should provide a more complete view of cloud structures and precipitating weather systems. Finally, one of the important features of MiRS is that, when run in operations, it does not use any real-time ancillary data. External data for the surface (especially emissivity) from a time-varying climatology or for the atmosphere (water vapor, temperature) from numerical weather prediction systems is anticipated to be beneficial to the retrieval products, but needs to be quantified and balanced against the needs of some users for satellite products that are independent of the numerical models.

References

Aires, F., Prigent, C., Rossow, W. B., & Rothstein, M. (2001). A new neural network approach including first guess for retrieval of atmospheric water vapor, cloud liquid water path, surface temperature, and emissivities over land from satellite microwave observations. *Journal of Geophysical Research, 106*, 14887–14907. https://doi.org/10.1029/2001JD900085.

Baldwin M. E., & Mitchell, K. E. (1998). *Progress on the NCEP hourly multisensory U.S. precipitation analysis for operations and GCIP research*. Preprints 2nd symposium on integrated observing systems (pp. 10–11), Phoenix, AZ, American Meteorological Society.

Boukabara, S. A., Garrett, K., & Grassotti, C. (2018). Dynamic inversion of global surface microwave emissivity using a 1DVAR approach. *Remote Sensing, 10*, 679–696. https://doi.org/10.3390/rs10050679.

Boukabara, S. A., Garrett, K., Chen, W., Iturbide-Sanchez, F., Grassotti, C., Kongoli, C., Chen, R., Liu, Q., Yan, B., Weng, F., Ferraro, R., Kleespies, T. J., & Meng, H. (2011). MiRS: An all-weather 1DVAR satellite data assimilation and retrieval system. *IEEE Transactions on Geoscience and Remote Sensing, 49*, 3249–3272. https://doi.org/10.1109/TGRS.2011.2158438.

Boukabara, S.-A., Garrett, K., Grassotti, C., Iturbide-Sanchez, F., Chen, W., Jiang, Z., Clough, S. A., Zhan, X., Liang, P., Liu, Q., Islam, T., Zubko, V., & Mims, A. (2013). A physical approach for a simultaneous retrieval of sounding, surface, hydrometer, and cryospheric parameters from SNPP/ATMS. *Journal of Geophysical Research, 118*, 12,600–12,619. https://doi.org/10.1002/2013JD020448.

Chen, Y., Weng, F., Han, Y., & Liu, Q. (2008). Validation of the community radiative transfer model (CRTM) by using CloudSat data. *Journal of Geophysical Research, 113*, 2156–2202. https://doi.org/10.1029/2007JD009561.

Chirokova, G., DeMaria, M., DeMaria, R., Dostalek, J., & Beven, J. (2015). *Use of JPSS ATMS-MiRS retrievals to improve tropical cyclone intensity forecasting*. 20th conference on satellite meteorology and oceanography, Phoenix, AZ, American Meteorological Society, P157. Available at https://ams.confex.com/ams/95Annual/webprogram/Paper263652.html, last accessed 7 Nov 2018.

Ding, S., Yang, P., Weng, F., Liu, Q., Han, Y., Delst, P. V., Li, J., & Baum, B. (2011). Validation of the community radiative transfer model. *Journal of Quantitative Spectroscopy & Radiative Transfer, 112*, 1050–1064. https://doi.org/10.1016/j.jqsrt.2010.11.009.

Doswell, C. A., III, Davies-Jones, R., & Keller, D. L. (1990). On summary measures of skill in rare event forecasting based on contingency tables. *Weather and Forecasting, 5*, 576–585. https://doi.org/10.1175/1520-0434(1990)005<0576:OSMOSI>2.0.CO;2.

Forsythe, J. M., Kidder, S. Q., Fuell, K. K., LeRoy, A., Jedlovec, G. J., & Jones, A. S. (2015). A multisensor, blended, layered water vapor product for weather analysis and forecasting. *Journal of Operational Meteorology, 3*, 41–58. https://doi.org/10.15191/nwajom.2015.0305.

Guardian. (2015). *Typhoon Soudelor: Death toll rises as storm crosses Taiwan*. Available at https:// www.theguardian.com/world/2015/aug/08/taiwan-hit-by-typhoon-soudelor, last accessed 7 Nov 2018.

Han, Y., Van Delst, P., Liu, Q., Weng, F., Yan, B., Treadon, R., & Derber, J. (2006). *Community Radiative Transfer Model (CRTM) – Version 1* (NOAA technical report 122). 33 pp. Available at https://repository.library.noaa.gov/view/noaa/1157, last accessed 7 Nov 2018.

Iturbide-Sanchez, F., Boukabara, S.-A., Chen, R., Garrett, K., Grassotti, C., Chen, W., & Weng, F. (2011). Assessment of a variational inversion system for rainfall rate over land and water surfaces. *IEEE Transactions on Geoscience and Remote Sensing, 49*, 3311–3333. https://doi.org/10.1109/TGRS.2011.2119375.

Jones, A. S., & Vonder Haar, T. H. (1990). Passive microwave remote sensing of cloud liquid water over land regions. *Journal of Geophysical Research, 95*, 16673–16683. https://doi.org/10.1029/JD095iD10p16673.

Joyce, R. J., & Xie, P. (2011). Kalman filter based CMORPH. *Journal of Hydrometeorology, 12*, 1547–1563. https://doi.org/10.1175/JHM-D-11-022.1.

Joyce, R. J., Janowiak, J. E., Arkin, P. A., & Xie, P. (2004). CMORPH: A method that produces global precipitation estimates from passive microwave and infrared data at high spatial and temporal resolution. *Journal of Hydrometeorology, 5*, 487–503. https://doi.org/10.1175/1525-7541(2004)005<0487:CAMTPG>2.0.CO;2.

Lin, Y., & Mitchell, K. E. (2005). *The NCEP Stage II/IV hourly precipitation analyses: Development and applications*. 19th conference on hydrology, San Diego, CA, American Meteorological Society, 1.2. Available at https://ams.confex.com/ams/pdfpapers/83847.pdf, last accessed 7 Nov 2018.

Liu, Q., & Lu, S. (2016). Community radiative transfer model for air quality studies (chapter 2). In *Light scattering reviews* (Vol. 11, pp. 67–115). Berlin/Heidelberg: Springer Praxis Books/Springer.

Liu, Q., & Weng, F. (2005). One-dimensional retrieval algorithm of temperature, water vapor, and cloud water profiles from advanced microwave sounding unit (AMSU). *IEEE Transactions on Geoscience and Remote Sensing, 43*, 1087–1095. https://doi.org/10.1109/TGRS.2004.843211.

Liu, S., Grassotti, C., Chen, J., & Liu, Q. (2017). GPM products from the microwave-integrated retrieval system. *IEEE Journal of Selected Topics in Applied Earth Observations and Remote Sensing, 10*, 2565–2574. https://doi.org/10.1109/JSTARS.2017.2716356.

NOAA. (2015). JPSS NESDIS ESPC requirements document volume 2: Science Requirements Document (JERD), JPSS-REQ1004, 49 pp. Available at https://www.star.nesdis.noaa.gov/jpss/documents/Requirements/JERDV2_JPSS-REQ-1004_Version2.0.pdf, last accessed 7 Nov 2018.

Rodgers, C. D. (2000). *Inverse methods for atmospheric sounding: Theory and practice*. Singapore, 238 pp: World Scientific. https://doi.org/10.1142/3171.

Weng, F., Han, Y., Van Delst, P., Liu, Q, Kleespies, T., Yan, B., & LeMarshall, J. (2005). *JCSDA Community Radiative Transfer Model (CRTM)*. In Procedings of 14th TOVS conference (pp. 217–222), Beijing.

Chapter 10
Introduction to Radar Rain Retrieval Methods

Toshio Iguchi and Ziad S. Haddad

Abstract This chapter describes basic principles of precipitation measurement with radar and algorithms to retrieve precipitation rate from the data obtained. The emphasis is on the space-borne radar measurement of precipitation. It concerns peculiar characteristics of spaceborne precipitation radar and algorithms that retrieve precipitation parameters such as rainfall rate. A formulation of radar equation is made in a general form in which the effect of inhomogeneous distribution of rain within a scattering volume can be traced. A coupled equation that can retrieve two drop size distribution parameters from dual-frequency measurement is given. Major error sources in precipitation retrieval with space-borne radar are described.

Keywords Precipitation · Rainfall · Satellite · Radar · Reflectivity · Range · Drop size distribution · GPM · DPR · Backscattering · Refractive index · Hitschfeld-Bordan solution · Surface reference technique · Attenuation · Path integrated attenuation · Non-uniform beam filling · Uncertainty estimation

10.1 Introduction

Radar is an acronym for RAdio Detection And Ranging. A radar is an active sensor that transmits radio signals, and receives and processes the backscattered radiation to detect the targets that produced it and to quantify the parameters of these backscattered signals. From the backscattered signals for the known transmitted signal, some properties of the targets can be estimated together with their locations. In the case of weather radar, the targets are precipitation particles that form rain, snow, graupel and hail. Wind profilers and other kind of weather radars are excluded

T. Iguchi (✉)

National Institute of Information and Communications Technology (NICT), Koganei, Japan
e-mail: tiguchi@umd.edu

Z. S. Haddad

Jet Propulsion Laboratory, California Institute of Technology, Pasadena, CA, USA

in this article. Recent radars are often equipped with capability of measuring not only the amplitude of received echo power but also other electromagnetic properties such as the phase relative to the transmitted signal, Doppler shift and polarization. However, since no spaceborne weather radar equipped with Doppler or polarimetric capabilities has been realized yet, this article does not concern itself with such functions.

The wavelength of radar is chosen according to the purpose of measurement. In the case of ground-based radar for rain measurement, microwaves in the range from 3 GHz (S band) to 10 GHz (X band) are generally used. In the case of space-borne radar, however, much higher frequencies are used because of the peculiarities of observation geometry and the constraints on the dimensions of the system. For example, the Dual-frequency Precipitation Radar (DPR) onboard the Global Precipitation Measurement (GPM's) core observatory uses Ku band (13.6 GHz) and Ka band (35.5 GHz) to realize the required footprint diameter of about 5 km at nadir from the nominal altitude of 407 km with the antenna aperture dimensions of 2.1 m × 2.1 m and 0.81 m × 0.81 m, respectively.

There are a few issues in the retrieval of rainfall rate from precipitation echo data obtained with a space-borne radar. The first is the difficulty of converting the measured radar reflectivity factors into rainfall rates, which is a common issue with ground-based weather radars. As described in detail below, the precipitation echo power is not a simple function of the rainfall rate, but varies substantially for a given rainfall rate if the size distribution of precipitating particles changes.

The second issue is the attenuation correction. High frequency microwaves used in space-borne radar suffer from attenuation when they propagate through rain. The magnitude of attenuation depends on the intensity of rain and the radio frequency used. The higher the frequency, the larger the attenuation. As a result, attenuation correction is imperative to estimate the reflectivity of rain. In fact, the attenuation correction is the most important part of the rain retrieval algorithm for space-borne weather radar.

The third issue is the inhomogeneity of rain distribution within a scattering volume of radar. Non-uniformity of rain distribution within a footprint of radar complicates the attenuation correction and the conversion of radar reflectivity into rainfall rate when rain is heavy (Nakamura 1991).

There are, of course, several other minor issues. In this article, however, rain retrieval algorithms are described with these three issues emphasized. We first formulate the radar equation with the non-uniform distribution of scatterers in mind, and show how the non-uniformity of rain will modify the apparent relationships among the radar reflectivity factor, rainfall rate, specific attenuation and other quantities averaged in the scattering volume or the footprint dimensions.

10.2   Formulation of Radar Measurement of Rain

In a single-frequency non-Doppler radar measurement of rain, the measurable quantity is the received echo power P_r of the electromagnetic waves scattered by rain drops as a function of time t. If we assume that the propagation of electromagnetic waves follows ray optics and that the multiple scattering effect can be ignored, the expected value of the received power $E(P_r)$ is given by

$$
E(P_r(t)) = \int_V \frac{P_t(t - 2r/c)G_t(\theta,\phi)G_r(\theta,\phi)\lambda^2\eta(r,\theta,\phi)}{(4\pi)^3 r^4} \\
\exp\left(-2q\int_0^r k(s,\theta,\phi)ds\right)dV,
\tag{10.1}
$$

where the position relative to the radar is expressed in a standard polar coordinate system (r,θ,ϕ) with the radar at the origin, c is the speed of light, $P_t(t)$ is the transmitting power at time t, $G_t(\theta,\phi)$ and $G_r(\theta,\phi)$ are respectively the transmitting and receiving antenna gains in the direction specified by angles θ and ϕ, λ is the wavelength, η is the radar reflectivity or volume scattering cross section per unit volume, k is the specific attenuation expressed in dB per unit length, V is the volume over which the integral is calculated, and $q = 0.1 \ln 10$ (Meneghini and Kozu 1990). dV can be written as $r \sin(\theta)\, dr\, d\theta\, d\phi$. The actual received power fluctuates around this expected value because of Rayleigh fading.

When the scatterers are rain drops, the radar reflectivity η consists of the radar backscattering cross sections of all particles ($\sigma_j, j = 1,\ldots,n$) in a unit volume dV around the position $r = (r,\theta,\phi)$:

$$
\eta(\tau,\theta,\phi) = \frac{1}{dV}\sum_{j=1}^n \sigma_j\delta(\mathbf{r} - \mathbf{r}_j).
\tag{10.2}
$$

Here, $\delta(\mathbf{r})$ is the three-dimensional delta function, and $\mathbf{r}_j$ ($j = 1,\ldots,n$) is the position of the j-th particle. We assume that the unit volume is much smaller than the dimensions that correspond to the radar resolution, but sufficiently large so that η can be treated as a continuous function of position. With this approximation, η can be expressed in terms of the effective radar reflectivity factor Z_e:

$$
\eta(r,\theta,\phi) = \frac{\pi^5|K_w|^2}{\lambda^4}Z_e(r,\theta,\phi),
\tag{10.3}
$$

where

$$Z_e(r, \theta, \phi) = \frac{\lambda^4}{\pi^5 |K_w|^2} \int_D \sigma_b(D; T(r, \theta, \phi), p_s) N(D; r, \theta, \phi) dD, \qquad (10.4)$$

and K_w is the dielectric factor defined by

$$K_w = \frac{m^2 - 1}{m_i^2 + 2}. \qquad (10.5)$$

Here, $\sigma_b(D; T, p_s)$ is the backscattering cross section of a precipitating particle with diameter D and temperature T, m is the complex refractive index of water, and $N(D; r, \theta, \phi)$ is the raindrop size distribution function and $N(D)\Delta D$ expresses the number concentration of rain drops with diameter between D and $D + \Delta D$ in the unit volume at (r, θ, ϕ). p_s is a parameter that specifies the kind and state of precipitation particles.

Rainfall rate R can be expressed by using $N(D)$ and the terminal velocity $v(D)$ of a rain drop with diameter D.

$$R(r, \theta, \phi) = \frac{\pi}{6} \int_D v(D; r, \theta, \phi, p_s) D^3 N(D; r, \theta, \phi) dD. \qquad (10.6)$$

The specific attenuation k consists of attenuation by precipitation (k_p) and that by other media (k_o) such as cloud water droplets and water vapor. The effect of k_o can be ignored at the Ku band in most cases. k_p is expressed in terms of $N(D)$ and extinction cross section σ_e:

$$k_p(r, \theta, \phi) = \frac{1}{q} \int_D \sigma_e(D; T(r, \theta, \phi), p_s) N(D; r, \theta, \phi) dD. \qquad (10.7)$$

If the precipitation consists not only of rain but also of snow, graupel or other forms of water, the backscattering cross section σ_b and the extinction cross section σ_e also depends upon another parameter p_s that specifies the state of precipitating particles. The fall velocity $v(D)$ depends very much on p_s as well as the air density and vertical wind speed. If the particles are not melted water, we have to multiply (10.6) by the ratio of the effective density of the particles to the melted water density to calculate the equivalent rainfall rate. To simplify the equations, however, we will not express this dependence explicitly, but include it in p_s.

The fundamental question of radar meteorology is how to estimate $R(r, \theta, \phi)$ from $P_r(t)$. If we have a large number of independent samples of radar echo from the same scattering volume in a short time in which the distribution of rain drops is essentially the same, we can estimate the expectation $E(P_r(t))$ from the average of samples. In the case of GPM's DPR, about 100 samples are taken at each range bin and the magnitude of fluctuation due to Rayleigh fading after averaging the log-detected signal is approximately 0.56 dB. Since this fluctuation is relatively insignificant except when the echo power is close to the noise level, we do not concern ourselves with the difference between $E(P_r)$ and the sample average of P_r in the following.

Let us define the apparent radar reflectivity factor Z_m by

$$Z_m(r, \theta, \phi) = Z_e(r, \theta, \phi) \exp\left(-2q \int_0^r k(s, \theta, \phi) ds\right).$$ (10.8)

If the transmitting pulse has a short duration (τ) and peaks at $t = 0$, we generally regard $P_r(2r/c)$ as the echo power from range r. In fact, (10.1) can be rewritten as a convolution integral with respect to r of $P_t(2r/c)$ and $Z_m(r)/r^3$:

$$E(P_r(2r/c)) = \frac{\pi^2 |K_w|^2}{4^3 \lambda^2}$$
$$\int_V \frac{P_t(2(r - r')/c) G_t(\theta, \phi) G_r(\theta, \phi) Z_m(r', \theta, \phi)}{r'^4} r' \sin(\theta) dr' d\theta d\phi.$$ (10.9)

As long as the pulse width ($c\tau$) is much shorter than the range r, we can treat the denominator in the integrand constant over the range in which $P_t(2(r-r')/c)$ is non-zero, and take the range dependence of ($1/r'^4$) from inside the integral to the outside.

The antenna pattern is often expressed in terms of two orthogonal directions from the maximum direction of antenna gain instead of θ and ϕ. If we denote these two directions θ_1 and θ_2, and if both the transmitting and receiving antenna gains have a Gaussian shape, and if their beam widths are very small, we can express the antenna gain function, for example of the transmitting antenna gain, as

$$G_t(\theta_1, \theta_2) = G_{t0} \exp\left[-4 \ln(2)\left(\frac{(\theta_{t1} - \theta_{t10})^2}{\theta_{tw1}^2} + \frac{(\theta_{t2} - \theta_{t20})^2}{\theta_{tw2}^2}\right)\right]$$ (10.10)

where G_{t0} is the maximum gain and θ_{t10} and θ_{t20} are the maximum gain direction expressed in the (θ_{t1}, θ_{t2}) coordinates. θ_{tw1} and θ_{tw2} are the beam width (full width at half maximum) in the respective directions. The receiving antenna gain function is similarly expressed.

If $Z_m(r', \theta, \phi)$ does not depend on θ and ϕ where the antenna gain factor $G_t G_r$ is significant, which means if the rain distribution at a given range is uniform within the radar beam, assuming the transmitting and receiving antenna directions are the same ($\theta_{t10} = \theta_{r10}$ and $\theta_{t20} = \theta_{r20}$), we obtain the following equation after integration with respect to θ and ϕ.

$$E(P_r(2r/c)) = \frac{\pi^3 |K_w|^2}{\lambda^2 2^9 \ln 2} \frac{P_{t0} G_{t0} G_{r0} \sqrt{\theta_{tw1} \theta_{tw2} \theta_{rw1} \theta_{rw2}}}{r^2}$$
$$\int u_t(2(r - r')/c) Z_e(r') \exp\left(-q \int_0^{r'} k(s) ds\right) dr'.$$ (10.11)

where $u_t(2(r-r')/c)$ is the pulse shape of transmitted radio waves expressed as a function of r. If the attenuation term $\exp\left(-q\int_0^{r'} k(s)ds\right)$ does not change much over the distance corresponding to the pulse width, and if the pulse shape is rectangular with duration τ, (10.10) can be further simplified to

$$E(P_r(2r/c)) = \frac{\pi^3 |K_w|^2}{\lambda^2 2^{10} \ln 2} \frac{P_{t0} G_{t0} G_{r0} \sqrt{\theta_{tw1} \theta_{tw2} \theta_{rw1} \theta_{rw2}} c\tau}{r^2}$$
$$Z_e(r) \exp\left(-q\int_0^r k(s)\,ds\right). \tag{10.12}$$

In the case of the DPR, the transmitting and receiving antennas have the same gains and patterns. As a result, (10.11) becomes

$$E(P_r(2r/c)) = \frac{\pi^3 |K_w|^2}{\lambda^2 2^{10} \ln 2} \frac{P_{t0} G_0^2 \theta_{w1} \theta_{w2} c\tau}{r^2}$$
$$Z_e(r) \exp\left(-q\int_0^r k(s)ds\right). \tag{10.13}$$

This equation is the one often used in radar meteorology. The current DPR algorithm also uses this equation as the starting point.

A few assumptions are used to derive this equation. The homogeneity assumption is a serious assumption for space-borne radar because a relatively large footprint of a few km may invalidate it. Nevertheless, without knowing the actual fine-scale distribution of precipitation, it is impossible to retrieve $Z_e(r,\theta,\phi)$ or an average of it over the resolution volume without any bias.

Among the parameters in (10.13), P_{t0}, G_0, θ_{w1}, θ_{w2} and λ are determined by calibration of the instrument. r is determined by the sampling time. $|K_w|^2$ depends on the dielectric constant of scattering particles, and hence on the particles' temperature and the wavelength of radar to some extent. In practice, a fixed value of $|K_w|^2$ is used irrespective of the temperature of the particles for a given wavelength. In the DPR data processing, $|K_w|^2 = 0.9255$ is used for KuPR and $|K_w|^2 = 0.8989$ for KaPR. With these parameters defined, $Z_m(r)$ is calculated as

$$Z_m(r) = P_r(2r/c) \times \frac{r^2}{C_r} \tag{10.14}$$

where C_r is

$$C_r = \frac{\pi^3 |K_w|^2}{\lambda^2 2^{10} \ln 2} P_{t0} G_0^2 \theta_{w1} \theta_{w2} c\tau \tag{10.15}$$

10.3   Rain Retrieval Algorithm

The main purpose of rain retrieval algorithm is to estimate the rainfall rate or precipitation rate R from measured Z_m. This process can be divided into two parts; conversion from Z_m to attenuation corrected radar reflectivity factor Z_e, and conversion from Z_e to R. As shown in Eqs. (10.4), (10.6) and (10.7), all k_p, Z_e and R depend on the integral of the drop size distribution (DSD) function with different weighting functions $\sigma_e(D)$, $\sigma_b(D)$ and $v(D)D^3$, respectively. As long as precipitation is rain and not solid precipitation particles, these weighting functions are relatively well defined as functions of D.

Since raindrops tend to be oblate spheroids, with a symmetry axis near the vertical, $\sigma_e(D)$, $\sigma_b(D)$ depend on the polarization of the electromagnetic (EM) waves used. For most space-borne radars, however, that operate at near-nadir incidence, the polarization state of the EM field is not a critical factor. In the case of $v(D)$, the vertical wind speed must be taken into account if the true rainfall rate as a flux must be calculated. The DSD function $N(D)$ has an infinite number of degrees of freedom, but if the variation of $N(D)$ in nature can be expressed in terms of a small number of parameters, the variations of k_p, Z_e and R can also be expressed in terms of these parameters. In fact, $N(D)$ is often approximated by a model function with one, two or three parameters. For example, in the case of the TRMM/PR and GPM/DPR algorithms, a Gamma distribution model is adopted.

$$N(D) = N_0 D^\mu \exp\left(-\Lambda D\right) = N_0 D^\mu \exp\left(-(4+\mu)D/D_m\right) \qquad (10.16)$$

In this case, DSD is uniquely determined by three parameters (N_0, Λ, μ) or (N_0, D_{m}, μ). Here, D_{m} is the volume weighted diameter of DSD.

$$D_m = \frac{\int D^4 N(D)dD}{\int D^3 N(D)dD} = \frac{4+\mu}{\Lambda} \qquad (10.17)$$

If the Gamma distribution model represents the true DSD well, and if the natural variations of the DSD parameters follow a certain model and if their effects on k_p, Z_e and R can be represented by a single parameter $p_{\mathrm{dsd}}(N_0,D_{\mathrm{m}},\mu)$, then all $k_p(p_{\mathrm{dsd}})$, $Z_e(p_{\mathrm{dsd}})$ and $R(p_{\mathrm{dsd}})$ are related to each other without any uncertainty. In this case, if the effect of attenuation due to non-precipitation particles are already corrected, since both $Z_e(r)$ and $k_p(r)$ can be expressed in terms of $p_{\mathrm{dsd}}(r)$,

$$Z_m(r) = Z_e(r) \exp\left(-2q \int_0^r k_p(s)ds\right) \qquad (10.18)$$

becomes an integral equation of $p_{\mathrm{dsd}}(r)$ for given $Z_m(r)$ and its solution gives $Z_e(r)$ and $k_p(r)$.

In reality, however, the relations among k_p, Z_e and R cannot be expressed by a single parameter very well. It is empirically known that two independent DSD

parameters are necessary to express the variations of k_p, Z_e and R well. Nevertheless, in the case of retrieving R from data obtained with a single frequency radar, the use of a single DSD parameter model is unavoidable. For example, in the rain retrieval algorithm for TRMM/PR, a fixed value of $\mu = 3$ and a particular relation between N_0 and D_m are assumed for each type of storm so that the DSD change can be expressed in a single parameter effectively (Iguchi et al. 2009). In the case of the GPM/DPR algorithm, the same Gamma DSD model with $\mu = 3$ is adopted, but the R-D_m relation is used to define the N_0-D_m relation indirectly. The advantage of the use of the R-D_m relation is that both R and D_m can be measured directly by a disdrometer and enables the comparisons with other kinds of measurements easily.

Note that variables k_p, Z_e and R are dependent only on the local variables and parameters in the scattering volume, whereas Z_m depends on the variables in the volume that extends from the radar to the scattering volume because of the attenuation term in (10.8). In a single parameter DSD model, k_p becomes a function of Z_e. If this relation can be approximated by a power law,

$$k_p = \alpha Z_e^\beta \tag{10.19}$$

then Eq. (10.18) can be solved analitically.

$$Z_e(r) = \frac{Z_m(r)}{\left[C - 2q\beta \int_0^r \alpha(s) Z_m^\beta(s) ds\right]^{1/\beta}} \tag{10.20}$$

This solution is called the Hitschfeld-Bordan solution (Hitschfeld and Bordan 1954). Here, α can be a function of range r, but β must be a constant. The denominator of the right-hand side corresponds to the attenuation factor. C is an integral constant and can be determined by an initial condition. A natural choice of C is $C = 1$ because at $r = 0$ (or at the first range where echo is detected) there must be no attenuation and hence $Z_e = Z_m$ there if the radar is well calibrated. If the radar is not well calibrated and if Z_m includes some bias, C can be different from unity (Iguchi and Meneghini 1994).

The Hitschfeld-Bordan solution is known to give a reasonable correction if the attenuation is small, but when the attenuation is significant, its performance becomes very poor. The denominator often becomes an imaginary number. If the attenuation to a certain range is known, the denominator can be equated to the value corresponding to that attenuation. In this case, the attenuation correction up to this range is always stable.

In the TRMM/PR case, $C = 1$ is used, but α is adjusted by a factor ϵ over the entire path so that

$$-\frac{10}{\beta} \log_{10}\left(1 - 2q\beta \int_0^r \epsilon \alpha(s) Z_m^\beta(s) ds\right) \tag{10.21}$$

is equal to the given attenuation. The surface reference technique that will be explained below gives an estimate of the path-integrated attenuation to the surface. By using this estimate of attenuation at the farthest range of radar echo, ϵ can be determined and the solution becomes stable over the entire range of measurement.

Since Eq. (10.19) is derived from a single parameter DSD model, if α is modified by ϵ, the DSD parameter must be modified accordingly. When Z_e is converted into R, the Z_e-R relation defined by the modified DSD model must be used for consistency.

In the case of dual-frequency radar, Z_m can be obtained from the same scattering volume at two frequencies. If the propagation and scattering properties of radar waves for precipitation particles are different at two frequencies, Z_m at two frequencies give two pieces of information at each sampling volume. This fact implies that two independent DSD parameters can, in principle, be estimated from acquired data. In fact, it is possible to formulate the deterministic equations that must be satisfied by two DSD parameters for given Z_m at two frequencies (Iguchi 2005). For example, if the frequency dependent variables such as k_p, Z_e and Z_m at two frequencies are distinguished by subscript f ($f = 1, 2$), and if the DSD model function is parameterized by two parameters p_{dsd1} and p_{dsd2}, Eq. (10.18) becomes

$$Z_{mf}(r) = Z_{ef}(r) \exp\left(-2q \int_0^r k_{pf}(s)ds\right), \qquad (f = 1, 2) \qquad (10.22)$$

where Z_e and k_p can be expressed as functions of DSD parameters p_{dsd1} and p_{dsd2}.

$$Z_{ef}(p_{dsd1}, p_{dsd2}) = C_{Zf} \int \sigma_{bf}(D) N_{model}(D; p_{dsd1}, p_{dsd2}) dD \qquad (10.23)$$

and

$$k_{pf}(p_{dsd1}, p_{dsd2}) = \frac{1}{q} \int \sigma_{ef}(D) N_{model}(D; p_{dsd1}, p_{dsd2}) dD \qquad (10.24)$$

where $C_{Zf} = \lambda^4/(\pi^5|K_f|^2)$ with $K_f = \left(m_f^2 - 1\right)/\left(m_f^2 + 2\right)$. If we define $X_{mf} = 10\log_{10}(Z_{mf})$ and $X_{ef} = 10\log_{10}(Z_{ef})$ for brevity, and express Z_{ef} and k_{pf} in terms of the DSD parameters, (10.22) becomes a pair of integral equations for these DSD parameters which are equivalent to a set of the following differential equations.

$$\begin{pmatrix} \dfrac{dp_{dsd1}(r)}{dr} \\ \dfrac{dp_{dsd2}(r)}{dr} \end{pmatrix} = \mathcal{A}^{-1} \begin{pmatrix} \dfrac{dX_{m1}(r)}{dr} + 2k_1(p_{dsd1}(r), p_{dsd2}(r)) \\ \dfrac{dX_{m2}(r)}{dr} + 2k_2(p_{dsd1}(r), p_{dsd2}(r)) \end{pmatrix} \qquad (10.25)$$

where

$$\mathcal{A} = \begin{pmatrix} \dfrac{\partial X_{e1}}{\partial p_{dsd1}} & \dfrac{\partial X_{e1}}{\partial p_{dsd2}} \\ \dfrac{\partial X_{e2}}{\partial p_{dsd1}} & \dfrac{\partial X_{e2}}{\partial p_{dsd2}} \end{pmatrix}. \tag{10.26}$$

For given $Z_{mf}(r)$ ($f = 1,2$), it is theoretically possible to solve a set of Eq. (10.25) numerically. Once $p_{dsd1}(r)$ and $p_{dsd2}(r)$ are obtained, $R(r)$ can be calculated easily. Essentially the same, but seemingly different formulation can be found in Meneghini et al. (1992).

In practice, however, it turns out that the solutions become rather unstable even if the total path-integrated attenuations at two frequencies are given as constraints when the method is applied to real GPM/DPR data. In the case of DPR, $f = 1$ corresponds to the Ku band, and $f = 2$ to the Ka band. Possible error sources may be fluctuation of data, deviation of the actual DSD from the model function, errors associated with discretization of continuous data in range and non-uniform beam filling effect. Another source of error comes from the fact that the DFR-D_m (DFR, Dual-Frequency Ratio) relationship is not single-valued when DFR < 0 where DFR is defined as DFR=$10\log_{10}(Z_{e1}) - 10\log_{10}(Z_{e2})$. The theoretical relationship between D_m and DFR takes a minimum value at a certain D_m at which $\frac{dDFR}{dD_m} = 0$ and $\mathcal{A}$ becomes singular there. At this point, the inverse $\mathcal{A}^{-1}$ does not exist and a numerical solution of the discretized equation becomes unstable in the vicinity of this point. This fact can be checked by taking $p_{dsd1} = N_0$ and $p_{dsd2} = D_m$. A different selection of the DSD parameters does not remove the singularity of $\mathcal{A}$.

10.4   Surface Reference Technique (SRT)

As explained in the previous section, attenuation correction is essential in the rain retrieval algorithm for space-borne radar data. When the Z_e profile is estimated from the measured Z_m profile, it is necessary to relate k_p with Z_e regardless of the correction method employed. In any case, the error in attenuation estimate increases with range simply because the error in Z_m is amplified by the factor of attenuation correction and the errors at different ranges are accumulated recursively as the range increases (Hitschfeld and Bordan 1954).

If the total attenuation to the farthest range of measurement is known, however, it is possible to use it as a constraint not only to avoid the explosion of error but also to stabilize the solution over the entire range.

In the case of space-born radar, surface echoes can be measured in addition to echoes from precipitation. In fact, surface echoes are much stronger than precipitation echoes except when the attenuation due to heavy rain decreases the surface echo substantially. The strength of surface echo is a function of the surface radar cross section and the attenuation of radar signal through precipitation. Therefore, if we know the surface radar cross section behind the precipitation echo, the difference

between the true and apparent measured cross sections corresponds to the path-integrated attenuation to surface. A technique that uses this attenuation estimate to correct for the attenuation in Z_m is called the Surface Reference Technique (SRT) (Meneghini et al. 1983, 2000, 2004).

Since the true radar cross section of the surface behind rain is not known exactly, it is estimated from its statistics of nearby surrounding area without precipitation, or the cross-section data at the same area measured and accumulated under the no precipitation condition previously. These two kinds of reference data are called spatial reference and temporal reference, respectively. In the actual algorithm, a combination of these two types of reference is used.

10.5   Errors in Retrievals

There are several error sources in the retrieval of precipitation. Calibration error affects almost all estimates in the retrieval. One exception may be the attenuation estimate obtained by the SRT because taking the difference between the surface cross sections measured under rain and without rain cancels the bias in measurements.

The difference between the actual DSD and the DSD model creates the errors in the relations among k_p, Z_e and R. It is known that a single parameter DSD model, which is equivalent to the use of fixed $Z_e - R$ and $k_p - Z_e$ relations, gives only mediocre performance. As mentioned above, a fixed $k_p - Z_e$ relation often gives unreliable estimates when it is used in the Hitschfeld-Bordan method for attenuation correction if the attenuation is large.

A DSD model with two adjustable parameters may improve the situation. Nevertheless, it may still not be good enough for accurate rain retrieval. For example, in a dual-frequency retrieval, if the DSD is modeled by a function (10.16) with two adjustable parameters N_0 and D_m and a fixed μ, since both Z_{e1} and Z_{e2} are proportional to N_0, the ratio Z_{e1}/Z_{e2} becomes a function of only D_m. Therefore, once attenuation correction is reliably carried out and Z_{e1}/Z_{e2} is given, then D_m should be able to be estimated. When actual data of Z_{e1}/Z_{e2} is plotted against D_m, however, data points spread around the theoretical curve so that it is obvious that D_m cannot be determined accurately by using the model relation. Another important problem is that the theoretical relationship between D_m and Z_{e1}/Z_{e2} becomes a double-value function if D_m is treated as a function of Z_{e1}/Z_{e2}.

Up to this point, precipitation particles are assumed to be liquid water or rain. If they are solid particles such as snow, graupel and hail, cross sections σ_b in (10.4), σ_e in (10.7) and fall speed v in (10.6) depend not only on the particle size D but also on their melting fraction and shape. All such dependence is included in multi-dimensional parameter p_s in (10.4), (10.6) and (10.7). If the phase state and kind of particles are known, the same retrieval algorithm for rain can be used with modification of some constants and parameters to estimate the precipitation rate. In practice, however, the state of precipitation particles is not known. In a stratiform

rain system, a bright band is often observed in radar echo and it is possible to define the height at which ice particles melt into liquid particles. In a convective system, however, it is known that supercooled liquid particles often exist above the 0 °C height lifted by a strong updraft. Even with dual-frequency measurement, identifying the phase transition height is impossible in most convective cases. We need to rely on some empirical fact to choose the transition height and retrieve the precipitation rate. Errors in the identification of the transition height results in the error in the attenuation correction because the extinction cross section σ_e for ice differs significantly from that for water for the same dimension. Consequently, the error will propagate into all kinds of estimates.

The error in SRT will affect the attenuation estimate. There are a few possible error sources in SRT. Non-uniformity of rain is the most serious error source when the attenuation is large. For example, if a fraction f of the whole footprint is clear of rain, no matter how heavy the rain is in the remaining part of the footprint and no matter how significantly the echo from the surface is attenuated, the surface echo does not decrease to a value less than the fraction f.

The second source of error in SRT is the change of the surface condition. For example, surface canopy or vegetation changes with season and snow accumulation alters the cross section substantially. Winds over sea surface affect the wave conditions and hence the surface cross section. Since the winds within a storm may differ substantially from those outside the storm, the reference data taken outside the storm or taken at different time may not give the correct attenuation estimates. Rain itself may change the surface conditions (Seto and Iguchi 2007). In fact, it is known that the same land surface has generally larger radar cross section when it is wet than when it is dry. Over ocean, small ripples are created by rain drops hitting the surface. These ripples modify the backscattering cross section slightly. They decrease the cross section near nadir but increase it at incidence angles larger than a few degrees.

In the case of the dual-frequency radar, surface echoes are obtained at two frequencies. Since the variation of the surface cross section affects the scattering cross sections at two frequencies in the same way, if we take the difference of the two attenuation estimates at these frequencies, common errors caused by the variation of surface conditions are cancelled out substantially (Meneghini et al. 2012). This PIA difference between two frequencies can be used as a reliable constraint in the DPR retrieval algorithm.

The retrieval algorithm described above ignores the effect of attenuation caused by non-precipitation particles. They include cloud liquid water, water vapor and atmospheric oxygen molecules. The distribution of oxygen molecules is well known and very stable so that the correction for them is not an issue. The total attenuation to the surface is about 0.4 dB at the Ka band and is less than 0.1 dB at the Ku band. Attenuation due to cloud liquid water and water vapor cannot be ignored for radar that uses high-frequency microwaves, in particular, the Ka band and above. Since the scale height of water vapor is rather small and of the order of 2 km, and its concentration can be assumed to be nearly 100% in rain, as long as the temperature profile is well known, the attenuation due to water vapor can be estimated pretty

well. The attenuation to the surface is about 1.5 dB at the Ka band at most. The most difficult component for attenuation correction is cloud liquid water. Its distribution may extend to near the top of troposphere with a concentration that varies significantly in space and time. The absolute value of attenuation by cloud liquid water in an intense convective storm may exceeds a few dB at the Ka band. Note that the attenuation estimates given by the SRT includes the excess attenuation caused by those non-precipitation components.

The assumption of homogeneous distribution of precipitation particle within each scattering volume is critical. Without it, Eq. (10.9) could not be simplified to Eq. (10.13), which depends only on the variations in Z_e and k with range r. If we denote the average quantity of a variable x over the scattering volume by an overbar as $\overline{x}$, the relation between $\overline{Z}_e$ and $\overline{R}$ does not change significantly even if the precipitation is spatially non-uniform. In fact, for example, if the DSD is represented by the Gamma model (10.16), and if the non-uniformity is caused by only the change in N_0, then since both $\overline{Z}_e$ and $\overline{R}$ are linearly proportional to N_0, the $\overline{Z}_e - \overline{R}$ relation remains the same. The effect of non-uniform beam filling (NUBF) on the attenuation is very serious. As can be expected from (10.8), the dependence of k_p on the location within the beam affects the distribution of Z_m in a complicated way. Its magnitude depends exponentially on the distribution of k_p over the entire volume within the beam up to the range in question. As a result, the correction for the NUBF effects remains a difficult issue. Some attempts to account for it can be found in Iguchi et al. (2009).

The formulation in this article assumes that the effect of multiple scattering can be totally ignored. This assumption is valid in the Ku-band radar except for very intense storms that are associated with graupel or hail. In the Ka band or a higher frequency band, however, multiply-scattered echoes are not necessarily insignificant in intense storms with graupel or hail. Ignoring the multiple scattering effect creates some errors in rain retrievals.

The formulation also assumes that received signal is available at continuous range of r. In an actual system, the received signal is sampled at discrete ranges. Integrals used in equations for retrieval may be approximated by summations. An echo signal sampled at range r is assumed to represent the average of Z_m not only in the lateral directions of the radar beam, but also along the range direction within the pulse length. The effect of attenuation within the range resolution must be taken into account in intense rain when it is significant. Such is often the case in the Ka band.

10.6   Summary

Rain retrieval algorithms have been described in general terms with special attention to applications to spaceborne radar data. The measurement equation is formulated in a way to facilitate an understanding of the NUBF effect. The various forms of the meteorological radar equation show the relationship between the measured signal and the characteristics of the rain, including the drop size distribution (DSD). The

parameters to specify the DSD are treated in a general way so that the discussion can be applicable to different models of DSD. Several possible error sources in the current algorithms are described. A more specific algorithm used in the precipitation retrieval algorithm for the GPM/DPR is described in Chap. 11.

References

Hitschfeld, W., & Bordan, J. (1954). Errors inherent in the radar measurement of rainfall at attenuating wavelengths. *Journal of Meteorology, 11*, 58–67. https://doi.org/10.1175/1520-0469(1954)011<0058:EIITRM>2.0.CO;2.

Iguchi, T. (2005). *Possible algorithms for the Dual-Frequency Precipitation Radar (DPR) on the GPM core satellite*. Preprints 32nd conference on radar meteorology, Albuquerque, NM, American Meteor Society, 5R.4.

Iguchi, T., & Meneghini, R. (1994). Intercomparison of single-frequency methods for retrieving a vertical rain profile from airborne radar data. *Journal of Atmospheric and Oceanic Technology, 11*, 1507–1516. https://doi.org/10.1175/1520-0426(1994)011<1507:IOSFMF>2.0.CO;2.

Iguchi, T., Kozu, T., Kwiatkowski, J., Meneghini, R., Awaka, J., & Okamoto, K. (2009). Uncertainties in the rain profiling algorithm for the TRMM Precipitation Radar. *Journal of the Meteorological Society of Japan, 87A*, 1–30. https://doi.org/10.2151/jmsj.87A.1.

Meneghini, R., & Kozu, T. (1990). *Spaceborne weather radar*. Boston: Artech House, 199 pp, ISBN:0890063826.

Meneghini, R., Eckerman, J., & Atlas, D. (1983). Determination of rain rate from a spaceborne radar using measurements of total attenuation. *IEEE Transactions on Geoscience and Remote Sensing, 21*, 34–43. https://doi.org/10.1109/TGRS.1983.350528.

Meneghini, R., Kozu, T., Kumagai, H., & Boncyk, W. C. (1992). A study of rain estimation methods from space using dual-wavelength radar measurements at near-nadir incidence over ocean. *Journal of Atmospheric and Oceanic Technology, 9*, 364–382. https://doi.org/10.1175/1520-0426(1992)009<0364:ASOREM>2.0.CO;2.

Meneghini, R., Iguchi, T., Kozu, T., Liao, L., Okamoto, K., Jones, J. A., & Kwiatkowski, J. (2000). Use of the surface reference technique for path attenuation estimates from the TRMM Precipitation Radar. *Journal of Applied Meteorology, 39*, 2053–2070. https://doi.org/10.1175/1520-0450(2001)040<2053:UOTSRT>2.0.CO;2.

Meneghini, R., Jones, J. A., Iguchi, T., Okamoto, K., & Kwiatkowski, J. (2004). A hybrid surface reference technique and its application to the TRMM Precipitation Radar. *Journal of Atmospheric and Oceanic Technology, 21*, 1645–1658. https://doi.org/10.1175/JTECH1664.1.

Meneghini, R., Liao, L., Tanelli, S., & Durden, S. L. (2012). Assessment of the performance of a dual- frequency surface reference technique over ocean. *IEEE Transactions on Geoscience and Remote Sensing, 50*, 2968–2977. https://doi.org/10.1109/TGRS.2011.2180727.

Nakamura, K. (1991). Biases of rain retrieval algorithms for spaceborne radar caused by nonuniformity of rain. *Journal of Atmospheric and Oceanic Technology, 8*, 363–373. https://doi.org/10.1175/1520-0426(1991)008<0363:BORRAF>2.0.CO;2.

Seto, S., & Iguchi, T. (2007). Rainfall-induced changes in actual surface backscattering cross sections and effects on rain-rate estimates by spaceborne precipitation radar. *Journal of Atmospheric and Oceanic Technology, 24*, 1693–1709. https://doi.org/10.1175/JTECH2088.1.

Chapter 11
Dual-Frequency Precipitation Radar (DPR) on the Global Precipitation Measurement (GPM) Mission's Core Observatory

Toshio Iguchi

Abstract This chapter describes major specification of the Dual-Frequency Precipitation Radar (DPR) onboard the Global Precipitation Measurement (GPM) Mission's core observatory, and the specific algorithm that is used to retrieve precipitation rate from its data. Emphasis is on the level 2 algorithm that retrieves instantaneous rainfall profiles. Major functions of the six modules that form the level 2 algorithm and special features in the dual-frequency algorithm are described.

Keywords Precipitation · Rainfall · Hydrometeors · Phase · Satellite · Radar · Reflectivity · Range · Bright band · Drop size distribution · GPM · TRMM · PR · DPR · Path integrated attenuation · Surface reference technique

11.1 Dual-Frequency Precipitation Radar

The Dual-Frequency Precipitation Radar (DPR) on the Global Precipitation Measurement (GPM) mission's core satellite is the second space-borne precipitation radar, following the first such radar, the Precipitation Radar (PR), launched on the Tropical Rainfall Measuring Mission (TRMM) satellite in November, 1997. The PR was a single frequency radar that operated at Ku-band (13.8 GHz), whereas the DPR consists of Ku-band (13.6 GHz) and Ka-band (35.5 GHz) channels. They are abbreviated as KuPR and KaPR, respectively, in this chapter. The addition of the Ka-band radar to the Ku-band radar enables the use of dual-frequency algorithms that improve the estimates of rainfall rates and other quantities. Since radar is an active sensor, these Earth-pointing KuPR and KaPR instruments provide precipitation echoes over land and ocean, and day and night with essentially the same quality.

The GPM's core satellite was launched on 28 February 2014 and has been flying at a nominal altitude of 407 km with the inclination angle of 65°. Both KuPR and

T. Iguchi (✉)
National Institute of Information and Communications Technology (NICT), Koganei, Japan

KaPR are designed to have the same beam widths so that they can measure the precipitation echoes from the same volume simultaneously. KuPR scans the full swath of 250 km with 49 beams. KaPR also has 49 beams in one scan, but 25 of them have the same range resolution, 250 m, as the KuPR, and their scattering volumes are adjusted to match the corresponding KuPR's scattering volumes at the central 25 beams of KuPR, which makes the inner swath of 125 km. The KaPR data acquired with these 25 beams are designated as KaMS, where MS denotes "Matched Scan". The remaining 24 beams of KaPR have a range resolution of 500 m. The KaPR data acquired with these 24 beams are designated as KaHS, where HS denotes "High Sensitivity", because the signal-to-noise ratio of KaHS is about 5.5 dB better than that of KaMS. From the launch of the satellite until May 21, 2018, the scan pattern of the KaHS channel was interleaved in the inner swath with that of the KaMS scan pattern to provide information on non-uniform beam filling (Fig. 11.1, left-hand side). Beginning on May 21, 2018 the KaHS beams were shifted to the outer swath to provide coincident Ku/Ka-band data over the full 245 km swath (Fig. 11.1, right-hand side).

The diameter of the footprint is about 5 km at nadir for both KuPR and KaPR when the satellite is at the nominal altitude of 407 km. Off-nadir, the footprint is an ellipse with an eccentricity that increases with incidence angle so that at the swath edge ($\pm18°$) the semi-major and semi-minor axes, in the cross-track and along-track directions, are about 5.9 and 5.2 km, respectively, Since the Earth is slightly oblate, the actual altitude of the satellite varies from the nominal altitude by about ±10 km or about $\pm2.5\%$. The footprint dimensions change accordingly.

The echo data are over-sampled at every 125 m for KuPR and KaMS and 250 m for KaHS. Sampled data from the DPR cover, at minimum, heights from 0 to 19 km above sea level. Received echo signals are log-detected and averaged. Data at each range bin is an average of about 100 independent samples. The exact number of samples depends on the scan angle and the satellite altitude because of the use of variable pulse repetition rate. The received signal fluctuates according to Rayleigh
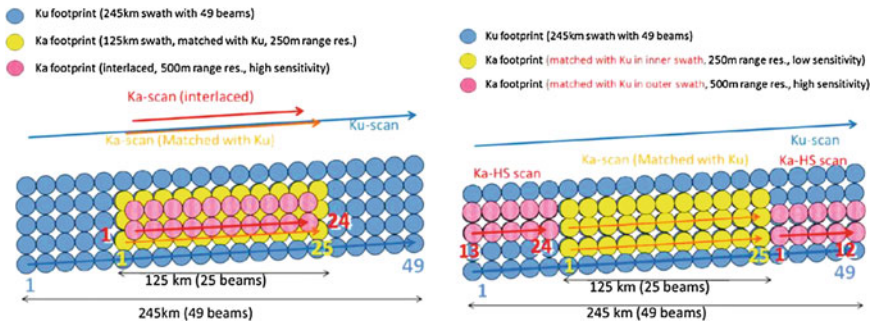
Fig. 11.1 DPR's scan pattern before May 21 2018 (left) and after May 21 2018 (right). KaHS beams scan in the inner swath before May 21 2018, but now they scan in the outer swath and match with KuPR's beams. Numbers in color indicate angle bin numbers for KuPR (blue), KaMS (yellow), and KaHS (red)

fading which follows an exponential power distribution with a standard deviation in the received power that is equal to the mean. Averaging N independent samples of the log-detected signal gives a standard deviation of $5.57/\sqrt{N} dB$. As a result, when the radar echo is much larger than the noise level, the error in the echo power, and hence in radar reflectivity measurement, is about 0.56 dB.

Note, however, that when the echo power is close to the noise level, the relative error after noise subtraction increases as the echo power decreases. As explained in Chap. 10, if the threshold for rain detection is set to 2.5 σ_{rm}, where σ_{rm} is the standard deviation of signal fluctuation, the error in estimated measured radar reflectivity factor Z_m becomes about ± 2 dB near the threshold. Details of other design specifications can be found in Kojima et al. (2012).

11.2 Outline of the DPR Data Processing Algorithm

The data processing algorithm for DPR consists of Level 1 (L1), Level 2 (L2) and Level 3 (L3) processing. The major role of L1 processing is to convert the received signals from KuPR and KaPR that are recorded in count values into the received power in engineering units by combining various radar parameters. Some of the parameter values and the overall conversion factors are determined according to the calibrations after launch.

The L2 algorithm consists of three sets of algorithms (Iguchi et al. 2017). They are the two single frequency algorithms for KuPR and KaPR, and the dual frequency algorithm. The flows of the three algorithms are basically the same, and their common framework is shown in Fig. 11.2. It consists of 7 modules: Main module, Preparation (PRE) module, Vertical (VER) module, Classification (CSF) module, Surface Reference Technique (SRT) module, Drop Size Distribution (DSD) module, and Solver (SLV) module. The main module controls the flow of the overall processing: it will open and close files, call other modules, and read/write all the input and output files and variables. The roles and functions of each module in the L2 algorithm are described in the next section.

The L3 algorithm collects various output variables of L2 products, and takes their monthly statistics at each grid box defined over the globe. There are two kinds of grid boxes: one is $5° \times 5°$ boxes and the other is $0.25° \times 0.25°$ boxes. Statistics of more than 30 variables are taken. For each variable, the number of measurement counts, the mean, and the standard deviation in the box are stored in the output. Histograms are also created for the coarse grid boxes of $5° \times 5°$. The statistics are taken separately for the algorithm used (Ku, KaMS and KaHS single frequency products and dual-frequency products), rain type (stratiform, convective, other), and surface type (ocean, land, all). Statistics of some variables are further categorized by height and angle bins when applicable.
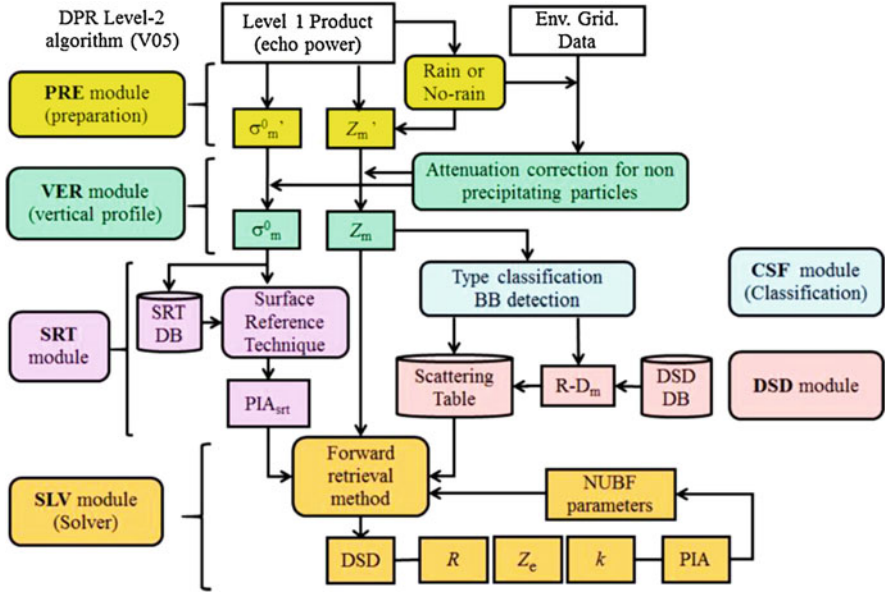
Fig. 11.2 DPR L2 algorithm flow

11.3 Outline of the DPR L2 Algorithm Modules

The preparation (PRE) module reads the received power data from L1 products, classifies each footprint into either rain or no-rain, and converts the received power P_r into measured reflectivity factor Z'_m at each range bin and into apparent normalized surface cross section $\sigma^{0\prime}_m$. When Z'_m and $\sigma^{0\prime}_m$ are calculated, the background noise P_n is subtracted in linear scale from the received power P_r. No attenuation corrections are applied at this stage. The rain/no-rain judgment is carried out at each angle bin by comparing P_r and P_n in logarithmic scale because these powers are log-detected and averaged. If $10\log_{10}(P_r) - 10\log_{10}(P_n)$ is larger than the predefined threshold $a \times \sigma_{rn}$ for m consecutive range bins, the beam in question is judged to contain precipitation echoes. Here a is a constant and $\sigma_{rn} = \sqrt{\sigma_r^2 + \sigma_n^2}$ where σ_r^2 and σ_n^2 are the variances of received signal and noise in dB, respectively. The actual values of σ_{rn} are 0.58, 0.57 and 0.60 dB for KuPR, KaMS and KaHS, respectively. Constants a and m are selected as small as possible to detect light rain but large enough to avoid misjudging a no-rain pixel as a rain pixel. In version 05 of the algorithm, a is set to 2.5 and m, which depends on the sample bin size, is set to a number that corresponds to 750 m. Since the magnitude of $10\log_{10}(P_n)$ over land corresponds to about 19.5, 23.3 and 17.6 dBZ for KuPR, KaMS and KaHS, the thresholds for rain detection are approximately 15, 19 and 14 dBZ, respectively. Note that the background noise changes depending on the surface type and the existence of rain itself to a small extent. Sidelobe clutter is removed in this module,

too (Kubota et al. 2016). This module also converts the satellite coordinates used in L1 data into the coordinates relative to the Earth's geoid surface that are used in L2 data, and defines several geometrical and geophysical parameters such as storm height, surface height, surface type and clutter-free bottom range bin.

The vertical (VER) module reads ancillary atmospheric profile data to calculate the temperature profile and the attenuation due to cloud and atmospheric gases. As described in the previous chapter, the specific attenuation k consists of the specific attenuation by precipitation k_p and that by cloud and atmospheric gases k_o, i.e., $k = k_p + k_o$. The VER module calculates the vertical profile of k_o by assuming model profiles of water vapor, molecular oxygen and cloud liquid water. It then gives measured reflectivity factor Z_m as a function of range r and the apparent normalized surface cross section σ_m^0, both corrected for the attenuation by cloud and atmospheric gases:

$$Z_m(r) = Z_m' \exp\left(2q \int_0^r k_o(s)ds\right) = Z_e \exp\left(-2q \int_0^r k_p(s)ds\right) \tag{11.1}$$

$$\sigma_m^0 = \sigma_m^{0\,'} \exp\left(2q \int_0^{r_s} k_o(s)ds\right) = \sigma^0 \exp\left(-2q \int_0^{r_s} k_p(s)ds\right) \tag{11.2}$$

where $q = 0.1 \ln(10)$, σ^0 is the true surface cross section, and r_s is the range to surface.

The classification (CSF) module classifies rain pixels into three major classes; stratiform, convective, or other. These classes are further divided into several sub-classes. Classification is carried out by two different methods; a vertical profiling method (V-method) and a horizontal pattern method (H-Method). The V-method classifies the rain as stratiform if it detects a bright-band in the profile. If it detects an intense echo that exceeds a certain threshold, the rain type is judged to be convective. The H-method looks at a horizontal pattern of radar reflectivity factor and classifies the rain types. These methods used in the DPR algorithm are basically the same as those used in the TRMM PR algorithm (Awaka et al. 2009). The results from these methods are merged to create unified output rain types. The classification module also outputs a few other parameters that include bright-band parameters and flags for anvil, shallow rain and intense ice precipitation.

The surface reference technique (SRT) module computes the path-integrated attenuation (PIA) from the change in the apparent surface cross section σ_m^0 in rain. The SRT rests on the assumption that the difference between the measured values of σ_m^0 in dB, within and outside rain provides an estimate of the PIA. The normalized radar cross section in no-rain condition is taken from areas in the vicinity of the raining area in question in the same orbit or from the same area with the same incidence angle in the same season of previous years under no-rain condition. The former reference is called the spatial reference and the latter the temporal reference. The spatial reference data are created by looking at σ_m^0 in no-rain either at the same

incidence angle along the track before the rain area (forward along-track) or after it (backward along-track), or estimating the true surface cross section σ_0 at the incidence angle in question by fitting a model curve to no-rain pixel data across the scan direction (cross-track direction) before the rain area or after it. Variances of all these reference data are compared and a weighted average is used to give the best estimate of PIA (Meneghini et al. 2004, 2012, 2015).

The DSD module defines the phase state as a function of range and provides at each range bin various variables that depend on the DSD parameters. It uses the environmental temperature data to define the phase state unless a bright band is detected. If a bright band is detected, a certain bright-band model is used to define the phase state as a function of height within the bright band. The drop size distribution model is expressed in terms of the R-D_m relation at one atmospheric pressure with an adjustable parameter ϵ. Here, R denotes the rainfall rate and D_m is the volume weighted mean diameter of precipitation particles. Parameter ϵ can be regarded as a second DSD parameter. Specifying D_m with a given ϵ will determine not only R but also other necessary variables that include effective radar reflectivity factor Z_e and specific attenuation k at both Ku and Ka bands. All such variables at various temperatures are pre-calculated and stored in a table. Once the phase state and the temperature are given, the values of Z_e and k needed for attenuation correction can be picked up from the table. Unlike the TRMM PR algorithm, the attenuation correction algorithm in the solver module does not assume a power law relationship between k and Z_e because there are no consistent power law relations at both Ku and Ka bands that can be derived from a single-parameter DSD model.

The solver module is the core of the rain retrieval algorithm. It estimates D_m at each range bin that can best reproduce the measured profiles of Z_m at both Ku and Ka bands with constraints that include: agreement between the computed PIA and the SRT-derived estimate; restrictions on how large ϵ can deviate from its nominal value of one. Note that ϵ is not adjusted at each range bin but is common at all range bins in a beam. The basic idea of the attenuation correction is described in the Chap. 10. Since no power law is assumed between k and Z_e in the DPR algorithm, however, the attenuation correction is made at each range bin numerically by using the k-Z_e relations stored in the look-up table. Since the actual echo data have a finite range resolution and are sampled at discrete ranges, the attenuation within the range bin is also taken into account in this process (Seto et al. 2013). The effect of NUBF is considered and corrected for (Seto et al. 2015). Once the best combination of ϵ and D_m profile are chosen, all other variables such as R, Z_e and k are calculated and written in the output file.

11.4   Special Features in the DPR Algorithm

The algorithm flow described in the previous section is applicable to both single-frequency and dual-frequency L2 algorithms. The single-frequency algorithms for KuPR and KaPR are developed not only because KuPR and KaPR have unmatched

beams along which data from only one of them are available, but also because the mission requires output data even if one of the radars stops its measurement for some unexpected operational reasons or accidents. Before 21 May 2018, the dual-frequency algorithm was applicable only to the data from the matched beams of the inner swath. Estimates of rain parameters derived from these data are presumed to be more accurate than single-frequency estimates because of the availability of more information obtained simultaneously at the same resolution cell.

As mentioned in Chap. 10, attenuation correction is the major issue in rain retrieval with a spaceborne radar. Instead of using the Hitschfeld-Bordan solution that requires a power law relation between k and Z_e, the attenuation correction in the DPR algorithm is carried out successively along the range direction by numerically solving the equation that relates Z_m, Z_e, and k by assuming an R-D_m relation with adjustable parameter ϵ. The PIA estimate provided by the SRT is used as a constraint. Since the PIA estimates by SRT include some errors whose relative magnitude increases when the PIA becomes small, there is a minimum PIA above which the SRT is applicable (Seto et al. 2015). This minimum level is much higher for KuPR than for KaPR because the attenuation in the Ka-band is about 6 times larger than that in the Ku-band. As a result, SRT can be used in KuPR only for rain rates larger than approximately a few mm h^{-1} whereas it can be used in KaPR for rain rates larger than about 1 mm h^{-1} if rain extends from surface to a few km in height. The exact level of the threshold depends on the incidence angle, surface type, storm height and other conditions. On the other hand, if rain is quite heavy and if the attenuation is so large that the surface echo disappears, SRT cannot be used either. This latter condition often happens in KaPR measurement. In such a case, echoes from rain near the surface disappear because their powers become much smaller than the noise level of the radar receiver. As a result, KaPR often fails to estimate the rainfall rate near surface in heavy rain. These facts imply that the accuracy of rain estimates from KuPR and KaPR depends on the intensity of rain and other conditions, but their dependence on the rain rate differs substantially between KuPR and KaPR. By combining information from KuPR and KaPR, it is possible not only to extend the usable range of SRT, but also to improve the accuracy of PIA estimates over the PIA range where both Ku and Ka PIA can be estimated by SRT. The differential PIA that is defined as the difference between Ku and Ka band PIAs can be estimated with a smaller error than the errors associated with individual PIA estimates. A major error in PIA estimates by the single-frequency SRT generally originates because of differences between the actual surface cross section in rain and the reference value constructed from rain-free surface cross sections. In the dual-frequency case, the variance of the difference in the surface cross sections σ_0(Ka) – σ_0 (Ku) is typically smaller than in the single-frequency case so the errors in the estimate of differential path attenuation tend to be smaller than those associated with the path attenuation derived from single-frequency data (Meneghini et al. 2015). In version 05 of the DPR's dual-frequency algorithm, this differential PIA estimates by SRT is used as a constraint in the solver module.

As described in Chap. 10, a dual-frequency algorithm that tries to retrieve two DSD parameters at each range bin becomes unstable in many cases. Because of this

problem, the current solver module adopts a different approach to effectively use the dual-frequency information. The new dual-frequency algorithm is an extension of the Ku-only algorithm. The parameter called ϵ, which corresponds to the second adjustable DSD parameter and is common over the entire vertical profile, is adjusted to correct for the attenuation in such a way that the retrieved vertical profile of D_m and hence the precipitation profile will reproduce both the measured vertical profiles of KuPR and KaPR as close as possible and also make the differential PIA calculated from it agree with the differential PIA given by SRT in a probabilistic way.

Dual-frequency information is used in other parts of the algorithm as well. The measured dual-frequency ratio defined by

$$\mathrm{DFR_m} = 10\log_{10}Z_m(\mathrm{Ku}) - 10\log_{10}Z_m(\mathrm{Ka}) \qquad (11.3)$$

is used in three places in version 05 of the DPR L2 algorithm. It is used to estimate the melting top and bottom in the vertical profile of stratiform rain with a bright band (Le and Chandrasekar 2013). This method is a kind of vertical profiling method and classifies each angle bin into either stratiform, convective or transitional. The output is merged in the classification output as a subcategory of rain types. These parameters provide additional information about the precipitation structure.

$\mathrm{DFR_m}$ is also used to set a flag in flagHeavyicePrecip which indicates the existence of intense ice precipitation above the $-10\,^\circ\mathrm{C}$ isotherm (Iguchi et al. 2018). Finally, it is used to calculate the snow index that defines a flag called flagSurfaceSnowfall which indicates the phase state of precipitation at surface (Le et al. 2017).

11.5   Future of the DPR Algorithm

The parameters and flags derived by the use of $\mathrm{DFR_m}$ turn out to be very useful. Because of the advantage of accurate estimation of rainfall rate with the dual-frequency data together with additional useful information derived from the use of $\mathrm{DFR_m}$, the GPM project decided to change the scan pattern of KaHS so that dual-frequency matched beam data can be obtained over the full swath even though the information about the non-uniformity of rain distribution provided by using KaHS's interlaced scan would be sacrificed. The new scan pattern of KaHS is also expected to improve rain/no-rain judgement in the outer swath where KuPR profiles are often contaminated by sidelobe surface clutter at certain ranges. The classification of rain types may also be improved by using the dual-frequency information.

At the same time, some effort has been made to improve the DPR algorithm in several aspects. In the current algorithm, for example, the PIA estimates by SRT is the only additional constraint to the attenuation correction. But the increase of the background noise of KuPR due to rain over ocean should be usable for attenuation correction. Since the radar's receivers are not designed for radiometric use, the

radiometric information provided by the radar can be used only for heavy rain or in limited cases. However, it can improve the reliability of the output especially when the SRT fails to estimate the PIA correctly under some exceptional conditions where the distribution of σ^0 is unusual. Such an unusual surface return occurs, for example, when the sea is very calm and σ^0 as a function of incidence angle changes substantially, or when a part of the ocean surface has very different surface winds due to the existence of an island. Attenuation estimates inferred with DFR_m are implicitly used in the current algorithm when it adjusts the DSD parameters so that the retrieved Z_e and k profiles at both Ku and Ka bands will reproduce the measured Z_m profiles at these frequencies. But, there may be a more explicit use of DFR_m near surface in attenuation correction if two DSD parameters are not estimated at each range bin (Seto and Iguchi 2015).

Research is also going on to improve the reliability of reference data of the surface cross section used in SRT by combining different sizes and different areas of statistics of σ^0 (Meneghini and Kim 2017). Multiple scattering effects appear, especially in Ka-band echoes, in heavy convective rain system that contains a large amount of ice particles (Battaglia et al. 2015). Such effects are not taken into account in the current retrieval algorithm. Correction of multiple scattering effects is a very difficult issue together with the non-uniform beam filling effects. Some efforts to alleviate these effects are under way.

References

Awaka, J., Iguchi, T., & Okamoto, K. (2009). TRMM PR standard algorithm 2A23 and its performance on bright band detection. *Journal of the Meteorological Society of Japan, 87A*, 31–52. https://doi.org/10.2151/jmsj.87A.31.

Battaglia, A., Tanelli, S., Mroz, K., & Tridon, F. (2015). Multiple scattering in observations of the GPM dual-frequency precipitation radar: Evidence and impact on retrievals. *Journal of Geophysical Research, 120*, 4090–4101. https://doi.org/10.1002/2014JD022866.

Iguchi, T., Seto, S., Meneghini, R., Yoshida, N., Awaka, J., Le, M., Chandrasekar, V., & Kubota, T. (2017). GPM/DPR Level-2 algorithm theoretical basis document, JAXA-NASA Tech. Rep., 81 pp. Available online at https://pmm.nasa.gov/resources/documents/gpmdpr-level-2-algorithm-theoretical-basis-document-atbd, last accessed 9 Oct 2018.

Iguchi, T., Kawamoto, N., & Oki, R. (2018). Detection of intense ice precipitation with GPM/DPR. *Journal of Atmospheric and Oceanic Technology, 35*, 491–502. https://doi.org/10.1175/JTECH-D-17-0120.1.

Kojima, M., Miura, T., Furukawa, K., Hyakusoku, Y., Ishikiri, T., Kai, H., Iguchi, T., Hanado, H., & Nakagawa, K. (2012). *Dual-Frequency Precipitation Radar (DPR) development on the Global Precipitation Measurement (GPM) core observatory*. In Proceedings of SPIE earth observing missions and sensors: Development, implementation, and characterization II, *85281A*. https://doi.org/10.1117/12.976823.

Kubota, T., Iguchi, T., Kojima, M., Liao, L., Masaki, T., Hanado, H., Meneghini, R., & Oki, R. (2016). A statistical method for reducing sidelobe clutter for the Ku-band precipitation radar on board the GPM Core Observatory. *Journal of Atmospheric and Oceanic Technology, 33*, 1413–1428. https://doi.org/10.1175/JTECH-D-15-0202.1.

Le, M., & Chandrasekar, V. (2013). Precipitation type classification method for Dual-Frequency Precipitation Radar (DPR) onboard the GPM. *IEEE Transactions on Geoscience and Remote Sensing, 51*, 1784–1790. https://doi.org/10.1109/TGRS.2012.2205698.

Le, M., Chandrasekar, V., & Biswas, S. (2017). An algorithm to identify surface snowfall from GPM DPR observations. *IEEE Transactions on Geoscience and Remote Sensing, 55*, 4059–4071. https://doi.org/10.1109/TGRS.2017.2687420.

Meneghini, R., & Kim, H. (2017). Minimizing the standard deviation of spatially-averaged surface cross section data from the Dual-Frequency Precipitation Radar (DPR). *IEEE Transactions on Geoscience and Remote Sensing, 55*, 1709–1716. https://doi.org/10.1109/TGRS.2016.2630669.

Meneghini, R., Jones, J. A., Iguchi, T., Okamoto, K., & Kwiatkowski, J. (2004). A hybrid surface reference technique and its application to the TRMM precipitation radar. *Journal of Atmospheric and Oceanic Technology, 21*, 1645–1658. https://doi.org/10.1175/JTECH1664.1.

Meneghini, R., Liao, L., Tanelli, S., & Durden, S. L. (2012). Assessment of the performance of a dual-frequency surface reference technique over ocean. *IEEE Transactions on Geoscience and Remote Sensing, 50*, 2968–2977. https://doi.org/10.1109/TGRS.2011.2180727.

Meneghini, R., Kim, H., Liao, L., Jones, J. A., & Kwiatkowski, J. M. (2015). An initial assessment of the surface reference technique applied to data from the Dual-Frequency Precipitation Radar (DPR) on the GPM satellite. *Journal of Atmospheric and Oceanic Technology, 32*, 2281–2296. https://doi.org/10.1175/JTECH-D-15-0044.1.

Seto, S., & Iguchi, T. (2015). Intercomparison of attenuation correction methods for the GPM Dual-Frequency Precipitation Radar. *Journal of Atmospheric and Oceanic Technology, 32*, 915–926. https://doi.org/10.1175/JTECH-D-14-00065.1.

Seto, S., Iguchi, T., & Oki, T. (2013). The basic performance of a precipitation retrieval algorithm for the Global Precipitation Measurement missions single/dual-frequency radar measurements. *IEEE Transactions on Geoscience and Remote Sensing, 51*, 52395251. https://doi.org/10.1109/TGRS.2012.2231686.

Seto, S., Iguchi, T., Shimozuma, T., & Hayashi, S. (2015). NUBF correction methods for the GPM/DPR level-2 algorithms. *IEEE International Geoscience Remote Sensing Symposium (IGARSS)*, 2612–2614. https://doi.org/10.1109/IGARSS.2015.7326347.

Chapter 12
DPR Dual-Frequency Precipitation Classification

V. Chandrasekar and Minda Le

Abstract Profile classification is a critical module in the microphysics retrieval algorithm for the dual-frequency precipitation radar (DPR) that on board the global precipitation measurement (GPM) core satellite. It does rain type classification, hydrometeor profile characterization, and surface snowfall identification at each Ku- and Ka- band matched footprint of DPR. Vertical characteristics of measured dual-frequency ratio (DFRm), defined as the difference between measured reflectivity at two frequency channels (Ku- and Ka- band) in dB scale, were key information that extensively used in various algorithms. This chapter introduces the theoretical basis of these algorithms. Validation activities are illustrated as well.

Keywords Precipitation · Radar · Rainfall · Dual frequency ratio · Convective/stratiform classification · Snow · Crystals · Dendrites · Hail · Graupel · Melting layer · Bright band · Reflectivity · GPM · TRMM · PR · DPR · Linear depolarization ratio · Surface snowfall · Validation

12.1 Introduction

The Dual-frequency precipitation radar (DPR) on board the GPM core satellite operates at Ku- (13.6 GHz) and Ka- (35.5 GHz) band. DPR improves our knowledge of precipitation relative to the single-frequency (Ku- band) radar used in TRMM (Tropical Rainfall Measurement Mission). New Ka-band observation of DPR helps improve the detection thresholds for light rain and snow (Hou et al. 2014). Measurements from both frequency bands suffer from attenuation when a radar beam propagates through precipitation such as the melting layer and moderate to heavy rain. However, attenuation from the Ka-band is larger than from the Ku- band. Non-Rayleigh scattering occurs in precipitation at both Ku- and Ka-bands.

V. Chandrasekar (✉) · M. Le
Department of Electrical and Computer Engineering, Colorado State University, Ft. Collins, CO, USA
e-mail: chandra@colostate.edu; leminda@engr.colostate.edu

Meanwhile, non-Rayleigh scattering is more severe at Ka-band than at Ku-band. This makes the difference between these two DPR measurements a viable parameter for making inferences about the profile.

The difference in the measured radar reflectivity at the two frequencies is a quantity often called the measured dual-frequency ratio (DFR$_m$). It is defined as

$$DFR_m = 10 \log_{10}(Z_m(K_u)) - 10 \log_{10}(Z_m(K_a)) \tag{12.1}$$

Z_m is the measured equivalent radar reflectivity factor in linear scale. DFR$_m$ is in dB scale.

Figure 12.1 shows a schematic plot of a typical DFR$_m$ profile with key points A, B, C, and D marked. These key points are DFR$_m$ slope peak where the gradient of DFR$_m$ profile reaches its maximum magnitude (point A); DFR$_m$ local maximum (point B); DFR$_m$ local minimum (point C), and DFR$_m$ value toward surface (point D).

Dual-frequency classification module is a module in the GPM DPR level 2 algorithms. The module is developed using observations from both Ku- and Ka-bands. The outputs of the module follow the legacy format used for TRMM precipitation radar. It includes two parts, namely precipitation type classification and melting layer detection. The flow chart of GPM-DPR level 2 algorithm is shown in Fig. 11.2 of Chap. 11. From the figure, the outputs of the classification module determine the nature of microphysical models and algorithms to be used in the retrievals (Iguchi et al. 2017).

Fig. 12.1 Schematic plot of DFR$_m$ profile with key points A, B, C, and D. Point A: slope of DFR$_m$ has peak value. Point B: local maximum of DFR$_m$. Point C: local minimum of DFR$_m$. Point D: DFR$_m$ value near surface
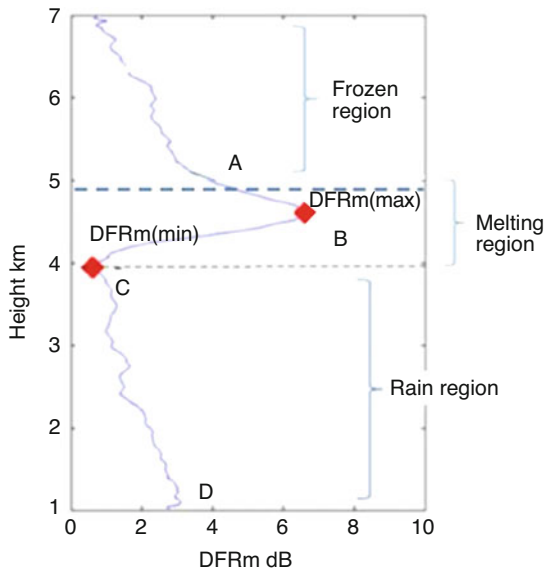
12.2 Precipitation Type Classification

The measured dual-frequency ratio (DFR_m) and its vertical variation compose the main parameters used in the model. In order to quantify the features of DFR_m, a set of indices are defined. Let V1 be

$$V1 = \frac{DFR_{ml}(\,max\,) - DFR_{ml}(\,min\,)}{DFR_{ml}(\,max\,) + DFR_{ml}(\,min\,)} \qquad (12.2)$$

DFR_m (max) and DFR_m (min) are shown in Fig. 12.1. DFR_{ml} used in (12.2) means DFR_m in linear scale. Let V2 be the absolute value of the mean slope for DFR_m below the local minimum point

$$V2 = abs(mean(DFR_m, slope)) \qquad (12.3)$$

The DFRm slope is defined as the difference of DFRm values between two successive DPR range bins, divided by range resolution. The parameters of V1 and V2 are normalized and are not dependent on the height or depth of the melting layer. In general, stratiform rain has larger V1 value than convective rain. While, convective rain has larger V2 value than stratiform rain. To further enlarge the difference between stratiform and convective rain types, a third index V3 is defined as

$$V3 = \frac{V1}{V2} \qquad (12.4)$$

The index V3 is an effective parameter and provides a separable threshold for performing precipitation type classifications.

Statistical studies are performed on V3 using GPM DPR real data. Cumulative Density Function (CDF) of index V3 is calculated for convective rain. 1-CDF of index V3 is calculated for stratiform rain. Different rain type databases are separated using Ku only classification algorithm (Awaka et al. 1997). Separable thresholds of C1 and C2 can be found on index V3 for two rain types with around 70% of CDF. Here C1 = 0.18 and C2 = 0.2. In other words, for stratiform rain: V3 > C2; convective rain: V3 < C1; transition: C1 $\leq$ V3 $\leq$ C2. C1 is smaller than C2. "Transition" is neither a stratiform, nor a convective rain type. The histogram of index V3 and its cumulative density functions are shown in Fig. 12.2. The calculation is based on data from 73 storms with 121,859 vertical profiles in total. Fig. 12.3 illustrates the flowchart of precipitation type classification method in the dual-frequency classification module. Details of algorithms can be found in Le and Chandrasekar (2013a).
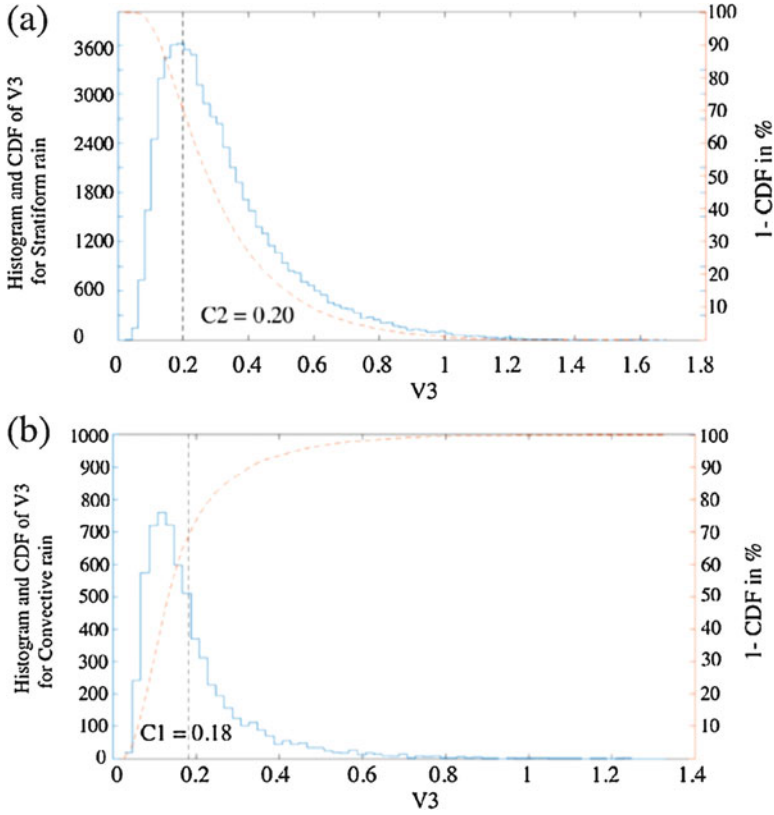
Fig. 12.2 Histogram of DFR$_m$ index V3 and CDFs (cumulative density function) using total of 121,859 vertical profiles from GPM real data. (**a**) Histogram and 1-CDF of V3 for Stratiform rain. Red dashed line represents 1-CDF. (**b**) Histogram and CDF of V3 for Convective rain. Red dashed line represents CDF

12.3 Melting Layer Detection

In the GPM DPR dual-frequency classification module, melting layer top and bottom heights for each qualified vertical profile are detected. The main information used in the model is the DFR$_m$ profile and its vertical variation. Referring to Fig. 12.1, we consider "DFR$_m$ pair" exists when both point B and C are detected. Then the melting layer top is defined as the height at which the slope of the DFR$_m$ hits a peak value. The melting layer bottom is defined as the height at which the DFR$_m$ has a local minimum value. Two horizontal dashed lines in Fig. 12.1 illustrate the melting layer top and bottom height for the profile using the above definition.
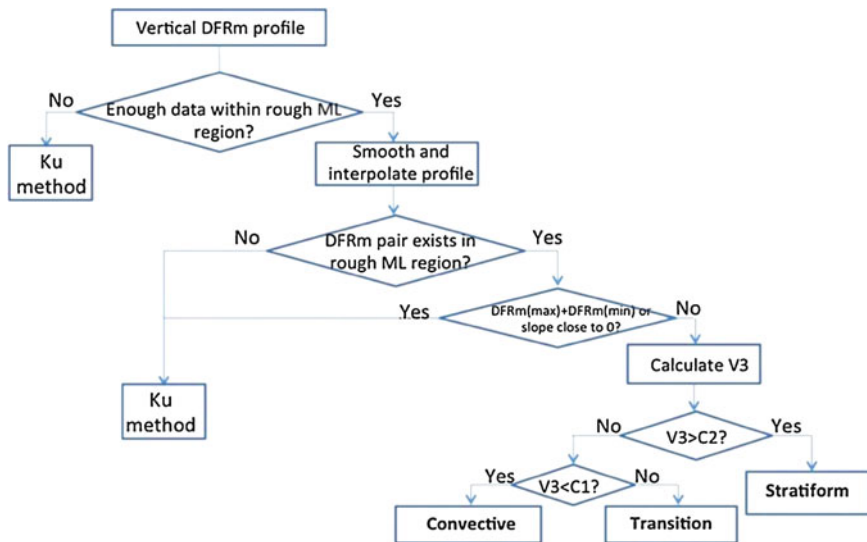
Fig. 12.3 Block diagram of precipitation type classification model

The criteria described above have been compared with other existing criteria in the literature using different radar parameters. Tilford et al. (2001) used the gradient of reflectivity (Z_m) to detect the bright band top and bottom for stratiform rain type. The linear depolarization ratio (LDR) has been pointed out by many researchers as an important signature in melting phase detection, with certain thresholds determined for different hydrometeor particles (Smyth and Illingworth 2006; Bandera et al. 1998; Tan and Goddard 1995; Hines 1983). Typical vertical profiles of reflectivity as well as the corresponding velocity for stratiform and convective type were extensively studied by Fabry and Zawadzki (1995). Baldini and Gorgucci (2006) mentioned that the rapid change of the hydrometeor fall velocity is an implication of the melting layer. The curvature of velocity was used by Zrnić et al. (1994) in characterizing the melting boundaries. Klaassen (1988) found that the melting bottom can be detected by maximum of velocity. Table 12.1 summarize the comparison of melting layer detections between criteria in DFR_m method and other existing criteria. The comparison results using airborne radar data (NAMMA, GRIP and Wakasa Bay experiment). From the table, estimations from the DFR_m method match best with velocity-based criteria with normalized bias of 1.3% and 2.2% for melting layer top and bottom respectively. The DFR_m method also compares well with the LDR criteria, with a −28 dB threshold, the bias between these two criteria is around −2.8%. Details can be found in Le and Chandrasekar (2013b). Figure 12.4 is the block diagram of melting layer detection used in the most updated version of dual-frequency classification module.

Table 12.1 Comparisons of melting layer boundaries between different criteria for NAMMA, GRIP and Wakasa Bay data

	Criteria	DFR_m slope peak (NAMMA)		DFR_m slope peak (GRIP)		DFR_m slope peak (Wakasa Bay)	
		NB	NSE	NB	NSE	NB	NSE
Melting layer top comparison	Z_m slope peak	−2.6%	3.6%	−2.5%	3.6%	−4.9%	6.6%
	Z_m curvature peak	1.6%	3.3%	1.5%	3.0%	2.8%	5.2%
	LDR	−2.8%	4.5%	−3.3%	4.2%	−6.0%	7.2%
	Velocity curvature peak	−1.3%	3.6%	−1.4%	3.7%	−1.9%	5.6%
Melting layer bottom comparison	Z_m curvature peak	4.3%	5.5%	3.7%	5.0%	4.3%	6.9%
	LDR	4.5%	5.9%	4.0%	5.4%	5.4%	11.2%
	Velocity curvature min	2.2%	4.9%	1.7%	4.4%	−0.08%	7.0%
	Velocity max	1.6%	5.9%	1.9%	4.3%	−2.6%	13.9%
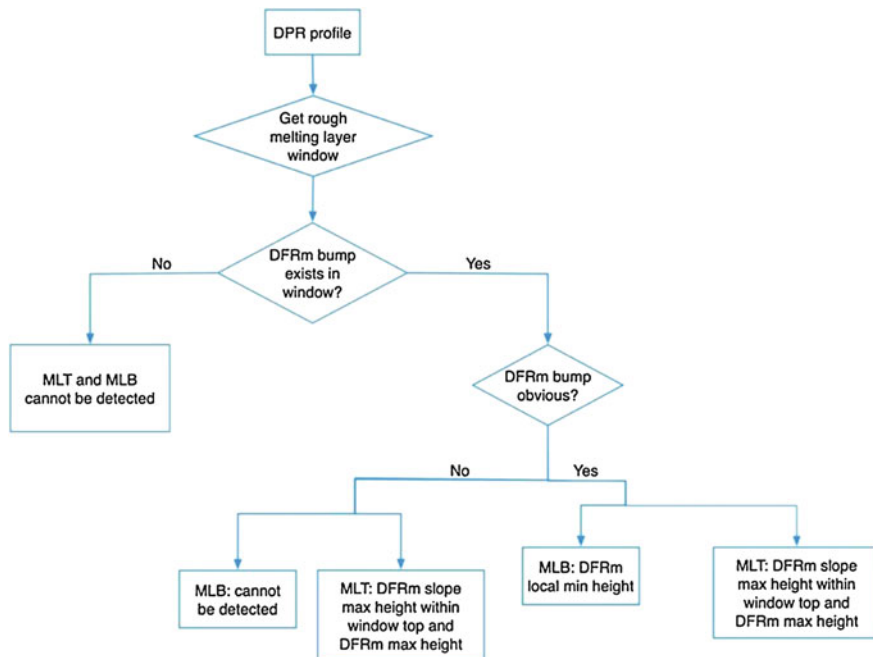
Fig. 12.4 Block diagram of melting layer detection for DFR_m method

12.4   Evaluation of the Dual-Frequency Classification Module

Extensive evaluations have been conducted of the dual-frequency classification algorithm ever since GPM's launch. Results from the dual-frequency classification algorithm are compared with both space radar algorithm and ground radar methods. The single frequency (Ku-band) algorithm from TRMM legacy is applied to the full swath of DPR overpass, while the dual-frequency algorithm is applied to the inner swath. It is critical to show consistency of classification results from two different algorithms. We compare different rain type counts using both algorithms and perform statistical studies on the melting layer top and bottom heights using tropical storm datasets.

12.4.1   Comparison Between Dual-Frequency and TRMM Legacy Single Frequency Methods

Table 12.2 is a contingency table summarizing a comparison of rain type counts between dual-frequency classification method and TRMM legacy Ku only method using GPM data from total of 15 orbits. 'S', 'C' and 'O' in the table represent stratiform, convective and other rain types. The count of stratiform rain that is detected by both methods is 73,190. The count of convective rain and other rain type is 14,094 and 9414 respectively. With a total of 110,794 rain type counts in this comparison, the percentage of matches between dual-frequency method and TRMM legacy Ku only method is around 87.3%. In addition to general profile comparisons, the evaluation is also performed on tropical storms. A total of 61 tropical storms with 7 from cyclones, 27 from hurricanes and 27 from typhoons are used in the evaluation of melting layer top and bottom between the dual-frequency classification method and the single frequency approach.

In Fig. 12.5, histograms for melting layer top and bottom for these three storm types illustrate similar ranges. Median value for melting layer top and bottom are the same for dual-frequency classification method and Ku only method for hurricanes and typhoons. For cyclones, median value of melting layer bottom from the dual-frequency classification method is slightly lower than the estimations from

Table 12.2 Comparison of stratiform, convective and other rain types between dual-frequency classification method and Ku only method

Count	Dual-frequency method			
Ku only method		S	C	O	Total
	S	73,190	4364	303	77,857
	C	2914	14,094	45	17,053
	O	6095	375	9414	15,884
	Total	82,199	18,833	9762	110,794

A total of 15 GPM DPR orbits data are used in comparison

'S' represents for stratiform rain; 'C' for convective rain and 'O' for other type
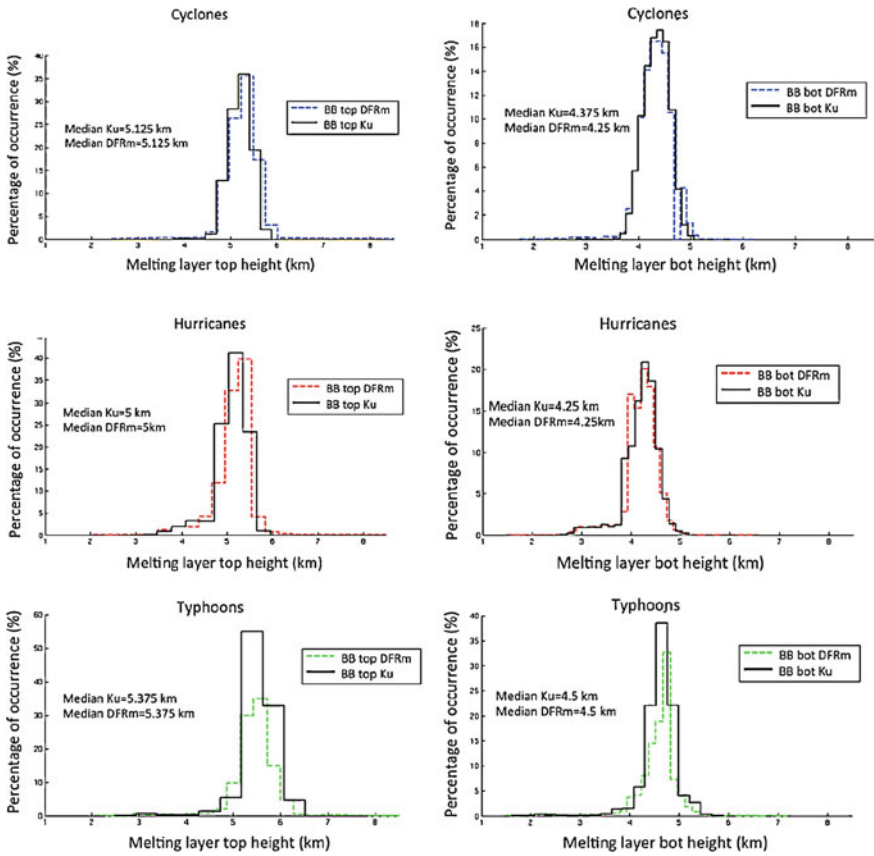
Fig. 12.5 Left column (from top to bottom): comparison of melting layer top height (in km) between dual-frequency classification method and Ku only method for cyclone, hurricane and typhoons shown in Table 12.2. Right column illustrates similar results for melting layer bottom height (in km)

Table 12.3 Count of melting layer top match between dual-frequency method of DPR and Ku only method using GPM DPR data from tropical storms including cyclones, typhoons and hurricanes

Count	Match of MLT ($\Delta \leq 0.25$ km)?		
	Yes	No	Total
Cyclone	7234	173	7407
Typhoon	37,137	832	37,969
Hurricane	19,278	469	19,747

Ku only method. We assume the results from both methods match if the absolute difference of the melting layer top (or bottom) between two methods is within 0.25 km. We counted the number of profiles that have melting layer top (or bottom) match (or not match) for cyclone, typhoon and hurricane storms. Tables 12.3 and 12.4 summarize this comparison for melting layer top and melting layer bottom,

Table 12.4 Count of melting layer bottom match between dual-frequency method and Ku only method using GPM DPR data from tropical storms including cyclones, typhoons and hurricanes

Count	Match of MLB ($\Delta \leq 0.25$ km)?		
	Yes	No	Total
Cyclone	7406	1	7407
Typhoon	37,950	19	37,969
Hurricane	19,736	11	19,747

respectively. Tables 12.3 shows that there are 7234 matched melting layer tops detected out of 7407 cyclone profiles, while there are 37,137 matched melting layer top detections out of 37,969 typhoon profiles and 19,278 matched detections out of 19,747 hurricane profiles. The percentage of melting layer top matches between the dual-frequency method and the TRMM legacy Ku only method is higher than 97% for different tropical storm types. Table 12.4 shows the similar results for melting layer bottom detection. The percentage of matches for melting layer bottom is more than 99%.

From histogram plots and tables shown below, results from the dual-frequency classification method match well with Ku only method, which is the TRMM legacy method. In this way, consistency can be expected between the inner swath (where dual-frequency classification method is applied) and the outer swath.

12.4.2   Surface Snowfall Identification

The GPM mission extends observation coverage from the tropical regions to the whole globe including cold regions compared to TRMM mission. In those cold regions, snow is the dominant precipitation type. It is important to study snowfall precipitation and provide a surface snowfall flag to each vertical profile in the GPM products. In this section, we describe an algorithm to identify surface snowfall using information from vertical observations from radar such as the dual-frequency ratio.

This is a new approach to detect snow because traditional methods rely on surface temperature or surface echo to detect snow. This algorithm has been implemented as an experimental version in the dual-frequency classification module. Adding this surface snowfall identification function is considered as an enhancement of the current classification module. It should be pointed out that this method is not for detecting snow aloft.

Figure 12.6a shows the first snow observation caught by GPM DPR with overpass #272 on 17 March 2014. Within that overpass, there is snow, stratiform and convective rain precipitation within a 160 scan (around 800 km) range. A, B and C indicate the locations of snow, stratiform and convective rain. Figure 12.6b shows the averaged reflectivity profile for snow at Ku-, Ka- band and the measured dual-frequency ratio. As expected, reflectivity at Ku- band is, most of the time, below 25 dBZ. However, the difference between Ku- and Ka- band (indicated by DFR_m) is
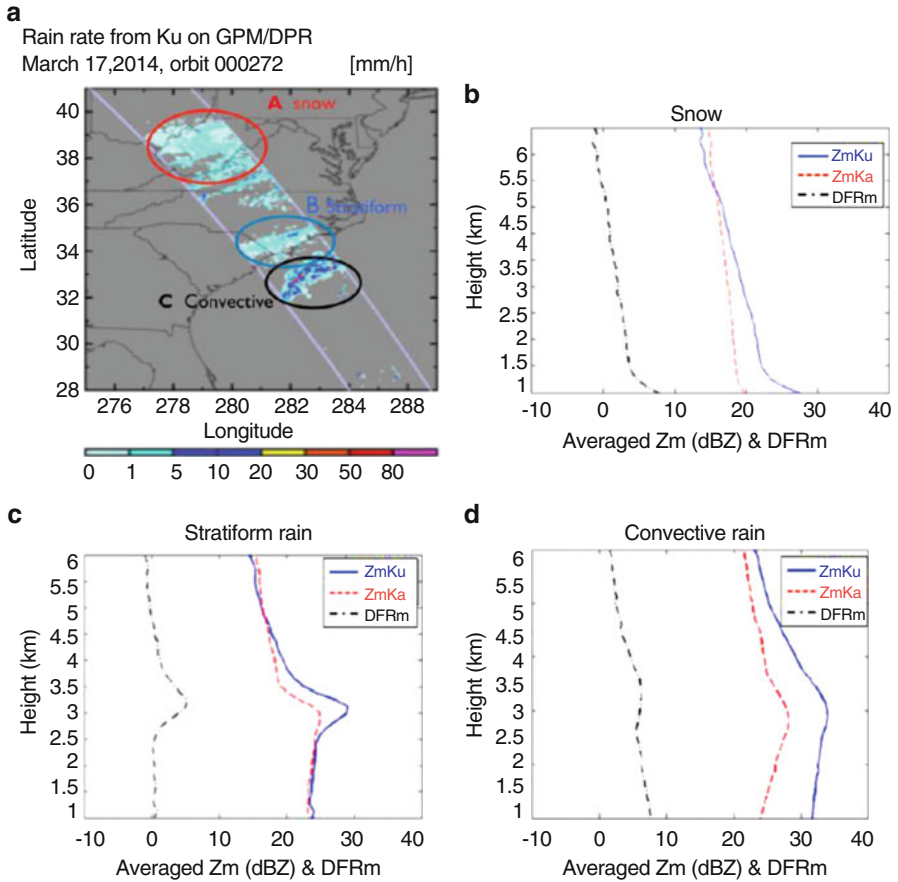
Fig. 12.6 (**a**) GPM DPR overpass of rainfall rate on March 17, 2014 (#000272). Circled A, B and C represents snow, stratiform rain, and convective rain. (**b**) Averaged reflectivity profiles as well as dual-frequency ratio profile for snow. (**c**) Same as (**b**) for stratiform rain. (**d**) Same as (**b**) for convective rain

several dBs, even when reflectivity at Ku- band remains a relatively small value. Figure 12.6c shows an averaged vertical profile for stratiform rain. The bright band is obvious from Ku- band reflectivity. Values of DFR_m below the melting region (or the bright band) are very small indicating that attenuation at Ka- band is very small when reflectivity at Ku- band is less than around 25 dBZ in the rain region. In contrast, DFRm values above the melting layer is several dBs, with values similar to the snow in Fig. 12.6b. For convective rain, from Fig. 12.6d, the maximum of reflectivity at Ku- band is equal or larger than 35 dBZ, while DFRm values are considerable in the rain region. Large DFRm values in rain are contributed from both the attenuation difference and the non-Rayleigh scattering effect, while the former factor plays a more important role. Comparing Fig. 12.6b, c, DFR_m values are larger
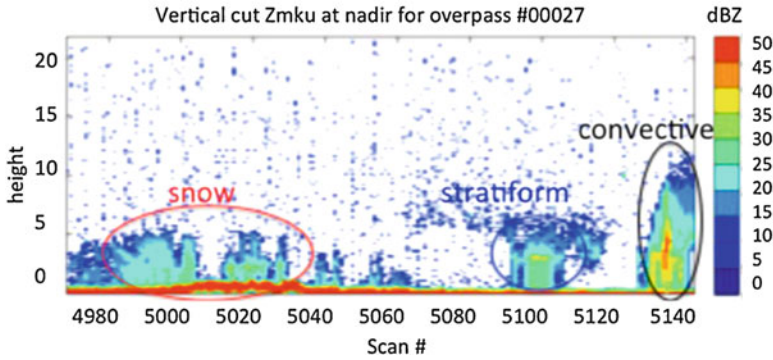
Fig. 12.7 Vertical cross section at nadir of DPR overpass shown in Fig. 12.6a

for snow than stratiform rain even when reflectivity values are of similar magnitude. This is a useful indication to help perform snow- and rain-fall separation. Comparing Fig. 12.6b, d, DFR_m values for snow are in the similar range compared to convective rain. However, reflectivity at Ku- band is much smaller for snow than convective rain. One of the features of a convective storm is that it is normally formed at a higher altitude in the atmosphere (except for some warm rain or orographic rain) compared to stratiform and snow precipitation (Houze 1997). Figure 12.7 shows the vertical cross section at nadir for the DPR overpass shown in Fig. 12.6a. Red, blue and black circles indicate snow, stratiform and convective precipitation, which correspond to Fig. 12.6a. It is straightforward that storm top height is lower for snow and stratiform, which is around 5 km. In contrast, storm top height is around 10 km for convective precipitation.

Based on the above analysis, three ingredients including DFR_m, the maximum value of reflectivity at Ku- band, as well as the storm top height become important, are then used in the development of the algorithm to identify surface snowfall. To avoid calibration issues, we use the slope of DFR_m instead of DFR_m itself. Figure 12.8a–c illustrate histograms of DFR_m mean slope (absolute value), maximum of reflectivity at Ku-band, and storm top height for snow, stratiform and convective rain using DPR overpass #000272 (scan # 4980–5140). In Fig. 12.8a, the mode value is around 5, 3 and 3.5 dB km^{-1} for snow, stratiform and convective rain, respectively. In Fig. 12.8b, the mode value of Z_{mku} max is less than 15 dBZ with the mean value around 20 dBZ for snow. For stratiform rain, the mode value is around 30~35 dBZ, and 35~40 dBZ for convective rain. Storm top height value is much larger for convective rain compared to snow and stratiform rain, shown in Fig. 12.8c. All these findings from the histogram plots match the features we observe from averaged vertical profiles shown in Fig. 12.6.

A closer inspection of DPR profiles shows some features: (i) DFR_m slope is appreciable for snow compared to stratiform rain; (ii) maximum of reflectivity for snow is less than 30 dBZ, while for convective rain is around 35–40 dBZ; (iii) storm top height for snow is lower than convective rain in a general sense. Combining
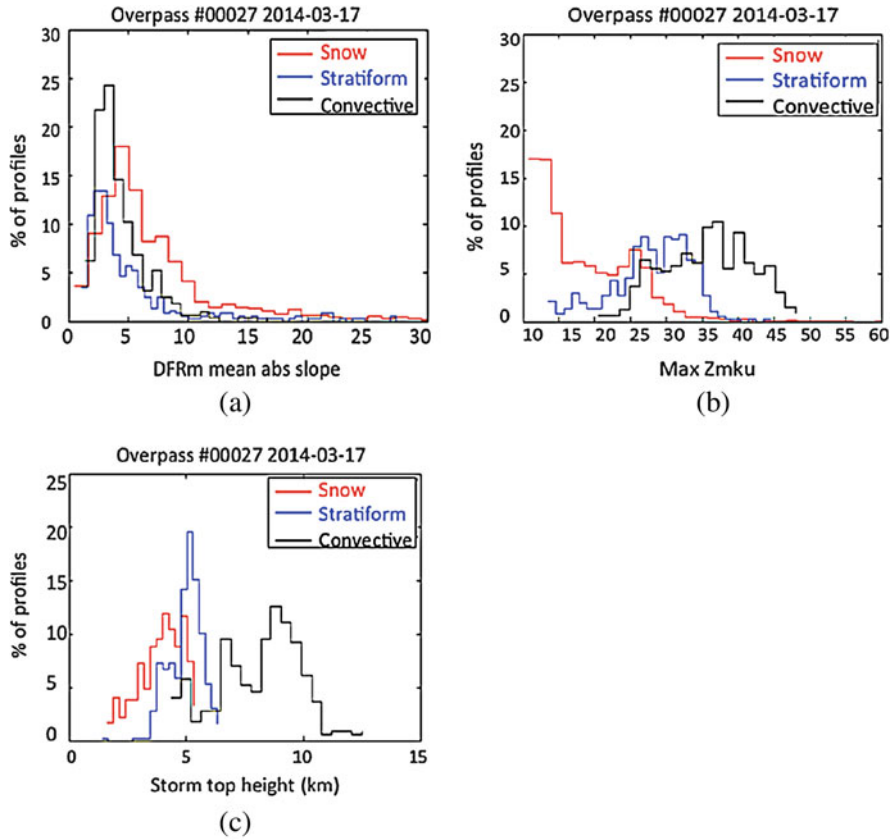
Fig. 12.8 GPM DPR overpass of rainfall rate on March 17, 2014. Scan # from 4894 to 5142. (**a**) Histogram of mean DFR_m slope in absolute value. (**b**) Histogram of maximum reflectivity at Ku band. (**c**) Histogram of storm top height

these features, a snow index to perform effective separation between snowfall and rain (includes stratiform and convective) is designed. The snow Index (SI) is carefully chosen from the features discussed above. The definition of SI is

$$SI = \frac{mean\big(abs\big(DFRm_{slope}\big)\big)}{Zmku_{max} * Storm\_top\_height} \tag{12.5}$$

where the DFR_m slope (in dB km^{-1}) is used instead of the DFR_m value due to its immunity to calibration change. Zmku_max (in dBZ) represents maximum of reflectivity at Ku- band along the profile. Storm_top_height represents the altitude of the storm top in km. In general, the absolute value of DFR_m slope in the numerator of (12.5) is larger for snow than for stratiform rain. Zmku_max value in the denominator is larger for convective rain than for snow, while storm top height in the denominator is lower for snow and stratiform rain than for convective rain.
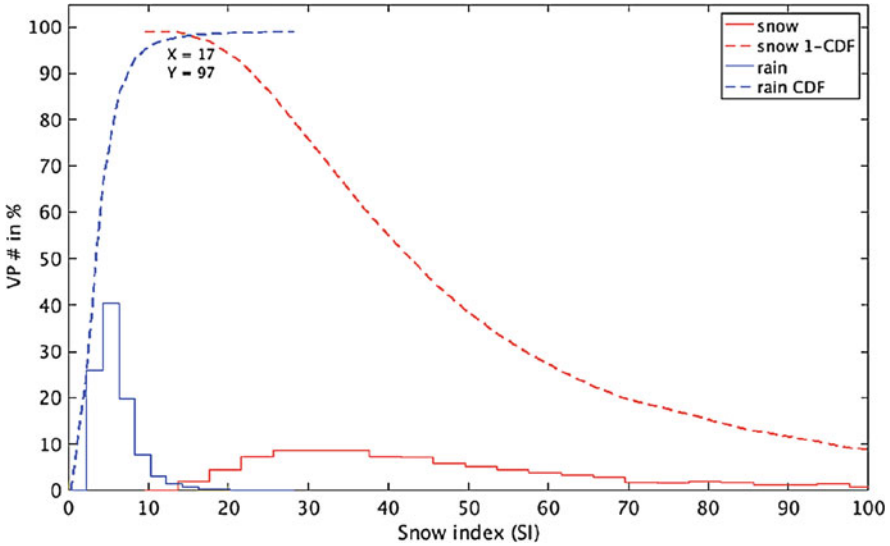
Fig. 12.9 Large scale study of the snow index using GPM DPR profiles. Histograms of the snow index are shown for rain (blue) and snow (red). The blue dashed curve is the cumulative density function (CDF) for rain. The red dashed curve is 1-CDF for snow

Therefore, SI is expected to be a larger value for snow profile than for rain. In the algorithm, we use the normalized value of Zmku_max and Storm_top_height.

A total of 353,166 rain profiles and 4935 snow profiles are used in the statistical study of the snow index. Rain profiles are chosen from tropical regions during the summer season and snow profiles are chosen from northern Europe and the northern US in the winter season. Information of 0 °C isotherm is used in profile selection. Fig. 12.9 shows the histogram of the snow index (SI) defined in (12.5) for snow and rain profiles respectively. In general, as expected, snow index is larger for snow profiles. The cumulative density function (CDF) is calculated for rain, and illustrated as a blue dashed curve in Fig. 12.9, while the red dashed curve represents 1-CDF for snow profiles. At around 97% of the CDF (or 1-CDF), the SI index can separate snow and rain profiles. In other words, 97% of snow profiles have SI > 17, while 97% of rain profiles have SI ≤ 17.

Figure 12.10 shows a flow chart of the surface snowfall identification algorithm that uses the snow index. Besides snow index, other auxiliary information such as 0 °C isotherm and clutter free height are used in the algorithm. Although the 0 °C isotherm (or surface temperature) plays an important role in snowfall detection, its accuracy is a challenge for space-borne weather radars such as GPM. Therefore, in this algorithm, the 0 °C isotherm is not the dominant parameter but rather a constraint parameter. In many research efforts, snowfall detection is associated with near surface reflectivity values (Kulie and Bennartz 2009). However, for DPR radar, surface reflectivity at Ku- and Ka- bands is easily falls below the GPM noise level (~18 dBZ) due to attenuation, which limits the detectability of snowfall.
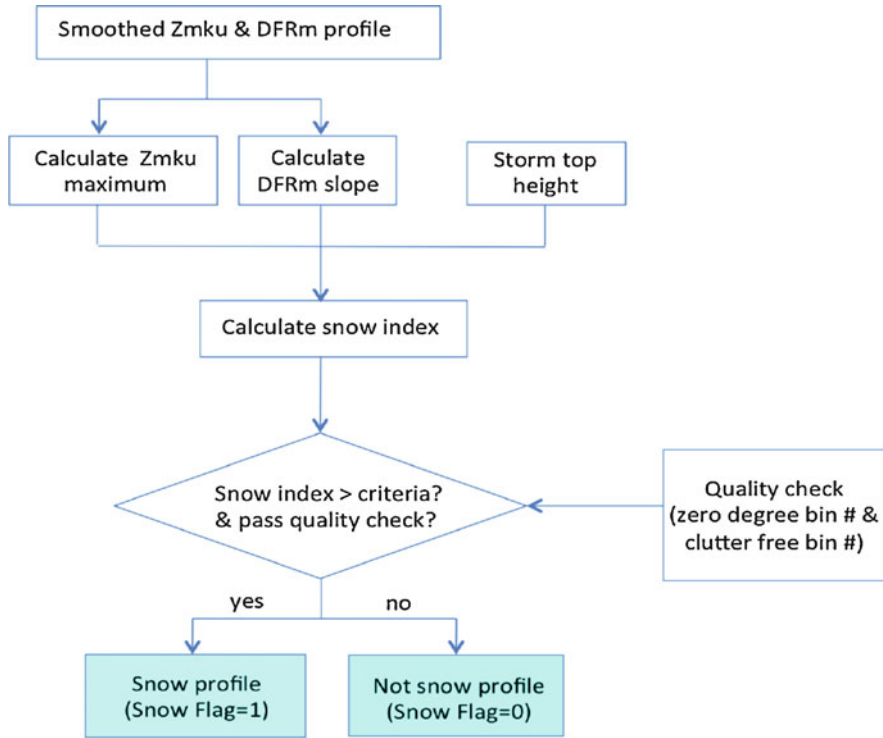
Fig. 12.10 Flowchart to perform surface snowfall identification in profile classification module of GPM DPR level 2 algorithm

However, the current snowfall identification algorithm uses profile information to detect snow rather than the information solely from the surface, which is considered as another advantage. More details of the surface snowfall identification algorithm can be found in Le et al. (2017).

12.4.3 Ground Validation for the Surface Snowfall Identification Algorithm

The surface snowfall identification algorithm has been gone through extensive validations with ground observations. Ground observations include ground-based validation radars and in situ instruments. Among various validation instruments, ground-based dual-polarization radar has shown great advantages to conduct precipitation observation over a wide area in a relatively short time span. Therefore, radar is always a key component in all the validation field experiments. Validation cases are carefully selected to demonstrate the algorithm's stability under different

Table 12.5 Information on snow validation cases

Radar	Date	Surface type	GPM DPR orbit#
KILX (Lincoln, IL)	2014-12-22	Flat land	4638
KOKX (Upton, NY)	2015-01-09	Coastline	4914
KEAX (Kansas, MO)	2015-01-31	Flat land	5263
KBUF (Buffalo, NY)	2015-03-14	Lake	5908
KIWX (North Webster, IN)	2015-03-23	Lake	6052
NPOL (Olympic peninsula, WA)	2015-11-14	Coastline	9722
KDVN (Davenport, IA)	2015-11-21	Flat land	9828
NPOL (Olympic peninsula, WA)	2015-12-03	Coastline	10,019
KAKQ (Wakefield, WA)	2016-02-05	Coastline	11,011
KAPX (Gaylord, MI)	2016-02-25	Lake	11,319
KARX (La Crosse, WI)	2016-03-24	Flat land	11,755
CSU-CHILL (Greeley, CO)	2016-04-16	Mountain	12,119
KGRR (Grand Rapids, MI)	2017-11-18	Lake	21,160
KCLE (Cleveland, OH)	2017-12-14	Lake	21,554
KOTX (Spokane, WA)	2017-12-20	Flat land	21,648
KDOX (Dover, AFB, DE)	2018-01-04	Coastline	21,882

Table 12.6 Meaning of abbreviation used for ground radar hydrometeor identification

Type	RH	HA	GR	DS	RA	DRZ	WS
	Rain and hail	Hail	Graupel	Dry snow	Rain	Drizzle	Wet snow

geophysical conditions including mountain, lake, flat land and coastline at different season of the year. Table 12.5 contains a list of radars and events we have successfully done validation with.

In the validation process, precipitation events that were simultaneously captured by both GPM DPR and ground radar are chosen first. Then, the hydrometeor type is classified using ground radar for choosing snow events. Third, the surface snowfall identification algorithm is applied to DPR observations during these events. Finally, comparisons are done between hydrometeor type results from two radars. The output of the surface snowfall algorithm is a snow flag (0 or 1), where "1" means that there is surface snowfall, while "0" means there is no surface snowfall. No snowfall could be rain, wet snow, graupel or hail etc. The algorithm used to perform hydrometeor identification for the ground radar is described in Bechini and Chandrasekar (2015). The match ratio between DPR and ground radar is calculated within the overlapped region. Whenever DPR footprint has a valid "0" or "1" value from the surface snowfall flag, we search the ground radar hydrometeor type at the closest latitude and longitude data point. When the snow flag is "1" (surface snowfall exists), we consider hydrometeor types of dendrite ("DN"), crystal ("CR") and dry snow ("DS") from ground radar to be a match. When the snow flag is "0" (surface snowfall does not exist), the other hydrometeor types from the ground radar identification algorithm are considered a match. The hydrometeor type identified from the ground radar is summarized in Table 12.6 (details can be found in Bechini and Chandrasekar 2015). The match ratio is calculated as

$$Match\ Ratio = \frac{of\ match\ points}{of\ valid\ points\ of\ DPR} \qquad (12.6)$$

If the match ratio equals 1, it means all DPR footprints can find a match of snow/ no snow with ground radar. DPR has limited detectability due to its attenuation at higher frequencies compared to ground radar. It is therefore normal that DPR observes fewer valid points than the ground radar.

Figure 12.11 shows the match ratio for all 16 cases in Table 12.5. The validation radars are NPOL, NEXRAD and CSU-CHILL. Validation cases are chosen from different surface types, including 5 from flat land, 5 from lake, 5 from coastline and 1 from mountain. In the figure, 11 out of 16 cases have a match ratio above 85%. The rest are all above 70%. In Table 12.7, we illustrate the total number of data points in the comparison and the averaged match ratio for each surface type. Lake and mountain cases have higher match ratio above 90%, although there is only 1 available mountain case in this study so far. The average ratio for flat land is the lowest but still above 85%. Averaged match ratios among all 16 cases is 87.8%, which is a promising result. More details on the validation of the surface snowfall algorithm can be found in Le and Chandrasekar (2019).
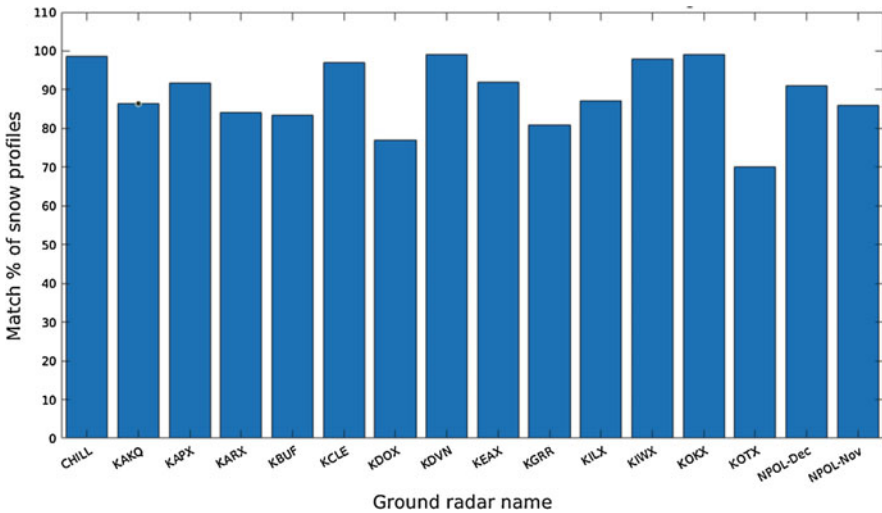
Fig. 12.11 Match ratio for 16 validation cases during the years 2014–2018

Table 12.7 Average match ratio for validation cases under different surface types

Surface type	Flat land	Coastline	Lake	Mountain	All
Total valid points	2498	3338	2668	298	8802
Average match ratio (%)	85.6	86.5	90.8	98.5 (1 case)	87.8

References

Awaka, J., Iguchi, T., Kumagai, H., & Okamoto, K. (1997). Rain type classification algorithm for TRMM precipitation radar. *Proceedings of the IEEE International Geoscience Remote Sensing Symposium (IGARSS)*, 4, 1633–1635, Singapore. https://doi.org/10.1109/IGARSS.1997. 608993.

Baldini, L., & Gorgucci, E. (2006). Identification of the melting layer through dual-polarization radar measurements at vertical incidence. *Journal of Atmospheric and Oceanic Technology, 23*, 829–839. https://doi.org/10.1175/JTECH1884.1.

Bandera, J., Papatsoris, A. D., Watson, P. A., & Goddard, J. W. (1998). Method for detecting the extent of the melting layer. *Electronics Letters, 34*, 2104–2105. https://doi.org/10.1049/ el:19981462.

Bechini, R., & Chandrasekar, V. (2015). A semisupervised robust hydrometeor classification method for dual-polarization radar applications. *Journal of Atmospheric and Oceanic Technology, 32*, 22–47. https://doi.org/10.1175/JTECH-D-14-00097.1.

Fabry, F., & Zawadzki, I. (1995). Long-term radar observations of the melting layer of precipitation and their interpretation. *Journal of the Atmospheric Sciences, 52*, 838–850. https://doi.org/10. 1175/1520-0469(1995)052<0838:LTROOT>2.0.CO;2.

Hines, E. L. (1983). *Image processing techniques for the detection of the radar bright band*. Ph. D. thesis, University of Bradford, Bradford, UK.

Hou, A. Y., Kakar, R. K., Neeck, S., Azarbarzin, A. A., Kummerow, C. D., Kojima, M., Oki, R., Nakamura, K., & Iguchi, T. (2014). The Global Precipitation Measurement Mission. *Bulletin of the American Meteorological Society, 95*, 701–722. https://doi.org/10.1175/BAMS-D-13-00164.1.

Houze, R. A. (1997). Stratiform precipitation in regions of convection: A meteorological paradox? *Bulletin of the American Meteorological Society, 78*, 2179–2196. https://doi.org/10.1175/1520-0477(1997)078<2179:SPIROC>2.0.CO;2.

Iguchi, T., Seto, S., Meneghini, R., Yoshida, N., Awaka, J., Le, M., Chandrasekar, V., & Kubota, T. (2017). GPM/DPR level-2 algorithm theoretical basis document, JAXA-NASA Tech. Rep., 81 pp. [Available online at https://pmm.nasa.gov/resources/documents/gpmdpr-level-2-algo rithm-theoretical-basis-document-atbd. Last accessed 9 Oct 2018]

Klaassen, W. (1988). Radar observations and simulation of the melting layer of precipitation. *Journal of the Atmospheric Sciences, 45*, 3741–3753. https://doi.org/10.1175/1520-0469 (1988)045<3741:ROASOT>2.0.CO;2.

Kulie, M. S., & Bennartz, R. (2009). Utilizing space borne radars to retrieve dry snowfall. *Journal of Applied Meteorology and Climatology, 48*, 2564–2580. https://doi.org/10.1175/ 2009JAMC2193.1.

Le, M., & Chandrasekar, V. (2013a). Precipitation type classification method for Dual-Frequency Precipitation Radar (DPR) onboard the GPM. *IEEE Transactions on Geoscience and Remote Sensing, 51*, 1784–1790. https://doi.org/10.1109/TGRS.2012.2205698.

Le, M., & Chandrasekar, V. (2013b). Hydrometeor profile characterization method for dual-frequency precipitation radar Onboard the GPM. *IEEE Transactions on Geoscience and Remote Sensing, 51*, 3648–3658. https://doi.org/10.1109/TGRS.2012.2224352.

Le, M., & Chandrasekar, V. (2019). Ground validation of surface snowfall algorithm in GPM dual-frequency precipitation radar. *Journal of Atmospheric and Oceanic Technology*. https://doi.org/ 10.1175/JTECH-D-18-0098.1.

Le, M., Chandrasekar, V., & Biswas, S. (2017). An algorithm to identify surface snowfall from GPM DPR observations. *IEEE Transactions on Geoscience and Remote Sensing, 55*, 4059–4071. https://doi.org/10.1109/TGRS.2017.2687420.

Smyth, T. J., & Illingworth, A. J. (2006). Radar estimates of rainfall rates at the ground in bright band and non-bright band events. *Quarterly Journal of the Royal Meteorological Society, 124*, 2417–2434. https://doi.org/10.1002/qj.49712455112.

Tan, J., & Goddard, J. W. F. (1995). The use of dual-polarisation techniques for bright-band detection with PPI-based radars. In *IEEE Colloquium on Radar Meteorology*, 11/1–11/6. https://doi.org/10.1049/ic:19950204.

Tilford, K. A., Cluckie, I. D., Griffith, R. J., & Lane, A. (2001). Vertical reflectivity characteristics and bright band correction. In *Radar Hydrology for Real Time Flood Forecasting, Proceedings of an advanced course*, 47–65, European Communities.

Zrnić, D. S., Raghavan, R., & Chandrasekar, V. (1994). Observations of copolar correlation coefficient through a bright band at vertical incidence. *Journal of Applied Meteorology, 33*, 45–52. https://doi.org/10.1175/1520-0450(1994)033<0045:OOCCCT>2.0.CO;2.

Chapter 13
Triple-Frequency Radar Retrievals

Alessandro Battaglia, Simone Tanelli, Frederic Tridon, Stefan Kneifel, Jussi Leinonen, and Pavlos Kollias

Abstract With triple frequency radars becoming more and more popular both at ground-based facilities and on airborne platforms and with the prospect of a space mission with a triple-frequency radar payload on the horizon, triple-frequency radar retrievals are becoming fertile areas of active research. In this chapter the benefits and potentials of a triple-frequency radar approach for retrieving rain and ice microphysics will be discussed first on a theoretical basis and then demonstrated for a stratiform case study extracted from the OLYMPEX field campaign with Ku-Ka-W band radar observations. Challenges and recommendations for future work are included in the chapter.

Keywords Precipitation · Rainfall · Snow · Hydrometeors · Phase · Aircraft · OLYMPEX · Satellite · Radar · Reflectivity · Attenuation · Drop size distribution · Cloud resolving model · GPM · DPR · CloudSat · CPR · Path integrated attenuation · T-matrix · Rayleigh scattering · Dual frequency ratio · Non-uniform beam filling · Triple frequency radar.

A. Battaglia (✉)
Department of Physics and Astronomy, University of Leicester, Leicester, UK
e-mail: ab474@le.ac.uk

S. Tanelli · J. Leinonen
Jet Propulsion Laboratory (JPL), California Institute of Technology, Pasadena, CA, USA

F. Tridon
Earth Observation Science, Department of Physics and Astronomy, University of Leicester, Leicester, UK

S. Kneifel
Institute for Geophysics and Meteorology, University of Cologne, Cologne, Germany

P. Kollias
School of Marine and Atmospheric Sciences, Stony Brook University, Stony Brook, NY, USA

13.1   Introduction

In order to adequately understand the role of clouds and precipitation and improve their representation in numerical models, global-scale satellite measurements of cloud microphysics and dynamics are required to complement detailed ground-based process studies on all scales important to cloud formation, evolution and dissipation (Bony et al. 2006). Contrary to the case for infrared and visible, micro-wave radiation can penetrate deep convective systems and profile the interior of a precipitating system. Multi-frequency radars are considered the gold standard for clouds and precipitation observations because they offer unmatched vertical profil-ing capabilities and they have the potential to provide a holistic view of cloud-precipitation processes. In addition, by providing improved microphysical charac-terization of the different hydrometeors in the column, they promise to shed light into the "processes" operating within the atmosphere which link clouds to precipi-tation. For instance, accurate measurements of Drop Size Distributions (DSD) are fundamental for understanding the processes (e.g., coalescence, evaporation and droplet breakup) governing cloud microphysics and improving liquid precipitation representation in numerical models. Similarly, Cloud Resolving Models (CRM) tend to incorrectly represent ice microphysical processes (e.g., deposition, aggregation and riming), inducing significant inaccuracies in the partitioning between liquid and ice water species, the depth of the mixed-phase cloud region, the vertical redistri-bution and location of ice and liquid water, and upper-level detrainment of water vapor. A huge effort has been dedicated by modelers to better describing such processes in CRMs by using two-moment or spectral microphysics schemes (e.g., Seifert and Beheng 2001; Morrison and Grabowski 2007; Kumjian and Prat 2014). Improved observations and retrievals are required for evaluating the enhanced complexity of microphysics schemes both from the ground and from space. This premise calls for a paradigm shift away from current systems that largely observe microphysical variables to future observing systems that can in addition capture snapshots of "processes". Triple-frequency radar systems can play a key role in this area by providing unique observations that can be used to verify models of cloud-precipitation processes.

13.1.1   Why Triple-Frequency Radars?

Figure 13.1, which depicts almost coincident observations from the CloudSat CPR (see Chap. 2) and the GPM DPR (see Chap. 1), epitomizes the potential of spaceborne multi-frequency radar observations of the same precipitating system. Two aspects of the multi-frequency approach are paramount.

Complementarity: cm and mm-radars are effective in mapping different parts of the precipitating system. Thanks to its better sensitivity compared to the GPM DPR, the CloudSat CPR is capable of detecting the high cloud structure, the anvil
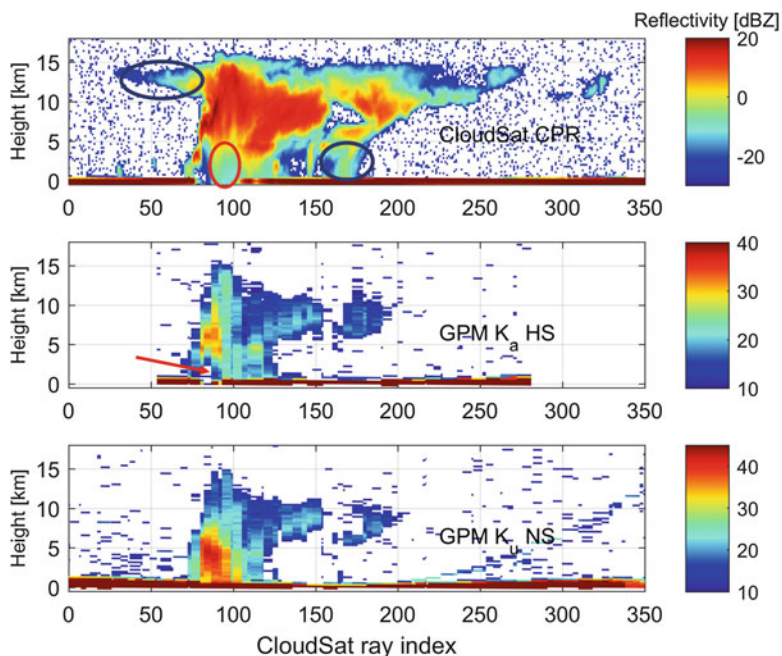
Fig. 13.1 CloudSat and GPM coincident overpass observations of a convective precipitation system developed over the Banda Sea in the Maluku Islands of Indonesia. Measurements from a suite of microwave sensors are shown. Top row: CloudSat W-band reflectivity; second row: GPM Ka-band reflectivities for the high sensitivity (HS) scan; third row: GPM Ku-band reflectivity for the normal scan (NS). The dataset of coincident overpasses is from the GPM product 2B-CSATGPM from the NASA Precipitation Processing System developed by J. Turk, JPL

outflow and the region of lighter stratiform precipitation (black circles). On the other hand, because of its much higher attenuation, the CPR signal is strongly affected by attenuation and multiple scattering[1] in the most intense part of precipitation (i.e., where even the Ka-GPM observations are fully attenuated, red circle).

Synergy: in the regions where they all produce detectable signals cm and mm radars can be used synergistically in order to better retrieve cloud microphysical properties. For instance, in Fig. 13.1 the large-ice and low-precipitation regions are detected both by the DPR and by the CPR. The signal detected by these radars is the result of the complex interplay between non-Rayleigh and attenuation effects. If the attenuation of the signal from one of the radars becomes too strong[2] then the signal vanishes below the minimum detection threshold.

---

[1]This effect is identified by the absence of a detectable surface peak, see detailed discussion in Battaglia and Simmer (2008), Battaglia et al. (2010).

[2]In a retrieval study Battaglia et al. (2016a) identified as a rule of thumb the condition that the optical thickness from the radar to the target whose properties must be retrieved should not exceed three units (i.e., a two-way attenuation of less than ~25 dB). Above such levels, attenuation corrections become prohibitive.

Unfortunately, such observations are currently available only during "coincident overpasses" of the CloudSat and GPM-core satellites (e.g., for the example shown in Fig. 13.1 there is a 319 s gap between the two satellite observations). Since the latest Decadal Survey (2017) conducted by the US National Academy of Sciences adopts Ku-Ka and W band frequencies as a baseline for the Cloud and Precipitation Process (CCP) mission, these three frequency bands will be the focus of this chapter.

Leinonen et al. (2015) studied in detail the complementarity and synergy of a triple-frequency radar for global cloud and precipitation observations with detection levels enhanced with respect to current capabilities (see also discussion in Sect. 13.1.1.1). They found (see their Fig. 4) that for a 450-km orbit a third of the whole system is only detected by W-band, a quarter by the Ka-W and 38.5% by the triple-frequency Ku-Ka-W. This latter percentage tends to increase when moving away from the top of the cloud, e.g. it is 49% at 3 °C and 54% at −15 °C. This highlights the potential benefit of retrievals techniques capable of fully exploiting triple-frequency observations.

The premise of all multi-wavelength retrievals is that the scattering properties of mm- and cm-size particles strongly depend on the wavelength of the impinging electromagnetic radiation. Radar-measured reflectivity factors (Z_m) at range r and at frequency f are the result of intrinsic effective reflectivity factors[3] (Z_e) within the backscattering volume and of attenuation (α) between the radar transmitter/receiver and the target:

$$Z_{m,f}(r) = Z_{e,f}(r) - 2\int_0^r \big(\alpha_f(s)\big)ds. \tag{13.1}$$

where reflectivities are in dBZ and attenuation in dB units. Thus, Z_m at different frequencies may differ because of:

(a) the effective reflectivity factors of the targets; this becomes relevant when the hydrometeor sizes are comparable to the radar wavelength (i.e., in the presence of "non-Rayleigh effect", (Bohren and Huffman 1983; Lhermitte 1990);

(b) the attenuation properties of the medium, with higher attenuation produced at higher frequencies (Lhermitte 1990).

The contribution of these two sources in dual frequency ratios (DFR), defined as the ratio of reflectivity factor measurements in linear units (or, like here, their difference in logarithmic units) from two radars operating at different frequencies f_1 and f_2 ($f_1 < f_2$), can be written as:

---

[3]Hereafter we use the following convention of effective reflectivity factor:

$Z_{e,\lambda}(r) = \frac{\lambda^4}{\pi^5|K|^2}\eta(r)$

where η is the radar reflectivity, λ is the radar wavelength and $|K|^2 = 0.93$. With this definition small ice particles have the same Z_e (e.g., Hogan et al. 2006).

$$DFR_{f_1,f_2}(r)[dB] \equiv Z_{m,f_1}(r) - Z_{m,f_2}(r) = \underbrace{Z_{e,f_1}(r) - Z_{e,f_2}(r)}_{Non-Rayleigh\ effect} + \underbrace{2\int_0^r (\alpha_{f_2}(s) - \alpha_{f_1}(s))ds}_{Attenuation\ effect}.$$

$$(13.2)$$

The two differential terms on the right-hand side can provide PSD information beyond the simple Rayleigh radar reflectivity factor (which is proportional to the sixth moment of the PSD) of a profoundly different nature, with non-Rayleigh effects, useful in gauging intensive quantities (e.g., characteristic size) and attenuation effects, useful for deducing extensive quantities (e.g., rain rate or water content). Because of the complexity of disentangling non-Rayleigh and attenuation effects, dual-frequency retrieval algorithms typically have been developed for regimes where one effect is dominant. For instance, Hogan et al. (2005) and Ellis and Vivekanandan (2011) have proposed dual-wavelength differential attenuation methods for the estimation of the cloud, drizzle, or light rain liquid water content while Matrosov (1998), Wang et al. (2005) and Liao and Meneghini (2011) have exploited non-Rayleigh effects for sizing and for hydrometeor classification in snow and ice clouds. Radar observations at three (or more) frequencies have the potential to be effective in retrieving microphysical properties for a larger gamut of cloud and precipitation regimes where the simultaneous presence of both attenuation and non-Rayleigh effects can substantially complicate the inversion process.

13.1.1.1   Why a Triple-Frequency Approach for Rain?

Raindrops increasingly behave as non-Rayleigh targets when moving from Ku to W band (see Fig. 2 in Tridon and Battaglia 2015) with the single particle backscattering cross sections deviating from Rayleigh dependence (proportional to the sixth power of the diameter) and exhibiting consecutive maxima and minima. At Ka the first maximum (minimum) is localized close to a radius of 1.8 mm (2.3 mm) while at W-band the first maximum (minimum) appears at 0.6 mm (0.85 mm) followed by a second maximum (minimum) at 1.2 mm (1.45 mm). Radar reflectivities tend to decrease with increasing frequency with the only exception being the Ku-Ka pair for raindrops with radii lower than 1.1 mm. This implies that increasing DFRs correspond to larger sizes (e.g., see Figure 1 in Gaussiat et al. 2003, or Figure 8 in Battaglia et al. 2016a). The left panel in Fig. 13.2 demonstrates the possibility of retrieving a characteristic size (mean mass-weighted diameter) and the shape parameter, μ, of Γ-parameterized DSD (Ulbrich 1983) if triple-frequency radar measurements are available and effective DFRs for the pair K_u-K_a and K_a-W can be derived. Clearly having only knowledge of DFR_{Ku-Ka} leaves ambiguities relating to the bifurcation of the curves for different shape parameter at $D_m > 1$ mm but also in the region where $DFR_{Ku-Ka} < 0$ (see Chap. 11). The addition of W-band helps in disentangling such ambiguities, particularly in the region of $D_m < 1.5$ mm.
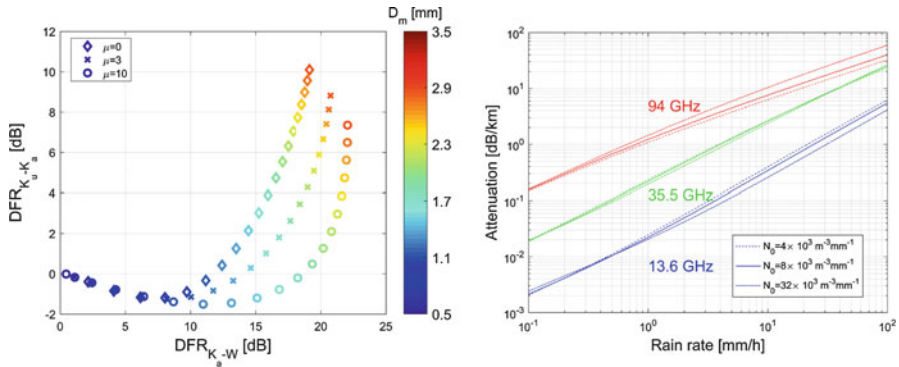
Fig. 13.2 Left: effective DFR$_{Ka-W}$ vs DFR$_{Ku-Ka}$ for population of raindrops at 15 °C with Γ DSDs with different μ as indicated in the legend and with color-coded mean mass-weighted diameter. Right: extinction coefficient vs rain rate for exponential DSDs with intercept parameters as indicated in the legend. Scattering properties are computed using T-matrix

The main obstacle to performing such a triple-frequency retrieval resides however in the assumption that effective DFR can be derived from the measurements, i.e. that the attenuation term on the right-hand side of Eq. 13.3 can be corrected for. In fact, as shown in the right panel of Fig. 13.2, attenuation increases rapidly with frequency and with rain rate and can be challenging to account for, not to say that it can drive the radar received power from ranges beyond heavy rain layers into the noise level (e.g., for the Ka band in correspondence with the red arrow in Fig. 13.2). Additional sources of attenuation (e.g., caused by cloud liquid droplets or melting particles, Matrosov 2008) can further add complication to the problem. Though the Ku-band radar reflectivity can be used to correct the Ka- and W-band signals, integral constraints are highly desirable to stabilize the inversion problem (L'Ecuyer and Stephens 2002; Haynes et al. 2009). Examples of these are provided by radar path-integrated attenuations (PIA), typically derived by the surface reference technique, and by radiometer brightness temperatures (TBs). Of course, attenuation itself, which often dominates the vertical gradient of reflectivity observed in rain at mm-wavelengths, can be used as a source of information, e.g. for estimating rainfall rate. In fact, especially at Ka-band (green lines in Fig. 13.2), attenuation is almost linearly proportional to rain rate (Matrosov 2005; Matrosov et al. 2006; Giangrande et al. 2010).

13.1.1.2 Why a Triple-Frequency Approach for Ice?

The basic idea of using multi-frequency for ice and snow is similar to the concept described for rain: when combining frequencies for which different parts of the size distribution transition from the Rayleigh to the non-Rayleigh scattering regime, Z_e of the frequency which is more affected by non-Rayleigh scattering will be reduced. While for Rayleigh scattering all components of the particle experience the same

electric field of the impinging wave, in the non-Rayleigh scattering regime, resonance effects inside the particle lead in general to a less than the square of the particle mass increase of the backscattering cross section. For rain drops, the shape as function of size as well as the refractive index of liquid water is well defined. Hence, the effective DFR is mainly dependent on the PSD parameters. For ice and snow particles, neither the shape nor the overall effective refractive index of the ice-air mixture is well defined. Early studies (Matrosov 1992, 1998) approximated snowflakes with a spheroidal shape and calculated the effective refractive index of the ice-air mixture with an effective medium approximation (see also Chap. 15). Interestingly, this leads to a very small sensitivity of the DFR to density and aspect ratio so that the DFR should be usable to infer the characteristic size of the PSD. Unfortunately, this insensitivity to density and shape seems to disappear once more realistic representations of snowflakes are used (Kneifel et al. 2011). In their theoretical analysis of aggregates (Petty and Huang 2010), single ice crystals (Liu 2008) and spheroidal scattering approximations for Ku, Ka, and W-Band, they found large uncertainties introduced in the PSD parameters derived from standard DFR. However, once three frequencies are combined, a separation between aggregates and the more spheroidal shapes appears. The typical hook signature of low-density aggregates in combination with the more slowly increasing signature of denser and more spherical particles (e.g., graupel) was confirmed by other theoretical studies using a large variety of snowflake scattering computations (Leinonen et al. 2012; Tyynelä and Chandrasekar 2014; Leinonen and Moisseev 2015; Leinonen and Szyrmer 2015; Stein et al. 2015). First triple-frequency observations from airborne platforms (Leinonen et al. 2012; Kulie et al. 2014) confirmed the existence of the main signatures predicted by the scattering models. The first observational evidence of a direct link between these triple-frequency signatures and snow particle properties was provided by a comparison of ground-based triple-frequency observations and collocated in-situ observations (Kneifel et al. 2015). The triple-frequency signatures revealed the expected dependence on characteristic size of the PSD but also a sensitivity to the overall particle density. It is important to note that shape (an intrinsically ambiguous defined property) and overall density are often connected (e.g., in case of riming). Currently, the available scattering datasets (see Chap. 15 for a detailed overview) are still unable to fully cover the observed range of triple-frequency signatures (see for instance Fig. 13.3 where several scattering models have been used, details in Tridon et al. (2019). However, in order to quantify the sensitivity and added value of triple-frequency observations for PSD and density retrievals using e.g. optimal estimation methods, a representative set of scattering computations is key.

13.2 Triple-Frequency Datasets

Airborne cloud and precipitation radar data have been acquired since the 1980s in support of mission concepts such as TRMM, CloudSat and then GPM. A majority of these datasets were acquired by single-band or dual-band radar systems in such as
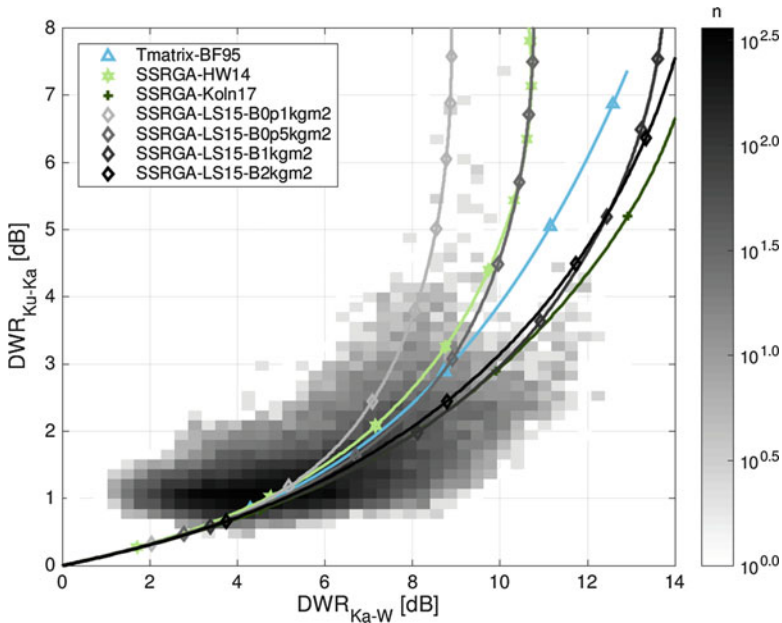
Fig. 13.3 Effective DFR$_{Ka-W}$ vs DFR$_{Ku-Ka}$ for population of ice crystals computed different scattering tables. The density plots show the distribution measured by a triple-frequency radar during one of the GPM field campaigns

ARMAR, ELDORA/ASTRAIA, EDOP, CRS, ACR, and others (e.g., Durden et al. 1994; Hildebrand et al. 1993; Heymsfield et al. 1996). In a few experiments some of these instruments were positioned on the same airborne platform, and one experiment in particular received significant attention in the last decade for the specific purpose of exploring the value of triple-frequency radar measurements: the Wakasa Bay experiment conducted in 2003 as part of a joint campaign by NASA and JAXA to validate the Aqua products. In that experiment the APR-2 (Ku- and Ka-band, Sadowy et al. 2003) and the ACR (W-band (Sadowy et al. 1997) were installed in the forward and aft sections of the NASA P-3, respectively. The resulting dataset, has been analyzed in the context of triple-frequency retrievals mainly to investigate the value of such measurements in reducing the ambiguities associated with the retrieval of frozen hydrometeors (e.g., the previously mentioned "hook feature" in the DFR_{Ka-W} vs DFR_{Ku-Ka} plane). While small airborne datasets of 3 or even 4 radar frequencies were acquired during other field experiments (e.g., TC4, Costa Rica 2007; see Toon et al. 2010; Jensen et al. 2009) by flying in formation two aircrafts carrying cloud or precipitation radars operating at different bands, the community had to wait until IPHEX/RADEX14 for the next extensive dataset of multi-frequency airborne radar data. IPHEX (Integrated Precipitation and Hydrology Experiment, https://pmm. nasa.gov/iphex, last accessed 11 Oct. 2018) was planned for 2014 as part of the GPM Ground Validation program with a primary complement of ground-based

radars and airborne in situ instruments. During its early definition phases, the ACE (Aerosol/Clouds/Ecosystem) mission concept Science Working Group identified it as an excellent opportunity to synergistically pursue overlapping needs linking cloud and precipitation science and supported its augmentation (as RADEx'14, the first ACE Radar Definition Experiment) that enabled acquisition of a new extensive dataset of multi frequency radar data by including on the ER-2 payload three radars: EXRAD (X-band), HIWRAP (Ku- and Ka-band in nadir pointing configuration) and CRS (W-band) and a number of other active and passive sensors to simulate candidate measurements by the ACE mission concept. Two key new elements were introduced by this dataset with respect to Wakasa Bay: the completely different range of cloud and precipitation systems, and the addition of X-band data to the collocated measurements. As a result, the focus of this dataset insofar has been mostly on deep convective systems (e.g., Battaglia et al. 2016a) and warm rain or cumulus congestus. The collaboration between GPM GV and ACE SWG continued to grow even as IPHEX/RADEX'14 was still in its planning stages, and a second major joint effort was conducted in November/December 2015 when the OLYMPEX field experiment (Houze et al. 2017) originally selected within the GPM GV was also augmented by ACE to deliver what is the most extensive (to date) dataset of triple-frequency airborne cloud and precipitation radar data. Three aircraft participated in OLYMPEX/RADEx'15 (Radar Definition Experiment): the NASA DC-8 carrying the APR-3 triple-frequency scanning radar (Ku-, Ka- and W-band), the NASA ER-2 carrying the EXRAD, HIWRAP and CRS, and the University of North Dakota Citation flying under them with cloud probes. The DC-8 and ER-2 also included a number of passive sensors for microwave and polarimetric observations of clouds and precipitation. This dataset includes a large amount of airborne observations of clouds and precipitation in prefrontal, frontal and post-frontal regimes, either over ocean or in the context of significant orographic effects induced by the Olympic mountains. Many instances of multi-frequency airborne radar observations are augmented with collocated and simultaneous in situ sampling by the Citation. The dataset is also characterized by the availability of a vast amount of ground-based data spanning from radars to in situ measurements, and is actively studied by several research groups on a number of topics (e.g., Heymsfield et al. 2018; Chase et al. 2018; Tridon et al. 2019). Extensive ground-based datasets of triple frequency observations have also been collected in several ARM field campaigns such as the Biogenic Aerosols – Effects on Clouds and Climate (BAECC) campaign (Petäjä et al. 2016) with comprehensive in-situ ground observations, and the ARM West Antarctic Radiation Experiment (AWARE, https://www.arm.gov/research/campaigns/amf2015aware, last accessed 11 Oct. 2018), with the first triple frequency dataset in Antarctica. Other supersites (e.g., Chilbolton and Jülich) conducted several measurement campaigns and plan to continuously record triple frequency data (Stein et al. 2015). These long-term datasets could shed more light on certain aspects that cannot be monitored by airborne data.

13.3 Triple-Frequency Retrievals

The development and testing of triple-frequency retrieval are relatively new because of the only recent availability of triple-frequency airborne radar observation datasets. When attenuation severely affects the higher frequency channels (as in the presence of supercooled liquid or heavily rimed precipitation and/or when the microphysical retrieval is run for the entire precipitation column) triple-frequency retrievals are based on optimal estimation (L'Ecuyer and Stephens 2002; Grecu et al. 2011; Mason et al. 2017) approaches, which disentangle non-Rayleigh and attenuation effects by optimizing a cost function via an iterative process based on a forward model radar operator (e.g., Haynes et al. 2007; Hogan and Battaglia 2008; Battaglia et al. 2016a). Bayesian approaches have also been recently developed for retrieving ice only microphysics under the assumption that effective reflectivities can be recovered (Leinonen et al. 2018)). But to date only few have been applied to three (or more) frequency radar observations (Battaglia et al. 2015, 2016a, b; Leinonen et al. 2018).

An example of an optimal estimation retrieval applied to the data collected by the Airborne Third Generation Precipitation Radar (APR-3; Sadowy et al. 2003) flown on board the NASA DC-8 aircraft during the OLYMPEX field campaign (details in Houze et al. 2017) and shown in Fig. 13.4 is depicted in Fig. 13.5. Results are presented for two different retrieval methodologies. The first is the method proposed
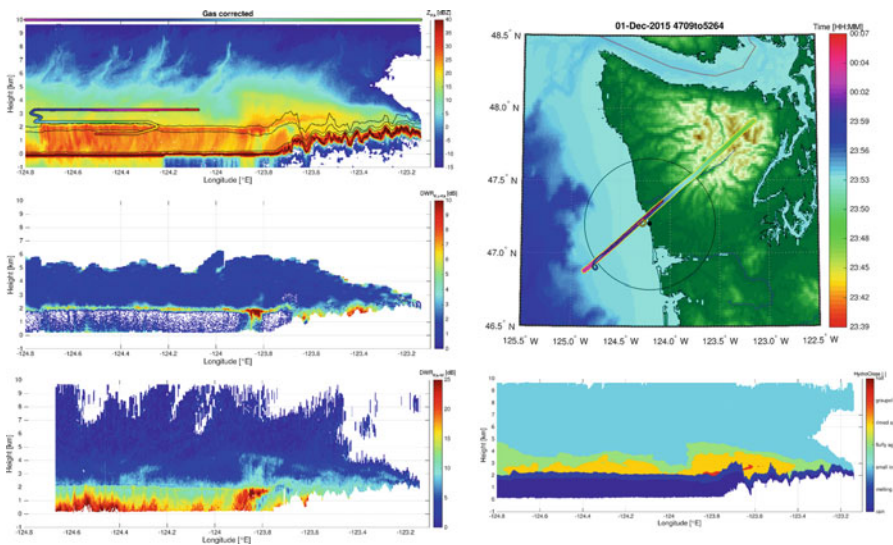
Fig. 13.4 Left: gas-corrected Ka-band reflectivity (top), DFR_{Ku-Ka} (center) and DFR_{Ka-W} (bottom) for a flight on the 1 December 2016. Right top: flight tracks across the Olympic Peninsula from the Olympic Mountains range toward and beyond the NPOL radar (black dot) on the Pacific coastline. The UTC time of DC-8 (external contour) and Citation (internal contour) aircraft paths are modulated in color (see color bar). The position of the Citation is shown in the top left panel. Right bottom: hydrometeor classification according to the multi-frequency method of Tridon et al. (2019)
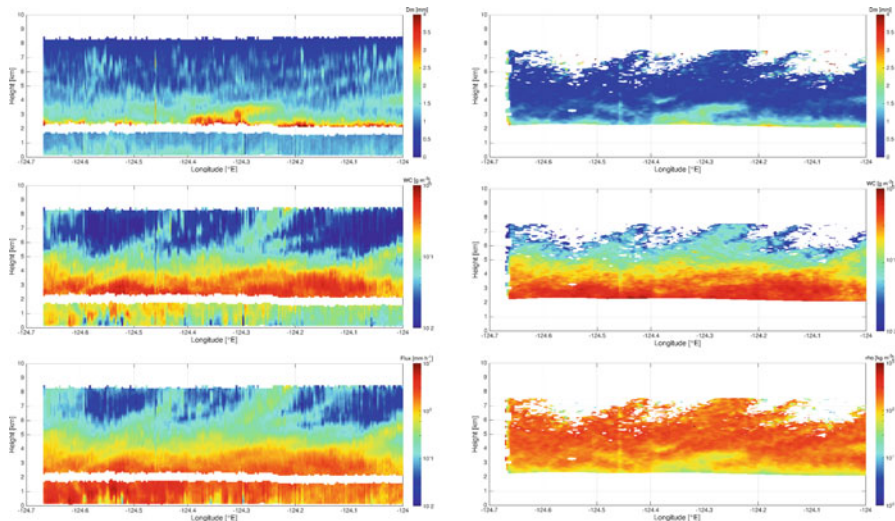
Fig. 13.5 Retrieved parameters for the leg shown in Fig. 13.4: mean mass-weighted maximum size (top), IWC (center) and flux (bottom). The right bottom panel shows the bulk ice density as defined in Leinonen et al. (2018)

in Tridon et al. (2019) (referred as "TRI18") and it is applicable to the whole precipitation column (left column panels) with the only exception of the melting layer (white band). A preliminary classification mask allows the identification of ice, melting and rain region (bottom right panel in Fig. 13.4) and a rough categorization of the different types of ice. Only results for one scattering model, the lightly rimed B-model with LWP = 100 g m^{-2} proposed by Leinonen and Szyrmer (2015), are shown here (left panels). Such model was found to be the best one for reconciling in-situ and radar remote sensing measurements for the whole campaign. The second is the retrieval described in Leinonen et al. (2018) (referred as "LEI18"), which is applicable only for the ice phase and uses lookup tables mapping the measurement space to the state space (right column). Microphysics are illustrated in terms of mean mass weighted particle size (top panels) and equivalent water content (center panels). The bulk ice density as defined in Leinonen et al. (2018) (bottom right) clearly shows a vertical evolution of ice particles from bulk ice density at the top of the cloud (small ice crystals) to much smaller densities corresponding to fluffier snowflakes close to the freezing level. From a direct comparison of the two retrievals it is clear that LEI18 is producing ice particles smaller than TRI18 and slightly larger ice water contents. Figure 13.5 also shows that for the full-column retrieval (left) there is reasonable flux continuity between the top and the bottom of the melting level (bottom panel).

In situ validation data are provided by the Citation that was flying below the DC-8 (track highlighted in the top panels of Fig. 13.4). An intercomparison between in-situ and retrieved microphysical properties in the ice part for the upper leg is shown in Fig. 13.6. The retrieved values are comparable but it remains challenging, given the
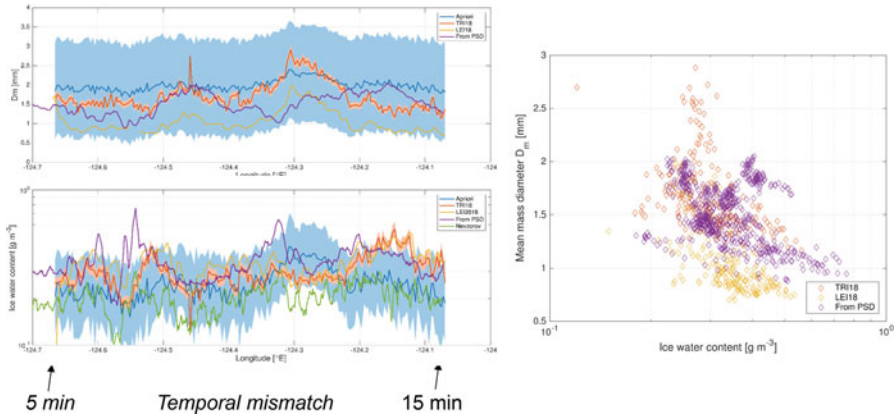
Fig. 13.6 Comparison between in-situ and retrieved microphysical properties as sample by the Citation aircraft in the ice part corresponding to the upper leg as shown in Fig. 13.4. Left column: mean mass weighted particle size (top) and ice water content (bottom) for the in-situ and for the two retrievals considered in this paper. The blue lines and the blue bands correspond to the a-priori and its standard deviation. Right panel: scatterplot of IWC vs D_m for the in-situ and for the two retrievals. Note that the in-situ D_m and IWC are derived from the PSD measurements based on the assumption that the mass-size follows that of lightly rimed B-model of Leinonen and Szyrmer (2015)

uncertainties in the in-situ measurements and the co-location/sampling issues, to draw definitive conclusions about the quality of the two retrievals.

13.4 Critical Issues and Open Questions

As discussed in previous sections, there is a growing body of literature that deals with the numerical computation and evaluation of the appropriate scattering libraries especially for non-spherical particles, the development of appropriate a priori conditions and the introduction of physically-based parameterizations that connect the radar observables to the microphysical parameters of interest. However, conducting dual- and triple-wavelength radar observations from spaceborne (GPM-DPR), airborne (Battaglia et al. 2016a) and ground-based (Kneifel et al. 2015; Stein et al. 2015) platforms requires trades-off that can affect quality and information content of the multi-wavelength radar observations. High quality multi-wavelength radar observations require matched sampling volumes to address the large natural variability of precipitation microphysics and sufficient number of samples and signal-to-noise conditions to reduce the error in the reflectivity measurements for all the radars.

Although we have seen synergistic data products from radar and lidar observations performed from different spaceborne platforms (CloudSat-Calipso, Delanoë

and Hogan 2010), multi-wavelength radar observations should be conducted from the same platform using the same antenna. The error in Dual-Wavelength Ratio (DWR) from radars that use noncoincident footprints can be very large (2–3.5 dB), thus significantly affecting the interpretation of the multi-wavelength radar observations for deriving particle size information (Hogan et al. 2000). The DPR offers an example of volume matched dual-wavelength radar observations. Due to size restrictions in space, the matched antenna beamwidth (0.71°) is controlled by the lower radar frequency (Ku-band) and results to a 5-km footprint in the troposphere. Furthermore, the vertical resolution (250 m) is also controlled by the minimum detectable signal requirement for the Ku-band radar. Thus, the requirement for matched sampling volumes comes at the expense of reducing the performance of the higher frequency radar. In addition, the large DPR matched sampling volume (250 m vertical, 5000 m horizontal) is inherently a problem because of the large variability in the radar reflectivity field (the so called non-uniform beam filling (NUBF) conditions). Hogan et al. (2000) attempted to assess the impact of the selected sampling volume on the quality of the DWR measurements using the horizontal structure function of the radar reflectivity field as estimated from ground-based observations and their conclusion was that the error in ice clouds can be ≤0.2 dB for frequency combinations that include 35-GHz and higher frequencies. One way to demonstrate the NUBF conditions for different sampling volumes is to estimate the single radar frequency (Ka-band) standard deviation within different sampling volumes as depicted by high spatiotemporal observations from ground- and air-based observations using higher resolution observations. As expected, at coarser resolution, the standard deviation increases. The averaging effect of the sampling volume affects also the observed pdfs of radar reflectivity at different wavelengths and of the DFR. This change on the absolute magnitude of the DFR translates into an error in the retrieval of the particle size: on average, the simultaneous sampling of high and low radar reflectivity areas causes a shift of the radar DFR pdfs towards lower values, thus, shifting the retrieved particle size distributions towards lower sizes, as demonstrated in Fig. 13.7.

Another factor to consider that affects the quality of DFR measurements is the uncertainty in the radar reflectivity estimate at low signal-to-noise ratio (SNR) conditions and/or at small number of independent samples M_I. The uncertainty of radar reflectivity measurement (ΔZ), Hogan et al. (2000), is approximately equal to:

$$\Delta Z \,[dB] = \frac{4.343}{\sqrt{M_I}}\left(1 + \frac{1}{SNR}\right) \tag{13.3}$$

Assuming that the random error in Z_{f_1} and Z_{f_2} is independent, the uncertainty of DFR can be estimated as: $\sqrt{\Delta Z_{f_1}^2 + \Delta Z_{f_2}^2}$. Thus, the error in the DFR measurements is controlled by the radar with lower sensitivity. Let's assume a single pulse noise level of -10 dBZ for a future Ka-band spaceborne radar system and $M = 200$ averaging samples. At typical PRFs, due to the large Doppler fading introduced by platform motion, all the samples are independent ($M = M_I$), so that the uncertainty in

Fig. 13.7 Shift of the retrieved particle size distributions towards lower sizes. Figure prepared by L. Pfitzenmaier (see Pfitzenmaier et al. 2019 for details)
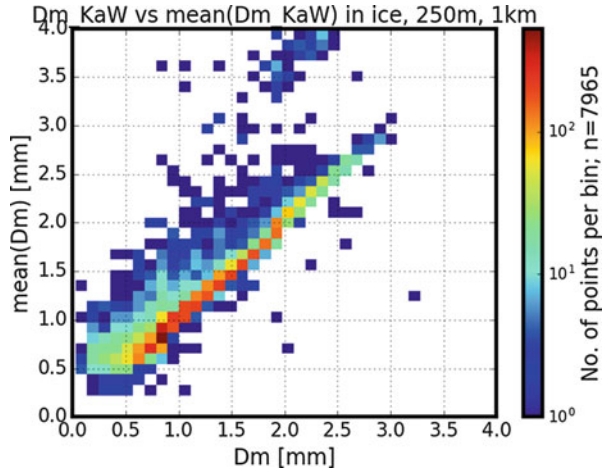
the radar reflectivity measurements (ΔZ) is 3.3781, 0.6142, 0.3378, and 0.3102 dB for SNR values of -10, 0, 10, 20 dB. Thus, SNR values of $+10$ dB or higher (i.e., reflectivities higher than 0 dBZ) are required to reduce the DFR error below 0.35 dB.

Apart from the impact of NUBF and of the noise into triple-frequency retrievals other questions remain to be answered.

1. Doppler capabilities could be added to the next generation of multi-frequency space-borne radars. This will enable a direct link to the cloud dynamics (e.g., via mass fluxes) and should allow a deeper understanding of precipitation processes like riming, aggregation or evaporation/sublimation, a key leap forward for the improvement of cloud models.
2. Though Ku-Ka-W are generally recognized as the most comprehensive way forward for a holistic monitoring of cloud-precipitation processes from space other frequencies can offer unique insights in studying specific regimes. X-band space-borne radars, though presenting challenges due to increased antenna size and coarser spatial resolution, can enhance observations in deep convection cores and extreme precipitation where Ku systems can suffer from severe attenuation and multiple scattering (Battaglia et al. 2016a; Heymsfield et al. 2013). Similarly, ice and mixed-phase clouds can be better characterized if frequencies in the G-band are exploited (Hogan et al. 2000; Battaglia et al. 2014). Technological challenges (large antennas for X-band and larger transmitted powers for G-band) need to be overcome to accomplish these ideas.

13.5 Recommendations for Future Work

Triple-frequency retrievals are in their infancy. Progress can be made in several directions along these proposed research avenues.

1. Intercomparison studies between retrieval techniques developed by different research groups should be performed for golden cases (i.e., with in-situ validation). This could help to better assess the relevance of different a-priori assumptions, the validity of the scattering tables utilized in the retrieval, the uncertainties introduced by using different single scattering properties (see Chap. 15) and the impact of the uncertainties in the calibration and cross calibrations of the radars. This will implicitly establish whether retrieval errors are properly estimated.

2. In-situ validation studies are key to assess the performances of triple-frequency retrievals. New datasets are needed particularly in regions where the multifrequency signal is present, e.g. in rain or in presence of ice particles exceeding 1 mm, as typically found in the aggregation areas close to the melting level. Such in-situ measurements could also contribute in refining a-priori assumptions (e.g., how ice D_m and IWC at a given temperature are related to reflectivities and how they co-vary). In-situ measurements below the freezing level remain essential to validate full-column retrievals.

3. The effective benefits, potentials and limitations of triple- vs double- and single-frequency retrievals have not yet been fully unfolded, e.g. the improved accuracy of precipitation retrievals for triple-frequency systems in different regimes (light/moderate/heavy rain rain, snow,...) must be properly quantified. Moreover, the impact and added value of additional information like Doppler velocities and co-located brightness temperatures and/or PIA must be better understood.

References

Battaglia, A., & Simmer, C. (2008). How does multiple scattering affect the spaceborne W-band radar measurements at ranges close to and crossing the sea surface range? *IEEE Transactions on Geoscience and Remote Sensing, 46*(6), 1644–1651. https://doi.org/10.1109/TGRS.2008.916085.

Battaglia, A., Tanelli, S., Mroz, K., & Tridon, F. (2015). Multiple scattering in observations of the GPM dual-frequency precipitation radar: Evidence and impact on retrievals. *Journal of Geophysical Research, 120*, 4090–4101. https://doi.org/10.1002/2014JD022866.

Battaglia, A., Mroz, K., Lang, T., Tridon, F., Tanelli, S., Heymsfield, G., & Tian, L. (2016a). Using a multi-wavelength suite of microwave instruments to investigate the microphysical structure of deep convective cores. *Journal of Geophysical Research, 121*, 9356–9381. https://doi.org/10.1002/2016JD025269.

Battaglia, A., Mroz, K., Tridon, F., Tanelli, S., & Kirstetter, P.-E. (2016b). Multiple-scattering-induced "ghost echoes" in GPM-DPR observations of a tornadic supercell. *Journal of Applied Meteorology and Climatology, 55*, 1653–1666. https://doi.org/10.1175/JAMC-D-15-0136.1.

Battaglia, A., Tanelli, S., Kobayashi, S., Zrnić, D., Hogan, R., & Simmer, C. (2010). Multiple-scattering in radar systems: A review. *Journal of Quantitative Spectroscopy & Radiative Transfer, 111*(6), 917–947. https://doi.org/10.1016/j.jqsrt.2009.11.024.

Battaglia, A., Westbrook, C. D., Kneifel, S., Kollias, P., Humpage, N., Löhnert, U., Tyynelä, J., & Petty, G. W. (2014). G-band (140-220 GHz) atmospheric radars: New frontiers in cloud physics. *Atmospheric Measurement Techniques, 7*, 1527–1546. https://doi.org/10.5194/amt-7-1527-2014.

Bohren, C. F., & Huffman, D. R. (1983). *Absorption and scattering of light by small particles*. New York, 530 pp: Wiley. https://doi.org/10.1002/9783527618156.

Bony, S., Colman, R., Kattsov, V. M., Allan, R. P., Bretherton, C. S., Dufresne, J.-L., Hall, A., Hallegatte, S., Holland, M. M., Ingram, W., Randall, D. A., Soden, B. J., Tselioudis, G., & Webb, M. J. (2006). How well do we understand and evaluate climate change feedback processes? *Journal of Climate, 19*, 3445–3482. https://doi.org/10.1175/JCLI3819.1.

Chase, R. J., Finlon, J. A., Borque, P., McFarquhar, G. M., Nesbitt, S. W., Tanelli, S., Sy, O. O., Durden, S. L., & Poellot, M. R. (2018). Evaluation of triple-frequency radar retrieval of snowfall properties using coincident airborne in-situ observations during OLYMPEX. *Geophysical Research Letters, 45*. https://doi.org/10.1029/2018GL077997.

Delanoë, J., & Hogan, R. (2010). Combined CloudSat-CALIPSO-MODIS retrievals of the properties of ice clouds. *Journal of Geophysical Research, 115*, D00H29. https://doi.org/10.1029/2009JD012346.

Durden, S., Im, E., Li, F., Ricketts, W., Tanner, A., & Wilson, W. (1994). ARMAR: An airborne rain-mapping radar. *Journal of Atmospheric and Oceanic Technology, 11*, 727–737. https://doi.org/10.1175/1520-0426(1994)011<0727:AAARMR>2.0.CO;2.

Ellis, S. M., & Vivekanandan, J. (2011). Liquid water content estimates using simultaneous S and Ka band radar measurements. *Radio Science, 46*(2). https://doi.org/10.1029/2010RS004361.

Gaussiat, N., Sauvageot, H., & Illingworth, A. J. (2003). Cloud liquid water and ice content retrieval by multiwavelength radar. *Journal of Atmospheric and Oceanic Technology, 20*, 1264–1275. https://doi.org/10.1175/1520-0426(2003)020¡1264:CLWAIC¿2.0.CO;2.

Giangrande, S. E., Luke, E. P., & Kollias, P. (2010). Automated retrievals of precipitation parameters using non-Rayleigh scattering at 95 GHz. *Journal of Atmospheric and Oceanic Technology, 27*, 1490–1503. https://doi.org/10.1175/2010JTECHA1343.1.

Grecu, M., Tian, L., Olson, W. S., & Tanelli, S. (2011). A robust dual-frequency radar profiling algorithm. *Journal of Applied Meteorology and Climatology, 50*, 1543–1557. https://doi.org/10.1175/2011JAMC2655.1.

Haynes, J. M., L'Ecuyer, T., Stephens, G. L., Miller, S. D., Mitrescu, C., Wood, N. B., & Tanelli, S. (2009). Rainfall retrieval over the ocean with spaceborne W-band radar. *Journal of Geophysical Research: Atmospheres, 114*, D00A22. https://doi.org/10.1029/2008JD009973.

Haynes, J. M., Marchand, R. T., Luo, Z., Bodas-Salcedo, A., & Stephens, G. L. (2007). A multipurpose radar simulation package: QuickBeam. *Bulletin of the American Meteorological Society, 88*, 1723–1727. https://doi.org/10.1175/BAMS-88-11-1723.

Heymsfield, A., Bansemer, A., Wood, N., Liu, G., Tanelli, S., Sy, O., Poellot, M., & Liu, C. (2018). Toward improving ice water content and snow-rate retrievals from radars. Part II: Results from three wavelength radar collocated in situ measurements and CloudSat-GPM-TRMM radar data. *Journal of Applied Meteorology and Climatology, 57*, 365–389. https://doi.org/10.1175/JAMC-D-17-0164.1.

Heymsfield, G. M., Tian, L., Li, L., Mclinden, M., & Cervantes, J. (2013). Airborne radar observations of severe hail storms: Implications for future spaceborne radar. *Journal of Applied Meteorology and Climatology, 52*, 1851–1867. https://doi.org/10.1175/JAMCD-12-0144.1.

Heymsfield, G. M., Bidwell, S. W., Caylor, I. J., Ameen, S., Nicholson, S., Boncyk, W., Miller, L., Vandemark, D., Racette, P. E., & Dod, L. R. (1996). The EDOP radar system on the high-altitude NASA ER-2 aircraft. *Journal of Atmospheric and Oceanic Technology, 13*, 795–809. https://doi.org/10.1175/1520-0426(1996)013<0795:TERSOT>2.0.CO;2.

Hildebrand, P., Walther, C., Frush, C., Testud, J., & Baudin, F. (1993). The ELDORA/ASTRAIA airborne Doppler weather radar: Goals, design, and first field tests. *Proceedings of the IEEE, 82*, 1873–1990. https://doi.org/10.1109/5.338076.

Hogan, R. J., & Battaglia, A. (2008). Fast lidar and radar multiple scattering models: Part 2: Wide-angle scattering using the time-dependent two-stream approximation. *Journal of the Atmospheric Sciences, 65*, 3636–3651. https://doi.org/10.1175/2008JAS2643.1.

Hogan, R. J., Gaussiat, N., & Illingworth, A. (2005). Stratocumulus liquid water content from dual-wavelength radar. *Journal of Atmospheric and Oceanic Technology, 22*, 1207–1218. https://doi.org/10.1175/JTECH1768.1.

Hogan, R. J., Illingworth, A. J., & Sauvageot, H. (2000). Measuring crystal size in cirrus using 35- and 94-GHz radars. *Journal of Atmospheric and Oceanic Technology, 17*, 27–37. https://doi.org/10.1175/1520-0426(2000)017<0027:MCSICU>2.0.CO;2.

Hogan, R. J., Mittermaier, M. P., & Illingworth, A. J. (2006). The retrieval of ice water content from radar reflectivity factor and temperature and its use in the evaluation of a mesoscale model. *Journal of Applied Meteorology, 45*, 301–317. https://doi.org/10.1175/JAM2340.1.

Houze, R. A., Jr., McMurdie, L. A., Petersen, W. A., Schwaller, M. R., Baccus, W., Lundquist, J. D., Mass, C. F., Nijssen, B., Rutledge, S. A., Hudak, D. R., Tanelli, S., Mace, G. G., Poellot, M. R., Lettenmaier, D. P., Zagrodnik, J. P., Rowe, A. K., DeHart, J. C., Madaus, L. E., Barnes, H. C., & Chandrasekar, V. (2017). The Olympic Mountains experiment (OLYMPEX). *Bulletin of the American Meteorological Society, 98*, 2167–2188. https://doi.org/10.1175/BAMS-D-16-0182.1.

Jensen, E. J., Lawson, P., Baker, B., Pilson, B., Mo, Q., Heymsfield, A. J., Bansemer, A., Bui, T. P., McGill, M., Hlavka, D., Heymsfield, G., Platnick, S., Arnold, G. T., & Tanelli, S. (2009). On the importance of small ice crystals in tropical anvil cirrus. *Atmospheric Chemistry and Physics, 9*, 5519–5537. https://doi.org/10.5194/acp-9-5519-2009.

Kneifel, S., Kulie, M. S., & Bennartz, R. (2011). A triple-frequency approach to retrieve microphysical snowfall parameters. *Journal of Geophysical Research, 116*, D11203. https://doi.org/10.1029/2010JD015430.

Kneifel, S., von Lerber, A., Tiira, J., Moisseev, D., Kollias, P., & Leinonen, J. (2015). Observed relations between snowfall microphysics and triple-frequency radar measurements. *Journal of Geophysical Research, 120*, 6034–6055. https://doi.org/10.1002/2015JD023156.

Kulie, M. S., Hiley, M. J., Bennartz, R., Kneifel, S., & Tanelli, S. (2014). Triple-frequency radar reflectivity signatures of snow: Observations and comparisons with theoretical ice particle scattering models. *Journal of Applied Meteorology and Climatology, 53*, 1080–1098. https://doi.org/10.1175/JAMC-D-13-066.1.

Kumjian, M. R., & Prat, O. P. (2014). The impact of raindrop collisional processes on the polarimetric radar variables. *Journal of the Atmospheric Sciences, 71*, 3052–3067. https://doi.org/10.1175/JAS-D-13-0357.1.

L'Ecuyer, T. S., & Stephens, G. L. (2002). An estimation-based precipitation retrieval algorithm for attenuating radars. *Journal of Applied Meteorology, 41*, 272–285. https://doi.org/10.1175/1520-0450(2002)041<0272:AEBPRA>2.0.CO;2.

Leinonen, J., & Moisseev, D. (2015). What do triple-frequency radar signatures reveal about aggregate snowflakes? *Journal of Geophysical Research, 120*, 229–239. https://doi.org/10.1002/2014JD022072.

Leinonen, J., & Szyrmer, W. (2015). Radar signatures of snowflake riming: A modeling study. *Earth and Space Science, 2*, 346–358. https://doi.org/10.1002/2015EA000102.

Leinonen, J., Kneifel, S., Moisseev, D., Tyynelä, J., Tanelli, S., & Nousiainen, T. (2012). Evidence of nonspheroidal behavior in millimeter-wavelength radar observations of snowfall. *Journal of Geophysical Research, 117*, D18205. https://doi.org/10.1029/2012JD017680.

Leinonen, J., Lebsock, M., Tanelli, S., Suzuki, K., Yashiro, H., & Miyamoto, Y. (2015). Performance assessment of a triple-frequency spaceborne cloud-precipitation radar concept using a global cloud-resolving model. *Atmospheric Measurement Techniques, 8*, 3493–3517. https://doi.org/10.5194/amt-8-3493-2015.

Leinonen, J., Lebsock, M. D., Tanelli, S., Sy, O. O., Dolan, B., Chase, R. J., Finlon, J. A., von Lerber, A., & Moisseev, D. (2018). Retrieval of snowflake microphysical properties from multi-frequency radar observations. *Atmospheric Measurement Techniques, 11*, 5471–5488. https://doi.org/10.5194/amt-11-5471-2018.

Lhermitte, R. (1990). Attenuation and scattering of millimeter wavelength radiation by clouds and precipitation. *Journal of Atmospheric and Oceanic Technology, 7*, 464–479. https://doi.org/10.1175/1520-0426(1990)007<0464:AASOMW>2.0.CO;2.

Liao, L. A., & Meneghini, R. (2011). A study on the feasibility of dual-wavelength radar for identification of hydrometeor phases. *Journal of Applied Meteorology and Climatology, 50*, 449–456. https://doi.org/10.1175/2010JAMC2499.1.

Liu, G. (2008). Deriving snow cloud characteristics from CloudSat observations. *Journal of Geophysical Research, 113*, D00A09. https://doi.org/10.1029/2007JD009766.

Mason, S. L., Chiu, J. C., Hogan, R. J., & Tian, L. (2017). Improved rain rate and drop size retrievals from airborne Doppler radar. *Atmospheric Chemistry and Physics, 17*, 11567–11589. https://doi.org/10.5194/acp-17-11567-2017.

Matrosov, S. Y. (1992). Radar reflectivity in snowfall. *IEEE Transactions on Geoscience and Remote Sensing, 30*, 454–461. https://doi.org/10.1109/36.142923.

Matrosov, S. Y. (1998). A dual-wavelength radar method to measure snowfall rate. *Journal of Applied Meteorology, 37*, 1510–1521. https://doi.org/10.1175/1520-0450(1998)037<1510:ADWRMT>2.0.CO;2.

Matrosov, S. (2005). Attenuation-based estimates of rainfall rates aloft with vertically pointing Ka-band radars. *Journal of Atmospheric and Oceanic Technology, 22*, 43–54. https://doi.org/10.1175/JTECH-1677.1.

Matrosov, S. (2008). Assessment of radar signal attenuation caused by the melting hydrometeor layer. *IEEE Transactions on Geoscience and Remote Sensing, 46*, 1039–1047. https://doi.org/10.1175/2007JAMC1768.1.

Matrosov, S., May, P., & Shupe, M. (2006). Rainfall profiling using atmospheric radiation measurement program vertically pointing 8-mm wavelength radars. *Journal of Atmospheric and Oceanic Technology, 23*, 1478–1491. https://doi.org/10.1175/JTECH1957.1.

Morrison, H., & Grabowski, W. W. (2007). Comparison of bulk and bin warm-rain microphysics models using a kinematic framework. *Journal of the Atmospheric Sciences, 64*, 2839–2861. https://doi.org/10.1175/JAS3980.

Petäjä, T., O'Connor, E. J., Moisseev, D., Sinclair, V. A., Manninen, A. J., Väänänen, R., von Lerber, A., Thornton, J. A., Nicoli, K., Petersen, W., Chandrasekar, V., Smith, J. N., Winkler, P. M., Krüger, O., Hakola, H., Timonen, H., Brus, D., Laurita, T., Asmi, E., Riekkola, M.-L., Mona, L., Massoli, P., Engelmann, R., Komppula, M., Wang, J., Kuang, C., Bäck, J., Virtanen, A., Levula, J., Ritsche, M., & Hickmon, N. (2016). BAECC: a field campaign to elucidate the impact of biogenic aerosols on clouds and climate. *Bulletin of the American Meteorological Society, 97*, 1909–1928. https://doi.org/10.1175/BAMS-D-14-00199.1.

Petty, G. W., & Huang, W. (2010). Microwave backscatter and extinction by soft ice spheres and complex snow aggregates. *Journal of the Atmospheric Sciences, 67*, 769–787. https://doi.org/10.1175/2009JAS3146.1.

Pfitzenmaier, L., Battaglia, A., & Kollias, P. (2019). The impact of the radar-sampling volume on multiwavelength Spaceborne radar measurements using airborne radar observations. *Remote Sensing, 11*(19), 2263. https://doi.org/10.3390/rs11192263.

Sadowy, G. A., Berkun, A. C., Chun, W., Im, E., & Durden, S. L. (2003). Development of an advanced airborne precipitation radar. *Microwave Journal, 46*(1), 84–98.

Sadowy, G. A., McIntosh, R. E., Dinardo, S. J., Durden, S. L., Edelstein, W. N., Li, F. K., Tanner, A. B., Wilson, W. J., Schneider, T. L., & Stephens, G. L. (1997) The NASA DC-8 airborne cloud radar: Design and preliminary results. In Proceedings of IGARSS '97, Singapore, *4*, 1466–1469. https://doi.org/10.1109/IGARSS.1997.608896.

Seifert, A., & Beheng, K. (2001). A double-moment parameterization for simulating autoconversion, accretion and self collection. *Atmospheric Research, 59-60*, 265–281. https://doi.org/10.1016/S0169-8095(01)00126-0.

Stein, T. H. M., Westbrook, C. D., & Nicol, J. C. (2015). Fractal geometry of aggregate snowflakes revealed by triple-wavelength radar measurements. *Geophysical Research Letters, 42*, 176–183. https://doi.org/10.1002/2014GL062170.

Survey, D. (Ed.). (2017). *Thriving on our changing planet: A decadal strategy for earth observation from space*. Washington, DC., 716 pp: The National Academies Press. https://doi.org/10.17226/24938.

Toon, O. B., Starr, D. O., Jensen, E. J., Newman, P. A., Platnick, S., Schoeberl, M. R., Wennberg, P. O., Wofsy, S. C., Kurylo, M. J., Maring, H., Jucks, K. W., Craig, M. S., Vasques, M. F., Pfister, L., Rosenlof, K. H., Selkirk, H. B., Colarco, P. R., Kawa, S. R., Mace, G. G., Minnis, P., & Pickering, K. E. (2010). Planning, implementation, and first results of the tropical composition, cloud and climate coupling experiment (TC4). *Journal of Geophysical Research, 115*, D00J04. https://doi.org/10.1029/2009JD013073.

Tridon, F., & Battaglia, A. (2015). Dual-frequency radar Doppler spectral retrieval of rain drop size distributions and entangled dynamics variables. *Journal of Geophysical Research, 120*, 5585–5601. https://doi.org/10.1002/2014JD023023.

Tridon, F., Battaglia, A., Chase, R. J., Finlon, J., Turk, F. J., Bansemer, A., Kneifel, S., Leinonen, J., Mroz, K., Tanelli, S., Nesbitt, S. W., & Heymsfield, A. J. (2019). The microphysics of stratiform precipitation during OLYMPEX: Compatibility between 3-frequency radar and airborne in situ observations. *Journal of Geophysical Research, 124*, 8764–8792. https://doi.org/10.1029/2018JD029858.

Tyynelä, J., & Chandrasekar, V. (2014). Characterizing falling snow using multifrequency dual-polarization measurements. *Journal of Geophysical Research, 119*. https://doi.org/10.1002/2013JD021369.

Ulbrich, C. W. (1983). Natural variations in the analytical form of the raindrop size distribution. *Journal of Climate and Applied Meteorology, 22*, 1764–1775. https://doi.org/10.1175/1520-0450(1983)022<1764:NVITAF>2.0.CO;2.

Wang, Z., Heymsfield, G. M., Li, L., & Heymsfield, A. J. (2005). Retrieving optically thick ice cloud microphysical properties by using airborne dual-wavelength radar measurements. *Journal of Geophysical Research, 110*, D19201. https://doi.org/10.1029/2005JD005969.

Chapter 14
Precipitation Retrievals from Satellite Combined Radar and Radiometer Observations

Mircea Grecu and William S. Olson

Abstract This chapter provides a unified perspective on a broad class of approaches to derive precipitation estimates from satellite combined radar and radiometer observations based on the optimal estimation theory. These approaches are based on the optimal estimation theory and are numerical equivalent to an optimization problem. Irrespective of the procedure used to address the optimization, challenges related to mismatch between the large mismatches between the radar and radiometer footprint sizes, the ill-posed character of the mathematical problem and errors in the forward models need to be effectively mitigated. Approaches used in the TRMM and GPM combined algorithms as well as their benefits and limitations are discussed in the chapter. Aspects requiring improvement and potential solutions are also presented in the chapter.

Keywords Precipitation · Rainfall · Snow · Hydrometeors · Satellite · Radar · Radiometers · Brightness temperature · Path integrated attenuation · Surface reference technique · Normalized radar cross section · GPM · TRMM · Radiative transfer · Non-uniform beam filling · Particle size distribution · Optimal estimation · Deconvolution · Validation · MRMS.

M. Grecu (✉)
Morgan State University, Baltimore, MD, USA

NASA, Goddard Space Flight Center, Greenbelt, MD, USA
e-mail: mircea.grecu-1@nasa.gov

W. S. Olson
University of Maryland Baltimore County, Baltimore, MD, USA

NASA, Goddard Space Flight Center, Greenbelt, MD, USA

14.1 Introduction

Space-borne weather radar observations may be subject to significant attenuation due to precipitation and clouds. To derive precipitation estimates from such observations, it is, therefore, necessary to incorporate an attenuation correction procedure in the estimation methodology. While efficient attenuation correction procedures exist (Iguchi and Meneghini 1994), they are affected by the same type of uncertainties that usually affect the precipitation estimation from un-attenuated ground radar observations. The inclusion of reliable independent estimates of the Path Integration Attenuation (PIA) in the attenuation correction has been shown to mitigate uncertainties in the attenuation correction process and improve the accuracy of associated precipitation estimates (Iguchi and Meneghini 1994; Ferreira et al. 2001). However, although estimates of the PIA from space borne radar observations using a Surface Reference Technique (SRT, Meneghini et al. 2000) are in many instances sufficiently accurate to have a positive impact on the precipitation estimation process, they are not always reliable enough to be usable in the attenuation correction procedure (Meneghini et al. 2000). Alternative PIA estimates are therefore beneficial in mitigating uncertainties in the attenuation correction procedure. Early studies determined that radiometer observations at frequencies lower than 10-GHz are strongly related to the PIA at X-band and Ku-band (Weinman et al. 1990) and can be used to derive information that can be incorporated into radar precipitation profiling algorithms. Motivated by the work of Weinman et al. (1990) Smith et al. (1997) developed a relationship to estimate the PIA at Ku-band (13.8 GHz) from 10.7-GHz radiometer observations. This relationship was used in the first Tropical Rainfall Measuring Mission (TRMM) (Kummerow et al. 1998; Grecu and Bolvin 2018) combined radar-radiometer algorithm (Haddad et al. 1997).

The main challenge in deriving PIA estimates from satellite radiometer observations is that the typical footprints of low frequency radiometer channels are significantly larger than the typical footprints of space-born radars. This makes the direct application of the formulations derived by Weinman et al. (1990) and Smith et al. (1997) problematic. To circumvent this difficulty, the TRMM Day-1 combined algorithm (Haddad et al. 1997) made use of a procedure to simultaneously perform the attenuation correction and precipitation estimation for all radar profiles falling within the intersection of four adjacent 10.7-GHz radiometer footprints. Alternative approaches were developed by Grecu et al. (2004), Masunaga and Kummerow (2005), and Munchak and Kummerow (2011), but, irrespective of the approach, the radar-footprint PIA was not directly estimated from the radiometer observations. Instead, radar estimates were derived to maximize the agreement between model predicted radiometer observations and actual radiometer observations.

Despite discrepancies between radar and radiometer footprint sizes that make the direct investigation of the impact of the radiometer observations on the accuracy of the PIA estimates difficult, the estimation of precipitation from satellite combined radar-radiometer observations has been an area of active research in recent years due to the benefits that combined approaches provide in the development of satellite radiometer precipitation estimation algorithms. Specifically, given that combined

radar radiometer precipitation estimates are optimized to maximize the agreement between simulated and actual satellite radiometer observations, they can be used to derive large databases of precipitation and associated radiometer observations for the development of "Bayesian" precipitation estimation algorithms from satellite radiometer-only observations (Grecu and Olson 2006; Kummerow et al. 2011; Hou et al. 2014). As a consequence, combined precipitation estimates have been adopted as the optimal solution to develop unified precipitation retrievals from the constellation of satellite microwave radiometers that comprise the Global Precipitation Mission (GPM) (Hou et al. 2014). Given the increased focus on the development of radiometer algorithms, the potential of combined radar-radiometer algorithms to mitigate uncertainties in satellite radar precipitation estimates has been somewhat less intensively studied since the deployment of the main GPM core observatory. However, given the quality of the radar and radiometer instruments aboard the GPM core observatory (Hou et al. 2014; Skofronick-Jackson et al. 2017), the problem of how well the PIA can be estimated from collocated radiometer observations and how effective such estimates are in mitigating uncertainties in precipitation estimates derived from space-borne radar observations needs to be revisited.

The chapter is organized as follows. In the next section, we will briefly describe the GPM combined radar-radiometer algorithm (Grecu et al. 2016). The GPM combined algorithm incorporates several ideas and techniques developed over the previous 3 years, and can therefore serve as a basis for a discussion on the components that any current or future algorithm is likely to require to effectively address the challenges associated with the estimation of precipitation from satellite combined radar and radiometer observations. We also discuss some deficiencies in the current GPM combined algorithm and avenues to overcome them in Sect. 14.2.2. In Sect. 14.3, we provide an analysis of the statistical relationships between the GPM Microwave Imager (GMI) observations and the differential Ku-band and Ka-band PIA derived from the application of the SRT technique (Meneghini et al. 2015) to observations from the Dual-Frequency Precipitation Radar (DPR) onboard the GPM core satellite. The differential PIA has been found to be significantly more accurate than single frequency SRT PIA estimates (Meneghini et al. 2015). This is because the differences between normalized radar cross sections (NRCS) of the surface at the two DPR frequencies is less variable in clear sky regions than the individual surface NRCSs. This makes the differential SRT PIA estimates significantly more accurate than single frequency SRT PIA estimates. However, differential SRT PIA estimates are not always available for inclusion in the estimation process. From this perspective, it is useful to quantify how well the differential SRT PIA can be estimated exclusively from GMI observations. In addition to providing direct insight into how brightness temperature information can impact a radar-only retrieval procedure, the explicit estimation of the PIA from observed brightness temperatures leads to partial mitigation of the underestimation of precipitation that is too light or shallow to be detected by the DPR. This aspect is also discussed in Sect. 14.3. A summary and conclusions are provided in Sect. 14.4.

14.2   The GPM Combined Algorithm

As previously mentioned, a significant challenge in the development of satellite combined radar radiometer algorithms is that the footprints of low frequency radiometer channels are significantly larger than the typical footprints of space-borne radars. This makes the direct application of the approach developed by Weinman et al. (1990) impossible. To circumvent this problem, the agreement between the radar and radiometer observations is evaluated in terms of brightness temperatures (Grecu et al. 2004; Munchak and Kummerow 2011; Grecu et al. 2016). That is, brightness temperatures computed from the radar retrievals are either convolved to the radiometer footprint size resolution (Grecu et al. 2004, 2016; Munchak and Kummerow 2011) or the radiometer observations are deconvolved to the radar footprint resolution as shown in Fig. 14.1 (Grecu et al. 2016). The work flow associated with the evaluation of the agreement between simulated and observed brightness temperatures at radiometer resolution is shown in blue, while the work flow associated with the brightness temperatures evaluation at radar resolution is shown in green. To maximize the agreement between the simulated and observed brightness temperatures, an optimization procedure is used. This procedure iteratively updates assumptions about the Particle Size Distributions (PSD) associated with the radar observations. Specifically, it was shown by (Willis 1984; Testud et al. 2001) that two parameters are generally sufficient to capture most of the PSD variability. One of these parameters is the normalized PSD intercept, while the other is a bulk size-related parameter. At the same time, the relationships between Ku-band radar-reflectivity and the associated specific attenuation were shown to depend mostly on the PSD intercept (Ferreira et al. 2001). Since single frequency radar observations cannot be used to reliably estimate both the PSD intercept and the bulk size-related parameter in a space-borne radar profiling algorithm, it is convenient to express the bulk size-related parameter as a function of the intercept and the radar reflectivity profile, and then tune the intercept based on other considerations

Fig. 14.1 Illustration of two possible strategies to mitigate the large mismatches between the radar and radiometer footprint sizes in satellite combined retrievals
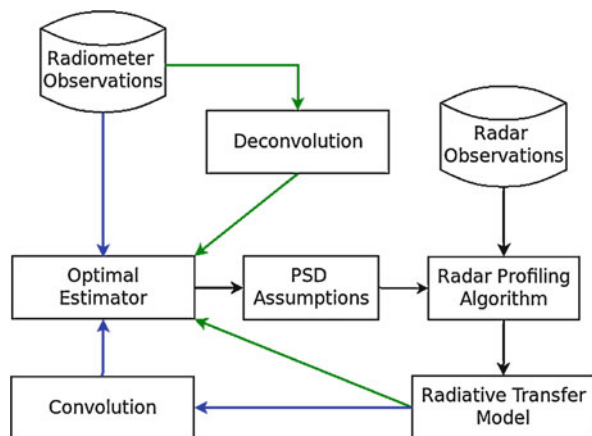
such as the agreement of calculated PIA with SRT PIA (Ferreira et al. 2001) or the agreement between simulated and observed brightness temperatures (Grecu et al. 2004). This is the reason why an optimal estimation component is generally required in combined radar-radiometer estimation algorithms; see Fig.14.1.

14.2.1   Formulation

The GPM combined algorithm is based on a Ku-band radar profiling algorithm (Grecu et al. 2011) and physical models that simulate satellite Ka-band radar and multichannel radiometer observations as a function of the Ku-band radar estimates and relevant geophysical variables (Grecu et al. 2016). A detailed description is given in Grecu et al. (2016). Numerically, it requires the minimization of a function defined as

$$
\begin{aligned}
J = \frac{1}{2} (y_{\text{sim}}(x) - y_{\text{obs}})^{\text{T}} W_{\text{T}}^{-1} (y_{\text{sim}}(x) - y_{\text{obs}}) + \\
\frac{1}{2} (x - x_{\text{N}})^{\text{T}} W_{\text{T}}^{-1} (x - x_{\text{N}})
\end{aligned}
\tag{14.1}
$$

where $\mathbf{x}$ is the set of geophysical variables to be estimated, $\mathbf{y_{sim}(x)}$ is the physically-based forward model, $\mathbf{y_{obs}}$ are the satellite Ka-band radar and multichannel radiometer observations, $\mathbf{W_T}$ is the covariance matrix of forward model errors and noise in the observations, $\mathbf{x_N}$ is the a priori mean of $\mathbf{x}$ and $\mathbf{W_X}$ is its covariance matrix. The first term in Eq. 14.1 quantifies the agreement between simulations and observations, while the second term penalizes the departure of the estimated values from their climatological values. The purpose of the second term is to prevent the derivation of highly inaccurate estimates that fit well the observations, i.e. minimize to 0.0 the first term of Eq. 14.1. Such estimates are possible because although the GPM core observatory features a Ka-band radar and a microwave radiometer in addition to a Ku-band radar, the information provided by the combined radar and radiometer observations is not sufficient to uniquely determine the properties of the underlying precipitation PSDs. The inclusion of the second term, usually referred to as the regularization term (Doicu et al. 2011), makes the estimates derived through the minimization of Eq. 14.1 better determined, less noisy and consistent with an independent climatology.

Despite its conceptual simplicity, the optimal estimation approach outlined in the above paragraph is computationally intensive and requires efficient practical implementations. To minimize the number of iterations required to determine the minimum of J, the GPM combined algorithm makes use of an elimination technique (Fletcher 2013) to reduce the size of the optimization problem. Specifically, instead of including all the PSD parameters in $\mathbf{x}$ and estimate them through the minimization of J, only the PSD intercepts (Testud et al. 2001) are optimized, and the other PSD parameters are derived as a function of the Ku-band GPM radar observations using the radar profiling method of Grecu et al. (2011). In addition to reducing the number

of variables in **x**, this approach makes the optimization problem simpler than that associated with a full-rank formulation, because the Ku-band radar algorithm narrows the space of PSD parameters that can explain a given set of combined GPM radar and radiometer observations. In addition to the PSD intercept, variables describing the vertical distribution of water vapor and cloud water for each profile of observed reflectivities and the sea surface wind over oceans (and surface emissivities over land) are included in **x** (Grecu et al. 2016). The minimization of J is achieved using an ensemble filtering technique (Evensen 2006). Specifically, a formula to update the estimates **x** based on the agreement between the model predictions $\mathbf{y_{sim}(x)}$ and actual observations $\mathbf{y_{obs}}$ is derived from the equation $\mathbf{r_J} = 0$. Ensemble methodologies in general have the advantage of not requiring the explicit calculation of the forward model's Jacobian, i.e. $H = \nabla y_{sim}(x)$ (Evensen 2006; Grecu et al. 2016). Instead, the H-dependent matrices involved in the derivation of the optimal estimates are statistically estimated from an ensemble of simulations of observations $\mathbf{y_{sim}}$ associated with a set of potential solutions **x**.

As illustrated in Fig. 14.1 and discussed in the previous paragraphs, to reconcile the mismatches between the radiometer and radar footprint sizes, special operations (either convolution or deconvolution) are required. The GPM combined algorithm relies on statistical procedure to deconvolve the GMI brightness temperatures to the radar footprint resolution. Thus, simulated brightness temperatures at the radar resolution are evaluated against deconvolved GMI brightness temperature in Eq. 14.1. In addition to the radar-resolution brightness temperatures, Ka-band radar observations and PIAs at two frequencies are included in **y**. This is because a dual-frequency precipitation radar (DPR) (Skofronick-Jackson et al. 2017) is deployed on the GPM satellite observatory. The first DPR frequency is 13.6 GHz (Ku-band), which is the operating frequency of the TRMM radar (13.8 GHz) (Kummerow et al. 1998; Grecu and Bolvin 2018). The second frequency is 35.0 GHz (Ka-band) (Skofronick-Jackson et al. 2017). GPM Ka-band observations were collected only within 12 rays from nadir before 28 May 2018. A new scan pattern permitting the collection of Ka-band observations across the entire Ku-band swath was implemented after 28 May 2018.

The benefit of dual-frequency radar observations is that they allow for the derivation of more accurate precipitation estimates relative to those derived from single frequency radar observations. It should be noted that the Ka-band radar observations and the PIA estimates derived from the Surface Reference Techniques (SRT) can be significantly impacted by Multiple Scattering (MS) (Battaglia et al. 2006; Grecu et al. 2016) and Non-Uniform Beam Filling (NUBF) effects (Short et al. 2015; Grecu et al. 2016). Specifically, MS, i.e. the scattering of radar pulse energy several times off atmospheric targets before returning to the receiver, can significantly enhance the observed GPM Ka-band radar observations and may be misinterpreted as reduced attenuation (Battaglia et al. 2006; Grecu et al. 2016). Similarly, NUBF can significantly distort the interpretation of the average extinction associated with an observed reflectivity profile. This is because electromagnetic energy originating in an unattenuated sub-volume of radar observing volume may still reach the radar and be interpreted as an indication of low PIA, even though the energy originating in the remaining portion of the observing volume is completely

attenuated. For example, a column of very intense precipitation that fills half of the radar's field of view (FOV) may be associated with a total SRT PIA of only 3-dB, because the normalized radar cross section of the surface decreases only by half (in natural units) when half of the FOV is precipitation free. However, 3-dB attenuation is rather weak at Ka-band and is suggestive of light precipitation in the case of uniform beam filling. To prevent MS and NUBF effects from biasing the estimates, an advanced multiple scattering model (Hogan and Battaglia 2008) and a simple downscaling procedure (Grecu et al. 2016) are included in the GPM combined algorithm. The downscaling procedure statistically generates, for every Ku-band reflectivity profile, a set of Ku-band reflectivity profiles whose average is equal to the profile from which they are generated. The Ku-band radar profiling algorithm is applied to each sub-profile and the resulted PIAs are aggregated to the original radar resolution. The statistical parameter used to describe the variability of generated observations with every radar FOV has been tuned to improve the long-term consistency between single and dual-frequency combined estimates (Grecu et al. 2016). The MS model is applied at the original resolution of the data because it is one-dimensional, making it questionable for applications at very high horizontal spatial resolution. The inclusion of the MS model and NUBF parameterization significantly improved the consistency between single and dual-frequency retrievals (Grecu et al. 2016). Although the evaluation of the GPM combined precipitation estimates is still work in progress, several studies suggests that, as expected, estimates incorporating the Ka-band observations are more accurate than those based exclusively on Ku-band and GMI observations (Grecu et al. 2016; Naud et al. 2018).

14.2.2 Areas Requiring Improvement

As apparent from the previous section, the accuracy of the simulation models in Eq. 14.1 is of paramount importance in the derivation of unbiased, minimum variance precipitation estimates from combined radar and radiometer observations. While some of these models can be improved through theoretical work, e.g. the attenuation correction procedure (Grecu et al. 2011) and the multiple scattering model (Hogan and Battaglia 2008) (whose performance depends on the accurate quantification of electromagnetic scattering properties), others, i.e. the NUBF parameterization, will require empirical evidence and validation for further improvements. In this respect, a particularly useful product has been the Multi-Radar Multi-Sensor (MRMS) (Zhang et al. 2016) precipitation rate product. The MRMS product is a quality-controlled, rain gauge-calibrated radar precipitation product. The MRMS surface precipitation rate estimates are gridded at 0.01-degree resolution every 2 min and are provided along with a Radar Quality Index (RQI) that can be used to filter out unreliable estimates. An example of GPM combined surface precipitation estimates and associated MRMS estimates are shown in Fig. 14.2. It may be inferred from the figure that there is a good agreement between the GPM combined and MRMS estimates. In addition to the MRMS estimates being smoother, which is most likely
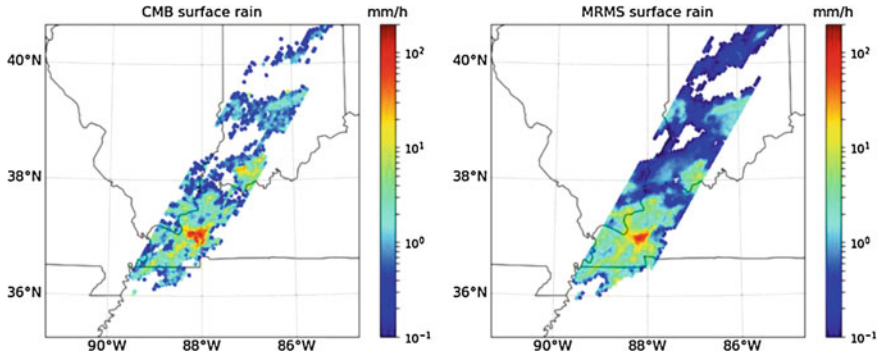
Fig. 14.2 (Left) Example of combined surface precipitation estimates for GPM orbit 605 on 1 October 2014. (Right) The associated Multi-Radar/Multi-Sensor (MRMS) estimates

a consequence of how the gauge information is incorporated in the estimation procedure, an obvious difference between the combined and MRMS surface precipitation is the extent of light precipitation (below 0.2 mm h^{-1}) area. This is the consequence of the DPR not being able to reliably detect precipitation with a radar echo below 12.0 dBZ. The convective precipitation estimates appear to be in good agreement with no obvious systematic differences. It should be noted that although rigorous statistical analyses of the differences between combined and MRMS estimates can be carried out at DPR resolution, such analyses may be biased by temporal and spatial mismatches between the two types of estimates. Specifically, the combined precipitation estimates are derived from ground-clutter-free radar observations that can be as much as 2.0 km from the ground. However, reflectivity observations not very close to the ground are likely to be better correlated with surface precipitation that is horizontally displaced relative to their projection on the ground (Lauri et al. 2012). Therefore, unless such displacements are accounted for using numerical weather prediction model (NWP) (Lauri et al. 2012) or 3D dimensional time-dependent radar observations (Anagnostou and Krajewski 1999), the conditional distribution of combined precipitation estimates, given the MRMS precipitation, is likely to exhibit features that have nothing to do with the performance of the combined algorithm. This is because convective precipitation, in particular, exhibits large spatial gradients and significant displacement errors that result in low precipitation estimates in one dataset being systematically associated with high precipitation estimates in the other dataset and vice-versa.

To overcome this behavior, which is apparent in combined-MRMS comparisons at the footprint level, while avoiding the use of intensive NWP or reflectivity tracking methodologies (Lauri et al. 2012; Anagnostou and Krajewski 1999), one can aggregate the combined and MRMS estimates at spatial scales that reduce the spatial displacement artifacts, while retaining information about the physical context in which large discrepancies between the two estimates are observed. For example, while large discrepancies between combined and MRMS estimates of convective precipitation at the DPR footprint resolution are always expected, discrepancies between the means of large contiguous areas of convective precipitation are expected to be indicative of systematic differences in the two estimates.

Fig. 14.3 Density scatterplot of GPM combined V06 vs reference MRMS convective precipitation (mm h^{-1}) at the footprint scale over the period April 2014– October 2014
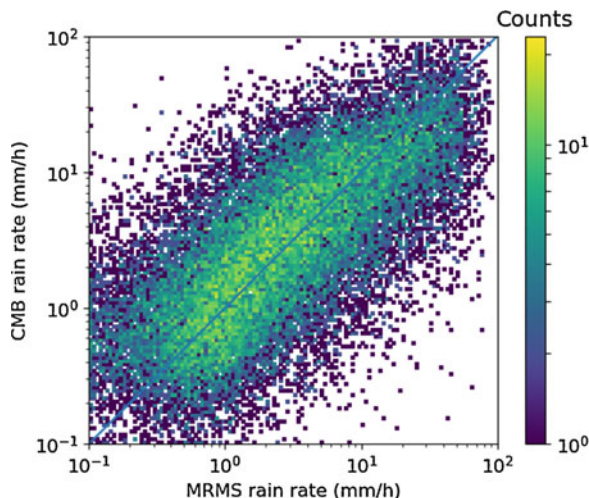
A direct comparison between MRMS surface precipitation and combined convective surface precipitation estimates at the DPR footprint resolution is shown in Fig. 14.3. Although the overall agreement between the two sets of estimates is fairly good, the number of combined precipitation estimates with values >10 mm h^{-1} appears to be smaller than that of MRMS estimates >10 mm h^{-1}. As explained in the previous paragraph, due to displacements, a profile by profile analysis is not likely to allow for a robust identification of underestimated GPM combined convective precipitation. However, using the contiguous area aggregation strategy described in the previous paragraph, it is possible to identify orbits that exhibit significant underestimation relative to the MRMS product. Several such orbits in the period 1 April – 31 October 2014 have been identified in the Version 6 (V6) of the GPM combined product, and the extension of this analysis to the entire GPM-MRMS record is expected to identify a significant number of additional orbits that exhibit underestimation relative to the MRMS product. The causes of this apparent deficiency are not yet clear. As discussed in Grecu et al. (2016), NUBF-related parameterizations and the a priori distribution of particle size intercepts have a significant impact on the combined estimates and, most likely, their representation in V6 is still sub-optimal. A detailed analysis based on the GPM-MRMS coincident dataset, as described above, is expected to lead to the resolution of this issue.

In addition, the underestimation of precipitation due to the DPR'S sensitivity can be effectively mitigated over ocean surfaces. Shown in Fig. 14.4 are estimates of liquid water path (LWP) derived from GMI observations using the formulation of Weng et al. (1997) and associated combined near-surface precipitation estimates. While some of the non-zero precipitation areas also exhibit non-zero LWP, there are also areas with significant LWP but no precipitation. This is likely a consequence of the limited DPR sensitivity. An analysis of the CloudSat-GPM coincidence Dataset (Turk 2016) (not shown in the chapter) reveals that, indeed, a large fraction of the precipitation at high latitudes over oceans is associated with echo not detected by the DPR. The current formulation of the combined algorithm provides precipitation
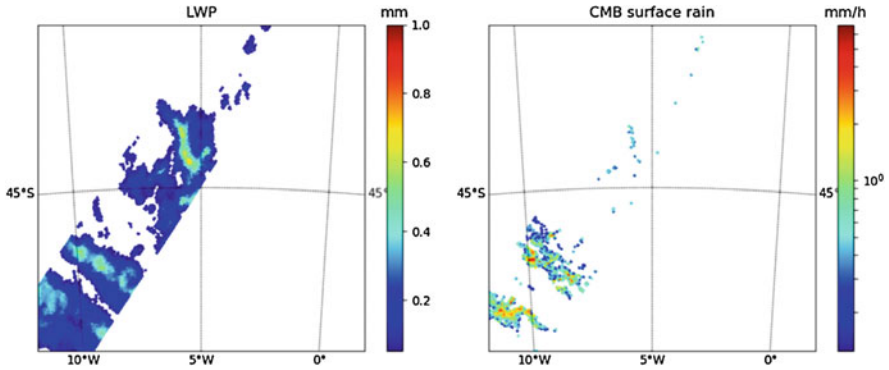
Fig. 14.4 (Left) Example of liquid water path (LWP) derived from GMI observations over oceans for orbit 003351 on 1 October 2014. (Right) The associated combined surface precipitation. The magnitude of the LWP suggests that light precipitation is undetected by the DPR

estimates only for the DPR pixels deemed as precipitating by the DPR rain/no rain discrimination algorithm (Iguchi et al. 2010). However, the inclusion of a radiometer-only component to provide estimates for precipitation systems too light or too shallow to be detected by the DPR is possible. A relatively simple approach may be derived, based on the premise that the joint distribution of the precipitation and associated brightness temperatures derived by the current version of the combined algorithm is a truncated distribution (Rao 1997). That is, while only the portion of the joint distribution characterized by radar echo above the DPR noise level is quantified in terms of precipitation intensity by the combined algorithm, a robust statistical methodology may be used to extrapolate the truncated distribution for echoes below the DPR noise level. This methodology draws upon an analysis of the relationships between observed radiometer brightness temperatures and the differential PIA derived from a dual surface reference technique (Meneghini et al. 2015), as explained in the next section.

14.3 Brightness Temperature – PIA Relationships, Revisited

As described in Sect. 14.1, direct relationships between brightness temperatures and path integrated attenuation are conceptually appealing because they permit the straightforward integration of radiometer information into space-borne radar retrievals (Weinman et al. 1990; Smith et al. 1997, Grecu et al. 2004). From a practical perspective, however, such relationships are problematic, as the typical footprint of a 10-GHz satellite radiometer channel is much larger than that of a satellite radar footprint (Kummerow et al. 1998; Skofronick-Jackson et al. 2017). This does not necessarily mean that relationships between satellite radiometer observations and radar resolution PIA are weak, but rather than the derivations of

accurate relationships are difficult. Formulations derived by radiative transfer calculations (Weinman et al. 1990; Smith et al. 1997) require the radiometer's footprint size be the same as the radar's footprint size. Although more general (and accurate) relationships may be derived, using, for example, cloud resolving models, such relationships are likely to be biased if the variability of precipitation and associated geophysical variables with the radiometer's field of view is not properly captured. These challenges may be circumvented by constructing a database of radiometer brightness temperatures and associated PIAs directly from GPM observations. As shown by Meneghini et al. (2015), the differential (Ku-Ka) surface normalized radar cross section (NRCS) exhibits significantly smaller variability in clear sky regions over oceans, which allows for the derivation of accurate differential (as well as single frequency) PIA estimates from the analysis of the surface return. To investigate the relationships of differential Surface Return Technique (SRT) PIA to brightness temperatures, a database of deconvolved GMI brightness temperature and coincident differential SRT PIA estimates is derived from 1 month (October 2014) of observations over mid-latitude oceans in the northern hemisphere. It should be noted that for global evaluation and application, a global database needs to derived and stratified as a function of geophysical parameters (e.g., sea surface temperature, total precipitable water) that are likely to have a strong impact on the relationships between brightness temperatures and associated PIAs. For simplicity, in this study, only a regional database is considered. The deconvolution procedure is based on a simple regression procedure derived from simulations of brightness temperatures at GMI resolution (Grecu et al. 2016). For evaluation purposes, this database is randomly split into two disjoint, equal-size, subsets and one set is used for deriving a statistical relationship between deconvolved brightness temperatures and PIA, while the other is used for evaluation. From a practical perspective, a simple analytical brightness temperature – PIA relationship is preferable to more complex non-parametric statistical relationships such as those available in open machine learning libraries (e.g., Pedregosa et al. 2011), because, as previously explained, the brightness temperature-PIA joint distribution is truncated, and its extrapolation to brightness temperatures characterized by Ku-radar echo below 12.0 dBz is problematic in the case of non-parametric models.

A very simple approach that works satisfactorily can be developed by extending the formulation of Smith et al. (1997) to two radiometer channels (i.e., 10-GHz V and 19-GHz V) and statistically estimating the three associated parameters in PIA = a0 + a1 × TB10 + a2 × TB19. The cross-validation analysis described above indicates a good performance. Specifically, the correlation coefficients between estimated values and those in the evaluation datasets are about 0.8 for both the differential and Ku-band PIAs, while the root mean squared error is 3.0 dB for the differential PIA and 0.6 dB for the Ku-band PIA. The Ku-PIA is derived by assuming that the average ratio of the Ka-band PIA to the Ku-band PIA is 6.0, which is what the analysis of the surface Ku-band and Ka-band NRCSs suggest (Meneghini et al. 2015). The Ku-band PIA estimates derived from the analysis of Ku-band surface echo are in greater disagreement, i.e. correlation coefficient of 0.5 and root mean squared error of 0.9 dB, with the dual frequency SRT PIA estimates, relative to the PIA values derived from brightness temperatures. This is not surprising, given that Ku-band

surface NRCSs exhibit significant variations that are not necessarily related to attenuation, making only large-value estimates (i.e., significantly larger that the clear sky NRCS variability) reliable. However, a significant fraction of large value SRT PIA estimates derived from Ku-band-only observations, although deemed reliable (because of their value relative to the clear sky NRCS variability), are actually erroneous rather than a measure of strong attenuation in the associated radar fields of view. This results in medium to low correlation and increased root-mean-squared error in relation to the differential SRT PIA estimates. Regarding the use of PIA in the radar retrieval process, the PIA uncertainties need to be correctly specified and, consequently, the more uncertain the Ku-band only SRT PIA estimates are, the less likely they are to have a significant impact on the final precipitation estimates. It should be mentioned, however, that the dual-frequency SRT cannot generally be used to estimate dual frequency PIA greater than 40.0 dB, because, beyond this value, the Ka-band surface return tends first to become insensitive to changes in PIA and eventually becomes undetectable. From this perspective, a good strategy for future versions of the GPM combined is to quantify the uncertainties in the brightness-temperature-based and single-frequency SRT PIA estimates as a function of their actual values, which will allow for the optimal use of the information in both types of PIA estimates. The brightness-temperatures PIA estimates are also expected to supplement dual-frequency SRT PIA estimates simply because the differential SRT PIA estimates are deemed not reliable about 30% of the time. Moreover, before 28 May 2018, dual frequency radar observations were only available in the inner half of the DPR swath. Therefore, without the brightness temperature derived PIA estimates, Ku SRT PIA estimates provide the only PIA information in the outer portions of the swath that can be used in the radar profiling algorithm.

Shown in Fig. 14.5 are the Ku-band PIA derived by the GPM combined algorithm (left panel) and directly estimated from the observed brightness temperatures
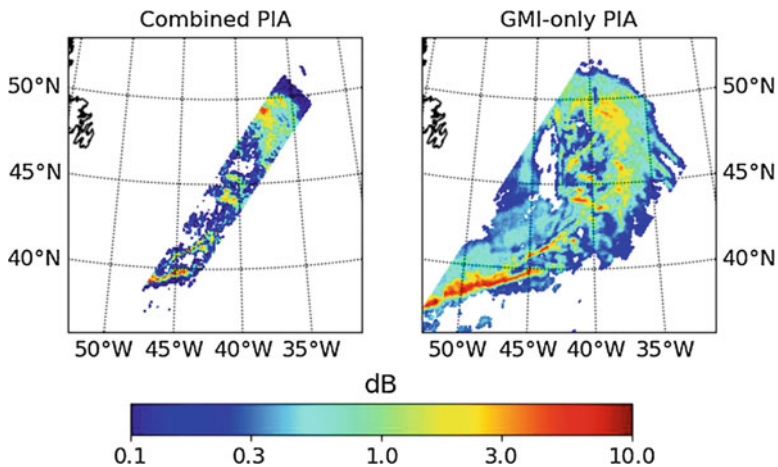
Fig. 14.5 (Left) Example of Ku-band PIA derived by the combined algorithm for orbit 003539 on 13 October 2014. (Right) The associated Ku-band PIA estimated exclusively from GMI observations

using the approach described in the previous paragraphs. As seen in the figure, there is very good correlation between the two estimates. However, some differences are also apparent. Specifically, there are areas of PIA between 0.3 and 1.0 dB in the brightness temperature-based estimates that correspond to very low values of the combined estimates. This may be an indication of missed precipitation due to the DPR's limited sensitivity. Some differences are also apparent in the mostly stratiform precipitation region defined by the 40°–35°W and 45°–50°N window, but their potential impact on final PIA and precipitation estimates, had the brightness-temperature-based PIAs been included in the combined algorithm, is difficult to assess. Future work that explicitly investigates the differences between combined retrievals including and not including the brightness-temperature-based PIAs is expected to provide insight into this issue.

As previously mentioned, one advantage of the extended Smith et al. (1997) formulation is that it can be applied even to brightness temperatures that are not associated with radar echoes above the noise level. Non-negligible brightness-temperature PIA estimates may then be an indication of precipitation not detected by the space-borne radar. The incorporation of such an approach in an operational algorithm obviously requires a reliable methodology to determine whether the brightness-temperature PIA estimates (associated with radar echo below the noise level) are more likely to be the result of not-detected precipitation than not. A χ^2 approach (Elsaesser and Kummerow 2008) applied to clear sky retrievals may be used to provide such a methodology. Specifically, a physical clear sky retrieval procedure may be applied to all brightness temperatures associated with radar echo below the noise level, and the discrepancy between simulated and observed brightness temperature may then be used to quantify the probability of precipitation (Elsaesser and Kummerow 2008). Large discrepancies would be an indication that the underlying physical models (which do not account for precipitation) are unable to explain the observed brightness temperatures, which further implies that precipitation is a variable required to explain the observed brightness temperatures. Another possibility is to apply more ad-hoc, data-driven, approaches (Ferraro et al. 1998) to identify precipitation-affected footprints and apply the brightness-temperature-based PIA estimator to all those footprints. The application of the latter approach to observations from a GMI orbit on 1 October 2014 is illustrated in Fig. 14.6. As seen in the figure, there are significant differences between the combined derived Ku-band PIA and the Ku-band PIA estimated directly from the brightness temperatures. In particular, there is band of precipitation in the region between 10°–5°W and 40°–45°S that produces only a few DPR profiles above the noise level. The brightness-temperature-based PIA estimates can be converted into surface precipitation estimates using simple, but realistic, parameterizations and thus provide a relatively direct solution to the DPR precipitation detection problem at high latitudes. The accuracy of such a solution depends on the accuracy of brightness temperature – PIA relationships (as previously described) and the performance of the rain discrimination procedure. Fortunately, both of these can be investigated using the CloudSat GPM coincidence dataset (Turk 2016). This is because the coincidence dataset includes estimates of W-band PIA associated with observed GPM brightness
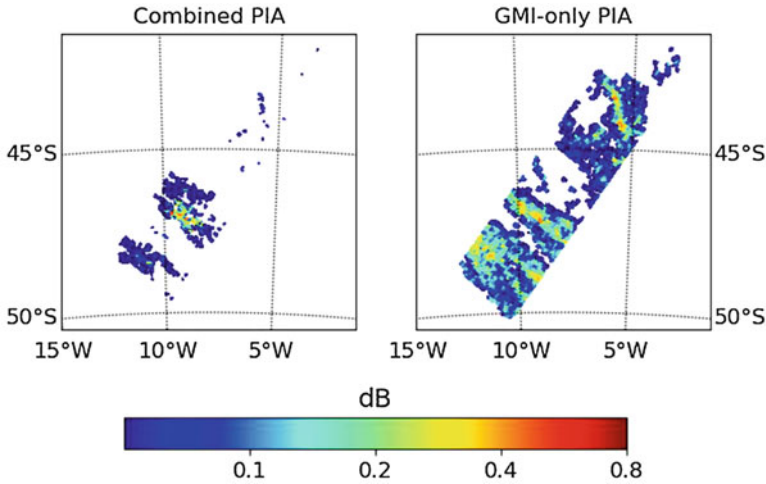
Fig. 14.6 (Left) Ku-band PIA derived by the combined algorithm for orbit 003351 on 1 October 2014. (Right) The associated Ku-band PIA derived from GMI brightness temperatures using the extended formulation described in the text

temperatures. The W-band PIA estimates can be converted into Ku-band PIA and compared to the values derived from the GMI brightness temperatures in the coincidence data. A direct comparison indicates the Ku-band PIA's derived from GMI observations using the extended Smith et al. (1997) are practically unbiased relative to the estimates derived from the coincident W-band estimates. Similarly, the rain discrimination procedure derived by Ferraro et al. (1998) can be adjusted to be unbiased relative to CloudSat rain/no rain discrimination.

14.4 Summary and Conclusions

In this chapter, topics relevant to the estimation of precipitation from combined space-borne radar and radiometer observations are discussed. The discussion is mostly driven by challenges and questions raised during the development and refinement of the GPM combined algorithm (Grecu et al. 2016). This is not meant to imply that the approaches formulated in Grecu et al. (2016) has greater merit than other combined satellite radar-radiometer approaches, but rather that many of the challenges and questions relevant to the approach, and the GPM mission more badly, are also relevant to other approaches and missions.

Section 14.2 contains a brief description of the GPM combined algorithm. Some of the components the GPM combined algorithm, i.e. the multiple scattering model and the non-uniform beamfilling (NUBF), are likely to be required in other formulations or for other missions featuring different radars. While the resolution of future space borne radars is expected to increase, the emphasis on higher frequencies,

which make it possible to detect smaller particles, is likely to result in the development of radar systems that are subject to the effects of multiple scattering. Moreover, while traditionally it is believed that matched beams are essential in the development of multiple-frequency radar retrievals (Bringi and Chandrasekar 2001), the GPM DPR experience suggests that a new paradigm driven by the overall information content is needed. Specifically, since one-dimensional multiple scattering and NUBF models and parameterizations are necessary to interpret multiple frequency radar observations at a given (apparent) range, the requirement that the beams be matched does not simplify the problem at hand and does not necessarily improve the informational content. At the same time, higher resolution observations, although less affected by multiple scattering and NUBF, are inherently going to be characterized by poorer spatial sampling (i.e., smaller areal coverage). To achieve a trade-off between accuracy and areal coverage, future space-borne systems may, therefore, may need to rely of a combination of radars with different measurement resolutions and operating at different frequencies. As a consequence, multiple scattering and NUBF may still affect the observations, but from the technological standpoint, space-borne radars can be built to minimize multiple scattering and NUBF effects.

The complexity of spaceborne measurements and estimation methods makes performance evaluation strategies such as those based on the MRMS product presented in Sect. 14.2 very import for the refinement of satellite combined precipitation retrievals. The challenge in making use of collocated high-quality ground estimates, such as the MRMS products, is that due to spatial displacements (Lauri et al. 2012) between near-surface satellite estimates and the ground, the combined algorithm estimated precipitation distributions are intrinsically biased relative to that of the ground product. Nevertheless, ground products may still be used to identify and correct deficiencies in the satellite estimates of precipitation. The evaluation of the GPM precipitation estimates over oceans is not discussed in this chapter, but the methodology based on independent, climatologically-accurate products such as the GPCP product (Adler et al. 2003) can be used to credibly assess future versions of the combined algorithm (Grecu et al. 2016).

An analysis of the relationships between GMI observed brightness temperatures and associated PIA over oceans is presented in Sect. 14.3. The PIA estimates are derived using a differential surface reference technique (SRT) procedure (Meneghini et al. 2015), which makes the analysis model-free. Strong relationships between the observed brightness temperatures and associated PIA are found. These relationships make it possible to derive PIA estimates more accurately than those derived from the application the SRT procedure to Ku-band observations (for Ku-band PIA below 7–8 dB), and brightness-temperature-based PIA estimates may be used to supplement both single frequency and differential PIA estimates. It is anticipated that the inclusion of these estimates in the combined estimation framework will have a positive impact, although rigorous quantification necessitates a systematic analysis not undertaken in this chapter. Moreover, the application of the derived brightness temperature – PIA relationships to observations with radar echo below noise level is expected to improve the detection and quantification of light precipitation over oceans.

References

Adler, R. F., Huffman, G. J., Chang, A., Ferraro, R., Xie, P., Janowiak, J., Rudolf, B., Schneider, U., Curtis, S., Bolvin, D., Gruber, A., Susskind, J., Arkin, P., & Nelkin, E. (2003). The version 2 Global Precipitation Climatology Project (GPCP) monthly precipitation analysis (1979-present). *Journal of Hydrometeorology, 4*(6), 1147–1167. https://doi.org/10.1175/1525-7541 (2003)004<1147:TVGPCP>2.0.CO;2.

Anagnostou, E. N., & Krajewski, W. F. (1999). Real-time radar rainfall estimation. Part I: Algorithm formulation. *Journal of Atmospheric and Oceanic Technology, 16*, 189197. https:// doi.org/10.1175/1520-0426(1999)016<0189:RTRREP>2.0.CO;2.

Battaglia, A., Ajewole, M. O., & Simmer, C. (2006). Evaluation of radar multiple-scattering effects from a GPM perspective. Part I: Model description and validation. *Journal of Applied Meteorology and Climatology, 45*, 1634–1647. https://doi.org/10.1175/JAM2424.1.

Bringi, V. N., & Chandrasekar, V. (2001). *Polarimetric doppler weather radar: Principles and applications*. Cambridge, UK, 636 pp: Cambridge University Press. https://doi.org/10.1017/ CBO9780511541094.

Doicu, A., Trautmann, T., & Schreier, F. (2011). Regularization of inverse problems in atmospheric remote sensing. In M. I. Mishchenko, Y. S. Yatskiv, V. K. Rosenbush, & G. Videen (Eds.), *Polarimetric detection, characterization and remote sensing* (pp. 79–116). Dordrecht: Springer, ISBN:978-94-007-1636-0.

Elsaesser, G. S., & Kummerow, C. D. (2008). Toward a fully parametric retrieval of the nonraining parameters over the global oceans. *Journal of Applied Meteorology and Climatology, 47*, 1599–1618. https://doi.org/10.1175/2007JAMC1712.1.

Evensen, G. (2006). *Data assimilation: The ensemble Kalman filter*. Dordrecht: Springer, 280 pp, ISBN:978-3-642-03711-5.

Ferraro, R. R., Smith, E. A., Berg, W., & Huffman, G. J. (1998). A screening methodology for passive microwave precipitation retrieval algorithms. *Journal of the Atmospheric Sciences, 55*, 1583–1600. https://doi.org/10.1175/1520-0469(1998)055<1583:ASMFPM>2.0.CO;2.

Ferreira, F., Amayenc, P., Oury, S., & Testud, J. (2001). Study and tests of improved rain estimates from the TRMM precipitation radar. *Journal of Applied Meteorology, 40*, 1878–1899. https:// doi.org/10.1175/1520-0450(2001)040<1878:SATOIR>2.0.CO;2.

Fletcher, R. (2013). *Practical methods of optimization*. Padstow/Cornwall: Wiley, 456 pp, ISBN:978-0-471-49463-8.

Grecu, M., & Bolvin, D. T. (2018). The tropical rainfall measuring mission. In C. Andronache (Ed.), *Remote sensing of clouds and precipitation*. Dordrecht: Springer, 155-174, ISBN978-3-319-72583-3.

Grecu, M., & Olson, W. S. (2006). Bayesian estimation of precipitation from satellite passive microwave observations using combined radar retrievals. *Journal of Applied Meteorology and Climatology, 45*, 416–433. https://doi.org/10.1175/JAM2360.1.

Grecu, M., Olson, W. S., & Anagnostou, E. N. (2004). Retrieval of precipitation profiles from multiresolution, multifrequency active and passive microwave observations. *Journal of Applied Meteorology, 43*, 562–575. https://doi.org/10.1175/1520-0450(2004)043<0562:ROPPFM>2.0. CO;2.

Grecu, M., Tian, L., Olson, W. S., & Tanelli, S. (2011). A robust dual-frequency radar profiling algorithm. *Journal of Applied Meteorology and Climatology, 50*, 1543–1557. https://doi.org/10. 1175/2011JAMC2655.1.

Grecu, M., Olson, W. S., Munchak, S. J., Ringerud, S., Liao, L., Haddad, Z., Kelley, B. L., & McLaughlin, S. F. (2016). The GPM combined algorithm. *Journal of Atmospheric and Oceanic Technology, 33*, 2225–2245. https://doi.org/10.1175/JTECH-D-16-0019.1.

Haddad, Z. S., Smith, E. A., Kummerow, C. D., Iguchi, T., Farrar, M. R., Durden, S. L., Alves, M., & Olson, W. S. (1997). The TRMM day-1 radar/radiometer combined rain-profiling algorithm. *Journal of the Meteorological Society of Japan, 75*, 799–809. https://doi.org/10.2151/jmsj1965. 75.4_799.

Hogan, R. J., & Battaglia, A. (2008). Fast lidar and radar multiple-scattering models. Part II: Wide-angle scattering using the time-dependent two-stream approximation. *Journal of the Atmospheric Sciences, 65*, 3636–3651. https://doi.org/10.1175/2008JAS2643.1.

Hou, A. Y., Kakar, R. K., Neeck, S., Azarbarzin, A. A., Kummerow, C. D., Kojima, M., Oki, R., Nakamura, K., & Iguchi, T. (2014). The global precipitation measurement mission. *Bulletin of the American Meteorological Society, 95*, 701–722. https://doi.org/10.1175/BAMS-D-13-00164.1.

Iguchi, T., & Meneghini, R. (1994). Intercomparison of single-frequency methods for retrieving a vertical rain profile from airborne or spaceborne radar data. *Journal of Atmospheric and Oceanic Technology, 11*, 1507–1516. https://doi.org/10.1175/1520-0426(1994)011.

Iguchi, T., Seto, S., Meneghini, R., Yoshida, N., Awaka, J., & Kubota, T. (2010). GPM/DPR level-2 algorithm theoretical basis document. NASA Goddard Space Flight Center, Greenbelt, MD, USA, Tech. Rep. Available at https://pmm.nasa.gov/resources/documents/gpmdpr-level-2-algorithm-theoretical-basis-document-atbd, last accessed 6 Nov 2018.

Kummerow, C. D., Barnes, W., Kozu, T., Shiue, J., & Simpson, J. (1998). The Tropical Rainfall Measuring Mission (TRMM) sensor package. *Journal of Atmospheric and Oceanic Technology, 15*, 809–817. https://doi.org/10.1175/1520-0426(1998)015<0809:TTRMMT>2.0.CO;2.

Kummerow, C. D., Ringerud, S., Crook, J., Randel, D., & Berg, W. (2011). An observationally generated a priori database for microwave rainfall retrievals. *Journal of Atmospheric and Oceanic Technology, 28*, 113–130. https://doi.org/10.1175/2010JTECHA1468.1.

Lauri, T., Koistinen, J., & Moisseev, D. (2012). Advection-based adjustment of radar measurements. *Monthly Weather Review, 140*, 1014–1022. https://doi.org/10.1175/MWR-D-11-00045.1.

Masunaga, H., & Kummerow, C. D. (2005). Combined radar and radiometer analysis of precipitation profiles for a parametric retrieval algorithm. *Journal of Atmospheric and Oceanic Technology, 22*, 909–929. https://doi.org/10.1175/JTECH1751.1.

Meneghini, R., Iguchi, T., Kozu, T., Liao, L., Okamoto, K., Jones, J. A., & Kwiatkowski, J. (2000). Use of the surface reference technique for path attenuation estimates from the TRMM precipitation radar. *Journal of Applied Meteorology, 39*, 2053–2070. https://doi.org/10.1175/1520-0450(2001)040<2053:UOTSRT>2.0.CO;2.

Meneghini, R., Kim, H., Liao, L., Jones, J. A., & Kwiatkowski, J. M. (2015). An initial assessment of the surface reference technique applied to data from the Dual-Frequency Precipitation Radar (DPR) on the GPM satellite. *Journal of Atmospheric and Oceanic Technology, 32*, 2281–2296. https://doi.org/10.1175/JTECH-D-15-0044.1.

Munchak, S. J., & Kummerow, C. D. (2011). A modular optimal estimation method for combined radar-radiometer precipitation profiling. *Journal of Applied Meteorology and Climatology, 50*, 433448. https://doi.org/10.1175/2010JAMC2535.1.

Naud, C. M., Booth, J. F., Lebsock, M., & Grecu, M. (2018). Observational constraint for precipitation in extratropical cyclones: Sensitivity to data sources. *Journal of Applied Meteorology and Climatology, 57*, 991–1009. https://doi.org/10.1175/JAMC-D-17-0289.1.

Pedregosa, F., Varoquaux, G., Gramfort, A., Michel, V., Thirion, B., Grisel, O., Blondel, M., Prettenhofer, P., Weiss, R., Dubourg, V., Vanderplas, J., Passos, A., Cournapeu, D., Brucher, M., Perrot, M., & Duchesnay, E. (2011). Scikit-learn: Machine learning in Python. *Journal of Machine Learning Research*, *12*, 2825–2830. Available at http://www.jmlr.org/papers/volume12/pedregosa11a/pedregosa11a.pdf, last accessed 3 Nov 2018

Rao, R. C. (1997). *Statistics and truth: Putting chance to work*. Singapore: World Scientific, 210 pp, ISBN:978-9810231118.

Short, D. A., Meneghini, R., Emory, A. E., & Schwaller, M. R. (2015). Reduction of nonuniform beamfilling effects by multiple constraints: A simulation study. *Journal of Atmospheric and Oceanic Technology, 32*, 2114–2124. https://doi.org/10.1175/JTECH-D-15-0021.1.

Skofronick-Jackson, G., Petersen, W. A., Berg, W., Kidd, C., Stocker, E. F., Kirschbaum, D. B., Kakar, R., Braun, S. A., Huffman, G. J., Iguchi, T., & Kirstetter, P. E. (2017). The Global Precipitation Measurement (GPM) mission for science and society. *Bulletin of the American Meteorological Society, 98*, 1679–1695. https://doi.org/10.1175/BAMS-D-15-00306.1.

Smith, E. A., Turk, F. J., Farrar, M. R., Mugnai, A., & Xiang, X. (1997). Estimating 13.8-GHz path-integrated attenuation from 10.7-GHz brightness temperatures for the TRMM combined PRTMI precipitation algorithm. *Journal of Applied Meteorology, 36*, 365–388. https://doi.org/10.1175/1520-0450(1997)036<0365:EGPIAF>2.0.CO;2.

Testud, J., Oury, S., Black, R. A., Amayenc, P., & Dou, X. (2001). The concept of normalized distribution to describe raindrop spectra: A tool for cloud physics and cloud remote sensing. *Journal of Applied Meteorology, 40*, 1118–1140. https://doi.org/10.1175/1520-0450(2001)040<1118:TCONDT>2.0.CO;2.

Turk, F. J. (2016). CloudSat-GPM coincidence dataset (Version 1C). NASA technical report. Available at https://pmm.nasa.gov/resources/documents/cloudsat-gpm-coincidence-dataset-version-1c, last accessed 3 Nov 2018.

Weinman, J. A., Meneghini, R., & Nakamura, K. (1990). Retrieval of precipitation profiles from airborne radar and passive radiometer measurements: Comparison with dual-frequency radar measurements. *Journal of Applied Meteorology, 29*, 981–993. https://doi.org/10.1175/1520-0450(1990)029<0981:ROPPFA>2.0.CO;2.

Weng, F., Grody, N. C., Ferraro, R., Basist, A., & Forsyth, D. (1997). Cloud liquid water climatology from the special sensor microwave/imager. *Journal of Climate, 10*, 1086–1098. https://doi.org/10.1175/1520-0442(1997)010<1086:CLWCFT>2.0.CO;2.

Willis, P. T. (1984). Functional fits to some observed drop size distributions and parameterization of rain. *Journal of the Atmospheric Sciences, 41*, 1648–1661. https://doi.org/10.1175/1520-0469(1984)041<1648:FFTSOD>2.0.CO;2.

Zhang, J., Howard, K., Langston, C., Kaney, B., Qi, Y., Tang, L., Grams, H., Wang, Y., Cocks, S., Martinaitis, S., & Arthur, A. (2016). Multi-Radar Multi-Sensor (MRMS) quantitative precipitation estimation: Initial operating capabilities. *Bulletin of the American Meteorological Society, 97*, 621–638. https://doi.org/10.1175/BAMS-D-14-00174.1.

Chapter 15
Scattering of Hydrometeors

**Stefan Kneifel, Jussi Leinonen, Jani Tyynelä, Davide Ori,
and Alessandro Battaglia**

Abstract A profound understanding of the scattering properties of hydrometeors is key to extract information from passive and active MW observations. The natural variety of hydrometeor properties also leads to the complexity of how they interact with electromagnetic radiation. The challenge of calculating hydrometeor scattering properties is not only the scattering method itself but starts with an accurate characterization of the hydrometeors themselves. The number and sophistication of those hydrometeor models has rapidly grown during recent years, as has the number of publicly available databases of their scattering properties. This development opens up new possibilities to improve the quality of retrievals but also raises new questions on how to best coordinate the scattering community efforts in the future. While sufficient confidence exists for liquid hydrometeor scattering properties, frozen hydrometeors remain challenging and the questions of how to best model their physical properties and how to derive average properties representative for global applications are still under discussion.

Keywords Scattering · Hydrometeors · Liquid · Ice · Snow · Snowflake · Riming · Melting · Rain · Microwave · Rayleigh scattering · Mie regime · T-matrix · SSRGA · EBCM · DDA · ADDA · DDSCAT · GMM · EMA · RGA · Refractive index · Fast Fourier transform · Backscattering cross section.

S. Kneifel (✉) · D. Ori
Institute for Geophysics and Meteorology, University of Cologne, Cologne, Germany
e-mail: skneifel@meteo.uni-koeln.de

J. Leinonen
Jet Propulsion Laboratory (JPL), California Institute of Technology, Pasadena, CA, USA

J. Tyynelä
Finnish Meteorological Institute, Helsinki, Finland

A. Battaglia
Department of Physics and Astronomy, University of Leicester, Leicester, UK

15.1   Scattering Methods

Microwave remote sensors are well suited to observe liquid and frozen hydrometeors because in most regions in the MW, radiation is able to penetrate even thick clouds. In order to utilize the "cloudy" MW observations for retrievals or data assimilation, the absorption and scattering properties of the hydrometeors must be accurately characterized. In this chapter, we will mainly focus on the hydrometeors' scattering properties.

The structure of this chapter mirrors the three major challenges of characterizing the scattering properties of the multitude of hydrometeors present in clouds. First, a suitable scattering method has to be found. A number of scattering approximations exists which have been widely used in the past because they allow a fast and cost-effective calculation of the scattering properties. As computing power drastically increased during the last decades, more numerically expensive methods have been applied to a quickly increasing number of more and more complex particle shapes (Kneifel et al. 2018). These more recent calculations revealed limitations of commonly used scattering approximations particularly for higher frequencies and larger and more complex hydrometeors. On the other hand, the availability of scattering simulation tools which can handle very complex structures, motivated the development of more realistic hydrometeor models. Hydrometeor models are inevitably important in order to ensure that the physical properties (for example mass-size relation of ice particles) of the hydrometeors used for the scattering computations match the properties found for example in in-situ observations. Finally, once the scattering properties of a representative ensemble of realistic hydrometeor structures has been calculated, the question remains as to which snow particle or ensemble average to choose as representative for the scattering properties of a particular snowfall event or for satellite retrievals applied on a global scale.

The scattering behavior of hydrometeors is often assigned to certain regimes such as Rayleigh or Mie scattering regime. In fact, this grouping mainly indicates which approximations might be applicable to certain hydrometeors depending on the frequency range being considered. The most widely used parameter, which describes the "electrical size" of the particle is the size parameter $x = 2\pi r/\lambda$; it simply relates the characteristic dimension of a particles such as a sphere's radius r to the wavelength λ of the electromagnetic wave. For $x \ll 1$, the wavelength is much larger than the particle and hence all parts of the particle experience nearly the same electric field. As will be briefly discussed in the next section, the Rayleigh approximation can be applied to scattering problems with low size parameter.

This chapter shall provide a broad overview of hydrometeor scattering properties rather than going into details of scattering theory; the interested reader is referred to common textbooks such as the ones by Bohren and Huffman (1983) or Mishchenko et al. (2002). A common way (Bohren and Huffman 1983) to describe the scattering interactions of an incident and scattered electric field is to use the complex amplitude scattering matrix

$$\mathbf{S}(\theta, \phi) = \begin{bmatrix} S_2 & S_3 \\ S_4 & S_1 \end{bmatrix} \tag{15.1}$$

with the azimuth angle ϕ and the scattering angle θ. Commonly used scattering variables, such as backscattering σ_{bsc}, scattering σ_{sca}, absorption σ_{abs} cross section, or asymmetry parameter g can be directly calculated from $\mathbf{S}$

$$\sigma_{\text{bsc}} = \frac{2\pi}{k^2} \left(|S_1(\pi, 0)|^2 + |S_2(\pi, 0)|^2 \right) \tag{15.2}$$

$$\sigma_{\text{sca}} = \frac{1}{2k^2} \int_0^{2\pi} \int_0^{\pi} \left(|S_1(\theta, \phi)|^2 + |S_2(\theta, \phi)|^2 \right) \sin\theta \mathrm{d}\theta \mathrm{d}\phi \tag{15.3}$$

$$\sigma_{\text{abs}} = \frac{2\pi}{k^2} \left(\operatorname{Re} \left[S_1(0, 0) + S_2(0, 0) \right] \right) \tag{15.4}$$

$$g = \frac{1}{2k^2 C_{\text{sca}}} \int_0^{2\pi} \int_0^{\pi} \left(|S_1(\theta, \phi)|^2 + |S_2(\theta, \phi)|^2 \right) \sin\theta \cos\theta \mathrm{d}\theta \mathrm{d}\phi \tag{15.5}$$

It should be noted that there exists a large number of numerical methods to calculate scattering of complex particles (see for example the overview given in Kahnert (2003); a large number of scattering software is also available from http://www.scattport.org (last accessed 12 Oct. 2018). We will focus in the following on the most common methods used to calculate scattering properties of hydrometeors in the MW.

15.1.1   Rayleigh, Mie, and T-Matrix Methods

If the particle is small compared with the wavelength of the incident radiation, the Rayleigh approximation can be applied which simplifies the calculation of $\mathbf{S}$ to

$$\mathbf{S} = \begin{bmatrix} S_2 & 0 \\ 0 & S_2 \cos(\theta) \end{bmatrix} \tag{15.6}$$

$$S_2 = \frac{3k^2}{4\pi} K_{CM} V \tag{15.7}$$

$$K_{CM} = \frac{\varepsilon - 1}{\varepsilon + 2} \tag{15.8}$$

where $k = 2\pi/\lambda$ is the wavenumber, V is the volume of the spherical hydrometeor, and K_{CM} is the Clausius-Mossotti factor with the complex dielectric constant of the particle ε. In (15.8) it is assumed that the polarizability of the particle is the same in all direction as it is the case for a homogeneous sphere. For nonspherical ice particles (even with $x \ll 1$), modified formulas for K_{CM} have to be applied which have been derived for idealized ice particle shapes (Westbrook 2014, Hogan et al. 2017). This

adjustment of the K_{CM} factor is also necessary for approximations derived for aggregates composed of different ice monomers such as the Self-Similar Rayleigh Gans Approximation (SSRGA, Sect. 15.1.3). The definition of the radar reflectivity factor Z as the sixth moment of the particle size distribution (PSD) is closely connected to the Rayleigh approximation. Since the early days of radar meteorology, low frequencies (for example at C or S band) were used for precipitation radars focusing on the detection and quantification of nearly spherical rain drops for which the Rayleigh approximation holds. As one can see from (15.2) and (15.7), in the Rayleigh approximation, the backscattering cross sections σ_{bsc} of the rain drops in a certain volume are directly related to the square of their volumes and hence to the sixth power of their diameters.

For spherical particles which cannot be treated as Rayleigh scatterers, an analytical solution for their scattering properties has been derived by Mie (1908) using spherical wave vector functions to describe the incident, scattered, and internal field. A full derivation of the Mie theory can be found in scattering textbooks such as that of Bohren and Huffman (1983). Mie theory has been widely applied for raindrops and also ice and snow particles because it allows a very fast computation of the scattering properties. An important parameter for the calculation of Mie scattering is the definition of the particle's complex dielectric constant which can be challenging for particles consisting of mixtures of different materials (see Sect. 15.1.2). The Mie theory and associated software has been also expanded to multi-layer spheres where individual dielectric properties can be defined for the different layers (Aden and Kerker 1951).

Extended boundary condition method (EBCM), which is a scattering formulation for non-spherical particles using spherical wave vector functions to describe the electromagnetic fields has been developed by Waterman (1965). The coefficients used for the expansions of the basis functions, which relate incident and scattered fields, are combined in a so-called transition matrix or T-matrix (for a complete derivation see Mishchenko et al. 2002). A particular advantage of the T-matrix formalism is that the T-matrix only has to be calculated once for a particular particle size and shape. The scattering properties can then be derived from it for any orientation of the scatterer and observation geometry. EBCM is theoretically applicable to any homogeneous particle having a radially single-valued surface. However, shapes that are numerically convergent, are more restricted due to the boundary conditions. Also, symmetries in the particle shapes can be utilized to make the method more efficient. Due to this, most of the available codes assume some symmetries in the shapes, such as spheroids, cylinders and Chebyshev particles (Mishchenko and Travis 1998); polyhedral (Kahnert et al. 2001) and more arbitrary shapes (Petrov et al. 2011) are also available. The method of discrete sources by Wriedt and Doicu (1998) also uses the T-matrix formalism for more arbitrary shapes. In atmospheric sciences, it became common to denote the use of spheroidal shapes which are often calculated with code provided by Mishchenko and Travis (1998) as T-matrix method (a convenient python interface based on the same source code has recently been made available, Leinonen 2014).

15.1.2 Effective Medium Approximation

Only cloud, drizzle, and raindrops can be considered to be composed of a homogeneous medium. Ice particles, dry and melting snowflakes, graupel, and even hailstones, if they contain air inclusions or have a liquid coating, are characterized by a complex structure of different materials such as ice, air, or liquid water. Some scattering methods, for example the Discrete Dipole Approximation (DDA, Sect. 15.1.4) or the Generalized Multiparticle Mie-solution (GMM, Sect. 15.1.5), allow for the explicit treatment of this complex structure if the detailed hydrometeor models provide this information. Scattering approximations such as Mie theory or T-matrix, usually approximate the hydrometeor structure with a simplified, often spheroidal geometry. They require the user to assign a specific complex dielectric constant to the particle, which in the case of heterogeneous materials can be calculated with so-called effective medium approximations (EMA) or dielectric mixing formulas.

The most widely used EMAs are those of Maxwell-Garnett (1904) and Bruggeman (1935). In both formulations the average or effective dielectric constant ε_{eff} is calculated with dielectric constants of the particle's components and their volume fractions f. The differences between the methods are illustrated and thoroughly discussed in Bohren and Battan (1982) and Bohren (1986). In the Maxwell-Garnett formulation, it is assumed that one material is present as small, disconnected, spherical inclusions (ε_i, f_i) embedded in a continuous, homogeneous matrix (ε_m).

$$f_i \frac{\varepsilon_i - \varepsilon_m}{\varepsilon_i + 2\varepsilon_m} = \frac{\varepsilon_{eff} - \varepsilon_m}{\varepsilon_{eff} + 2\varepsilon_m} \tag{15.9}$$

As the Maxwell-Garnett relation (15.9) is non-symmetric, the result depends on whether the snowflake is assumed as air with "grains" of ice or vice versa. Obviously, one or the other might seem more appropriate depending on whether ε_{eff} is needed for a fluffy, low-density snowflake or a lumpy graupel particle.

In the symmetric Bruggeman relation, the two components are indistinguishable and hence an arbitrary decision when to use ice or air as the matrix or the inclusions is not necessary. A generalized EMA combining the Maxwell-Garnett and Bruggeman formulation is provided by Shivola (1989)

$$\frac{\varepsilon_{eff} - \varepsilon_1}{\varepsilon_{eff} + 2\varepsilon_1 + v(\varepsilon_{eff} - \varepsilon_1)} - f_2 \frac{\varepsilon_2 - \varepsilon_1}{\varepsilon_2 + 2\varepsilon_1 + v(\varepsilon_{eff} - \varepsilon_1)} = 0. \tag{15.10}$$

The parameter v is a positive number. Setting $v = 0$ in (15.10) gives the Maxwell-Garnett relation while $v = 2$ yields the Bruggeman formula. Comparisons of DDA simulations of ice-air spheres of various densities with ε_{eff} calculated with different EMA and applied to Mie theory revealed the best agreement for $v = 0.85$ which is neither of the "classical" EMAs (Petty and Huang 2010).

15.1.3 Rayleigh Gans and Self-Similar Rayleigh Gans Approximation

It is possible under certain conditions to simplify the scattering problem by assuming that the single scattering elements of a particle only interact with the incident wave. The resulting scattered wave is then simply the superposition of the scattering contributions by the single elements. This so-called Rayleigh-Gans approximation (RGA, Bohren and Huffman 1983) extends the Rayleigh formulation (15.7) by introducing a form factor f,

$$S_2 = \frac{3i}{4\pi} K_{CM} k^3 V f \tag{15.11}$$

with i being the imaginary unit. The form factor is a dimensionless number and can be interpreted as a description of the deviation from Rayleigh scattering ($f = 1$ reduces (15.11) to the Rayleigh approximation (15.7)). The form factor can be calculated for a particular particle structure by integrating the phase of the electromagnetic wave over the particle volume V

$$f = \frac{1}{V} \int_V \exp{(i\delta(\mathbf{R}))} d\mathbf{R} \tag{15.12}$$

$$\delta(\mathbf{R}) = \mathbf{R} \cdot (\mathbf{k}_{\text{inc}} - \mathbf{k}_{\text{sca}}) \tag{15.13}$$

where $\mathbf{R}$ describes the position within the particle and δ is related to the difference of the phases between the incident wave vector k_{inc} and the scattered wave vector k_{sca}. If all waves from the scattering elements of the particle are in phase, δ becomes 0 and the form factor is equal to unity. This situation can be expected if the particle is small compared to the wavelength as assumed in the Rayleigh approximation. It is worth noting that in (15.12) the integral is done only over the ice elements of the particle. Therefore, no EMA as for Mie or T-matrix method is needed which eliminates a potential source of uncertainty.

A particularly interesting aspect of the RGA is that the form factor can be calculated with the Fourier transform of the mass distribution along the propagation direction of the incident wave (a detailed discussion is given in Sorensen 2001). The inherent mass fluctuations present in a snowflake – no matter how complex the shape might be – can thus be taken into account in the RGA while in methods requiring an EMA, these fluctuations are represented by an average value. In fact, Leinonen et al. (2013) showed that these missing mass fluctuations in Mie or T-matrix methods are mainly responsible for their deficiencies in representing the scattering properties of larger, low-density complex particles. The direct connection of mass distribution and scattering properties in the RGA thus provides an interesting opportunity to link microphysics and scattering properties.

The formal conditions for the applicability of RGA are provided by Bohren and Huffman (1983).

$$| m - 1 | \ll 1 \qquad (15.14)$$

$$2kD \, | m - 1 | \ll 1 \qquad (15.15)$$

with $m = \sqrt{\varepsilon}$ is the complex index of refraction of the particle material and D is the particle's maximum dimension. A heuristic interpretation provided in Bohren and Huffman (1983) of these conditions is that (15.14) ensures that reflections of the incident wave on the particle-medium interface are small; this is the case if m of the surrounding medium and the particle are similar. The condition (15.15) requires that the phase and amplitude of the incident wave is not changing significantly while passing through the particle. The RGA appears to be well applicable to snowflakes considering the low refractive index of ice in the microwave and assuming a "fluffy" structure of the particle which limits the coupling between the different scattering elements.

During recent years, the RGA was increasingly applied to single, complex snowflake shapes. Its ability to accurately predict radar backscattering cross sections has been intensively studied (Matrosov 1992; Westbrook et al. 2006; Tyynelä et al. 2013; Leinonen et al. 2013, 2018a, b; Hogan et al. 2012). The RGA results can be validated with accurate numerical methods, such as the Discrete Dipole Approximation (DDA, Sect. 15.1.4), which takes all internal and external scattering interactions of the particle and the incident wave into account. Good agreement between RGA and DDA has been found for various low-density snow aggregates and different scattering parameters (Tyynelä et al. 2013). The differences are larger for σ_{bsc} than for integrated quantities such as σ_{sca} or single scattering albedo. Some of the biases found in Tyynelä et al. (2013) are likely to be caused by using the classical Clausius-Mossotti factor for spheres (15.8) instead of a modified K_{CM} which better represents the non-symmetric polarizability of the aggregate monomers (Hogan et al. 2017). In order to better understand the limits of the applicability of the RGA for snow, Leinonen et al. (2018a, b) performed a similar validation study for various rimed aggregates. As expected, the deviations from single particle scattering properties increase with higher degrees of riming due to increasing internal scattering interactions. Interestingly, the average scattering properties of an ensemble of particles for a given degree of riming and size were found to be in good agreement between DDA and RGA except for the most heavily rimed particle category.

For a radar, the backscattered wave is indeed the superposition or average of many individual hydrometeor backscattering signals rather than the response of a single particle. In case of aggregates, a number of studies found that their structure can be described as being self-similar or fractal (Sorensen 2001; Westbrook et al. 2004; Ishimoto 2008, among others). The self-similarity assumption was the basis for Hogan and Westbrook (2014) to derive an analytical expression for the ensemble backscattering cross section of snow aggregates with similar fractal properties. The SSRGA requires five parameters which describe the average mass distribution and the individual fluctuations from this average distribution along a certain direction. In order to derive the coefficients, only an ensemble of discretized snowflake structures

(similar to the input structure files required by many DDA methods) is needed. The method has been recently extended (Hogan et al. 2017) by the calculation of the scattering phase function without need for additional coefficients. As long as polarimetric quantities can be neglected (they inherently depend on the interaction of the particle's scattering elements which are neglected in RGA and SSRGA), the SSRGA can be used for active and passive MW radiative transfer. The same coefficients can be used to calculate scattering properties for any frequency as long as the formal criteria (15.14) and (15.15) for the applicability of the RGA are valid. SSRGA coefficients have been derived for different aggregate models (Hogan and Westbrook 2014; Hogan et al. 2017) and also for rimed aggregates (Leinonen et al. 2018a, b). It should be noted that the classical RGA formulation (15.11) does not produce depolarization due to the lack of multiple scattering between the volume elements. Without rigorously including the mutual interactions between the elements as in DDA, this contribution can be estimated in a mean-field sense (Berry and Percival 1986) or by computing the second-order scattering (Acquista 1976).

15.1.4 Discrete Dipole Approximation (DDA)

The Discrete Dipole Approximation is a popular technique to compute the scattering and absorption properties of particles with arbitrary shape and composition. The first derivation of this method (Purcell and Pennypacker 1973) followed the intuitive idea of substituting the scatterer shape with a cluster of point dipoles. Those dipoles interact with the incident wave and with each other modifying their own polarization state. The scattered field is computed by the superposition of the field radiated by those polarized dipoles. A more mathematically rigorous way of deriving the DDA technique comes from the discretization of the integral volume equation of the electric field. This approach shows the equivalence of DDA to other scattering method based on the same mathematical background (Kahnert 2003; Petty and Huang 2010; Piller and Martin 1998).

The subdivision of the scatterer volume into n polarizable dipoles makes the DDA formulation a set of n linear equations to be solved with respect to the dipole polarization states. This formulation leads to a memory occupancy and a computational complexity that scales as $O(n^2)$. The computational cost of the algorithm makes it only feasible for targets that are either small or very sparse (i.e., with a large number of internal cavities). The computational cost of DDA can be greatly reduced if it is assumed that the discrete dipoles belong to a regular lattice grid. With this restriction, the system of n equations can be solved in the dual space in $O(N \log N)$ by applying a combination of Fast Fourier Transform and an iterative solver (Goodman et al. 1991). Here N is the number of cells in the lattice bounding box. This accelerated algorithm comes with the drawback of increasing the memory occupancy scaling to $O(n^3)$ and because of that the DDA algorithm is well known to be memory bounded.

The popularity of DDA is certainly related to the increasingly available computational resources but also to the availability of publicly available software packages. The Discrete Dipole Scattering (DDSCAT, Draine and Flatau 1994) and Amsterdam DDA (ADDA, Yurkin and Hoekstra 2011) software packages are probably the most widely used DDA implementations. Both algorithms are actively developed and include several options for the DDA formulation. These codes can also scale well on large parallel computer clusters, which mitigates the memory restrictions imposed by the DDA formulation.

The accuracy of DDA has been repeatedly tested against analytic expressions such as the Mie solution for homogeneous and layered spheres and the T-matrix (Ori and Kneifel 2018; Yurkin et al. 2006; Tyynelä et al. 2009; Petty and Huang 2010). The results of these tests show how strongly the DDA accuracy depends on particle shape, size, dielectric properties and DDA formulation. However, it is possible to derive two general criteria for the validity of the DDA solution. The first requires that the scatterer shape is well represented by the cluster of polarizable dipoles, i.e. the size of each dipole should be much smaller than any constitutive length of the scattering target. The second criterion ensures that the electric field within the scatterer is well represented by the superposition of the electric fields radiated by the oscillating electric dipoles. The latter requirement is usually summarized by ensuring that $|m|kd \ll 1$, where $|m|k$ is the wavenumber within the scatterer and d is the size of the dipoles. This last requirement is generally assumed as the only criterion to be checked to ensure the validity of DDA. However, especially if the value of the refractive index of the scattering particle is high, additional criteria for the DDA accuracy have to be applied (Ori and Kneifel 2018).

DDA has been used in a wide range of scattering applications ranging from the characterization of interstellar dust to blood cells. Particularly, after the publication of a first publicly available database of ice particles by Liu (2008), DDA has been increasingly used to compute scattering properties of various non-spheroidal hydrometeors; an overview of recently available scattering databases if provided in Table 15.1.

As an example of single particle scattering properties, extinction and backscattering efficiency for raindrops at X, Ka and W band are shown in Fig. 15.1. Scattering properties are computed for spheres and for perfectly oriented spheroids with axial ratios parameterized according to Andsager et al. (1999) at vertical illumination. Rayleigh approximation is also plotted as a reference. Generally speaking, the spheroid approximation produces slightly larger extinction (but only for large raindrops); the same applies for the backscattering for raindrops with equivalent volume radii larger than 1.2, 1.5 and 2 mm at 94, 35.5 and 9.6 GHz, respectively. These differences tend to be smoothed out when bulk scattering properties are computed by averaging the single scattering properties over a particle size distribution. As an example, the reflectivity expected for an exponentially distributed population of raindrops with a water content of 1 g m^{-3} and different mean mass-weighted equi-volume diameters (D_m) is plotted in Fig. 15.2. Clearly, there is no large difference between spheres and perfectly oriented spheroids. The non-Rayleigh scattering effects tend to strongly reduce the reflectivity when moving

Table 15.1 Databases of scattering properties for snow particles at microwave frequencies

Publication	Particle habits	Morphology	Size range (μm)	Frequency range (GHz)	Orientations	Scattering Method	Availability
Liu (2008)	N1e, C1e, C1g, C2a, P1a, P1c, P1f	Pristine	50–10000	13.4–340	Random	DDA	https://github.cam/rhoneyagar/scatdb
Pelty and Huang (2010)	N1e, P1e	Aggregated	125–10000	13.4–89	Random	DDA	Author
Botta et al. (2010)	N1e	Aggregated, melted	500–11000	3, 35.6	Horizontal	GMM	Author
Tyynelä et al. (2011)	P1e, P1f	Aggregated	200–24000	5.6–94	Horizontal	DDA	http://helios.fmi.fi/~tyynelaj/
Tyynelä et al. (2013)	N1e, P1a, P1d, C2a	Pristine, aggregated	450–8500	3–220	Horizontal	DDA	http://helios.fmi.fi/~tyynelaj/
Nowell et al. (2013)	C2a	Aggregated	800–12000	10.7–183.3	Random	DDA	https://github.com/rhoneyager/scatdb
Ori et al. (2014)	C1e	Aggregated, melted	1000–15000	5.6–157	Random	DDA	Author
Tyynelä and Chandrasekar (2014)	N1e, C1e, P1a, P1e, P1f, C2a, R4b	Pristine. aggregated	100–24000	2.7–220	Horiz., random	DDA	http://helios.fmi.fi/~tyynelaj/

Reference	Habits	Type	Size range	Frequency	Orientation	Method	Source
Leinonen and Szyrmer (2015)	P1e	Aggregated, rimed	700–20000	9.7–94	Gaussian	DDA	Author
Leinonen and Moisseev (2015)	Nle, Pla, P1e, C2a	Aggregated	200–10000	13.6–94	Gaussian	DDA	Author
Lu et al. (2016)	Nle, Cle, Pla, Plc, Pld, R4c	Pristine, aggregated	100–62000	9.4–94	Horizontal	GMM, DDA	https://www.arm.gov/data/data-sources/icepa.rt-mod-120
Kuo et al. (2016)	N1e, P1a, P1c, P1d, P1e, P1f, P2c	Pristine, aggregated	260–14000	3–190	Random	DDA	https://storm.pps.eosdis.nasa.gov/storm/OSSPTest.jsp
Johnson et al. (2016)	N1e, P1e	Aggregated, melted	100–14000	13.4–183	Random	DDA	Author
Ding et al. (2017)	Cle, C1f, Pla, C2a	Pristine, aggregated	2–10000	1–874	Random	II-TM, IGOM	Author
Eriksson et al. (2018)	N1e, Cle, C1g, P1a, C2a, P1c, P1f	Pristine, aggregated	10–22000	1–886	Random	DDA, Mie	https://doi.org/10.5281/zenodo.1175572

Particle habits are listed according to the classification by Magono and Lee (1966)
Note that some of the databases include also particle types that are not classified, such as soft/solid spheroids
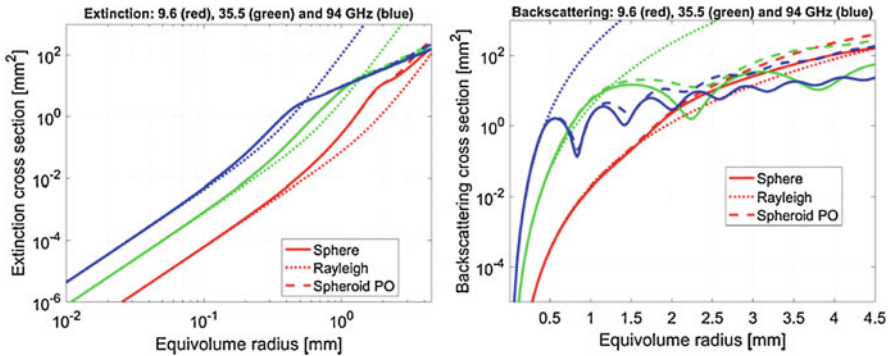
Fig. 15.1 Extinction (left) and backscattering (right) cross sections for spheres (continuous lines), perfectly oriented spheroids (dashed) and Rayleigh spheres (dotted) for single raindrops at 9.6 (red), 35.5 (green) and 94 (blue) GHz

Fig. 15.2 Reflectivity per unit mass for an exponential drop size distribution vs mean mass-weighted equi-volume diameter for spheres (continuous lines), perfectly oriented spheroids (dashed) at 9.6 (red), 35.5 (green) and 94 (blue) GHz
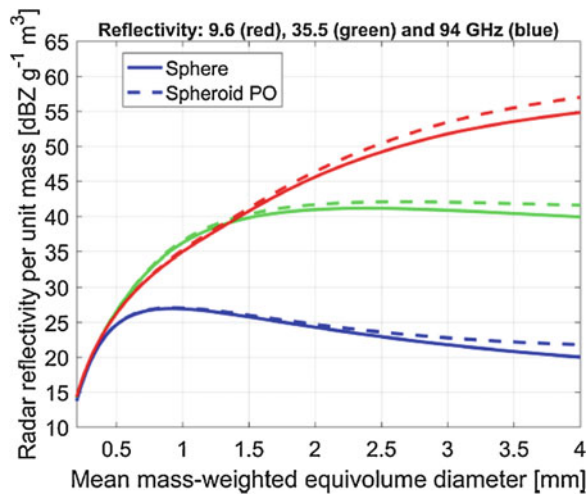
to higher frequency. The only exception is represented by the 9.6–35.5 GHz pair when considering D_m smaller than 1.4 mm (see also the related discussion about the Dual Precipitation Radar on GPM, Chap. 11).

15.1.5 Generalized Multiparticle Mie-Solution (GMM)

A generalization of the Mie theory to two spheres was introduced by Liang and Lo (1967) and Bruning and Lo (1971). Later, Borghese et al. (1979), Wang and Chew (1983), Mackowski (1991) and Xu (1995) generalized the method for an arbitrary number of spheres and improved its numerical efficiency. They also used the

T-matrix formalism for computing the scattering properties of the particles. The only restriction in these methods is that the sphere surfaces are not allowed to overlap. However, some of the publicly available codes, such as the one by Mackowski and Mishchenko (2011), allow the spheres to be inside each other.

GMM has been used mainly for modeling light scattering by dust and soot particles, but Botta et al. (2010) applied it to partially melted snow particles at microwave frequencies. They approximated long columns by a chain of spheres and aggregated these chains together in a random way. Recently, Lu et al. (2016) published a comprehensive database, which includes these aggregates as well as single dendrites also modeled as a regular grid of spheres. The database described in Lu et al. (2016) is the first which includes the full scattering matrix for the full sphere of incident angles. Due to the air between the spheres, the dielectric constant had to be modified in order to match that of a solid ice particle. A limitation in GMM is the maximum number of spheres that can be used to approximate the shapes, which is more limited than the number of dipoles in DDA.

15.2 Hydrometeor Models

Without being able to accurately characterize the physical properties of real hydrometeors, even a perfectly accurate scattering method would be useless for realistically characterizing their scattering properties. Hydrometeor models are therefore needed to realistically reproduce key hydrometeor properties such as size, mass, shape, internal structure, mixture of different components, or falling behavior. For some hydrometeors, those models have been available for a long time but for more complex particles, such as melted or rimed particles, accurate hydrometeor models are still under development.

15.2.1 Liquid Hydrometeors

While cloud droplets are perfectly spherical, raindrops with size exceeding $\approx$ 1.0 mm in radius and falling at terminal velocity in air tend to have shape similar to asymmetric oblate spheroids with a flattened base. The shapes of water drops were first described by Pruppacher and Pitter (1971) using a series of Chebyshev polynomial but they can also be well described by oblate spheroids with size-dependent axial ratios (e.g., Mishchenko and Travis 1998, their chapter 16). Raindrops tend to be horizontally aligned with the major axis on the horizontal plane. In the presence of turbulence, small canting angles are observed with a Gaussian probability distribution about a mean value of zero and with standard deviation less than 5° (Beard and Jameson 1983). The refractive index of liquid water is also well known, (e.g., Ellison 2007). Recent studies (Turner et al. 2016) have also thoroughly characterized its behavior at very cold temperatures (which are relevant for supercooled droplets).

15.2.2   Ice and Snow

In contrast to liquid water drops, icy hydrometeors found in nature exhibit diverse
shapes, structures and densities owing to the interaction of three growth processes:
ice crystal growth by vapor deposition, aggregation, and riming. Deposition growth
alone creates widely variable shapes depending mainly on temperature and ice
supersaturation (Magono and Lee 1966). This complexity is further compounded
by aggregation and riming. Ice crystals have been grown in diffusion chambers
under different atmospheric conditions (e.g., Bailey and Hallet 2004; Libbrecht
2005; Libbrecht and Rickerby 2013), but it is difficult to simulate the full complexity
of the natural environment in the laboratory. Consequently, properties of icy hydro-
meteors have been mostly derived from field measurements on the ground or from
aircraft. The downside of these is that the conditions can vary a great deal between
campaigns and even during the measurements, which can limit their utility. More-
over, some properties like the mass and 3D structure of the particle are difficult to
measure directly, and need to be estimated. Some new in situ measurement devices
try to solve this problem by using multiple cameras Garrett et al. (2012) or holog-
raphy Kaikkonen et al. (2014).

Due to the relative complexity of snowflakes, developers of scattering models
have often tried to simplify the shape to a degree that still gives acceptable scattering
properties. The approximation of snowflakes as spheres in the Rayleigh scattering
regime was already used by Marshall and Gunn (1952). Due to its simplicity and fast
computation, the T-matrix method with spheroidal shapes has also been utilized for
snow (e.g., Matrosov 2007; Hogan et al. 2012; Liao et al. 2013). To simulate the
variable density of icy hydrometeors, EMA is typically used to calculate the dielec-
tric properties of an air–ice mixture. This "soft" spheroidal model has only a few free
parameters, and can therefore be easily fitted to empirical formulas. For some
scattering properties, the lack of irregularity in the particle shape can be partly
compensated by a distribution of orientations.

The study of Evans and Vivekanandan (1990) was among the first to model
scattering by non-spheroidal ice particles at the microwave frequencies. The shapes
they used for the ice crystals were hexagonal plates, columns and needles. This
development was motivated mainly by the availability of high frequency cloud radar
and radiometer data at that time. DDA also had become feasible to utilize as
computing resources had increased. Later, e.g., Dungey and Bohren (1993), Evans
and Stephens (1995) and Tang and Aydin (1995) extended these studies to even
higher frequencies up to 340 GHz. Note that many of these models assumed
horizontally oriented particles due to the observations made by, e.g., Cho et al.
(1981) and Thomas et al. (1990). More recent efforts to systematically compute
scattering by complex ice crystals at high microwave frequencies have been
performed by Kim (2006), Liu (2008), Hong et al. (2009) and Kuo et al. (2016).
In these studies, however, particles were assumed to be in random orientations.

It was shown by Westbrook et al. (2006), Ishimoto (2008), Petty and Huang
(2010), Botta et al. (2010) and Tyynelä et al. (2011) that for higher radar frequencies,

especially at Ka and W bands, the soft spheroidal models for snow significantly underestimates the backscattering cross sections when compared to more complex shapes. The underestimation is caused by the resonance behavior of the symmetric shape and homogeneous structure of the soft spheroid model in the Mie resonance region (see examples in Fig. 15.3). This is a concern particularly with aggregates, which can reach sizes of the order of 1 cm, comparable to or larger than the radar wavelengths. In recent years, studies that also include aggregates of ice crystals, as well as rimed snowflakes, have become more common. This has driven the need to develop detailed models of snowflake growth that produce shapes that can be used as input to scattering calculations.

In remote sensing measurements, precise information of atmospheric conditions is rarely known. Air motion in clouds and precipitation can be turbulent such that particle orientation is also uncertain, and the volumes observed are large enough to entail thousands of differently shaped particles. It is therefore not practical to model ice crystals in a deterministic way by using detailed physical models. Instead, researchers have tried to find a compromise between theoretical and empirical information of ice particles in many different ways, which can be roughly divided into two categories: *physical and empirical modeling*.

The *physical simulation of ice crystal growth* by deposition is complicated by the continuing lack of detailed knowledge of the physics involved, and its dependence on temperature, pressure and vapor density (Libbrecht 2005). Mathematical or semi-
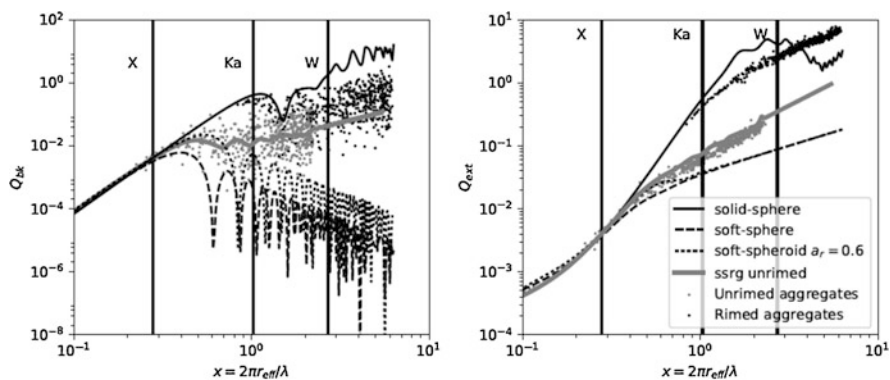
Fig. 15.3 Backscattering (Q_{bk}, left) and extinction (Q_{ext}, right) efficiencies defined as $Q = \sigma/\pi r_{eff}^2$ with r_{eff} being the radius of the equal mass ice sphere and σ the corresponding cross section. The size parameter x combines the dependence of the scattering variables on particle mass and wavelength. Spheroid approximations include spheres of solid ice (continuous black line), spheres with an ice-air mixture (black long-dashed) representing the mass-size relation of Brown and Francis (1995), and spheroids with the same mass-size relation but with an aspect ratio of 0.6 (black dotted). Scattering properties for unrimed (gray dots) and rimed (black dots) calculated with DDA in Leinonen and Szyrmer (2015) (results shown are for particle model B and the second most rimed particles). The SSRGA (gray solid line) has been derived for the same ensemble of unrimed aggregates (Leinonen et al. 2018a). The vertical lines denote the size parameter for X, Ka and W band assuming a particle mass of 10 mg which corresponds for example for the unrimed aggregates to a maximum snowflake size of 3 cm

physical models approximating the growth in 2D (Reiter 2005) and 3D (Gravner and Griffeath 2009) have been developed, but purely physical models have not yet been achieved, owing to the uncertainties in molecular scale physics of ice surfaces. The physics-based modeling of aggregation was formulated by Westbrook (2004) and Maruyama and Fujiyoshi (2005) and later extended to riming by Leinonen and Szyrmer (2015). These methods are stochastic and take into account the mutual probabilities of particle collisions, which depend on particle sizes and velocities. This method also produces fractal-like structures for the aggregates with the fractal dimension close to 2, while the dimensions for purely rime-grown particles are closer to 3. The aggregating particles are usually frozen in place at the contact point, but some methods allow some overlap. Rimed droplets were also assumed to freeze immediately on contact with ice in Leinonen and Szyrmer (2015). The results of these models are typically only semi-physical in practice because the complexity of the physics and the variability of environmental conditions require simplifying assumptions and approximations to be made. Many of the models also use empirical formulas for the dimensions of the original ice crystals, although Kuo et al. (2016) used the 3D-crystal growth algorithm of Gravner and Griffeath (2009). The shapes produced with the physical approach are qualitatively realistic, but may demand a lot of computer resources. Further examples of studies using this method are those by Tyynelä et al. (2011), Tyynelä and Chandrasekar (2014), Leinonen and Moisseev (2015), Kuo et al. (2016) and Ekelund et al. (2018).

In *empirical growth models*, the particles are generated in an ad hoc way by fitting the particle models to empirical formulas. As size and shape are the two most easily measured physical properties of snowflakes, other properties (e.g., mass) tend to be defined with respect to these in simple mathematical forms, such as the power law αD^{β}, where α and β are empirically fitted constants for a given type of snowflake. There have been many studies that give different values for the constants (Pruppacher and Klett 1997). The shapes of ice crystals are often fairly simple, while the physics that they arise from is not, so the empirical approach is well suited for generating these models. Empirical models of aggregates have also been developed. In these, the shape models themselves are not necessarily qualitatively realistic, but only incorporate some kind of randomness. Even though the shapes may not be realistic, the other properties (typically mass and aspect ratio) are guaranteed to obey the formulas that were used during the fitting. Common formulas that are used for mass are by Mitchell (1996) and Brandes and Ikeda (2007). When compared to the physical-based models, the properties of empirically generated particles show much less variance. The models are computationally fast, but the downside of this approach is that the results may not be generally usable due to the fitting. Examples of such studies include Botta et al. (2010), Nowell et al. (2013), Ori et al. (2014), Johnson et al. (2016), and Lu et al. (2016).

There are also studies that incorporate both of these approaches, such as the fractal model by Ishimoto (2008). The fractal model is a mathematical model that mimics the fractal nature of natural snowflakes, but is not necessarily realistic in any other way. The fractal size can be scaled arbitrarily and its mass can be fitted to empirical formulas.

15.2.3   *Melting Ice*

Creating realistic, detailed scattering models of melting snowflakes remains particularly challenging. These bodies combine the physical phenomena of both liquid and solid hydrometeors, and consequently many of the simplifying assumptions applicable to those cannot be used with melting particles. Most importantly, unlike frozen hydrometeors, melting particles cannot be well approximated as rigid bodies, nor do they assume smooth, near-spherical shapes like liquid ones. The surface tension between liquid and ice plays a major role in the determination of the shape of melting particles, and leads to a very inhomogeneous mixture of liquid water and ice (Knight 1979; Fujiyoshi 1986; Mitra et al. 1990; Oraltay and Hallett 2005). Nevertheless, understanding the microwave scattering properties of melting snowflakes remains important because of their unique characteristics: most notably, they are responsible for the bright band, a horizontal layer near the 0 °C isotherm where radar reflectivity is higher than either in the snow above or the rain below it (Austin and Bermis 1950; Battan 1973; Fabry and Zawadzki 1995). The melting layer also has a distinct effect on the observations of both polarimetric radars (Brandes and Ikeda 2004; Giangrande et al. 2008) and passive microwave radiometers (Bauer et al. 1999; Olson et al. 2001), and attenuates microwave signals strongly (Klaassen 1990; Kharadly and Hulays 1994). The melting layer attenuation can strongly affect radar signals crossing it, and properly correcting for it is important to satellite-based radar estimates of rain rate, as well as ground-based radar observations where the shallow elevation angle of the radar beam may require the signal to travel for a long distance inside the melting layer (von Lerber et al. 2015).

   Because of the complexity of the physics of melting snowflakes, they were long modeled as spheres whose air–liquid water–ice mixture was treated using an EMA (Bohren 1986; Klaassen 1988). In some studies, these spheres were layered, each layer having a different mixture of the constituents, reflecting the initial formation of meltwater preferentially on the outer edges of the snowflake (Fabry and Szyrmer 1999).

   At wavelengths much larger than the scatterer diameter, the sphere models, combined with Mie scattering calculations, can simulate the radar reflectivity in the melting layer quite accurately (Fabry and Szyrmer 1999). However, they drastically underestimate the cross-polarized signal from the scatterers. Moreover, at shorter wavelengths they suffer from the same fundamental problems as similar models of dry snow: the microstructure of the snowflake affects the scattering signal in a manner that cannot be simulated by the homogeneous or layered spherical approximations. Thus DDA, and other numerical scattering methods that work with arbitrary shapes, are also attractive for simulating the scattering from melting snow.

   DDA and GMM simulations of melting snow follow the same principles as those of dry snowflakes. With DDA, the higher refractive index of liquid water compared to ice requires the use of smaller dipoles, leading to higher computational and memory requirements. Nevertheless, performing the scattering simulations for a given shape model is reasonably straightforward. The main challenge, then, is

producing appropriate shape models, which is particularly complicated for the reasons outlined above.

A few studies have investigated the scattering properties of melting snowflakes using DDA or GMM. The study of Tyynelä et al. (2014) used an uneven distribution of meltwater within spheroids to investigate its effect on polarimetric ground-based weather radar signals, but found little difference between this approach and homogeneous spheroids. On the other hand, Botta et al. (2010), Ori et al. (2014) and Johnson et al. (2016) used a heuristic model to imitate melting of detailed aggregate snowflake models, and found substantial differences to bulk models. Recently, Leinonen and von Lerber (2018) used a physical model to simulate snowflake melting at a detailed level, but as of this writing, this has not yet been used for scattering studies. Thus, considerable work remains to be done in fully understanding the scattering properties of melting hydrometeors in simulations.

15.3 Scattering Properties and Scattering Databases

Rather than providing an in-depth comparison of the scattering properties included in the growing number of scattering databases, which would certainly be out of the scope of this chapter, we aim to provide a basic overview of the main scattering characteristics of the different hydrometeor classes illustrated with examples from different hydrometeor models and scattering methods. We also hope to provide the reader a useful overview of currently available scattering databases for ice and snow particles which usually requires a laborious literature and internet research.

15.3.1 Liquid Hydrometeors

Due to the impact of raindrop non-sphericity on radar polarimetry and microwave radiometry, the modeling of raindrops scattering properties has been extensively investigated. Typically, the Rayleigh ellipsoidal approximation or T-matrix methodology has been adopted for computing the scattering matrix (Oguchi 1973; Mishchenko et al. 2008; Bringi and Chandrasekar 2001; Battaglia and Simmer 2007). These computations have been historically performed for low incidence angles and at the frequency characteristic of precipitation radars (i.e., S, C, X band); more recently, with the advent of spaceborne cloud radars, more attention has been paid to Ka and W bands. Differently from ground-based applications, for space-borne applications the interest resides mainly at vertical incidence where, unfortunately, polarimetric signatures tend to disappear.

15.3.2   *Ice Crystals, Aggregates, and Rimed Particles*

The number of scattering databases and the complexity of the particles included largely increased during recent years (see Table 15.1 or also Figure 1 in Kneifel et al. 2018). Rather than comparing the scattering properties of all published particles – a task which we leave to an extensive review study – we show in Fig. 15.3 an exemplary selection of particles for the different (non-melted) ice hydrometeor categories. The scattering efficiencies are plotted as function of the size parameter defined with the radius of the mass-equivalent ice sphere r_{eff}.

The solid ice sphere represents the high density extreme, potentially only applicable to simulate scattering properties of spherical hail. The 'soft' sphere and the soft spheroid results were calculated with a widely used mass-size relation provided by Brown and Francis (1995) and using the Maxwell-Garnett EMA (15.9); for the spheroid we also assume a commonly used constant aspect ratio of 0.6 (e.g., Hogan et al. 2012). Typical characteristics of the spheroidal approximations are the oscillating behavior of the scattering properties, as a function of size, caused by the internal reflection of the electromagnetic wave outside the Rayleigh regime. The high symmetry of the spheroids causes these 'dips' – a result of destructive interferences – to be particularly pronounced especially for backscattering. These resonance effects are averaged out for scattering efficiency which is an integrated quantity over the scattering angle. The multiple orders of magnitude difference in the backscattering efficiencies for the solid and the soft sphere are a result of the very different refractive indices. For the soft sphere calculations, mass-size relations are often used which have been empirically derived from in-situ observations. This ice mass is then homogeneously distributed in the spheroidal volume which leads to a rapid decrease of the average density and consequently also of the effective refractive index. As a result, the backscattering efficiency is drastically decreasing with larger size parameters. For an illustration of the problem, imagine a sphere (or spheroid) circumscribed to a long ice needle. A large fraction of the sphere's volume is filled with air and only a very small fraction of the volume is filled with solid ice. This extreme example illustrates the main inconsistency of the sponge-like assumption of a homogeneous ice-air mixture in the spheroidal approximation. In fact, the mass fluctuations inside the particle volume seem to be key for an accurate calculation of the particles scattering properties (e.g., Sorensen 2001) especially when approaching large size parameters. An increasing number of studies related to RGA and SSRGA indicate that their main advantage is the ability to better account for these mass fluctuations.

Scattering calculations by the computationally costlier methods such as DDA or GMM are nowadays the basis of most scattering databases (Table 15.1). Most datasets include a large number of particle shapes and their associated single particle scattering properties. However, the databases still differ even in key assumptions such as whether calculations include the results for single particle orientations or whether averaging over random orientations is applied. While for single ice crystals there is little debate that they have a preferential orientation during fall, this is still

less clear for aggregates. Other differences are, for example, the range of particle size and frequencies included, definition of scattering variables, consideration of polarization, ice refractive index model used, or simply the question whether the full scattering matrix or only scattering cross sections are included. Very recently, database developers also started to include rimed snow particles in addition to single crystals and aggregates.

As an example of single-particle DDA calculations, the results for unrimed and strongly rimed snow aggregates from Leinonen and Szyrmer (2015) are plotted in Fig. 15.3. The range of variability found for a particular size parameter illustrates the inherent uncertainty of scattering properties for single ice particles. The uncertainty for individual particles is much larger for backscattering than for extinction due to the relation of the backscattering to one particular scattering angle. The rimed particles tend to populate more towards the solid sphere curve than the unrimed aggregates. This is mainly an effect of the overall larger refractive index. Usually, a remote sensor receives the scattered radiation of a large ensemble of ice particles. One unsolved question is thus, how to generate a reasonable average of the scattering properties. For particles, which are not too rimed and for applications where polarimetric information is not needed, the SSRGA approach seems to be a reasonable solution (Leinonen et al. 2018a). Several comparisons with DDA results (Leinonen et al. 2018a; Hogan et al. 2017; Hogan and Westbrook 2014) reveal that SSRGA provides a sufficiently accurate ensemble average of the scattering properties (see also DDA and SSRGA results for unrimed aggregates in Fig. 15.3). Especially for backscatter, the overall behavior of the SSRGA is much closer to DDA as compared to the strongly deviating soft spheroidal approximation.

Many databases also include scattering computations for single ice crystals of various shapes such as columns, plates, bullet rosettes, sector snowflakes, or dendrites. Due to their smaller sizes (less than 5 mm) and relatively small size parameters, their curves would be difficult to see in Fig. 15.3. Their scattering properties would populate within the range presented in Fig. 15.3 with individually large differences especially if no orientation averaging is applied (e.g., Eriksson et al. 2018). It is obvious from Fig. 15.3 that different scattering variables show different sensitivity to varying particle properties. Any approximation or average needs therefore to be carefully tested with respect to how well it is able to approximate the different scattering variables over a wide frequency range.

15.3.3   Melting Ice

As discussed in Sect. 15.2.3, only a limited number of scattering databases include partially melted snowflakes (Botta et al. 2010; Ori et al. 2014; Johnson et al. 2016). The available databases still have several limitations in terms of particle size range, number of orientations, melted fractions and frequencies. Nevertheless, they already provide some interesting information about melting snow scattering properties. Figure 15.4 shows the extinction and backscattering characteristics of melted snow
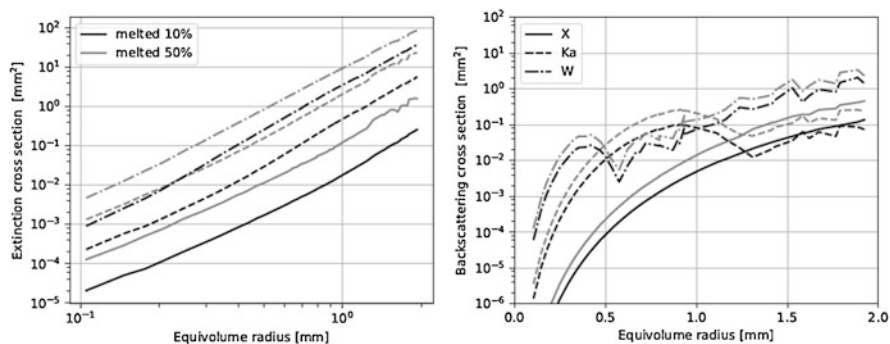
Fig. 15.4 Extinction (left) and backscattering (right) cross sections for partially melted snow aggregates at 10% (dark) and 50% (gray) melted fractions. Results are from DDA scattering simulations (Ori et al. 2014) at 9.6 (continuous), 35.5 (dashed) and 94 (dash-dotted) GHz

as a function of the radius of the corresponding melted sphere. As the particle melted fraction increases, its scattering properties increase in response of the larger value of the water refractive index with respect to ice. The differences are largest at the lowest frequencies (below 30 GHz) since this is the region of the microwave spectrum where the differences in ice and water dielectric properties are largest. At 9.6 GHz, increasing snowflake melted fraction from 10% to 50% leads to a fivefold increase of backscattering and one order of magnitude in the extinction cross section. This translates into a 7 dB increase in the unattenuated radar reflectivity due to melting.

15.3.4 Future Directions

Significant progress has been achieved during recent years with respect to our general understanding of MW scattering of ice and snow particles but still a number of open questions remain. Several particle classes such as rimed particles, aggregates of mixed monomers, melting particles, or secondary ice are still underrepresented or even completely missing in currently available databases. While there is much confidence in the scattering methods themselves (i.e., if computational resources are available DDA can be readily applied), the hydrometeor modeling needs to be more tightly linked to in-situ studies. Developers of hydrometeor models should also communicate more with developers of microphysical parametrizations. In this way, a larger consistency between radiative transfer calculations and numerical weather and climate prediction models could be achieved. Another urgent aspect which has been discussed at the meetings of the International Precipitation Working Group (Levizzani et al. 2018) and also during the last International Summer Snowfall Workshop (Kneifel et al. 2018) is to develop standards and conventions how to store the growing number of scattering databases. Such conventions would help to make the datasets easier to compare, would simplify the combined use of several

datasets, and would help to reproduce results or to extend existing datasets with calculations of e.g. new particles or frequencies.

References

Acquista, C. (1976). Light scattering by tenuous particles: A generalization of the Rayleigh-Gans-Rokard approach. *Applied Optics, 15*, 2932–2936. https://doi.org/10.1364/AO.15.002932.

Aden, A. L., & Kerker, M. (1951). Scattering of electromagnetic waves from two concentric spheres. *Journal of Applied Physics, 22*, 1242–1246. https://doi.org/10.1063/1.1699834.

Andsager, K., Beard, K. V., & Laird, N. S. (1999). Laboratory measurements of axis ratios for large raindrops. *Journal of the Atmospheric Sciences, 56*, 2673–2683. https://doi.org/10.1175/1520-0469(1999)056<2673:LMOARF>2.0.CO;2.

Austin, P., & Bemis, A. (1950). A quantitative study of the bright band in radar precipitation echoes. *Journal of Meteorology, 7*, 145–151. https://doi.org/10.1175/1520-0469(1950)007h0145:AQSOTBi2.0.CO;2.

Bailey, M., & Hallett, J. (2004). Growth rates and habits of ice crystals between 20 and 70°C. *Journal of the Atmospheric Sciences, 61*, 514–544. https://doi.org/10.1175/1520-0469(2004)061h0514:GRAHOIi2.0.CO;2.

Battaglia, A., & Simmer, C. (2007). Explaining the polarization signal from rain dichroic media. *Journal of Quantitative Spectroscopy and Radiative Transfer, 105*, 84–101. https://doi.org/10.1016/j.jqsrt.2006.11.012.

Battan, L. J. (1973). *Radar observation of the atmosphere*. Chicago: University of Chicago Press, 324 pp, ISBN:0226039196.

Bauer, P., Poiares Baptista, J. P. V., & de Iulis, M. (1999). The effect of the melting layer on the microwave emission of clouds over the ocean. *Journal of the Atmospheric Sciences, 56*, 852–867. https://doi.org/10.1175/1520-0469(1999)056h0852:TEOTMLi2.0.CO;2.

Beard, K. V., & Jameson, A. (1983). Raindrop canting. *Journal of the Atmospheric Sciences, 40*, 448–454. https://doi.org/10.1175/1520-0469(1983)040<0448:RC>2.0.CO;2.

Berry, M. V., & Percival, I. C. (1986). Optics of fractal clusters such as smoke. *Optica Acta, 33*, 577–591. https://doi.org/10.1080/713821987.

Bohren, C. F. (1986). Applicability of effective-medium theories to problems of scattering and absorption by nonhomogeneous atmospheric particles. *Journal of the Atmospheric Sciences, 43*, 468–475. https://doi.org/10.1175/1520-0469(1986)043h0468:AOEMTTi2.0.CO;2.

Bohren, C. F., & Battan, L. J. (1982). Radar backscattering of microwaves by spongy ice spheres. *Journal of the Atmospheric Sciences, 39*, 2623–2628. https://doi.org/10.1175/1520-0469(1982)039h2623:RBOMBSi2.0.CO;2.

Bohren, C. F., & Huffman, D. R. (1983). *Absorption and scattering of light by small particles*. New York, 530 pp: Wiley. https://doi.org/10.1002/9783527618156.

Borghese, F., Denti, P., Toscano, G., & Sindoni, O. I. (1979). Electromagnetic scattering by a cluster of spheres. *Applied Optics, 18*, 116–120. https://doi.org/10.1364/AO.18.000116.

Botta, G., Aydin, K., & Verlinde, J. (2010). Modeling of microwave scattering from cloud ice crystal aggregates and melting aggregates: A new approach. *IEEE Geoscience and Remote Sensing Letters, 7*, 572–576. https://doi.org/10.1109/LGRS.2010.2041633.

Brandes, E. A., & Ikeda, K. (2004). Freezing-level estimation with polarimetric radar. *Journal of Applied Meteorology, 43*, 1541–1553. https://doi.org/10.1175/JAM2155.1.

Brandes, E. A., & Ikeda, K. (2007). A statistical and physical description of hydrometeor distributions in Colorado snowstorms using a video disdrometer. *Journal of Applied Meteorology and Climatology, 46*, 634–650. https://doi.org/10.1175/JAM2489.1.

Bringi, V. N., & Chandrasekar, V. (2001). *Polarimetric Doppler weather radar, principles and applications*. Cambridge, 536 pp: Cambridge University Press. https://doi.org/10.1017/CBO9780511541094.

Brown, P. R. A., & Francis, P. N. (1995). Improved measurements of the ice water content in cirrus using a total-water probe. *Journal of Atmospheric and Oceanic Technology, 12*, 410–414. https://doi.org/10.1175/1520-0426(1995)012h0410:IMOTIWi2.0.CO;2.

Bruggeman, D. A. G. (1935). Berechnung verschiedener physikalischer Konstanten von heterogenen Substanzen. I. Dielektrizitätskonstanten und Leitfähigkeiten der Mischkörper aus isotropen Substanzen. *Annalen der Physik, 416*(7), 636–664. https://doi.org/10.1002/andp.19354160705.

Bruning, J., & Lo, Y. (1971). Multiple scattering of em waves by spheres part i. multipole expansion and ray-optical solutions. *IEEE Transactions on Antennas and Propagation, 19*, 378–390. https://doi.org/10.1109/TAP.1971.1139944.

Cho, H. R., Iribarne, J. V., & Richards, W. G. (1981). On the orientation of ice crystals in a cumulonimbus cloud. *Journal of the Atmospheric Sciences, 38*, 1111–1114. https://doi.org/10.1175/1520-0469(1981)038h1111:OTOOICi2.0.CO;2.

Ding, J., Bi, L., Yang, P., Kattawar, G. W., Weng, F., Liu, Q., & Greenwald, T. (2017). Single-scattering properties of ice particles in themicrowave regime: Temperature effect on the ice refractive indexwith implications in remote sensing. *Journal of Quantitative Spectroscopy and Radiative Transfer, 190*, 26–37.

Draine, B. T., & Flatau, P. J. (1994). Discrete-dipole approximation for scattering calculations. *Journal of the Optical Society of America A, 11*(4), 1491–1499. https://doi.org/10.1364/JOSAA.11.001491.

Dungey, C. E., & Bohren, C. F. (1993). Backscattering by nonspherical hydrometeors as calculated by the coupled-dipole method: An application in radar meteorology. *Journal of Atmospheric and Oceanic Technology, 10*, 526–532. https://doi.org/10.1175/1520-0426(1993)010h0526:BBNHACi2.0.CO;2.

Ekelund, R., Brath, M., Mendrok, J., & Eriksson, P. (2018). ARTS microwave single scattering properties database. https://doi.org/10.5281/zenodo.1175573.

Ellison, W. J. (2007). Permittivity of pure water at standard atmospheric pressure over the frequency range 0-25 THz and the temperature range 0-100°C. *Journal of Physical and Chemical Reference Data, 36*(**1**), 1–18. https://doi.org/10.1063/1.2360986.

Eriksson, P., Ekelund, R., Mendrok, J., Brath, M., Lemke, O., & Buehler, S. A. (2018). A general database of hydrometeor single scattering properties at microwave and sub-millimetre wavelengths. *Earth System Science Data, 10*, 1301–1326. https://doi.org/10.5194/essd-10-1301-2018.

Evans, K. F., & Stephens, G. L. (1995). Microwave radiative transfer through clouds composed of realistically shaped ice crystals. Part I: Single scattering properties. *Asia-Pacific Journal of Atmospheric Sciences, 52*, 2041–2057. https://doi.org/10.1175/1520-0469(1995)052<2041:MRTTCC>2.0.CO;2.

Evans, K., & Vivekanandan, J. (1990). Multiparameter radar and microwave radiative transfer modeling of nonspherical atmospheric ice particles. *IEEE Transactions on Geoscience and Remote Sensing, 28*(4), 423–437. https://doi.org/10.1109/TGRS.1990.572908.

Fabry, F., & Szyrmer, W. (1999). Modeling of the melting layer. Part II: Electromagnetic. *Journal of the Atmospheric Sciences, 56*, 3593–3600. https://doi.org/10.1175/1520-0469(1999)056h3593:MOTMLPi2.0.CO;2.

Fabry, F., & Zawadzki, I. (1995). Long-term radar observations of the melting layer of precipitation and their interpretation. *Journal of the Atmospheric Sciences, 52*, 838–851. https://doi.org/10.1175/1520-0469(1995)052h0838:LTROOTi2.0.CO;2.

Fujiyoshi, Y. (1986). Melting snowflakes. *Journal of the Atmospheric Sciences, 43*(3), 307–311. https://doi.org/10.1175/1520-0469(1986)043h0307:MSi2.0.CO;2.

Garrett, T. J., Fallgatter, C., Shkurko, K., & Howlett, D. (2012). Fall speed measurement and high-resolution multi-angle photography of hydrometeors in free fall. *Atmospheric Measurement Techniques, 5*, 2625–2633. https://doi.org/10.5194/amt-5-2625-2012.

Giangrande, S. E., Krause, J. M., & Ryzhkov, A. V. (2008). Automatic designation of the melting layer with a polarimetric prototype of the WSR-88D radar. *Journal of Applied Meteorology and Climatology, 47*(5), 1354–1364. https://doi.org/10.1175/2007JAMC1634.1.

Goodman, J. J., Draine, B. T., & Flatau, P. J. (1991). Application of fast-Fourier-transform techniques to the discrete-dipole approximation. *Optics Letters, 16*(15), 1198–1200. https://doi.org/10.1364/OL.16.001198.

Gravner, J., & Griffeath, D. (2009). Modeling snow-crystal growth: A three-dimensional mesoscopic approach. *Physical Review E, 79*, 011601. https://doi.org/10.1103/PhysRevE.79.011601.

Hogan, R. J., & Westbrook, C. D. (2014). Equation for the microwave backscatter cross section of aggregate snowflakes using the self-similar Rayleigh-Gans approximation. *Journal of the Atmospheric Sciences, 71*(9), 3292–3301. https://doi.org/10.1175/JAS-D-13-0347.1.

Hogan, R. J., Tian, L., Brown, P. R. A., Westbrook, C. D., Heymsfield, A. J., & Eastment, J. D. (2012). Radar scattering from ice aggregates using the horizontally aligned oblate spheroid approximation. *Journal of Applied Meteorology and Climatology, 51*(3), 655–671. https://doi.org/10.1175/JAMC-D-11-074.1.

Hogan, R. J., Honeyager, R., Tyynelä, J., & Kneifel, S. (2017). Calculating the millimetre-wave scattering phase function of snowflakes using the self-similar Rayleigh-Gans approximation. *Quarterly Journal of the Royal Meteorological Society, 143*, 1385–1395. https://doi.org/10.1002/qj.2968.

Hong, G., Yang, P., Baum, B. A., Heymsfield, A. J., Weng, F., Liu, Q., Heygster, G., & Buehler, S. A. (2009). Scattering database in the millimeter and submillimeter wave range of 100-1000 GHz for nonspherical ice particles. *Journal of Geophysical Research, 114*, D06201. https://doi.org/10.1029/2008JD010451.

Ishimoto, H. (2008). Radar backscattering computations for fractal-shaped snowflakes. *Journal of the Meteorological Society of Japan, 86*(3), 459–469. https://doi.org/10.2151/jmsj.86.459.

Johnson, B. T., Olson, W. S., & Skofronick-Jackson, G. (2016). The microwave properties of simulated melting precipitation particles: Sensitivity to initial melting. *Atmospheric Measurement Techniques, 9*(1), 9–21. https://doi.org/10.5194/amt-9-9-2016.

Kahnert, F. M. (2003). Numerical methods in electromagnetic scattering theory. *Journal of Quantitative Spectroscopy and Radiative Transfer, 79-80*, 775–824. https://doi.org/10.1016/S0022-4073(02)00321-7.

Kahnert, F. M., Stamnes, J. J., & Stamnes, K. (2001). Application of the extended boundary condition method to homogeneous particles with point symmetries. *Applied Optics, 40*, 3110–3123. https://doi.org/10.1364/AO.40.003110.

Kaikkonen, V. A., Ekimov, D., & Mäkynen, A. J. (2014). A holographic in-line imaging system for meteorological applications. *IEEE Transactions on Instrumentation and Measurement, 63*, 1137–1144. https://doi.org/10.1109/TIM.2013.2295658.

Kharadly, M. M. Z., & Hulays, R. A. (1994). Estimation of melting-snow layer attenuation and scattering on microwave communication links. In *Proceedings, 24th European Microwave Conf*erence (pp. 734–739). Cannes, France. https://doi.org/10.1109/EUMA.1994.337298.

Kim, M. J. (2006). Single scattering parameters of randomly oriented snow particles at microwave frequencies. *Journal of Geophysical Research, 111*, D14201. https://doi.org/10.1029/2005JD006892.

Klaassen, W. (1988). Radar observations and simulation of the melting layer of precipitation. *Journal of the Atmospheric Sciences, 45*, 3741–3753. https://doi.org/10.1175/1520-0469 (1988)045<3741:ROASOT>2.0.CO;2.

Klaassen, W. (1990). Attenuation and reflection of radio waves by a melting layer of precipitation. *IEEE Proceedings H Microwaves Antennas Propagation, 137*(1), 39–44. https://doi.org/10. 1049/ip-h-2.1990.0007.

Kneifel, S., Neto, J. D., Ori, D., Moisseev, D., Tyynelä, J., Adams, I. S., Kuo, K. S., Bennartz, R., Berne, A., Clothiaux, E. E., Eriksson, P., Geer, A. J., Honeyager, R., Leinonen, J., & Westbrook, C. D. (2018). The first international summer snowfall workshop: Scattering properties of realistic frozen hydrometeors from simulations and observations, as well as defining a new standard for scattering databases. *Bulletin of the American Meteorological Society, 99*(3), ES55–ES58. https://doi.org/10.1175/BAMS-D-17-0208.1.

Knight, C. A. (1979). Observations of the morphology of melting snow. *Journal of the Atmospheric Sciences, 36*, 1123–1130. https://doi.org/10.1175/1520-0469(1979)036h1123:OOTMOMi2.0.CO;2.

Kuo, K. S., Olson, W. S., Johnson, B. T., Grecu, M., Tian, L., Clune, T. L., van Aartsen, B. H., Heymsfield, A. J., Liao, L., & Meneghini, R. (2016). The microwave radiative properties of falling snow derived from nonspherical ice particle models. Part I: An extensive database of simulated pristine crystals and aggregate particles, and their scattering properties. *Journal of Applied Meteorology and Climatology, 55*, 691–708. https://doi.org/10.1175/JAMC-D-15-0130.1.

Leinonen, J. (2014). High-level interface to t-matrix scattering calculations: Architecture, capabilities and limitations. *Optics Express, 22*(2), 1655–1660. https://doi.org/10.1364/OE.22.001655.

Leinonen, J., & Moisseev, D. (2015). What do triple-frequency radar signatures reveal about aggregate snowflakes? *Journal of Geophysical Research, 120*, 229–239. https://doi.org/10. 1002/2014JD022072.

Leinonen, J., & Szyrmer, W. (2015). Radar signatures of snowflake riming: A modeling study. *Earth and Space Science, 2*, 346–358. https://doi.org/10.1002/2015EA000102.

Leinonen, J., & von Lerber, A. (2018). Snowflake melting simulation using smoothed particle hydrodynamics. *Journal of Geophysical Research, 123*, 1811–1825. https://doi.org/10.1002/ 2017JD027909.

Leinonen, J., Moisseev, D., & Nousiainen, T. (2013). Linking snowflake microstructure to multi-frequency radar observations. *Journal of Geophysical Research, 118*(8), 3259–3270. https://doi. org/10.1002/jgrd.50163.

Leinonen, J., Kneifel, S., & Hogan, R. J. (2018a). Evaluation of the Rayleigh-Gans approximation for microwave scattering by rimed snowflakes. *Quarterly Journal of the Royal Meteorological Society, 144*(S1), 77–88. https://doi.org/10.1002/qj.3093.

Leinonen, J., Lebsock, M. D., Tanelli, S., Sy, O. O., Dolan, B., Chase, R. J., Finlon, J. A., von Lerber, A., & Moisseev, D. (2018b). Retrieval of snowflake microphysical properties from multi-frequency radar observations. *Atmospheric Measurement Techniques, 11*, 5471–5488. https://doi.org/10.5194/amt-2018-73.

Levizzani, V., Kidd, C., Aonashi, K., Bennartz, R., Ferraro, R. R., Huffman, G. J., Roca, R., Turk, F. J., & Wang, N.-Y. (2018). The activities of the International Precipitation Working Group. *Quarterly Journal of the Royal Meteorological Society, 144*(S1), 3–15. https://doi.org/10.1002/ qj.3214.

Liang, C., & Lo, Y. (1967). Scattering by two spheres. *Radio Science, 2*, 1481–1495. https://doi. org/10.1002/rds19672121481.

Liao, L., Meneghini, R., Nowell, H. K., & Liu, G. (2013). Scattering computations of snow aggregates from simple geometrical particle models. *IEEE Journal of Selected Topics in Applied Earth Observations and Remote Sensing, 6*, 1409–1417. https://doi.org/10.1109/JSTARS.2013. 2255262.

Libbrecht, K. G. (2005). The physics of snow crystals. *Reports on Progress in Physics, 68*, 855–895. https://doi.org/10.1088/0034-4885/68/4/R03.

Libbrecht, K. G., & Rickerby, M. E. (2013). Measurements of surface attachment kinetics for faceted ice crystal growth. *Journal of Crystal Growth, 377*, 1–8. https://doi.org/10.1016/j.jcrysgro.2013.04.037.

Liu, G. (2008). A database of microwave single-scattering properties for nonspherical ice particles. *Bulletin of the American Meteorological Society, 89*, 1563–1570. https://doi.org/10.1175/2008BAMS2486.1.

Lu, Y., Jiang, Z., Aydin, K., Verlinde, J., Clothiaux, E. E., & Botta, G. (2016). A polarimetric scattering database for non-spherical ice particles at microwave wavelengths. *Atmospheric Measurement Techniques, 9*, 5119–5134. https://doi.org/10.5194/amt-9-5119-2016.

Mackowski, D. W. (1991). Analysis of radiative scattering for multiple sphere configurations. *Proceedings of the Royal Society, 433*, 599–614. https://doi.org/10.1098/rspa.1991.0066.

Mackowski, D. W., & Mishchenko, M. I. (2011). A multiple sphere T-matrix Fortran code for use on parallel computing clusters. *Journal of Quantitative Spectroscopy and Radiative Transfer, 112*, 2182–2192. https://doi.org/10.1016/j.jqsrt.2011.02.019.

Magono, C., & Lee, C. W. (1966). Meteorological classification of natural snow crystals. *Journal of the Faculty of Science, Hokkaido University. Series 7, Geophysics 2*, 321–335. Available at http://hdl.handle.net/2115/8672, last accessed 12 Oct 2018.

Marshall, J. S., & Gunn, K. L. S. (1952). Measurement of snow parameters by radar. *Journal of Meteorology, 9*(5), 322–327. https://doi.org/10.1175/1520-0469(1952)009h0322:MOSPBRi2.0.CO;2.

Maruyama, K. I., & Fujiyoshi, Y. (2005). Montecarlo simulation of the formation of snowflakes. *Journal of the Atmospheric Sciences, 62*, 1529–1544. https://doi.org/10.1175/JAS3416.1.

Matrosov, S. Y. (1992). Radar reflectivity in snowfall. *IEEE Transactions on Geoscience and Remote Sensing, 30*, 454–461. https://doi.org/10.1109/36.142923.

Matrosov, S. Y. (2007). Modeling backscatter properties of snowfall at millimeter wavelengths. *Journal of the Atmospheric Sciences, 64*, 1727–1736. https://doi.org/10.1175/JAS3904.1.

Maxwell-Garnett, J. C. (1904). Colours in metal glasses and in metallic films. *Philosophical Transactions. Series A, Mathematical, Physical, and Engineering Sciences, 203*(359–371), 385–420. https://doi.org/10.1098/rsta.1904.0024.

Mie, G. (1908). Beiträge zur Optik trüber Medien, speziell kolloidaler Metallösungen. *Annalen der Physik, 330*, 377–445. https://doi.org/10.1002/andp.19083300302.

Mishchenko, M. I., & Travis, L. D. (1998). Capabilities and limitations of a current fortran implementation of the t-matrix method for randomly oriented, rotationally symmetric scatterers. *Journal of Quantitative Spectroscopy and Radiative Transfer, 60*, 309–324. https://doi.org/10.1016/S0022-4073(98)00008-9.

Mishchenko, M. I., Travis, L. D., & Lacis, A. A. (2002). *Scattering, absorption, and emission of light by small particles*. Cambridge, UK: Cambridge University Press, 110 pp., ISBN:052178252X.

Mishchenko, M. I., Videen, G., Khlebtsov, N. G., Wriedt, T., & Zakharova, N. T. (2008). Comprehensive T-matrix reference database: A 2006/07 update. *Journal of Quantitative Spectroscopy and Radiative Transfer, 109*, 1447–1460. https://doi.org/10.1016/j.jqsrt.2008.01.001.

Mitchell, D. L. (1996). Use of mass- and area-dimensional power laws for determining precipitation particle terminal velocities. *Journal of the Atmospheric Sciences, 53*, 1710–1723. https://doi.org/10.1175/1520-0469(1996)053h1710:UOMAADi2.0.CO;2.

Mitra, S. K., Vohl, O., Ahr, M., & Pruppacher, H. R. (1990). A wind-tunnel and theoretical study of melting behavior of atmospheric ice particles IV: Experiment and theory for snow flakes. *Journal of the Atmospheric Sciences, 47*(5), 584–591. https://doi.org/10.1175/1520-0469(1990)047<0584:AWTATS>2.0.CO;2.

Nowell, H., Liu, G., & Honeyager, R. (2013). Modeling the microwave single-scattering properties of aggregate snowflakes. *Journal of Geophysical Research, 118*, 7873–7885. https://doi.org/10.1002/jgrd.50620.

Oguchi, T. (1973). Scattering properties of oblate raindrops and cross polarization of radio waves due to rain: Calculations at 19.3 and 34.8 GHz. *Radio Research Laboratories, Journal, 20*, 79–118.

Olson, W., Bauer, P., Viltard, N., Johnson, D., Tao, W. K., Meneghini, R., & Liao, L. (2001). A melting-layer model for passive/active microwave remote sensing application. Part I: Model formulation and comparison with observations. *Journal of Applied Meteorology, 40*, 1145–1163. https://doi.org/10.1175/1520-0450(2001)040<1145:AMLMFP>2.0.CO;2.

Oraltay, R. G., & Hallett, J. (2005). The melting layer: A laboratory investigation of ice particle melt and evaporation near 0°C. *Journal of Applied Meteorology, 44*(2), 206–220. https://doi.org/10.1175/JAM2194.1.

Ori, D., & Kneifel, S. (2018). Assessing the uncertainties of the discrete dipole approximation in case of melting ice particles. *Journal of Quantitative Spectroscopy and Radiative Transfer, 217*, 396–406. https://doi.org/10.1016/j.jqsrt.2018.06.017.

Ori, D., Maestri, T., Rizzi, R., Cimini, D., Montopoli, M., & Marzano, F. S. (2014). Scattering properties of modeled complex snowflakes and mixed-phase particles at microwave and milli-meter frequencies. *Journal of Geophysical Research, 119*, 9931–9947. https://doi.org/10.1002/2014JD021616.

Petrov, D., Shkuratov, Y. G., & Videen, G. (2011). Electromagnetic wave scattering from particles of arbitrary shapes. *Journal of Quantitative Spectroscopy and Radiative Transfer, 112*, 1636–1645. https://doi.org/10.1016/j.jqsrt.2011.01.036.

Petty, G. W., & Huang, W. (2010). Microwave backscatter and extinction by soft ice spheres and complex snow aggregates. *Journal of the Atmospheric Sciences, 67*, 769–787. https://doi.org/10.1175/2009JAS3146.1.

Piller, N. B., & Martin, O. J. F. (1998). Increasing the performance of the coupled-dipole approximation: A spectral approach. *IEEE Transactions on Antennas and Propagation, 46*, 1126–1137. https://doi.org/10.1109/8.718567.

Pruppacher, H. R., & Klett, J. D. (1997). *Microphysics of clouds and precipitation*. Dordrecht: Boston, 954 pp, ISBN:0-79-234211-1.

Pruppacher, H. R., & Pitter, R. L. (1971). A semi-empirical determination of the shape of cloud and rain drops. *Journal of the Atmospheric Sciences, 28*, 86–94. https://doi.org/10.1175/1520-0469(1971)028<0086:ASEDOT>2.0.CO;2.

Purcell, E. M., & Pennypacker, C. R. (1973). Scattering and absorption of light by nonspherical dielectric grains. *The Astrophysical Journal, 186*, 705–714. https://doi.org/10.1086/152538.

Reiter, C. A. (2005). A local cellular model for snow crystal growth. *Chaos, Solitons and Fractals, 23*, 1091–1496. https://doi.org/10.1016/j.chaos.2004.06.071.

Shivola, A. H. (1989). Self-consistency aspects of dielectric mixing theories. *IEEE Transactions on Geoscience and Remote Sensing, 27*, 403–415. https://doi.org/10.1109/36.29560.

Sorensen, C. M. (2001). Light scattering by fractal aggregates: A review. *Aerosol Science and Technology, 35*, 648–687. https://doi.org/10.1080/02786820117868.

Tang, C., & Aydin, K. (1995). Scattering from ice crystals at 94 and 220 GHz millimeter wave frequencies. *IEEE Transactions on Geoscience and Remote Sensing, 33*, 93–99. https://doi.org/10.1109/36.368218.

Thomas, L., Cartwright, J. C., & Wareing, D. P. (1990). Lidar observations of the horizontal orientation of ice crystals in cirrus clouds. *Tellus B, 42*, 211–216. https://doi.org/10.3402/tellusb.v42i2.16290.

Turner, D. D., Kneifel, S., & Careddu, M. P. (2016). An improved liquid water absorption model at microwave frequencies for supercooled liquid water clouds. *Journal of Atmospheric and Oceanic Technology, 33*, 33–44. https://doi.org/10.1175/JTECH-D-15-0074.1.

Tyynelä, J., & Chandrasekar, V. (2014). Characterizing falling snow using multifrequency dual-polarization measurements. *Journal of Geophysical Research, 119*, 8268–8283. https://doi.org/10.1002/2013JD021369.

Tyynelä, J., Nousiainen, T., Göke, S., & Muinonen, K. (2009). Modeling C-band single scattering properties of hydrometeors using discrete-dipole approximation and T-matrix method. *Journal of Quantitative Spectroscopy and Radiative Transfer, 110*, 1654–1664. https://doi.org/10.1016/j.jqsrt.2009.02.020.

Tyynelä, J., Leinonen, J., Moisseev, D., & Nousiainen, T. (2011). Radar backscattering from snowflakes: Comparison of fractal, aggregate, and soft spheroid models. *Journal of Atmospheric and Oceanic Technology, 28*, 1365–1372. https://doi.org/10.1175/JTECH-D-11-00004.1.

Tyynelä, J., Leinonen, J., Westbrook, C. D., Moisseev, D., & Nousiainen, T. (2013). Applicability of the Rayleigh-Gans approximation for scattering by snowflakes at microwave frequencies in vertical incidence. *Journal of Geophysical Research, 118*, 1826–1839. https://doi.org/10.1002/jgrd.50167.

Tyynelä, J., Leinonen, J., Moisseev, D., Nousiainen, T., & von Lerber, A. (2014). Modeling radar backscattering from melting snowflakes using spheroids with nonuniform distribution of water. *Journal of Quantitative Spectroscopy and Radiative Transfer, 133*, 504–519. https://doi.org/10.1016/j.jqsrt.2013.09.013.

von Lerber, A., Moisseev, D., Leinonen, J., Koistinen, J., & Hallikainen, M. T. (2015). Modeling radar attenuation by a low melting layer with optimized model parameters at C-band. *IEEE Transactions on Geoscience and Remote Sensing, 53*, 724–737. https://doi.org/10.1109/TGRS.2014.2327148.

Wang, Y. M., & Chew, W. C. (1983). A recursive t-matrix approach for the solution of electromagnetic scattering by many spheres. *IEEE Transactions on Antennas and Propagation, 41*, 1633–1639. https://doi.org/10.1109/8.273306.

Waterman, P. C. (1965). Matrix formulation of electromagnetic scattering. *Proceedings of the IEEE, 53*(8), 805–812. https://doi.org/10.1109/PROC.1965.4058.

Westbrook, C. D. (2004). *Universality in snow formation* (Ph.D. thesis). University of Warwick, Coventry, UK, 109 pp.

Westbrook, C. D. (2014). Rayleigh scattering by hexagonal ice crystals and the interpretation of dual-polarisation radar measurements. *Quarterly Journal of the Royal Meteorological Society, 140*, 2090–2096. https://doi.org/10.1002/qj.2262.

Westbrook, C., Ball, R., Field, P., & Heymsfield, A. J. (2004). Universality in snowflake aggregation. *Geophysical Research Letters, 31*(15), L15104. https://doi.org/10.1029/2004GL020363.

Westbrook, C. D., Ball, R. C., & Field, P. R. (2006). Radar scattering by aggregate snowflakes. *Quarterly Journal of the Royal Meteorological Society, 132*, 897–914. https://doi.org/10.1256/qj.05.82.

Wriedt, T., & Doicu, A. (1998). Formulations of the extended boundary condition method for three-dimensional scattering using the method of discrete sources. *Journal of Modern Optics, 45*, 199–213. https://doi.org/10.1080/09500349808231681.

Xu, Y. (1995). Electromagnetic scattering by an aggregate of spheres. *Applied Optics, 34*, 4573–4588. https://doi.org/10.1364/AO.34.004573.

Yurkin, M. A., & Hoekstra, A. G. (2011). The discrete-dipole-approximation code ADDA: Capabilities and known limitations. *Journal of Quantitative Spectroscopy and Radiative Transfer, 112*, 2234–2247. https://doi.org/10.1016/j.jqsrt.2011.01.031.

Yurkin, M. A., Maltsev, V. P., & Hoekstra, A. G. (2006). Convergence of the discrete dipole approximation. II. An extrapolation technique to increase the accuracy. *Journal of the Optical Society of America A, 23*, 2592–2601. https://doi.org/10.1364/JOSAA.23.002592.

Chapter 16
Radar Snowfall Measurement

Guosheng Liu

Abstract Measuring snowfall by radars faces many extra challenges compared to radar rainfall measurements due to the facts that snow particles have low density and are non-spherical in shape. The low density makes their scattering intensity weak, therefore only detectable by highly sensitive radars. The non-sphericity of the snow particle, on the other hand, makes the conversion from radar reflectivity to snowfall rate extremely uncertain. Because of these difficulties, global snowfall maps were not available until the availability of CloudSat Cloud Profiling Radar (CPR) measurements, which operates at 94 GHz and has a minimum detectability better than -26 dBZ. In this article, using CPR measurements as an example, we first describe the theory and methods of measuring snowfall by space-borne radars, followed by new findings that have resulted from CloudSat observations and ideas on how to use CloudSat to guide passive microwave sensors for snowfall retrievals.

Keywords CPR · CloudSat · GPM · DPR · Snow · Snowfall · Snowflake · Dendrites · Rosettes · Aggregates · Rainfall · Radar · Reflectivity · Backscattering cross section · Particle size distribution · Power law · Attenuation · Radiometer

16.1 Introduction

Measuring snowfall is important for forecasting hazardous weather, understanding the hydrological cycle and evaluating the cooling and freshening effects of snow onto ocean. Over land, accumulated snow may stay on the ground for months, resulting in very different hydrological and radiative consequences from those from rain (e.g., Barnett et al. 1989; Walsh 1995). Over ocean, falling snow has complex interaction with the ocean because it both freshens and cools (through snow melting) the ocean surface water. Despite the importance of snow precipitation, there

G. Liu (✉)

Department of Earth, Ocean and Atmospheric Science, Florida State University, Tallahassee, FL, USA
e-mail: gliu@fsu.edu

have been no global climatologies of snowfall distributions produced on the basis of observational data until very recently when CloudSat Cloud Profiling Radar (CPR) observations became available.

Compared to rainfall measurements, measuring snowfall from space radars faces many extra challenges. First, snowflakes generally have very low and quite variable values of density, which leads to the intensity of their radar returns to be low and uncertain; detecting the low backscatter intensity requires that the radar have a very low value of minimum detection. Second, unlike raindrops, snowflakes are nonspherical and have countless types of shapes. The radar reflectivity depends on particles shapes, orientation and size distribution. Therefore, the nonspherical nature of snowflakes adds many dimensions of difficulty to the problem of converting radar reflectivity to snowfall intensity. Third, there are few surface-based reliable snowfall measurements; snow gauge measurements are spotty and the technique itself remains challenging (e.g., Rasmussen et al. 2012). This lack of ground truth makes it hard to validate snowfall retrievals, which in turn, does not help improve retrieval algorithms. Owing to these challenges, space-borne sensors that are suitable for use to estimate snowfall distributions have not been available until CloudSat CPR (Stephens et al. 2002).

In the following sections, using CloudSat CPR as an example, we first describe the theory and methods for estimating snowfall intensity from radar reflectivity factors, followed by introducing some applications of using CloudSat measurements to understand the characteristics of snowing clouds. Finally, an idea of using radar snowfall estimates as guide to train passive microwave radiometer snowfall observations is explained.

16.2 Radar Snowfall Retrieval Method

Ignoring the attenuation by atmospheric gases, cloud liquid drops and ice particles, the equivalent radar reflectivity factor, Z, derived from the returned power from a unit volume of snow particles may be expressed by

$$Z = \frac{\lambda^4}{\pi^5 |K|^2} \int_0^\infty n(D)\sigma_b(D)dD, \tag{16.1}$$

where D is the dimension of the snowflake, $n(D)$ the particle size distribution, λ the wavelength, K a function of dielectric constant of water, and $\sigma_b(D)$ the backscattering cross section. Meanwhile, snowfall rate (liquid water equivalent) is the volume flux of snowflakes, and is expressed by

$$S = \frac{1}{\rho_w} \int_0^\infty n(D)m(D)v(D)dD, \tag{16.2}$$

where $v(D)$ is terminal velocity, $m(D)$ the particle's mass, and ρ_w the density of liquid water. The task of converting radar reflectivity measurement to snowfall rate then comes down to how to linking Eqs. (16.1) and (16.2).

16.2.1   Factors Impacting Z – S Relations

From the equations above, the accuracy of radar snowfall retrievas is thus impacted primarily by the uncertainties in the following three factors: (1) the particle size distribution, (2) the particle terminal velocity and (3) the backscatter of the nonspherical particles. If dual-wavelength (e.g., Matrosov 1998) or additional Doppler spectrum measurements (e.g., Mace et al. 2002) are available, the uncertainties in the snowfall retrievals could be reduced by taking those additional pieces of information into account. However, since the current CloudSat CPR is a single wavelength radar without Doppler spectrum measurements, the retrieval uncertainty can only be reduced by introducing additional constraints using ancillary information. For example, Wood et al. (2013, 2014) introduced microphysical properties observed from field experiments to constrain ice particle shapes and densities.

Results from *in situ* observations showed that the snow particle size distributions generally follow an exponential form, while the intercept and slope vary, among other things, with the intensity of snowfall (e.g., Houze et al. 1979; Brandes et al. 2007). Observational data also indicated that the intercept and slope in the size distribution vary with air temperature (Brandes et al. 2007). Terminal velocity of snowflakes has been observed by many investigators (e.g., Locatelli and Hobbs 1974; Heymsfield et al. 2007; Brandes et al. 2008; Heymsfield and Westbrook 2010) and is customarily parameterized in the form $v(D) = \alpha D^{\beta}$, where α and β are parameters empirically determined by *in situ* measurements. For aggregates, the terminal velocity generally ranges from 0.5 to 2 m s^{-1}, depending on the density of the particles and the degree of riming. A study by Brandes et al. (2008) suggests that the terminal velocity of snowflakes increases with air temperature in the range of $-10\,^{\circ}C$ to $0\,^{\circ}C$, presumably due to the increase of riming at warmer temperatures.

The third factor governing the Z-S relation is the backscattering cross section for nonspherical snowflakes. Atlas et al. (1953) showed that if particle sizes are sufficiently small (in the Rayleigh regime), the backscattered intensity by a nonspherical snowflake could be approximated by that of an equivalent low-density sphere having the same mass. Many investigators have so far used this approximation (e.g., Braham et al. 1992; Liu and Illingworth 2000). However, as wavelength becomes shorter (such as the 3 mm of CloudSat CPR), this approximation becomes invalid. In fact, as shown by Liu (2004), single scattering properties differ substantially from those of equivalent low-density spheres as the particles' size parameter becomes larger than 0.5. To evaluate the backscattering cross section of snowflakes, several investigators modeled the scattering properties at microwave frequencies using discrete dipole approximation techniques (e.g., Liu 2008a; Tyynelä et al. 2009; Petty and Huang 2010; Kuo et al. 2016) for various types of particles (see also Chap. 15).
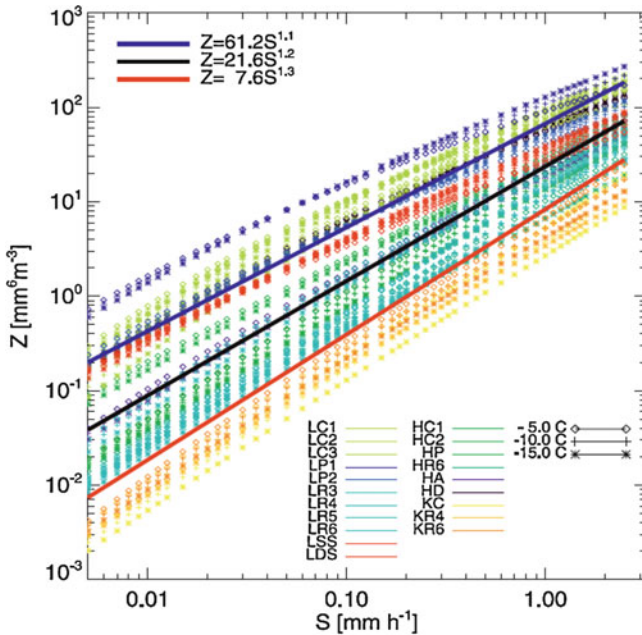
Fig. 16.1 The spread of Z-S relations under different assumptions of particle shapes. (Adapted from Hiley et al. 2011)

In radar meteorology, it is customary to relate Z and S by a power-law relation, i.e.,

$$Z = aS^b \qquad (16.3)$$

Clearly, the values of a and b strongly depend on the three factors discussed above. To illustrate the spread of this relation solely due to the assumption of particle shapes, Hiley et al. (2011) computed this relation using 20 ice particle shapes with Field et al. (2005) particle size distribution at 3 different air temperatures. As shown in Fig. 16.1, even without considering the uncertainties of particle size distributions and terminal velocities, the spread can be an order of magnitude among the *Z-S* relations assuming different particle shapes. Sims (2017) examined this problem by including the variation of particle size distribution and terminal velocity. In her study, 3 particle size distributions (Sekhon and Srivastava 1970; Field et al. 2007; Brandes et al. 2007), 3 terminal velocity relations (fitting the upper, middle and lower portion of the results of Locatelli and Hobbs 1974), and 4 types of ice particles (6-bullet rosettes, sectors, and dendrite from Liu 2008a, and aggregates from Nowell et al. 2013), were examined. The study concluded that the greatest uncertainty arises from the variability of particle shapes. Given the same snowfall rate, the low-density dendrite type snowflakes produce the weakest radar reflectivity while the rosettes produce the strongest. Therefore, better knowledge of weather dependent ice particle types and their scattering properties is the key to improve the accuracy of radar snowfall retrievals.

16.2.2 A Z-S Relation

Keeping these uncertainties in mind, Liu (2008b) derived a Z-S relation for CloudSat radar frequency (94 GHz) based on the averaged results of several particle shapes (Fig. 16.2). In his study, an exponential form of particle size distribution, $n(D) = n_0 \exp(-\Lambda D)$, was used with the values of n_0 and Λ taken from observational data published by Braham (1990) and Lo and Passarelli (1982). For terminal velocity, the 15 relations given by Locatelli and Hobbs (1974) for various types of ice particles are used. To be consistent with their observations, the size range of ice particles corresponding to these terminal velocity relations are also adopted from the Locatelli and Hobbs study. Figure 16.2 shows the Z-S relations computed using Eqs. (16.1) and (16.2) for rosettes, sectors and dendrites (Liu 2008a). A least square fitting of the data points in Fig. 16.2 gives $a = 11.5$ and $b = 1.25$ for the Z-S relation form given in Eq. (16.3), in which Z is in $mm^6 \, m^{-3}$, and S in $mm \, h^{-1}$ (liquid water equivalent). This relation is coincidentally quite similar to that of Matrosov (2007), which is also shown in Fig. 16.2 by a dashed line. Again, the spread of S values is quite large at any given Z (about an order of magnitude), indicating that not knowing the particle shape will introduce large uncertainties (random error) into the snowfall rate retrievals. On a logarithm scale, the correlation coefficient of the fitted line in Fig. 16.2 is 0.92 while the r.m.s difference of $\ln(S)$ between data points and computed by Eq. (16.3) is 0.47. Because of $d\ln(S) = dS/S$, it is estimated that the relative error ($\Delta S/S$) solely due to the spreading of data points around the fitting curve is about 50%.
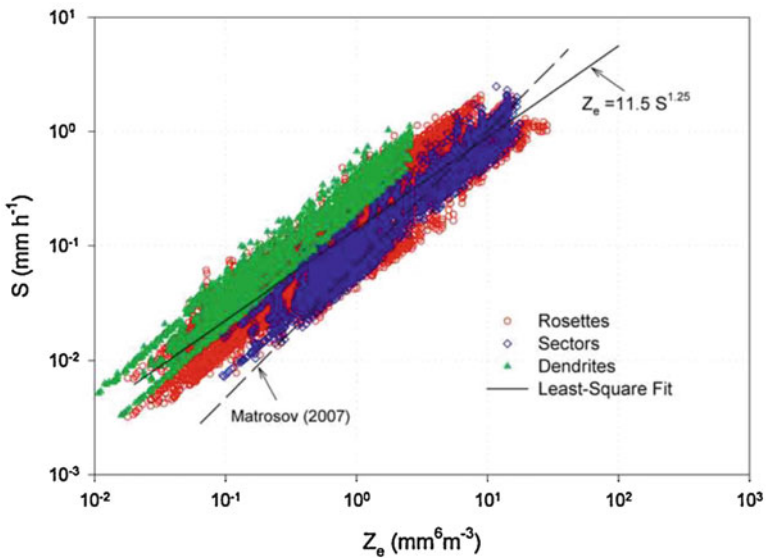
Fig. 16.2 Z-S relation for three nonspherical snowflakes. A least square fitting curve and relation by Matrosov (2007) are also shown. (Adapted from Liu 2008b)

16.2.3   Issues Related to Detectability and Attenuation

As discussed in the Introduction, snowfall can only be detected by radars that have a high detectability because the scattering intensity by low-density ice particles is weak. To illustrate this point, Fig. 16.3 shows a scatterplot of radar reflectivities from coincident observations by CloudSat CPR and GPM DPR (Global Precipitation Measurement Dual-frequency Precipitation Radar). The DPR operates at Ku- and Ka-band, with a minimum detection of 13 dBZ (Toyoshima et al. 2015); only data from Ku-band are shown in the plot. Below 13 dBZ, there is no meaningful information from DPR Ku radar (i.e., its reflectivity does not vary as CPR reflectivity changes). Above this level, Ku reflectivity varies in correspondent with CloudSat CPR variations, while the value of CPR reflectivity is several dBZ lower than that of Ku radar. This is consistent to our numerical calculations based on nonspherical ice scattering. Additionally, CPR reflectivity shows clear sign of attenuation for cases with Ku reflectivity higher than 20 dBZ (i.e., CPR reflectivity leveling off or decreasing as DPR reflectivity increases). Using estimates from Z-S relations described above for CPR and a similarly derived relation for DPR Ku-band, it was found that the ratio of the averaged snowfall rate by DPR Ku radar to that by CPR is 3:1 for the points shown in the green box in the figure, indicating that CloudSat underestimates snowfall rate for those cases that both DPR and CPR can detect.
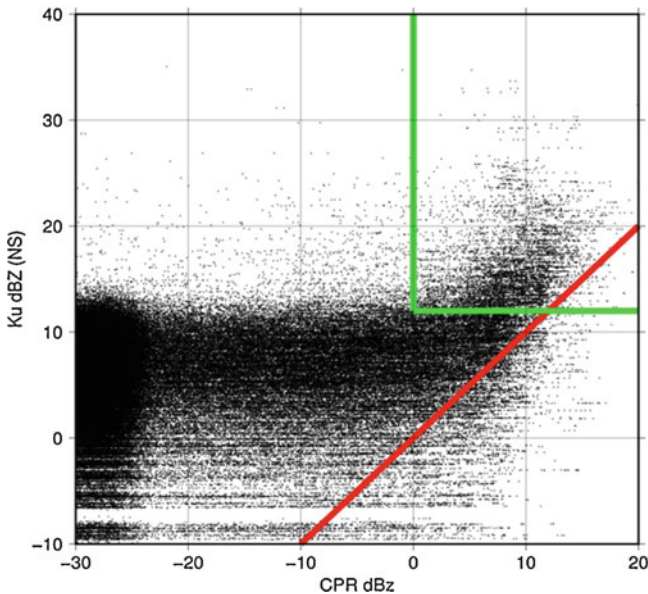
Fig. 16.3 Scatterplot of coincident CloudSat CPR and GPM/DPR Ku-band reflectivities for snowing cases. Data in the green box are those above the minimum detection for both Ku and CPR radars
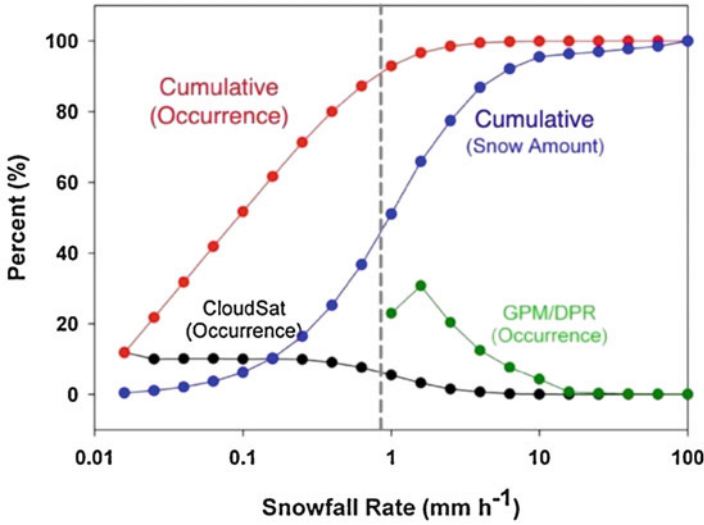
Fig. 16.4 PDFs and cumulative PDFs of snowfall occurrence and snowfall rate derived by coincident CPR and DPR observations using Z-S relations as discussed in the text. Data period for these plots is from March 2014 to December 2015

To estimate how much snowfall have been missed by the limited-detectability of the DPR radar, we analyzed the probability distribution functions (PDF) of occurrence and snowfall rate (estimated by Z-S relations) for both CPR and DPR observations for snowfall possible conditions (Sims and Liu 2015) for a period of March 2014 to December 2015. The results are shown in Fig. 16.4 with both PDFs and cumulative PDFs of snowfall occurrence and snowfall amount. The cumulative PDFs are computed using DPR data when DPR Ku-band reflectivity is >13 dBZ and CPR reflectivity is greater than 0 dBZ (within the green box). Otherwise, CPR data are used for the computation. From the cumulative PDFs, it is estimated that DPR misses ~50% of the snowfall amount while missing ~90% of snowfall occurrences detected by CloudSat CPR. Note that this result is based on coincident CPR and DPR data, which excludes the regions of 65° poleward since GPM satellite does not observe higher latitudes. Because there are more light snowfall events in higher latitudes, globally the proportion that DPR misses would be greater if the satellite were to cover entire the globe. Therefore, for snowfall observations, high detectability radars such as CPR are clearly necessary.

16.3   Results from CloudSat Measurements

Launched in April 2006, CloudSat is in the A-Train orbit. Its 94 GHz CPR makes nearly simultaneous Earth observations with various sensors onboard other satellites in the constellation (Stephens et al. 2002). Its pre-launch minimum detectable radar

reflectivity factor was designed to be -26 dBZ, although analysis of in-orbit data has shown that the sensitivity is better than the specification at about -30 dBZ. It has 500 m vertical resolution although the reflectivity data are sampled every 240 m in the archived standard products. The footprint size of radar reflectivity profiles is 1.4 km cross- and 2.5 km along-track. To avoid surface contaminated data, reflectivity data of the lowest 3 bins ($\sim$0.75 km) need to be excluded in the data analysis. In the following, the snowfall rate derived from radar reflectivity at the 4th bin above surface is used as "near surface snowfall".

Figure 16.5 shows two cases of CloudSat CPR observations of snowing clouds. Both are in the southern Hemisphere between 50 and 60°S. Using the rain-snow separation scheme of Sims and Liu (2015), it is determined that both cases correspond to conditions of snowfall at the surface. In the first case (top panel), snowing clouds associated with a frontal system have echo tops as high as 10 km and the maximum radar reflectivity reaches 15 dBZ. In the second case (bottom panel), shallow convective snowing cells can be seen between 50 and 56°S, with echo tops only reaching 2 km, but the maximum radar reflectivity can be over 10 dBZ.
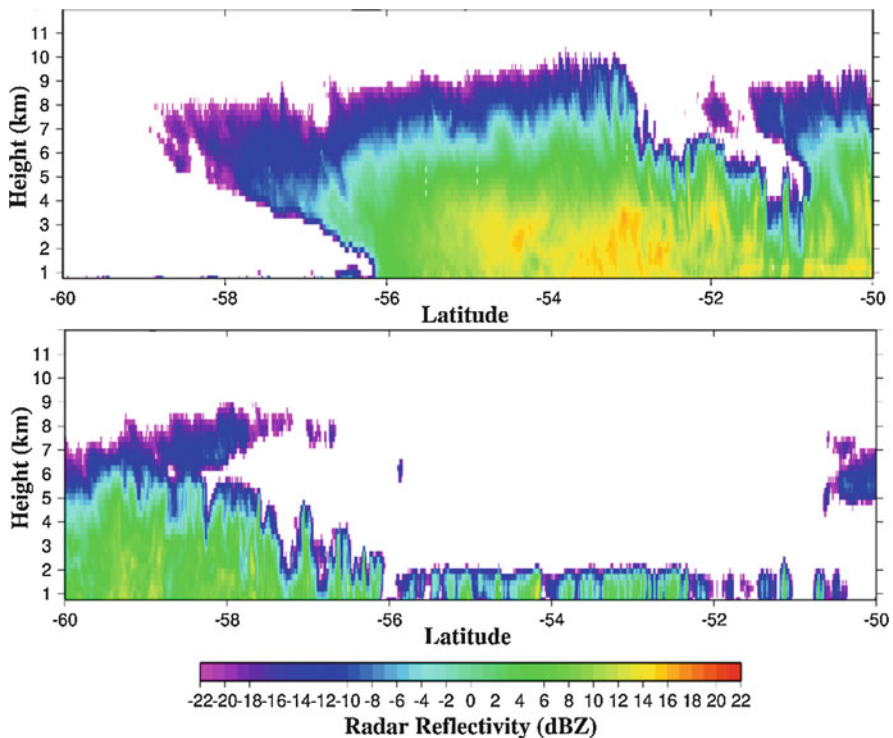
Fig. 16.5 CloudSat CPR radar reflectivity for 2 snowfall cases on 21 August 2007 (top) and 17 July 2006 (bottom) over 50–60°S. The top case is associated with deep snowing clouds cross a frontal system and the bottom case is associated with very shallow snowing cloud cells next to moderate deep snowing clouds

16.3.1   First Global Snowfall Map

Using CloudSat data over a 2-year period (July 2006 through June 2008), the global distributions of the frequency of total precipitation (rainfall and snowfall), the frequency of snowfall, and the averaged snowfall rate (Fig. 16.6) was analyzed. In generating these maps, it was assumed that the precipitation threshold for CPR is -15 dBZ and the rain-snow separation scheme of Sims and Liu (2015) was used. The results show that in the southern hemisphere, there is an almost zonally orientated high snowfall zone centered around $60°$S, where both snowfall frequency and rate are high. In the northern hemisphere, however, heavy/frequent snowfall areas are mostly locked to geographical locations associated with storm tracks. The zonal averages of these quantities are shown in Fig. 16.7 (with snowfall frequencies shown stacked over rainfall frequencies to display the total precipitation frequencies). In the regions poleward of $60°$, the majority of the precipitation is in the form of snowfall. The still significant values of mean precipitation show the importance of snowfall in the hydrologic cycle.

Another way to look at the snowfall statistics is to show how the number and volume (number times rate) fractions are distributed in the whole snowfall rate spectrum, which is shown in Fig. 16.8. The frequencies are calculated in the
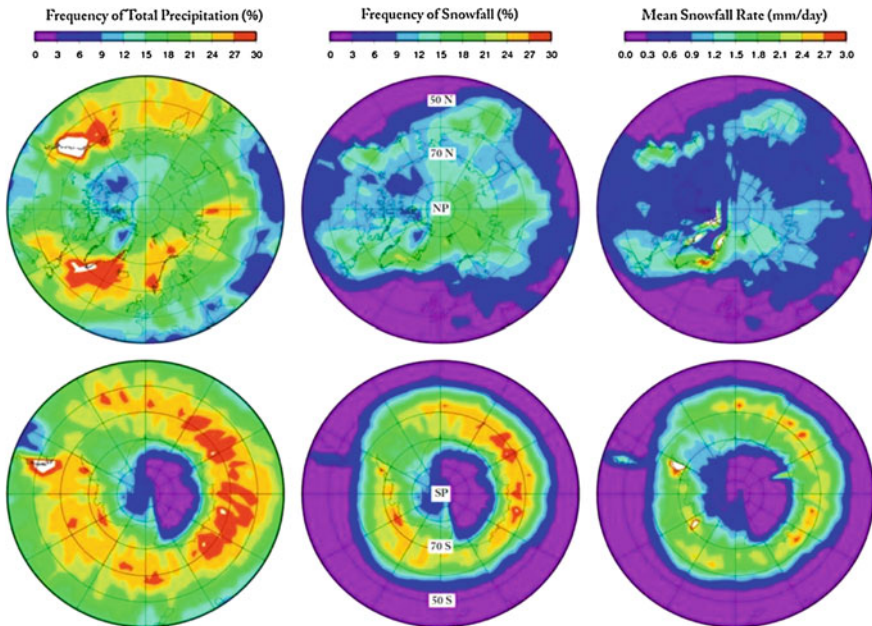
Fig. 16.6 Frequency of total precipitation (rain and snow, left), frequency of snowfall (middle) and mean snowfall rate (right) for northern (top) and southern (bottom) hemispheres derived from CloudSat observations from July 2006 to June 2008. The diagrams cover the area from the Poles to $40°$N/S. Detailed descriptions of the retrieval method can be found in Liu (2008b)
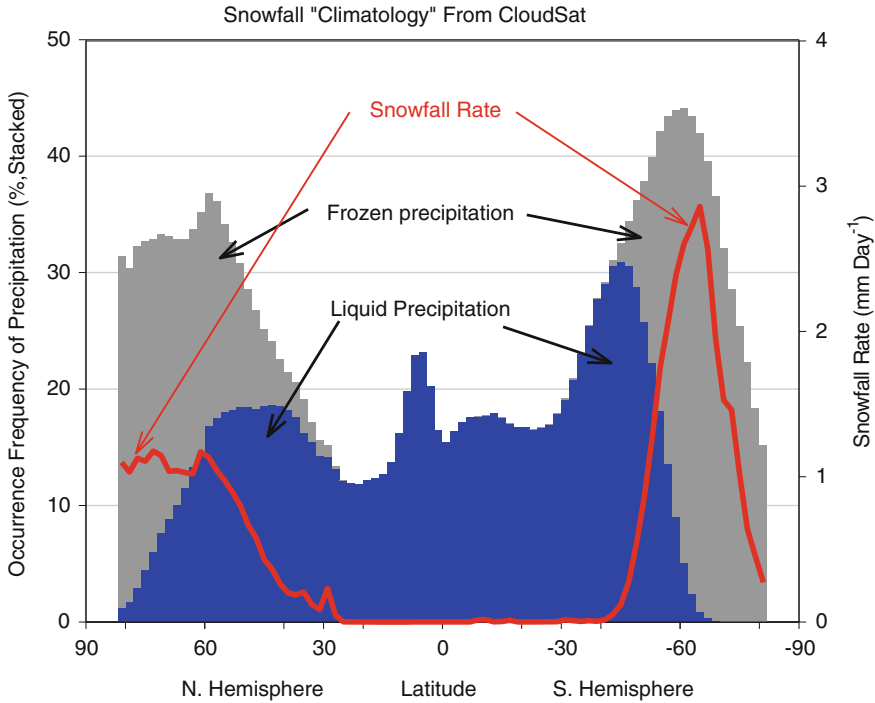
Fig. 16.7 Zonally averaged frequency of occurrence of rainfall (blue), frequency of snowfall (gray, stacked above blue) and snowfall rate (red). Derived using CPR −15 dBZ as precipitation threshold, rain-snow separation scheme of Sims and Liu (2015), and Z-S relation of Liu (2008b)
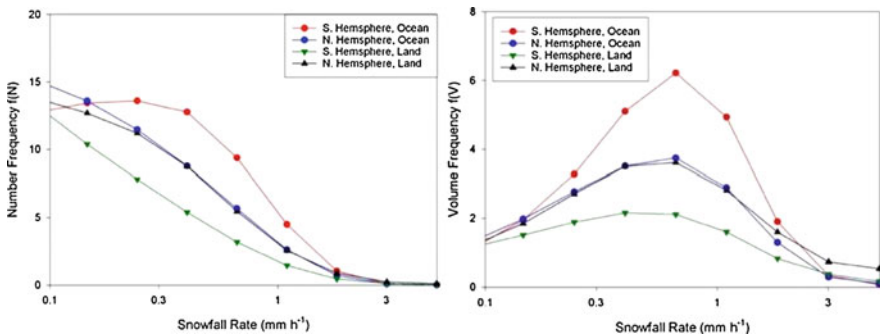
Fig. 16.8 Number and volume frequency distributions of snowfall rate derived from CloudSat observations. Note the frequencies are calculated in a snowfall rate interval on logarithm scale

logarithm of snowfall rate (i.e., the number and volume fractions are computed within a ln(S) interval). From this figure, it can be seen that for number frequency (or areal fraction) the largest contribution is by those snowfall events with lightest

intensities. For snowfall volume, the greatest contribution comes from those events with snowfall rate ~0.5 mm h^{-1}. Snowfall events over southern oceans seem to be somewhat different from those over other regions with a narrower snowfall volume frequency distribution (also peaked near 0.5 mm h^{-1}).

16.3.2   Snow Cloud Structures

The section focuses on the vertical distribution of snowfall for a given surface snowfall rate. Observed profiles from July 2006 to June 2007 were divided into several groups according to their near surface snowfall rate, partitioned between over ocean and over land. The mean profile was computed for each group. The averaged snowfall rate profiles are shown in Fig. 16.9. The averaged profiles for over-ocean and over-land environments are quite similar except that the over-land profiles are somewhat shallower than over-ocean profiles when surface snowfall rates are low.

Fig. 16.9 Mean profiles for a given near surface snowfall rate for (**a**) over ocean and (**b**) over land environments. CloudSat observations from July 2006 to June 2007 are used. (Adapted from Liu 2008b)
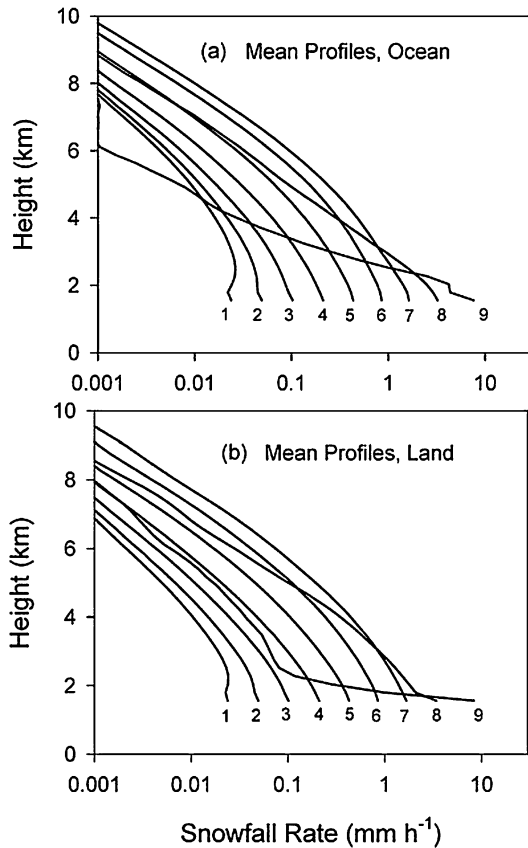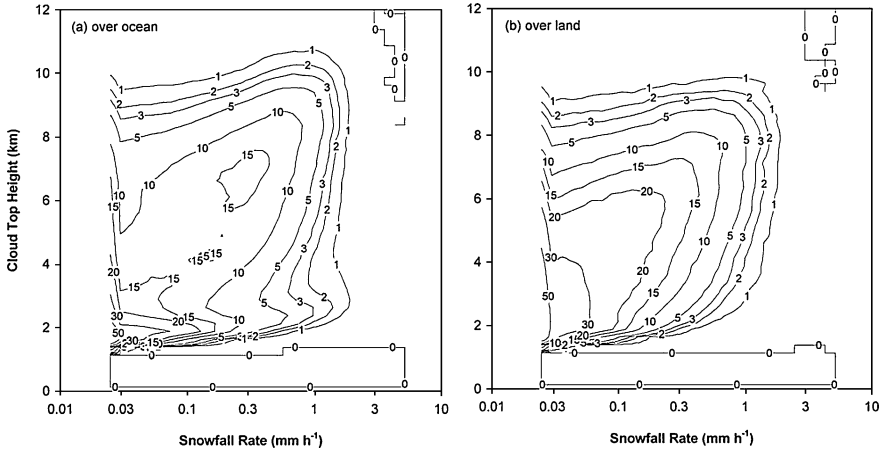
Fig. 16.10 Relation between near surface snowfall rate and cloud top height as expressed by snowfall profiles frequency distributions for snowfall events over (**a**) ocean and (**b**) land. The frequency values are normalized so that the maximum frequency is 100. (Adapted from Liu 2008b)

From profiles 1–7, as surface snowfall rate increases, the snow layer grows deeper, manifesting that heavier snowfall is generally associated with a thicker cloud layer. However, profiles 8 and 9 do not follow the same trend, indicating that the heaviest surface snowfalls are produced by rather shallow clouds. The explanation to this exception of trend is not immediately clear to the author although it is speculated that the last two groups may correspond to shallow convective clouds associated with "lake effect" (cold air overpasses warm water surfaces creating strong shallow convections), which, while shallow, often produce heavy snowfalls. The prevalence of the two different snow cloud regimes is supported by Fig. 16.10, which shows the 2-dimensional PDFs of CloudSat echoes in a cloud top height (as defined by $Z = -24$ dBZ) versus near surface snowfall rate diagram. It is seen that while near surface snowfall rate increases in response to increasing cloud top heights, there seem to exist two groups of clouds that have different growth rate, particularly for those profiles over oceanic environment. When surface snowfall rate increases to ~2 mm h^{-1}, one group has cloud top height around 10 km while the other group has cloud top height below 3 km. The abundance of shallow snowing clouds has been reported in detail by Kulie et al. (2016).

Although snowing clouds exist in cold environments, mostly below 0 °C, cloud liquid water is commonly found in these clouds in abundant amounts. To study the magnitude and feature of cloud liquid water in snowing clouds, Wang et al. (2013) retrieved liquid water path from the Advanced Microwave Scanning Radiometer for Earth Observing System (AMSR-E) observations on the Aqua satellite that are collocated with CloudSat CPR pixels. Figure 16.11 shows the averaged liquid water path as a function of near surface radar reflectivity and cloud top height are shown for different types of clouds. In the cloud classification, the term "isolated" is for continuous radar returns horizontally shorter than 40 km, otherwise it is called
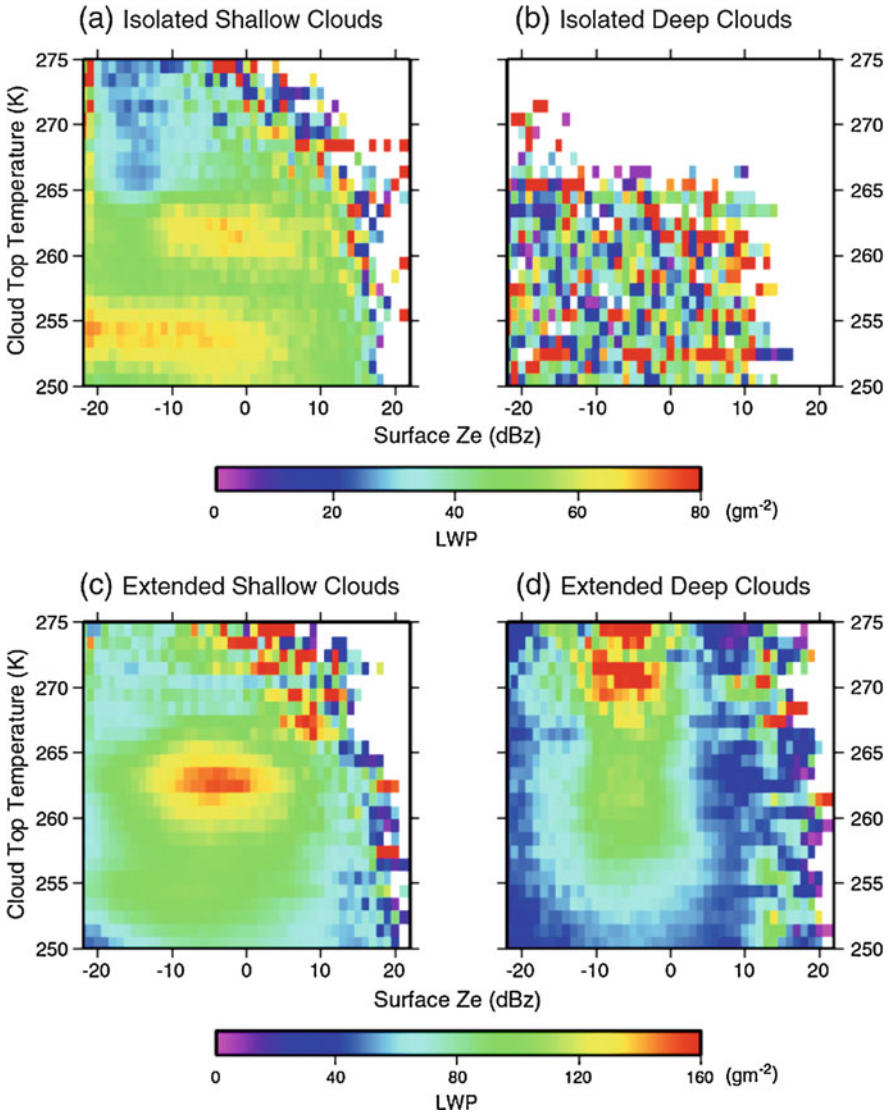
Fig. 16.11 Mean liquid water path as a function of cloud top temperature and near surface radar reflectivity for different snowing cloud types: (**a**) Isolated shallow clouds, (**b**) Isolated deep clouds, (**c**) extended shallow clouds, and (**d**) Extended deep clouds. Coincident CloudSat CPR and Aqua AMSR-E observations from June 2006 to June 2010 are used. Note that the LWP color scales for isolated and extended clouds are different. (Adapted from Wang et al. 2013)

"extended". Likewise, the term "shallow" is used for clouds with radar echo top height lower than 5 km, otherwise it is called "deep". Except for isolated deep clouds, in which the number of data samples appears too low to show a clear distribution pattern, liquid water path seems to show greater values when near

surface radar reflectivity ranges from -10 to 0 dBZ, corresponding to a weak snowfall of approximately 0.02 to 0.15 mm h^{-1}. Heavy snowfalls are commonly not accompanied by large values of cloud liquid water. Additionally, the diagram shows that larger values of liquid water paths often appear at several "favorite" cloud top temperature ranges, e.g., around $0\,^{\circ}\mathrm{C}$ (extended deep clouds), $-10\,^{\circ}\mathrm{C}$ (263 K, all except for isolated deep clouds), and $-19\,^{\circ}\mathrm{C}$ (254 K, isolated shallow clouds). To the author's best knowledge, this result does not seem to have an obvious explanation.

16.4 Guiding Passive Sensors for Snowfall Estimation

As shown in previous sections, the CloudSat CPR measurements provide the first opportunity to survey the horizontal and vertical snowfall (snowing cloud) structures in a globally complete manner. The usage of CPR data for snowfall studies can be two-fold. First, the CPR radar reflectivity can be converted into snowfall rate. The CPR snowfall retrieval has provided the first global snowfall distribution, although its representativeness for snowfall climatology is still questionable due to its narrow spatial sampling (~1.5 km per orbit) and its inability to resolve the diurnal cycle. Second, by combining CPR with high-frequency passive microwave satellite data, one can use the CPR snowfall retrievals as truth to "teach" the passive microwave sensors, which alone have several deficiencies in measuring snowfall such as surface contamination and cloud liquid water masking of ice scattering signature, so that snowfall retrievals can be performed in much greater spatial coverage and temporal frequency. Currently, there are multiple polar-orbiting satellites in operation that carry high-frequency (>85 GHz) passive microwave sensors; the swath width of these measurements is generally over one thousand kilometers. Given the fact that CPR only observes a 1.5 km width swath along the orbit, the second usage is unarguably important for deriving global snowfall climatologies.

Following the above strategy, Liu and Seo (2013) studied the possibility of using CloudSat to train high-frequency microwave observations of Microwave Humidity Sounder (MHS) over land for snowfall retrievals. Their results indicate that while it is difficult to isolate snowfall signatures at any single channel, the collective variation of brightness temperatures do contain signatures of snow precipitation. Accordingly, they extracted the primary information from brightness temperatures by using the 3 leading principle components derived by Empirical Orthogonal Function analysis, and developed a lookup table of snowfall probability and snowfall rate in the 3-dimensional principle component space based on coincident radar and radiometer observations. A similar approach has also been used by Kongoli et al. (2015) for Advanced Technology Microwave Sounder (ATMS) observations. This method recently advanced to train GPM Microwave Imager (GMI) observations using combined CloudSat CPR and GPM/DPR data to minimize the impact due to attenuation in CPR data (see Fig. 16.12).
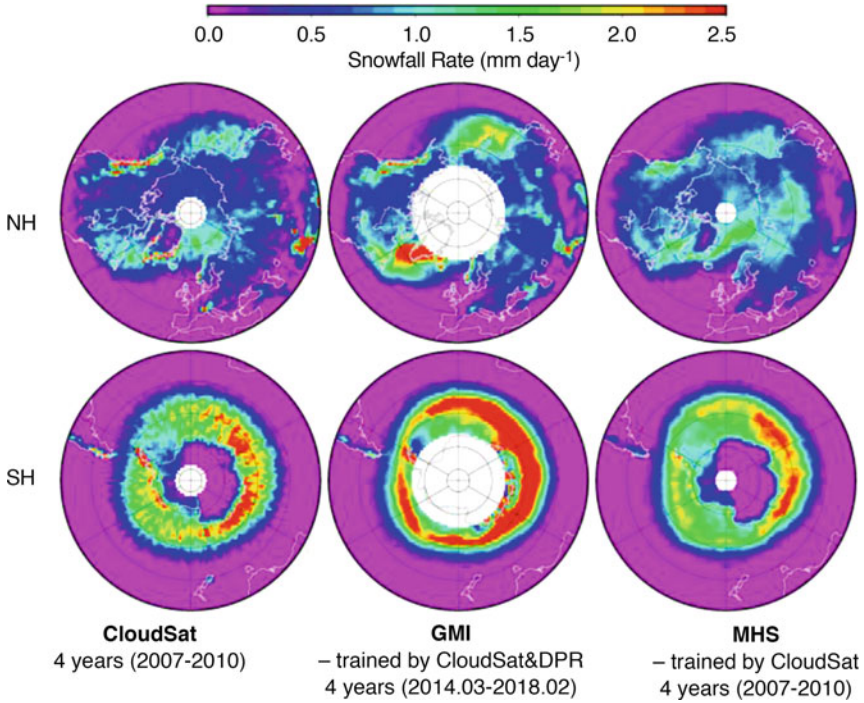
Fig. 16.12 Mean snowfall rate maps derived from multiple years of CloudSat (2007–2010), GMI (March 2014–Feb 2018), and MHS (2007–2010). GMI algorithm is trained by combined CloudSat and DPR radar data. No observations in blank areas. MHS algorithm is trained by CloudSat CPR

Using this radar-guided method, the mean global snowfall maps based on multiple years of CloudSat, GMI and MHS data are derived and shown in Fig. 16.12. In developing these mean snowfall maps, the GMI algorithm is trained by both CloudSat CPR and GPM DPR, while the MHS algorithm is trained by CloudSat CPR alone since there are very few coincident CloudSat CPR, GPM DPR and MHS observations. First, the patterns of the 3 maps are very consistent, which confirms that the active sensor trained passive microwave snowfall algorithms have captured the primary signature of snowfall and produced reasonable snowfall rate estimates. However, the estimates by GMI, which is trained by combined CloudSat CPR and GPM DPR, are clearly higher than the other 2 estimates, which relied on CloudSat radar alone. Recalling earlier discussions related to Fig. 16.3 that CloudSat underestimates snowfall rate for heavy snowfall cases, it can be argued that the GMI retrievals are more accurate. Although the accuracy of these snowfall algorithms needs further investigation, their ability to capture the primary pattern of global snowfall distribution offers a solid promise of this strategy.

16.5 Concluding Remarks

This article briefly summarized the theory and techniques used to derive snowfall from spaceborne radars. In particular, it discussed how to retrieve snowfall rate and global snowfall distributions from CloudSat observations. Compared to rainfall estimations, radar snowfall measurements face at least two extra challenges: the weak scattering intensity due to the low density of snow, and the uncertainty of scattering magnitude due to the nonsphericity of snow particles. The first challenge can be addressed by developing high sensitivity radars, such as CloudSat CPR (Stephens et al. 2002) and future EarthCare cloud profiling radar (EC-CPR, Kobayashi et al. 2002) both with a minimum detectability better than −26 dBZ. CloudSat opened the door for measuring snowfall globally and the "first look" of global snowfall has since been developed. To overcome the second challenge, a collective effort is required from a community consisting of scientists specializing in *in situ* microphysical measurement, electromagnetic wave scattering theory, and radar meteorology. Recently, a group of scientists (Kneifel et al. 2018) took this initiative and started to assemble existing nonspherical particles' scattering databases (see Chap. 15). It is hoped that this community effort will bear fruits in tackling the second challenge in coming years. As in radar rainfall estimations, particle size distributions are also a large factor of uncertainty for radar snowfall retrievals. Further technology development, such as dual-frequency radars and/or Doppler measurements are certainly helpful in alleviating this problem.

Combining active and passive sensors has shown great potentials for understanding microphysical processes of snowing clouds and advancing satellite snowfall remote sensing. Today, satellite radar observations have better sensitivity to snowfall while microwave radiometers have better spatial and temporal coverages. By skillfully combing the two, we can greatly increase the utility of satellite remote sensing in snowfall measurements. In this article, we only demonstrated some preliminary examples of this combination, i.e., understanding the abundance of supercooled cloud water in snowing clouds and training high-frequency microwave observations for snowfall retrievals. Other problems can also be investigated following this approach. For example, cloud ice is an important, yet poorly observed variable in determining global energy balance. CloudSat CPR can retrieve cloud ice water contents (Deng et al. 2010; Delanoë and Hogan 2010), but with narrow sampling coverage. In particular, its observations miss the diurnal cycle of cloud ice, which is extremely important for understanding cloud ice's radiative effect. If the diurnal cycle information can be provided by currently operational high-frequency passive microwave observations, this uncertainty can be significantly reduced.

References

Atlas, D., Kerker, M., & Hitschfeld, W. (1953). Scattering and attenuation by non-spherical atmospheric particles. *Journal of Atmospheric and Terrestrial Physics, 3*, 108–119. https://doi.org/10.1016/0021-9169(53)90093-2.

Barnett, T. P., Dumenil, L., Schlese, U., Roeckner, E., & Latif, M. (1989). The effect of Eurasian snow cover on regional and global climate variations. *Journal of the Atmospheric Sciences, 46*, 661–685. https://doi.org/10.1175/1520-0469(1989)046<0661:TEOESC>2.0.CO;2.

Braham, R. R., Jr. (1990). Snow particle size spectra in lake effect snows. *Journal of Applied Meteorology, 29*, 200–207. https://doi.org/10.1175/1520-0450(1990)029<0200:SPSSIL>2.0.CO;2.

Braham, R. R., Kristovich, D. A. R., & Dungey, M. J. (1992). Comparison of lake-effect snow precipitation rates determined from radar and aircraft measurements. *Journal of Applied Meteorology, 31*, 237–246. https://doi.org/10.1175/1520-0450(1992)031<0237:COLESP>2.0.CO;2.

Brandes, E., Ikeda, K., Zhang, G., Schönhuber, M., & Rasmussen, R. (2007). A statistical and physical description of hydrometeor distributions in Colorado snowstorms using a video disdrometer. *Journal of Applied Meteorology and Climatology, 46*, 634–650. https://doi.org/10.1175/JAM2489.1.

Brandes, E., Ikeda, K., Thompson, G., & Schönhuber, M. (2008). Aggregate terminal velocity/temperature relations. *Journal of Applied Meteorology and Climatology, 47*, 2729–2736. https://doi.org/10.1175/2008JAMC1869.1.

Delanoë, J., & Hogan, R. J. (2010). Combined CloudSat-CALIPSO-MODIS retrievals of the properties of ice clouds. *Journal of Geophysical Research, 115*, D00H29. https://doi.org/10.1029/2009JD012346.

Deng, M., Mace, G. G., Wang, Z., & Okamoto, H. (2010). Tropical composition, cloud and climate coupling experiment validation for cirrus cloud profiling retrieval using CloudSat radar and CALIPSO lidar. *Journal of Geophysical Research, 115*, D00J15. https://doi.org/10.1029/2009JD013104.

Field, P. R., Hogan, R. J., Brown, P. R. A., Illingworth, A. J., Choularton, T. W., & Cotton, R. J. (2005). Parametrization of ice-particle size distributions for mid-latitude stratiform cloud. *Quarterly Journal of the Royal Meteorological Society, 131*, 1997–2017. https://doi.org/10.1256/qj.04.134.

Field, P. R., Heymsfield, A. J., & Bansemer, A. (2007). Snow size distribution parametrization for midlatitude and tropical ice clouds. *Journal of the Atmospheric Sciences, 64*, 4346–4365. https://doi.org/10.1175/2007JAS2344.1.

Heymsfield, A. J., & Westbrook, C. D. (2010). Advances in the estimation of ice particle fall speeds using laboratory and field measurements. *Journal of the Atmospheric Sciences, 67*, 2646–2482. https://doi.org/10.1175/2010JAS3379.1.

Heymsfield, A. J., Bansemer, A., & Twohy, C. (2007). Refinements to ice particle mass dimensional and terminal velocity relationships for ice clouds: Part I: Temperature dependence. *Journal of the Atmospheric Sciences, 64*, 1047–1067. https://doi.org/10.1175/JAS3890.1.

Hiley, M., Kulie, M. S., & Bennartz, R. (2011). Uncertainty analysis for CloudSat snowfall retrievals. *Journal of Applied Meteorology and Climatology, 50*, 399–418. https://doi.org/10.1175/2010JAMC2505.1.

Houze, R., Hobbs, P., Herzegh, P., & Parsons, D. (1979). Size distributions of precipitation particles in frontal clouds. *Journal of the Atmospheric Sciences, 36*, 156–162. https://doi.org/10.1175/1520-0469(1979)036<0156:SDOPPI>2.0.CO;2.

Kneifel, S., Neto, J. D., Ori, D., Moisseev, D., Tyynelä, J., Adams, I. S., Kuo, K. S., Bennartz, R., Berne, A., Clothiaux, E. E., Eriksson, P., Geer, A. J., Honeyager, R., Leinonen, J., & Westbrook, C. D. (2018). The first international summer snowfall workshop: Scattering properties of realistic frozen hydrometeors from simulations and observations, as well as defining a new standard for scattering databases. *Bulletin of the American Meteorological Society, 99*, ES55–ES58. https://doi.org/10.1175/BAMS-D-17-0208.1.

Kobayashi, S., Kumagai, H., & Kuroiwa, H. (2002). A proposal of pulse-pair Doppler operation on a spaceborne cloud-profiling radar in W band. *Journal of Atmospheric and Oceanic Technology, 19*, 1294–1306. https://doi.org/10.1175/1520-0426(2002)019<1294:APOPPD>2.0.CO;2.

Kongoli, C., Meng, H., Dong, J., & Ferraro, R. (2015). A snowfall detection algorithm over land utilizing high-frequency passive microwave measurements—Application to ATMS. *Journal of Geophysical Research, 120*, 1918–1932. https://doi.org/10.1002/2014JD022427.

Kulie, M. S., Milani, L., Wood, N. B., Tushaus, S. A., Bennartz, R., & L'Ecuyer, T. S. (2016). A shallow cumuliform snowfall census using spaceborne radar. *Journal of Hydrometeorology, 17*, 1261–1279. https://doi.org/10.1175/JHM-D-15-0123.1.

Kuo, K.-S., Olson, W., Johnson, B., Grecu, M., Tian, L., Clune, T., van Aartsen, B., Heymsfield, A., Liao, L., & Meneghini, R. (2016). The microwave radiative properties of falling snow derived from nonspherical ice particle models. Part I: An extensive database of simulated pristine crystals and aggregate particles, and their scattering properties. *Journal of Applied Meteorology and Climatology, 55*, 691–708. https://doi.org/10.1175/JAMC-D-15-0130.1.

Liu, G. (2004). Approximation of single scattering properties of ice and snow particles for high microwave frequencies. *Journal of the Atmospheric Sciences, 61*, 2441–2456. https://doi.org/10.1175/1520-0469(2004)061<2441:AOSSPO>2.0.CO;2.

Liu, G. (2008a). A database of microwave single-scattering properties for nonspherical ice particles. *Bulletin of the American Meteorological Society, 89*, 1563–1570. https://doi.org/10.1175/2008BAMS2486.1.

Liu, G. (2008b). Deriving snow cloud characteristics from CloudSat observations. *Journal of Geophysical Research, 113*, D00A09. https://doi.org/10.1029/2007JD009766.

Liu, C.-L., & Illingworth, A. J. (2000). Toward more accurate retrievals of ice water content from radar measurements of clouds. *Journal of Applied Meteorology, 39*, 1130–1146. https://doi.org/10.1175/1520-0450(2000)039<1130:TMAROI>2.0.CO;2.

Liu, G., & Seo, E.-K. (2013). Detecting snowfall over land by satellite high-frequency microwave observations: The lack of scattering signature and a statistical approach. *Journal of Geophysical Research, 118*, 1376–1387. https://doi.org/10.1002/jgrd.50172.

Lo, K. H., & Passarelli, J. R. E. (1982). The growth of snow in winter storms: An airborne observational study. *Journal of the Atmospheric Sciences, 39*, 697–706. https://doi.org/10.1175/1520-0469(1982)039<0697:TGOSIW>2.0.CO;2.

Locatelli, J. D., & Hobbs, P. V. (1974). Fall speeds and masses of solid precipitation particles. *Journal of Geophysical Research, 79*, 2185–2197. https://doi.org/10.1029/JC079i015p02185.

Mace, G. G., Heymsfield, A. J., & Poellot, M. R. (2002). On retrieving the microphysical properties of cirrus clouds using the moments of the millimeter-wavelength Doppler spectrum. *Journal of Geophysical Research, 107*, 4815–4841. https://doi.org/10.1029/2001JD001308.

Matrosov, S. Y. (1998). A dual-wavelength radar method to measure snowfall rate. *Journal of Applied Meteorology, 37*, 1510–1521. https://doi.org/10.1175/1520-0450(1998)037<1510:ADWRMT>2.0.CO;2.

Matrosov, S. Y. (2007). Modeling backscatter properties of snowfall at millimeter wavelengths. *Journal of the Atmospheric Sciences, 64*, 1727–1736. https://doi.org/10.1175/JAS3904.1.

Nowell, H., Liu, G., & Honeyager, R. (2013). Modeling the microwave single-scattering properties of aggregate snowflakes. *Journal of Geophysical Research, 118*, 7873–7885. https://doi.org/10.1002/jgrd.50620.

Petty, G. W., & Huang, W. (2010). Microwave backscatter and extinction by soft ice spheres and complex snow aggregates. *Journal of the Atmospheric Sciences, 67*, 769–787. https://doi.org/10.1175/2009JAS3146.1.

Rasmussen, R. M., Baker, B., Kochendorfer, J., Meyers, T., Landolt, S., Fischer, A. P., Black, J., Theriault, J. M., Kucera, P. A., Gochis, D., Smith, C., Nitu, R., Hall, M., Ikeda, K., & Gutmann, E. (2012). How well are we measuring snow? *Bulletin of the American Meteorological Society, 93*, 811–829. https://doi.org/10.1175/BAMS-D-11-00052.1.

Sekhon, R. S., & Srivastava, R. C. (1970). Snow size spectra and radar reflectivity. *Journal of the Atmospheric Sciences, 27*, 299–307. https://doi.org/10.1175/1520-0469(1970)027<0299:SSSARR>2.0.CO;2.

Sims, E. M. (2017). *Improving satellite-based snowfall estimation: A new method for classifying precipitation phase and estimating snowfall rate*. PhD Dissertation. Florida State University, Tallahassee. Available at https://search.proquest.com/openview/9dc178ed8a6f58391ead bad256754a3a/1?pq-origsite=gscholar&cbl=18750&diss=y. Last accessed 9 Dec 2018.

Sims, E. M., & Liu, G. (2015). A parameterization of the probability of snow-rain transition. *Journal of Hydrometeorology, 16*, 1466–1477. https://doi.org/10.1175/JHM-D-14-0211.1.

Stephens, G. L., Vane, D. G., Boain, R. J., Mace, G. G., Sassen, K., Wang, Z., Illingworth, A. J., O'Connor, E. J., Rossow, W. B., Durden, S. L., Miller, S. D., Austin, R. T., Benedetti, A., Mitrescu, C., & the CloudSat Science Team. (2002). The CloudSat mission and the A-train: A new dimension of space-based observations of clouds and precipitation. *Bulletin of the American Meteorological Society, 83*, 1771–1790. https://doi.org/10.1175/BAMS-83-12-1771.

Toyoshima, K., Masunaga, H., & Furuzawa, F. A. (2015). Early evaluation of Ku- and Ka-band sensitivities for the Global Precipitation Measurement (GPM) Dual-frequency Precipitation Radar (DPR). *SOLA, 11*, 14–17. https://doi.org/10.2151/sola.2015-004.

Tyynelä, J., Nousiainen, T., Göke, S., & Muinonen, K. (2009). Modeling C-band single scattering properties of hydrometeors using discrete-dipole approximation and T-matrix method. *Journal of Quantitative Spectroscopy and Radiative Transfer, 110*, 1654–1664. https://doi.org/10.1016/j.jqsrt.2009.02.020.

Walsh, J. E. (1995). Continental snow cover and climate variability. In *Nation Climate Variability on Decade-to-Century Time Scales* (pp. 49–58). Washington, DC: National Academy Press.

Wang, Y., Liu, G., Seo, E.-K., & Fu, Y. (2013). Liquid water in snowing clouds: Implications for satellite remote sensing of snowfall. *Atmospheric Research, 131*, 60–72. https://doi.org/10.1016/j.atmosres.2012.06.008.

Wood, N. B., L'Ecuyer, T. S., Bliven, F. L., & Stephens, G. L. (2013). Characterization of video disdrometer uncertainties and impacts on estimates of snowfall rate and radar reflectivity. *Atmospheric Measurement Techniques, 6*, 3635–3648. https://doi.org/10.5194/amt-6-3635-2013.

Wood, N. B., L'Ecuyer, T. S., Heymsfield, A. J., Stephens, G. L., Hudak, D. R., & Rodriguez, P. (2014). Estimating snow microphysical properties using collocated multisensor observations. *Journal of Geophysical Research, 119*. https://doi.org/10.1002/2013JD021303.

Chapter 17
A 1DVAR-Based Snowfall Rate Algorithm for Passive Microwave Radiometers

Huan Meng, Cezar Kongoli, and Ralph R. Ferraro

Abstract This chapter introduces an overland snowfall rate algorithm for passive microwave radiometers. It relies on an embedded algorithm to detect the presence of snowfall. The retrieval of cloud properties is the foundation of the snowfall rate algorithm and is accomplished with a one-dimensional variational (1DVAR) model. The snowfall rate derived with the physical algorithm is further adjusted based on calibration against a ground radar and gauge combined precipitation product. Both the snowfall detection and the snowfall rate algorithms have been validated respectively against ground observations and radar and gauge combined analyses from the contiguous United States with satisfactory results. Specifically, the correlation coefficient of the validation data with the radar analyses reaches 0.50. Currently, the snowfall rate product is operationally generated at near real-time at the US National Oceanic and Atmospheric Administration.

Keywords Snow · Ice · Snowfall detection · Snowfall rate · NOAA · Logistic regression · 1DVAR · Microwave humidity sounders · Brightness temperature · MRMS · GFS · Radiative transfer model · Particle distribution function · Ice water content.

17.1 Introduction

Satellite remote sensing of snowfall is challenging due to the complexity of atmospheric processes involved and the lack of both the understanding about these processes and the information on the forcing variables. It is more difficult to estimate snowfall rate than rainfall rate because more information, such as ice particle shape

H. Meng (✉) · R. R. Ferraro
NOAA/NESDIS/STAR, College Park, MD, USA
e-mail: huan.meng@noaa.gov

C. Kongoli
University of Maryland, College Park, MD, USA

and density, is required for developing physically based snowfall rate algorithm that is generally unavailable. Consequently, snowfall retrieval algorithms have lagged significantly behind the development of satellite rain rate algorithms (Ferraro et al. 2005; Kummerow et al. 2011). However, snowfall retrieval from passive microwave (PMW) instruments has been gaining momentum in recent years. The observations from PMW are uniquely suitable for snowfall detection and retrieval. PMW has the ability to penetrate clouds, hence directly bearing the signature of snow particles. High frequencies, such as window channels around 160 GHz and water vapor sounding channels around 183 GHz, are particularly sensitive to the radiance depressing effect of ice scattering (Bennartz and Bauer 2003). Some snowfall rate algorithms have been developed utilizing this property (Noh et al. 2006; Kim et al. 2008; Liu and Seo 2013; Skofronick-Jackson et al. 2013; Kummerow et al. 2015; Kidd et al. 2016; You et al. 2017; Meng et al. 2017; Kongoli et al. 2015, 2018). It is noted that many microwave algorithms that retrieve precipitation (rainfall or snowfall) rely on the sensing of ice signatures.

The algorithm introduced in this chapter retrieves snowfall rate over land (hereafter denoted as SFR). It consists of two components: snowfall detection (SD) and snowfall rate estimation. The former is a statistical algorithm whiles the latter employs a 1DVAR-based approach to retrieve snowfall rate. Owing to its physically-based framework, the SFR algorithm can cover a wide range of snowfall conditions. Currently, the SFR product is operationally produced at near real-time at the US National Oceanic and Atmospheric Administration (NOAA).

17.2 Data and Models

17.2.1 Instruments and Data

The SFR algorithm utilizes measurements from two sets of PMW instruments: Advanced Microwave Sounding Unit-A (AMSU-A) and Microwave Humidity Sounder (MHS) pair, and the Advanced Technology Microwave Sounder (ATMS). AMSU-A and MHS are aboard four POES and Metop satellites, and ATMS is aboard S-NPP and NOAA-20 satellites. These are cross-track scanning, PMW sounders with channels ranging from 23.8 GHz to 190.31 (MHS)/183.31 (ATMS) GHz, i.e. a combination of window, temperature sounding and water vapor sounding frequencies. The sensors have variable footprint sizes depending on frequency and scan position. The nadir resolution is about 16 km for high frequencies which is the resolution of the SFR product.

Some Numerical Weather Prediction (NWP) model data are also employed where required environmental state observations are not available. The model data employed are from the Global Forecast System (GFS) produced at NOAA National Centers for Environmental Prediction (NCEP). The forecast data satisfy the latency requirement of the SFR production at near real-time.

The SD algorithm was trained with in-situ weather observations. The ground data were obtained from the Quality Controlled Local Climatology Data (QCLCD) product. This dataset is generated from surface meteorological observations from approximately 1600 U.S locations. The data undergo interactive and manual quality control at NOAA National Centers for Environmental Information (NCEI) in addition to automated quality control. It provides direct measurement of present weather including snowfall occurrence and other related variables at hourly intervals, making it a valuable independent ground truth reference for satellite snowfall identification studies.

The SFR algorithm was calibrated against the NCEP Stage IV precipitation analysis. This dataset takes the Multi-Radar Multi-Sensor (MRMS) precipitation data (Zhang et al. 2016) as input. It further incorporates gauge, model, and satellite data, and applies human quality controls. The hourly Stage IV data has a 4 km resolution over the contiguous United States (CONUS). It is a high-quality standard radar-based precipitation analyses used by the US National Weather Service.

17.2.2 Logistic Regression

The SD algorithm applies a Logistic Regression (LR) technique to derive the probability of snowfall (POS). LR estimates the probability of a binary outcome Y as an exponential continuous function of a set of predictor variables:

$$P = \frac{exp\left(\beta_0 + \beta_1 X_1 + \beta_2 X_2 + \ldots + \beta_n X_n\right)}{1 + exp\left(\beta_0 + \beta_1 X_1 + \beta_2 X_2 + \ldots + \beta_n X_n\right)} \qquad (17.1)$$

where P is the probability of success of the binary variable Y; X is the vector of independent variables; and β is the vector of regression coefficients. The logarithm of the probability of Y, called the logit, can be expressed as linear combination of independent variables as in multiple regression:

$$Logit(P) = Ln\left(\frac{P}{1 - P}\right) = \beta_0 + \beta_1 X_1 + \beta_2 X_2 + \ldots + \beta_n X_n \qquad (17.2)$$

The inverse of the logit function is called the logistic function:

$$P = \frac{exp\left(B\right)}{1 + exp\left(B\right)} \qquad (17.3)$$

where B is the logit function or the multiple linear regression term in Eq. (17.2). The fitting procedure consists in iteratively finding the set of regression coefficients using maximum likelihood estimation of the joint distribution of the response Y:

$$g(y_1, y_2, \ldots, y_n) = \prod_{i=1}^{n} P_i^{y_i} (1 - p_i)^{y_i} \qquad (17.4)$$

where y_i is an individual measured value of Y, and p_i is the probability that y_i takes on a certain value. Note that p_i is computed using Eq. (17.1). This differs from ordinary least squares regression where a unique analytic solution can be found in closed form.

17.2.3   Radiative Transfer Model and 1DVAR

A 1DVAR approach (Yan et al. 2008) is used in the SFR algorithm to retrieve cloud properties. The model retrieves ice cloud properties and snow emissivity at five microwave window and water vapor sounding channels: 23.8, 31.4, 89.0/88.2, 157.0/165.5, and 190.31/183.31 $\pm$ 7 GHz, respectively for AMSU-A and MHS/ATMS. The inversion method involves a set of iterations where brightness temperatures (T_bs) at the five frequencies are simulated using an RTM (Weng et al. 2001) at each iteration with given atmospheric and surface parameters (i.e., control vector). The differences between simulated and observed T_bs (ΔT_bs) are compared to preset thresholds. The iteration will terminate if the ΔT_bs fall below the thresholds, i.e. the retrieval converges. Otherwise, the elements of the control vector are adjusted and iteration will continue until it reaches the maximum allowed number of iterations, indicating that the retrieval is nonconvergent. The threshold for the first four frequencies is 1.5 K and for 190.31/183.31 $\pm$ 7 GHz is 3 K. The atmospheric and surface parameters from a successful run become the retrieved properties using the inversion method. The parameters include land surface emissivity at the five frequencies, total precipitable water (TPW), ice water path (I_w), effective size of ice particles (D_e), surface temperature (T_s), and cloud temperature (T_c).

The RTM utilized in this 1DVAR algorithm is a two-stream, one-layer model (Weng et al. 2001). The simulation error caused by the simplifications is mitigated by a correcting procedure developed by Weng and Grody (2000). Simulated T_bs are corrected with a set of empirical equations that were derived from a data set of T_b observations and the corresponding uncorrected simulations. According to Yan et al. (2008), the standard deviations of the corrected T_bs at frequencies 23.8, 31.4, 89, and 150 GHz are 0.21, 0.33, 0.72, and 0.68 K, respectively. Additional study shows that the standard deviation for 190.31 GHz and 183 $\pm$ 7 GHz are 4.06 and 2.62 K, respectively.

This 1DVAR model was adopted for the SFR algorithm for a few reasons. While a simple assumption of one-layer atmosphere is made in the RTM, it allows the model parameters, such as I_w, to be expressed in analytic forms and provides one with both qualitative and quantitative understanding of the connection among model parameters. The two-stream formula makes computation effective so retrieval can be completed quickly even with full-orbit data. Computation efficiency and product

latency can be important factors for operational applications such as weather forecasting. Lastly, the 1DVAR model was developed for retrieving snow emissivity. Its parameterization, such as bias correction and emissivity initialization, is consistent with emissivity properties of cold conditions. The close connection between snow emissivity and snowfall makes the 1DVAR an appropriate model to use in a snowfall rate algorithm.

17.2.4 Ice Particle Terminal Velocity

An important component of the SFR algorithm is the ice particle terminal velocity. Heymsfield and Westbrook (2010) modified Mitchell's (1996) formula for ice particle fall speed and developed a new equation:

$$V(D) = \frac{\eta \delta_0^2}{4\rho_a D} \left[\left(1 + \frac{4\sqrt{X}}{\delta_0^2 \sqrt{C_0}} \right)^{1/2} - 1 \right]^2 \tag{17.5}$$

where V is the ice particle terminal velocity, D the maximum dimension of the ice particle, η the dynamic viscosity of air, ρ_a the air density, δ_0 and C_0 the fitting parameters ($\delta_0 = 8.0$ and $C_0 = 0.35$), and the modified Best number X is defined as

$$X = \frac{8mg\rho_a}{\pi\eta^2 \sqrt{A_r}} \tag{17.6}$$

where m is the mass, $m = \pi D^3 \rho_I/6$ for spherical particles, ρ_I the density of ice particle and assumed to be 0.6 g cm^{-3}, g the gravitational constant, A_r the ice particle area ratio (the area of the particle projected normal to the flow divided by the area of a circumscribing disc) and is 1 for spherical particle. Heymsfield and Westbrook (2010) computed terminal velocities of ice particles of various shapes using this approach and compared them with measurements. Their results show that the predicted and measured particle fall velocities agree well for all particle shapes examined. This conclusion is the basis for selecting the Heymsfield and Westbrook (2010) model to compute ice particle terminal velocity in the SFR algorithm.

17.3 Snowfall Detection

Snowfall detection is an integral part of the snowfall rate retrieval. Only when snowfall is detected will the SFR algorithm be applied to retrieve snowfall rate. The QCLCD hourly data from two winter seasons between 2012 and 2014 were taken as ground truth to train the SD algorithm. The 'present weather' reported by QCLCD contains information on the type of precipitation, which was used for

classification of cases into falling snow or no-precipitation. When constructing the training dataset, the maximum time offset between the satellite and station-collocated pairs was set at 30 min with station time following satellite time. The maximum separation distance between satellite footprint centroid and station location was set at 25 km. Only the closest station within the 25 km distance from the satellite footprint centroid was matched.

The SD model is a hybrid algorithm that combines the output from a statistical model utilizing satellite passive microwave measurements with the output from a statistical model using meteorological variable forecasts from GFS. Both models were trained with the QCLCD in-situ data (Kongoli et al. 2018). Each module of the combined algorithm is described below.

17.3.1 Satellite Module

The satellite SD module computes POS using the LR technique and the principal components (PCs) of the five/seven high-frequency T_bs at 89.0/88.2 GHz and above for MHS/ATMS, respectively (Kongoli et al. 2015). PCs, instead of T_bs, are utilized as LR model predictors because the high frequency measurements are highly correlated with each other which can cause instability in the regression coefficients. Another predictor variable is the satellite local zenith angle (LZA) to account for the scan angle effect in satellite observations. The limb-corrected oxygen absorption channel at 53.6 GHz, T_{b53L}, (AMSU-A channel 5 and ATMS channel 6) is utilized as an atmospheric temperature proxy to define two retrieval regimes: cold and warm. To optimize retrievals, the PC weights and logistic regression coefficients are trained with in-situ station observations of snowfall and no-snowfall occurrence and pre-computed separately for the warmer (T_{b53L} between 244 and 252 K) and colder (T_{b53L} between 240 and 244 K) weather regimes. This approach is a major advancement compared to the previous version of Kongoli et al. (2003) in that it allows snowfall retrievals in much colder environments, down to near surface temperatures of about $-15\,°C$. In addition, the statistical probabilistic approach is a more robust method than the previous decision tree approach.

17.3.2 Weather Module

A similar probabilistic LR approach was adopted for snowfall detection using GFS meteorological variable forecasts as predictors. Experience with satellite PMW instruments and theoretical investigations (e.g., Munchak and Skofronick-Jackson 2013) indicate that the detectability of precipitation over snow cover surfaces deteriorates significantly compared to bare land. In addition, snowfall analysis and estimation from physical parameters would be desirable in and of itself, for providing alternative retrieval strategies and insights into the relative importance of these

parameters in snowfall processes. You et al. (2017) explored the influence of several environmental parameters on both rain and snowfall estimations and found that relative humidity and vertical velocity are related to the occurrence of snowfall, more so than that of rainfall. On the other hand, experience with the AMSU-A/MHS and ATMS satellite algorithms have shown that cloud thickness computed from forecast data is an efficient filter in reducing false alarms (Meng et al. 2017). Therefore, to develop the algorithm, the forecast variables considered include relative humidity at 2-m, 1-km, 2-km and 3-km height, cloud thickness, and vertical velocity at 2-km and 3-km height.

17.3.3 Hybrid Algorithm

The rationale for the hybrid algorithm (Kongoli et al. 2018) is to compute an output as a weighted average of outputs from the satellite and the weather-based SD algorithms:

$$P_{hyb} = W_{sat} * P_{sat} + W_{wea} * P_{wea} \qquad (17.7)$$

where P refers to POS, W refers to weight, and hyb, sat and wea refer to the hybrid, satellite and the weather-based SD algorithms, respectively. Note that $W_{sat} + W_{wea} = 1$. Equation (17.7) may therefore be written as:

$$P_{hyb} = W_{sat} * P_{sat} + (1 - W_{sat}) * P_{wea} \qquad (17.8)$$

where W_{sat} is between 0 and 1. Presented with a set of brightness temperatures and ancillary data, POS for the satellite and the weather models are computed. The POS for the hybrid algorithm is derived based on Eq. (17.8) for a specific weighting parameter W_{sat}. Next, the resulting probability value (P_{hyb}) is assigned to "snowfall" if it is greater than an *a priori* threshold probability.

17.3.4 SD Filters

Rainfall and snow cover can exhibit similar characteristics as snowfall in PMW measurements. Consequently, they can contaminate the outcome of the statistical SD model. In addition, the SD algorithm does not exclude rainfall in its detection so temperature-based screening is necessary to filter out rainfall. These considerations led to the development of a set of filters to further screen the snowfall identified by the SD model. Most filters use atmospheric and surface information from the GFS forecasts. The meteorological variables considered include 2-m temperature, maximum atmospheric temperature, 2-m relative humidity, T_{b53L}, and cloud thickness

(CT). For instance, one of the filters checks 2 m temperatures at the two consecutive GFS forecast times that encompass the satellite passing time. If both temperatures are above 1 °C, it indicates a persistently warm environment at the surface that generally cannot sustain snowfall (Meng et al. 2017). Another filter requires surface relative humidity to be above 60% because analysis has shown that this condition is almost always met during snowfall (Kongoli et al. 2015). The most important filter is a check on CT. It requires CT to be at least 1500 m. While this requirement is likely to remove shallow snowfall such as lake effect snow, it will not significantly lower the Probability of Detection (POD). This is because the SFR algorithm is not sensitive to very shallow snowfall due to the weak effect from the latter on PMW measurements. The exertion of a CT threshold eliminates most of the confusions between true snowfall and snow cover on the surface. Our analysis has shown that this is a very effective filter that can significantly reduce false snowfall detection (Meng et al. 2017).

17.4   Snowfall Rate

The SFR algorithm (Meng et al. 2017) is composed of three main elements: (i) retrieval of cloud properties from a 1DVAR, (ii) derivation of initial SFR, i.e. SFR_i, and (iii) SFR_i calibration to obtain the final SFR product. This section details the theoretical basis of the algorithm and the calibration approach.

17.4.1   *Methodology*

The Particle Distribution Function (PDF) of ice particles adopts the modified gamma distribution from Yan et al. (2008) and Weng et al. (2001):

$$N(D) = \frac{N_0 D^{\nu-1} e^{-D/D_m}}{\Gamma(\nu) D_m^{\nu}} \tag{17.9}$$

where D is the diameter of the ice particle (assuming spherical habit), D_m the nominal diameter of the particle, N_0 the intercept parameter, ν the shape parameter for the gamma distribution, and Γ the gamma function. Furthermore,

$$D_m = D_e \frac{\Gamma(\nu)}{\Gamma(\nu - 1)} \tag{17.10}$$

and

$$N_0 = \frac{6 I_w \Gamma^3 (\nu + 1)}{\pi \rho_I D_e^3 \Gamma(\nu + 3) \Gamma^2(\nu)} \tag{17.11}$$

where D_e is the effective diameter of the ice particles and I_w ice water path. If the shape parameter is assumed to be 1, the PDF in Eq. (17.9) reduces to an exponential distribution:

$$N(D) = \frac{I_w e^{-D/D_e}}{\pi \rho_I D_e^4} \tag{17.12}$$

Assuming the number of ice particles follows the above exponential distribution, the water equivalent snowfall rate, SFR_i, can be expressed as (Meng et al. 2017):

$$SFR_i = \int_0^\infty \frac{\pi \rho_I D^3 N(D) V(D)}{6 \rho_w} dD \tag{17.13}$$

or

$$SFR_i = \frac{I_w}{6 \rho_w D_e^4} \int_0^\infty D^3 e^{-\frac{D}{D_e}} V(D) dD \tag{17.14}$$

where ρ_w is the density of water.

An implicit assumption is made in the above equation, i.e. ice water content (IWC) is uniformly distributed in the cloud column. It is consistent with the one-layer RTM (Yan et al. 2008). However, this assumption is not a true representation of cloud physics. In snowing clouds, ice crystals grow in mass as they fall in the cloud through two mechanisms: i) Bergeron process, i.e. supersaturated water vapor deposition, and ii) accretion (riming), i.e. freezing of super cooled liquid droplets onto the surface of ice crystals. These processes generally lead to higher IWC at the lower portion of the cloud than in the upper portion. Figure 17.1 presents ten randomly selected, normalized IWC estimate profiles retrieved from CloudSat (Stephens et al. 2002). In general, these profiles show an increasing trend from cloud top to cloud base, and supports the notion that IWC is not uniformly distributed in most clouds. As a first step to mitigate the bias caused by the simple assumption about IWC, it is assumed that IWC has a linearly distribution through the cloud column. This effectively doubles the SFR_i in Eq. (17.14) at cloud base through simple trigonometric calculation.

By adopting Heymsfield and Westbrook's (2010) model (Eqs. 17.5 and 17.6) and assuming spherical ice habit, SFR_i can then be expressed as:

$$SFR_i = \frac{I_w \eta \delta_0^2}{12 \rho_w \rho_a D_e^4} \int_0^\infty D^2 e^{-\frac{D}{D_e}} \left[\left(1 + \frac{8 D^{3/2}}{\eta \delta_0^2} \sqrt{\frac{g \rho_I \rho_a}{3 C_0}} \right)^{1/2} - 1 \right]^2 dD \tag{17.15}$$

Fig. 17.1 CloudSat derived
ice water content (IWC)
profiles. The values have
been normalized
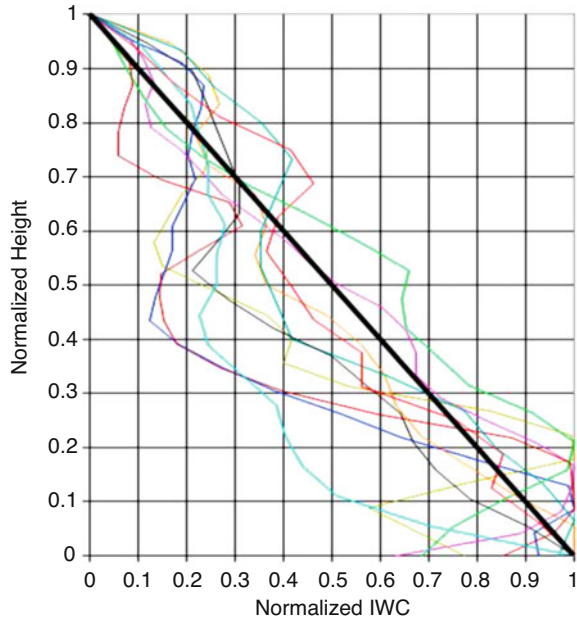
The above equation does not have an analytical solution. It is solved numerically using Romberg's method.

17.4.2 Calibration

Since the IWC profile is not known from the PMW measurements or the GFS model, SFR_i was calibrated against Stage IV precipitation analysis to improve retrieval accuracy. SFR_i data was collocated with Stage IV data from large snowstorms in the two winter seasons between 2015 and 2017. The spatial collocation was performed by convoluting higher resolution Stage IV data to lower resolution satellite Field-of-View (FOV). The SFR_i estimates were matched with Stage IV analyses within 1 h of the satellite overpass. The snowfall detected by the SD algorithm was utilized to identify snowfall pixels for Stage IV since the latter does not include precipitation phase.

The calibration adopts the histogram matching technique described in Kidder and Jones (2007). This approach matches the cumulative probability distribution functions (CDF) of two products (SFR_i and Stage IV in this case) through lease square method to achieve optimal overall agreement. The equation for estimating S-NPP ATMS SFR is:

$$SFR = 1.5813\ SFR_i - 0.2236\ SFR_i^2 + 0.0216\ SFR_i^3 \qquad (17.16)$$

Table 17.1 compares the S-NPP SFR statistics against Stage IV from before and after calibration. It shows that the calibration significantly reduces the bias in the initial SFR retrievals while largely maintaining the root mean square error (RMSE) and correlation with Stage IV. It is noted that, with the simple assumption of linear IWC distribution, the 1DVAR-based SFR retrieval has already achieved a correlation coefficient of 0.52 with Stage IV. It demonstrates the merit of this physical algorithm.

Figures 17.2 and 17.3 respectively present the scatter plots and the probability density functions (PDFs) for the same datasets as for Table 17.1. The underestimation in SFR_i below 1 mm h^{-1} is mitigated to a certain degree. So is the overestimation above about 3.5 mm h^{-1} (Fig. 17.2). The two PDFs also reach much better agreement through the calibration (Fig. 17.3). A low limit of 0.05 mm h^{-1} is set in the SFR product because false alarm rate (FAR) increases drastically for very light snowfall. This low limit results in the slight dip at the low end of the SFR PDF (Fig. 17.3).

Table 17.1 S-NPP SFR metrics before and after calibration

	Before calibration			After calibration	
Correlation coefficient	Bias (mm h^{-1})	RMS (mm h^{-1})	Correlation coefficient	Bias (mm/hr)	RMS (mm h^{-1})
0.52	−0.15	0.63	0.51	−0.02	0.64
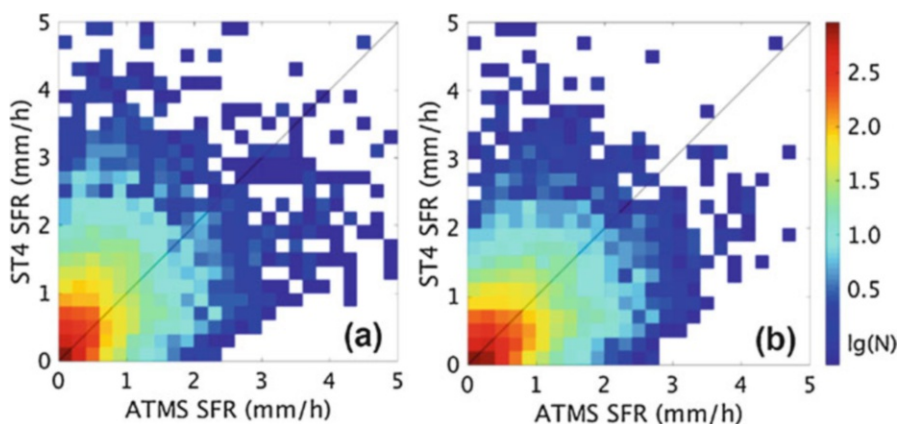
Fig. 17.2 Stage IV vs. S-NPP SFR scatter plot from (**a**) before calibration, and (**b**) after calibration
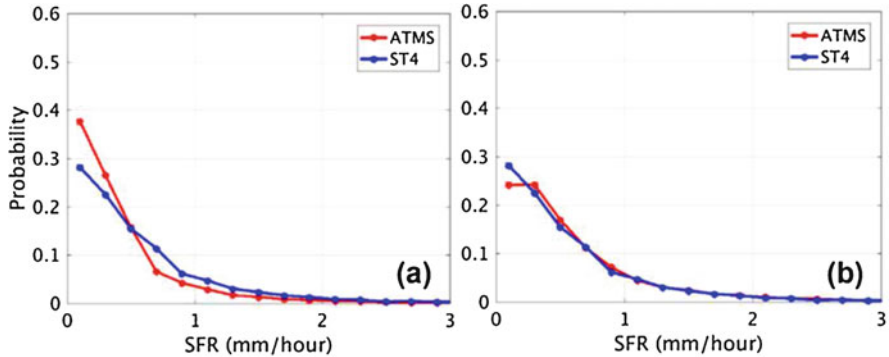
Fig. 17.3 PDFs of S-NPP SFR and Stage IV (**a**) before, and (**b**) after calibration

17.5   Validation

Separate validation studies were conducted to verify the performance of the SD and the SFR algorithms, respectively, since they are independent of each other.

17.5.1   SD Validation

The QCLCD in-situ hourly ground data were employed for SD algorithm validation. Periods during the three winter seasons between 2014 and 2017 were selected to sample snowfall events over CONUS. The satellite, weather-based and hybrid SD outputs at the satellite FOV scale were matched with in-situ data following the same spatio-temporal collocation criteria as for constructing the SD training data.

Table 17.2 presents the statistical results of the S-NPP ATMS satellite and the hybrid algorithm, the latter using a weighting coefficient f equal to 0.5, i.e., when GFS-based and satellite outputs have the same uncertainty information. Compared to the satellite-only algorithm, the hybrid algorithm has substantially improved POD, FAR and the Heidke Skill Score (HSS). It is important to emphasize that the statistical results reported here are computed from comparisons with in-situ measurements where light snowfall cases (reported as "trace" or with zero surface accumulation) were dominant. Generally, light snowfall is much more difficult to detect than heavier snowfall due to its weak impact on satellite measurements.

Figure 17.4 demonstrates the improvement of the hybrid model for a major snowfall event hitting the Northeast US on 5 February 2014. As shown in Fig. 17.4, a considerable snowfall area of this significant event was missed by the satellite algorithm but captured by the hybrid algorithm.

Table 17.2 S-NPP SD Metrics from satellite-only and hybrid algorithms

Model	POD	FAR	HSS
Satellite	0.41	0.18	0.23
Hybrid	0.52	0.11	0.44
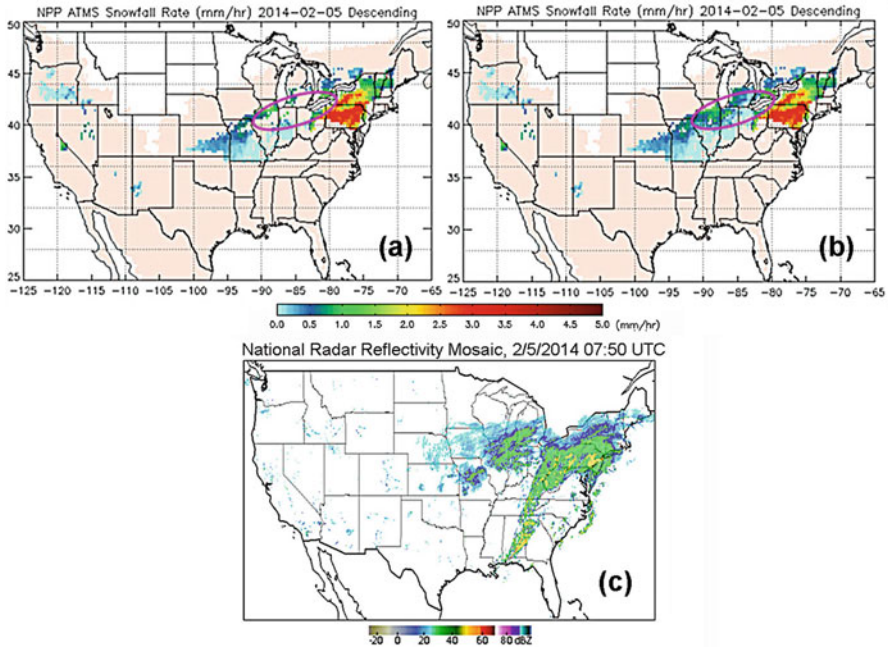
Fig. 17.4 S-NPP ATMS SFR using (**a**) satellite-only SD algorithm, and (**b**) hybrid SD algorithm during a major snowfall event on 5 February 2014 in the US Image (**c**) is the near coincident radar reflectivity which covers both snowfall and rainfall (in the southern part of CONUS). The noted oval areas in (a) and (b) show legitimate snowfall that was missed by the satellite-only algorithm but captured by the hybrid algorithm

17.5.2   SFR Validation

The SFR algorithm was validated against the Stage IV analyses from October 2016 to April 2017. SFR was retrieved using the abovementioned algorithm (Eqs. 17.15 and 17.16) for all snowfall FOVs over CONUS from this period. The data set was collocated with Stage IV data via convolution over sensor footprints. Table 17.3 lists the statistics of the S-NPP SFR validation data. The correlation and bias are comparable to those of the calibration data. The RMSE is somewhat higher. The scatter plot and PDF of the validation data are displayed in Fig. 17.5. As expected from the RMSE, data can be observed to scatter more than the calibration data. It is noted that, unlike the calibration dataset which is composed of data from large snowstorm systems, the validation data include all SFR retrievals that could be collocated with Stage IV from winter 2017. The fact that the validation data still

Table 17.3 S-NPP SFR validation metrics

Correlation Coefficient	Bias (mm/h)	RMS (mm/h)
0.50	0.06	0.74
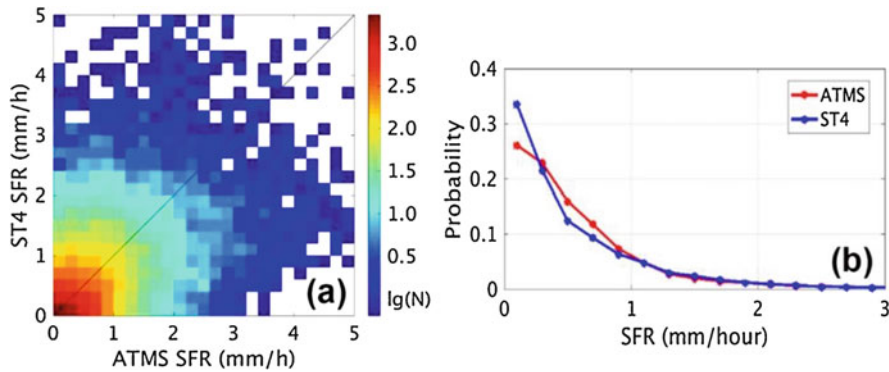
Fig. 17.5 (**a**) Scatter plot of Stage IV vs. collocated S-NPP SFR validation data, and (**b**) PDFs of the same data sets
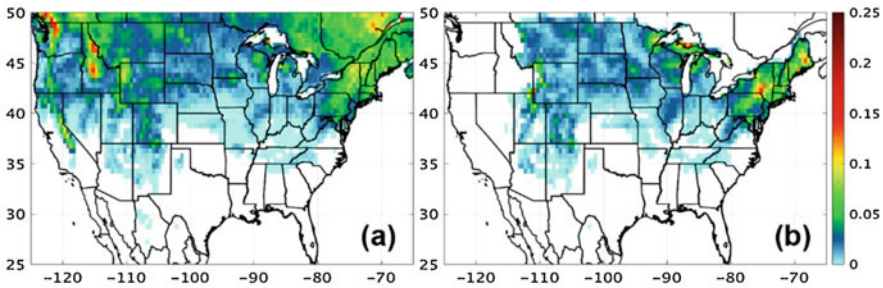
Fig. 17.6 Comparison of (**a**) S-NPP SFR 3-month average from January - March 2017 and (**b**) the corresponding Stage IV data

perform reasonably well demonstrates the strength of the SFR algorithm for both large-scale and localized snowfall.

As part of the validation study, the 3-month average S-NPP SFR from January ~ March 2017 was calculated and compared to the corresponding Stage IV average from the same period (Fig. 17.6). The SD detected snowfall was again used to determine snowfall for Stage IV. Stage IV does not cover most of the western US due to poor radar coverage in this region. This reveals one of the advantages of satellite snowfall rate product like SFR, i.e. satellite product can fill in radar gaps. The overall intensity patterns between the two images in Fig. 17.6 are rather similar, i.e. heavier snowfall in the Northeast of US, around the Great Lakes, and along the Rocky Mountains; and lighter snowfall in between. It is stressed that the 3-month snowfall average is based on the snowfall detected by the SFR algorithm. The current algorithm has low detection rate for shallow snowfall such as lake effect

Table 17.4 Metrics of S-NPP SFR 3-month (Jan–Mar 2017) average

Correlation Coefficient	Bias (mm/h)	RMS (mm/h)
0.65	0.00	0.02

snow and shallow orographic snow. It is most likely that the snowfall represented in Fig. 17.6 only includes a portion of such shallow snowfall. The statistics of the 3-month SFR average against the Stage IV data are given in Table 17.4. As expected, the metrics of the seasonal average are superior to the validation and even the calibration data.

17.6 Summary and Conclusions

An overland SFR algorithm has been developed for PMW radiometers (the AMSU-A/MHS pair aboard the NOAA POES and EUMETSAT Metop satellites, and ATMS aboard the S-NPP and NOAA-20 satellites). The algorithm relies on an embedded SD model to detect snowfall. Only when snowfall is detected will the SFR algorithm be applied to retrieve snowfall rate.

The SD model is a hybrid algorithm that combines the output from a satellite-based statistical model and the output from a GFS model-based statistical model. Both statistical algorithms were trained with QCLCD in-situ observations of snowfall and no-snowfall. The satellite model couples the PCs of PMW measurements at high frequencies with LR to produce the satellite-based POS. The other statistical model takes a set of meteorological variables from GFS forecast as predictors and produces the weather-based POS with a LR model. The final POS is a weighted average of the above two probabilities and is assigned to "snowfall" if it is greater than an *a priori* threshold. The SD algorithm is further enhanced with a set of mostly NWP model-based filters. These filters, especially the cloud thickness threshold, are effective at removing false alarms in the SD model output.

The SFR algorithm is a physically-based model and is composed of three main elements: retrieving cloud properties, estimating initial SFR, i.e. SFR_i, and determining the final SFR with an adjustment. Cloud properties, I_w and D_e, are retrieved using a 1DVAR approach that uses a two-stream RTM as the forward model to simulate T_bs at five window and water vapor sounding channels. An existing model is adopted to calculate ice particle terminal velocity. The retrieved cloud properties are used in the computation of the terminal velocity and IWC, and eventually SFR_i. Finally, SFR is determined by adjusting SFR_i with a cubic regression function. The adjustment function was derived from matching SFR_i histogram with that of the Stage IV precipitation data. The effect of the adjustment is to reduce the overall bias in SFR_i that is conceivably due to the uncertainty associated with the assumption about IWC linear distribution. The adjustment has little impact on the RMS and the correlation of SFR_i with Stage IV analyses.

The SD algorithm was validated against hourly in-situ ground data. Compared to the satellite-only model, the hybrid SD algorithm exhibits much improved performance in terms of POD, FAR, and HSS. For instance, the former has an HSS of 0.23 while the latter 0.44. The SFR product was validated using the Stage IV precipitation analyses. Both point and seasonal (January – March 2017) average SFR were compared to the corresponding Stage IV data. While the calibration dataset is composed of data from large snowstorm systems from winters 2015 and 2016, the validation data include all SFR retrievals that could be collocated with Stage IV from winter 2017. The validation data still perform well with correlation and bias comparable to the calibration data while have somewhat higher RMS. The results demonstrate the strength of the SFR algorithm for both large-scale and localized snowfall.

References

Bennartz, R., & Bauer, P. (2003). Sensitivity of microwave radiances at 85–183 GHz to precipitating ice particles. *Radio Science, 38*, 8075. https://doi.org/10.1029/2002RS002626.

Ferraro, R. R., Weng, F., Grody, N. C., Zhao, L., Meng, H., Kongoli, C., Pellegrino, P., Qiu, S., & Dean, C. (2005). NOAA operational hydrological products derived from the advanced microwave sounding unit. *IEEE Transactions on Geoscience and Remote Sensing, 43*, 1036–1049. https://doi.org/10.1109/TGRS.2004.843249.

Heymsfield, A. J., & Westbrook, C. D. (2010). Advances in the estimation of ice particle fall speeds using laboratory and field measurements. *Journal of the Atmospheric Sciences, 67*, 2469–2482. https://doi.org/10.1175/2010JAS3379.1.

Kidd, C., Matsui, T., Chern, J., Mohr, K., Kummerow, C., & Randel, D. (2016). Precipitation estimates from cross-track passive microwave observations using a physically based retrieval scheme. *Journal of Hydrometeorology, 17*, 383–400. https://doi.org/10.1175/JHM-D-15-0051.1.

Kidder, S. Q., & Jones, A. S. (2007). A blended satellite total precipitable water product for operational forecasting. *Journal of Atmospheric and Oceanic Technology, 24*(1), 74–81. https://doi.org/10.1175/JTECH1960.1.

Kim, M.-J., Weinman, J. A., Olson, W. S., Chang, D.-E., Skofronick-Jackson, G., & Wang, J. R. (2008). A physical model to estimate snowfall over land using AMSU-B observations. *Journal of Geophysical Research, 113*, D09201. https://doi.org/10.1029/2007JD008589.

Kongoli, C., Pellegrino, P., Ferraro, R., Grody, N. C., & Meng, H. (2003). A new snowfall detection algorithm over land using measurements from the Advanced Microwave Sounding Unit (AMSU). *Geophysical Research Letters, 30*(14), 1756. https://doi.org/10.1029/2003GL017177.

Kongoli, C., Meng, H., Dong, J., & Ferraro, R. (2015). A snowfall detection algorithm over land utilizing high-frequency passive microwave measurements—application to ATMS. *Journal of Geophysical Research, 120*, 1918–1932. https://doi.org/10.1002/2014JD022427.

Kongoli, C., Meng, H., Dong, J., & Ferraro, R. (2018). A hybrid snowfall detection method from satellite passive microwave measurements and global weather forecast models. *Quarterly Journal of the Royal Meteorological Society, 144*(S1), 120–132. https://doi.org/10.2002/qj3270.

Kummerow, C. D., Ringerud, S., Crook, J., Randel, D., & Berg, W. (2011). An observationally generated a priori database for microwave rainfall retrievals. *Journal of Atmospheric and Oceanic Technology, 28*, 113–130. https://doi.org/10.1175/2010JTECHA1468.1.

Kummerow, C. D., Randel, D., Kulie, M., Wang, N.-Y., Ferraro, R. R., Munchak, S. J., & Petkovic, V. (2015). The evolution of the Goddard profiling algorithm to a fully parametric scheme. *Journal of Atmospheric and Oceanic Technology, 32*, 2265–2280. https://doi.org/10.1175/JTECH-D-15-0039.1.

Liu, G., & Seo, E.-K. (2013). Detecting snowfall over land by satellite high-frequency microwave observations: The lack of scattering signature and a statistical approach. *Journal of Geophysical Research, 118*, 1376–1387. https://doi.org/10.1002/jgrd.50172.

Meng, H., Dong, J., Ferraro, R. R., Yan, B., Zhao, L., Kongoli, C., Wang, N.-Y., & Zavodsky, B. (2017). A 1DVAR-based snowfall rate retrieval algorithm for passive microwave radiometers. *Journal of Geophysical Research, 122*. https://doi.org/10.1002/2016JD026325.

Mitchell, D. L. (1996). Use of mass- and area-dimensional power laws for determining precipitation particle terminal velocities. *Journal of the Atmospheric Sciences, 53*, 1710–1723. https://doi.org/10.1175/1520-0469(1996)053<1710:UOMAAD>2.0.CO;2.

Munchak, S. J., & Skofronick-Jackson, G. (2013). Evaluation of precipitation detection over various surfaces from passive microwave imagers and sounders. *Atmospheric Research, 131*, 81–94. https://doi.org/10.1016/j.atmosres.2012.10.011.

Noh, Y.-J., Liu, G., Seo, E.-K., Wang, J. R., & Aonashi, K. (2006). Development of a snowfall retrieval algorithm at high microwave frequencies. *Journal of Geophysical Research, 111*, D22216. https://doi.org/10.1029/2005JD006826.

Skofronick-Jackson, G., Johnson, B. T., & Munchak, S. J. (2013). Detection thresholds of falling snow from satellite-borne active and passive sensors. *IEEE Transactions on Geoscience and Remote Sensing, 51*, 4177–4189. https://doi.org/10.1109/TGRS.2012.2227763.

Stephens, G. L., Vane, D. G., Boain, R. J., Mace, G. G., Sassen, K., Wang, Z., Illingworth, A. J., O'Connor, E. J., Rossow, W. B., Durden, S. L., Miller, S. D., Austin, R. T., Benedetti, A., Mitrescu, C., & the CloudSat Science Team. (2002). The CloudSat mission and the A-train: A new dimension of space-based observations of clouds and precipitation. *Bulletin of the American Meteorological Society, 83*, 1771–1790. https://doi.org/10.1175/BAMS-83-12-1771.

Weng, F., & Grody, N. (2000). Retrieval of ice cloud parameters using a microwave imaging radiometer. *Journal of the Atmospheric Sciences, 57*, 1069–1081. https://doi.org/10.1175/1520-0469(2000)057<1069:ROICPU>2.0.CO;2.

Weng, F., Yan, B., & Grody, N. (2001). A microwave land emissivity model. *Journal of Geophysical Research, 106*, 20,115–20,123. https://doi.org/10.1029/2001JD900019.

Yan, B., Weng, F., & Meng, H. (2008). Retrieval of snow surface microwave emissivity from the advanced microwave sounding unit. *Journal of Geophysical Research, 113*, D19206. https://doi.org/10.1029/2007JD009559.

You, Y., Wang, N.-Y., Ferraro, R. R., & Rudlosky, S. (2017). Quantifying the snowfall detection performance of the GPM microwave imager channels over land. *Journal of Hydrometeorology, 18*, 729–751. https://doi.org/10.1175/JHM-D-16-0190.1.

Zhang, J., Howard, K., Langston, C., Kaney, B., Qi, Y., Tang, L., Grams, H., Wang, Y., Cocks, S., Martinaitis, S., Arthur, A., Cooper, K., Brogden, J., & Kitzmiller, D. (2016). Multi-Radar Multi-Sensor (MRMS) quantitative precipitation estimation: Initial operating capabilities. *Bulletin of the American Meteorological Society, 97*. https://doi.org/10.1175/BAMS-D-14-00174.1.

Chapter 18
X-Band Synthetic Aperture Radar Methods

Saverio Mori, Frank S. Marzano, and Nazzareno Pierdicca

Abstract Spaceborne Synthetic Aperture Radars (SARs), operating at L-band and above, offer microwave observations of the Earth at very high spatial resolution in almost all-weather conditions. Nevertheless, precipitating clouds can significantly affect the signal backscattered from the ground surface in both amplitude and phase, especially at X band and beyond. This evidence has been assessed by numerous recent efforts analyzing data collected by COSMO-SkyMed (CSK) and TerraSAR-X (TSX) missions at X band. This sensitivity can be exploited to detect and quantify precipitations from SARs at the spatial resolution of a few hundred meters, a very appealing feature considering the current resolution of precipitation products from space. Forward models of SAR response in the presence of precipitation have been developed for analyzing SAR signature sensitivity and developing rainfall retrieval algorithms. Precipitation retrieval algorithms from SARs have also been proposed on a semi-empirical basis. This chapter will review experimental evidences, modelling approaches, retrieval methods and recent applications of X-band SAR data to rainfall estimation.

Keywords Synthetic aperture radar · High resolution · Clouds · Rainfall · Precipitation · Raindrops · Snowflakes · Reflectivity · Normalized radar cross section · Particle size distribution · Polarization · Regressive empirical algorithm · Probability matching algorithm · COSMO-SkyMed · TerraSAR-X

18.1 Introduction

The importance of monitoring global precipitations and their associated extreme events, such as floods, landslides, hurricanes, and droughts, is crucial for the management of daily life and environmental crises (Skofronick-Jackson et al.

S. Mori (✉) · F. S. Marzano · N. Pierdicca
Department of Information Engineering, Electronics and Telecommunications, University of Roma "La Sapienza", Rome, Italy
e-mail: saverio.mori@uniroma1.it

2017). Global-scale precipitation measurements are essential for the development and validation of both weather and climate models (Ebert et al. 2007). Cloud-resolving models require global, kilometer-scale observations to provide diagnoses of their performance and to develop adequate data assimilation procedures (e.g., Masunaga et al. 2008).

Since the 1980s much of our understanding of global precipitation has been provided by spaceborne passive microwave radiometers (e.g., Kummerow et al. 1998; Marzano et al. 2002; Skofronick-Jackson et al. 2017). Precipitation retrievals from microwave radiometer data over land is affected by a low spatial resolution, typically larger than tens of kilometers. Spaceborned infrared radiometers can offer an adequate resolution of few kilometers, but they are nearly saturated by the presence of precipitating clouds within the observed scene. Space-based weather radars, operating at Ku band (i.e., about 2-cm wavelength) and beyond, have represented a key advance in satellite precipitation monitoring. The Ku-band Precipitation Radar (PR) aboard the Tropical Rainfall Measurement Mission (TRMM) satellite has provided unprecedented and unique precipitation measurements over land, even though limited by a swath smaller than microwave radiometers (Kummerow et al. 1998). The development and launch of the Global Precipitation Measurement (GPM) mission has further advanced spaceborne radar technology by means of the Dual-Frequency Precipitation Radar (DPR) at Ku and Ka band (Hou et al. 2014). However, if significant shallow precipitation or rain cells smaller than few kilometers occur over land, then both PR and DPR may miss or underestimate the intensity of such precipitation fields (e.g., Marzano et al. 2011; Durden et al. 1998).

The high spatial resolution of Synthetic Aperture Radars (SARs) at X band (i.e., about 3 cm wavelength) and beyond can provide new insights into the structure of precipitating clouds and permit the observation of small precipitation cells at micro-alpha scale (between 0.2 and 2 km). Indeed, the nominal spatial resolution of SAR is of the order of meters, but it is degraded to hundreds of meters by the turbulent motion of the hydrometeors due the random broadening of the Doppler-frequency spectra with respect to fixed-target surface imaging (Atlas and Moore 1987). Spaceborne SARs at C-band and L-band (i.e., about 5 and 21 cm wavelengths, respectively) have a long heritage for Earth observation, but these space radars are relatively insensitive to rainfall. Space Shuttle missions in 1994 and 2000 carried the first X-band SAR (X-SAR) along with L-band and C-band SARs (Jordan et al. 1995). Since then, the possibility of detecting and quantifying precipitation from SARs has received more attention (e.g., Alpers and Melsheimer 2004; Atlas and Moore 1987; Ferrazzoli and Schiavon 1987; Melsheimer et al. 1998; Moore et al. 1997). In the last decade, new X-SARs such as four COSMO-SkyMed (CSK) satellites (ASI 2009) and two TerraSAR-X (TSX) satellites (Fritz and Eineder 2013) followed by other missions such as TecSAR and KOMPSAT-5 have been succesfully launched. First analyses of X-band SAR influence of precipitating clouds date back to the '80s (Atlas and Moore 1987).

Precipitating clouds can significantly alter the specabeorne backscattered SAR signal, introducing path attenuation and scattering as well as depolarization and

tropospheric scintillation (Ferrazzoli and Schiavon 1987; Quegan and Lamont 1986; Alpers and Melsheimer 2004). An extensive review of the atmospheric impacts on the retrieved TSX data, can be found in Weinman and Marzano (2008) and Danklmayer et al. (2009). The latter analyze a large dataset of TSX acquisitions finding evident precipitations effects in only 0.8% of cases. The analyzed cases confirm the effect of precipitation on X Band SAR data, but also have provided evidence that only intense events can produce significant effects at X band. Synergy and complementarity of X-band SAR with ground-based weather radars have been investigated in Marzano et al. (2010) and Fritz and Chandrasekar (2010, 2012). A forward model is generally needed to convert weather radar reflectivity into spaceborne SAR path attenuation and signal, taking into account polarimetric features as well (Marzano et al. 2012). Several steps are necessary to simulate a X-band SAR precipitation signature using weather radar (WR) reflectivity: (1) estimation of the specific differential phase; (2) path attenuation correction (if necessary); (3) gridding on an Earth-centric Cartesian grid; (4) hydrometeor classification, in order to use the correct particle distribution model; (5) scale frequency and look angle; (6) SAR geometry resampling and (7) integration to SAR observations. Obtainable polarimetric products include the differential reflectivity, and the differential phase, simulated at both X band and Ku band. Baldini et al. (2014) have carried out a review of the model of Fritz and Chandrasekar (2012) adding formulas for simulating X-band SAR observables from ground weather radar reflectivity at C and S band. An analysis of the CSK Ping-Pong mode (alternate HH-VV) was also carried out, showing some interesting features. Roberto et al. (2014) extend this model approach to marine environments, a fairly challenging goal due to the difficulties in modelling the SAR response of the sea surface background. The detection of the hurricane eye, hurricane tracking, and the estimation of wind fields from SAR data has also been recently attempted (Li 2017). Hydrological applications of X-band SARs are typically oriented to flood monitoring (e.g., Landuyt et al. 2018; Refice et al. 2018), but precipitation effects can be quantified as well (Marzano et al. 2011).

This chapter aims to provide an overview of X-band SAR techniques for precipitation signature characterization and detection, introducing both precipitation response simulations (forward models) and precipitation retrieval methods (inverse models). Sect. 18.2 shows an example of precipitation signatures on SAR imagery, whereas Sect. 18.3 describes a forward model of SAR response in the presence of precipitation. Section 18.4 illustrates some precipitation retrieval techniques used in literature, whereas Sect. 18.5 deals with an advanced approach and the applications of validation techniques. Finally, Sect. 18.6 contains a discussion on high-frequency SAR for hydrological applications and future perspectives.

18.2   Evidence of Precipitation Signatures on X-SAR Imagery

In Marzano et al. (2010) several examples of precipitation SAR signatures at X band are discussed. A very good example is represented by Hurricane Gustav, observed by TerraSAR-X (TSX) on 2 September 2008, from 11:58:44 to 11:59:06 UTC, a few hours after landfall on the US coast. The selected case study refers to the passage of Hurricane Gustav over Louisiana and Mississippi northwestward, moving at an average velocity of 24 km h^{-1} and delivering torrential rains to the central gulf coast of the US (e.g., Larto Lake, LA, reported a rainfall total accumulation of 533.4 mm). Ideally speaking, atmospheric effects could be detected, or at least appreciated, using a clear-sky image acquired by the same instrument in the same transmitting and receiving polarization and the same acquisition mode, and orbit direction, during a recent date. Such images are referred to as "SAR background images". Unfortunately, in this case no background image was available.

Figure 18.1 shows the synoptic view of an outer rain band of Hurricane Gustav over south-eastern Louisiana taken from the NEXRAD ground Weather Radar (WR) located in Mobile (Alabama) (e.g., Fulton et al. 1998). WR acquisition started at 11:59:44 UTC so the time difference with TSX is about 1 min. From the radiosonde available from Birmingham (AL) at 12:00 UTC, the freezing level height was about 4.5 km. The white box shows precipitation around 30.5° N × 89.5° W. The near-surface conical scan at 0.86° elevation angle and HH-polarized of NEXRAD rainfall data is compared to the ScanSAR map of TSX HH-polarized Normalized Radar Cross Section (NRCS) observation. Note that TSX ScanSAR product has a ground coverage of 154 × 105 km^2 and a ground resolution of about 18 × 18 m^2. WR reflectivity has a spatial resolution of about 0.25 km in range and 0.5° in azimuth and nominal coverage radius of about 209 km. In the previous figure it is evident that the correspondence over land between WR higher reflectivity areas and TSX dark ones. TSX returns over ocean are also detectable by a brighter incoherent feature with respect to the darker quasi-specular NRCS response, due to the sea surface. The southern portion of the rain band over ocean corresponds to WR reflectivity of about 20 dBZ. Values of Z are as high as 59.1 dBZ, indicating torrential convective rainfall connected to Hurricane Gustav, probably mixed with some hail.

The correlation between NRCS values σ_{SAR} [dB] (filtered and resampled) against co-located and co-registered WR reflectivity Z [dBZ] for a central Region of Interest (ROI) is shown in Fig. 18.2. The co-polar radar reflectivity factor Z is proportional to the radar reflectivity η of the WR through $Z = \eta \lambda^4/(\pi^5 |K|^2)$ with λ the wavelength and $|K|^2$ the dielectric factor equal to 0.93 for water (Bringi and Chandrasekar 2001). A significant negative correlation is present between X-Band σ_{SAR} and S-band Z, demonstrating that the X-SAR NRCS tends to decrease as the S-band WR reflectivity increases, mainly due to the increase of two-way rain path attenuation. The dynamic range of X-SAR NRCS due to rainfall is about 12 dB. Moreover, X-SAR NRCS tends to saturate for values of S-band Z of about 25 dBZ and below.
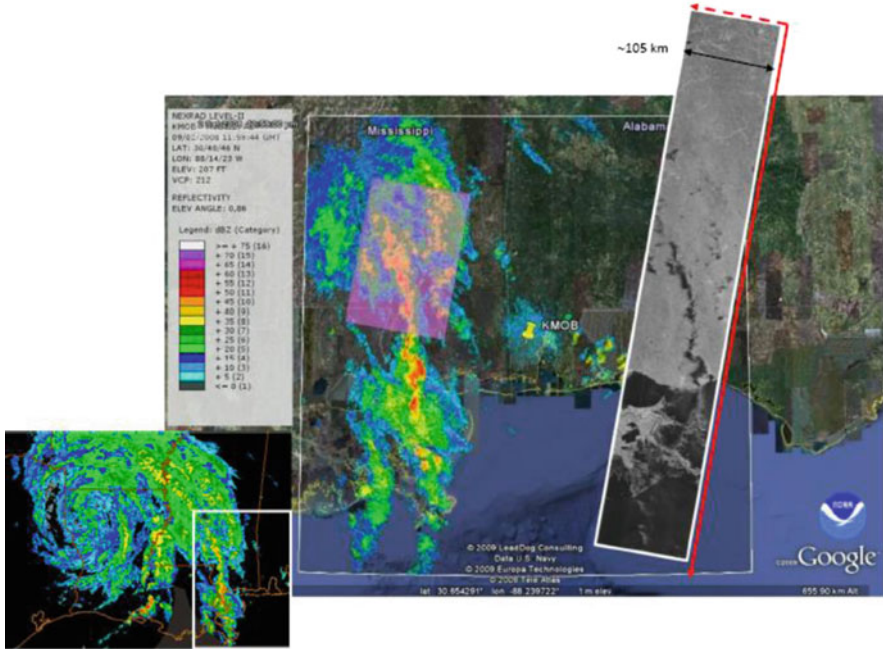
Fig. 18.1 (Lower left image) Synoptic view of Hurricane Gustav over south eastern Louisiana on September 2, 2008 12:00 UTC taken from NEXRAD weather radar reflectivity mosaic. The white box shows an outer rain band around 30.5° N × 89.5° W. (Central image) Geographic representation of the NEXRAD image at 0.86° elevation, acquired by the S-band radar (KMOB, in figure) near Mobile (Alabama). The semi-transparent rectangular box represents the scene of interest, acquired by TSX X-SAR on 2 September 2008 12:00 UTC in HH polarization and ScanSAR mode (100 km swath). (Upper right image) TSX quicklook of the acquisition in arbitrary units at 100-m resolution; flight direction is indicated. (Adapted from Marzano et al. 2010)

The dispersion between σ_{SAR} and Z is mainly due to the slant-view observation geometry, surface NRCS variability and the spatial inhomogeneity of hydrometeor distribution. The trend of this curve is similar to the one indicated in Fritz and Chandrasekar (2010).

The Tropical Rainfall Measuring Mission (TRMM) satellite observed the area at about 15:30 UTC of 2 September 2008. The significant time-difference makes a direct comparison with TSX data impractical. Nevertheless, the TRMM acquisition allows a qualitative comparison with MW radiometric and radar spaceborne imagers. In this respect, the principal TRMM instruments are the TRMM Microwave Imager (TMI), a passive microwave sensor, and the Precipitation Radar (PR), an active one. Figure 18.3 shows the acquired horizontally polarized TMI brightness temperatures (TB) at 37 GHz and 85.5 GHz (obtained from TRMM 1B11 product). The TMI image swath is about 760 km wide, while the ground resolution is about 16×9 km^2 at 37 GHz and 7×5 km^2 at 85.5 GHz. The hurricane signature is quite evident, but
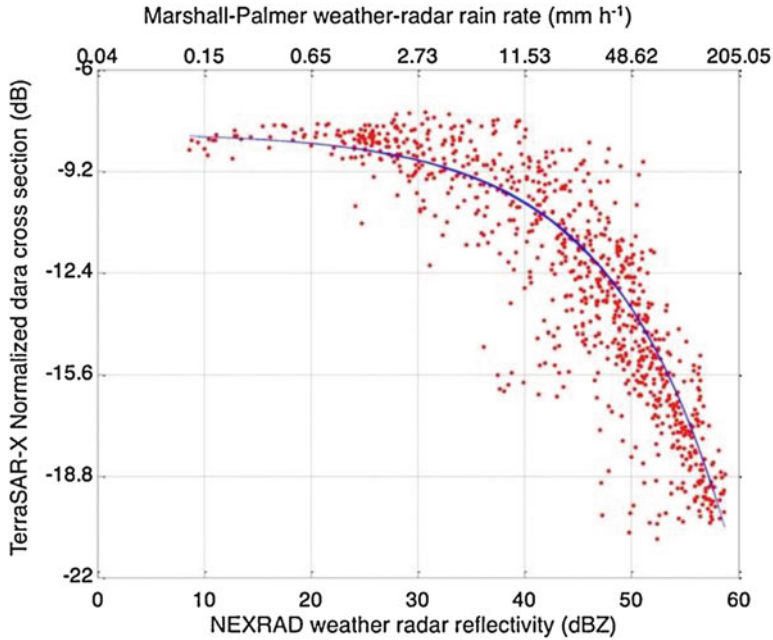
Fig. 18.2 Correlation diagram between NRCS values X-band σSAR against co-located and co-registered S-band NEXRAD weather-radar reflectivity Z, for a selected region of interest (ROI) of the scene. The upper axis provides the estimated rain-rate from NEXRAD data using the Marshall-Palmer relation (Bringi and Chandrasekar 2001). The best-fitting curve is also plotted. (Adapted from Marzano et al. 2010)

the impact of the different spatial resolution between the two radiometric channels is also striking. Figure 18.3 also illustrates the PR reflectivity factor (dBZ) at 14 GHz closest to the surface for both the "normal sampled" range bin 75 and the "rain oversampled" range bin 16 (as obtained from TRMM 1C21 product). The PR swath is 220 km for the "normal sampled" product, but it is reduced for the "rain oversampled" one due to oversampling; the height resolution is about 250 m. The "rain oversampled" product aims at registering the detailed vertical profile of the rain. The spiral bands of the hurricane are detectable with a moderate spatial resolution, but only the combination with TMI can provide the general features of the hurricane due to the relatively smaller swath. Spaceborne microwave radiometers (passive instruments) allow a wider swath, but with a rougher resolution with respect to radars (active instruments). Note that the radar resolution is coarser than the SAR, but the vertical ranging allows for atmospheric profiling, a feature not possible for SAR due to their slant observing geometry and surface-tuned receiving time-window (Marzano et al. 2011).
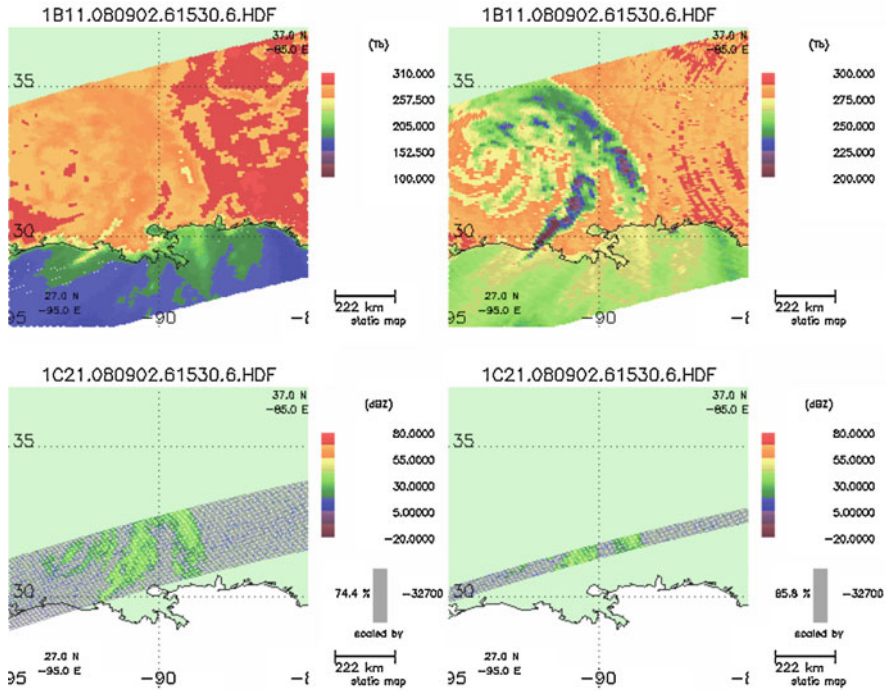
Fig. 18.3 TRMM observations, at 15:30 UTC, for the case study of Hurricane Gustav. (Top panels) TRMM 1B11 brightness temperature (TB) product relative to TMI channel 7 (37 GHz horizontal polarization, left), beam effective field-of-view (EFOV) of 16×9 km^2, and TMI channel 9 (85.5 GHz horizontal polarization, right) with a main-beam EFOV of 7×5 km^2. The cyclonic cell indicated in Fig. 18.2 is well captured. (Bottom panels) The TRMM 1C21 radar reflectivity (dBZ) product, relative to PR normal sample (left) range bin 75, and PR rain oversampled (right), range bin 16. Note that the PR swath is 220 km wide (reduced in the oversampled product) and the range resolution is 0.25 km; TMI swath is 760 km wide. (Adapted from Marzano et al. 2011)

18.3 Forward Model of SAR Response to Rainfall

Polarimetric radars are powerful tools for quantitative studies of the properties of atmospheric hydrometeors (e.g., Bringi and Chandrasekar 2001; Doviak and Zrnić 1993). Conventional radars measure the backscattered intensity from hydrometeors in a scattering volume defined by the antenna-beam width and the transmitted-pulse width. For a polydispersion of oblate ellipsoidal particles, with a random distribution of spherical volume-equivalent diameter D and zenithal canting angle ϕ, being λ the wavelength corresponding to a frequency f, we can define several RADAR observables related to the incoming signal power. In particular, η_{pq} is the pq-polarized radar reflectivity (in km^{-1}, or backscattering cross section per unit of volume) and can be expressed in terms of Particle Size Distribution (PSD) $N(D)$, particle orientation density $p_o(\phi)$ and the complex backscattering matrix element $S_{pq}(D, \phi)$. Instead of

reflectivity, radar reflectivity factors Z_{hh}, Z_{vv} and Z_{vh} (in mm^6 m^{-3} or dBZ) can be used. Note that the double subscript stands for the received (first index) and transmitted (second index) polarization state, which can be either horizontal (h) or vertical (v). K_{dp} is the specific differential phase shift (in ° km^{-1}) due to the forward propagation phase difference between the two polarizations. k_{pp} is the specific power attenuation at polarization p in km^{-1} (or A_{pp} if expressed in dB km^{-1}) and is the counterpart of K_{dp} in terms of power attenuation per unit length.

Given a volumetric distribution of atmospheric water particles, radar observables can be used to estimate the SAR signal when observing ground targets in the presence of atmospheric effects by means of a SAR response forward model. The next section illustrates the model proposed in Marzano et al. (2012) and Mori et al. (2017a).

18.3.1 SAR Observing Geometry and Response Model

The fundamental parameter, imaged by SARs, is the Radar Cross Section (RCS) σ_{pq} of the target, defined by $P_p = \sigma_{pq} \cdot S_q^{\ i}/4\pi$, where P_p is the power re-irradiated by the target at polarization p and $S_q^{\ i}$ is the incident power density at polarization q (Ulaby and Long 2014). While the previous definition corresponds to point targets, NRCS (also indicated as backscattering coefficient $\sigma_{pq}^{\ 0}$) is usually defined as the RCS normalized to the target area A for distributed targets, that is $\sigma_{pq}^{\ 0} = \sigma_{pq}/A$.

In the presence of precipitation, the SAR backscattering response has to account for the two-way attenuation of the surface echo due to the atmospheric particles, the atmospheric volume reflectivity and phase shift.

We can express the spaceborne SAR co-polar and cross-polar NRCS for a given pixel with coordinates (x,y) on the Earth surface, using a simplified model where the forward depolarization is neglected and the isorange lines, actually spherical, are supposed to be planar as shown in Fig. 18.4:

$$\sigma_{SARpq}^0(x,y) = 4\pi \left\langle \left| S_{SARpq} \right|^2 \right\rangle = \sigma_{SRFpq}^0(x,y) + \sigma_{VOLpq}^0(x,y) \tag{18.1}$$

$$\sigma_{SRFpq}^0(x,y) = \sigma_{pq}^{0ground}(x,y)\, exp\left(-\int\limits_{\Delta l(x,y)} k_{qq}(l)dl - \int\limits_{\Delta l(x,y)} k_{pp}(l)dl\right)$$

$$\sigma_{VOLpq}^0(x,y) = \sin(\theta) \int\limits_{\Delta t(x,y)} \eta_{pq}(t) \exp\left(-\int\limits_{\Delta l(t)} k_{qq}(l)dl - \int\limits_{\Delta l(t)} k_{pp}(l)dl\right) dt$$

where θ is the local incident angle, and S_{SARpq} are the elements of the SAR received backscattering matrix. $\sigma^0_{SRFpq}(x,y)$ (in m^2 m^{-2}) is the "surface-driven" backscattering coefficient, that is the surface target NRCS $\sigma^{0ground}_{pq}$ (superscript "ground" here
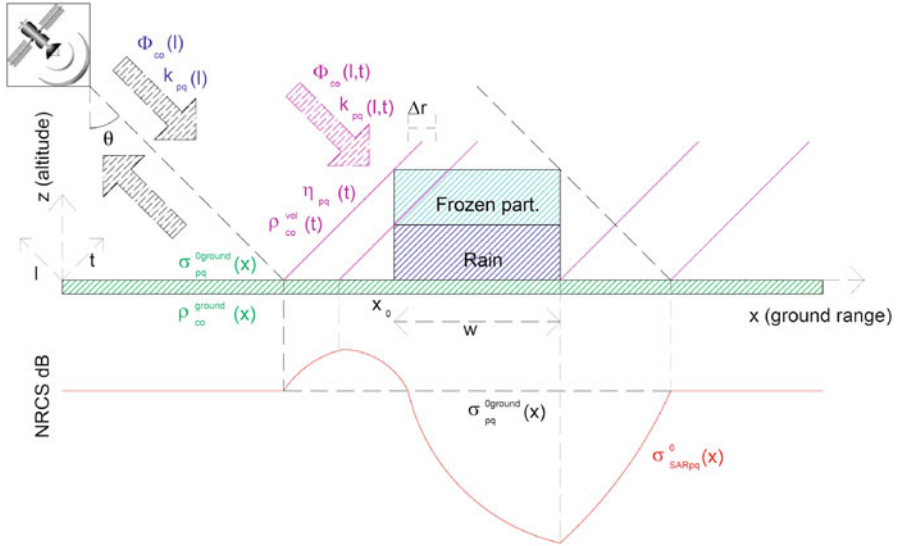
Fig. 18.4 Schematic SAR NRCS (in dB) as a function of cross-track scanning distance x, showing enhanced values on the left of the cross-over point caused by scattering from the cloud top and attenuation from rain in the lower cloud on the right. The viewing angle with respect to nadir (incidence angle) is θ, while the cloud extension is w. The symbol Δr indicates the width of the slant slice of the atmosphere representing the SAR side-looking resolution volume. The figure also shows the energy fluxes and the e.m. parameters of the model according to Marzano et al. (2012) and Mori et al. (2017a)

refers to the surface target property) attenuated by the two-way path through the precipitating atmosphere, whereas the term $\sigma^0_{VOLpq}(x,y)$ (m^2 m^{-2}) is the "volume-driven" backscattering due to hydrometeor reflectivity, weighted by the two-way path through the precipitating atmosphere. The spatial transverse coordinates l and t along the atmospheric path (in km), inherently depend on the Cartesian coordinate in the volume (x,y,z). The path from the radar to the surface target at (x,y) is $\Delta l(x,y)$. Note that the volume term accounts for the contributions to the SAR echo due to the atmospheric hydrometeors encountered by the path-attenuated SAR wave front aligned along the transverse coordinate t and in the same resolution cell Δr. The scattered wave from hydrometeors, encountered at position t along the transverse line, experiences an attenuation along the path $\Delta l(t)$ when propagating back to the radar. The SAR model geometry, shown in Fig. 18.4, depicts a possible enhancement of the background response at near range, due to frozen particle scattering at high altitudes, followed by an intense attenuation of the background signal, due to the path attenuation through the rain cloud. This pattern is evident in the case of Fig. 18.4.

Spaceborne satellite SARs usually allow the observation of the co-polar elements of the 3×3 ensemble-average scattering covariance matrix $\mathbf{C}_{SAR}$. Operational SAR systems may allow the measurement of the cross-polar elements, whereas co-polar backscattering coefficients are always available. We can define the following SAR

polarimetric observables (e.g., Bringi and Chandrasekar 2001; Marzano et al. 2012; Ulaby and Elachi 1990):

$$\sigma_{SARppqq}(x,y) = 4\pi \left\langle S_{SARpp}(x,y) S^*_{SARqq}(x,y) \right\rangle \tag{18.2}$$

$$\sigma_{SARpq}(x,y) = 4\pi \left\langle S_{SARpq}(x,y) S^*_{SARpq}(x,y) \right\rangle \tag{18.3}$$

$$Z_{SARco}(x,y) = \frac{\sigma_{SARhh}(x,y)}{\sigma_{SARvv}(x,y)} \tag{18.4}$$

$$\rho_{SARco}(x,y) = \frac{S_{SARvv}(x,y) S^*_{SARhh}(x,y)}{\sqrt{|S_{SARhh}(x,y)|^2}\sqrt{|S_{SARvv}(x,y)|^2}} = \tag{18.5}$$
$$|\rho_{SARco}(x,y)| \exp\left(j\Psi_{SARco}(x,y)\right)$$

where σ_{SARpq} is the pq-polarized NRCS (or backscattering coefficient, adimensional), and σ_{SARhv} the cross-polarizations and σ_{SARhh}, σ_{SARvv} the co-polarizations. The term $\sigma_{SARppqq}$ describes the cross term among orthogonal polarizations. Z_{SARco} is the co-polar ratio (or difference, if expressed in decibels), whereas ρ_{SARco} is the complex correlation coefficient (or degree of correlation, adimensional), expressed by an amplitude $|\rho_{SARco}|$ and a phase Ψ_{SARco}.

When dealing with the co-polar differential phase, the SAR polarimetric phase model needs to account for the slant observing geometry within a precipitation medium (see Fig. 18.4). In clear sky the SAR phase response is given by the ground polarimetric differential phase, indicated by $\delta^0_{co}(x,y)$, due to the surface interaction. The path through the hydrometeors adds a two-way rotation along the incident path, given by the path integral of the specific differential phase $K_{co}(x,y,z)$ (propagation phase shift). The precipitation-cell backscatter also introduces a differential phase, $\delta_{co}(t)$, i.e. the phase rotation between S_{hh} and S_{vv} of the scattering volume (depending on the cell position, t), additionally affected by the 2-way path from the same volume to the radar (Bringi and Chandrasekar 2001; Marzano et al. 2012). According to Matrosov et al. (1999), values of δ_{co} are small for S-band wavelengths even for intense rainfall rates; however, at X band it is negligible only for modest precipitation rates, wheras at Ka band values, δ_{co} can be very significant even for modest rainfall rates. A formulation of the observable SAR complex correlation coefficient for a ground point (x,y) is presented in Marzano et al. (2012) and revised in Mori and Marzano (2017a) in the form:

$$\rho_{SARco}(x,y) = \frac{f(\sigma^{0ground}_{vv}, \sigma^{0ground}_{hh}, \rho^0_{co}) \cdot L(k_{hh}, k_{hh}, K_{co}) + \sin(\theta)\int\limits_{\Delta t} C_{vol}(t)dt}{f'(\sigma_{SARhh}, \sigma_{SARvv})} \tag{18.6}$$

$$C_{vol}(t) = f''(\eta_{hh}, \eta_{hh}, \rho_{co}) \cdot L(k_{hh}, k_{hh}, K_{co})$$

where $\rho_{co}^0(x,y) = \left|\rho_{co}^0(x,y)\right| exp\left(j\delta_{co}^0(x,y)\right)$ is the complex correlation coefficient of the ground target and $\rho_{co}(x,y) = |\rho_{co}(x,y)| exp(j\delta_{co}(x,y))$ is the complex correlation coefficient of the atmospheric volume. $L(\cdot)$ is a functional term accounting for the two-way path attenuation and $f(\cdot), f'(\cdot), f''(\cdot)$ are complex functions of the surface and volume scattering matrix elements, depending respectively on ground target, SAR received signal and atmospheric volume. Note that in the literature, the computation of $\delta_{co}(x,y)$ is simplified as it is assumed equal to $\delta_{co} = arg(\rho_{co})$ of the scattering cell in position x,y (Marzano et al. 2012), or ignored as in Fritz and Chandrasekar (2012).

Marzano et al. (2012) suggest a significant correlation between the SAR NRCS and the slant-integrated water contents. The SAR response seems to be mainly governed by the surface contribution σ_{SRF}, except when the two-way path within precipitation is relatively long and medium attenuation is sufficiently strong. In the latter case, the volume contribution σ_{VOL} tends to saturate and the relation between SAR NRCS and integrated water contents is much more dispersed. Moreover, the SAR response appears strongly affected by ground surface response and, to a limited extent, by the observing incident angle. The analysis at different bands suggests different SAR responses, with the X-band NRCS not being strongly influenced by frozen hydrometeors, while this is not necessarily true for Ka-band NRCS.

The polarimetric modelling of SAR response requires knowledge of the electromagnetic signatures of each water particle class affecting the wave propagation. We can define a particle class as a group, such as "moderate rain" drops or "dry snow" flakes, characterized in terms of shape, radius, PSD, temperature, composition (e.g., Marzano et al. 2008). The complexity of this approach can be simplified using an approximate but reasonable approach where the electromagnetic signature of each class is expressed through semi-empirical models of a bulk parameter, such as the water content $W(x,y,z)$ (in g m^{-3}), defined for each classes. This is the approach followed in Marzano et al. (2012) at X-Band where the power-law formula has been used to model specific attenuation $k_{pq}(x,y,z)$ (in dB km^{-1}), equivalent reflectivity $Ze_{pq}(x,y,z)$ (in mm^6 m^{-3}), differential phase $K_{co}(x,y,z)$ (in ° km^{-1}), modulus and argument of the co-polar correlation coefficient $\rho_{co}(x,y,z)$ (adim). A typical parametric expression has the form of $k_{pq}(x,y,z) = a_{pq}W(x,y,z)^{b_{pq}}$.

18.3.2   Example of Precipitation-Affected SAR Scene

The model proposed in Sect. 18.3.1 can be used in order to numerically simulate the SAR response for a given scene. This requires a SAR ground response model and simulations of atmospheric water particle distributions. Realistic clouds are difficult to retrieve from in situ and remote measurements and, in this respect, synthetic clouds can be simulated more easily by cloud-resolving models. For sensitivity analysis, canonical clouds with a rectangular shape on the x-z plane and stratified in the vertical direction, composed by 1 or 2 uniform constituents (e.g., clouds,
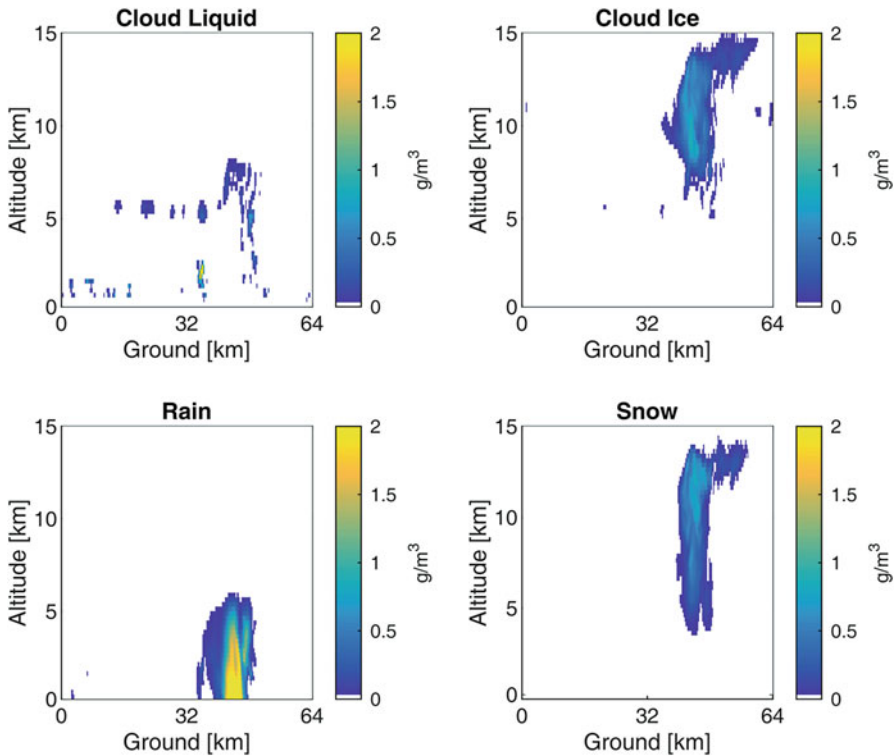
Fig. 18.5 Example of System for Atmospheric Model (SAM) vertical slice for a Compact Medium Single Cell cloud. Values indicate water content W in g m^{-3} of the simulated distributions of snow, rain, ice and cloud particles

moderate rain drops or dry snowflakes), can be also employed, as in Weinman and Marzano (2008) and Marzano and Weinman (2008).

Clouds can be simulated using the Weather Research and Forecasting (WRF) model (Michalakes et al. 2005) or the System for Atmospheric Model (SAM) Cloud Resolving Models (CRMs), as well as other Numerical Weather Prediction (NWP) models. SAM is a high-resolution (250 m) model, which simulates the 3-D water content distribution (g m^{-3}) of several kinds of hydrometeors, both precipitating (snow, graupel and rain) and non-precipitating (cloud ice, cloud liquid) (Blossey et al. 2007). A simulated SAM vertical section is given in Fig. 18.5 as an example.

A relatively simple surface target within the SAR response model is represented by bare soil. The Semi-Empirical Model (SEM) of Oh et al. (2002) allows simulation of the complete SAR polarimetric response of a realistic bare soil with a root mean square (RMS) height (k_s), a correlation length (k_l) and a volumetric soil moisture content (m_v). The simulation of Fig. 18.6 uses 1.5 cm, 5.0 cm and 0.25 cm^3 cm^{-3} as values of the three parameters, respectively. Other effective surface targets, representing many other targets and their combination, are represented by canonical targets including spheres, cylinders and dihedrals. Their combination may represent
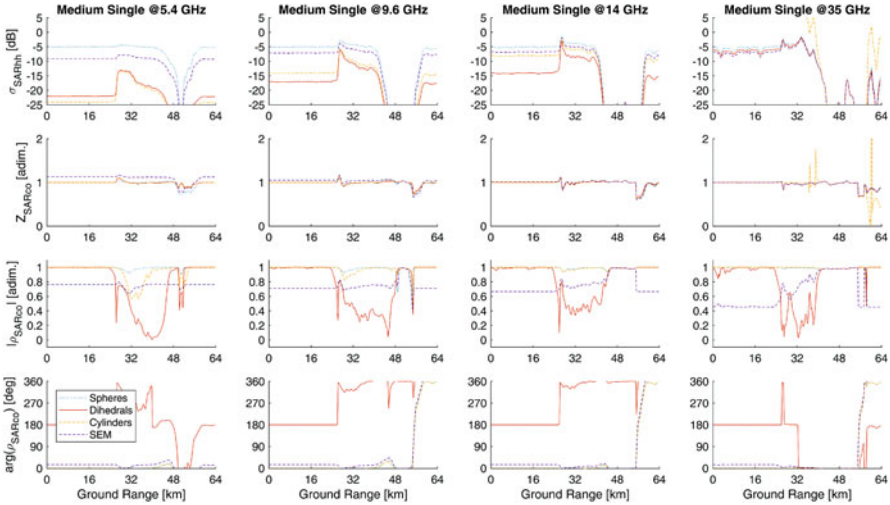
Fig. 18.6 SAR simulated response in terms of normalized Radar cross section σ_{SARhh} (horizontal transmitted and received), co-polar ratio Z_{SARco} and complex correlation coefficient ρ_{SARco} for the SAM realistic cell of Fig. 18.5. Four SAR frequencies are evaluated (5.4, 9, 14 and 35 GHz). Considered background are Spheres, Dihedrals, Cylinders, and a semi-empirical bare soil scattering model (SEM)

many natural targets according to the Freeman-Durden polarimetric decomposition (e.g., Cloude 2010). Their scattering matrix in BSA (BackScatter Alignment) convention is reported in Ulaby and Elachi (1990). The simulation of Fig. 18.6 considers spheres of 0.3 m, dihedrals of 0.025 m and cylinders of 0.030 m and 0.002 m radius, at 45° rotation. Note that NRCSs are function of target dimensions, differently from target complex correlation coefficients that are independent of dimension. In this simplified scenario, canonical targets are supposed to fill the ground scene, one target per ground cell.

Fig. 18.6 shows an example of realistic SAR responses in the presence of precipitation, for different ground targets and frequency using the model of Sect. 18.3.1. For NRCS the signal is sensitive to precipitation and frequency, as well as the precipitation pattern described in Sect. 18.3.1. At C band ground targets could be easily recognized, while at Ka band their response is similar; on the other hand, Ka-band response appears more sensitive to ice (the small peak at around km 48). Polarimetry can give useful information only at C Band. The interpretation of the complex correlation coefficient is more difficult, even if the volumetric effects is present in all bands as well as the sensitivity to different targets. The dihedral-type surface always allows the detection of clouds, whereas sphere-type surface rarely permit it. In terms of phase, the presence of a cloud introduces a significant phase rotation.

18.4 SAR Precipitation Retrieval Techniques

In order to convert X-SAR measurements into near-surface rain-rate $R(x,y)$ (in mm h^{-1}), it is necessary to apply an inversion algorithm, such as the ones proposed in Marzano and Weinman (2008) and Weinman and Marzano (2008), starting from the intuition of Pichugin and Spiridonov (1991). Other easier approaches have been proposed, based on the difference (in dB) between the background NRCS $\sigma_{pp}^{0ground}(x,y)$ and the retrieved NRCS $\sigma^{0}_{SARpp}(x,y)$:

$$\Delta\sigma_{SARdB}(x, y) = \sigma_{pp}^{0ground}(x, y) - \sigma_{SARpp}^{0}(x, y) \tag{18.7}$$

Note that $\Delta\sigma_{SARdB}$ is usually positive for rainfall observations and tends to be negative for significant backscattering effects due to edge effects from the upper rain-cloud, as discussed in Sect. 18.3.

18.4.1 Data Pre-processing

X-Band SAR products, distributed by space agencies, differ in their ground resolution and areal extent, usually with an inverse relation, depending on the observing method (e.g., Ulaby and Long 2014). Usually Spotlight, Stripmap or Scansar modes are available, whereas SAR products can vary with the processing level. Using the COSMO-SkyMed notation (but similar to TerraSAR-X), the Single-look Complex Slant (SCS) outputs are the basic product available for users. Multilook Ground Detected (MGD) products are obtained through a further processing where the focused SCS is detected, radiometrically equalized and projected in range-azimuth. Further data processing envisages the correction for ellipsoid (Geocoded Ellipsoid Corrected, GEC) or terrain (Geocoded Terrain Corrected, GTC) and consequent projection on a cartographic reference system (Fritz and Eineder 2013; ASI 2009). SCS, MGD, GEC and GTC are usually indicated as Level-1 products.

For X-SAR precipitation estimation the GTC product can be used, directly dowloadable from the archives or self-produced from a SCS product using a proper processing tool (such as ENVI-SARSCAPE®). GTC product has a reduced speckle, due to 6-look averaging and approximately a square resolution on the ground of about 18×18 m^2 with a pointing knowledge error of less than 20 m. Both Stripmap and Scansar acquisition modes are suitable for precipitation analysis. The Stripmap mode has a ground coverage of about 30×30 km^2 with a resolution of about 15 m/pixel, whereas Scansar has a coverage of 200×200 km^2 with a resolution of about 30 m/pixel. These numbers refer to CSK, but they are similar in TSX. With respect to the polarization, the horizontally transmitted and horizontally received (HH) signal is preferable, being more sensitive to raindrop oblate shapes.

Several of the proposed SAR-based retrieval methods require a calibration with ground measurements. Doppler weather radar data, which allows relatively wide

coverage, continuous monitoring and a suitable range resolution, is the most suitable one. The overlapping SAR/WR data is affected by the difference in acquisition geometry and frequency band (Fritz and Chandrasekar 2010). Weather radar co-polar horizontally-polarized (HH) reflectivity factor Z can be converted into rain rates using empirical relationships which generally have the form of a power law. The suggested retrieval relation for the rainfall field $R_{WR}(x,y)$ in the x-y horizontal plane is:

$$\widehat{R}_{WR}(x,y) = \left[\frac{Z(x,y)}{a_n}\right]^{1/b_n} \tag{18.8}$$

with $a_n = 300$ and $b_n = 1.4$ for S-band NEXRAD and $a_n = 200$ and $b_n = 1.6$ for a standard Marshall-Palmer formula where R is in mm h^{-1} and Z is in linear units mm^6 m^{-3} (e.g., Bringi and Chandrasekar 2001). For Z corresponding to 59.1 dBZ (such as the case presented in Sect. 18.2), the NEXRAD Z-R and Marshall-Palmer yield R of about 283 and 180 mm h^{-1}, respectively. Strictly speaking, it is not correct to invert a statistical relation Z-R to get R-Z as in (18.8) due to different error minimization; however, this approximation is a common practice in operational radar meteorology.

In order to make SAR observation comparable with WR data, both WR and X-SAR images have to be co-registered and X-SAR images degraded through an appropriate moving-average filter at the resolution of about 0.5-km size and down-sampled at about 0.5 km ground resolution. This resolution is an upper-limit estimate consistent with the effective resolution of SAR data processing applied to incoherent moving targets such as precipitation (Marzano et al. 2010).

18.4.2   Regressive Empirical Algorithm (REA)

An effective model for radar precipitation analysis is the power-law expression to estimate of the rain-rate profile $R_{REA}(x,y)$ (in mm h^{-1}), expressed by:

$$\widehat{R}_{REA}(x,y) = a_e[\Delta\sigma_{SARdB}(x,y)]^{b_e} \tag{18.9}$$

where X-band $\Delta\sigma_{SARdB} \geq 0$ and the empirical coefficients a_e and b_e may be geographically and climatologically dependent as it happens for WRs in terms of reflectivity and rain-rate. The X-SAR side-viewing geometry introduces a characteristic pattern of the observed NRCS due to the increasing attenuation path as the incident radar ray moves within the precipitation cell from near to far ranges (e.g., Weinman and Marzano 2008). This deformation is such that the X-SAR tends to underestimate rainfall intensity at the near-range edges and to overestimate it at the far-range edges with an apparent broadening of the rainfall footprint. In order to take these geometrical effects into account, Eq. (18.9) can be modified by introducing a

factor $f_G(x)$ that accounts for the location of a pixel with respect to the edge cell. For heavy rainfall intensity, the model of (18.9) tends to underestimate the volumetric backscattering contribution σ^0_{VOLhh}, but this effect may be partially corrected by a first-order approach. The derived formulation of (18.9), proposed in Marzano et al. (2011) and called Modified Regression Empirical Algorithm (MREA), is:

$$\widehat{R}_{MREA}(x) = \begin{cases} \left[\dfrac{\Delta\sigma_{SARdB}(x) + b_v \Delta\sigma_{SARdB}(x)^{c_v}}{a} \right]^{\frac{1}{b}} \left[\dfrac{1}{x - x_0} \right]^{c_e} & x_0 + \epsilon \leq x \leq x_0 + w \\ \\ 0 & \text{otherwise} \end{cases}$$

(18.10)

where the parameters a, b, b_v, c_v and c_e are empirical coefficients. Using WR reflectivities Z, Eq. (18.8) with Marshall-Palmer coefficients and corresponding SAR $\Delta\sigma_{SARdB}$ with an average background $\sigma_{hh}^{0ground} = -7.9$ dB, estimated coefficients are, respectively, 0.0089, 2.4595, 0.1216, 3.8979 and -0.0230 through a linear regression (Marzano et al. 2011). In (18.10) the along-track variable y has been omitted, since the formual is intended for across-track corrections only. The parameter x_0 is the near-range edge of the rain cloud with w its estimated across-track width. The parameter ε in (18.10) is introduced to prevent the singularity in $x = x_0$ and is usually equal to few pixels in the ground range. Eq. (18.10) applies to all the X-SAR pixels where $\Delta\sigma_{SARdB} \geq 1$ taking into account the $\sigma_{hh}^{0ground}$ background uncertainty.

Applying (18.10) to the Hurricane Gustav case of Sect. 18.2, a quantitative analysis of the error with respect to WR-based estimates shows that the correlation coefficient is 0.75, the error bias -0.66 mm h^{-1}, the root mean square error (RMSE) 22.28 mm h^{-1} and the Fractional RMSE (FRMSE) of about 0.98 (where FRMSE is defined as the ratio between estimation RMSE and root-mean-square value of R_{WR} over the whole dataset).

18.4.3 Probability Matching Algorithm (PMA)

A second approach, described in Marzano et al. (2010), employs a probability matching approach over a given target area (Calheiros and Zawadzki 1987). Once estimated the probability density function $p_{WR}(R_{WR})$ of WR-based rain rate RWR, and the probability density function $p_{SAR}(\Delta\sigma_{SARdB})$ of measured X-SAR differential NRCS $\Delta\sigma_{SARdB}$, the PMA method can be simply written as follows:

$$\int_{R_t}^{\widehat{R}_{PMA}} p_{WR}(R_{WR})dR_{WR} = \int_{\Delta\sigma_{dBt}}^{\Delta\sigma_{SARdB}} p_{SAR}(\Delta\sigma_{SARdB})d\Delta\sigma_{SARdB} \qquad (18.11)$$

where R_t and $\Delta\sigma_{dBt}$ are rain-rate and differential σ_{SARdB} lower threshold values (e.g., equal to 0.1 mm h^{-1} and 0.5 dB, respectively). The integrals in (18.11) represent a probability (or cumulative distribution function) and if computed for increasing values of the extremes, yield an expression for PMA:

$$\widehat{R}_{PMA}(x,y) = f_{PM}(\Delta\sigma_{SARdB}(x,y)) \qquad (18.12)$$

where f_{PM} is a functional which can be either implemented as a look-up table of RPMA and NRCS records or as a polynomial regressive curve. Applying PMA to the case of Sect. 18.2, yields an estimated mean error of 3.1 mm h^{-1}, an RMSE of about 13.2 mm h^{-1} and a correlation coefficient of 0.64.

18.5   Applications

18.5.1   Improving SAR Retrieval Using Background Estimation

The MREA methodology, described in Sect. 18.4.2, requires the knowledge of background NRCS in the absence of precipitating clouds. Moreover, MREA applies to the entire scene, including flooded areas, permanent water bodies and orographic shadows. These limitations can lead to severe estimation errors or misinterpretations of the scene. Improvements to MREA estimations can arise from a pre-processing step to select only areas affected by precipitations and trying to estimate the clear-sky background NRCS of these areas.

Pulvirenti et al. (2014) propose the classification methodology indicated as SAR Images Dark Object Classifier (SIDOC) that allows the differentiation of "water surfaces" from areas affected by precipitation, both appearing dark in X-SAR imagery. Water surfaces may include both permanent water bodies, such as lakes or rivers, and flooded areas and, in this respect, SIDOC shows its usefulness in both detecting areas affected by precipitations and in detecting flooded areas. SIDOC uses several ancillary data, such as Digital Elevation Model (DEM), static land cover and Local Incident Angle (LIA) maps. SIDOC consist of several steps, summarized in Fig. 18.7.

The SIDOC first step detects low backscatter areas in the input image, using a supervised Split Based Approach (SBA) and fuzzy logic that lead to determining a mean threshold, more or less suitable for the whole scene. Output of this step is a segmented map, in which the detected areas are distinguished and labelled as contiguous pixels, and a raw classification map, where pixel with high LIA (that clearly cannot be plain surfaces) are distinguished from the others. In the SIDOC second step, the remaining pixel are processed to extract shape features, such as area,
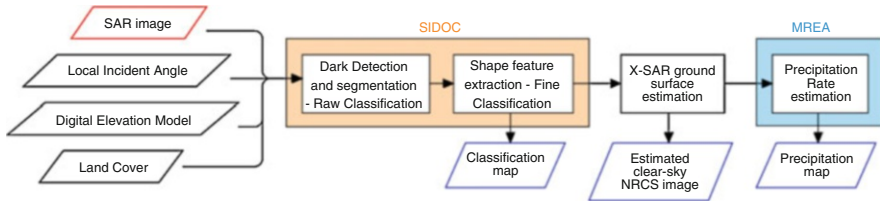
Fig. 18.7 Flowchart of the procedure described in Mori et al. (2016) for detecting flooded and cloud areas in X-SAR images and estimating the relative precipitation rate

perimeter and complexity (weighted ratio between area and perimeter): these features and fuzzy logic (together with land cover) are used to distinguish flooded areas from areas affected by precipitations.

In order to produce precipitation maps, two further steps are necessary (Mori et al. 2016). The first one consists of estimates the X-SAR ground surface response for those pixels detected as dark by SIDOC. The reconstructed $\sigma_{pp}^{0ground}$ is estimated as the mean value of the pixel near the outer border of the cloudy ones, belonging to the same land cover class and not affected by cloud or water effects. This realistic cloud-free image of the observed scene is then ingested in the MREA precipitation estimation procedure.

18.5.2 Statistical Approaches for Retrieval Validation

X-SAR precipitation detection and estimation errors should be ideally verified through ground-truth data of the analyzed area at the same time and at a similar resolution as the SAR acquisition. Unfortunately, this goal can rarely be achieved, due to the SAR high spatial resolution and relative wide coverage area and SAR near instantaneous acquisition time. A good compromise is available through the use of ground-based weather radars, that ensure a wide and uniform coverage, at a comparable ground resolution. WR volume acquisition time is quite long (about 5 min to complete a volume production) as compared to SAR, causing possible misalignments between the two data series. Moreover, the two acquisition geometries, the image formation and often the scanning frequency are quite different, resulting in another source of error. Note that WR precipitation real-time rain products can be affected by numerous sources of errors such as wet radome, spatial variability of particle size distribution, and system miscalibration (e.g., Bringi and Chandrasekar 2001).

Statistical approaches can be also considered for SAR-based retrieval analysis. The first and second order statistics of these errors can be evaluated (e.g., Stein et al. 2002). First-order statistics indicates a comparison of the spatial distribution of the retrieved rain values regardless the spatial organization of the retrieved rain fields. For this purpose, we can use the Complementary Cumulative Distribution Function (CCDF) defined as follows:

$$CCDF(X_{th}) = 1 - P(X(\mathbf{s}) > X_{th}) \quad \forall s \in D \tag{18.13}$$

In (18.13) P denotes probability, X_{th} is a threshold, D the spatial domain where the rain retrieval is carried out and $X(s)$ is a variable sampled at spatial and temporal position $s = (x,y,t)$. Second-order statistics characterizes the spatial correlation structure of the rain fields, describing the spatial variability of the variable under investigation at different spatial scales. In this respect, we can use a semi-variogram $\gamma_X(\mathbf{l})$ of the variable X, defined as:

$$\gamma_X(l) = \frac{1}{2} \left\langle |X(\mathbf{s} + \mathbf{l}) - X(\mathbf{s})|^2 \right\rangle_s \tag{18.14}$$

where l is the lag distance and s a generic position. These statistical approaches allow a comparison between WR and X-SAR data in terms of precipitation structure even though it reduces the SAR precipitation map to the resolution of the WR (Mori et al. 2016).

18.5.3   Case Study

The whole processing and validation chain of Sects. 18.5.1 and 18.5.2 is applied in Mori et al. (2016) to a couple of COSMO-SkyMed case studies. We have selected one of these cases as an application example, also for the geographical, spatial and instrumental differences with respect to the example of Sect. 18.2. The selected case is a CSK Ping-Pong acquisition over Italy (Voghera area), which occurred on 7 July 2007 at 05:18 UTC during a mid-latitude intense precipitation. The area is centered at 44.99°N – 8.94°E and covers 30×30 km^2 (Fig. 18.8).

Only the SCS HH channel has been processed in ENVI-SARSCAPE® in order to produce a calibrated multilooked product at 20-m pixel resolution together with DEM correction using SRTM data and UTM projected using WGS84 ellipsoid. Ground WR data are C-Band Vertical Maximum Intensities (VMI, in dBZ) obtained by the Italian national mosaic, with an acquisition frequency of 15 min and a ground resolution of about 1 km^2.

The precipitation maps, derived from SAR and WR data, are shown in Fig. 18.9. The land cover, used by SIDOC, is the Corine Land Cover (CLC) 2012, ensuring a minimum spatial resolution of 25 ha/100 m and 15 classes (at Level-II). The SAR map has been filtered with a texture filter and degraded to WR resolution in order to extract the map feature. WR precipitation map has been obtained using the standard Marshall-Palmer formula. Even if the SAR is sensitive only to moderate-to-intense precipitations areas, the geographic correspondence between WR and SAR precipitation map is fairly good with a displacement mainly due to the significant time difference between the two acquisitions (Fig. 18.10). In terms of accuracy, the mean error is -2.64 mm h^{-1} and RMSE is 15.78 mm h^{-1}. The CCDF comparison in Fig. 18.10 shows a tendency to overestimation, mainly due to the sensitivity of X-SAR to the intense portion of the rain event (leading to select only a part of the WR retrievals).
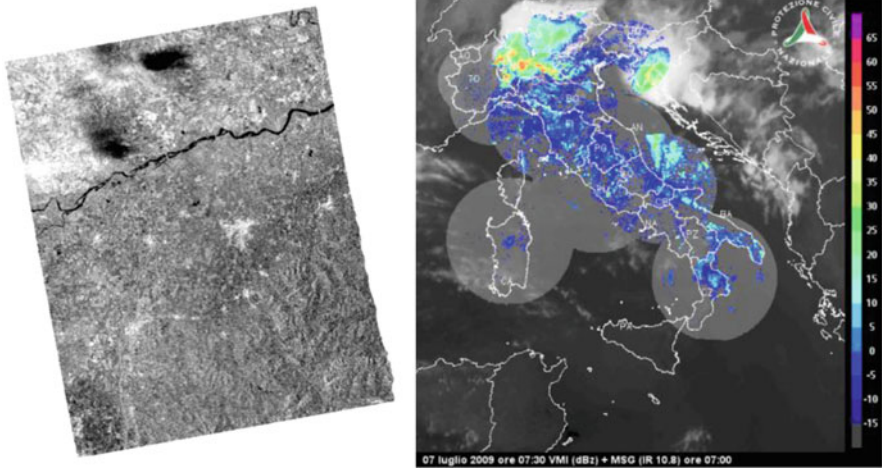
Fig. 18.8 Voghera case study. Left image is a geocoded quicklook of the CSK acquisition (at 05:18 UTC). Right figure shows the corresponding Italian National Mosaic Vertical Maximum Intensities (VMI) at 05:30 UTC (~15 min acquisition time); the ellipse approximately encloses the case study area. (Adapted from Mori et al. 2017b)
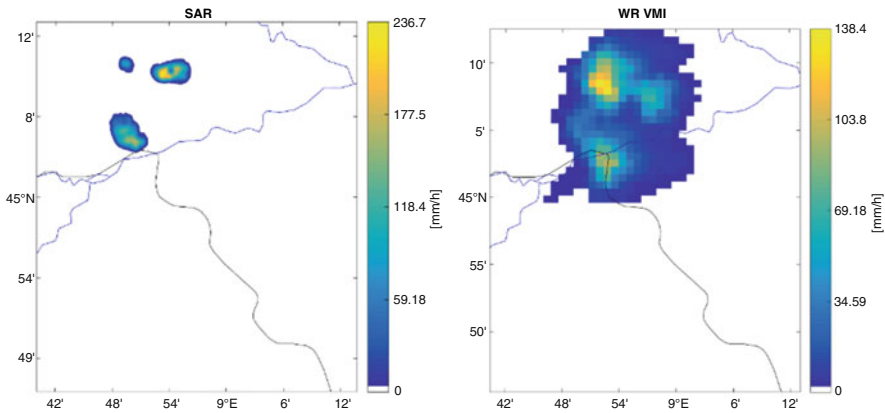
Fig. 18.9 Precipitation maps for the case study of Fig. 18.8. Left map is obtained from X-SAR data with the procedure of Sect. 18.5.1 (filtered and smoothed to WR resolution), right map is obtained by WR VMI data and a Marshall-Palmer formula. (Adapted from Mori et al. 2017b)
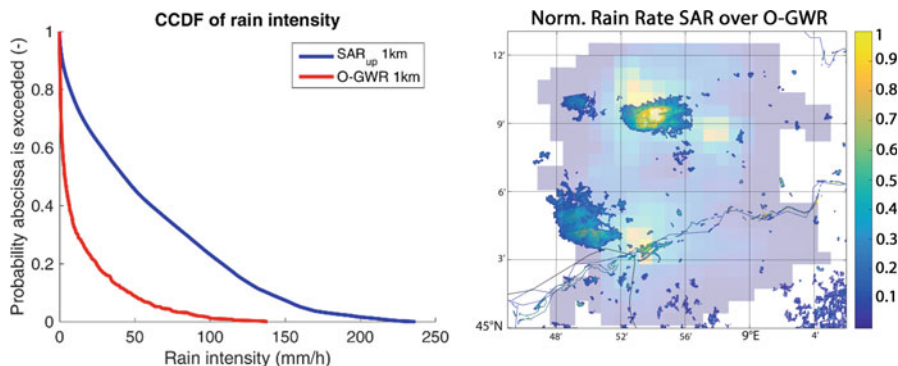
Fig. 18.10 Right plot shows the analysis of the position error between the WR precipitation map (shaded background) and the SAR one (foreground) for the case study of Fig. 18.8. Values have been normalized to the maximum of the dataset. Note that the WR data precedes the SAR data by ~12 min. Left plot shows Complementary Cumulative Distribution Function (CCDF) for the same case study. Blue lines represent SAR data degraded at WR resolution (1000 m); red lines represent WR data. (Adapted from Mori et al. 2017b)

18.6   Conclusion

Hydrometeorological applications can represent an appealing goal for spaceborne SAR missions, especially if high spatial resolution is requested. Forward and inverse models for SAR precipitation retrieval at X-band have been presented and discussed in this chapter. The SAR use at C band for flood monitoring is well established, but SAR observations can be also exploited for detecting marine winds and hurricanes. The use of Ku and Ka-band SARs for cryosphere applications has been also proposed, as in the CoRe-H2O mission concept (ESA 2012), but these SAR frequencies can be also exploited for precipitating cloud observation.

Spaceborne SARs can ensure a global coverage whose orbit duty cycle can be improved by satellite constellations, such as for COSMO-SkyMed, or operating in quasi-continuous acquisition mode, such as for Sentinel-1 satellites. Their ground spatial resolution remains unparalleled by other satellite microwave instruments. A multi-frequency SAR system can probe precipitating clouds with high-frequency sensors sensitive to stratiform rainfall and low-frequency sensors capable to sensing more intense near-surface precipitation. Most of the work to date has focused on rainfall retrievals over land while retrievals over the ocean are a future objective for X-SAR rain estimation at high spatial resolution. SAR slant-viewing geometry and precipitation retrieval processing still present several open issues to be explored in order to refine the physical-statistical retrieval approaches.

SAR future is characterized by the proposal of new space mission concepts and technologies. Recent studies exist for a geostationary SAR (e.g., Monti Guarnieri and Hu 2016) with possible hydrometeorological applications. The increasing of swath width without losing spatial resolution is under investigation by means of High Resolution Wide Swath (HRWS) SARs. Other researches explore the

feasibility and opportunity of SAR operating at Ka band for single pass interferometry, but also addressing the atmospheric influence. The KydroSAT mission concept (Mori et al. 2017b) proposes a SAR space mission entirely devoted to hydrology and cryology. KydroSAT mission concept foresees a miniaturized fully-digital SAR at Ku and Ka band (KydroSAR), specifically devoted to detecting and estimating atmospheric precipitation and surface snow; its baseline includes dual-polarization capability, high orbit duty cycle (>75%), flexible ground resolution (5–150 m), and a large variable swath (50–150 km), doubled by formation of two mini-satellites both carrying a KydroSAR. Moreover, the KydroSAT mission concept foresees the along-track convoy with the COSMO-SkyMed and SAOCOM SAR platforms, allowing the observation of the same scene at L, X, Ku and Ka bands. The challenging requirements of this architecture require the development of new technologies such as Digital Beam Forming and direct digital-to-radiofrequency conversion, which are current frontiers in SAR research. These candidate missions can effectively contribute and extend the capability to observe the precipitating clouds at high resolution, according to the principles and techniques discussed in this chapter.

References

Alpers, W., & Melsheimer, C. (2004) Rainfall. In: C. R. Jackson, & J. R. Apel (Eds.), *Synthetic Aperture Radar marine user's manual* (pp. 353–372). US Department of Commerce, NOAA. Available at http://www.sarusersmanual.com/, last accessed 15 Oct 2018.

ASI. (2009). *COSMO-SkyMed SAR products handbook rev. 2*. Available at http://www.e-geos.it/products/pdf/csk-product%20handbook.pdf, last accessed 15 Oct 2018.

Atlas, D., & Moore, R. K. (1987). The measurement of precipitation with synthetic Aperture Radar. *Journal of Atmospheric and Oceanic Technology, 4*, 368–376. https://doi.org/10.1175/1520-0426(1987)004<0368:TMOPWS>2.0.CO;2.

Baldini, L., Roberto, N., Gorgucci, E., Fritz, J. P., & Chandrasekar, V. (2014). Analysis of dual polarization images of precipitating clouds collected by the COSMO SkyMed constellation. *Atmospheric Research, 144*, 21–37. https://doi.org/10.1016/j.atmosres.2013.05.010.

Blossey, P. N., Bretherton, C. S., Cetrone, J., & Khairoutdinov, M. (2007). Cloud-resolving model simulations of KWAJEX: Model sensitivities and comparisons with satellite and radar observations. *Journal of the Atmospheric Sciences, 64*, 1488–1508. https://doi.org/10.1175/JAS3982.1.

Bringi, V. N., & Chandrasekar, V. (2001). *Polarimetric doppler weather radar, principles and applications*. Cambridge,. 536 pp: Cambridge University Press. https://doi.org/10.1017/CBO9780511541094.

Calheiros, R. V., & Zawadzki, I. I. (1987). Reflectivity rain-rate relationships for radar hydrology in Brazil. *Journal of Climate and Applied Meteorology, 26*, 118–132. https://doi.org/10.1175/1520-0450(1987)026<0118:RRRRFR>2.0.CO;2.

Cloude, S. R. (2010). *Polarisation – applications in remote sensing*. Oxford : Oxford University Press, Scholarship Online. https://doi.org/10.1093/acprof:oso/9780199569731.001.0001.

Danklmayer, A., Doring, B. J., Schwerdt, M., & Chandra, M. (2009). Assessment of atmospheric propagation effects in SAR images. *IEEE Transactions on Geoscience and Remote Sensing, 47*, 3507–3518. https://doi.org/10.1109/TGRS.2009.2022271.

Doviak, R. J., & Zrnić, D. S. (1993). *Doppler radar and weather observations*. San Diego: Academic, 562 pp, ISBN:978-0-12-221422-6.

Durden, S. L., Haddad, Z. S., Kitiyakara, A., & Li, F. K. (1998). Effects of non-uniform beam filling on rainfall retrieval for the TRMM precipitation radar. *Journal of Atmospheric and Oceanic Technology, 15*, 635–646. https://doi.org/10.1175/1520-0426(1998)015<0635:EONBFO>2.0. CO;2.

Ebert, E. E., Janowiak, J. E., & Kidd, C. (2007). Comparison of near-real-time precipitation estimates from satellite observations and numerical models. *Bulletin of the American Meteorological Society, 88*, 47–64. https://doi.org/10.1175/BAMS-88-1-47.

ESA. (2012). CoReH2O - Report for mission selection - an earth explorer to observe snow and ice. ESA SP-1324-2. http://esamultimedia.esa.int/docs/EarthObservation/SP1324-2_CoReH2Or. pdf, last accessed 15 Oct 2018

Ferrazzoli, P., & Schiavon, G. (1987). Rain-induced modification of SAR performance. *Advances in Space Research, 7*, 269–272. https://doi.org/10.1016/0273-1177(87)90323-1.

Fritz, J. P., & Chandrasekar, V. (2010). Simultaneous observations and analysis of severe storms using polarimetric X-band SAR and ground-based weather radar. *IEEE Transactions on Geoscience and Remote Sensing, 48*, 3622–3637. https://doi.org/10.1109/TGRS.2010.2048920.

Fritz, J. P., & Chandrasekar, V. (2012). A fully polarimetric characterization of the impact of precipitation on short wavelength synthetic Aperture Radar. *IEEE Transactions on Geoscience and Remote Sensing, 50*, 2037–2048. https://doi.org/10.1109/TGRS.2011.2170576.

Fritz, T., & Eineder, M. (Eds.) (2013) TerraSAR-X Ground segment. Basic product specification document. TX-GS-DD-3302, Issue 1.9. Available at https://sss.terrasar-x.dlr.de/docs/TX-GS-DD-3302.pdf, last accessed 15 Oct 2018

Fulton, R. A., Breidenbach, J. P., Seo, D.-J., Miller, D. A., & O'Bannon, T. (1998). The WSR-88d rainfall algorithm. *Weather and Forecasting, 13*, 377–395. https://doi.org/10.1175/1520-0434 (1998)013<0377:TWRA>2.0.CO;2.

Hou, A. Y., Kakar, R. K., Neeck, S., Azarbarzin, A. A., Kummerow, C. D., Kojima, M., Oki, R., Nakamura, K., & Iguchi, T. (2014). The Global Precipitation Measurement mission. *Bulletin of the American Meteorological Society, 95*, 701–722. https://doi.org/10.1175/BAMS-D-13-00164.1.

Jordan, R. L., Huneycutt, B. L., & Werner, M. (1995). The SIR-C/X SAR synthetic Aperture Radar system. *IEEE Transactions on Geoscience and Remote Sensing, 33*, 829–839. https://doi.org/10.1109/36.406669.

Kummerow, C., Barnes, W., Kozu, T., Shiue, J., & Simpson, J. (1998). The Tropical Rainfall Measuring Mission (TRMM) sensor package. *Journal of Atmospheric and Oceanic Technology, 15*, 809–817. https://doi.org/10.1175/1520-0426(1998)015<0809:TTRMMT>2.0.CO;2.

Landuyt, L., van Wesemael, A., Schumann, G. J., Hostache, R., Verhoest, N. E. C., & van Coillie, F. M. B. (2018). Flood mapping based on synthetic Aperture Radar: An assessment of established approaches. *IEEE Transactions on Geoscience and Remote Sensing*. https://doi.org/10.1109/TGRS.2018.2860054.

Li, X. (Ed.). (2017). *Hurricane monitoring with Spaceborne synthetic Aperture Radar*. Singapore: Springer, 396 pp, ISBN:978-981-10-2893-9.

Marzano, F. S., & Weinman, J. A. (2008). Inversion of spaceborne X-band synthetic Aperture Radar measurements for precipitation remote sensing over land. *IEEE Transactions on Geoscience and Remote Sensing, 46*, 3472–3487. https://doi.org/10.1109/TGRS.2008.922317.

Marzano, F. S., Mori, S., & Weinman, J. A. (2010). Evidence of rainfall signature on X-band synthetic Aperture Radar measurements over land. *IEEE Transactions on Geoscience and Remote Sensing, 48*, 950–964. https://doi.org/10.1109/TGRS.2009.2034843.

Marzano, F. S., Mugnai, A., & Turk, F. J. (2002). Precipitation retrieval from spaceborne microwave radiometers and combined sensors. In F. S. Marzano & G. Visconti (Eds.), *Remote sensing of atmosphere and ocean from space: Models, instruments and techniques* (pp. 107–126). Dordrecht: Kluwer Academic Publ, ISBN:1-4020-0943-7.

Marzano, F. S., Scaranari, D., Vulpiani, G., & Montopoli, M. (2008). Supervised classification and estimation of hydrometeors using C-band dual-polarized radars: A Bayesian approach. *IEEE Transactions on Geoscience and Remote Sensing, 46*, 85–98. https://doi.org/10.1109/TGRS. 2007.906476.

Marzano, F. S., Mori, S., Montopoli, M., & Weinman, J. A. (2012). Modeling polarimetric response of spaceborne synthetic Aperture Radar due to precipitating clouds from X to Ka band. *IEEE Transactions on Geoscience and Remote Sensing, 50*, 687–703. https://doi.org/10.1109/TGRS.2011.2163942.

Marzano, F. S., Mori, S., Chini, M., Pulvirenti, L., Pierdicca, N., Montopoli, M., & Weinman, J. A. (2011). Potential of high-resolution detection and retrieval of precipitation fields from X-band spaceborne synthetic Aperture Radar over land. *Hydrology and Earth System Sciences, 15*, 859–875. https://doi.org/10.5194/hess-15-859-2011.

Masunaga, H., Satoh, M., & Miura, H. (2008). A joint satellite and global cloud- resolving model analysis of a Madden-Julian oscillation event: Model diagnosis. *Journal of Geophysical Research, 113*, D17210. https://doi.org/10.1029/2008JD009986.

Matrosov, S. Y., Kropfli, R. A., Reinking, R. F., & Martner, B. E. (1999). Prospects for measuring rainfall using propagation differential phase in X- and Ka-radar bands. *Journal of Applied Meteorology, 38*, 766–776. https://doi.org/10.1175/1520-0450(1999)038<0766:PFMRUP>2.0.CO;2.

Melsheimer, C., Alpers, W., & Gade, M. (1998). Investigation of multifrequency/ multipolarization radar signatures of rain cells derived from SIR-C/X-SAR data. *Journal of Geophysical Research, 103*, 18867–18884. https://doi.org/10.1029/98JC00779.

Michalakes, J., Dudhia, J., Gill, D., Henderson, T., Klemp, J., Skamarock, W., & Wang, W. (2005). The weather research and forecast model: Software architecture and performance. In W. Zwieflhofer & G. Mozdzynski (Eds.), *Use of high performance computing in meteorology* (pp. 156–168). Singapore: World Scientific. https://doi.org/10.1142/9789812701831_0012.

Monti Guarnieri, A., & Hu, C. (2016). Geosynchronous and geostationary SAR: Face-to-face comparison. In *Proceedings of EUSAR 2016: 11th European conference on synthetic Aperture Radar*, Hamburg, Germany, 6–9 June.

Moore, R. K., Mogili, A., Fang, Y., Beh, B., & Ahamad, A. (1997). Rain measurement with SIR-C/X-SAR. *Remote Sensing of Environment, 59*, 280–293. https://doi.org/10.1016/S0034-4257(96)00147-2.

Mori, S., Montopoli, M., Pulvirenti, L., Marzano, F. S., & Pierdicca, N. (2016). Detection and quantification of precipitations signatures on synthetic Aperture Radar imagery at X band. In *Proceedings of SPIE 10003, SAR image analysis, modeling, and techniques XVI*, 1000306, Edinburgh, UK, 18 Oct. https://doi.org/10.1117/12.2241943.

Mori, S., Marzano, F. S., & Pierdicca, N. (2017a). Atmospheric distortions of spaceborne SAR polarimetric signatures at X and Ka-band. In *8th Int. Workshop on science and applications of SAR polarimetry and polarimetric interferometry (POLinSAR)*, Frascati, 23–27 January 2017.

Mori, S., Marzano, F. S., Pierdicca, N., Bombaci, O., Giancristofaro, D., Macelloni, G., Lemmetyinen, J., Giudici, D., & Poghosyan, A. (2017b). KydroSAT: A Ku/Ka band Synthetic Aperture Radar space mission concept for high-resolution mapping of hydrometeorological parameters. In *Proceedings of SPIE 10426, Active and passive microwave remote sensing for environmental monitoring XVI*, 1042603, Warsaw, Poland, 11–14 Sept. https://doi.org/10.1117/12.2277993.

Oh, Y., Sarabandi, K., & Ulaby, F. T. (2002). Semi-empirical model of the ensemble-averaged differential Muller matrix for microwave backscattering from bare soil surfaces. *IEEE Transactions on Geoscience and Remote Sensing, 40*, 1348–1355. https://doi.org/10.1109/TGRS.2002.800232.

Pichugin, A. P., & Spiridonov, Y. G. (1991). Spatial distributions of rainfall intensity recovery from space radar images. *Soviet Journal of Remote Sensing, 8*, 917–932.

Pulvirenti, L., Marzano, F. S., Pierdicca, N., Mori, S., & Chini, M. (2014). Discrimination of water surfaces, heavy rainfall and wet snow using COSMO-SkyMed observations of severe weather events. *IEEE Transactions on Geoscience and Remote Sensing, 52*, 858–869. https://doi.org/10.1109/TGRS.2013.2244606.

Quegan, S., & Lamont, J. (1986). Ionospheric and tropospheric effects on synthetic Aperture Radar performance. *International Journal of Remote Sensing, 7*, 525–539. https://doi.org/10.1080/01431168608954707.

Refice, A., D'Addabbo, A., & Capolongo, D. (2018). *Flood monitoring through remote sensing*. Cham: Springer, 208 pp, ISBN:978-3-319-63959-8.

Roberto, N., Baldini, L., Facheris, L., & Chandrasekar, V. (2014). Modelling COSMO-SkyMed measurements of precipitating clouds over the sea using simultaneous weather radar observations. *Atmospheric Research, 144*, 38–56. https://doi.org/10.1016/j.atmosres.2014.01.016.

Skofronick-Jackson, G., Petersen, W. A., Berg, W., Kidd, C., Stocker, E. F., Kirschbaum, D. B., Kakar, R., Braun, S. A., Huffman, G. J., Iguchi, T., Kirstetter, P.-E., Kummerow, C., Meneghini, R., Oki, R., Olson, W. S., Takayabu, Y. N., Furukawa, K., & Wilheit, T. (2017). The Global Precipitation Measurement (GPM) mission for science and society. *Bulletin of the American Meteorological Society, 98*, 1679–1695. https://doi.org/10.1175/BAMS-D-15-00306.1.

Stein, A., van der Meer, F. D., & Gorte, B. (Eds.). (2002). *Spatial statistics for remote sensing*. Dordrecht: Springer, 260 pp, ISBN:978-0-306-47647-1.

Ulaby, F. T., & Elachi, C. (1990). *Radar polarimetry for geoscience applications*. Boston: Artech House, 350 pp, ISBN:9780890064061.

Ulaby, F. T., & Long, D. G. (2014). *Microwave radar and radiometric remote sensing*. Ann Arbor: University of Michigan Press, 984 pp, ISBN:978-0-472-11935-6.

Weinman, J. A., & Marzano, F. S. (2008). An exploratory study to derive rainfall over land from spaceborne synthetic Aperture Radars. *Journal of Applied Meteorology and Climatology, 47*, 562–575. https://doi.org/10.1175/2007JAMC1663.1.

Part III
Merged Precipitation Products

Chapter 19
Integrated Multi-satellite Retrievals for the Global Precipitation Measurement (GPM) Mission (IMERG)

George J. Huffman, David T. Bolvin, Dan Braithwaite, Kuo-Lin Hsu, Robert J. Joyce, Christopher Kidd, Eric J. Nelkin, Soroosh Sorooshian, Erich F. Stocker, Jackson Tan, David B. Wolff, and Pingping Xie

Abstract The Integrated Multi-satellitE Retrievals for the Global Precipitation Measurement (GPM) mission (IMERG) is a US GPM Science Team precipitation product. IMERG uses inter-calibrated estimates from the international constellation of precipitation-relevant satellites and other data, including monthly surface precipitation gauge analyses, to compute half hour, $0.1° \times 0.1°$ gridded datasets over

G. J. Huffman (✉)
NASA, Goddard Space Flight Center, Greenbelt, MD, USA
e-mail: george.j.huffman@nasa.gov

D. T. Bolvin · E. J. Nelkin
NASA, Goddard Space Flight Center, Greenbelt, MD, USA

Science Systems and Applications, Inc., Lanham, MD, USA

D. Braithwaite · K.-L. Hsu · S. Sorooshian
University of California, Irvine, CA, USA

R. J. Joyce
Innovim, Greenbelt, MD, USA

NOAA/NWS, Climate Prediction Center, College Park, MD, USA

C. Kidd
NASA, Goddard Space Flight Center, Greenbelt, MD, USA

University of Maryland, ESSIC, College Park, MD, USA

E. F. Stocker
NASA/GSFC, Global Change Data Center, Greenbelt, MD, USA

J. Tan
NASA, Goddard Space Flight Center, Greenbelt, MD, USA

Universities Space Research Association, Columbia, MD, USA

D. B. Wolff
NASA/GSFC, Wallops Flight Facility, Wallops Island, VA, USA

P. Xie
NOAA/NWS, Climate Prediction Center, College Park, MD, USA

60°N-S (and partially outside of that latitude band) in three "Runs"—Early (4 h after obs time), Late (14 h after obs time), and Final (3.5 months after obs time). The concepts behind IMERG are briefly reviewed, together with major shifts related to changes in versions from the at-launch Version 03 to Version 05, and an outline of Version 06, which was released in late 2019.

Keywords Precipitation · Rainfall · Snowfall · IMERG · GPM · TRMM · TMPA · Microwave · Infrared · GEO · LEO · Raingauges · GPCC · NASA · CMORPH-KF weighting · PERSIANN-CCS estimates · Uncertainties

19.1 Introduction

The critical role of fresh water for life on Earth, and the necessity of using satellite data to estimate its ultimate source, precipitation, is a repeated theme throughout this book. Most of the relatively accurate satellite-based precipitation estimates are provided by passive microwave (PMW) sensors flying on low Earth orbit (LEO) platforms. Figure 19.1 shows the entire history of "modern" PMW sensors, which started in mid-1987 with the Special Sensor Microwave/Imager (SSM/I). It is also possible to estimate precipitation from infrared (IR) sensors, with geosynchronous Earth orbit (GEO) satellites providing convenient and relatively complete global coverage, except in polar latitudes, albeit with lower quality.

The proliferation of LEO-PMW satellites around the start of the millennium made it possible to create multi-satellite precipitation data sets that had uniform and increasingly finer-scale time/space grids. Typically, the focus has been on providing the best short-interval estimates (at the expense of less homogeneity in the data record), referred to as High Resolution Precipitation Products (HRPP). Examples include the Climate Prediction Center (CPC) Morphing algorithm (CMORPH; Joyce et al. 2004), the Global Satellite Mapping of Precipitation (GSMaP; Kubota et al. 2007), and the Tropical Rainfall Measuring Mission (TRMM) Multi-Satellite Precipitation Analysis (TMPA; Huffman et al. 2007, 2010).

With the launch of the Global Precipitation Measurement (GPM) mission Core Observatory (GPM-CO) in February 2014, the US GPM science team instituted the Integrated Multi-satellitE Retrievals for GPM (IMERG) merged precipitation product. This algorithm is intended to inter-calibrate, merge, and interpolate all available satellite PMW precipitation estimates, together with microwave-calibrated infrared (IR) satellite estimates, precipitation gauge analyses, and other precipitation estimators, to produce fine time- and space-scale estimates spanning the TRMM and GPM eras for the entire globe. IMERG is computed three times for each observation time, first providing an initial estimate and then successively better estimates as more data arrive. The final step uses monthly gauge data to create research-level products. The at-launch Version 03 and subsequent Versions 04 and (current) 05 only covered the GPM era, while Version 06 extends back through the TRMM era.
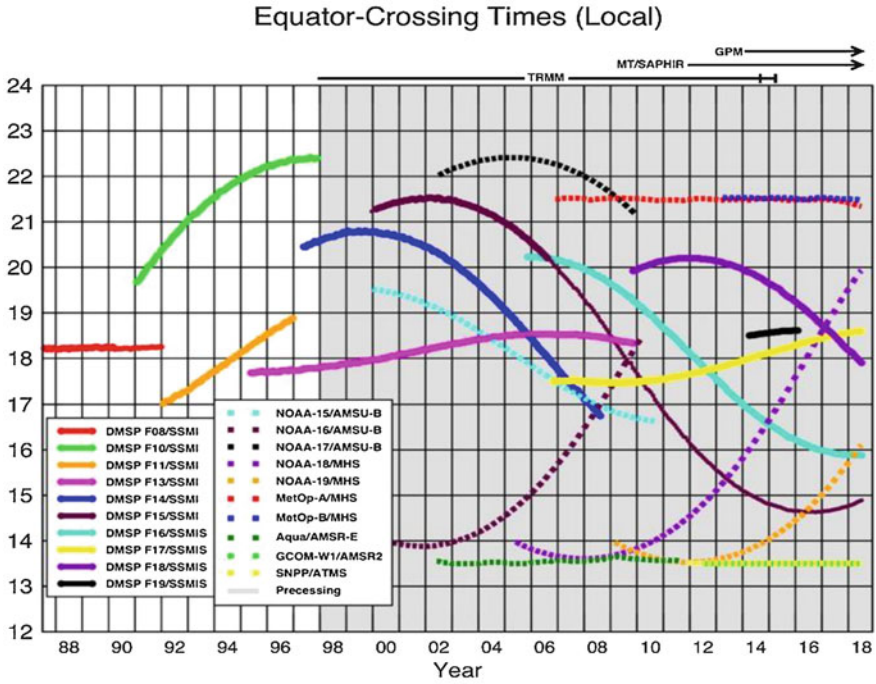
Ascending passes (F08 descending); satellites depicted above graph precess throughout the day.
Image by Eric Nelkin (SSAI), 12 July 2018, NASA/Goddard Space Flight Center, Greenbelt, MD.

Fig. 19.1 PMW sensor Equator-crossing times for 12-24 Local Time (LT; 0000-1200 LT is the same) for the modern PMW sensor era. These are all ascending passes, except F08 is descending. Shading indicates that the precessing TRMM, Megha-Tropiques, and GPM cover all times of day with changes that are too rapid to depict at this scale. (Image by Eric Nelkin (SSAI; GSFC), 12 July 2018; https://pmm.nasa.gov/sites/default/files/imce/times_allsat.jpg holds the current version, last accessed 1 Apr. 2019)

Focusing on the current Version 05, Sect. 19.2 describes the input data sets, while Sect. 19.3 describes the IMERG processing and Sect. 19.4 provides the status of the data sets. Section 19.5 describes some tests of the algorithm performance with examples of IMERG applied to typical applications. Section 19.6 presents the status for Version 06 and concluding remarks.

19.2 Input Data Sets

The precipitation-relevant satellites mentioned above all enter the IMERG computation as single-sensor precipitation estimates. Subsequently, inter-calibration is performed to ensure that these are as consistent as possible. The main groupings are:

1. GPM-CO: The GPM Microwave Imager (GMI) is a well-calibrated conical-scan multi-channel, dual-polarization PMW sensor, and is considered the standard for the other PMW sensors. Its precipitation retrievals (Kummerow et al. 2015 are used in IMERG as direct estimates, as well as contributing to the inter-calibration process. The GPM-CO also carries the scanning Dual-frequency Precipitation Radar (DPR) which is key to the inter-calibration process as part of the Combined Radar-Radiometer Algorithm (Olson et al. 2011 and Chap. 14) estimates.

2. PMW constellation: The rest of the GPM era constellation (cf. Figure 19.1) is composed of satellites of opportunity. The US Defense Meteorological Satellite Program (DMSP) F16, F17, F18, and F19 Special Sensor Microwave Imager/Sounder (SSMIS); the Japanese Global Change Observation Mission-Water (GCOM-W1) Advanced Microwave Scanning Radiometer (AMSR2); and TRMM Microwave Imager (TMI) are conically scanning imagers, while the Joint Polar Satellite System (JPSS-1) and Suomi National Polar-orbiting Partnership (SNPP) Advanced Technology Microwave Sounder (ATMS); and European Meteorological operational satellites (METOP-A and, METOP-B), and the US National Oceanic and Atmospheric Administration (NOAA-18 and NOAA-19) Microwave Humidity Sounder (MHS) are cross-track scan sounders. Observations from all of these sensors are processed using the Goddard Profiling (GPROF; Kummerow et al. 2015) algorithm to provide precipitation estimates.

3. GEO-IR constellation: IR data from the US Geostationary Operational Environmental Satellite (GOES), the Japanese Himawari, and the European Meteosat satellite series cover the central Atlantic through to the central Pacific, from there to the Indian Ocean, and from there to the central Atlantic, respectively. The data are processed into precipitation retrievals using Precipitation Estimation from Remotely Sensed Information using Artificial Neural Networks – Cloud Classification System (PERSIANN-CCS; Hong et al. 2004).

4. Work with previous datasets has shown that incorporating a uniform precipitation gauge analysis, even at the monthly scale, is important for controlling the biases that satellite precipitation estimates typically contain. We use the Deutscher Wetterdienst (DWD) Global Precipitation Climatology Centre (GPCC) V5 Monitoring Product (Becker et al. 2013; Schneider et al. 2014, 2017) through March 2018, and the V6 thereafter.

5. Ancillary products: The IMERG algorithm also accesses surface type (the standard static map of percent water coverage from the Precipitation Processing System [PPS]); snow/ice surface extent (AUTOSNOW from NOAA); and surface temperature, relative humidity, and surface pressure (Japan Meteorological Agency forecasts [for Early and Late] of meteorological data; and the European Centre for Medium-range Weather Forecasts [ECMWF] analysis [for Final, for consistency with the GPROF "climatological" run]).

19.3   IMERG Processing

The input data from the various satellite PMW sensors are assembled, received at PPS as Level 1 brightness temperatures (Tb) from the relevant providers, intercalibrated to GMI as GPM Level 1C brightness temperatures (Tc), then converted to Level 2 precipitation estimates using the V05 GPROF scheme. All estimates are gridded, inter-calibrated to the Ku swath Combined Radar-Radiometer (CORRA) product on a rolling 45-day basis using probability matching, and climatologically calibrated to the Global Precipitation Climatology Project (GPCP) monthly Satellite-Gauge estimates with a simple ratio in high latitude oceans (where GPM-CO Version 05 products are deficient in precipitation) and over all land areas (where the CORRA tends to be high). These "high quality" (HQ) data are combined into half-hourly fields, masked for surface snow and ice (due to uncertain quality in the GPM-CO products), and provided to both the recalibration of PERSIANN-CCS infrared estimates and to the semi-Lagrangian time interpolation scheme adapted from CMORPH-Kalman Filter (CMORPH-KF; Joyce et al. 2011). In parallel, CPC assembles the zenith-angle-corrected, inter-calibrated "even-odd" and merged geo-IR fields and forwards them to the PPS for use in the CMORPH-KF semi-Lagrangian time interpolation scheme and the PERSIANN-CCS computation routines, respectively. The PERSIANN-CCS estimates are computed (supported by an asynchronous 30-day re-calibration cycle) and sent to the CMORPH-KF weighting scheme. The CMORPH-KF weighting scheme (supported by an asynchronous KF weights 3-monthly updating cycle) uses the PMW and IR estimates to create half-hourly estimates. Note that various intermediate fields are carried through the processing as necessary to populate the fields in the output file (Table 19.1). Precipitation phase is computed in the PMW merger step as a diagnostic using surface type, surface pressure, surface temperature, and surface humidity (after Sims and Liu 2015). Finally, user requests for a simple Quality Index (QI) led to two distinctly different QI definitions for the half-hourly and monthly data sets in Version 05 (*https://pmm.nasa.gov/sites/default/files/document_files/IMERG_QI.pdf*, last accessed 17 Nov. 2018).

IMERG is processed twice in near-real time:

- "Early" multi-satellite product ∼ 4 h after observation time and
- "Late" multi-satellite product ∼ 14 h after observation time, and once after the monthly gauge analysis is received
- "Final" satellite-gauge product ∼ 3.5 months after the observation month.

For the Final product the half-hour multi-satellite estimates are adjusted to equal the monthly satellite-gauge combination computed in a monthly IMERG estimate (following the TMPA approach). In all Runs, the output contains multiple fields that provide information on the input data, selected intermediate fields, and estimation quality (Table 19.1).

To ensure a consistent archive of data for all users, all three runs of IMERG are retrospectively processed, including for Version 05. In practice, IMERG is first

Table 19.1 Lists of data field variable names and definitions to be included in each of the output datasets. Primary fields for users are in italics

Half-hourly data file (Early, Late, Final)	
precipitationCal	*Multi-satellite precipitation estimate with gauge calibration (recommended for general use)*
precpitationUncal	Multi-satellite precipitation estimate
randomError	*Random error for gauge-calibrated multi-satellite precipitation*
HQprecipitation	Merged microwave-only precipitation estimate
HQprecipSource	Microwave satellite source identifier
HQobservationTime	Microwave satellite observation time
IRprecipitation	IR-only precipitation estimate
IRkalmanFilterWeight	Weighting of IR-only precipitation relative to the morphed merged microwave-only precipitation
probabilityLiquidPrecipitation	*Probability of liquid precipitation phase*
PrecipitationQualityIndex	*Quality Index for precipitationCal field*
Monthly data file (Final)	
precipitation	*Merged satellite-gauge precipitation estimate (recommended for general use)*
randomError	*Random error for merged satellite-gauge precipitation*
gaugeRelativeWeight	Weighting of gauge precipitation relative to the multi-satellite precipitation
probabilityLiquidPrecipitation	*Accumulation-weighted probability of liquid precipitation phase*
PrecipitationQualityIndex	*Quality Index for precipitationCal field*

retrospectively processed as the Final Run, then again with calls that mimic the processing for Early and Late, but using the data available to the Final. Specifically, the selection of input data available to the retrospective Early Run is approximated by limiting the forward time span of data to the typical latency time (~3 h) before the Early run time (currently 4 h after observation time). The Late uses both backward- and forward-morphing, but neither the Early nor Late Runs are given gauge data. These choices cause the Early and Late Runs to be reprocessed with a superset of input data covering the original runs, and the input data from a particular sensor are produced by the climatological GPROF estimates (computed with more-carefully prepared reanalysis data). Retrospective processing for both the Early and Late Runs is carried out after retrospective processing for the Final Run.

All output data files have multiple data fields with project-mandated metadata and are written in HDF5, which is compatible with NetCDF4. All fields are produced for all Runs, as listed in Table 19.1. Since the PPS provides interactive data subsetting by time, region, and parameter, users are not required to download the entire file. Furthermore, both the PPS and the Goddard Earth Science Data and Information Services Center (GES DISC) create value-added products that give the user additional formats and/or periods of accumulation (*https://pmm.nasa.gov/data-access/downloads/gpm*, last accessed 17 Nov. 2018, provides a current summary).

19.4   IMERG Data Set Status

The at-launch IMERG V03 was processed using pre-launch calibrations, as were all the other GPM products such as GPROF. The cross-track sounder PMW precipitation retrievals computed from the MHS were processed using an alternative scheme (Kidd et al. 2016). Version 04 used initial GPM-based calibrations, as well as V04 GPROF for all PMW data, including the cross-track sounder retrievals. Among other changes, in this version we started dynamically calibrating PERSIANN-CCS to the HQ merged PMW data, and HQ was extended to cover the entire globe.

IMERG was upgraded to V05 in November 2017, with retrospective processing occurring over the following 2.5 months. In this version the fully global GPROF estimates were inserted into the complete precipitation fields (precipitationCal, precipitationUncal) outside the standard IR domain (60°N-S), although without morphing or IR fill-in. Recall that GPROF estimates over snowy/icy surface types are set to missing, so data coverage outside 60°N-S is quite limited. Version 05 also marked the introduction of the Quality Index. Because the Version 05 GPROF-TMI estimates had not been computed for the GPM era when the IMERG Runs were retrospectively processed, TMI retrievals are not included in the V05 IMERG datasets.

The Early, Late, and Final Runs all cover the practically useful data record from GPM, starting in March 2014. The Early and Late Runs occasionally suffer data dropouts and faults in the input data that are transient, but are not corrected until after processing. PPS consults with the IMERG team in such cases, usually allowing the deficiency to stand, but occasionally reprocessing the datasets. Such cases are recorded in the IMERG Technical Documentation (see the link to this document at *https://pmm.nasa.gov/data-access/downloads/gpm*, last accessed 17 Nov. 2018, for the latest listing).

One easy way to get a quick qualitative review of recent IMERG performance is by viewing the "last week of IMERG" visualization provided by the Goddard Science Visualization Studio (*https://svs.gsfc.nasa.gov/cgi-bin/details. cgi?aid=4285*, last accessed 17 Nov. 2018).

19.5   IMERG Performance and Examples

A number of studies are available that document IMERG performance, including the "V05 IMERG Final Run Release Notes" (*https://pmm.nasa.gov/sites/default/ files/document_files/IMERG_FinalRun_V05_release_notes-rev3.pdf*, last accessed 17 Nov. 2018), various hydrological assessments (e.g., Sharif et al. 2017; Yuan et al. 2018), and more-general statistical analyses (e.g., Beck et al. 2019; Kim et al. 2017). Additional studies are listed in the GPM citation list (*https://pmm.nasa.gov/ resources/gpm-publications*, last accessed 17 Nov. 2018).
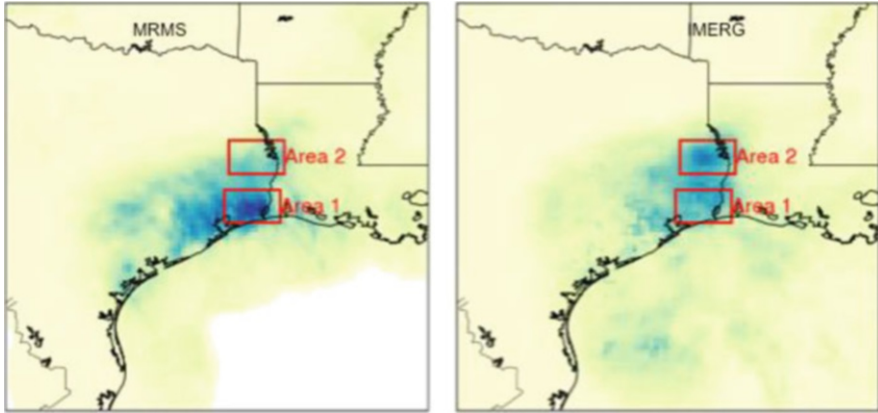
Fig. 19.2 Rainfall accumulations for the week of 25-31 August 2017 over the US Gulf Coast for NOAA Multi-Radar Multi-Sensor (MRMS) data (left) and IMERG V05 Late estimates (right). Houston, Texas is just west of Area 1

One interesting example of IMERG (Late) performance occurred during Hurricane Harvey, which deposited significant, and even all-time record rainfall in the Houston, Texas area in August 2017. The initial analysis showed that IMERG Late underestimated precipitation in the Houston area (just west of, and extending through, Area 1 on Fig. 19.2). However, as the figure shows, Area 2, inland to the north, showed IMERG overestimates. Furthermore, the time series of area-averages in Fig. 19.3 demonstrates that these under- and over-estimates occurred simultaneously. Clearly, the details of the meteorological setting in the two regions are driving systematic and different retrieval errors by GPROF. The IR-based precipitation (Fig. 19.3) is systematically low, a fact we ascribe to its trailing calibration to microwave data: if rain events similar to those in hurricanes have not occurred in the previous 45 days, the calibrations will very likely lead to weaker estimates than are needed to match the hurricane's rainfall.

19.6 Status for Version 06 and Concluding Remarks

The upgrade to Version 06 for IMERG computed in Fall 2019, after this manuscript went to press. The first major change in this version is carrying the retrospective processing back into the TRMM era. For dates before the launch of GPM, the TRMM satellite products will serve as the calibration standard, although some adjustments are necessary to ensure compatibility with GPM-CO products. For example, TRMM's orbital inclination is 35°, so calibration to CORRA must be approximated in the latitudinal band from that point to 65° (GPM's inclination) in both hemispheres. The initial start date is June 2000 to accommodate data
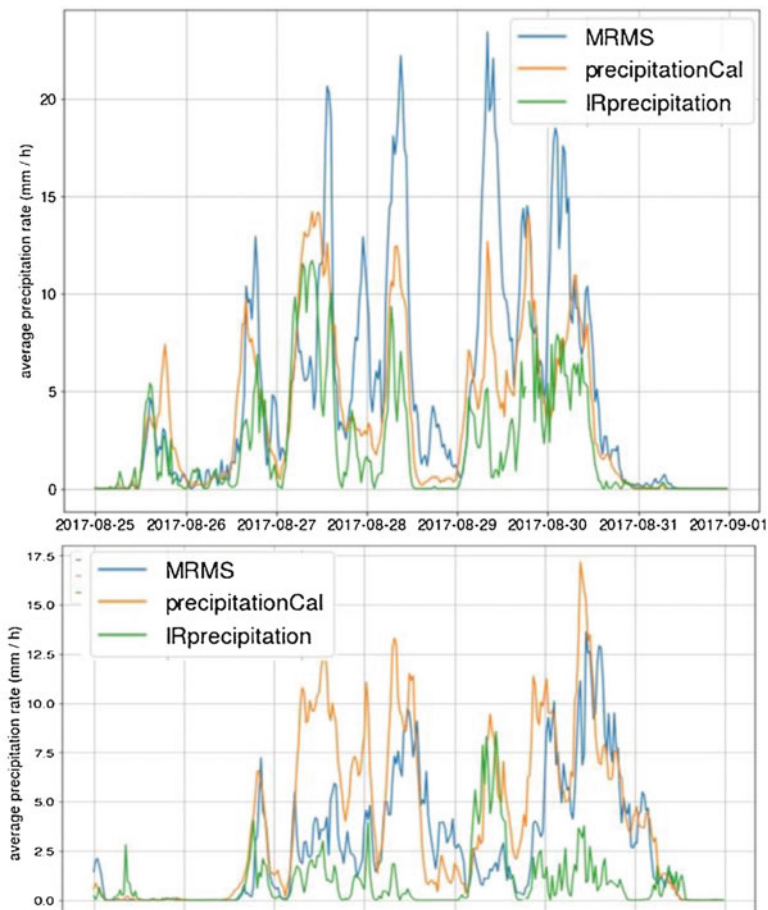
Fig. 19.3 Time series of area-average rainfall for the week of 25-31 August 2017 over the US Gulf Coast for the near-coastal Area 1 (top) and the more inland Area 2 (bottom). Houston, Texas is just west of Area 1. The IMERG Late averages are labeled precipitationCal, and the IR-based precipitation time series is IRprecipitation

availability, but the plan is to extend back to January 1998 when the necessary data are made available.

Another significant change in Version 06 is shifting the source of the motion vectors from IR to vertically integrated vapor (TQV) as depicted in the Modern-Era Retrospective analysis for Research and Applications, Version 2 (MERRA-2) for the Final Run, and in the Global Earth Observing System Forward Processing (GEOS FP) for the Early and Late Runs. This change was necessitated by data availability issues and our intent to extend the morphing technique beyond the 60° N-S latitude extent of the GEO-IR. Testing indicates that the TQV-based vectors have skill that equals or slightly exceeds the skill of the IR-based vectors.

The new TQV-based vectors are computed over the entire globe, so V06 includes morphed PMW estimates wherever the PMW GPROF estimates are considered reliable. Specifically, in the time available, the IMERG team was not able to develop the adjustments necessary to tune GPROF over ice and snow surface types, so areas with ice or snow cover continue to default to IR precipitation (as in previous versions) in the latitude band 60°N-S, and are set to missing at higher latitudes. Nonetheless, providing morphed PMW estimates at higher latitudes will provide a welcome increase in coverage, in summertime land areas, and year-round for open ocean water.

IMERG V06 processing was pursued during summer 2019, and all runs were processed for the complete long-record dataset in fall 2019. That milestone started the countdown to end the computation of the TMPA datasets, which had continued to be produced, even after the demise of TRMM using climatological calibrations, to support users who require a long, relatively homogeneous record. Production of the TMPA datasets was carried to the end of 2019 and ended.

References

Beck, H. E., Pan, M., Roy, T., Weedon, G. P., Pappenberger, F., van Dijk, A. I. J. M., Huffman, G. J., Adler, R. F., & Wood, E. F. (2019). Daily evaluation of 26 precipitation datasets using stage-IV gauge-radar data for the CONUS. *Hydrology and Earth System Sciences*, 23, 207–224. https://doi.org/10.5194/hess-23-207-2019.

Becker, A., Finger, P., Meyer-Christoffer, A., Rudolf, B., Schamm, K., Schneider, U., & Ziese, M. (2013). A description of the global land-surface precipitation data products of the Global Precipitation Climatology Centre with sample applications including centennial (trend) analysis from 1901-present. *Earth System Science Data, 5*, 71–99. https://doi.org/10.5194/essd-5-71-2013.

Hong, Y., Hsu, K.-L., Sorooshian, S., & Gao, X. (2004). Precipitation estimation from remotely sensed imagery using an artificial neural network cloud classification system. *Journal of Applied Meteorology, 43*, 1834–1852. https://doi.org/10.1175/JAM2173.1.

Huffman, G. J., Bolvin, D. T., Nelkin, E. J., Wolff, D. B., Adler, R. F., Gu, G., Hong, Y., Bowman, K. P., & Stocker, E. F. (2007). The TRMM Multi-satellite Precipitation Analysis: Quasi- global, multi-year, combined-sensor precipitation estimates at fine scale. *Journal of Hydrometeorology, 8*, 38–55. https://doi.org/10.1175/JHM560.1.

Huffman, G. J., Adler, R. F., Bolvin, D. T., & Nelkin, E. J. (2010). The TRMM Multi-satellite Precipitation Analysis (TMPA). In F. Hossain & M. Gebremichael (Eds.), *Satellite rainfall applications for surface hydrology*. New York: Springer, ISBN: 978-90-481-2914-0, 3-22.

Joyce, R. J., Janowiak, J. E., Arkin, P. A., & Xie, P. (2004). CMORPH: A method that produces global precipitation estimates from passive microwave and infrared data at high spatial and temporal resolution. *Journal of Hydrometeorology, 5*, 487–503. https://doi.org/10.1175/1525-7541(2004)005<0487%3ACAMTPG>2.0.CO%3B2.

Joyce, R. J., Xie, P., & Janowiak, J. E. (2011). Kalman filter based CMORPH. *Journal of Hydrometeorology, 12*, 1547–1563. https://doi.org/10.1175/JHM-D-11-022.1.

Kidd, C., Matsui, T., Chern, J., Mohr, K., Kummerow, C., & Randel, D. (2016). Global precipitation estimates from cross-track passive microwave observations using a physically based retrieval scheme. *Journal of Hydrometeorology, 17*, 383–400. https://doi.org/10.1175/JHM-D-15-0051.1.

Kim, K., Park, J., Baik, J., & Choi, M. (2017). Evaluation of topographical and seasonal feature using GPM IMERG and TRMM 3B42 over far-East Asia. *Atmospheric Research, 187*, 95–105. https://doi.org/10.1016/j.atmosres.2016.12.007.

Kubota, T., Shige, S., Hashizume, H., Aonashi, K., Takahashi, N., Seto, S., Hirose, M., Takayabu, Y. N., Nakagawa, K., Iwanami, K., Ushio, T., Kachi, M., & Okamoto, K. (2007). Global precipitation map using satellite-borne microwave radiometers by the GSMaP project: Production and validation. *IEEE Transactions on Geoscience and Remote Sensing, 45*, 2259–2275. https://doi.org/10.1109/TGRS.2007.895337.

Kummerow, C. D., Randel, D. L., Kulie, M., Wang, N.-Y., Ferraro, R., Munchak, S. J., & Petkovic, V. (2015). The evolution of the Goddard PROFiling algorithm to a fully parametric scheme. *Journal of Atmospheric and Oceanic Technology, 32*, 2265–2280. https://doi.org/10.1175/JTECH-D-15-0039.1.

Olson, W. S., Masunaga, H., & the GPM Combined Radar-Radiometer Algorithm Team. (2011). GPM combined radar-radiometer precipitation. Algorithm theoretical basis document (Version 2). PPS, NASA/GSFC, 58 pp. Available at *http://pps.gsfc.nasa.gov/Documents/GPM2011CombinedL2ATBD.pdf*, last accessed 17 Nov 2018.

Schneider, U., Becker, A., Finger, P., Meyer-Christoffer, A., Ziese, M., & Rudolf, B. (2014). GPCC's new land-surface precipitation climatology based on quality-controlled in-situ data and its role in quantifying the global water cycle. *Theoretical and Applied Climatology, 115*, 15–40. https://doi.org/10.1007/s00704-013-0860-x.

Schneider, U., Finger, P., Meyer-Christoffer, A., Rustemeier, E., Ziese, M., & Becker, A. (2017). Evaluating the hydrological cycle over land using the newly-corrected precipitation climatology from the Global Precipitation Climatology Centre (GPCC). *Atmosphere, 8*, 52. https://doi.org/10.3390/atmos8030052.

Sharif, H. O., Al-Zahrani, M., & El Hassan, A. (2017). Physically, fully-distributed hydrologic simulations driven by GPM satellite rainfall over an urbanizing arid catchment in Saudi Arabia. *Water, 9*. https://doi.org/10.3390/w9030163.

Sims, E. M., & Liu, G. (2015). A parameterization of the probability of snow–rain transition. *Journal of Hydrometeorology, 16*, 1466–1477. https://doi.org/10.1175/JHM-D-14-0211.1.

Yuan, F., Wang, B., Shi, C., Cui, W., Zhao, C., Liu, Y., Rena, L., Zhang, L., Zhu, Y., Chen, T., Jiang, S., & Yang, X. (2018). Evaluation of hydrological utility of IMERG final run V05 and TMPA 3B42V7 satellite precipitation products in the Yellow River source region, China. *Journal of Hydrology, 567*, 696–711. https://doi.org/10.1016/j.jhydrol.2018.06.045.

Chapter 20
Global Satellite Mapping of Precipitation (GSMaP) Products in the GPM Era

Takuji Kubota, Kazumasa Aonashi, Tomoo Ushio, Shoichi Shige, Yukari N. Takayabu, Misako Kachi, Yoriko Arai, Tomoko Tashima, Takeshi Masaki, Nozomi Kawamoto, Tomoaki Mega, Munehisa K. Yamamoto, Atsushi Hamada, Moeka Yamaji, Guosheng Liu, and Riko Oki

Abstract As the Japanese Global Precipitation Measurement (GPM) product, the Global Satellite Mapping of Precipitation (GSMaP) has been provided by the Japan Aerospace Exploration Agency (JAXA) to distribute hourly global precipitation map with $0.1° \times 0.1°$ lat/lon grid. Since JAXA started near-real-time processing of the GSMaP on November 2007, there have been various significant improvements to the GSMaP. This paper summarizes GSMaP products and related algorithms in the GPM era and shows validation results in Japan and the United States.

T. Kubota (✉) · M. Kachi · T. Tashima · M. Yamaji · R. Oki
Earth Observation Research Center (EORC)/Japan Aerospace Exploration Agency (JAXA), Ibaraki, Japan
e-mail: kubota.takuji@jaxa.jp

K. Aonashi
Meteorological Research Institute, Japan Meteorological Agency, Ibaraki, Japan

T. Ushio · T. Mega
Tokyo Metropolitan University, Tokyo, Japan

S. Shige · M. K. Yamamoto
Kyoto University, Kyoto, Japan

Y. N. Takayabu
Atmosphere and Ocean Research Institute, The University of Tokyo, Chiba, Japan

Y. Arai · T. Masaki · N. Kawamoto
Remote Sensing Technology Center of Japan (RESTEC), Tokyo, Japan

A. Hamada
University of Toyama, Toyama, Japan

G. Liu
Department of Earth, Ocean and Atmospheric Science, Florida State University, Tallahassee, FL, USA

20.1   Introduction

Satellite-based precipitation datasets have been developed to achieve higher spatial
and temporal resolutions using combined data from passive microwave (PMW)
sensors in low Earth orbit and infrared (IR) radiometers in geostationary Earth
orbit. Global Satellite Mapping of Precipitation (GSMaP) is a blended PMW–IR
precipitation product and has been developed in Japan for the Global Precipitation
Measurement (GPM) mission (Hou et al. 2014; Skofronick-Jackson et al. 2017) as
the Japanese GPM standard product.

The GSMaP algorithms have been improved based on various attributes derived
from the Tropical Rainfall Measuring Mission (TRMM) precipitation radar (PR),
which was the first spaceborne precipitation radar and operated during 1997–2015
(Kummerow et al. 1998; Kozu et al. 2001). The combined use of PR and the TRMM
microwave imager (TMI) has greatly improved rainfall estimation technique. Fur-
thermore, the GPM Core Observatory was launched in Feb. 2014, carrying the Dual-
frequency Precipitation Radar (DPR) and the GPM Microwave Imager (GMI). The
DPR and the GMI have further advanced techniques by expanding the coverage of
observations to higher latitudes than those obtained by the TRMM. Moreover,
precipitation information based on differential scattering properties of the dual
frequencies by the DPR can be helpful for improving the PMW algorithms.

The GSMaP project was initiated and sponsored by the Japan Science and
Technology Agency under the Core Research for Evolutional Science and Technol-
ogy from November 2002 (Okamoto et al. 2005; Kubota et al. 2007), and its major
activity was completed in March 2008. Since April 2008, GSMaP activities have
been implemented under the JAXA Precipitation Measuring Mission (PMM) Sci-
ence Team. Since JAXA started near-real-time processing of the GSMaP on
November 2007 (Kachi et al. 2011), there have been various significant improve-
ments of the GSMaP in the GPM era. This paper summarizes the recent progress of
the GSMaP products and related algorithms. Section 20.2 provides an overview of
the GPM-era GSMaP products. Section 20.3 describes recent GSMaP algorithms.
Section 20.4 illustrates validation results in Japan and the United States. Conclusions
are presented in Sect. 20.5.

20.2   GSMaP Product List in the GPM Era

The GSMaP products in the GPM era mainly comprise the "standard product,"
"near-real-time product," "real-time product", and "reanalysis product". Table 20.1
shows the GSMaP product list in the GPM era. The horizontal resolution is
0.1° × 0.1° lat/lon grid, and the temporal resolution is 1 h. All products are
accessible through the "JAXA Global Rainfall Watch" website (http://sharaku.
eorc.jaxa.jp/GSMaP/, last accessed 15 Oct. 2018) (see Fig. 20.1). In addition, the
standard products and the near-real-time products are also accessible via the JAXA
Globe-Portal (G-Portal) (https://www.gportal.jaxa.jp, last accessed 15 Oct. 2018).

Table 20.1 GSMaP product list in the GPM era

Product name	Variables	Resolution	Latency	Update interval
Standard product	Hourly Precip Rate (**GSMaP_MVK**)	Horizontal: 0.1 × 0.1 deg. lat/lon Temporal: 1 h	3 days	1 h
	Gauge-adjusted Hourly Precip Rate (**GSMaP_Gauge**)			
Near-real-time product	Hourly Precip Rate (**GSMaP_NRT**)		4 h	
	Gauge-adjusted Hourly Precip Rate (**GSMaP_Gauge_NRT**)			
Real-time product	Hourly Precip Rate (**GSMaP_NOW**)		0 h	0.5 h
Reanalysis product	Hourly Precip Rate (**GSMaP_RNL**)		Occasionally reprocesses past periods data	
	Gauge-adjusted Hourly Precip Rate (**GSMaP_Gauge_RNL**)			
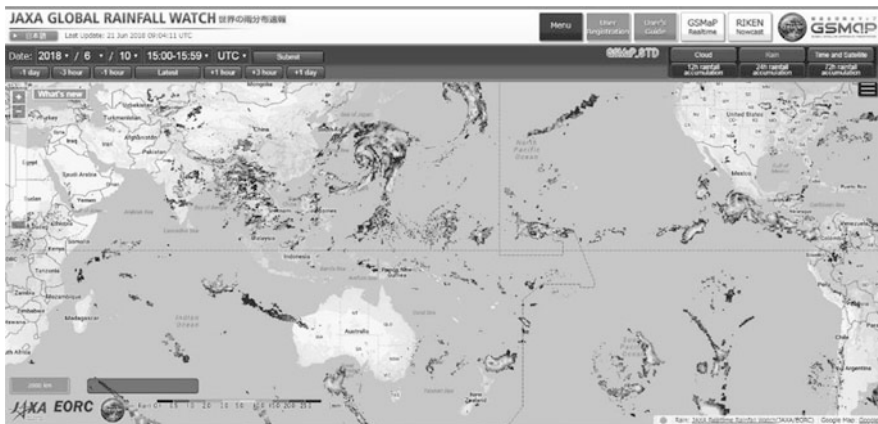
Fig. 20.1 Image of "JAXA Global Rainfall Watch" website (http://sharaku.eorc.jaxa.jp/GSMaP/, last accessed 15 Oct. 2018)

The standard products are processed 3 days after observations and consist of satellite-only hourly precipitation rate (GSMaP_MVK, hereafter, MVK) and gauge-adjusted hourly precipitation rate (GSMaP_Gauge, hereafter, GA).

On the other hand, the near-real-time products are processed 4 h after observations and consist of satellite-only hourly precipitation rate (GSMaP_NRT, hereafter, NRT) and gauge-adjusted hourly precipitation rate (GSMaP_Gauge_NRT, hereafter GA_NRT).

The near-real-time algorithm is based on the standard algorithm, but some simplifications in the processing are implemented to keep operability and data latency within near-real-time. The major differences between the near-real-time and standard processing are as follows.

- In the near-real-time processing, forecast data are used as atmospheric information.
- Latest available data are used for sea surface temperature (SST) information.
- Only temporarily forward cloud movement is used in the PMW–IR combined algorithm.
- Only statistical parameters are used in gauge-adjustment algorithm.

Furthermore, the real-time product "GSMaP_NOW" (hereafter, NOW) is processed to produce estimates at the current hour. The NOW has been provided over the Japan Meteorological Agency (JMA)'s geostationary satellite "Himawari-8" (Bessho et al. 2016) region since November 2015. Since November 2018, the NOW has been extended to regions of the European Organization for the Exploitation of Meteorological Satellites (EUMETSAT). Further extensions to other global domains were established using satellite data from the National Oceanic and Atmospheric Administration (NOAA) in June 2019. Major differences between real-time and near-real-time processing are as follows.

- In the real-time processing, data that is available within 0.5 h after observations are collected, while the data that is available within 3 h are collected in the near-real-time processing.
- Data received at direct readout stations for Advanced Microwave Scanning Radiometer-2 (AMSR2) and the Direct Broadcast Network (DBNet) are used to increase PMW data collection in the real-time processing.
- A 0.5-h forward extrapolation (future direction) applied by cloud motion vector is used to produce estimates at the current hour.
- The NOW product is updated half-hourly, while other products are updated hourly.

These features and differences among products are directly related to accuracies of the products, which are later verified in this paper using gauge-corrected ground-radar dataset.

Reanalysis products (GSMaP_RNL and GSMaP_RNL_Gauge) are calculated with Japanese 55-year reanalysis (JRA55) (Kobayashi et al. 2015; Harada et al. 2016) and occasionally reprocesses historical data. The data of March 2000 to February 2014 are now available in the reanalysis product. Our preliminary analyses show differences between the reanalysis and the standard products are small and therefore, users can combine these for long-term analyses. This reanalysis product has been scheduled to be integrated into the standard product around early 2020 in the JAXA GPM mission.

In addition, the RIKEN, a research institute in Japan, has provided GSMaP RIKEN Nowcast (GSMaP_RNC) data developed based upon Otsuka et al. (2016) since 2017. This data is also available from JAXA/EORC ftp site.

20.3   Algorithm Description

The GSMaP products were significantly updated on September 2014 and January 2017 after the GPM Core Observatory was launched. The product corresponding to the algorithm updates on September 2014 is referred to as Product version V03 and Algorithm version V6, and the product corresponding to the algorithm updates on January 2017 is referred to as Product version V04 and Algorithm version V7. In this section, algorithms are summarized referring to previous papers, and algorithm versions are used for classification between both updates. Evolutions of the algorithms from V6 to V7 are briefly summarized in Sect. 20.3.9. Currently, both V6 and V7 algorithms are processed at the JAXA.

20.3.1   Overall Algorithm Framework

Core algorithms of the GSMaP products are based on those provided by the GSMaP project: PMW precipitation retrieval algorithm, PMW–IR combined algorithm, and gauge-adjustment algorithm. Figure 20.2 shows a process flowchart for the GSMaP product.

The GSMaP algorithms use several ancillary data as operational inputs. JMA global analysis (GANAL) and forecast (FCST) data set, which have 6-hourly and 0.5° grid box resolution, are used as ancillary data of atmospheric conditions to calculate look-up tables (LUTs), which are referenced by the PMW algorithms.
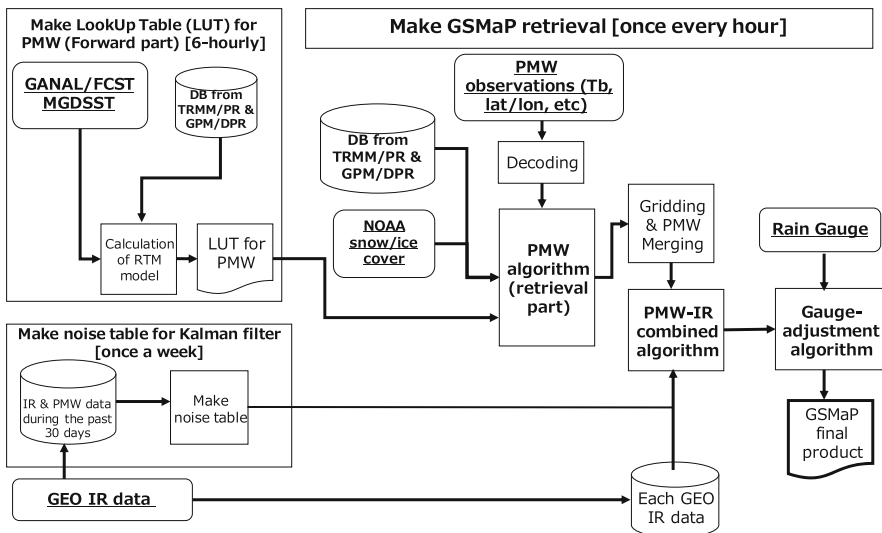
Fig. 20.2   Process flowchart for the GSMaP product

GANAL data are used to process standard products, and FCST data are used to process near-real-time products. In the reanalysis product, the JRA-55 data (6-hourly, TL319L60 model grid) are used instead of operational data. The JMA merged satellite and in situ data global daily SST (MGDSST) data, which are on a 0.25° grid box, are used as ancillary data of SST for calculating LUTs, which are referenced by the PMW algorithms.

The NOAA Climate Prediction Center (CPC) unified gauge-based analysis of global daily precipitation (Chen et al. 2008), which is on a 0.5° grid box, has been used as an input to calculate gauge-adjusted rainfall.

Climatological sea ice values from the JAXA Advanced Microwave Scanning Radiometer for EOS (AMSR-E) product were used for screening sea ices in V6, while ancillary data for surface snow were not used. In the V7, the NOAA National Environmental Satellite, Data, and Information Service (NESDIS) multi-sensor snow/ice cover maps were used as ancillary data to detect the sea ice and the surface snow, which are referenced by the PMW algorithms.

20.3.2 Outline of the PMW Algorithm

The PMW algorithm retrieves global precipitation rates from PMW sensor brightness temperatures (Tbs). The PMW algorithm has been improved based upon the Microwave Imager (MWI) algorithm of Aonashi et al. (2009). The basic idea of the PMW algorithm is to find precipitation rates that give Tb, computed through radiative transfer model, that best fit with the observed Tbs. The MWI algorithm employs polarization corrected temperatures (PCTs) at higher frequencies (37 and 85 GHz for the TMI) over land and coast, and Tbs with vertical polarization at lower frequencies (10, 19, and 37 GHz for the TMI) in addition to the higher frequency PCTs over ocean. Several modifications due to sensor specifications are highlighted in Sect. 20.3.5.

20.3.3 Methodology in the PMW Algorithm

The PMW algorithm consists of a forward calculation part and a retrieval part. In the forward calculation part, LUTs are calculated for homogeneous precipitation by incorporating atmospheric and surface variables of the GANAL or FCST data and precipitation physical models based on spaceborne precipitation radar observations into the RTM program of Liu (1998). The precipitation physical models have been developed in previous efforts (Takayabu 2008; Takahashi and Awaka 2005; Kozu et al. 2009; Yamaji et al. 2017). In the construction of the model, the TRMM/PR data were used in V6 algorithm, and both the TRMM/PR and GPM/DPR data were used in the V7 algorithm. The land surface emissivity was used from the TRMM observations (Furuzawa et al. 2012). LUTs for inhomogeneous precipitation are

derived from the above LUTs using the approximations of Aonashi and Liu (2000) and Kubota et al. (2009a).

The retrieval part of the PMW algorithm performs the detection of rainfall using scattering signals over land, and emission signals over ocean. Methods of Seto et al. (2005, 2008, 2016), Mega and Shige (2016), and Kida et al. (2009, 2010a) were adopted for the rainfall detection over land, coastal areas, and ocean, respectively. Seto et al. (2005) was used in both V6 and the V7 in the TMI over-land algorithm. In the algorithms for the other PMW sensors, Seto et al. (2008) was applied in V6, and a method using the DPR and the GMI (Seto et al. 2016), similar to Seto et al. (2005) of TRMM, was applied in V7. In addition, the over-ocean detection is improved in V7 by consideration of cloud liquid water estimated from 37 GHz Tbs (Aonashi et al. 2016).

Dual-frequency PCTs (at 37 and 85 GHz for TMI) are employed in retrievals using scattering signals. An adjustment method is introduced using indices of frozen precipitation depth and surface temperature. In the over-ocean retrieval using emission signals, a rainfall rate is derived by minimizing a cost function for lower frequency, vertically polarized Tbs (10, 19, and 37 GHz for the TMI), with the scattering retrievals as the first guess.

20.3.4   Orographic/Non-orographic Rainfall Classification Scheme

Over coastal mountain ranges, heavy rainfall can be caused by shallow orographic rainfall, which is inconsistent with the assumption in the PMW algorithm that heavy rainfall results from deep clouds with significant ice. For example, severe underestimation of the GSMaP rainfall estimates in old versions were found over orographic rainfall areas in Japan (Kubota et al. 2009b). Therefore, orographic/non-orographic rainfall classification scheme was developed (Shige et al. 2013; Taniguchi et al. 2013) and installed in the PMW algorithm. LUTs for orographic rainfall are calculated according to Shige et al. (2014). In addition, a detection scheme has been developed for orographic rainfall areas where the LUTs for orographic rainfall are applied. The scheme and modified one were installed in V6 (Yamamoto and Shige 2015) for the TMI and V7 (Yamamoto et al. 2017) for all sensors, respectively.

20.3.5   Modifications Due to Sensor Specifications

While the basic structure described above is common to the PMW algorithms, several modifications have been applied because of sensor specifications. Shige et al. (2009) developed a Microwave Sounder (MWS) algorithm which combines an emission-based estimate from Tb data at 23 GHz and a scattering-based estimate

from Tb data at 89 GHz over ocean, depending on a scattering index computed from Tb at both 89 and 150 GHz. The scattering index, which is designed on the basis that Tb decreases in response to scattering by precipitation at these frequencies, also responds to emission in light rain with a low concentration of cloud liquid water, leading to detection of light rain pixel (Kida et al. 2010b). In addition, the MWS algorithm adopts a rain/no-rain classification method over land using 150 and 183 GHz channels, as described in Kida et al. (2017).

The Special Sensor Microwave Imager/Sounder (SSMIS) or Special Sensor Microwave/Imager (SSM/I) do not have 10 GHz channels. Therefore, the over-ocean algorithms for the SSMIS and the SSM/I us the normalized polarization differences (Petty 1994) at 19 GHz, and combine them with emission-based estimates from Tb at 19 GHz vertical polarization and scattering-based estimates from the PCTs at 89 GHz (Hashizume et al. 2006; Kubota et al. 2011).

20.3.6 Snowfall Estimation Method

Recently, a snowfall estimation algorithm was implemented in the V7 algorithm (Kubota et al. 2018). In the V6 or earlier versions, there was no snowfall estimation in the GSMaP products. The snowfall estimation method can be divided into a method of classifying precipitation phase (rain/snow) and if determined to be snow, a method of estimating snowfall intensity. Here, the rain/snow classification method is based upon the method of Sims and Liu (2015), with inputs of the GANAL/FCST data. Based on the results of past ground observations, the method determines the precipitation phase, whether rain or snow. The snowfall intensity estimation method was developed using the CloudSat-GPM coincidence dataset, based upon the method of Liu and Seo (2013). This statistical method which uses radar observations to train the PMW data uses information contained in the first three principal components that resulted from an empirical orthogonal function. In the V7, the snowfall estimation method was installed for GMI and the SSMIS sensors.

20.3.7 PMW–IR Combined Algorithm

The PMW–IR combined algorithm integrates PMW data with infrared radiometer data to achieve high temporal (1 h) and spatial (0.1 degree) resolution global precipitation estimates. The product is produced based on a Kalman filter model that refines the precipitation rate propagation based on the atmospheric moving vector derived from two successive IR images (Ushio et al. 2009). Noise and coefficients in the Kalman filter model are calculated once a week using IR and PMW data during the past 30 days, as described in Fig. 20.2. As noted in Sect. 20.2, both temporarily forward and backward cloud motions are used in the MVK, while only temporarily forward cloud motion is used in the NRT and the NOW.

20.3.8   Gauge-Adjustment Algorithm

The GA algorithm adjusts the MVK estimates with the NOAA/CPC unified gauge-based analysis of global daily precipitation. The estimate is adjusted only over land. The rain rate over ocean from GA and GA_NRT are the same as those from MVK and NRT, respectively. The algorithm uses an optical estimation scheme, in which the solution is calculated by maximizing the probability density function defined in the system model (Mega et al. 2019). The hourly rain rate of the GA is adjusted by this algorithm so that the sum of the 24-h rain of the GA rate is roughly the same as the gauge measurement. A number of gauges available in each 0.5 deg. lat/lon grid box was considered in V7, while it was not considered in V6. While the parameters were assumed to be constant in the V6 GA_NRT, statistical parameters were improved to be calculated from data during the past 30 days in the V7 GA_NRT. On the other hand, a method similar to the GA_NRT V7 was also applied to the GA_NRT V6 as a minor version-upgrade in December 2018. Therefore, the GA_NRT method is essentially identical between V6 and V7 after December 2018.

20.3.9   Brief Summary of Evolutions from V6 to V7

In the above sub-sections, the algorithms were described for both V6 and the V7. Table 20.2 provides a brief summary of evolutions in the algorithms from V6 to V7.

Table 20.2 Brief summary of evolutions in the algorithms from V6 to V7

| Item	V6	V7
Utilization of spaceborne radar data in precipitation physical models	TRMM/PR	TRMM/PR and GPM/DPR
Ancillary data for sea ice	JAXA AMSR-E (climatological)	NESDIS
Ancillary data for surface snow	None	NESDIS
Detection over the land for MWI/SSMIS/GMI	Seto et al. (2008)	Seto et al. (2016)
Detection over the ocean for MWI/SSMIS/GMI	Kida et al. (2009, 2010a)	Kida et al. (2009, 2010a) and Aonashi et al. (2016)
Orographic/non-orographic rainfall classification scheme	Yamamoto and Shige (2015) for the TMI	Yamamoto et al. (2017) for all sensors
Snowfall estimation method	Not implemented	Implemented in GMI/SSMIS
Consideration of gauge numbers in the gauge-adjustment algorithm	Not included	Included

20.4 Validation Results of the GSMaP Products

The validation of satellite products using ground instruments can be helpful to understand the products strengths and limitations. Validation results using gauge-corrected radar data around Japan and the contiguous United States (CONUS) are shown in this section. The GSMaP V6 products are analyzed here, and the validation using the GSMaP V7 has been left for future works. As noted in the previous section, the GA_NRT V6 had significant improvements in December 2018, and thus not considered in the validations.

20.4.1 Comparisons of the GSMaP Products Around Japan

This sub-section compares the GSMaP Products listed in Sect. 20.2 around Japan with reference to a ground-radar dataset calibrated by rain gauges provided by the JMA, termed "Radar-AMeDAS" data. Here, observation areas of the Radar-AMeDAS were limited to within 250 km of radar sites. In addition, the NOAA/NESDIS hydro-estimator (H-E) (Vicente et al. 1998, 2002; Scofield and Kuligowski 2003) is also analyzed because the H-E is a well-known IR-based satellite rainfall product with a latency of less than 30 min. Although previous work (e.g., Ebert et al. 1996; Smith et al. 1998; Beck et al. 2017) indicate that the IR-based products are less accurate than the PMW-based product, the low latency of the IR-based products can be attractive for users. The NOW system was developed with a higher priority on low latencies, and comparisons between the H-E and the NOW are interesting as both products have similar latencies.

Figure 20.3 shows the horizontal distribution of the daily rain amount around Japan in 0.25 deg lat/lon grid on June 25, 2017. The rainfall pattern related to the Baiu front, which is typical in a rainy season around Japan, was around the southern coast of Japan's main islands. Here, root mean square error (RMSE) and correlation coefficient (CC) are adopted as statistical indices and noted in the figures. The CC is sensitive to the rainfall spatial pattern, and the RMSE is sensitive to the rainfall intensity. Among the GSMaP products, the GA has the lowest RMSE and highest CC, while the NOW has the highest RMSE and lowest CC. On the other hand, the NOW shows better results than the H-E for this case study (Fig. 20.3).

To obtain more reliable results, these analyses were extended to a 21-month period: Apr. 1, 2017 to Dec. 31, 2018. Figure 20.4 shows the time series of the CC for the GSMaP products and the H-E referenced to the JMA's Radar-AMeDAS around Japan, and Fig. 20.5 shows the time series of the RMSE. Table 20.3 shows the CC and RMSE averaged values over 21 months. Table 20.3 clearly indicates the accuracies of the GSMaP products, where GA > MVK > NRT > NOW. This tendency was stable in the time series of the CC (Fig. 20.4) and the RMSE (Fig. 20.5). The GA has the best accuracy because of the adjustment using the gauge. As in Kubota et al. (2009b) and Kachi et al. (2011), seasonal changes of the
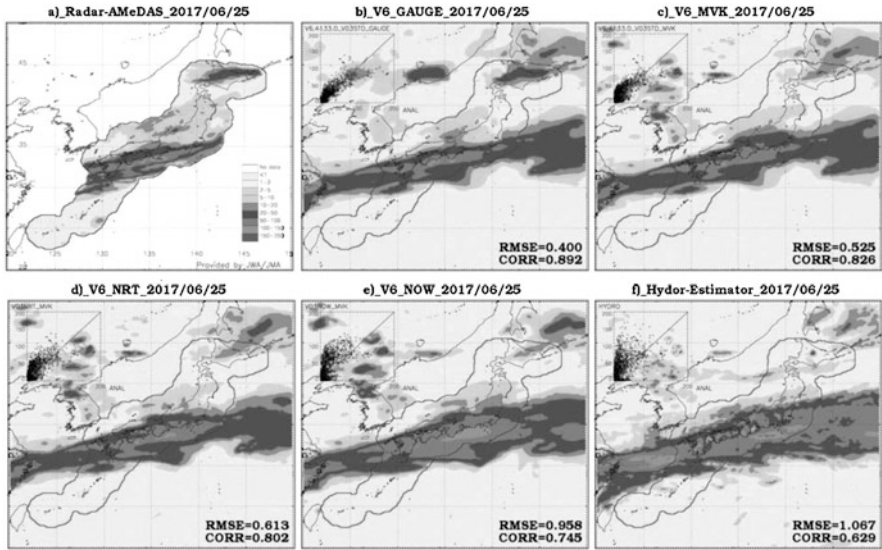
Fig. 20.3 Distribution of the daily rain amount around Japan on June 25, 2017 for (**a**) JMA radar-AMeDAS, (**b**) GA V6, (**c**) MVK V6, (**d**) NRT V6, (**e**) NOW V6, and (**f**) Hydro-Estimator (H-E)
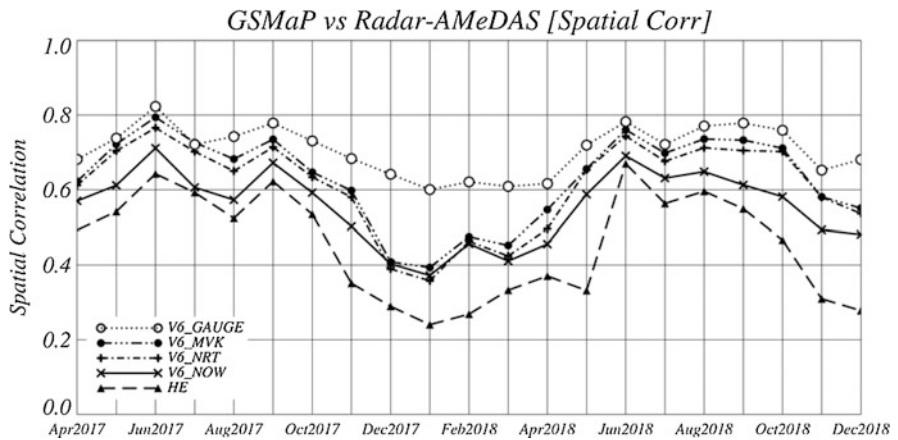
Fig. 20.4 Time series of the correlation coefficient (CC) for the GSMaP products and the H-E with reference to the JMA's Radar-AMeDAS around Japan in 0.25 deg lat/lon grid and daily accumulation from Apr. 1, 2017 to Dec. 31, 2018. Monthly mean was applied to the daily CC values. Open circles denote the GA; closed circles denote the MVK; plusses denote the NRT; crosses denote the NOW; and triangles denote the H-E

spatial correlation coefficients were found for the MVK, the NRT, and the NOW, because of poor skills caused by false signals related to surface snow in a cold season. On the other hand, amplitudes of the seasonal changes were smaller in the GA, and this suggests that the poor skills in the colder season were mitigated in the
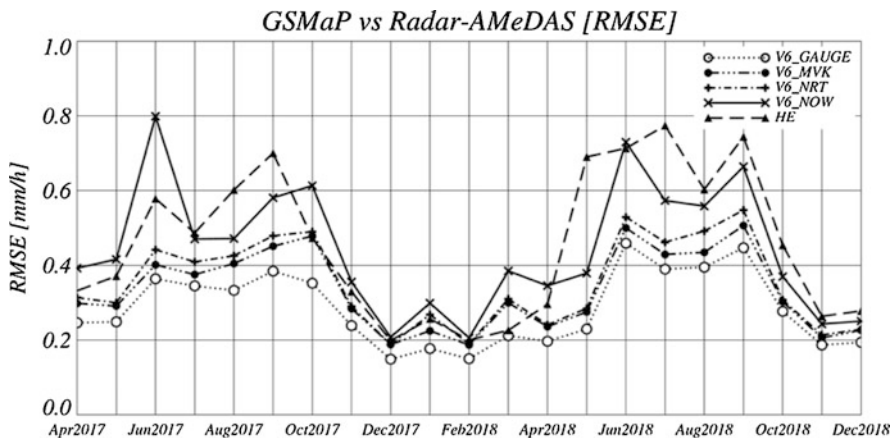
Fig. 20.5 Time series of the root mean square error (RMSE) for the GSMaP products and the H-E with reference to the JMA's Radar-AMeDAS around Japan in 0.25 deg lat/lon grid and daily accumulation from Apr. 1, 2017 to Dec. 31, 2018. Monthly mean was applied to the daily RMSE values. Open circles denote the GA; closed circles denote the MVK; plusses denote the NRT; crosses denote the NOW; and triangles denote the H-E

Table 20.3 Values of the CC and RMSE averaged during 21 months: April 2017 to December 2018

Product name	GA	MVK	NRT	NOW	H-E
CC	0.71	0.63	0.61	0.56	0.46
RMSE (mm/h)	0.28	0.33	0.35	0.44	0.45

GA. As noted in Sect. 20.3.2, some simplifications in the processing are implemented in the NRT to keep operability and data latency in near-real-time, and thus, results of the MVK are better than those of the NRT. With respect to comparison of the NRT and the NOW, the NOW uses the PMW–IR combined algorithm in wider areas than the NRT, due to decreases of the PMW coverage caused by its earlier data collection. As noted in Sect. 20.3.2, the NOW adopted a 0.5-h forward extrapolation. However, degradation of the 0.5-h forward extrapolation was examined with reference to JMA's Radar-AMeDAS, and results showed that this can be regarded as small (not shown). Therefore, the poorest accuracy of the NOW may be due to the decreases of the PMW coverage. These results suggest an evident trade-off between latency and accuracy, and the choice of a GSMaP product should be dependent upon its purposes.

The H-E has the worst CC averaged value, and its RMSE average is slightly worse than that of the NOW (Table 20.3). While the CC values for the NOW were better than those for the H-E in all periods (Fig. 20.4), the H-E has the better RMSE values than the NOW over some periods (Fig. 20.5). In the NOW, displacements of rain peaks can occur because the cloud motion may be inconsistent with the rain movement in areas of strong wind shear. Worse results of the NOW in RMSE

implies such rain peak displacements may be problematic in the NOW. Thus, the PMW-based real-time technique in the NOW showed better performances than the IR-based estimates from the H-E, in particular, for spatial patterns evaluated by the CC, while there can be still future tasks in the NOW, including issues of strong wind shear.

20.4.2 Validation Using the US Radar Network

This sub-section provides validation results over the CONUS using Multi-Radar Multi-Sensor (MRMS) precipitation data (Zhang et al. 2011, 2016). The MRMS is a system with automated algorithms that quickly and intelligently integrates data streams from multiple radars, surface observations, and various data sources. Here, the Level-3 MRMS dataset processed in support of the GPM Mission (Kirstetter et al. 2012; Tan et al. 2016) was used. The analysis is conducted over 3 months: June 2015 to August 2015. The original spatial resolution of the Level-3 MRMS is 0.01 degrees, and it was converted to the same grid of $0.1° \times 0.1°$ as the GSMaP.

Figure 20.6 shows distributions of rainfall over June to August 2015 (92 days) for the MRMS, MVK V6, and GA V6. In this paper, the MRMS was analyzed over areas where the radar quality index (RQI) was more than 50. The RQI ranges between from 0 (lowest confidence) to 100 (highest confidence) and observations of the MRMS over Rocky Mountains were partly excluded by the condition of the RQI > 50. In all the figures, rainfall is largest in the central portion of the US, decreasing to the eastern as well as western parts.

Two-dimensional distribution functions between the MRMS and the GSMaP are shown in Fig. 20.7. Here, daily rain amounts of the MRMS and the GSMaP were calculated with 379 boxes of the $1.5° \times 1.5°$ lat/lon grids over the CONUS, and Fig. 20.7 shows that both GSMaP estimates corresponded well with that of the MRMS. The statistical values denoted in Fig. 20.7 were calculated for every 0.2 mm h^{-1} bins of the MRMS up to 2.0–2.2 mm h^{-1} with more than 10 samples.
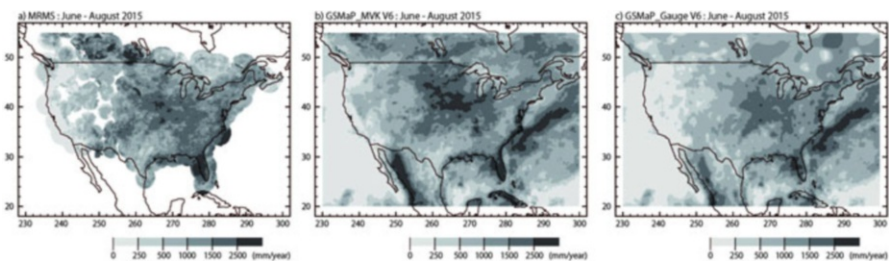
Fig. 20.6 Accumulated rainfall (mm year^{-1}) over 3 months: June to August 2015 for (**a**) MRMS, (**b**) MVK V6, and (**c**) GA V6. The MRMS was analyzed over areas where the RQI was more than 50
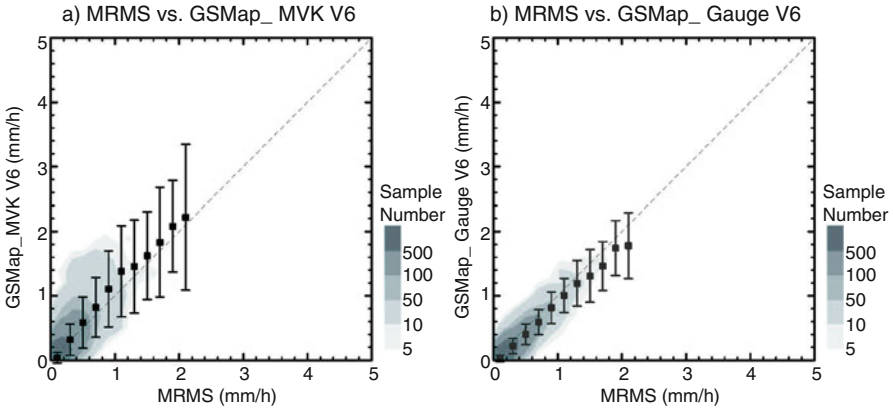
Fig. 20.7 Two-dimensional distribution function of daily precipitation over 3 months from June to August 2015. Horizontal axis shows the rain rate of the MRMS, and vertical axis shows rain rates of (**a**) MVK and (**b**) GA. Hatch color shows the sample number of occurrences. The average value (squares) and the standard deviation (1 sigma, bars) are shown for bins of 0.2 mm h^{-1} of the MRMS with the horizontal axis as a reference. The broken line is a one-to-one line

For the MVK and GA, the averages are basically distributed along the one-to-one line, which suggests biases in both GSMaP products are relatively small. Here, errors were calculated as normalized absolute differences, i.e., |GSMaP-MRMS|/MRMS (%), in the bins. The largest value among the error for the MVK is 26.59%, found in the bin of 1.0–1.2 mm h^{-1}, and that for the GA is 22.75% found in the bin of 0.2–0.4 mm h^{-1}. On the other hand, standard deviations of the GSMaP in bins of the MRMS, denoted by the bars, were much larger in the MVK than in the GA. The largest value among the standard deviations for the MVK is 1.13 mm h^{-1}, and that for the GA is 0.51 mm h^{-1}, found in the bin of 2.0–2.2 mm h^{-1}. This suggests that the adjustment using the gauge data largely reduced the daily variation of the errors.

20.5 Conclusions

As the Japanese GPM product, the GSMaP products have been provided by JAXA to distribute hourly global precipitation map with 0.1° × 0.1° lat/lon grid. Since JAXA started near-real-time processing of the GSMaP on November 2007, there have been various significant updates to the GSMaP. This paper describes the GSMaP products and related algorithms in the GPM era. It also shows validation results over Japan and CONUS. Based upon the validation results around Japan, the accuracy of the GSMaP products have been verified to be as follows: GA > MVK > NRT > NOW. This suggests the evident trade-off between latency and accuracy, and the choice of a GSMaP product should depend upon its purposes. The comparison

between the NOW and the H-E suggests that the PMW-based real-time technique in the NOW can be better than the IR-based estimates, in particular, for the spatial patterns. The validation results over the CONUS during Jun.-Aug. 2015 suggest that the adjustment using the gauge data largely reduced the daily variation of the errors.

The Algorithm V6 released on September 2014 and V7 released on January 2017 after the launch of the GPM Core Observatory were described in this paper. The following version, V8 is now scheduled to be released in 2020. Algorithm developments toward V8 are currently in progress. These will be described in future articles.

References

Aonashi, K., & Liu, G. (2000). Passive microwave precipitation retrievals using TMI during the Baiu period of 1998. Part I: Algorithm description and validation. *Journal of Applied Meteorology, 39*, 2024–2037. https://doi.org/10.1175/1520-0450(2000)039<2024:PMPRUT>2.0.CO;2.

Aonashi, K., Awaka, J., Hirose, M., Kozu, T., Kubota, T., Liu, G., Shige, S., Kida, S., Seto, S., Takahashi, N., & Takayabu, Y. N. (2009). GSMaP passive, microwave precipitation retrieval algorithm: Algorithm description and validation. *Journal of the Meteorological Society of Japan, 87A*, 119–136. https://doi.org/10.2151/jmsj.87A.119.

Aonashi, K., Ohwada, H., Okamoto, K., Ishimoto, H., & Yamaguchi, M. (2016). Development of the next-generation microwave imager precipitation retrieval algorithm (No. 4). *MSJ spring meeting 2016*, C154, Tokyo, Japan, May 2016 (in Japanese).

Beck, H. E., Vergopolan, N., Pan, M., Levizzani, V., van Dijk, A. I. J. M., Weedon, G. P., Brocca, L., Pappenberger, F., Huffman, G. J., & Wood, E. F. (2017). Global-scale evaluation of 22 precipitation datasets using gauge observations and hydrological modeling. *Hydrology and Earth System Sciences, 21*, 6201–6217. https://doi.org/10.5194/hess-2017-508.

Bessho, K., Date, K., Hayashi, M., Ikeda, A., Imai, T., Inoue, H., Kumagai, Y., Miyakawa, T., Murata, H., Ohno, T., Okuyama, A., Oyama, R., Sasaki, Y., Shimazu, Y., Shimoji, K., Sumida, Y., Suzuki, M., Taniguchi, H., Tsuchiyama, H., Uesawa, D., Yokota, H., & Yoshida, R. (2016). An introduction to Himawari-8/9— Japan's new-generation geostationary meteorological satellites. *Journal of the Meteorological Society of Japan, 94*, 151–183. https://doi.org/10.2151/jmsj.2016-009.

Chen, M., Shi, W., Xie, P., Silva, V. B. S., Kousky, V. E., Wayne Higgins, R., & Janowiak, J. E. (2008). Assessing objective techniques for gauge-based analyses of global daily precipitation. *Journal of Geophysical Research, 113*, D04110. https://doi.org/10.1029/2007JD009132.

Ebert, E. E., Manton, M. J., Arkin, P. A., Allam, R. J., Holpin, G. E., & Gruber, A. J. (1996). Results from the GPCP algorithm Intercomparison programme. *Bulletin of the American Meteorological Society, 77*, 2875–2887. https://doi.org/10.1175/1520-0477(1996)077<2875:RFTGAI>2.0.CO;2.

Furuzawa, F. A., Masunaga, H., & Nakamura, K. (2012) Development of a land surface emissivity algorithm for use by microwave rain retrieval algorithms. In *Proceedings of SPIE, Remote*

Sensing of the Atmosphere, Clouds, and Precipitation IV, 8523, W1-12, Kyoto. https://doi.org/10.1117/12.977237.

Harada, Y., Kamahori, H., Kobayashi, C., Endo, H., Kobayashi, S., Ota, Y., Onoda, H., Onogi, K., Miyaoka, K., & Takahashi, K. (2016). The JRA-55 reanalysis: Representation of atmospheric circulation and climate variability. *Journal of the Meteorological Society of Japan, 94*, 269–302. https://doi.org/10.2151/jmsj.2016-015.

Hashizume, H., Kubota, T., Aonashi, K., Shige, S., & Okamoto, K. (2006). Development of over-ocean SSM/I rain retrieval algorithm in the GSMaP project. In *Proceedings of IGARSS 2006*, 2588-2591, Denver, CO. https://doi.org/10.1109/IGARSS.2006.669.

Hou, A. Y., Kakar, R. K., Neeck, S., Azarbarzin, A. A., Kummerow, C. D., Kojima, M., Oki, R., Nakamura, K., & Iguchi, T. (2014). The Global Precipitation Measurement mission. *Bulletin of the American Meteorological Society, 95*, 701–722. https://doi.org/10.1175/BAMS-D-13-00164.1.

Kachi, M., Kubota, T., Ushio, T., Shige, S., Kida, S., Aonashi, K., & Okamoto, K. (2011). Development and utilization of "JAXA global rainfall watch" system. *IEEJ Transactions Fundamentals and Materials, 131*, 729–737. (In Japanese with English abstract).

Kida, S., Shige, S., Kubota, T., Aonashi, K., & Okamoto, K. (2009). Improvement of rain/no-rain classification methods for microwave radiometer observations over ocean using the 37-GHz emission signature. *Journal of the Meteorological Society of Japan, 87A*, 165–181. https://doi.org/10.2151/jmsj.87A.165.

Kida, S., Shige, S., Manabe, T., L'Ecuyer, T. S., & Liu, G. (2010a). Cloud liquid water path for the rain/no-rain classification method over ocean in the GSMaP algorithm. Transaction JSASS Aerospace Tech. Japan, 8, No. ists27, Pn_19-Pn_23.

Kida, S., Shige, S., & Manabe, T. (2010b). Comparison of rain fractions over tropical and sub-tropical ocean obtained from precipitation retrieval algorithms for microwave sounders. *Journal of Geophysical Research, 115*, D24101. https://doi.org/10.1029/2010JD014279.

Kida, S., Kubota, T., Shige, S., & Mega, T. (2017). Development of a rain/no-rain classification method over land for the microwave sounder algorithm. In T. Islam, Y. Hu, A. Kokhanovsky, & J. Wang (Eds.), *Remote sensing of aerosols, clouds, and precipitation* (pp. 249–265). Amsterdam: Elsevier, ISBN:9780128104378.

Kirstetter, P.-E., Hong, Y., Gourley, J. J., Chen, S., Flamig, Z., Zhang, J., Schwaller, M., Petersen, W., & Amitai, E. (2012). Toward a framework for systematic error modeling of spaceborne precipitation radar with NOAA/NSSL ground radar–based National Mosaic QPE. *Journal of Hydrometeorology, 13*, 1285–1300. https://doi.org/10.1175/JHM-D-11-0139.1.

Kobayashi, S., Ota, Y., Harada, Y., Ebita, A., Moriya, M., Onoda, H., Onogi, K., Kamahori, H., Kobayashi, C., Endo, H., Miyaoka, K., & Takahashi, K. (2015). The JRA-55 reanalysis: General specifications and basic characteristics. *Journal of the Meteorological Society of Japan, 93*, 5–48. https://doi.org/10.2151/jmsj.2015-001.

Kozu, T., Kawanishi, T., Kuroiwa, H., Kojima, M., Oikawa, K., Kumagai, H., Okamoto, K., Okumura, M., Nakatsuka, H., & Nishikawa, K. (2001). Development of precipitation radar onboard the Tropical Rainfall Measuring Mission (TRMM) satellite. *IEEE Transactions on Geoscience and Remote Sensing, 39*, 102–116. https://doi.org/10.1109/36.898669.

Kozu, T., Iguchi, T., Kubota, T., Yoshida, N., Seto, S., Kwiatkowski, J., & Takayabu, Y. N. (2009). Feasibility of raindrop size distribution parameter estimation with TRMM Precipitation Radar. *Journal of the Meteorological Society of Japan, 87A*, 53–66. https://doi.org/10.2151/jmsj.87A.53.

Kubota, T., Shige, S., Hashizume, H., Aonashi, K., Takahashi, N., Seto, S., Hirose, M., Takayabu, Y. N., Ushio, T., Nakagawa, K., Iwanami, K., Kachi, M., & Okamoto, K. (2007). Global precipitation map using satellite-borne microwave radiometers by the GSMaP project: Production and validation. *IEEE Transactions on Geoscience and Remote Sensing, 45*, 2259–2275. https://doi.org/10.1109/TGRS.2007.895337.

Kubota, T., Shige, S., Aonashi, K., & Okamoto, K. (2009a). Development of nonuniform beamfilling correction method in rainfall retrievals for passive microwave radiometers over

ocean using TRMM observations. *Journal of the Meteorological Society of Japan, 87A*, 153–164. https://doi.org/10.2151/jmsj.87A.153.

Kubota, T., Ushio, T., Shige, S., Kida, S., Kachi, M., & Okamoto, K. (2009b). Verification of high resolution satellite-based rainfall estimates around Japan using gauge-calibrated ground radar dataset. *Journal of the Meteorological Society of Japan, 87A*, 203–222. https://doi.org/10.2151/jmsj.87A.203.

Kubota, T., Shige, S., Kachi, M., & Aonashi, K.. (2011). Development of SSMIS rain retrieval algorithm in the GSMaP project. In *Proceedings of 28th ISTS*, 2011-n-46.

Kubota, T., Liu, G., Tashima, T., & Oki, R. (2018). Development of snowfall estimation method in Global Satellite Mapping of Precipitation (GSMaP) product. *JpGU meeting 2018*, Chiba, Japan, May 2018.

Kummerow, C., Barnes, W., Kozu, T., Shiue, J., & Simpson, J. (1998). The tropical rainfall measuring Mission (TRMM) sensor package. *Journal of Atmospheric and Oceanic Technology, 15*, 809–817. https://doi.org/10.1175/1520-0426(1998)015<0809:TTRMMT>2.0.CO;2.

Liu, G. (1998). A fast and accurate model for microwave radiance calculation. *Journal of the Meteorological Society of Japan, 76*, 335–343. https://doi.org/10.2151/jmsj1965.76.2_335.

Liu, G., & Seo, E.-K. (2013). Detecting snowfall over land by satellite high-frequency microwave observations: The lack of scattering signature and a statistical approach. *Journal of Geophysical Research, 118*, 1376–1387. https://doi.org/10.1002/jgrd.50172.

Mega, T., & Shige, S. (2016). Improvements of rain/no-rain classification methods for microwave radiometer over coasts by dynamic surface-type classification. *Journal of Atmospheric and Oceanic Technology, 33*, 1257–1270. https://doi.org/10.1175/JTECH-D-15-0127.1.

Mega, T., Ushio, T., Matsuda, T., Kubota, T., Kachi, M., & Oki, R. (2019). Gauge-adjusted Global Satellite Mapping of Precipitation (GSMaP_Gauge). *IEEE Transactions on Geoscience and Remote Sensing*. https://doi.org/10.1109/TGRS.2018.2870199.

Okamoto, K., Iguchi, T., Takahashi, N., Iwanami, K., & Ushio, T. (2005). The global satellite mapping of precipitation (GSMaP) project. In *Proceedings of IGARSS 2005*, Seoul, 3414–3416. https://doi.org/10.1109/IGARSS.2005.1526575.

Otsuka, S., Kotsuki, S., & Miyoshi, T. (2016). Nowcasting with data assimilation: A case of global satellite mapping of precipitation. *Weather and Forecasting, 31*, 1409–1416. https://doi.org/10.1175/WAF-D-16-0039.1.

Petty, G. W. (1994). Physical retrievals of over-ocean rain rate from multichannel microwave imagery. Part I: Theoretical characteristics of normalized polarization and scattering indices. *Meteorology and Atmospheric Physics, 54*, 79–99. https://doi.org/10.1007/BF01030053.

Scofield, R. A., & Kuligowski, R. J. (2003). Status and outlook of operational satellite precipitation algorithms for extreme-precipitation events. *Weather and Forecasting, 18*, 1037–1051. https://doi.org/10.1175/1520-0434(2003)018<1037:SAOOOS>2.0.CO;2.

Seto, S., Takahashi, N., & Iguchi, T. (2005). Rain/no-rain classification methods for microwave radiometer observations over land using statistical information for brightness temperatures under no-rain conditions. *Journal of Applied Meteorology, 44*, 1243–1259. https://doi.org/10.1175/JAM2263.1.

Seto, S., Kubota, T., Takahashi, N., Iguchi, T., & Oki, T. (2008). Advanced rain/no-rain classification methods for microwave radiometer observations over land. *Journal of Applied Meteorology and Climatology, 47*, 3016–3029. https://doi.org/10.1175/2008JAMC1895.1.

Seto, S., Kubota, T., & Shige, S. (2016). Production of the rain/no-rain classification database for GPM microwave radiometer observations over land. *MSJ spring meeting 2016*, D405, Tokyo, Japan, May 2016 (in Japanese).

Shige, S., Yamamoto, T., Tsukiyama, T., Kida, S., Ashiwake, H., Kubota, T., Seto, S., Aonashi, K., & Okamoto, K. (2009). The GSMaP precipitation retrieval algorithm for microwave sounders. Part I: Over-ocean algorithm. *IEEE Transactions on Geoscience and Remote Sensing, 47*, 3084–3097. https://doi.org/10.1109/TGRS.2009.2019954.

Shige, S., Kida, S., Ashiwake, H., Kubota, T., & Aonashi, K. (2013). Improvement of TMI rain retrievals in mountainous areas. *Journal of Applied Meteorology and Climatology, 52*, 242–254. https://doi.org/10.1175/JAMC-D-12-074.1.

Shige, S., Yamamoto, M. K., & Taniguchi, A. (2014). Improvement of TMI rain retrieval over the Indian subcontinent. In V. Lakshmi (Ed.), *Remote sensing of the terrestrial water cycle* (Geophysical Monograph) (Vol. 206, pp. 27–42). AGU. ISBN:9781118872031.

Sims, E. M., & Liu, G. (2015). A parameterization of the probability of snow–rain transition. *Journal of Hydrometeorology, 16*, 1466–1477. https://doi.org/10.1175/JHM-D-14-0211.1.

Skofronick-Jackson, G., Petersen, W. A., Berg, W., Kidd, C., Stocker, E. F., Kirschbaum, D. B., Kakar, R., Braun, S. A., Huffman, G. J., Iguchi, T., Kirstetter, P. E., Kummerow, C., Meneghini, R., Oki, R., Olson, W. S., Takayabu, Y. N., Furukawa, K., & Wilheit, T. (2017). The Global Precipitation Measurement (GPM) mission for science and society. *Bulletin of the American Meteorological Society, 98*, 1679–1695. https://doi.org/10.1175/BAMS-D-15-00306.1.

Smith, E. A., Lamm, J. E., Adler, R. F., Alishouse, J., Aonashi, K., Barrett, E., Bauer, P., Berg, W., Chang, A., Ferraro, R., Ferriday, J., Goodman, S., Grody, N., Kidd, C., Kniveton, D., Kummerow, C., Liu, G., Marzano, F., Mugnai, A., Olson, W., Petty, G., Shibata, A., Spencer, R., Wentz, F., Wilheit, T., & Zipser, E. (1998). Results of the WetNet PIP-2 project. *Journal of the Atmospheric Sciences, 55*, 1483–1536. https://doi.org/10.1175/1520-0469(1998)055<1483:ROWPP>2.0.CO;2.

Takahashi, N., & Awaka, J. (2005). Introduction of a melting layer model to a rain retrieval algorithm for microwave radiometers. In *Proceedings of 25th IGARSS*, (pp. 3404–3409). https://doi.org/10.1109/IGARSS.2005.1526573.

Takayabu, Y. N. (2008). Observing rainfall regimes using TRMM PR and LIS data. *GEWEX Newsletter, 18*(2), 9–10. Available at https://www.gewex.org/gewex-content/files_mf/1432208504May2008.pdf, last accessed 16 Oct 2018.

Tan, J., Petersen, W. A., & Tokay, A. (2016). A novel approach to identify sources of errors in IMERG for GPM ground validation. *Journal of Hydrometeorology, 17*, 2477–2491. https://doi.org/10.1175/JHM-D-16-0079.1.

Taniguchi, A., Shige, S., Yamamoto, M. K., Mega, T., Kida, S., Kubota, T., Kachi, M., Ushio, T., & Aonashi, K. (2013). Improvement of high-resolution satellite rainfall product for Typhoon Morakot (2009) over Taiwan. *Journal of Hydrometeorology, 14*, 1859–1871. https://doi.org/10.1175/JHM-D-13-047.1.

Ushio, T., Kubota, T., Shige, S., Okamoto, K., Aonashi, K., Inoue, T., Takahashi, N., Iguchi, T., Kachi, M., Oki, R., Morimoto, T., & Kawasaki, Z. (2009). A Kalman filter approach to the Global Satellite Mapping of Precipitation (GSMaP) from combined passive microwave and infrared radiometric data. *Journal of the Meteorological Society of Japan, 87A*, 137–151. https://doi.org/10.2151/jmsj.87A.137.

Vicente, G. A., Scofield, R. A., & Menzel, W. P. (1998). The operational GOES infrared rainfall estimation technique. *Bulletin of the American Meteorological Society, 79*, 1883–1898. https://doi.org/10.1175/1520-0477(1998)079<1883:TOGIRE>2.0.CO;2.

Vicente, J., Davenport, C., & Scofield, R. A. (2002). The role of orographic and parallax corrections on real time high resolution satellite rainfall rate distribution. *International Journal of Remote Sensing, 23*, 221–230. https://doi.org/10.1080/01431160010006935.

Yamaji, M., Kubota, T., Hamada, A., Takayabu, Y. N., Kachi, M., & Aonashi, K. (2017) Drop size distribution observed by Dual-frequency precipitation radar onboard Global Precipitation Measurement core satellite. In *Proceedings of ISTS 2017*, 2017-n-17.

Yamamoto, M. K., & Shige, S. (2015). Implementation of an orographic/nonorographic rainfall classification scheme in the GSMaP algorithm for microwave radiometers. *Atmospheric Research, 163*, 36–47. https://doi.org/10.1016/j.atmosres.2014.07.024.

Yamamoto, M. K., Shige, S., Yu, C.-K., & Cheng, L.-W. (2017). Further improvement of the heavy orographic rainfall retrievals in the GSMaP algorithm for microwave radiometers. *Journal of Applied Meteorology and Climatology, 56*, 2607–2619. https://doi.org/10.1175/JAMC-D-16-0332.1.

Zhang, J., Howard, K., Langston, C., Vasiloff, S., Kaney, B., Arthur, A., Van Cooten, S., Kelleher, K., Kitzmiller, D., Ding, F., Seo, D., Wells, E., & Dempsey, C. (2011). National mosaic and multi-sensor QPE (NMQ) system: Description, results, and future plans. *Bulletin of the American Meteorological Society, 92*, 1321–1338. https://doi.org/10.1175/2011BAMS-D-11-00047.1.

Zhang, J., Howard, K., Langston, C., Kaney, B., Qi, Y., Tang, L., Grams, H., Wang, Y., Cocks, S., Martinaitis, S., Arthur, A., Cooper, K., Brogden, J., & Kitzmiller, D. (2016). Multi-radar multi-sensor (MRMS) quantitative precipitation estimation: Initial operating capabilities. *Bulletin of the American Meteorological Society, 97*, 621–638. https://doi.org/10.1175/BAMS-D-14-00174.1.

Chapter 21
Improving PERSIANN-CCS Using Passive Microwave Rainfall Estimation

Kuo-Lin Hsu, Negar Karbalee, and Dan Braithwaite

Abstract Re-calibrated PERSIANN-CCS is one of the algorithms used in "Integrated Multi-satellitE Retrievals for GPM" (IMERG) to provide high-resolution precipitation estimations from the NASA Global Precipitation Measurement (GPM) program and retrospective data generation for the period covered by the Tropical Rainfall Measurement Mission (TRMM). This study presents the development of a re-calibrated PERSIANN-CCS algorithm for the next-generation GPM multi-sensor precipitation retrieval algorithm (IMERG). The activities include implementing the probability matching method to update PERSIANN-CCS using passive microwave (PMW) rainfall estimation from low earth orbit (LEO) satellites and validation of precipitation estimation using radar rainfall measurement. Further improvement by the addition of warm rain estimation to the PERSIANN-CCS algorithm using warmer temperature thresholds for cloud image segmentation is also presented. Additionally, developments using multispectral image analysis and machine learning approaches are discussed and proposed for future studies.

Keywords Precipitation · Rainfall · PERSIANN · GPM · TRMM · Microwave · Infrared · GEO · LEO · Raingauges · Multispectral imagery · Cloud classification · Deep neural network

21.1 Introduction

Satellite-based precipitation algorithms use information from the visible to infrared (IR) bands of Geosynchronous Earth Orbit (GEO) satellites and the passive microwave bands from Low Earth Orbit (LEO) satellites. Samples are available every 15–30 min from GEO satellites, but the information is indirectly related to surface rainfall. Some improvements have been reported with cloud classification

K.-L. Hsu (✉) · N. Karbalee · D. Braithwaite
Department of Civil and Environmental Engineering, Center for Hydrometeorology and Remote Sensing (CHRS), University of California, Irvine, CA, USA
e-mail: kuolinh@uci.edu

approaches that use texture measures and cloud-patch identification as well as combining information from multi-spectral imagery (Adler and Negri 1988; Ba and Gruber 2001; Behrangi et al. 2009a, 2010b; Bellerby 2004; Capacci and Conway 2005; Griffith et al. 1978; Hong et al. 2004; Scofield 1987; Turk and Miller 2005; Wu 1985; Vicente et al. 1998). Microwave (MW) sensors on LEO satellites can provide sensing of rain clouds more directly. Their low sampling frequency, however, limits the effectiveness of the rainfall retrievals. Effective integration of multiple LEO and GEO satellite information sources can be used to improve rainfall retrievals at short-time scales. Improvements in precipitation retrieval have been reported by locally adjusting GEO-IR retrievals using near-real-time LEO PMW-based rainfall estimation (Behrangi et al. 2009b; Bellerby et al. 2009; Bellerby 2004; Hsu et al. 1997; Hsu and Sorooshian 2009; Huffman et al. 2007; Kidd et al. 2003; Marzano et al. 2004; Sorooshian et al. 2000; Tapiador 2008; Todd et al. 2001; Turk and Miller 2005; Xu et al. 1999). The Self-Calibrating Multivariate Precipitation Retrieval (SCaMPR) algorithm estimates rainfall at a fine temporal resolution using PMW and GEO satellites. SCaMPR uses Special Microwave Sensor Imager (SSM/I) data to distinguish between rain/no-rain pixels, and then uses Geostationary Operational Environmental Satellites (GOES) data to calibrate the relationship between Tb-RR via linear regression for the precipitating pixels (Kuligowski 2002, 2010, 2016). Kidd (2003) used the histogram matching technique between PMW rainfall data and IR cloud-top temperature to estimate rainfall over Africa during a 4-month calibration period. More recent developments that include morphing PMW rainfall according to cloud advection from GEO-IR imagery have been found to be effective in improving rainfall retrievals (Behrangi et al. 2010b; Bellerby et al. 2009; Hsu and Sorooshian 2009; Joyce et al. 2004; Joyce and Xie 2011; Ushio et al. 2009). The Climate Prediction Center morphing method (CMORPH) uses motion vectors from dynamic GEO-IR images to fill the temporal gaps between two available PMW rainfall estimates (Joyce et al. 2004). The Tropical Rainfall Measuring Mission's (TRMM) Multisatellite Precipitation Analysis (TMPA) combined precipitation estimates from multiple satellites, as well as gauges where feasible, to generate rainfall data with a $0.25° \times 0.25°$ resolution every 3 h.

The PERSIANN algorithm is an adaptive, multi-platform precipitation estimation algorithm, which uses an artificial neural network model to merge high quality, sparsely sampled data from NASA, NOAA, and DMSP low-altitude polar-orbit satellites with frequently sampled data from geosynchronous satellites (Hsu et al. 1997, 1999; Sorooshian et al. 2000). The near-global product is available at 0.25° spatial resolution and hourly temporal resolution. Since the original development work on PERSIANN, further enhancements and improvements have been ongoing at UC Irvine. Some relevant activities include: (1) extending cloud classifications from individual cloud pixels to individual cloud patches based on the PERSIANN-Cloud Classification System (PERSIANN-CCS) (Hong et al. 2004, 2005; Hsu et al. 2007, 2010; Behrangi et al. 2010a); (2) improving rainfall estimates using enhanced multi-spectral data from the GOES-R satellite (PERSIANN-MSA: Behrangi et al. 2010a, b); (3) developing rainfall estimates based on cloud patch dynamic tracking (LMODEL: Bellerby et al. 2009; Hsu and Sorooshian 2009); (4) developing rainfall

estimates based on the combination of LEO and GEO satellite information (REFAME; Behrangi et al. 2010b, 2012); and (5) using machine learning algorithms for rainfall estimation from multiple spectral images (Akbari Asanjan et al. 2018; Hayatbini et al. 2019; Pan et al. 2019; Tao et al. 2016, 2017).

Building upon the success of TRMM, which operated from November 1997 to April 2015, the Global Precipitation Measurement (GPM) satellite was launched in February 2014. GPM is a concept based on using the available LEO-PMW satellite data and adding GEO-IR-based precipitation data to provide global precipitation estimation at near real time. One key dataset from the NASA GPM program is the Integrated Multi-Satellite Retrievals for GPM (IMERG). IMERG integrates LEO and GEO satellite information as well as surface precipitation gauge analysis to provide global precipitation (IMERG ATBD V.5.1, Huffman et al. 2018). IMERG is a merged retrieval using algorithms developed from (1) TRMM Multi-satellite Precipitation Analysis (TMPA), (2) Climate Prediction Center Morphing with Kalman Filter (CMORPH-KF), and (3) microwave re-calibrated PERSIANN-CCS (Huffman et al. 2007, Joyce and Xie 2011, Hong et al. 2004). IMERG was developed to provide better quality and shorter time latency for global precipitation monitoring at $0.1° \times 0.1°$ and half-hourly samples. The time latencies are around 4 and 12 h from observation time for the "Early" and "Late" near real-time IMERG data products, respectively. The "final" satellite-gauge merged product is available around 2-months after observation time (IMERG ATBD V.5.1, Huffman et al. 2018).

This study presents the improvements made to PERSIANN-CCS. Specifically, we highlight the results of incorporating precipitation data from various sources which is essential to improve estimates of PERSIANN-CCS. This is primarily because the original algorithm uses IR data to estimate precipitation indirectly from the cloud-top temperature and that is associated with some inherent uncertainties. The scope of this manuscript is as follows. Re-calibration of PERSIANN-CCS is described in Sect. 21.3. Evaluation of the re-calibrated PERSIANN-CCS is provided in Sect. 21.4. Improvements made in warm rain estimation are discussed in Sect. 21.4. Finally, conclusions and future directions are provided in Sect. 21.5.

21.2   Re-calibration of PERSIANN-CCS

High-resolution satellite rainfall products are needed for many hydro-meteorological applications. In the NASA Global Precipitation Mission (GPM) program, the Integrated Multi-satellitE Retrieval for GPM (IMERG) is designed to provide an effective near global precipitation retrieval by combining precipitation estimates from the morphed passive microwave estimation (CMORPH-KF, Joyce and Xie 2011) and the re-calibrated PERSIANN-CCS estimation (see Fig. 21.1) (Huffman et al. 2018). The IMERG products are made available to provide half-hourly and monthly precipitation estimates and related fields on $0.1° \times 0.1°$ lat./long. grid over the domain 60°N-60°S. The UC Irvine team has been working closely with NASA's GPM Multi-Satellite Working Group to develop a GPM multi-sensor precipitation retrieval algorithm.
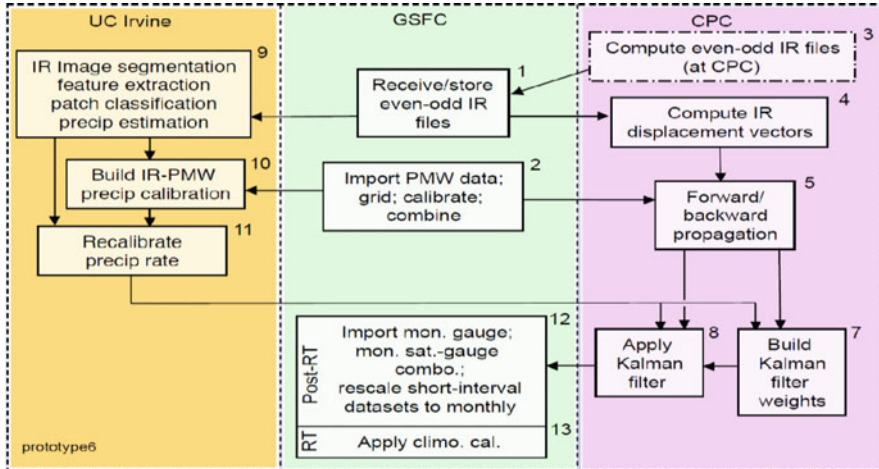
Fig. 21.1 The major processing modules and data flows in IMERG. The blocks are organized by contributing institution; the final code package is an integrated system. (Adapted from Huffman et al. 2018)

21.2.1 PERSIANN-CCS

Rainfall estimations from PERSIANN-CCS consist of four major steps: (1) GEO-IR cloud image segmentation, (2) feature extraction from GEO-IR cloud patches, (3) patch feature classification, and (4) rainfall estimation. The classification and rainfall estimation using PERSIANN-CCS is shown in Fig. 21.2 (Hong et al. 2004, Hsu et al. 2010). PERSIANN-CCS implements image processing and pattern classification techniques based on analysis of GEO-IR (10.7 μm) cloud images. During low-level image processing, a "watershed delineation process" using brightness temperature ($Tb = 253$ K) is applied to separate cloud patches from their image background. This is followed by image extraction and interpretation, in which cloud patches are treated as independent objects and described by object features such as patch coldness, size, shape, and texture. Classification of cloud patch objects is based on an unsupervised self-organizing feature map clustering scheme. When rainfall is assigned to a classified patch group, it establishes an interpretative relationship between the cloud patch property and rainfall. Finally, the classified patch group's rainfall distribution is described by a set of GEO-IR brightness temperature and rainfall rate (Tb-R) functions. Parameters of the nonlinear Tb-R function are calibrated from spatially and temporally co-located satellite image and radar/PMW rainfall maps.

Figure 21.3a shows cloud images as classified into 400 groups, where each group is associated with a unique Tb-R function; for groups that are close to each other, the Tb-R curves are similar. Here we have selected regions G0 through G6 showing cloud groups with similar Tb-R functions, as labeled in Fig. 21.3a and b. For the groups in region G0, the cloud Tb is high (clear weather pattern) and has no rain
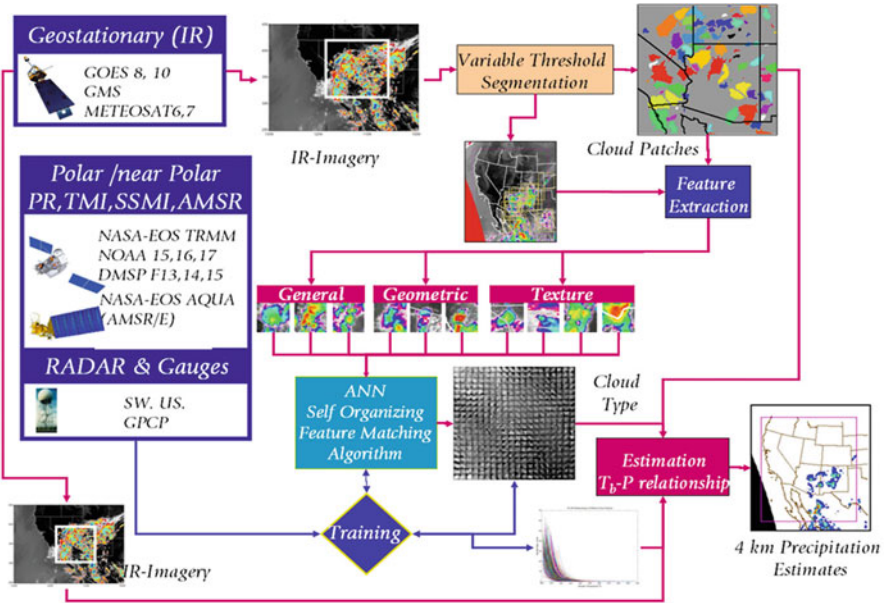
Fig. 21.2 Cloud image segmentation, feature extraction, classification, and rainfall estimation of the PERSIANN-CCS algorithm
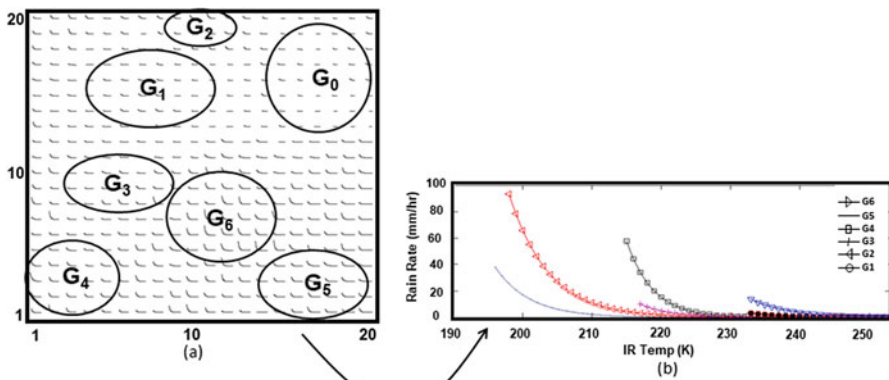
Fig. 21.3 (**a**) The Tb-R relationship of 20 × 20 SOFM cloud patch groups and (**b**) the Tb-R curves with respect to the SOFM groups G0~G6

associated with it. The slopes of the *Tb-R* curves are steeper for the G2, G4, and G6 regions; these have higher corresponding rainfall rates, implying that those cloud groups are relevant to the convective clouds of low, medium, and high altitudes. The regions covered by G1, G3, and G5, however, have slopes of *Tb-R* that are less steep and are associated with light or no-rain clouds at low, medium, and high altitudes, respectively (Hong et al. 2004).

21.2.2   Passive Microwave Adjustment of PERSIANN-CCS Estimation

Effective integration of LEO PMW rainfall with the more frequent samples from GEO images can improve the sampling for precipitation events in space and time. Figure 21.4 shows the constellation of LEO satellites with PMW sensors in the modern era. Compared to GEO satellites, LEO satellites provide fewer sampled data points per day and have significantly fewer samples altogether before 2002.

Multiple years (2008–2011) of concurrent and co-located PMW and PERSIANN-CCS rainfall were used in this experiment. The probability matching method was used to transfer PERSIANN-CCS rainfall toward the PMW rainfall distribution based on all the available co-located samples. This method assumes that rainfall from PERSIANN-CCS (Rccs) and PMW (Rpmw) are functionally related and that a transformation can be used:

$$p(Rccs_i)dR = p(Rpmw_i)dR \tag{21.1}$$

where the pairs of *(Rccs_i, Rpmw_i)* define the probability matching of the Rccs-Rpmw relationship, with *i* varying to encompass probabilities ranging from 0 to 100%. The cumulative distribution functions can be shown as:
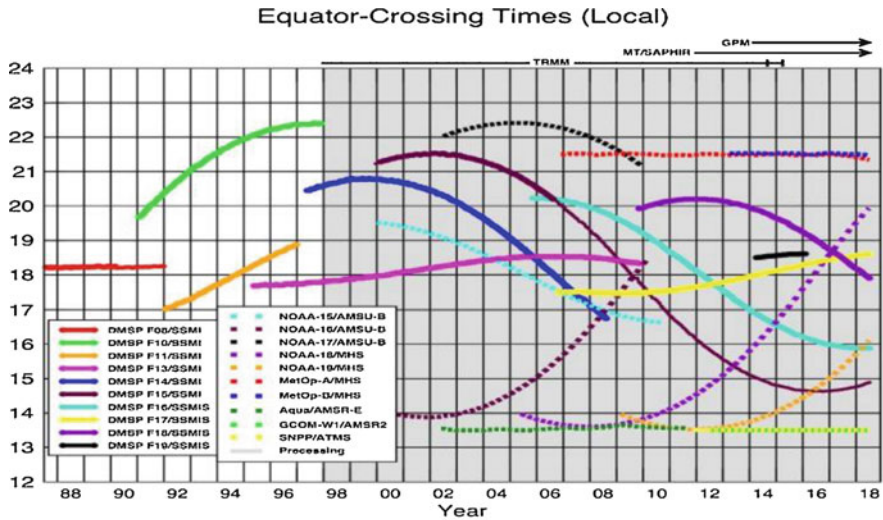
Fig. 21.4 PMW sensor Equator-crossing time for 1200–2400 local time for the modern PMW sensor era. Image by Eric Nelkin (SSAII GSFC, 5 july 2017; current version at https://precip.gsfc.nasa.gov/times_allsat.jpg, last accessed 5 Apr. 2019; also see Huffman et al. 2018)

$$\int_0^{Rccs_i} p(Rccs_i)dR = \int_0^{Rpmw_i} p(Rpmw_i)dR \qquad (21.2)$$

For the unconditional probability distribution function (*PDF*), integration is from 0 to $Rccs_i$; for a non-zero conditional PDF_i, the integration begins at a threshold (Rosenfeld et al. 1995). Figure 21.5 shows how PERSIANN-CCS rainfall is adjusted with PMW rainfall estimates based on the Cumulative Distribution Function (CDF) computed from the Probability Distribution Function (PDF). The left-side graph in Fig. 21.5 describes the PDF for PMW (solid line) and CCS (dashed line) calculated based on the concurrent samples of climatology data showing the probability of rainfall rate. The right-side graph is the CDF function calculated based on the PDF of PMW and PERSIANN-CCS data.

In this experiment, the PMW precipitation dataset (MWCOMB) was obtained from the NOAA Climate Prediction Center (CPC). MWCOMB is a blended precipitation data from multiple sensors and orbits, such as DMSP SSM/I, NOAA AMSU-B, and TRMM TMI (Ferraro et al. 1994, Kummerow et al. 2001, Weng et al. 2003, Huffman et al. 2007). MWCOMB data is at 8 km resolution from 60°N to 60°S and 0° to 360°, but is regridded to 0.25° lat-long for this study.

Precipitation estimation from PERSIANN-CCS is at a 0.04° × 0.04° spatial resolution every 0.5 h. The Cumulative Distribution Functions (CDFs) of both datasets must be calculated from concurrent samples at the same spatial resolution. Therefore, PERSIANN-CCS was also regridded to a 0.25° × 0.25° spatial resolution. To account for regional and seasonal variability, the PDFs were calculated for 5° × 5° overlapping subareas of the global coverage and for each month separately. The probability matching adjustment is calculated separately for each month and performed by using the long record of collocated PMW and PERSIANN-CCS rain rates on a 0.25° × 0.25° grid, aggregated for each overlapping 5° × 5°. Once computed, the probability mapping coefficients will be stored (as a table) for each 5° × 5° grid by calendar month and used as a lookup table for rainfall adjustment.
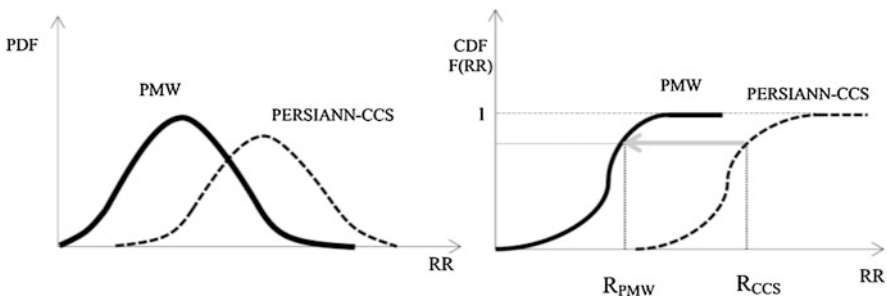
Fig. 21.5 Matching rainfall from PMW satellites with the rainfall from PERSIANN-CCS using PMM rainfall. (Adapted from Karbalaee et al. 2017)
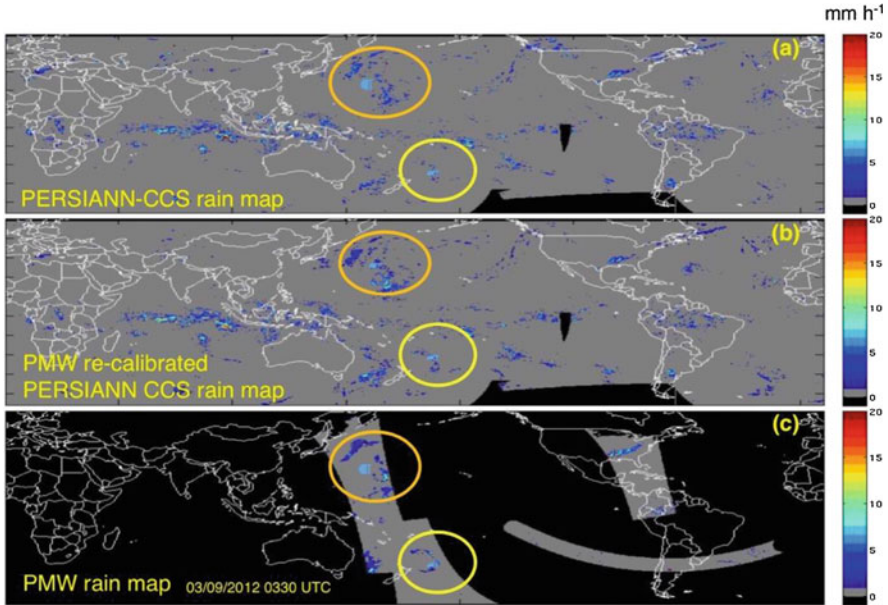
Fig. 21.6 (**a**) PERSIANN-CCS rainfall, (**b**) PMW recalibrated PERSIANN rainfall and (**c**) PMW rainfall maps at 0330 UTC, 9 March 2012. (rain rate: mm h^{-1})

Figure 21.6 shows a sample comparison of (a) PERSIANN-CCS rainfall, (b) PMW re-calibrated PERSIANN-CCS rainfall, and (c) PMW rainfall, at 0330 UTC 2 August 2011. The rainfall distribution and intensity of the PMM-adjusted PERSIANN rainfall is similar to that of PMW rainfall.

21.3 Evaluation of Re-calibrated PERSIANN-CCS Estimation

For the validation of the microwave-adjusted PERSIANN-CCS (hereafter MA-PERSIANN-CCS) estimates, one year of data (2012) was examined. The results from using the PMM method show improvement in both the summer and winter months, with the CDF of PERSIANN-CCS rainfall data adjusting toward the CDF of PMW rainfall. PERSIANN-CCS rainfall estimates are available every 30 min from geostationary satellite imagery and cover the near-global area from 60°N to 60°S and 0° to 360°. On the other hand, PMW rainfall estimates, due to the polar orbiting LEO satellites, are only available at limited spatial and temporal resolutions. The PDF of PERSIANN-CCS adjusts toward PMW rainfall estimation in a systematic way using the PMM method, while keeping the re-calibrated MA-PERSIANN-CCS estimation at the original high spatial and temporal scales.

For global validation the study area was divided into 8 longitudinal regions, 15° each from 60°N to 60°S, in order to ensure the regions have sufficient samples. The sample size is relatively higher during the warmer months, winter in the southern hemisphere and summer in the northern hemisphere. Table 21.1 and Table 21.2 show the summary of statistical parameters calculated for each zone during summer and winter months for 2012, namely bias, correlation coefficient, and root mean square error (RMSE). Table 21.1 shows the seasonal statistical evaluations for December, January, and February. During the winter (northern hemisphere) the evaluation is more reliable from 0° to 60°S, with zones located in the southern hemisphere showing improved bias, correlation coefficient, and RMSE values after bias adjustment. Table 21.2 shows the seasonal statistical parameters calculated for each zone for June, July, and August 2012 (summer in northern hemisphere). Table 21.2 shows that bias, correlation coefficient, and RMSE have improved for MA-PERSIANN-CCS in comparison with PERSIANN-CCS during summer 2012.

Table 21.1 Statistical parameters used for global validation calculated for 8 zones (December, January, and February 2012). Statistics is provided based on the concurrent samples of test data over the 3-month period. Bias & corr (no unit); RMSE (mm/3-month)

	Winter-2012					
	PERSIANN-CCS			MA-PERSIANN-CCS		
Zone	bias	corr	rmse	bias	corr	rmse
60 N–45 N	0.72	0.61	14.16	−0.23	0.86	6.62
45 N–30 N	0.26	0.71	15.28	−0.13	0.89	9.60
30 N–15 N	−0.13	0.38	11.58	−0.19	0.68	8.96
15N-0	−0.06	0.83	12.12	−0.05	0.92	8.63
0-15S	0.27	0.90	18.63	0.0008	0.94	9.32
15S–30S	0.08	0.87	13.72	−0.08	0.92	8.53
30S–45S	−0.39	0.79	11.83	−0.12	0.86	9.32
45S–60S	−0.51	0.69	8.71	−0.37	0.80	6.97

Table 21.2 Statistical parameters used for global validation calculated for 8 zones (June, July, and August 2012). Statistics is provided based on the concurrent samples of test data over the 3-month period. Bias & corr (no unit); RMSE (mm/3-month)

	Summer-2012					
	PERSIANN-CCS			MA-PERSIANN-CCS		
Zone	bias	corr	rmse	bias	corr	rmse
60 N–45 N	−0.50	0.52	13.95	−0.23	0.71	9.34
45 N–30 N	−0.25	0.80	12.29	−0.11	0.89	8.96
30 N–15 N	0.06	0.91	13.24	−0.08	0.94	10
15N-0	0.05	0.87	16.55	−0.01	0.93	12.11
0-15S	−0.07	0.91	7.36	−0.04	0.93	6.79
15S–30S	−0.44	0.86	7.79	−0.28	0.88	6.49
30S–45S	−0.25	0.70	11.81	−0.29	0.85	9.55
45S–60S	0.32	0.5	10.15	−0.30	0.72	7.08

Further validation was performed, using Q2 radar data, over CONUS for PERSIANN-CCS and MA-PERSIANN-CCS for winter (December, January, and February) and summer (June, July, and August) of the year 2012. For evaluating the performance of PERSIANN-CCS and MA-PERSIANN-CCS in comparison with PMW and radar Q2, statistical parameters such as bias, correlation coefficient and, root mean square error (RMSE) were calculated for winter and summer 2012 (see Table 21.3 and Table 21.4). Table 21.3 gives the statistical results for PERSIANN-CCS and MA-PERSIANN-CCS compared to PMW data and Table 21.4 shows the statistical performance of PERSIANN-CCS, MA-PERSIANN-CCS, and PMW against Q2 radar data as ground truth. During winter 2012, bias, correlation coefficient and RMSE between MA-PERSIANN-CCS and PMW shows improvement compared to the same statistics for PERSIANN-CCS and PMW. This shows that implementation of climatology data over the validation year 2012 has improved the PERSIANN-CCS rainfall estimation toward PMW rainfall data. MA-PERSIANN-CCS does not show improvement, however, for the winter season, compared with radar Q2. The statistical parameters show the bias value of −0.37 for PERSIANN-CCS decreased to −0.69 (more underestimation) between MA-PERSIANN-CCS and radar Q2, for winter 2012. The reason for this is due to inconsistencies between PMW and radar Q2 data. Statistical validation results for summer are also exhibited in Table 21.3 and Table 21.4. As expected, all the statistics for MA-PERSIANN-CCS show improvement over PERSIANN-CCS, for summer 2012. As compared to radar Q2, MA-PERSIANN-CCS shows an improvement in bias of 53% during the summer season with no significant changes in the other two statistics. In summary, this is a systematic approach for reducing the bias between the GEO-based PERSIANN-CCS and PMW estimates.

Table 21.3 Comparison between PERSIANN-CCS and MA-PERSIANN-CCS with PMW satellite data over CONUS during winter and summer 2012. Statistics is provided based on the concurrent samples of test data over the 3-month period. Bias & corr (no unit); RMSE (mm/3-month)

| | CONUS year 2012 | | | | | |
| | PERSIANN-CCS | | | MA-PERSIANN-CCS | | |
	bias	corr	rmse	bias	corr	rmse
Winter	0.59	0.61	8.35	−0.23	0.86	4.86
Summer	−0.25	0.8	13.51	−0.07	0.84	10.93

Table 21.4 Comparison between PERSIANN-CCS, MA-PERSIANN-CCS, and PMW with Q2 ground based radar over CONUS during winter and summer 2012. Statistics is provided based on the concurrent samples of test data over the 3-month period. Bias & corr (no unit); RMSE (mm/3-month)

| | CONUS year 2012 | | | | | | | | |
| | PERSIANN-CCS | | | MA-PERSIANN-CCS | | | PMW | | |
	bias	corr	rmse	bias	corr	rmse	bias	corr	rmse
Winter	−0.37	0.67	13.78	−0.69	0.7	16.83	−0.6	0.76	14.86
Summer	−0.3	0.82	14.41	−0.14	0.72	14.75	−0.07	0.8	12.95

21.4 Improving Warm Rain Estimation

The PERSIANN-CCS uses three Tb threshold levels (253, 235, and 220 K) to extract the spatial features of each individual cloud patch. With the IR cloud segmentation threshold at 253 K, the *Tb-RR* relationship of cloud patch groups, as shown in Fig. 21.7a and b, can only cover the cloud pixels with brightness temperatures lower than 253 K. Under this IR Tb threshold (253 K), rainfall from warm clouds (*Tb* > 253 K) are not included. This experiment demonstrated that the warm rainfall from the PERSIANN-CCS algorithm can be estimated using longwave IR temperature thresholds greater than 253 K.

Figure 21.7a shows the cloud image from the longwave infrared channel and the cloud coverage under the segmentation thresholds of IR *Tb* = 253 K (Fig. 21.7b), *Tb* = 260 K (Fig. 21.7c) and *Tb* = 280 K (Fig. 21.7d). As shown in Fig. 21.7d, the segmentation threshold at higher brightness temperatures (e.g., 280K) can cover warm clouds effectively.

The rainfall rate mapping curves (*Tb-RR*) of segmentation threshold *Tb* = 253 and 280 K are presented in Fig. 21.8. By extending the IR brightness temperature thresholds from *Tb* = 253 to 280 K, the rainfall rate mapping curves (*Tb-RR*) of
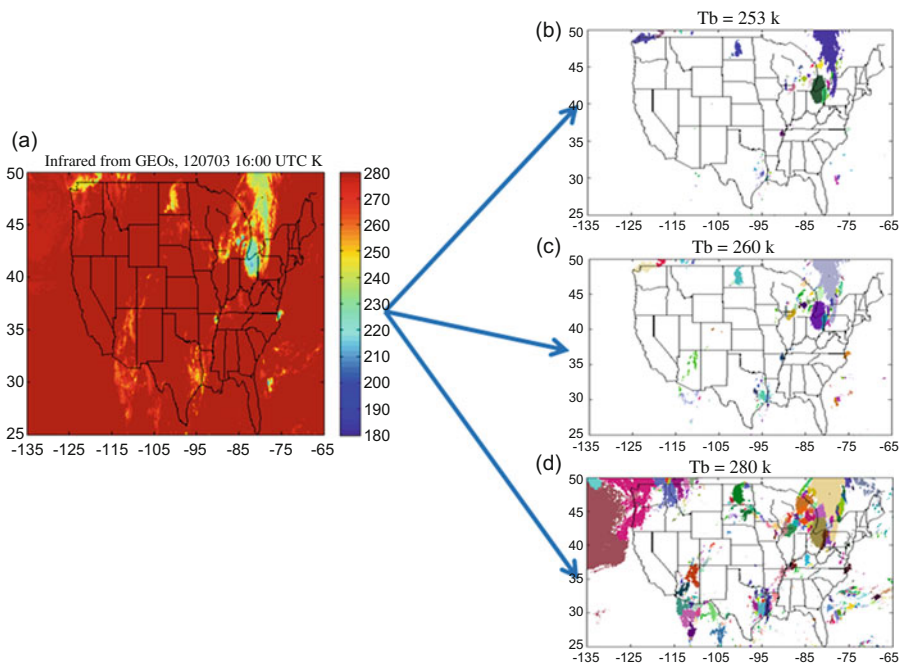
Fig. 21.7 (**a**) cloud image from longwave infrared channel; (**b**) segmentation of IR cloud image at Tb = 253 K, (**c**) segmentation of cloud image at Tb = 260 K, and (**d**) segmentation of cloud image at Tb = 280 K
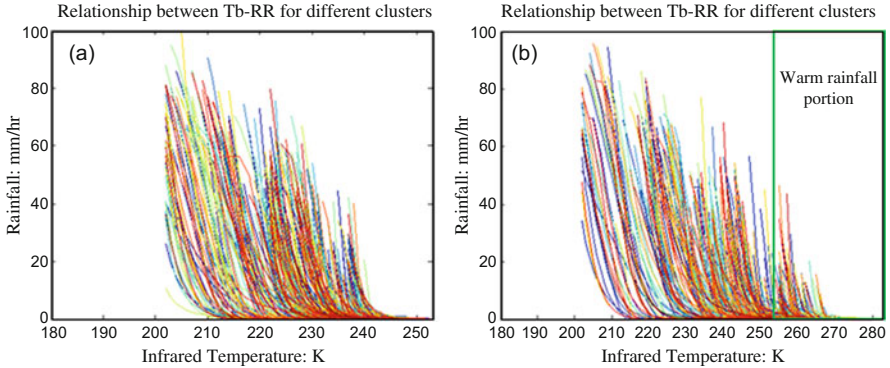
Fig. 21.8 PERSIANN-CCS mapping curves using IR Tb thresholds at (**a**) 253 and (**b**) 280 K
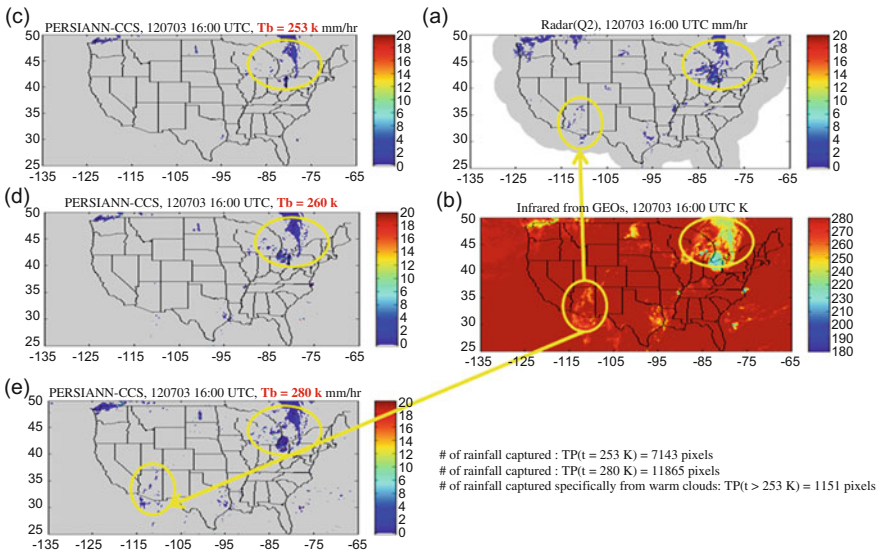
Fig. 21.9 Rainfall map at 1600 UTC time 3 July 2012, from (**a**) Q2 radar map, (**b**) satellite image of IR brightness temperature, and the rainfall maps estimated from segmentation using thresholds from Tb = (**c**) 253, (**d**) 260, and (**e**) 280 K

PERSIANN-CCS are extended to the clouds of warmer brightness temperature $Tb > 253$ K.

Figure 21.9 demonstrates rainfall rates estimated using the mapping curves from segmentation at three different brightness temperature thresholds ($Tb = 253$, 260 and 280 K). The satellite image of IR brightness temperature is displayed in Fig. 21.9b, while the Q2 radar map is displayed in Fig. 21.9a. Rainfall maps from three different segmentation thresholds ($Tb = 253$, 260 and 280 K) are listed in the

Fig. 21.9c–e. As shown in the figures, heavy rainfall with low brightness temperatures over the Great Lakes region and northern Ohio are retrieved from mapping curves using $Tb = 253$, 260 and 280 K. Another storm from warm clouds with warmer brightness temperatures near Arizona is displayed in the radar map Fig. 21.9a and satellite brightness temperature Fig. 21.9b. As shown in Fig. 21.9e, rainfall estimation using mapping curves from segmentation $Tb = 280$ K can cover the warm rains effectively. Rainfall maps using segmentation thresholds from $Tb = 253$ K and $Tb = 260$ K alone, however, cannot cover the warm rain effectively from this event, as displayed in Fig. 21.9c and d.

21.5 Conclusions and Future Directions

Precipitation observations from satellites continue to be developed to improve the spatial and temporal resolutions as well as the quality and reliability of the data. Taking advantage of multi-sensor satellite observations in combination with different in-situ measurements to generate a global precipitation map has become a primary goal of the research community. In this study, we have reported methods for improving PERSIANN-CCS using PMW rainfall estimation. A Probability Matching Method was used for the bias correction of PERSIANN-CCS. The regional and global evaluations of MA-PERSIANN-CCS show the statistics – bias, correlation coefficient, and root mean square error, with respect to the PMW data globally and radar Q2 measurements over CONUS – are improved, especially in mid latitude regions. Experiments also extended to the improvement of rain estimation from warm clouds. Our case study shows that warm rain can be detected by PERSIANN-CCS by increasing the segmentation temperature threshold from $Tb = 253$ to 280 K.

For improving the estimation of warm rainfall, we will continue exploring the use of a novel gradient-based segmentation technique that can integrate and segment multiple spectral images. The newly developed technique is more flexible, and is able to include a full temperature range of clouds from warm to cold with different cloud top height. This algorithm is extendable from single-channel to hyperspectral and high-spatial-resolution remote sensing data such as the current GOES-16 and 17 Advanced Baseline Imager (ABI) channels. Another focus of our development is on the development of remote sensing of precipitation using advanced machine learning techniques. Machine learning based methods have recently become very popular in many earth science and remote sensing applications. Experiments show that, when provided with a large amount of data and enhanced computing power, Deep Neural Networks (DNNs) are capable of generating effective results. Our studies have investigated the potential of Deep Neural Networks (DNNs) to improve precipitation estimation (Tao et al. 2016, 2017) and will continue the development of remotely-sensed precipitation based on emerging disciplines and techniques in machine learning, computational statistics, and data mining.

References

Adler, R. F., & Negri, A. J. (1988). A satellite infrared technique to estimate tropical convective and stratiform rainfall. *Journal of Applied Meteorology, 27*, 30–51. https://doi.org/10.1175/1520-0450(1988)027<0030:ASITTE>2.0.CO;2.

Asanjan, A. A., Yang, T., Hsu, K., Sorooshian, S., Lin, J., & Peng, Q. (2018). Short-term precipitation forecast based on the PERSIANN system and LSTM recurrent neural networks. *Journal of Geophysical Research: Atmospheres, 123*(22), 12,543-12,563. https://doi.org/10.1029/2018JD028375.

Ba, M. B., & Gruber, A. (2001). GOES multispectral rainfall algorithm (GMSRA). *Journal of Applied Meteorology, 40*, 1500–1514. https://doi.org/10.1175/1520-0450(2001)040<1500:GMRAG>2.0.CO;2.

Behrangi, A., Hsu, K.-L., Imam, B., Sorooshian, S., Huffman, G. J., & Kuligowski, R. J. (2009a). PERSIANN-MSA: A precipitation estimation method from satellite-based multispectral analysis. *Journal of Hydrometeorology, 10*, 1414–1429. https://doi.org/10.1175/2009JHM1139.1.

Behrangi, A., Hsu, K.-L., Imam, B., Sorooshian, S., & Kuligowski, R. J. (2009b). Evaluating the utility of multispectral information in delineating the areal extent of precipitation. *Journal of Hydrometeorology, 10*, 684–700. https://doi.org/10.1175/2009JHM1077.1.

Behrangi, A., Hsu, K.-L., Imam, B., & Sorooshian, S. (2010a). Daytime precipitation estimation using bispectral cloud classification system. *Journal of Applied Meteorology and Climatology, 49*, 1015–1031. https://doi.org/10.1175/2009JAMC2291.1.

Behrangi, A., Imam, B., Hsu, K.-L., Sorooshian, S., Bellerby, T. J., & Huffman, G. J. (2010b). REFAME: Rain estimation using forward-adjusted advection of microwave estimates. *Journal of Hydrometeorology, 11*, 1305–1321. https://doi.org/10.1175/2010JHM1248.1.

Behrangi, A., Kubar, T., & Lambrigtsen, B. (2012). Phenomenological description of tropical clouds using CloudSat cloud classification. *Monthly Weather Review, 140*, 3235–3249. https://doi.org/10.1175/MWR-D-11-00247.1.

Bellerby, T. J. (2004). A feature-based approach to satellite precipitation monitoring using geostationary IR imagery. *Journal of Hydrometeorology, 5*, 910–921. https://doi.org/10.1175/1525-7541(2004)005<0910:AFATSP>2.0.CO;2.

Bellerby, T. J., Hsu, K.-L., & Sorooshian, S. (2009). LMODEL: A satellite precipitation methodology using cloud development modeling. Part I: Algorithm construction and calibration. *Journal of Hydrometeorology, 10*, 1081–1095. https://doi.org/10.1175/2009JHM1091.1.

Capacci, D., & Conway, B. J. (2005). Delineation of precipitation areas from MODIS visible and infrared imagery with artificial neural networks. *Meteorological Applications, 12*, 291–305. https://doi.org/10.1017/S1350482705001787.

Ferraro, R. R., Grody, N. C., & Marks, G. F. (1994). Effects of surface conditions on rain identification using the DMSP-SSM/I. *Remote Sensing Reviews, 11*, 195–209. https://doi.org/10.1080/02757259409532265.

Griffith, C. G., Woodley, W. L., Grube, P. G., Martin, D. W., Stout, J., & Sikdar, D. N. (1978). Rain estimation from geosynchronous satellite imagery—Visible and infrared studies. *Monthly Weather Review, 106*, 1153–1171. https://doi.org/10.1175/1520-0493(1978)106<1153:REFGSI>2.0.CO;2.

Hayatbini, N., Hsu, K.-l., Sorooshian, S., Zhang, Y., & Zhang, F. (2019). Effective cloud detection and segmentation using a gradient-based algorithm for satellite imagery: Application to improve PERSIANN-CCS. *Journal of Hydrometeorology, 20*(5), 901–913. https://doi.org/10.1175/JHM-D-18-0197.1.

Hong, Y., Hsu, K.-L., Sorooshian, S., & Gao, X. (2004). Precipitation estimation from remotely sensed imagery using an artificial neural network cloud classification system. *Journal of Applied Meteorology, 43*, 1834–1853. https://doi.org/10.1175/JAM2173.1.

Hong, Y., Hsu, K.-L., Sorooshian, S., & Gao, X. (2005). Self-organizing nonlinear output (SONO): A neural network suitable for cloud patch–based rainfall estimation at small scales. *Water Resources Research, 41*, W03008. https://doi.org/10.1029/2004WR003142.

Hsu, K.-L., & Sorooshian, S. (2009). Satellite-based precipitation measurement using PERSIANN system. In S. Sorooshian, K.-L. Hsu, E. Coppola, B. Tomassetti, M. Verdecchia, & G. Visconti (Eds.), *Hydrological modelling and the water cycle* (pp. 27–48). Berlin/Heidelberg: Springer, ISBN:978-3-540-77843-1.

Hsu, K.-L., Gao, X., Sorooshian, S., & Gupta, H. V. (1997). Precipitation estimation from remotely sensed information using artificial neural networks. *Journal of Applied Meteorology, 36*, 1176–1190. https://doi.org/10.1175/1520-0450(1997)036<1176:PEFRSI>2.0.CO;2.

Hsu, K.-L., Gupta, H. V., Gao, X., & Sorooshian, S. (1999). Estimation of physical variables from multichannel remotely sensed imagery using a neural network: Application to rainfall estimation. *Water Resources Research, 35*, 1605–1618. https://doi.org/10.1029/1999WR900032.

Hsu, K.-L., Hong, Y., & Sorooshian, S. (2007). Rainfall estimation using a cloud patch classification map. In V. Levizzani, P. Bauer, & F. J. Turk (Eds.), *Measuring precipitation from space* (pp. 329–342). Dordrecht: Springer, ISBN:978-1-4020-5835-6.

Hsu, K.-L., Behrangi, A., Imam, B., & Sorooshian, S. (2010). Extreme precipitation estimation using satellite-based PERSIANN-CCS algorithm. In M. Gebremichael & F. Hossain (Eds.), *Satellite rainfall applications for surface hydrology* (pp. 49–67). Dordrecht: Springer, ISBN:978-90-481-2915-7.

Huffman, G. J., Bolvin, D. T., Nelkin, E. J., Wolff, D. B., Adler, R. F., Gu, G., Hong, Y., Bowman, K. P., & Stocker, E. F. (2007). The TRMM multisatellite precipitation analysis (TMPA): Quasi-global, multiyear, combined-sensor precipitation estimates at fine scales. *Journal of Hydrometeorology, 8*, 38–55. https://doi.org/10.1175/JHM560.1.

Huffman, G. J., Bolvin, D. T., Braithwaite, D., Hsu, K.-L., Joyce, R., Kidd, C., Nelkin, E. J., Sorooshian, S., Tan, J., & Xie, P. (2018). *NASA Global Precipitation Measurement (GPM) Integrated Multi-satellitE Retrievals for GPM (IMERG)*. Algorithm Theoretical Basis Document, version 5.2, 31 pp. Available at https://pmm.nasa.gov/resources/documents/gpm-integrated-multi-satellite-retrievals-gpm-imerg-algorithm-theoretical-basis-. Last accessed 6 Dec 2018.

Joyce, R. J., & Xie, P. (2011). Kalman filter–based CMORPH. *Journal of Hydrometeorology, 12*, 1547–1563. https://doi.org/10.1175/JHM-D-11-022.1.

Joyce, R. J., Janowiak, J. E., Arkin, P. A., & Xie, P. (2004). CMORPH: A method that produces global precipitation estimates from passive microwave and infrared data at high spatial and temporal resolution. *Journal of Hydrometeorology, 5*, 487–503. https://doi.org/10.1175/1525-7541(2004)005<0487:CAMTPG>2.0.CO;2.

Karbalaee, N., Hsu, K.-L., Sorooshian, S., & Braithwaite, D. (2017). Bias adjustment of infrared-based rainfall estimation using passive microwave satellite rainfall data. *Journal of Geophysical Research, 122*, 3859–3876. https://doi.org/10.1002/2016JD026037.

Kidd, C., Kniveton, D. R., Todd, M. C., & Bellerby, T. J. (2003). Satellite rainfall estimation using combined passive microwave and infrared algorithms. *Journal of Hydrometeorology, 4*, 1088–1104. https://doi.org/10.1175/1525-7541(2003)004<1088:SREUCP>2.0.CO;2.

Kuligowski, R. J. (2002). A self-calibrating real-time GOES rainfall algorithm for short-term rainfall estimates. *Journal of Hydrometeorology, 3*, 112–130. https://doi.org/10.1175/1525-7541(2002)003<0112:ASCRTG>2.0.CO;2.

Kuligowski, R. J. (2010). GOES-R Advanced Baseline Imager (ABI) algorithm theoretical basis document for rainfall rate (QPE). *Algorithm Theoretical Basis Doc.,* V. 2.0, NOAA/NESDIS, 44 pp. Available at https://www.goes-r.gov/products/ATBDs/baseline/Hydro_RRQPE_v2.0_no_color.pdf. Last accessed 6 Dec 2018.

Kuligowski, R. J., Li, Y., Hao, Y., & Zhang, Y. (2016). Improvements to the GOES-R rainfall rate algorithm. *Journal of Hydrometeorology, 17*, 1693–1704. https://doi.org/10.1175/JHM-D-15-0186.1.

Kummerow, C. D., Hong, Y., Olson, W. S., Yang, S., Adler, R. F., McCollum, J., Ferraro, R. R., Petty, G., Shin, D.-B., & Wilheit, T. T. (2001). The evolution of the Goddard Profiling Algorithm (GPROF) for rainfall estimation from passive microwave sensors. *Journal of Applied Meteorology, 40*, 1801–1820. https://doi.org/10.1175/1520-0450(2001)040<1801:TEOTGP>2.0.CO;2.

Marzano, F. S., Palmacci, M., Cimini, D., Giuliani, G., & Turk, F. J. (2004). Multivariate statistical integration of satellite infrared and microwave radiometric measurements for rainfall retrieval at the geostationary scale. *IEEE Transactions on Geoscience and Remote Sensing, 42*, 1018–1032. https://doi.org/10.1109/TGRS.2003.820312.

Pan, B., Hsu, K., AghaKouchak, A. A., & Sorooshian, S. (2019). Improving precipitation estimation using convolutional neural network. *Water Resources Research, 55*(3), 2301–2321. https://doi.org/10.1029/2018WR02409.

Rosenfeld, D., Amitai, E., & Wolff, D. B. (1995). Classification of rain regimes by the three-dimensional properties of reflectivity fields. *Journal of Applied Meteorology, 34*, 198–211. https://doi.org/10.1175/1520-0450(1995)034<0198:CORRBT>2.0.CO;2.

Scofield, R. A. (1987). The NESDIS operational convective precipitation-estimation technique. *Monthly Weather Review, 115*, 1773–1793. https://doi.org/10.1175/1520-0493(1987)115<1773:TNOCPE>2.0.CO;2.

Sorooshian, S., Hsu, K.-L., Gao, X., Gupta, H. V., Imam, B., & Braithwaite, D. (2000). Evaluation of PERSIANN system satellite-based estimates of tropical rainfall. *Bulletin of the American Meteorological Society, 81*, 2035–2046. https://doi.org/10.1175/1520-0477(2000)081<2035:EOPSSE>2.3.CO;2.

Tao, Y., Gao, X., Hsu, K.-L., Sorooshian, S., & Ihler, A. (2016). A deep neural network modeling framework to reduce bias in satellite precipitation products. *Journal of Hydrometeorology, 17*, 931–945. https://doi.org/10.1175/JHM-D-15-0075.1.

Tao, Y., Gao, X., Ihler, A., Sorooshian, S., & Hsu, K.-L. (2017). Precipitation identification with bispectral satellite information using deep learning approaches. *Journal of Hydrometeorology, 18*, 1271–1283. https://doi.org/10.1175/JHM-D-16-0176.1.

Tapiador, F. J. (2008). A physically based satellite rainfall estimation method using fluid dynamics modelling. *International Journal of Remote Sensing, 29*, 5851–5862. https://doi.org/10.1080/01431160802029677.

Todd, M. C., Kidd, C., Kniveton, D. R., & Bellerby, T. J. (2001). A combined satellite infrared and passive microwave technique for estimation of small-scale rainfall. *Journal of Atmospheric and Oceanic Technology, 18*, 742–755. https://doi.org/10.1175/1520-0469(2001)058<0742:ACSIAP>2.0.CO;2.

Turk, F. J., & Miller, S. D. (2005). Toward improved characterization of remotely sensed precipitation regimes with MODIS/AMSR-E blended data techniques. *IEEE Transactions on Geoscience and Remote Sensing, 43*, 1059–1069. https://doi.org/10.1109/TGRS.2004.841627.

Ushio, T., Sasashige, K., Kubota, T., Shige, S., Okamoto, K. I., Aonashi, K., Inoue, T., Takahashi, N., Iguchi, T., Kachi, M., & Oki, R. (2009). A Kalman filter approach to the Global Satellite

Mapping of Precipitation (GSMaP) from combined passive microwave and infrared radiometric data. *Journal of the Meteorological Society of Japan, 87*, 137–151. https://doi.org/10.2151/jmsj.87A.137.

Vicente, G. A., Scofield, R. A., & Menzel, W. P. (1998). The operational GOES infrared rainfall estimation technique. *Bulletin of the American Meteorological Society, 79*, 1883–1898. https://doi.org/10.1175/1520-0477(1998)079<1883:TOGIRE>2.0.CO;2.

Weng, F., Zhao, L., Ferraro, R. R., Poe, G., Li, X., & Grody, N. C. (2003). Advanced microwave sounding unit cloud and precipitation algorithms. *Radio Science, 38*. https://doi.org/10.1029/2002RS002679.

Wu, M. L. C. (1985). Remote sensing of cloud-top pressure using reflected solar radiation in the oxygen A-band. *Journal of Climate and Applied Meteorology, 24*, 539–546. https://doi.org/10.1175/1520-0450(1985)024<0539:RSOCTP>2.0.CO;2.

Xu, L., Gao, X., Sorooshian, S., Arkin, P. A., & Imam, B. (1999). A microwave infrared threshold technique to improve the GOES precipitation index. *Journal of Applied Meteorology, 38*, 569–579. https://doi.org/10.1175/1520-0450(1999)038<0569:AMITTT>2.0.CO;2.

Chapter 22
TAMSAT

Ross Maidment, Emily Black, Helen Greatrex, and Matthew Young

Abstract Rainfall monitoring over Africa using satellite imagery is essential given the lack of land-based rainfall measurements and the dependency of economies largely based on climate-sensitive practices. Motivated by a need to monitor rainfall deficits and its impact on crop yield over the Sahel, the TAMSAT Group have, since the 1980s, helped pioneer the use of Meteosat thermal infrared (TIR) imagery for rainfall estimation using cold cloud duration (CCD). Unlike other TIR-based algorithms, the TAMSAT algorithm, which is calibrated using rain gauges, varies spatially and temporally to account for the strong spatial and seasonal changes in the rainfall climate across Africa. TAMSAT produce high-resolution (0.0375°), operational rainfall estimates from 1983 to the delayed present for all Africa, at the daily to seasonal time-step. Currently, TAMSAT is only one of a handful of datasets that provide long-term (+30 years) and sub-monthly rainfall estimates for Africa. The data, whose skill is comparable or better (depending on the metric) than other satellite products, are used by a variety of stakeholders in the commercial, humanitarian, agricultural and financial sectors. The temporal consistency and longevity of the TAMSAT record makes it a valuable dataset for climate monitoring and risk assessment.

Keywords Precipitation · Rainfall · TAMSAT · Infrared · GEO · LEO · Raingauges · Cold cloud duration · Africa · GPI · Meteosat · Climate services · Weather index insurance

---

The original version of this chapter was previously published non-open access. A Correction to this chapter is available at https://link.springer.com/chapter/10.1007/978-3-030-24568-9_25

R. Maidment (✉) · E. Black · H. Greatrex · M. Young
Department of Meteorology, University of Reading, Reading, Berkshire, UK
e-mail: r.i.maidment@reading.ac.uk

22.1   The History of TAMSAT

The African continent is a region where rainfall information is of utmost importance. This is especially the case in semi-arid regions such as the Sahel and southern Africa where the majority of livelihoods are highly sensitive to even small deviations in the expected rainfall patterns, resulting in adverse socioeconomic problems that may persist for many years (e.g., Boyd et al. 2013; Funk et al. 2013; Shiferaw et al. 2014).

With the exception of a few countries, the real-time African rain gauge network is extremely sparse compared to other inhabited continents (see Fig. 22.1), making it difficult to monitor real-time changes in rainfall using rain gauges alone. Several countries also have poor historical rain-gauge records, making long-term assessment of changes in rainfall challenging. As such, the use of satellite-derived rainfall information over areas where there are few or no rain gauges is of great value.

The "Tropical Applications of Meteorology using SATellite and ground-based observations" (TAMSAT) Group, was created in the late 1970s with the introduction of the European Organisation for the Exploitation of Meteorological Satellites (EUMETSAT)'s flagship Meteosat programme. The group, based within the Department of Meteorology at the University of Reading (United Kingdom) – a world-leading centre for weather and climate research – have pioneered the use of thermal infra-red (TIR) satellite imagery in rainfall estimation over Africa since the 1980s. Since this time, TAMSAT have been producing rainfall estimates operationally for Africa, based on the use of satellite-derived cold cloud duration (CCD), which has its roots in the work of Arkin and Meisner (1987) and the subsequent GOES Precipitation Index (GPI) rainfall product. The TAMSAT method was originally devised in
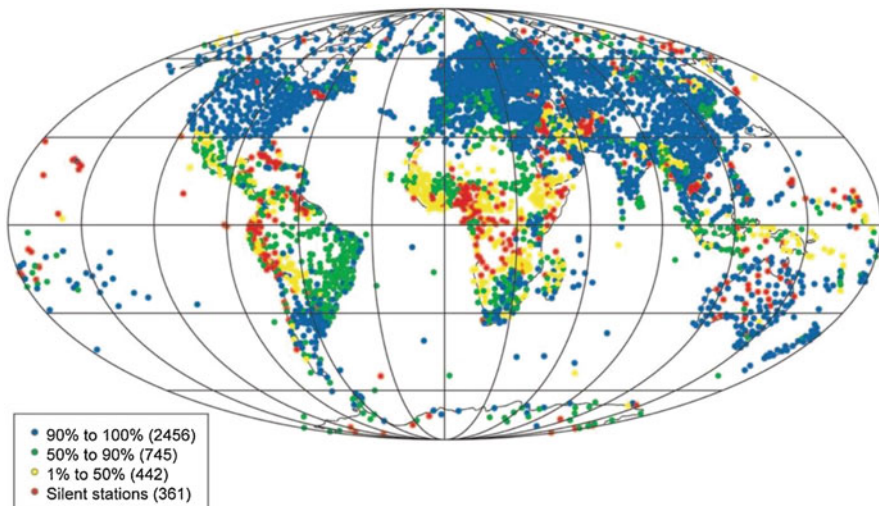
Fig. 22.1 The WMO World Weather Watch global distribution of the Regional Basis Synoptic Network weather stations providing SYNOP (surface synoptic observations) reports during October 2002. (WMO 2003). The colour denotes each station's reporting rate

response to the need for rapid in-season detection of below-average rainfall and potential losses in crop yield across the Sahel, but has since been extended to all Africa and is now used in a range of applications. Although the TAMSAT approach for estimating rainfall was significantly revised in 2017, the essence of the estimation method has remained unchanged in over 35 years.

The changes to the TAMSAT estimation approach in 2017 (used to generate TAMSAT v3.0), aimed at addressing shortcomings in the previous methodology and made possible by the availability of long (30+ years) daily rain gauge records for many stations, have resulted in vast improvements to the rainfall estimates. In particular, it has eliminated spatial discontinuities in the rainfall estimates that arose from boundaries between large climatologically similar "calibration zones" that were used in previous versions, and has reduced a large dry bias that was characteristic in previous estimates (Maidment et al. 2017; Dinku et al. 2018).

There is currently a variety of satellite-based rainfall datasets that provide coverage for Africa (see Table 22.1). Each has varying characteristics (including data inputs, temporal and spatial coverage/resolution, and latency) leading to different levels of skill for different applications. There is therefore, no one perfect dataset for all end-user applications. For example, some products that incorporate multiple sensor inputs might be more suited to event-based estimation (see the 'Primary Function' column in Table 22.1), but the incorporation of multiple sensors leads to relatively short records which limits their use for rainfall monitoring. The TAMSAT product falls in a different classification of multi-decadal products which also provide near-real time updates, making them useful for seasonal monitoring. Today, the TAMSAT Group are very active in ensuring the evolution of TAMSAT products using new technologies and data, and continue to promote TAMSAT products and related-research by regular attendance at the biennial EUMETSAT Africa User Forum and other relevant meetings.

22.2 TAMSAT Products

TAMSAT produces Africa-wide rainfall estimates at the daily, pentadal (5-day), dekadal (10-day), monthly and seasonal time-steps from January 1983 to the present on a regular $0.0375° \times 0.0375°$ (~ 4 km) grid. The primary product is the pentadal rainfall total (pentads are defined as *1st–5th, 6th–10th, 11th–15th, 16th–20th, 21st–25th and 26th*-last day of the month). Daily rainfall estimates are derived by disaggregating the pentadal rainfall total to daily rainfall totals by using the daily CCD fractions (described in Maidment et al. 2017), while the dekadal, monthly and seasonal estimates are derived by summing the respective pentadal estimates.

TAMSAT also produce rainfall anomalies for each time-step (except daily) against a 30-year climatology (1983–2012) and quick-look images for all rainfall estimates. The data files are released within 2 days after each pentad and available on

Table 22.1 Summary of widely used satellite rainfall datasets providing coverage for Africa

Name	Data input[a]	Spatial resolution	Temporal resolution (*only shorted listed*)	Spatial coverage	Start year	Primary function[b]	Reference
TAMSAT	TIR, gauge	0.0375°	Daily	Africa	1983	Climate	Maidment et al. (2014, 2017) and Tarnavsky et al. (2014)
CHIRP	TIR, TMPA-3B42	0.05°	Daily	50°N-S, 0°–360°E	1981	Climate	Funk et al. (2015a, b)
CHIRPS	TIR, TMPA-3B42, gauge	0.05°	Daily	50°N-S, 0°–360°E	1981	Climate	Funk et al. (2015a, b)
ARC	TIR, gauge	0.1°	Daily	40°N-S, 20°W-55°E	1983	Climate	Novella and Thiaw (2013)
RFE	TIR, PMW, gauge	0.1°	Daily	40°N-S, 20°W-55°E	1995	Weather	Herman et al. (1997)
GPCP	TIR, PMW, gauge	2.5°	Monthly	Global	1979	Climate	Huffman et al. (2009)
GPCP-1DD	TIR, PMW, gauge	1°	Daily	Global	1996	Weather	Huffman et al. (2001)
GPI	TIR	2.5°	Monthly	40°N-S	1986	Climate	Arkin and Meisner (1987)
IMERG	TIR, PMW, radar, gauge	0.1°	30-min	Global	2014	Weather	Huffman et al. (2015)
TRMM 3B42	TIR, PMW, radar, gauge	0.25°	3 hourly	50°N-S, 0°–360°E	1997 (end 2015)	Weather	Huffman et al. (2007) and Kummerow et al. (2000)
TRMM 3B43	TIR, PMW, radar, gauge	0.25°	Monthly	50°N-S, 0°–360°E	1997 (end 2015)	Climate	
CMORPH	TIR, PMW	0.07°	30-min	60°N-S	2002	Weather	Joyce et al. (2004)
PERSIANN	TIR, PMW	0.25°	6 hourly	60°N-S	2000	Weather	Hsu and Sorooshian (2008)

Table 22.1 (continued)

Name	Data input[a]	Spatial resolution	Temporal resolution (*only shorted listed*)	Spatial coverage	Start year	Primary function[b]	Reference
CMAP	TIR, PMW, gauge, model	2.5°	Pentad	Global	1979	Climate	Xie and Arkin (1997)
EPSAT-SG	TIR, PMW, radar, gauge	0.0375°	15-min	Africa	2004	Weather	Bergès et al. (2010)

[a]*TIR* thermal infra-red, *PMW* passive microwave

[b]The primary function gives the intended use of the dataset, although some datasets may have interchangeable use. Datasets designated as *climate* refer to those products suited for climate applications, such as climate research and long-term monitoring analysis, whilst datasets designated *weather* refer to those products aimed at weather analysis, such as event-scale rain rates and rainfall coverage

Adapted from Maidment et al. (2014)
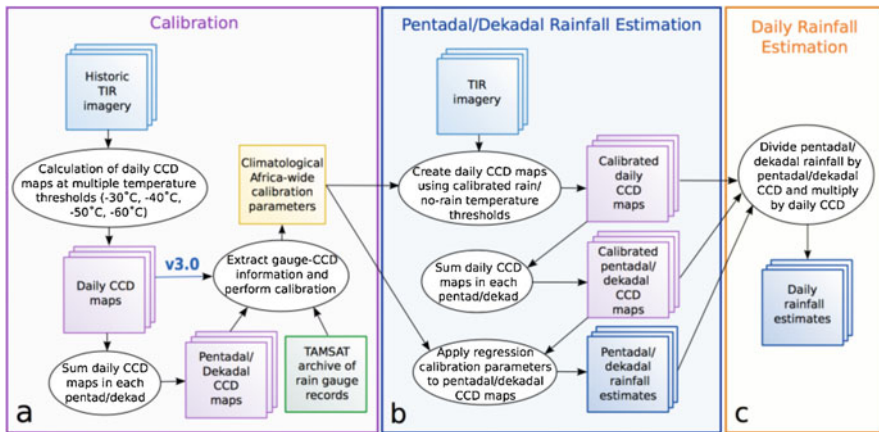
Fig. 22.2 Schematic summarising the TAMSAT calibration and rainfall estimation process. Squares denote inputs or outputs and ovals denote processes. (Adapted from Maidment et al. 2017)

the TAMSAT website (http://www.tamsat.org.uk) in netCDF format. The calibration (described in the next section) and estimation process is summarised in Fig. 22.2, with an example of a monthly estimate and anomaly given in Fig. 22.3.
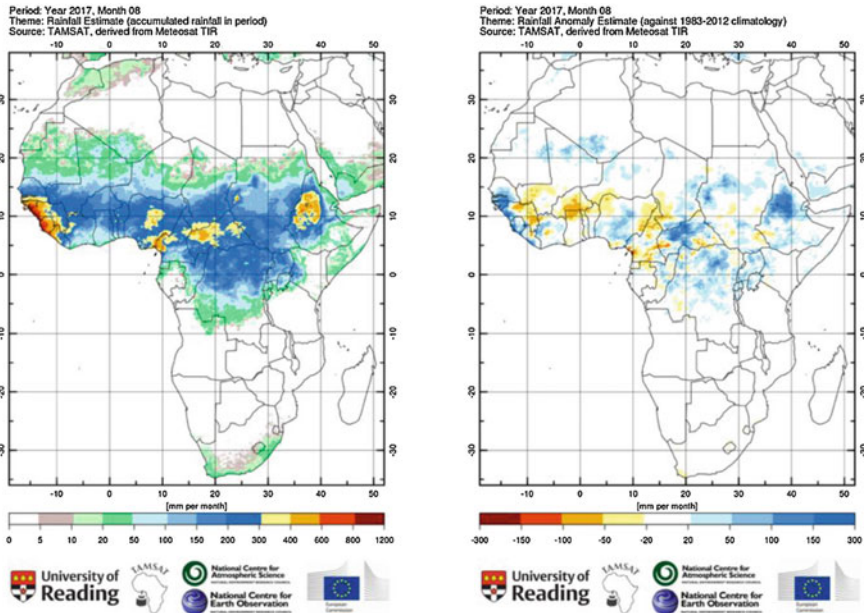
Fig. 22.3 TAMSAT v3.0 rainfall total (left) and rainfall anomaly (right) for August 2017

22.3 The TAMSAT Rainfall Estimation Approach

22.3.1 Overview

TAMSAT rainfall estimates are derived primarily from two inputs; Meteosat TIR imagery from EUMETSAT, and in situ rainfall measurements from rain gauges, used for calibration. The premise of the TAMSAT rainfall estimation methodology is based on the detection of precipitating storm clouds, characterised by their cold cloud tops, using TIR. Such clouds are readily identified from the warmer land surface or shallow non-precipitating clouds below (this is illustrated in Fig. 22.4).

The assumptions behind the TAMSAT method are:

1. Rainfall predominantly comes from convective cumulonimbus storm clouds.
2. These clouds will only start precipitating once their tops have reached a certain height. As temperature decreases with height throughout the atmosphere, the height of the cloud top can be inferred by the temperature from the TIR imagery. This is the threshold temperature (T_t), and can be defined as the cloud top temperature that best distinguishes between rain and no rain (illustrated in Fig. 22.5).
3. The amount of rainfall can be determined by the length of time the cloud top temperature is colder than T_t. This is the cold cloud duration or CCD.
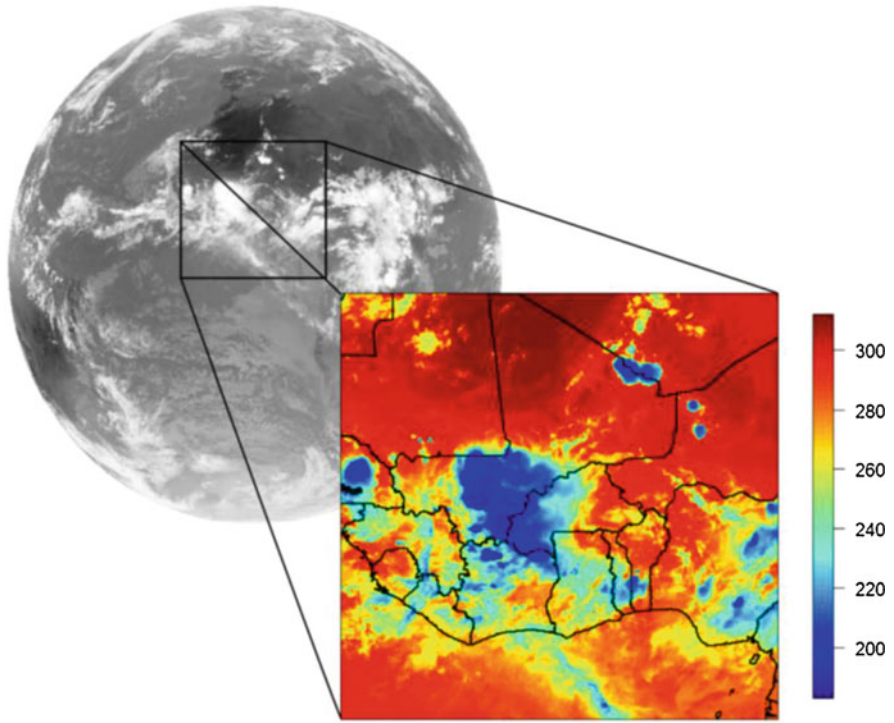
Fig. 22.4 Full disc (background) Meteosat-8 thermal-infrared image captured at 1800 UTC on 12 August 2005. The grey scale assigned signifies warmer (colder) surfaces as the darker (whiter) regions. A subset (foreground) of this image projected onto a longitude-latitude grid over West Africa giving the brightness temperature (scale in K) of the scene observed

Fig. 22.5 Schematic illustrating the assumptions in the TAMSAT algorithm. Clouds with tops colder than the threshold temperature (T_t) are assumed to be raining, while clouds with tops warmer than T_t are assumed not to be raining (schematic by David Grimes)
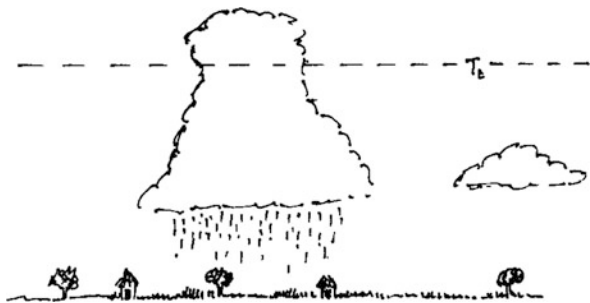
4. Rainfall is linearly related to CCD, provided sufficient averaging of the data in space and/or time.

The TAMSAT method can thus be categorised as a cloud indexing approach, in that TIR imagery is used to identify areas of cold cloud, and in turn, maps of CCD. To convert CCD to rainfall, we apply the following equations:

$$If \ (CCD_T = 0), \ R = 0$$
$$If(CCD_T > 0), \ R = a_0 + a_1 CCD_T$$

(22.1)

where R is rainfall, CCD_T is the cold cloud duration at a given threshold temperature, and a_0, a_1 are the offset and slope of the linear regression between R and CCD_T.

The regression coefficients (a_0 and a_1) and the threshold temperature (T_t) at which the CCD_T is calculated are derived during the calibration stage. Where CCD_T is equal to zero, it is assumed rainfall is also zero.

The long-standing ethos of the TAMSAT system has been to provide a fully automated, and pre-calibrated algorithm. As such, the TAMSAT calibration compares gauges and CCD to derive the threshold temperature and regression coefficients, in the form of Africa-wide calibration maps, which are applied in near-real time to estimate rainfall from satellite imagery. This approach overcomes the need for contemporaneous rain gauge records, simplifying the operational implementation of the method.

22.3.2 Calibration Method

The calibration process, which is carried out periodically when additional rain gauge records become available, can be summarised as follows:

- For all available daily gauge records in the TAMSAT archive, pixel-scale daily CCD values at multiple threshold temperatures (213 K/−60 °C to 243 K/ −30 °C at 10 K intervals) are extracted. Gauge-CCD pairs for CCD values at 1 K intervals between 213 and 243 K are then derived by interpolating between the existing CCD thresholds.
- The daily gauge-CCD pairs are then spatially binned into $1° \times 1°$ grid squares across Africa to determine the T_t for each grid. A $1° \times 1°$ grid is deemed large enough to contain sufficient gauge-CCD pairs to derive stable calibration parameters, yet small enough to capture local variations in the rainfall climate. For each threshold temperature, a contingency table is constructed (see Table 22.2) which compares the occurrence of rainfall and CCD for all gauge-CCD pairs in each

Table 22.2 Contingency table for determining T_t. The occurrence threshold is set at zero for both rainfall (mm) and CCD (hours). All gauge-CCD pairs are split into one of four possible groups (n_{11}: n_{22}) with the counts for each group recorded

	CCD = 0	CCD > 0
Gauge = 0	n_{11}	n_{12}
Gauge > 0	n_{21}	n_{22}

n_{11} is the number of occasions where both zero rainfall and CCD is observed
n_{12} is the number of occasions where zero rainfall is recorded but CCD is detected
n_{21} is the number of occasions where rainfall is recorded but no CCD is detected
n_{22} is the number of occasions where both rainfall and CCD are greater than zero

grid box (by considering the hits, misses, false alarms and correct negatives). The T_t is the threshold temperature which maximises agreement and minimises disagreement between rainfall and CCD. In practice, T_t is therefore the threshold temperature whose occurrence of misses and false alarms are roughly balanced, thus minimising any underestimation or overestimation of rainfall occurrence. Given the lack of gauge observations in places, this is only done for boxes where at least 100 gauge-CCD pairs exist. The derived T_t values are then spatially interpolated to produce Africa-wide maps for each calendar month (see Fig. 22.6).

- The derivation of a_0 and a_1 is based on 5-day sums of the daily gauge-CCD pairs. For each $1° \times 1°$ grid box, the gauge-CCD pairs are binned (by CCD value) and regressed by comparing the mean rainfall against the mean CCD for each bin, to obtain a_0 and a_1 respectively. This is repeated for each CCD threshold value across all grid boxes and months. All regression coefficients are then modelled as a function of T_t to produce maps of a_0 and a_1 based on the T_t map for the respective month. Finally, these maps are then adjusted by the Climate Hazards Group's Precipitation Climatology (CHPclim) pentadal rainfall climatology (described in Funk et al. 2015a, b) to account for geographical rainfall artefacts (e.g., orographic enhancement) that the CCD and available rain gauge measurements alone do not capture. This results in a set of 72 maps (one for each pentad) of a_0 and a_1.

A novel feature of the TAMSAT approach that differs from other existing TIR-based algorithms is that the parameters T_t, a_0 and a_1 vary both spatially and temporally to account for the strong geographical and seasonal changes in the rainfall climate across the African continent. While some other TIR-based approaches use fixed calibration parameters (e.g., GPI), several studies have
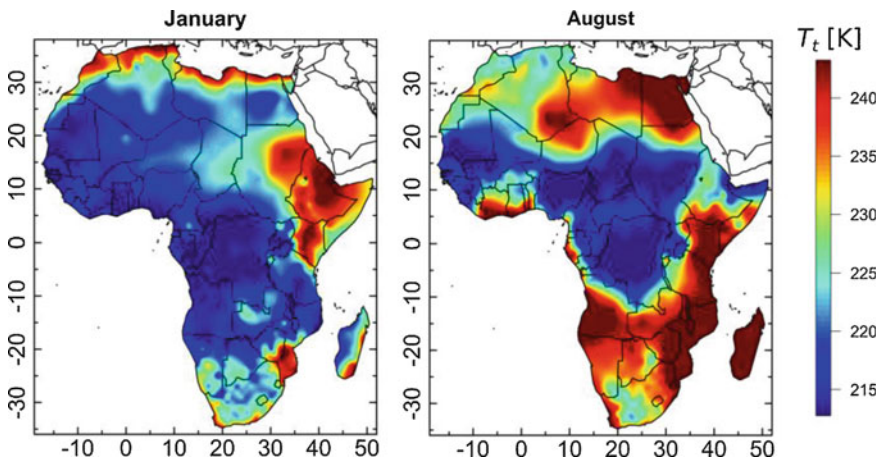
Fig. 22.6 TAMSAT v3.0 threshold temperature (T_t) maps for January (left) and August (right) respectively

indicated that a single rainfall-CCD relationship is inadequate over Africa, especially for products that depend entirely on satellite imagery (e.g., Dugdale et al. 1991; Todd et al. 1999, 1995; Dybkjær 2003; Chadwick et al. 2010). This is evident in Fig. 22.6 for example, which shows the T_t map used in the TAMSAT v3.0 calibration for January and August respectively. Across southern West Africa for example, the T_t varies by around 30 K between the dry season (January) and peak of the West African Monsoon (August), and also by a similar magnitude between the Guinea Coast and the Sahel (between 10°W and 5°E) during August. These drastic changes over southern West Africa during the rainy season are a result of a large influx of low-level moisture from the Gulf of Guinea and enhanced mid-tropospheric subsidence towards the coast (Omotosho 1988) which promotes the development of considerably shallower rainfall systems (Schumacher and Houze 2003; Liu and Zipser 2009; Mülmenstädt et al. 2015; Young et al. 2018), and necessitates the need for a warmer threshold. Conversely, during the dry season, rainfall typically only occurs when convective systems are very deep, reflected by a colder threshold. This is also the case as one moves northward towards the Sahel where moisture availability becomes more limited, and only the deepest of storm systems precipitate.

22.3.3   Strengths and Limitations

Many studies that have evaluated TAMSAT rainfall estimates using rain gauges, in conjunction with other satellite products, have generally demonstrated that TAMSAT data performs well and has comparable, or better skill than other datasets (Laurent et al. 1998; Thorne et al. 2001; Tucker and Sear 2001; Dinku et al. 2007, 2018; Chadwick et al. 2010; Jobard et al. 2011; Maidment et al. 2013, 2017; Ayehu et al. 2018; Young et al. 2014), although performance does vary depending on the time-step and spatial aggregation of the data, as well as region and season in question. Of the studies evaluating TAMSAT v3.0 against v2.0, the results indicate that v3.0 is a major improvement over v2.0 and compares favourably with other satellite products, particularly in regards to reducing bias (Maidment et al. 2017; Dinku et al. 2018). The skill of the TAMSAT data is notable given that no rain gauge measurements are directly included in the TAMSAT estimates, indicating that a locally calibrated, TIR-based approach can provide reliable rainfall information.

The success of the TAMSAT method can be attributed to several reasons:

- Where rainfall is primarily convective in nature, CCD can act as a useful proxy for rainfall. As the duration of cold cloud increases with the number of rain storms that passes over a given point, the association between rainfall and CCD increases. As such, the TAMSAT method is very well-suited for tropical regions where precipitation is predominantly convective in origin, such as the flat, semi-arid inland regions of Africa such as the Sahel and central southern Africa.
- As TAMSAT is locally calibrated, it is tuned to the expected CCD-rainfall relationship for a given region.

- As the Meteosat satellites follow a geostationary orbit, the on-board sensor is able to provide full spatial coverage of the African continent (see Fig. 22.4) and at frequent intervals (every 30-min for Meteosat First Generation of satellites and every 15-min since the introduction of the Meteosat Second Generation in 2002). Such coverage and sampling enable the CCD product to adequately capture the rapid evolution of such systems anywhere across the continent.

Despite the skill, there are some notable shortcomings to the TAMSAT method that users need to consider:

- Persistent cirrus, which is cold enough to be mistaken as precipitating storm clouds, can lead to an overestimation of rainfall. In practice though, this is typically not a significant problem across most months and locations.
- Extreme rainfall events are often underestimated as there is not enough information in the CCD product to capture intense rain rates over short periods. In practice, this is only a concern for daily rainfall amounts.
- The influence of large bodies of water (i.e. around lakes and near the coast) and presence of complex topography (e.g., Ethiopian highlands) can create microclimates that modulate the CCD-rainfall relationship.
- Long-lived shallow precipitating systems (e.g., stratiform rainfall) are non-distinguishable from non-raining cloud, leading the TAMSAT algorithm to have considerably lower skill during such events.

22.4 Usage and Applications

The TAMSAT Group have built up strong relationships with many African National Meteorological and Hydrological Services (NMHS) and other stakeholders, across a range of sectors, and have established themselves as a dependable source of reliable rainfall information. TAMSAT have worked closely with many African agencies – by developing TAMSAT products during TAMSAT-led workshops, and by providing capacity building through training Met Service staff to operate TAMSAT rainfall estimation software and applying TAMSAT rainfall estimates appropriately. In recent years, the bond between TAMSAT and African NMHS has strengthened further by a WMO-led programme supporting forecasters to study at the University of Reading and work with the TAMSAT Group. The value of such relationships is paramount not only to the effective use of TAMSAT data, but also to the development and evolution of TAMSAT rainfall estimates and related products, through improved access to climate records and trialling newly developed tools.

TAMSAT data plays a key role in supporting climate services in many African countries, for example, through the various agencies that access the data through EUMETSAT's EUMETCast distribution service, as well as the Enhancing National Climate Services (ENACTS) (Dinku et al. 2016) and Rainwatch (Tarhule et al. 2009) programmes, that provide value-added services using TAMSAT data. The data is also well used by the research community, for example, by furthering our

understanding of rainfall variability and trends across Africa (e.g., Maidment et al. 2015; Dunning et al. 2016; Cattani et al. 2018).

In recent years, the focus of TAMSAT has broadened to encompass a range of stakeholders in the commercial, humanitarian, agricultural and financial sectors. The temporal consistency and longevity of the TAMSAT record makes it a valuable dataset for risk assessment. In particular, as TAMSAT's primary rainfall product does not incorporate contemporaneous rain gauge measurements, its skill is unaffected by changes in gauge coverage that can introduce time-dependent biases into the rainfall record (Maidment et al. 2015). As an example of TAMSAT's adoption for risk management, TAMSAT rainfall is now widely used in weather index insurance – a form of insurance that pays out in the event of a weather index being breached (Black et al. 2016a, b). A temporally consistent record is especially important in the insurance industry where premium rates are often calculated using a historical burn analysis of long time-series. In 2017–2018, TAMSAT rainfall estimation enabled over 1 Million farmers to be insured using weather index insurance.

The myriad of publicly available Earth Observation and reanalysis products provide many opportunities to improve drought risk assessment. This raises the question of how users can assess risk in the face of multiple sources of information. The development of the TAMSAT-ALERT system (Brown et al. 2017; Asfaw et al. 2018) meets this need by deriving objective agricultural risk assessments based on seasonal weather, the historical climatology, the condition of the land surface and meteorological forecasts. Over the next years, TAMSAT will work with the humanitarian and agricultural sectors, as well as NMHS to implement TAMSAT-ALERT across Africa.

References

Arkin, P. A., & Meisner, B. N. (1987). The relationship between large-scale convective rainfall and cold cloud over the western hemisphere during 1982–84. *Monthly Weather Review, 115*, 51–74. https://doi.org/10.1175/1520-0493(1987)115%3C0051:TRBLSC%3E2.0.CO.

Asfaw, D., Black, E., Brown, M., Nicklin, K. J., Otu-Larbi, F., Pinnington, E., Challinor, A., Maidment, R., & Quaife, T. (2018). TAMSAT-ALERT v1: A new framework for agricultural decision support. *Geoscientific Model Development, 11*, 2353–2371. https://doi.org/10.5194/gmd-11-2353-2018.

Ayehu, G. T., Tadesse, T., Gessesse, B., & Dinku, T. (2018). Validation of new satellite rainfall products over the Upper Blue Nile Basin, Ethiopia. *Atmospheric Measurement Techniques, 11*, 1921–1936. https://doi.org/10.5194/amt-11-1921-2018.

Bergès, J., Jobard, I., Chopin, F., & Roca, R. (2010). EPSAT-SG: a satellite method for precipitation estimation; its concepts and implementation for the AMMA experiment. *Annales Geophysicae, 28*, 289–308. https://doi.org/10.5194/angeo-28-289-2010.

Black, E., Greatrex, H., Young, M., & Maidment, R. (2016a). Incorporating satellite data into weather index insurance. *Bulletin of the American Meteorological Society, 97*, ES203–ES206. https://doi.org/10.1175/BAMS-D-16-0148.1.

Black, E., Tarnavsky, E., Maidment, R., Greatrex, H., Mookerjee, A., Quaife, T., & Brown, M. (2016b). The use of remotely sensed rainfall for managing drought risk: A case study of

Weather Index Insurance in Zambia. *Remote Sensing, 8*, 342. https://doi.org/10.3390/rs8040342.

Boyd, E., Cornforth, R. J., Lamb, P. J., Tarhule, A., Lélé, M. I., & Brouder, A. (2013). Building resilience to face recurring environmental crisis in African Sahel. *Nature Climate Change, 3*, 631–637. https://doi.org/10.1038/nclimate1856.

Brown, M., Black, E., Asfaw, D., & Otu-Larbi, F. (2017). Monitoring drought in Ghana using TAMSAT-ALERT: a new decision support system. *Weather, 72*(7), 201–205. https://doi.org/10.1002/wea.3033.

Cattani, E., Merino, A., Guijarro, J. A., & Levizzani, V. (2018). East Africa rainfall trends and variability 1983–2015 using three long-term satellite products. *Remote Sensing, 10*, 931. https://doi.org/10.3390/rs10060931.

Chadwick, R. S., Grimes, D. I. F., Saunders, R. W., Francis, P. N., & Blackmore, T. A. (2010). The TAMORA algorithm: satellite rainfall estimates over West Africa using multi-spectral SEVIRI data. *Advances in Geosciences, 25*, 3–9. https://doi.org/10.5194/adgeo-25-3-2010.

Dinku, T., Ceccato, P., Grover-Kopec, E., Lemma, M., Connor, S. J., & Ropelewski, C. F. (2007). Validation of satellite rainfall products over East Africa's complex topography. *International Journal of Remote Sensing, 28*(7), 1503–1526. https://doi.org/10.1080/01431160600954688.

Dinku, T., Cousin, R., del Corral, J., Ceccato, P., Thomson, M., Faniriantsoa, R., Khomyakov, I., & Vadillo, A. (2016). *The ENACTS approach: Transforming climate services in Africa one country at a time*. World Policy Papers, 24 pp. Available at: https://worldpolicy.org/wp-content/uploads/2016/03/The-ENACTS-Approach-Transforming-Climate-Services-in-Africa-One-Country-at-a-Time.pdf. Last accessed 16 Oct 2018.

Dinku, T., Funk, C., Peterson, P., Maidment, R., Tadesse, T., Gadain, H., & Ceccato, P. (2018). Validation of the CHIRPS satellite rainfall estimates over eastern Africa. *Quarterly Journal of the Royal Meteorological Society, 144*(S1), 292–312. https://doi.org/10.1002/qj.3244.

Dugdale, G., McDougall, V. D., & Milford, J. R. (1991). Rainfall estimates in the Sahel from cold cloud statistics: Accuracy and limitations of operational systems. *Proceedings of workshop "Soil water balance in the Sudano-Sahelian Zone"*. Niamey, IAHS 199, 65–74.

Dunning, C. M., Black, E. C. L., & Allan, R. P. (2016). The onset and cessation of seasonal rainfall over Africa. *Journal of Geophysical Research, 121*, 11405–11424. https://doi.org/10.1002/2016JD025428.

Dybkjær, G. (2003). A simple self-calibrating cold cloud duration technique applied in West Africa and Bangladesh. *Geografisk tidskrift, 103*, 83–98. https://doi.org/10.1080/00167223.2003.10649482.

Funk, C., Husak, G., Michaelsen, J., Shukla, S., Hoell, A., Lyon, B., Hoerling, M. P., Liebmann, B., Zhang, T., Verdin, J., Galu, G., Eilerts, G., & Rowland, J. (2013). Attribution of 2012 and 2003–12 rainfall deficits in Eastern Kenya and Southern Somalia. [In: "Explaining Extreme Events of 2012 from a Climate Perspective"]. *Bulletin of the American Meteorological Society, 94*, S45–S48. https://doi.org/10.1175/BAMS-D-13-00085.1.

Funk, C., Verdin, A., Michaelsen, J., Peterson, P., Pedreros, D., & Husak, G. (2015a). A global satellite-assisted precipitation climatology. *Earth System Science Data, 7*, 275–287. https://doi.org/10.5194/essd-9-389-2017.

Funk, C., Peterson, P., Landsfeld, M., Pedreros, D., Verdin, J., Shukla, S., Husak, G., Rowland, J., Harrison, L., Hoell, A., & Michaelsen, J. (2015b). The climate hazards infrared precipitation with stations—A new environmental record for monitoring extremes. *Scientific Data, 2*, 150066. https://doi.org/10.1038/sdata.2015.66.

Herman, A., Kumar, V. B., Arkin, P. A., & Kousky, J. V. (1997). Objectively determined 10-day African rainfall estimates created for famine early warning systems. *International Journal of Remote Sensing, 18*, 2147–2159. https://doi.org/10.1080/014311697217800.

Hsu, K.-L., & Sorooshian, S. (2008). Satellite-based precipitation measurement using PERSIANN system. In S. Sorooshian, K.-L. Hsu, E. Coppola, B. Tomassetti, & M. Verdecchia (Eds.), *Hydrological modelling and the water cycle* (pp. 27–48). Berlin/Heidelberg: Springer. https://doi.org/10.1007/978-3-540-77843-1_2.

Huffman, G. J., Adler, R. F., Morrissey, M. M., Bolvin, D. T., Curtis, S., Joyce, R., McGavock, B., & Susskind, J. (2001). Global precipitation at one-degree daily resolution from multisatellite observations. *Journal of Hydrometeorology, 2*, 36–50. https://doi.org/10.1175/1525-7541 (2001)002<0036:GPAODD>2.0.CO;2.

Huffman, G. J., Bolvin, D. T., Nelkin, E. J., Wolff, D. B., Adler, R. F., Gu, G., Hong, Y., Bowman, K. P., & Stocker, E. F. (2007). The TRMM Multisatellite Precipitation Analysis (TMPA): Quasi-global, multiyear, combined-sensor precipitation estimates at fine scales. *Journal of Hydrometeorology, 8*, 38–55. https://doi.org/10.1175/JHM560.1.

Huffman, G. J., Adler, R. F., Bolvin, D. T., & Gu, G. (2009). Improving the global precipitation record: GPCP Version 2.1. *Geophysical Research Letters, 36*, L17808. https://doi.org/10.1029/2009GL040000.

Huffman, G. J., Bolvin, D. T., Braithwaite, D., Hsu, K., Joyce, R., Kidd, C., Nelkin, E. J., & Xie, P. (2015). *NASA Global Precipitation Measurement (GPM) Integrated Multi-satellitE Retrievals for GPM (IMERG)*. Algorithm Theoretical Basis Doc., version 4.5, 26 pp. Available online at http://pmm.nasa.gov/sites/default/files/document_files/IMERG_ATBD_V4.5.pdf.

Jobard, I., Chopin, F., Berges, J. C., & Roca, R. (2011). An intercomparison of 10-day satellite precipitation products during West African monsoon. *International Journal of Remote Sensing, 32*, 2353–2376. https://doi.org/10.1080/01431161003698286.

Joyce, R. J., Janowiak, J. E., Arkin, P. A., & Xie, P. (2004). CMORPH: A method that produces global precipitation estimates from passive microwave and infrared data at high spatial and temporal resolution. *Journal of Hydrometeorology, 5*, 487–503. https://doi.org/10.1175/1525-7541(2004)005<0487:CAMTPG>2.0.CO;2.

Kummerow, C., Simpson, J., Thiele, O., Barnes, W., Chang, A. T. C., Stocker, E., Adler, R. F., Hou, A., Kakar, R., Wentz, F., Ashcroft, P., Kozu, T., Hong, Y., Okamoto, K., Iguchi, T., Kuroiwa, H., Im, E., Haddad, Z., Huffman, G., Ferrier, B., Olson, W. S., Zipser, E., Smith, E. A., Wilheit, T. T., North, G., Krishnamurti, T., & Nakamura, K. (2000). The status of the Tropical Rainfall Measuring Mission (TRMM) after two years in orbit. *Journal of Applied Meteorology, 39*, 1965–1982. https://doi.org/10.1175/1520-0450(2001)040<1965:TSOTTR>2.0.CO;2.

Laurent, H., Jobard, I., & Toma, A. (1998). Validation of satellite and ground-based estimates of precipitation over the Sahel. *Atmospheric Research, 47*, 651–670. https://doi.org/10.1016/S0169-8095(98)00051-9.

Liu, C., & Zipser, E. J. (2009). "Warm Rain" in the Tropics: Seasonal and regional distributions based on 9 yr of TRMM data. *Journal of Climate, 22*, 767–779. https://doi.org/10.1175/2008JCLI2641.1.

Maidment, R. I., Grimes, D. I. F., Allan, R. P., Greatrex, H., Rojas, O., & Leo, O. (2013). Evaluation of satellite-based and model re-analysis rainfall estimates for Uganda. *Meteorological Applications, 20*, 308–317. https://doi.org/10.1002/met.1283.

Maidment, R. I., Grimes, D., Allan, R. P., Tarnavsky, E., Stringer, M., Hewison, T., Roebeling, R., & Black, E. (2014). The 30 year TAMSAT African Rainfall Climatology And Time Series (TARCAT) data set. *Journal of Geophysical Research, 119*, 10,619–10,644. https://doi.org/10.1002/2014JD021927.

Maidment, R. I., Allan, R. P., & Black, E. (2015). Recent observed and simulated changes in precipitation over Africa. *Geophysical Research Letters, 42*, 8155–8164. https://doi.org/10.1002/2015GL065765.

Maidment, R. I., Grimes, D., Black, E., Tarnavsky, E., Young, M., Greatrex, H., Allan, R. P., Stein, T., Nkonde, E., Senkunda, S., & Uribe Alcántara, E. M. (2017). Data Descriptor : A new, long-term daily satellite-based rainfall dataset for operational monitoring in Africa. *Scientific Data, 4*, 170063. https://doi.org/10.1038/sdata.2017.63.

Mülmenstädt, J., Sourdeval, O., Delanoë, J., & Quaas, J. (2015). Frequency of occurrence of rain from liquid-, mixed-, and ice-phase clouds derived from A-Train satellite retrievals. *Geophysical Research Letters, 42*(15), 6502–6509. https://doi.org/10.1002/2015GL064604.

Novella, N. S., & Thiaw, W. M. (2013). African Rainfall Climatology Version 2 for famine early warning systems. *Journal of Applied Meteorology and Climatology, 52*, 588–606. https://doi.org/10.1175/JAMC-D-11-0238.1.

Omotosho, J. B. (1988). Spatial variation of rainfall in Nigeria during the "little dry season". *Atmospheric Research, 22*(2), 137–147. https://doi.org/10.1016/0169-8095(88)90004-X.

Schumacher, C., & Houze, R. A., Jr. (2003). The TRMM Precipitation Radar's view of shallow, isolated rain. *Journal of Applied Meteorology, 42*, 1519–1524. https://doi.org/10.1175/1520-0450(2003)042<1519:TTPRVO>2.0.CO;2.

Shiferaw, B., Tesfaye, K., Kassie, M., Abate, T., Prasanna, B. M., & Menkir, A. (2014). Managing vulnerability to drought and enhancing livelihood resilience in sub-Saharan Africa: Technological, institutional and policy options. *Weather Climate Extremes, 3*, 67–79. https://doi.org/10.1016/j.wace.2014.04.004.

Tarhule, A., Saley-Bana, Z., & Lamb, P. J. (2009). Rainwatch. *Bulletin of the American Meteorological Society, 90*, 1607–1614. https://doi.org/10.1175/2009BAMS2697.1.

Tarnavsky, E., Grimes, D., Maidment, R., Black, E., Allan, R. P., & Stringer, M. (2014). Extension of the TAMSAT satellite-based rainfall monitoring over Africa and from 1983 to present. *Journal of Applied Meteorology and Climatology, 53*, 2805–2822. https://doi.org/10.1175/JAMC-D-14-0016.1.

Thorne, V., Coakeley, P., Grimes, D., & Dugdale, G. (2001). Comparison of TAMSAT and CPC rainfall estimates with raingauges, for southern Africa. *International Journal of Remote Sensing, 22*, 1951–1974. https://doi.org/10.1080/01431160118816.

Todd, M. C., Barrett, E. C., Beaumont, M. J., & Green, J. L. (1995). Satellite identification of rain days over the Upper Nile river basin using an optimum infrared rain/no-rain threshold temperature model. *Journal of Applied Meteorology, 34*, 2600–2611. https://doi.org/10.1175/1520-0450(1995)034<2600:SIORDO>2.0.CO;2.

Todd, M. C., Barrett, E. C., Beaumont, M. J., & Bellerby, T. J. (1999). Estimation of daily rainfall over the upper Nile river basin using a continuously calibrated satellite infrared technique. *Meteorological Applications, 6*, 201–210. https://doi.org/10.1017/S1350482799001206.

Tucker, M. R., & Sear, C. B. (2001). A comparison of Meteosat rainfall estimation techniques in Kenya. *Meteorological Applications, 8*, 107–117. https://doi.org/10.1017/S1350482701001098.

WMO. (2003). *World Weather Watch – Twenty-second status report on implementation*, Rep. 957, 60 pp. Available at: https://library.wmo.int/index.php?lvl=notice_display&id=10171#.W8YDh6dabPA. Last accessed 16 Oct 2018.

Xie, P., & Arkin, P. A. (1997). Global precipitation: A 17-year monthly analysis based on gauge observations, satellite estimates, and numerical model outputs. *Bulletin of the American Meteorological Society, 78*, 2539–2558. https://doi.org/10.1175/1520-0477(1997)078<2539:GPAYMA>2.0.CO;2.

Young, M. P., Williams, C. J. R., Chiu, J. C., & Maidment, R. I. (2014). Investigation of discrepancies in satellite rainfall estimates over Ethiopia. *Journal of Hydrometeorology, 15*, 2347–2369. https://doi.org/10.1175/JHM-D-13-0111.1.

Young, M. P., Chiu, J. C., Williams, C. J. R., Stein, T. H. M., Stengel, M., Fielding, M. D., & Black, E. (2018). Spatio-temporal variability of warm rain events over southern West Africa from geostationary satellite observations for climate monitoring and model evaluation. *Quarterly Journal of the Royal Meteorological Society, 144*, 2311–2330. https://doi.org/10.1002/qj.3372.

Chapter 23
Algorithm and Data Improvements for Version 2.1 of the Climate Hazards Center's InfraRed Precipitation with Stations Data Set

Chris Funk, Pete Peterson, Martin Landsfeld, Frank Davenport, Andreas Becker, Udo Schneider, Diego Pedreros, Amy McNally, Kristi Arsenault, Laura Harrison, and Shraddhanand Shukla

Abstract To support global drought early warning, the Climate Hazards Center (CHC) at the University of California, Santa Barbara developed the Climate Hazards center InfraRed Precipitation with Stations (CHIRPS) dataset, in collaboration with the US Geological Survey and NASA SERVIR. Specifically designed to support early warning applications, CHIRPS has high a spatial resolution (0.05°), a long period of record (1981 to the near present), and relatively low latencies. Here we will describe a brief formal analysis of distributional bias in CHIRPS2.0. This analysis reveals, as expected, that CHIRPS2.0 means are very similar to observed station

C. Funk (✉)
United States Geological Survey, Earth Resources Observation and Science Center, Sioux Falls, SD, USA

Climate Hazards Center, University of California, Santa Barbara, CA, USA
e-mail: chris@geog.ucsb.edu

P. Peterson · M. Landsfeld · F. Davenport · L. Harrison · S. Shukla
Climate Hazards Center, University of California, Santa Barbara, CA, USA

A. Becker · U. Schneider
Global Precipitation Climatology Centre (GPCC), Deutscher Wetterdienst (DWD), Offenbach, Germany

D. Pedreros
United States Geological Survey, Earth Resources Observation and Science Center, Sioux Falls, SD, USA

A. McNally
Earth Systems Science Interdisciplinary Center, University of Maryland, College Park, MD, USA

NASA, Goddard Space Flight Center, Greenbelt, MD, USA

K. Arsenault
NASA, Goddard Space Flight Center, Greenbelt, MD, USA

SAIC, Inc, McLean, VA, USA

data. However, a closer look suggests that low precipitation values are underestimated and high values are over-estimated in the CHIRPS2.0. We describe a potential correction for this below.

23.1 Context – Increasing Food Insecurity and the CHIRPS2.0 Dataset

Agricultural production shortfalls and food price volatility are severe problems for millions of people. Global food production will need to increase by 70% by 2050 to meet global demand (FAO 2009; Brown et al. 2017), as stagnating yield growth and rapid population growth reduces per capita cereal production in many poorer nations (Brown et al. 2017; FAO 2009; Funk and Brown 2009). The United Nations (UN) Food and Agriculture Organization (FAO) estimates of food insecurity indicate that the number of hungry people increased from 777 million in 2015 to 815 million in 2017. According to estimates from the FEWS NET, the number of people facing near-famine conditions has increased 60% since 2015. In 2018, some 76 million individuals faced severe food shortages (https://fews.net/sites/default/files/Food_assistance_needs_Peak_Needs_2018-Final.pdf, last accessed 29 Oct. 2018). Severe weather events in major food producing countries were a major factor in recent (2007/8; 2011/12) food-price spikes, pushing the number of food insecure people to over 1 billion and leading to civil unrest, economic strife, and geopolitical tension (Anderson et al. 2014; Janetos et al. 2017). The most recent catastrophic droughts in southern (2015–16) and eastern (2017) Africa led to major food shortages (GEOGLAM Crop Monitor for Early Warning Bulletins Nos. 5&13, www.cropmonitor.org, last accessed 29 Oct. 2018) requiring a timely international response (FEWSNET 2017; Funk et al. 2018).

However, as food insecurity increases, so does our ability to describe, model, and predict the Earth's agro-hydrological variations. These expansions arise through enhanced earth observing systems, improved tools for interpreting these observations, and better developed networks of collaborating scientists. FEWS NET scientists seek to entrain these advances to provide enhanced hydrological and agricultural assessments which will, in turn, support food security monitoring in the developing world. The outcomes of this project will directly support the UN Sustainable Development Goal of Ending Hunger by 2030 through data sets that will improve agricultural planning and productivity.

Recent crises in eastern and southern Africa underscore the importance of timely and accurate monitoring of hydroclimatic extremes, mitigating food supply crises, and mobilizing humanitarian assistance, yet many national governments are poorly

positioned to understand crop conditions in their own countries and make necessary decisions concerning food supply (Carletto et al. 2015).

Satellite precipitation retrievals are an absolute necessity to support global precipitation and agricultural monitoring (Funk et al. 2007; Kirschbaum et al. 2017). The combined collection area of all operationally available global rainfall gauges only covers two basketball courts (Kidd et al. 2017). Furthermore, the spatial distribution of these gauges is highly skewed, with most observations available in Europe, North America, Australia, and India. Since many of the most serious hydrologic impacts are experienced in poor countries, rainfall gauge data are typically sparsest where the need is greatest. The problem of sparse data is getting worse, as many meteorological agencies do not share their data. For example, at present, only about 500 stations are available for Africa or South America (Fig. 23.1). The reasons for this decline are diverse and not well understood; the degradation of existing rain gauge networks in many countries and the adoption of cost recovery-based proscriptions of data sharing are thought to be the most important causes. This decline in station density increases the important role played by satellite precipitation estimates. While new hydrologic monitoring tools like the Famine Early Warning Networks System (FEWS NET) Land Data Assimilation System (FLDAS) offer exciting new opportunities for improved drought detection (McNally et al. 2017), they also rely on sub-daily precipitation fields.
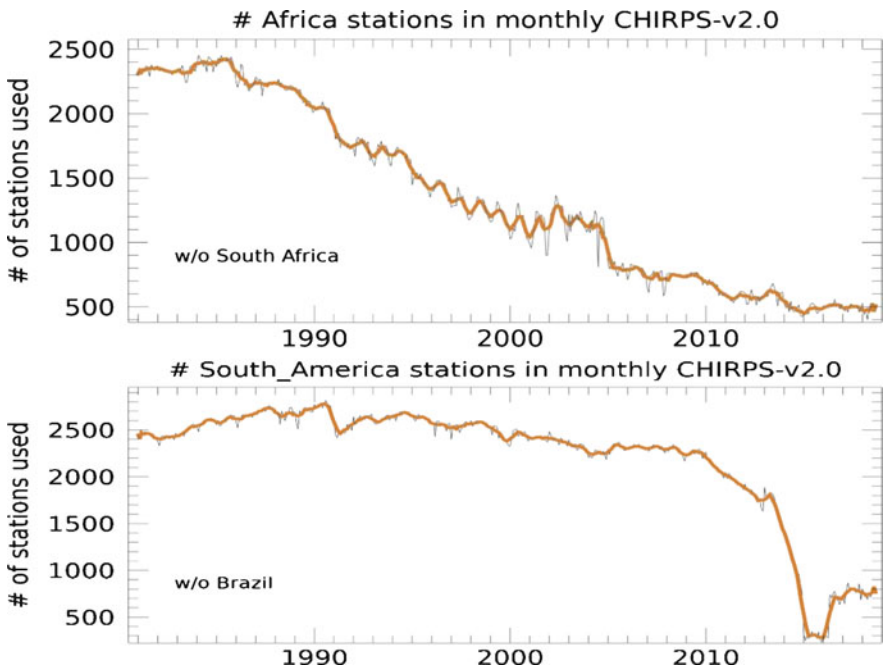
Fig. 23.1 The number of monthly station data used in the production of the CHIRPS Final precipitation data

To support global drought early warning, the Climate Hazards Center (CHC) at the University of California, Santa Barbara developed the Climate Hazards center InfraRed Precipitation with Stations (CHIRPS) dataset, in collaboration with the US Geological Survey and NASA SERVIR (Funk et al. 2015b). Specifically designed to support early warning applications, CHIRPS has a high spatial resolution (0.05°), a long period of record (1981 to the near present), and relatively low latencies. It integrates a high-resolution climatology (Funk et al. 2015a), cold cloud duration (CCD)-based precipitation estimates, and in situ gauge observations. Released in 2015, CHIRPS has rapidly become a fairly widely-used resource. Relief agencies like FEWS NET need monitoring products with deep historical coverage that are high resolution, reasonably accurate, and routinely updated in a timely fashion (Ross et al. 2009). In September 2018, 1027 unique internet protocol addresses downloaded 400,000 CHIRPS 2.0 products. CHIRPS has become an important input into the early warning and hydrologic monitoring activities carried out by FEWS NET and partner agencies such as the World Food Programme, the UN's FAO, the GEOGLAM Crop Monitor, and US Department of Agriculture's Foreign Agricultural Service (FAS). CHIRPS data, for example, helped catalyze (http://fews. net/east-africa/somalia/special-report/february-21-2017, last accessed 29 Oct. 2018) an early and effective response to the 2017 Somalia drought crisis, inform the 2016 Southern African Development Communities humanitarian appeal (https:// reliefweb.int/sites/reliefweb.int/files/resources/appeal_document_final_20160711. pdf, last accessed 29 Oct. 2018), effectively capture (http://fews.net/sites/default/ files/documents/reports/FEWS%20NET_Ethiopia%202015%20Drought%20Map% 20Book_20151217_0.pdf, last accessed 29 Oct. 2018) Ethiopia's 2015 drought— the worst in 50 years—, and drive Afghanistan hydrologic models, indicating record low snowpack levels in Afghanistan (https://earthobservatory.nasa.gov/images/ 91851/record-low-snowpack-in-afghanistan, last accessed 29 Oct. 2018).

CHIRPS occupies a unique space within the universe of satellite-precipitation estimates. The CHC's approach to enhancing satellite remote sensing products draws from "traditional" geostatistical climate analysis, in line with products like those developed by the Global Precipitation Climatology Centre (GPCC, Becker et al. 2013) or PRISM (Daly et al. 1994). The utilization of high resolution climatologies is central to these approaches. Conceptually, this approach is similar to a standard geostatistical decomposition in which a space-time data set is broken into long-term mean and stationary time-varying components (Cressie and Wikle 2015). As described, CHIRPS is constructed around the Climate Hazards Center Precipitation Climatology (CHPclim). This ensures relatively low bias (Dinku et al. 2018; Toté et al. 2015) relative to many other products. A secondary, but equally important, aspect of CHIRPS' use of CHPclim is that changes in station data networks (Fig. 23.1), which can cause spurious trends, appear to be mitigated in CHIRPS (Maidment et al. 2015). This arises when the station data and satellite precipitation estimates have similar mean fields, since such similarity reduces discontinuities when stations' observations appear and disappear in the historical record. We will discuss below, however, how the CHPclim-focused estimation process can also be a

limitation, especially in arid regions where the mean is low and precipitation arrives in infrequent pulses.

While the CHIRPS data set has proven useful, there are also several shortcomings that have been identified—namely (i) systematic undercatch biases in the CHIRPS precipitation climatology and (ii) a tendency to underestimate precipitation in arid regions like eastern portion of East Africa, North Africa, and the Arabian Peninsula.

Another major advance employed in the CHPclim2.1 will be the inclusion of many more high-quality climate normals and the gauge-undercatch correction of these normals. On this front, scientists from the GPCC have kindly contributed the 79,200 quality-controlled climate normals used to produce the GPCC's latest climatology (Schneider et al. 2017). Another 27,917 stations were derived from the FAO LocClim data archive (Raymo et al. 1996). Additional CHC normals (3964 stations) were added for selected countries or regions where the CHC archive had especially good coverage (Table 23.1). For Central America and Africa, these observations were provided by collaborating national and regional experts.

A major limitation of the CHPclim, especially for mountainous extra-tropical regions, has been the fact that CHPclim station normals were not corrected for systematic gauge undercatch (Beck et al. 2017). As discussed in Schneider et al. (2017), a systematic gauge-measuring error is generally an undercatch of the true precipitation. The magnitude of the undercatch error varies with the physical features

Table 23.1 Counts of CHC station climate normals added to the GPCC and FAO archive

Country/region	Count
Belize	9
Central America/Alfaro	77
Colombia	1971
Brazil	203
Central America/CATIE	190
El Salvador	24
Nicaragua	18
Panama	98
Guatemala	41
Haiti	10
GHA-Sahel	601
Mozambique	28
Ethiopia	188
Togo	9
Nigeria	40
Bangladesh	32
Thailand	57
Cambodia	19
Nepal	99
Sri Lanka	92
Vietnam	158
Total	**3964**

of the measurement device, the nature of the precipitation phase (liquid, solid, mixed) and intensity, and the local meteorological conditions. Many data sets have used spatial maps of the seasonally varying gauge-measuring error (Legates and Willmott 1990) to correct gauge undercatch (hereafter LW1990). Schneider et al. (2017) uses an improved method for estimating systematic gauge errors based on Fuchs et al. 2001). This method takes into account monthly weather conditions: wind, temperature, relative humidity, precipitation phase, and intensity.

While correcting undercatch gauge data using time-varying weather data, as in Schneider et al. (2017) is generally preferable to the static correction factors produced by LW1990, the CHIRPS2.1 process will need to use LW1990 estimates to correct time-varying gauge data in near-real time. The CHIRPS process focuses on producing satellite-only estimates (CHIRP) that are as close as possible to the mean of the observed gauge observations. Hence the training data for the CHPclim 2.1 will begin with the 29,689 quality-controlled CHC 'anchor' stations that are routinely blended into the existing CHIRPS2.0 final product. These stations will be used to calculate LW1990 corrected 1981–2010 climate normals. Next, normals from 3964 stations collected by the CHC for Asia and Latin America (Table 23.1) will be screened and added if they are more than 10 km from an existing CHC anchor stations. Estimates indicate that 601 stations will be added at this stage. A similar process will be carried out for the ~72,000 GPCC climate normals, resulting in an addition of ~28,229 long term mean values. Finally, ~5532 LW1990 undercatch-corrected normals from the FAO LocClim archive will be added if they are more than 10 km away from any previously selected stations. We anticipate that this step may be mostly beneficial in Madagascar, parts of the Middle East, and the Maritime Continent/Oceania region.

Poor performance in arid regions has been another potential concern reported by drought early warning practitioners. For example, FEWS NET comparisons of CHIRPS and livestock herd sizes in arid land regions in East Africa indicate weaker relationships than those found for more "direct" products like the African Rainfall Climatology version 2 (ARC2). "Direct" is used here in the sense that the satellite-based component of the ARC2 (Novella and Thiaw 2013) is estimated using the GOES Precipitation Index (GPI) regression with CCD values. While this simpler approach can lead to large mean bias errors (Dinku et al. 2018; Toté et al. 2015), it may be more effective at capturing rainfall in arid regions. While a full exploration of this topic is beyond the scope of this chapter, we will describe a brief formal analysis of distributional bias in CHIRPS2.0. This analysis reveals, as expected, that CHIRPS2.0 means are very similar to observed station data. However, a closer look suggests that low precipitation values are underestimated and high values are over-estimated in the CHIRPS2.0. We describe a potential correction for this below. Once sufficiently vetted, we anticipate that the enhanced CHPclim and bias-corrected CHIRP will form the basis of the next major CHIRPS2.1 release.

23.2 Description of the CHIRPS2.1 Methods

23.2.1 The CHIRPS2.1 Modeling Process

The CHIRPS2.1 modeling process consists of five steps (Fig. 23.2, Eqs. 23.1, 23.2 and 23.3): (1) First, an updated set of undercatch-corrected climate normals is combined with the existing 0.05° CHPclim. (2) Then, for each pentad and grid cell, a regression with the TRMM Multisatellite Precipitation Analysis (TMPA) (Adler et al. 2010; Huffman et al. 2007) is used to translate 1999-present Climate Prediction Center (CPC) (Janowiak et al. 2001) and 1983–1998 GridSat (Knapp et al. 2011) geostationary satellite Thermal Infrared (TIR) cold cloud duration (CCD) values into Infrared Precipitation Estimates (IRP, Eq. 23.1), which are then expressed as percentage anomalies. (3) These percentage anomalies are then multiplied against the CHPclim, producing CHIRP estimates in mm. (4) In the experimental CHIRP2.1 development process, a systematic relationship (described below) between the IRP and CHIRP errors is used to calculate error estimates F(IRP), which are subtracted from the CHIRP producing CHIRP2.1. Finally, (5) monthly and pentadal station observations are integrated into CHIRP2.1, producing the CHIRPS2.1 product (Eq. 23.2). The bias anomalies (S%) are based on station data (S) corrected with LW1990 correction factors (Eq. 23.3). A small value (ε) is added to the numerator and denominator to handle cases when $S \rightarrow 0$.

$$\mathbf{IRP} = b_0 + b_1 IRP \qquad (23.1)$$

$$\mathbf{C_{2.1}} = IDW\left(CHP_{clim}\left(\frac{IRP + \varepsilon}{\overline{IRP} + \varepsilon}\right) + F(IRP), s_\% \right) \qquad (23.2)$$
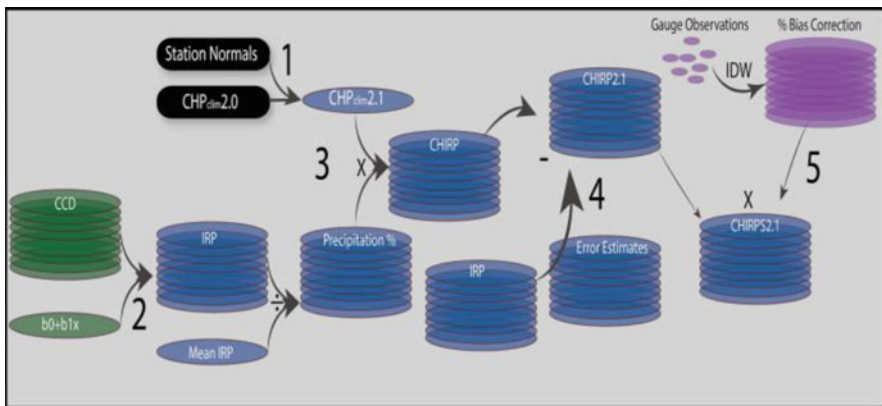

Fig. 23.2 CHIRPS2.1 schema

$$s_\% = \left(\frac{LW * S + \varepsilon}{CHP_{clim}\left(\frac{IRP+\varepsilon}{\overline{IRP}+\varepsilon}\right) + F(IRP) + \varepsilon} \right) \tag{23.3}$$

Working backwards, the CHIRPS2.1 product is an inverse distance weighted (IDW) blend of TIR CCD-based estimates and time varying station observations (Eq. 23.2). These CCD-based IRP estimates begin with local calibrations at every pixel for every pentad with the TMPA data set (Eq. 23.1). In the 2.1 process, an updated CHPclim is used and an IRP-based bias correction F(IRP) is also included. This correction was based on IRP rather than $CHP_{clim}\left(\frac{IRP+\varepsilon}{\overline{IRP}+\varepsilon}\right)$ to limit the influence of extremely low CHPclim values. In the final estimation of the CHIRPS2.1 predictions, LW1990 gauge undercatch correction ratios are used to adjust the station data (Eq. 23.3).

The CHIRPS process explicitly seeks similarity with a high-quality merged satellite product (TMPA) and high-quality interpolated gauge data sets like the GPCC. Typically, the CHIRPS process results in precipitation estimates that perform about as well as these data sets, but in a unique time frame (1981-now) suitable for monitoring hydroclimatic extremes.

23.2.2   The CHPclim 2.1 Climatology

The climatology modeling methodology is a more sophisticated version of the process used to derive the precipitation climatology underlying the CHIRPS product (Funk et al. 2015a). Rather than breaking the globe into 56 modeling regions, a modification of the R code now defines a continuous field. This field, furthermore, is associated with a variable-modeling radius. Areas with dense observation networks (like the United States) use a small modeling radius (d_{max} ~50 km), allowing the modeling process to capture fine details. Areas with sparse observation networks use a large radius (d_{max} ~300 km). The first step of the climatological modeling process involves a series of moving window regressions (MWR) to create an initial prediction of a 0.05° resolution temperature grid. The second step calculates the at-station residuals from step 1 (station observations minus regression estimates), and then interpolates these values using a modified inverse-distance weighting (IDW) interpolation scheme to create grids of MWR model residuals. A third step adjusts our background climatology to a 1981–2010 baseline using undercatch-corrected CHC precipitation observations.

23.2.2.1   Localized Correlation Estimates

Our process relies heavily on local regressions between our target variable and background field. To produce the revised CHPclim, a single predictor was used –

the original CHPclim climatology (Funk et al. 2015a). In this instance, MWR becomes a distance weighted bivariate regression. At a certain location, we can sample a number of points and background variables that fall within a certain distance (d_{max}) and calculate distance weighted localized regression slopes. The localized regression process finds a set of n neighboring points (within d_{max}) and estimates their weighted correlation, $w(d)$. As in Funk et al. (2015a), this study uses a cubic function of the distance (d). The new version of the MWR model adjusts d_{max} dynamically, based on the number of surrounding stations. In areas with dense networks, d_{max} will be smaller.

$$
\begin{aligned}
w(d) &= 0 & d &> d_{max} \\
w(d) &= \left[(1 - d/d_{max})^3 \right]^3 & d &\leq d_{max}
\end{aligned}
\tag{23.4}
$$

These weights are then used to estimate a localized regression slope.

$$
S_{x,y} = (n-1)^{-1} \left(\sum_{i=1}^{n} w(d_i) \right)^{-1} \sum_{i=1}^{n} w(d_i)[(x_i - \bar{x})][(y_i - \bar{y})]
\tag{23.5}
$$

$$
S_{x,x} = (n-1)^{-1} \left(\sum_{i=1}^{n} w(d_i) \right)^{-1} \sum_{i=1}^{n} w(d_i)[(x_i - \bar{x})]^2
\tag{23.6}
$$

$$
b_1 = \frac{S_{x,y}}{S_{x,x}}
\tag{23.7}
$$

Local distance-weighted estimates of the covariance (Eq. 23.5) and predictor variance (Eq. 23.6) are used to produce an estimate of the local slope (Eq. 23.7).

For each location, a set of neighboring observations is obtained and a regression model estimated using weighted least squares, with the weight of each observation determined by its distance from the regression centroid (d in Eqs. 23.5, 23.6 and 23.7). For each region and month, a grid of center points is defined over land-only locations. At each center point, station values within the radius (d_{max}) are collected, and a regression model is fit based on weights determined by Eqs. 23.5, 23.6 and 23.7. The d_{max} values are defined individually for each location based on the density of the available data.

23.2.2.2   Interpolation of Model Residuals

Following the MWR modeling procedure, at-station anomalies (the arithmetic difference between the station normals and the nearest 0.05° regression estimate) are calculated and interpolated using a modified IDW interpolation procedure. For

each $0.05°$ grid cell, the cube of inverse distances is used to produce a weighted average of the surrounding station residuals, r. This value is then modified based on a local interpolation radius, d_{IDW}, and the distance to the closest neighboring station (d_{min}).

$$r^* = \left(1 - d_{min}/d_{IDW}\right)r \qquad (23.8)$$

This simple thresholding procedure forces the interpolated residual field to relax towards zero based on the distance to the closest station. The d_{min} values change based on the local-station density.

23.2.2.3 Adjusting the CHTclim Climatology

The GPCC/FAO/CHC station normals used to drive the MWR and IDW steps of the climatology were selected to provide representative spatial coverage in data-sparse areas like South America, Africa, and Central Asia. This coverage was maximized, because we would like to have a reasonable CHPclim surface even in sparsely gauged areas like Madagascar and Yemen. These two countries represent a range of challenges. In Madagascar, we find rapid topographically-induced changes in local precipitation. In Yemen, where rainfall is much lower, we also find such changes, but the high level of aridity makes it difficult to model. Hence, we include a heterogeneous set of climate normals. The GPCC and FAO climate normals are based on a ~1950–1980 baseline, and the CHC normals are based on a 1981–2010 averaging period. The GPCC normals are undercatch-corrected using the time-varying Fuchs algorithm. The FAO and CHC normals are undercatch-corrected using LW1990. As previously described, the CHC normals were identified first, and then additional normals were added from the GPCC and, finally, the FAO archive.

After the MWR process is complete, a final bias correction pass is taken based on arithmetic anomalies from LW1990-adjusted 1981–2010 normals from the CHC monthly precipitation archive. This step aligns the climatologies with the 1981–2010 World Meteorological Organization (WMO) baseline. A secondary benefit is that this alignment minimizes discrepancies between the CHIRP2.1 estimates and the gauge-undercatch corrected CHC gauge observations. Finally, temporal resampling and smoothing of the 12-monthly mean fields were used to derive 72 pentadal mean fields.

23.3   Experimental Results for the CHIRPS 2.1 Redistribution Process

We next describe experimental results for the CHIRPS2.1 "redistribution" process, F (IRP) in Eq. 23.2. Redistribution refers to the manner in which we adjust low precipitation values up, and high precipitation values down.

23.3.1 CHIRP2.0 Systematic Bias Analysis

We begin by analyzing pentadal station, IRP, and CHIRP data. Daily Global Historical Climate Network, Global Telecommunication System, and Conagua stations from Mexico were pooled, and 14,197 stations identified for further analysis (Fig. 23.3). These stations had at least 50% complete records in each pentad between 1981 and 2017. Each month is divided into six pentads, with the first five pentads always having 5 days, and the last pentad containing the remainder of days in each month. We also applied a spatial constraint, only examining data south of 40°N. This selection, which made little difference in our results, was based on a primary interest in evaluating CHIRP and IRP in tropical and semi-tropical regions. Individual pentads having at least 1 mm of observed precipitation were selected, resulting in a total of 9,880,569 total observations. Overall, the correlation between the IRP, CHIRP, and the stations was modest (0.5), which is not surprising given that we are comparing point observations at gauges with gridded satellite retrievals.

Next, systematic biases within this archive were quantified by using CHIRP2.0 values to stratify the data into 2 mm-wide bins ranging between 1 and 120 mm. The station, IRP, and CHIRP2.0 means for each of these bins are shown in Fig. 23.4 together with a 1-to-1 line. While the overall means of the stations, IRP, and CHIRP are in fairly close alignment, systematic biases at low and high precipitation values can be observed (Fig. 23.4). At low precipitation events, when CHIRP2.0 is between 1 and 20 mm, the Mean Bias Error (MBE) of the CHIRP2.0 is 13 mm (Table 23.2). For wet events when CHIRP2.0 is between 80 and 120 mm, we find a systematic overestimation. Many more events are between 1 and 20 mm, resulting in a substantial overall dry bias in the CHIRP2.0: -8.3 mm. Mid-range precipitation events, between 60 and 80 mm, exhibit little systematic bias.
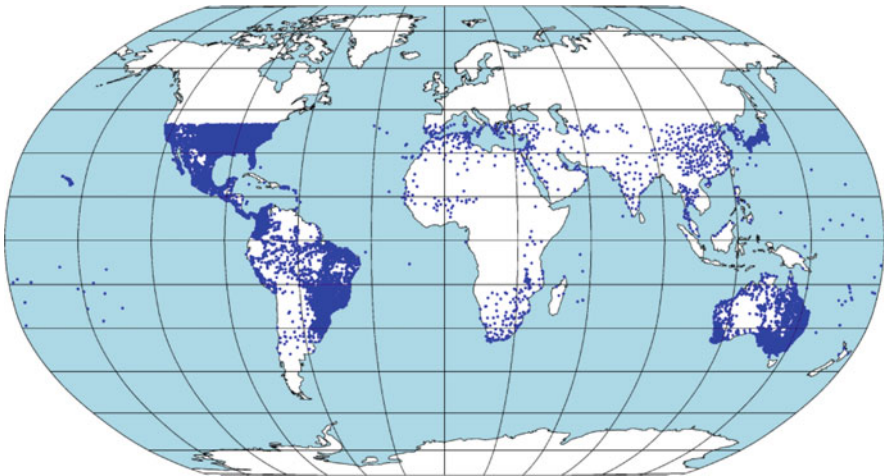
Fig. 23.3 Map of 14,197 stations used in the validation analysis

Fig. 23.4 Plots of station means (x-axis) and IRP (red diamonds), CHIRP2.0 (blue skinny diamonds) and CHIRP2.1 (yellow circles) means (y-axis). Data stratified binned by CHIRP2.0 values
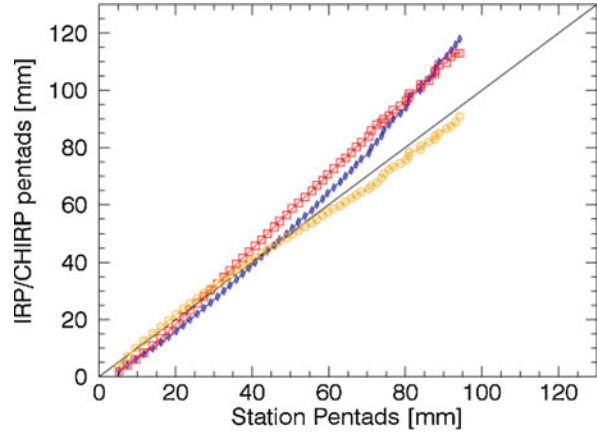
Table 23.2 Mean Bias Error (MBE) and Mean Absolute Error (MAE) by precipitation stratification. All statistics in mm per pentad

CHIRP ranges	Obs Counts	Stn Mean	CHIRP2 MBE	CHIRP2.1 MBE	CHIRP2 MAE	CHIRP2.1 MAE
1 mm < P < 20 mm	8,653,967	13	−4	0	9	9
20 mm < P < 40 mm	3,456,028	30	−1	+4	19	21
40 mm < P < 60 mm	1,906,035	48	+1	0	29	29
60 mm < P < 80 mm	761,252	63	+5	−3	37	37
80 mm < P < 120 mm	365,034	79	+14	−4	47	45
120 mm < P	71,228	108	+40	+1	68	61
All data, 10 mm < P	15,954,854	26.5	−2	−0.4	16	17

Fig. 23.5 Empirical correction factors obtained from the station data and IRP averages (yellow circles) along with regression estimates based on the IRP means
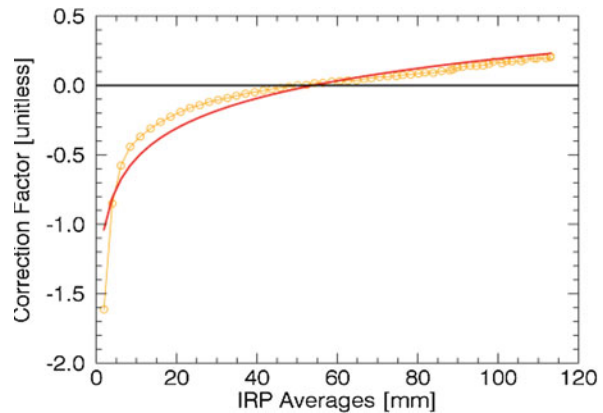
The CHIRP2.0 bias structure has a systematic relationship with changes in IRP values. Figure 23.5 shows the same binned mean IRP values as in Fig. 23.4 (x-axis) along with the ratio between the binned bias errors and IRP means: biasbin/IRPbin

(y-axis). Also shown on this plot is a regression estimate, F(IRP), based on the natural log of the IRP averages. F(IRP) = −1.24 + 0.31 × ln(IRP), R2 = 0.94. We chose to estimate our errors as a function of IRP, as opposed to CHIRP2.0, because it has been noted that low CHPclim values provide a severe limit when heavy precipitation occurs in historically very dry regions. The multiplicative formulation of the CHIRP and station unbiasing process makes CHIRPS2.0 unresponsive when CHPclim → zero. Locations with CHPclim values of zero will never have non-zero CHIRPS2.0 values, no matter what the IRP or station data values are. Adding an IRP-based bias correction may ameliorate this problem. Plans for CHIRP3.0 development may involve a more ambitious approach based on a conditional estimation process where the assumed mean value is allowed to vary with changing environmental conditions.

23.3.2 CHIRP2.1 Systematic Bias Corrections

Next, we briefly explore the potential utility of IRP-based bias corrections. We define a multiplicative bias coefficient, β, and use this to define our bias correction factor F(IRP).

$$\beta = b_0 + b_1 \ln(IRP) \tag{23.9}$$

$$F(IRP) = -1\beta IRP \tag{23.10}$$

When applying this correction, one sets all IRP values with zero to a very small non-zero value, so ln(IRP) → 1. At low values, when IRP is equal to 10, β is equal to −1.9, so the bias correction process (Eqs. 23.9 and 23.10) is essentially adding $2 \times$ IRP estimates to the CHIRP estimates for low IRP values. When used to produce experimental CHIRPS2.1 values for our pentadal data set, we find that the bias correction process does in fact reduce systematic biases for low CHIRP values (Table 23.2). Overall, however, little change was found in mean absolute error values or the overall correlation between CHIRPS2.1 and the station pentads ($r \approx 0.5$). At low precipitation ranges (< 20 mm), the IRP-based correction reduces the bias by 4 mm, reducing the percent bias from ∼ 33 to 0%. About half of precipitation events belong to this category, so this change may be important, especially in very arid regions. Across all precipitating events, where station precipitation was at least 1 mm, the bias is reduced from −2 to −0.2 mm, or from −7 to −1%. At high precipitation values CHIRPS2.0 over-estimates rainfall. The IRP-based bias correction reduces this systematic error as well.

The bias correction also affects both the variance of the CHIRP and the detection frequencies of low precipitation events. F(IRP) increases CHIRP2.1 at low values and reduces it at high values, such that we find a ∼ 4 mm/20% reduction in the overall standard deviation (Fig. 23.3). This shift in variance, however, has a distinct spatial pattern (Fig. 23.6). In general, drier regions exhibit modest decreases in variance while humid regions have small increases in variability (Table 23.3).
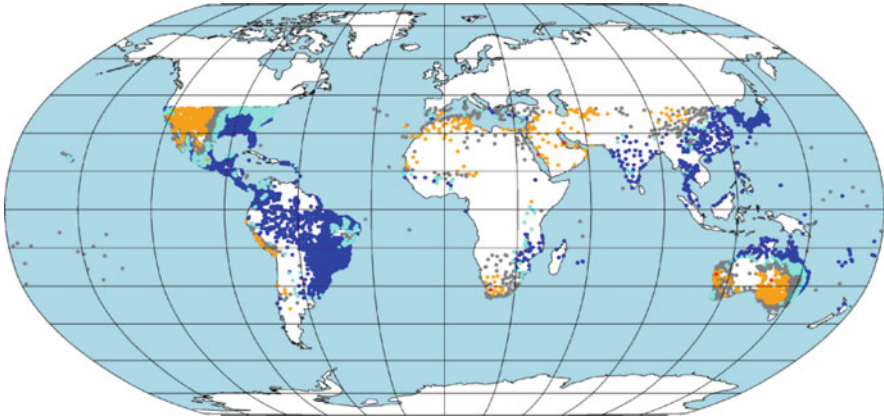
Fig. 23.6 Change in standard deviation (CHIRPS2.1 minus 2.0). Red circles indicate a decline of −2 mm or more, orange circles indicate decreases of between −1 and − 2 mm, grey circles indicate change values between −1 and 1 mm, cyan circles had changes between +1 and + 2 mm, blue circles had changes greater than +2 mm

Table 23.3 Pentad validation statistics for events when stations observed at least 1 mm of rainfall

Statistic	CHIRP2.0	CHIRP2.1
Mean [mm]	24	26
Standard deviation [mm]	23	19
Mean error [mm]	−1.7 mm	−0.2
Percent bias [Mean Error/Mean]	−7%	−1%
Correlation	0.59	0.55
MAE [mm]	16.2 mm	16.7 mm
Hit percent, >20 mm	48%	56%
False alarm percent, > 20 mm	23%	35%
Miss percent, P > 20 mm	19%	11%
Probability of detection, >20 mm	72%	83%
False alarm ratio, > 20 mm	33%	38%
Hit percent, >30 mm	29	33
False alarm percent, > 30 mm	19	26
Miss percent, P > 30 mm	18	14
Probability of detection, >30 mm	61	70
False alarm ratio, > 30 mm	39	44
Hit percent, > 50 mm	10	9
False alarm percent, > 50 mm	9	9
Miss percent, P > 50 mm	15	16
Probability of detection, >50 mm	41	36
False alarm ratio, > 50 mm	48	49

Based on comparisons with station observations between 40°N and 40°S with at least 50% valid observations between 1981 and 2017. If A, B, C, D represent hits, false alarms and misses, then the Probability of Detection (POD) = A/(A + C) and the False Alarm Ratio (FAR) = B/(B + A)

23.3.3   Changes in the Ability to Detect Low Precipitation Events

While our objective in this chapter has been to simply describe some possible enhancements to the CHIRPS climatology and algorithm, we do conclude with a brief assessment of changes in detection skill. We focus primarily on accuracy characteristics associated with events of 20 mm or more, though Fig. 23.3 also presents results for 30 + mm and 50 + mm categories. Overall, for the 20+ mm case, we find substantial reductions in systematic bias. The overall frequency of hits increases from 48 to 56%, while the number of misses decreases from 19 to 11%. CHIRPS2.1 misses half the number of precipitation events greater than 20 mm. The probability of detection increases from 72 to 83%. These changes, however, do come at the cost of increases in the frequency of false alarms, which shifts from ~23% to ~35%, resulting in change of the FAR from 33 to 38%. Examining 30 + mm events POD values reveals a shift from 61 to 70% as FAR values increase from 39 to 44%. At 50 + mm, POD and FAR values exhibit relatively little change.

Calculating CHIRPS2.1 and 2.0 POD scores at each station location, for 20 + mm precipitation events, indicated overall average POD scores of 61% and 71%. The average POD increase between 2.0 and 2.1 was 11%, with tenth and 90th percentile changes of 4% and 18%. The IRP-based correction consistently improved POD scores. A map of these increases (Fig. 23.7, middle) shows a fairly consistent pattern of positive changes. There are some locations, however, in North Africa and the Middle East where the improvements were very low. These very arid areas may have IRP estimates that are very close to zero, presumably because the TMPA data used to train the CCD-based IRP estimates also had very low precipitation totals. The increase in POD, however, also increases the chance of false detections. The bottom panel of Fig. 23.7 shows changes in CHIRPS2.1 versus 2.0 FAR values. Most stations were found to have increases in FAR of between 1 and 8%. The average increase in FAR was 5%.

23.4   Conclusions

The CHIRPS2.1 algorithm is still a work in progress, but here we have described our anticipated new algorithm and our process for developing an enhanced CHPclim2.1. These changes are expected to help CHIRPS2.1 reduce dry biases, especially for low precipitation intensities. These corrections will be achieved in two ways (1) by correcting for systematic gauge undercatch both in the CHPclim2.1 and in the station data used in the CHIRPS2.1, and by (2) modifying the CHIRP precipitation estimates based on estimates of systematic errors. These errors appear to underestimate precipitation at low values and overestimate at high values. Modeling these errors as a function of the CCD-based regression estimates (IRP) may help boost rainfall values in areas where the CHPclim is very low. The results presented here suggest

Fig. 23.7 Top – CHIRP POD for events with at least 20 mm of precipitation and change in +20 mm POD (CHIRPS2.1 minus 2.0). Middle – Map of changes in 20 + mm POD (CHIRPS2.1 minus 2.0). Cyan circles indicate POD increases between 5 and 10 percent, blue circles had changes greater than 10 percent. Average increase in POD was 11%. Bottom – Map of changes in FAR (CHIRPS2.1 minus 2.0). Orange circles indicate POD increases between 0 and 5 percent, red circles had changes greater than 5 percent. Average increase in FAR was 4%
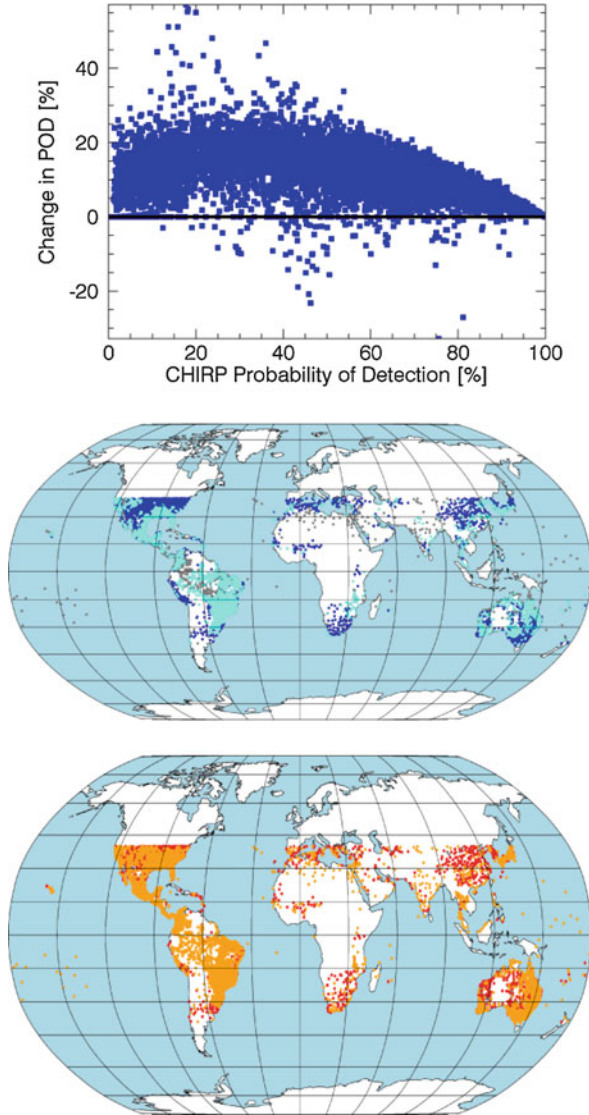
modest improvements in hit rate metrics for low precipitation categories. More validation and testing with the 2.1 beta version of the CHIRPS2.1 will be required to assess the value of these changes. Hydrologic simulations using the FLDAS (McNally et al. 2017) will also be run and compared to existing simulations based on CHIRPS2.0. The results presented here, however, are quite promising. Anecdotal evidence based on FLDAS simulations suggests that CHIRPS2.0 faces issues at low precipitation levels, a common occurrence in the Middle East and northern and eastern Africa. Similar performance issues have been reported by FEWS NET

analysts modeling livestock herd dynamics in eastern Africa. The new research examined here indicates that these errors appear to be quite systematic and, at least in aggregate, correctable.

Ultimately, however, the CHIRPS development team is working towards a substantially different CHIRPS3.0 framework - a framework in which the assumed 'prior' distribution is allowed to change with environmental conditions. As a thought experiment, assume we are estimating pentadal precipitation at the Santa Barbara airport. Like many arid and semi-arid regions, southern California precipitation totals are typically comprised of a few intense events. So, the pentadal CHPclim mean will be small. The mean in such arid regions is not very meaningful. In place of this static mean we will explore conditional relationships, probably comprised of three terms: the probability of rain (p) and the shape and scale of a Gamma distribution (α, β) associated with precipitation intensity, in mm per pentad. Local estimates of these distribution parameters could be allowed to change in time, increasing when large scale weather conditions (W) indicate shifts towards heavy precipitation events. These conditional parameter sets (p|W, α|W, β|W) could be calibrated such that their expected values converged on a distribution whose central location matched the desired long term mean. In theory, such an approach could provide the long-term low bias performance of the current CHIRPS algorithm while allowing dry areas to receive high levels of precipitation when large-scale conditions indicate large weather disturbances. The CHC's new global MWR modeling framework makes the developing of a set of global parameter grids describing the p|W, α|W, β|W plausible.

References

Adler, R. F., Huffman, G. J., Bolvin, D. T., & Nelkin, E. J. (2010). The TRMM Multi-Satellite Precipitation Analysis (TMPA). In M. Gebremichael & F. Hossain (Eds.), *Satellite rainfall applications for surface hydrology* (pp. 3–22). Dordrecht: Springer. https://doi.org/10.1007/978-90-481-2915-7_1.

Anderson, K., Ivanic, M., & Martin, W. J. (2014). Food price spikes, price insulation, and poverty. In J.-P. Chavas, D. Hummels, & B. D. Wright (Eds.), *The economics of food price volatility* (pp. 311–339). Chicago: University of Chicago Press. 9780226128924.

Beck, H. E., Vergopolan, N., Pan, M., Levizzani, V., van Dijk, A. I. J. M., Weedon, G. P., Brocca, L., Pappenberger, F., Huffman, G. J., & Wood, E. F. (2017). Global-scale evaluation of

22 precipitation datasets using gauge observations and hydrological modeling. *Hydrology and Earth System Sciences, 21*, 6201–6217. https://doi.org/10.5194/hess-21-6201-2017.

Becker, A., Finger, P., Meyer-Christoffer, A., Rudolf, B., Schamm, K., Schneider, U., & Ziese, M. (2013). A description of the global land-surface precipitation data products of the Global Precipitation Climatology Centre with sample applications including centennial (trend) analysis from 1901-present. *Earth System Science Data, 5*, 71–99. https://doi.org/10.5194/essd-5-71-2013.

Brown, M. E., Carr, E. R., Grace, K. L., Wiebe, K., Funk, C. C., Attavanich, W., Backlund, P., & Bujah, L. (2017). Do markets and trade help or hurt the global food system adapt to climate change? *Food Policy, 68*, 154–159. https://doi.org/10.1016/j.foodpol.2017.02.004.

Carletto, C., Jolliffe, D., & Banerjee, R. (2015). From tragedy to renaissance: Improving agricultural data for better policies. *The Journal of Development Studies, 51*, 133–148. https://doi.org/10.1080/00220388.2014.968140.

Cressie, N., & Wikle, C. K. (2015). *Statistics for spatio-temporal data*. John Wiley & Sons. World wide agroclimatic database, FAOCLIM CD-ROM v. 2.01, 2001.

Daly, C., Neilson, R. P., & Phillips, D. L. (1994). A statistical-topographic model for mapping climatological precipitation over mountainous terrain. *Journal of Applied Meteorology, 33*, 140–158. https://doi.org/10.1175/1520-0450(1994)033<0140:ASTMFM>2.0.CO;2.

Dinku, T., Funk, C., Peterson, P., Maidment, R., Tadesse, T., Gadain, H., & Ceccato, P. (2018). Validation of the CHIRPS satellite rainfall estimates over eastern of Africa. *Quarterly Journal of the Royal Meteorological Society, 144*(S1), 292–312. https://doi.org/10.1002/qj.3244.

FAO. (2009). *How to feed the world in 2050*. Rome: High-Level Expert Forum. Available at http://www.fao.org/fileadmin/templates/wsfs/docs/expert_paper/How_to_Feed_the_World_in_2050.pdf. Last accessed 29 Oct 2018.

FEWSNET. (2017). *Persistent drought in Somalia leads to major food security crisis*. Available at https://reliefweb.int/sites/reliefweb.int/files/resources/wfp290554.pdf. Last accessed 29 Oct 2018.

Fuchs, T., Rapp, J., Rubel, F., & Rudolf, B. (2001). Correction of synoptic precipitation observations due to systematic measuring errors with special regard to precipitation phases. *Physics and Chemistry of the Earth, Part B: Hydrology, Oceans and Atmosphere, 26*, 689–693. https://doi.org/10.1016/S1464-1909(01)00070-3.

Funk, C., & Brown, M. E. (2009). Declining global per capita agricultural production and warming oceans threaten food security. *Food Security, 1*, 271–289. https://doi.org/10.1007/s12571-009-0026-y.

Funk, C., Husak, G., Michaelsen, J., Love, T, & Pedreros, D. (2007). Third generation rainfall climatologies: Satellite rainfall and topography provide a basis for smart interpolation. In *Proceedings of the JRC—FAO Workshop, Nairobi, Kenya*.

Funk, C., Verdin, A., Michaelsen, J., Peterson, P., Pedreros, D., & Husak, G. (2015a). A global satellite assisted precipitation climatology. *Earth System Science Data, 7*, 275–287. https://doi.org/10.5194/essd-7-275-2015.

Funk, C., Peterson, P., Landsfeld, M., Pedreros, D., Verdin, J., Shukla, S., Husak, G., Rowland, J., Harrison, L., Hoell, A., & Michaelsen, J. (2015b). The climate hazards infrared precipitation with stations—A new environmental record for monitoring extremes. *Science Data, 2*, 150066. https://doi.org/10.1038/sdata.2015.66.

Funk, C., Harrison, L., Shukla, S., Pomposi, C., Galu, G., Korecha, D., Husak, G., Magadzire, T., Davenport, F., Hillbruner, C., Eilerts, G., Zaitchik, B., & Verdin, J. (2018). Examining the role of unusually warm Indo-Pacific sea surface temperatures in recent African droughts. *Quarterly Journal of the Royal Meteorological Society, 144*(S1), 360–383. https://doi.org/10.1002/qj.3266.

Huffman, G. J., Bolvin, D. T., Nelkin, E. J., Wolff, D. B., Adler, R. F., Gu, G., Hong, Y., Bowman, K. P., & Stocker, E. F. (2007). The TRMM multisatellite precipitation analysis (TMPA): Quasi-global, multiyear, combined-sensor precipitation estimates at fine scales. *Journal of Hydrometeorology, 8*, 38–55. https://doi.org/10.1175/JHM560.1.

Janetos, A., Justice, C., Jahn, M., Obersteiner, M., Glauber, J., & Mulhern, W. (2017). *The risks of multiple breadbasket failures in the 21st century: A science research agenda*. Boston University Frederick S. Pardee Center for the Study of the Longer-Range Future. Available at http://www.bu.edu/pardee/the-risks-of-multiple-breadbasket-failures-in-the-21st-century-a-science-research-agenda/. Last accessed 29 Oct 2018.

Janowiak, J. E., Joyce, R. J., & Yarosh, Y. (2001). A real-time global half-hourly pixel-resolution infrared dataset and its applications. *Bulletin of the American Meteorological Society, 82*, 205–217. https://doi.org/10.1175/1520-0477(2001)082<0205:ARTGHH>2.3.CO;2.

Kidd, C., Becker, A., Huffman, G. J., Muller, C. L., Joe, P., Skofronick-Jackson, G., & Kirschbaum, D. B. (2017). So, how much of the Earth's surface is covered by rain gauges? *Bulletin of the American Meteorological Society, 98*, 69–78. https://doi.org/10.1175/BAMS-D-14-00283.1.

Kirschbaum, D. B., Huffman, G. J., Adler, R. F., Braun, S., Garrett, K., Jones, E., McNally, A., Skofronick-Jackson, G., Stocker, E., Wu, H., & Zaitchik, B. F. (2017). NASA's remotely sensed precipitation: A reservoir for applications users. *Bulletin of the American Meteorological Society, 98*, 1169–1184. https://doi.org/10.1175/BAMS-D-15-00296.1.

Knapp, K. R., Ansari, S., Bain, C. L., Bourassa, M. A., Dickinson, M. J., Funk, C., Helms, C. N., Hennon, C. C., Holmes, C. D., Huffman, G. J., Kossin, J. P., Lee, H.-T., Loew, A., & Magnusdottir, G. (2011). Globally gridded satellite (GriSat) observations for climate studies. *Bulletin of the American Meteorological Society, 92*, 893–907. https://doi.org/10.1175/2011BAMS3039.1.

Legates, D. R., & Willmott, C. J. (1990). Mean seasonal and spatial variability in gauge-corrected, global precipitation. *International Journal of Climatology, 10*, 111–127. https://doi.org/10.1002/joc.3370100202.

Maidment, R. I., Allan, R. P., & Black, E. (2015). Recent observed and simulated changes in precipitation over Africa. *Geophysical Research Letters, 42*, 8155–8164. https://doi.org/10.1002/2015GL065765.

McNally, A., Arsenault, K., Kumar, S., Shukla, S., Peterson, P., Wang, S., Funk, C., Peters-Lidard, C. D., & Verdin, J. P. (2017). A land data assimilation system for sub-Saharan Africa food and water security applications. *Science Data, 4*, 170012. https://doi.org/10.1038/sdata.2017.12.

Novella, N. S., & Thiaw, W. M. (2013). African rainfall climatology version 2 for famine early warning systems. *Journal of Applied Meteorology and Climatology, 52*, 588–606. https://doi.org/10.1175/JAMC-D-11-0238.1.

Ross, K., Brown, M. E., Verdin, J., & Underwood, L. (2009). Review of FEWS NET biophysical monitoring requirements. *Environmental Research Letters, 4*, 024009. https://doi.org/10.1088/1748-9326/4/2/024009.

Schneider, U., Finger, P., Meyer-Christoffer, A., Rustemeier, E., Ziese, M., & Becker, A. (2017). Evaluating the hydrological cycle over land using the newly-corrected precipitation climatology from the Global Precipitation Climatology Centre (GPCC). *Atmosphere, 8*, 52. https://doi.org/10.3390/atmos8030052.

Toté, C., Patricio, D., Boogaard, H., van der Wijngaart, R., Tarnavsky, E., & Funk, C. (2015). Evaluation of satellite rainfall estimates for drought and flood monitoring in Mozambique. *Remote Sensing, 7*, 1758–1776. https://doi.org/10.3390/rs70201758.

Chapter 24
Merging the Infrared Fleet and the Microwave Constellation for Tropical Hydrometeorology (TAPEER) and Global Climate Monitoring (GIRAFE) Applications

Rémy Roca, Adrien Guérou, Rômulo A. Jucá Oliveira, Philippe Chambon, Marielle Gosset, Sophie Cloché, and Marc Schröder

Abstract Improved monitoring of the precipitation at global scale and in conventional data sparse regions is needed to enhance our understanding of the functioning of the water and energy cycle and our ability to forecast its evolution at various scales. Decades of precipitation remote sensing research have shown that the merging of the high frequency cloud top information derived from geostationary infrared observations with the column hydrometeors vertical fluxes estimated from much less frequent passive microwave observations could mitigate the short comings of each approach and provide accurate accumulated rainfall estimates. The classical merging technique is introduced in detail and some more recent developments on the estimation of the uncertainty of the daily accumulation are presented. The products from tropical hydrometeorology and climate monitoring implementations are shown. Their performances and sensitivity are discussed, with emphasis on the configuration of the constellation. Finally, an outlook for future developments is provided.

R. Roca (✉) · A. Guérou
CNRS/LEGOS, Toulouse, France
e-mail: remy.roca@legos.obs-mip.fr

R. A. Jucá Oliveira · M. Gosset
Geoscience Environnement, Toulouse, France

P. Chambon
Météo France, CNRM/GMAP/OBS, Toulouse, France

S. Cloché
CNRS/IPSL, Palaiseau, France

M. Schröder
Deutscher Wetterdienst, Offenbach, Germany

24.1 Introduction

The knowledge of the accumulated precipitation amount and its uncertainty is important to the water budget, be it at the global scale in relation to the energy budget of the planet or at the catchment scale in relation to possible flooding. The strong intermittency of the precipitation field nevertheless makes the estimation of accumulation difficult by adding sampling issues to the instantaneous rates intensity determination. Rain occurrence together with rain intensity when it rains are all important aspect of the accumulated precipitation. The merging of the high frequency cloud top information derived from geostationary infrared observations with the column hydrometeors vertical fluxes estimated from much less frequent passive microwave observations could mitigate the short comings of each approach and provide accurate accumulated rainfall estimation (Kidd 2001) that accounts for the highly variable precipitation.

Despite strong progress in the performances of the satellite remote sensing products over the last decades as shown in this book or as reported under the International Precipitation Working Group (IPWG) activities (Levizzani et al. 2018), new and more stringent requirements are arising that call for more accurate accumulated estimation at various scales and latency. For instance, climate model evaluation requires a long term accurate climatology at finer scales than before (Tapiador et al. 2017), with global means that are consistent with the energy budget (Tapiador et al. 2019) of the planet. Flood forecasting in the tropics used to require only low latency products but with the advance in hydrological modeling, it now also requires unbiased data in addition to low latency (Cassé et al. 2015; Gosset et al. 2018). On the user hand, the general demand for high quality global precipitation products comes from an ample variety of user categories, such as, for example, hydro-meteorological services, research institutions, universities, civil and environmental protection agencies, governments, insurance and reassurance companies, United Nations agencies (e.g., WMO, FAO, UNESCO, UNEP), water management authorities, agriculture and food production ministries, transportation companies and authorities. These specific demands are also reflected by the priority areas of the WMO Global Framework for Climate Services (GFCS) that are agriculture and food security, disaster risk reduction, health, and water availability. All these priority areas need high-quality precipitation observations.

These various incentives have prompted the development and improvements of a suite of accumulated precipitation products with multiple specifications, but all based on the merging of infrared data from the geostationary fleet with the observations from the passive microwave constellation. The next two sections are dedicated

to introducing the background underlying the estimation of accumulated precipitation and the associated uncertainty. Implementations of the merging method dedicated to the tropical water cycle science are then presented. Preliminary results from an ongoing effort to provide a climate monitoring implementation are detailed, with emphasis on its sensitivity to the constellation configuration. The final section describes the plan for the future.

24.2 Merging Satellite Observations for Accumulation and Uncertainty Estimation

24.2.1 Estimation of the Accumulated Precipitation

24.2.1.1 Background

The accumulated amount of precipitation over a domain and a period, A, can be written as

$$A = RR_{con} \times \alpha \qquad (24.1)$$

where RR_{cond} is the conditional instantaneous rain rate and α the precipitating fraction of the domain (in space and time). The estimation problem is easily separated into two separate steps: (i) the computation of the RR_{cond}, and (ii) the computation of the fraction.

Among the various approaches (Kummerow and Giglio 1995), the adjusted GOES Precipitation Index technique (Xu et al. 1999) provides a direct way to use both LEO microwave observations and GEO infrared measurements to constraint the estimation of the two values. First, a space-time training volume is defined for which all the instantaneous conditional rain rates estimates derived from the microwave data are used. The average of these observations is built to estimate RR_{cond}. Second, over another training volume, the instantaneous precipitation detection results are collocated with the geostationary infrared data and a histogram is built that permits the identification of the IR Brightness Temperature thresholds that would fit, over the training volume, the microwave derived precipitation fraction. This latter information is further used over the application domain to estimate the precipitation fraction using all the infrared observations.

24.2.1.2 Performance Sensitivity

The overall performances of such an estimation of accumulated precipitation depends upon the overall performance of the microwave retrieval in both the detection and the estimation steps, the statistical robustness of the average computation and its representativeness. Both are functions of the size of the relative training

volume and density of observations from the constellation and of the application volume.

The current generation of the L2 algorithm is based on a statistical approach to identify the relevant hydrometeors profiles and surface rain-rate from microwave channels observations (see Chap. 8) in a reference database. In most of these algorithms, the retrieved profile is the most likely one or a combination of most likely profiles (Kidd et al. 2016b). If the current meteorological situation is very unlikely or poorly represented in the database, the individual retrieval is unlikely to provide a relevant solution. On the other hand, assuming an accurate reference database, these profiles are likely to provide a good estimate of the reference database average conditions. In short, Bayesian retrievals are better when the method finds many profiles to averaged together to compute RR_{cond}. If the L2 retrievals are still characterized by a systematic bias, its propagation into the final accumulation products is not linear and usually damped as revealed by earlier error propagation studies (Chambon et al. 2012a). Finally, the bias correction scheme also acts as to mitigate the issue for the final product (Huffman et al. 2001; Roca et al. 2018).

The deterministic detection step is also an important source of performances sensitivity. While recent advances promote the ability of the passive microwave imagers to detect rainrates as low as 0.25 mm h^{-1} (Casella et al. 2015) the inclusion of the very light rain part of the distribution in the adjustment approach is very sensitive. It lowers the estimate of RR_{cond}, thus decreasing the overall rainfall estimation but simultaneously enhances the precipitating fraction. This is likely the reason for the good performance of the actual method over convectively dominated regions where the impact of this limitation is minimum. The treatment of the detection/minimum rain rate threshold requires a careful approach.

Apart from issues pertaining to the quality of the Level 2 product, there is an additional difficulty in the trade-off between training and application volume for statistical robustness vs. representativeness. For instance, a large training volume (for both RR_{cond} and α estimation) of $10° \times 10° \times 1$ month will allow a large number of microwave data to be ingested even with a modest constellation. When used for the IR threshold determination, however, that threshold might not be representative of the cloud top temperature-precipitation detection for a given daily event in the month. Similarly using a very dense constellation might ensure statistical robustness for a small area, and consequently, a more representative training volume but might not by itself grant the ability to use a short time (like hourly) application volume.

The optimization of such a retrieval thus requires comprehensive sensitivity studies to adjust the free parameters. Fortunately, the design of such approach makes it a particularly well-suited framework for data denial experiments.

24.2.1.3   Sensitivity to the Configuration of the Microwave Constellation

An observing system simulation experiment was performed by (Chambon et al. 2013) in order to evaluate the sensitivity of the estimated accumulated precipitation to the microwave sensor constellation. Within this idealized framework, it was

shown that algorithms of precipitation estimation, like the Tropical Amount of Precipitation with an Estimate of ERrors (TAPEER), need to be adapted in order to benefit from a dense constellation. In particular, it was only possible to detect the improvements arising from the temporal sampling of Megha-Tropiques by decreasing the size of the training volumes of the fusion algorithm. These results were confirmed with real observations by Roca et al. (2018).

24.2.2 Estimation of the Uncertainty

24.2.2.1 Background

The total uncertainty on the final accumulated precipitation arises from all of the individual source of uncertainty and their propagation at various levels of the complex, highly nonlinear series of operations needed along the merging procedure. Assuming all uncertainty sources are uncorrelated a general uncertainty budget of a physical measure can be written as

$$\varepsilon_{total} \sim \varepsilon_{calibration} + \varepsilon_{algorithm} + \varepsilon_{sampling} \qquad (24.2)$$

The calibration term relates to both the infrared geostationary data as well as the microwave instruments of the constellation. The algorithm term encompasses both the merging algorithm as well as the instantaneous rainrates retrieval uncertainty. The sampling term is more straightforward and is directly related to the number of available samples used for constructing the accumulation as detailed in the next section. Both the use of an ad-hoc bias correction scheme with ancillary data and the detection uncertainty further introduce non-linearity in the uncertainty budget and make it difficult to estimate the individual terms. At the instantaneous retrieval level, the impact of the uncertainty of the calibration (and other offsets in the simulated brightness temperatures) of the microwave imagers to the rain rates estimates has been explored (Elsaesser and Kummerow 2015) showing systematic error propagation, mainly in the low rain rates range. The systematization of such uncertainty model to the full-blown constellation, including sounders is nevertheless not straightforward. A systematic investigation of the various terms comprising the total uncertainty budget for a merged product (Chambon et al. 2012a) led to a number of generic elements. They used a Monte Carlo approach to deal with the non-linearity of the process and have shown that.

- The random errors in the level 2 data do not affect the final products performances very much but systematic errors do propagate to the final daily accumulated precipitation estimates.
- The response is precipitation-regime dependent. Low and high rain rate systematic errors (respectively $\leqq 2 \; mm \, h^{-1}$ and $\geqq 10 \; mm \, h^{-1}$) do not significantly affect the final daily accumulated precipitation estimates, even with strong errors

(~100%). Systematic errors on intermediate rain rates (between 2 and 10 mm h^{-1})
do propagate more efficiently to the final daily accumulated precipitation
estimates.

- The response is not linear. In the most sensitive case, (medium rain rates, systematic errors), a + 40% perturbation in the level 2 data yield a + 25% bias in the final daily accumulated precipitation.

While a more systematic approach for the propagation of uncertainty from the
microwave algorithm part is clearly needed, these early studies suggests that to a
first approximation, the random uncertainty budget can be simplified to

$$\varepsilon_{total} \sim \varepsilon_{sampling} \tag{24.3}$$

and the systematic part of the uncertainty budget can be mitigated through the bias
correction scheme.

24.2.2.2 The Sampling Uncertainty

Roca et al. (2010) proposed a model for the computation of the sampling uncertainty
for accumulated precipitation. It takes the form of a standard error and is given by

$$\varepsilon_{samp} = \frac{\sigma}{\sqrt{N_{ind}}} \tag{24.4}$$

where σ is the variance of the geostationary derived rain mask over the $1° \times 1° \times 1$ day
volume multiplied by the RR_{cond} and N_{ind} is the number of independent sample in the
computation of the mean and variance. The estimation of N_{ind} is based on the
computations of variograms from the geostationary rain mask and is given by

$$N_{ind} = \frac{A}{d^2} \frac{T}{\tau} \tag{24.5}$$

where d and τ are the decorrelation scales, both in space and time, obtained from the
variograms (Roca et al. 2010). Figure 24.1 shows the monthly averaged map of the
relative uncertainty obtained from TAPEER1.5 products (see Sect. 24.3.2).

The uncertainty is computed on a $10° \times 10°$ grid every 10 days to both minimize
the computational burden and while keeping the major variability of the variance
fields (Chambon et al. 2012a). In the intense rainfall areas, the sampling relative
uncertainty varies from 15% to 20% and tends to 15% as the rainfall increases.
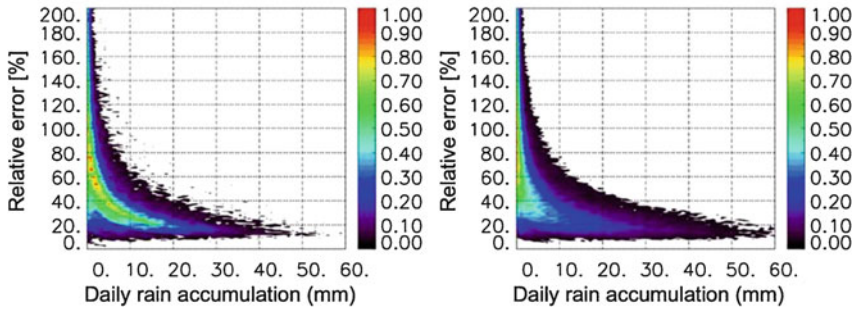
Fig. 24.1 The relative uncertainty in % as a function of daily rain accumulation for land (left) and ocean (right) conditions for July 2012 all over the Tropics

### 24.2.2.3   Bias Correction Scheme

The final step of the product realization is the application of the Bias Correction Scheme (BCS). This ensures some consistency between the satellite derived products mentioned above with respect to selected other products. This step is often, although improperly, called the calibration step of the final product. This statistical adjustment depends on various hypotheses.

Indeed, it is possible to adjust the bias of the product either at the global scale based on water and energy cycle closure arguments or at local scales making use of ground data rich regions where available, or both. Each of these adjustment approaches has its own advantages and weaknesses. It also relies strongly on the reference dataset selection. For instance, over the ocean a budget approach can be employed to characterize the products to first order by computing the water budget over various ocean basins using multi-year averaged seasonal cycle (Rodell et al. 2015; Brown and Kummerow 2014) with the help of evaporation data from SeaFlux and water vapour transport from ECMWF Reanalysis. Over the global land, the use of the GPCC reference can be used to compute multi-year seasonal cycles for comparison over various continental masses (Rodell et al. 2015), or simply used as a part of the product (e.g., Huffman et al. 2001).

24.2.2.4   Summary and the $1° \times 1° \times 1$ Day Optimum

Figure 24.2 presents a schematic summarizing the steps in producing the accumulated rainfall and associated uncertainty.

The accumulated rainfall estimation using this merging technique requires enough IR and microwave observations to ensure that the relationship between rain/no rain IR threshold and the actual rain fraction are robust. This relationship, between the cloud and the rain, is basically a statistical relationship that requires data to be aggregated to some space/time resolution for it to hold. The physical constraints of the observing system used to characterize the high frequency/small scales
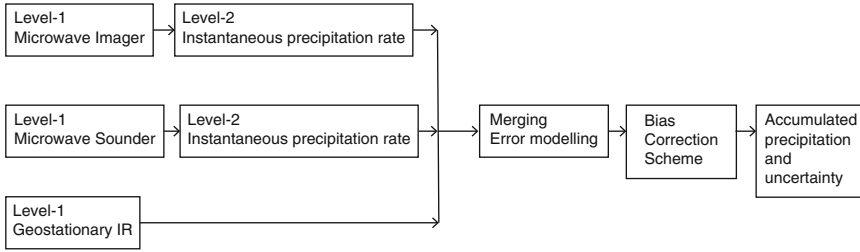
Fig. 24.2 Flow chart of the merging algorithm

in the intermittent precipitation field put a physical limit on the scale of the accumulation estimate. As a result, for a given set of observations, if the accumulation is computed over a small space domain, the random uncertainty will grow strongly (Bell and Kundu 2000) preventing its use for applications. Over large domain, the random uncertainty vanishes as does the physical variability of interest. A trade-off must be found. The merit of such an approach aggregated at the 1°/1 day scale has already been discussed and is pursued here. Theoretically, it is nevertheless possible to also consider lower resolutions of the products within our framework assuming the representativeness of the IR-rain statistics is conserved in order to avoid random error growth. Recent investigation for tropical conditions, in West Africa, indeed suggests that the skill of such a merging technique at $1°$ day^{-1} would still hold at 0.5°/6 h assuming observing conditions from the recent microwave constellation and the MSG satellite (Guilloteau et al. 2016). Further research is needed to assess whether it still holds in the past and in other regions. Similarly, one can think of a product that complements the 1°/1 day baseline but could address, for instance, 1°/30 min to resolve the diurnal cycle or 0.25°/daily scale for which the statistical robustness of the estimate is more easily achieved.

Finally, the observing system limitation (Guilloteau et al. 2018) prevent the use of this kind of approach for estimation at finer joint space and time scale that can nevertheless be explored thanks to statistical downscaling techniques as pointed out in Sect. 24.5.

24.3 Implementations for Tropical Water Cycle

24.3.1 Data

24.3.1.1 The Geostationary Data

Table 24.1 details the configuration of the geostationary infrared fleet for the month of August and reveals the spectral similarities of the thermal channels as well as the variety of space and time resolutions to deal with in the colocation step.

Table 24.1 The configuration of the geostationary infrared fleet for August 2016 used in the precipitation products

Nominal configuration	GOES-W	GOES-E	MSG	MFG	HIMAWARI
Satellite	GOES-15	GOES-13	MSG3	METEOSAT-7	HIMAWARI-8
IR channel (μm)	10.7	10.7	10.8	11.5	10.4
Nadir location	135°W	75°W	0°E	57°E	140.7°E
Time resolution (min)	30	30	15	30	20[a]
Resolution at nadir (km)	4	4	3	5	2
Effective long. Span	175°W–120°W	120°W–40°W	40°W–40°E	40°E–100°E	100°E–175°W

[a]The nominal resolution is 10 min

In the framework of both the TAPEER and the GIRAFE implementation, a specific quality control procedure has been devised to handle the technical issues found in the data (Szantai et al. 2011).

24.3.1.2 The BRAIN Data

The Bayesian Rain Algorithm including Neural Networks (BRAIN) algorithm originates from the GPROF algorithm (Viltard et al. 2006) and differs some the original versions by the use of a TRMM-PR database in the Bayesian scheme. In the version used for the tropical water cycle implementation, for all of the microwave imagers, the instantaneous rain rates are retrieved at a common resolution of 12 km, making the collocation with IR and the multiplatform merging straightforward. The analysis of the performance of the retrieval shows a rather good detection capability over tropical West Africa but a systematic underestimation of the rain intensity (Kacimi et al. 2013; Kirstetter et al. 2013; Roca et al. 2015, 2018).

24.3.2 The TAPEER Implementation

24.3.2.1 Common Aspects

The general implementation of the TAPEER algorithm has been presented in various publications (Chambon et al. 2012b, 2013; Roca et al. 2018). The algorithm merges the IR data (Table 24.1) with the BRAIN Level 2 from various platforms (Table 24.2) and outputs the 1° × 1° daily accumulated precipitation amount and the uncertainty estimate using the error model introduced in the previous section.

Table 24.2 The configuration of the passive microwave constellation (imagers and sounders) used for the various TAPEER and GIRAFE products

Algorithm	Imagers	Sounders
TAPEER 1.0	AMSR-2, TMI, F15SSM/I, F16/F17/F18 SSMIS, MADRAS	None
TAPEER 1.5	AMSR-2, TMI, F15SSM/I, F16/F17/F18 SSMIS	SAPHIR (Hong)
TAPEER 2.0	AMSR-2, GMI, F15SSM/I, F16/F17/F18 SSMIS, MADRAS	NPP, ATMS, METOPA.MHS, METOPB.MHS, NOAA18.MHS, NOAA19.MHS, SAPHIR (PRPS)
GIRAFE 1.0	AMSR-2, GMI, F15SSM/I, F16/F17/F18 SSMIS, MADRAS	NPP, ATMS, METOPA.MHS, METOPB.MHS, NOAA18.MHS, NOAA19.MHS
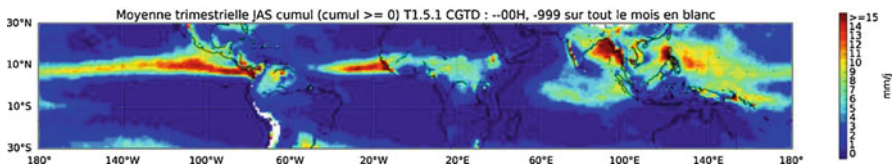
**Fig. 24.3** Map of the July–September 2012–2016 average daily precipitation from TAPEER 1.5

24.3.2.2 TAPEER 1.0 with MADRAS

Early tests of the TAPEER algorithm have been implemented using the MADRAS observations in conjunction with other imagers. The initial results were found very encouraging but the sudden demise of the instrument stopped the operational implementation (Roca et al. 2015). It prompted the team to explore mitigation solutions for the loss of the tropical sampling introduced by Megha-Tropiques and the development of TAPEER 1.5.

24.3.2.3 TAPEER 1.5 with SAPHIR

As discussed in Sect. 24.2, the conditional rain rate and the rain fraction can be estimated independently using different training volumes. Here we go one step further and use to configuration of the constellation, one with only the imagers used for the RR_{cond} computations and another one, including rain detection results from imagers and a rain-no rain mask derived from the SAPHIR sounder for the computation of the rain fraction. A SAPHIR-derived rain-no rain mask based on (Hong 2005) is available from the Megha-Tropiques water vapor products (Roca et al. 2015). This two-constellations implementation benefits from a TRMM-PR based bias correction scheme (Roca et al. 2018).

The boreal summer climatology of the products (Fig. 24.3) reveals the well-known features of the monsoons and the ITCZ as well as the heavy rainfall
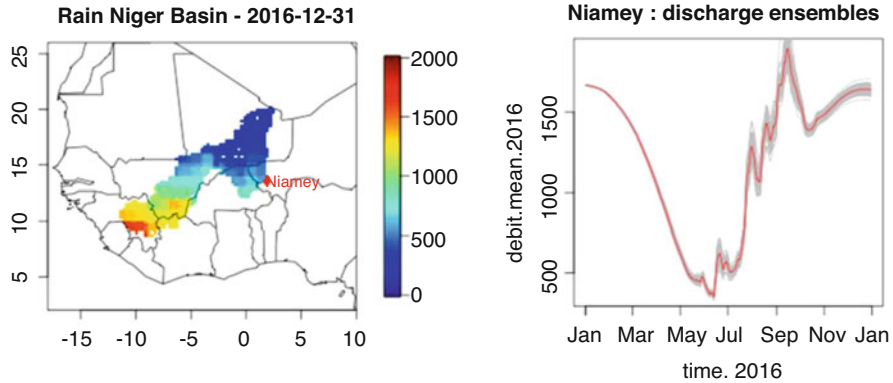
Fig. 24.4 Hydrological application of TAPEER 1.5 over the Niger River basin. The left figure shows the total rainfall accumulated over the Niger river basin in 2016 (1 January–31 December), the right plot illustrates the simulation of the discharge in Niamey based on the hydrological model MGB (Fleischmann et al. 2018) with TAPEER rainfall as forcing

characteristics of the Bay of Bengal. The patterns as well as the intensity are in good agreement with existing similar scale products. The product shows significant sensitivity of to the presence of the SAPHIR data (Roca et al. 2018). It is now being used to investigate tropical meteorology and hydrometeorology science questions as summarized in Chap. 3). An important aspect of the product is the very multiyear steady performance when compared to other global products over West Africa (Gosset et al. 2018) that enables hydrometeorological studies.

Recent applications indicate that one key feature for rainfall product relevance for hydrometeorology in West Africa is the reproduction of the early rise of the Niger in July followed by several sharp peaks during the "red-flood" period (Cassé et al. 2015, 2016) which creates severe floods in Niamey. Reproducing this feature requires a good representation of the convective systems' rainfall near Niamey – a skill shown by TAPEER 1.5 (Gosset et al. 2018). Figure 24.4 further illustrates the usefulness of the uncertainty information of the product when used as the forcing to a hydrological model for the 2016 season in Niger. The TAPEER 1.5 product is in operation in the French scientific ground segment for the Megha-Tropiques mission and the data are freely available at http://www.icare.univ-lille1.fr/mt (last accessed 16 Oct. 2018).

24.3.3 TAPEER-GPROFv5-PRPS

The most recent implementation of the algorithm is based on the use of a larger amount of instantaneous rain rates retrievals made available via PPS of GPM based on the GPROF and the PRPS algorithms.

24.3.3.1 The GPROF and PRPS Data

GPROF has been enhanced for the GPM constellation and its actual version (GPROF2017) is applicable to different PMW radiometers, such as imagers (SSM/I, TMI, SSMI/S, GMI and AMSR-2) and sounders as well (i.e., MHS, NPP). Given that GPROF is a physically-based Bayesian scheme which uses an a-priori database and relates to the brightness temperatures for rainfall retrievals (see Chap. 8), the GPM Version 5 (V5) a-priori database is used in GPROF2017 algorithm version. In this case, the GMI radiances are matched with 3 hydrometeor sources: (i) Combined MS, (ii) DPR Ku, and (iii) Multi-Radar/MultiSensor System (MRMS) ground-based radars (Kummerow et al. 2015; Kidd et al. 2016a).

In order to keep the full benefit of the MT orbit in the Tropics (demonstrated in Roca et al. 2018), GPROF pwv retrieval (which does not yet include SAPHIR) is complemented by PRPS retrieval (Kidd 2018) on SAPHIR. Precipitation Retrieval and Profiling Scheme (PRPS) is also a Level 2 physically-based scheme for rainfall retrieval, but developed uniquely for sounders (in this case for SAPHIR). The estimate of precipitation from PRPS for SAPHIR considers the Level 1C SAPHIR data and other four a-priori data as input: (i) database of DPR (rain rate) – SAPHIR (Tc radiances); (ii) database index; (iii) topography data; and (iv) scan-position correction database (Kidd et al. 2016a, 2018).

24.3.3.2 TAPEER 2.0

TAPEER 2.0 retains the principles of TAPEER 1.5, but uses different inputs. As with previous implementations, the algorithm allows for diverse constellations to be used for calculating the daily rain fraction and the constellation used for calculating the conditional rain rate. With this flexible approach, the use of sounders and imagers can thus be optimized according to the skills of the retrievals on each type of platform. Sensitivity tests are currently carried out in order to finalize the choice of parameters in TAPEER 2.0. Another novelty in TAPEER 2.0 is that unlike BRAIN, the spatial resolution of GPROF (version 5) retrieval is platform dependent. The co-location module of TAPEER 2.0, which creates the coincident data bases between the geostationary data and the PMW retrieval, has thus been modified to account for size and shape differences in the FOV of the different sensors.

24.3.3.3 Future Evolution

Future plans will focus on:

- The error model will continue to evolve the initial work by Chambon et al. (2012a) in order to account for the propagation of level 2 uncertainties (bias; random errors) into the level 4 data.

- While TAPEER 1.5 is provided at the $1° \times 1$ day resolution, the work by Guilloteau et al. (2017, 2018) demonstrated that information on rainfall at much smaller scales can be extracted from satellite information by using stochastic approaches. This will be implemented in TAPEER in some hot spot regions (e.g., targeted tropical basins such as Niger river).
- The type and amount of information provided at level 2 is expected to evolve rapidly in coming years. The TAPEER approach is flexible enough to absorb and take advantages of these changes by

  - Integrating level 2 data from the new constellations of satellites available in the Tropics (e.g., nano satellites like in the TROPICS mission, Blackwell et al. 2018).
  - Integrating the merging technique with probabilistic information which is becoming available at level 2 (e.g., probability of rain rather than a simple rain masks; quantiles of rain rates rather than a single rain values).

24.4   Implementation for Climate Monitoring

The demand for an improved precipitation climate product and service is related to the need for better information on medium– and long-term trends of precipitation and its extremes in various regions of the globe, especially those that are exposed to floods, droughts and/or water scarcity. The changing climatic regimes impose a serious reconsideration of our knowledge of the water cycle mechanisms, precipitation above all. The accurate knowledge of precipitation distribution and variability on a daily, monthly, seasonal, yearly, and decadal basis is vital as a support to decisions by the national, European and other authorities. It is deemed relevant and beneficial that Europe enters the arena of precipitation product provision for climate services; and that the development, generation and provision of a global precipitation climate data record will be pursued in a joint European effort.

This effort benefits from sustained European observing systems (e.g., Meteosat Third Generation and EUMETSAT Polar System Second Generation), a maximized utilization of well characterized radiances and brightness temperatures, i.e. Fundamental Climate Data Records (FCDRs), traceability through the full processing chain from Level 1 to Level 4, and a close cooperation with the in-situ community, in particular the Global Precipitation Climatology Centre. The precipitation product would further be based on a suite of physically based algorithms for instantaneous rain and snow rates, applicable to microwave sounders and imagers, on a sound approach for blending the geostationary observations for accumulated rainfall computations, and on an innovative uncertainty propagation model.

Initial elaborations of such products are ongoing within the EUMETSAT Climate Monitoring SAF under the name Global Interpolated RAinFall Estimation (GIRAFE). The preliminary outcomes of this long-term development are presented in the next section.

24.4.1   *GIRAFE 1.0 – GPROFv5*

This first implementation of GIRAFE is focused on estimating the $1° \times 1°$ daily liquid precipitation accumulation over the 55°S-55°N region. It follows the general flow chart of the merging algorithm (Fig. 24.5). It relies on the use geostationary observations of Table 24.1 and use the instantaneous rainfall estimation from GPROF v5 (see Sect. 3.6.4.4) for both the imagers and the sounders as summarized in Table 24.2. The rain-no rain detection step is deterministic with a flat threshold of 0.5 mm h^{-1} for each platform.

24.4.1.1   First Results

The map of estimated rainfall using GIRAFE and GPROF (Fig. 24.5) exhibits the well-known structures of the tropical and extra-tropical precipitation climatology. Under the current preliminary implementation, the intensity distribution is biased low with respect to other climatologies.

24.4.1.2   Sensitivity to the Constellation Configuration

Using the ability of the merging approach to exercise data denial experiments, a second run of GIRAFE is performed using only the imagers and no sounders. All other things are equal to the baseline integration. Figure 24.6 shows the map of the monthly mean difference between the two computations. While difference generally span negative to positive values over the oceanic regions, the northern midlatitude oceans are characterized by a systematic increase in monthly rainfall amount when
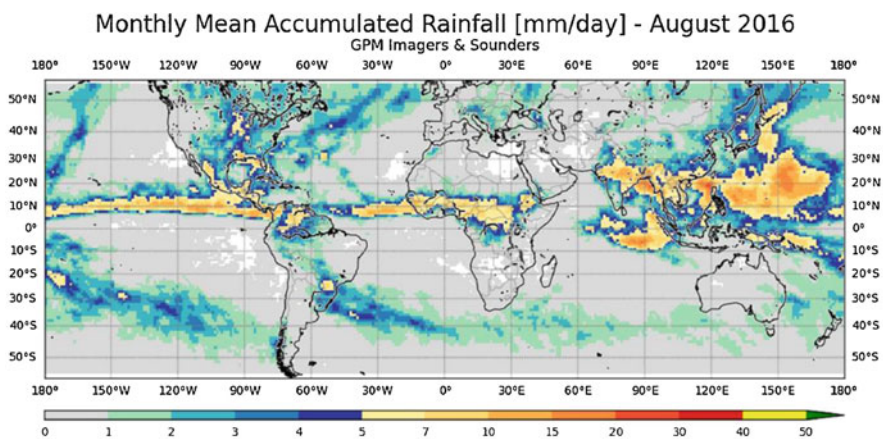
Fig. 24.5 Map of the monthly precipitation accumulation in mm for August 2016 from the full run of GIRAFE
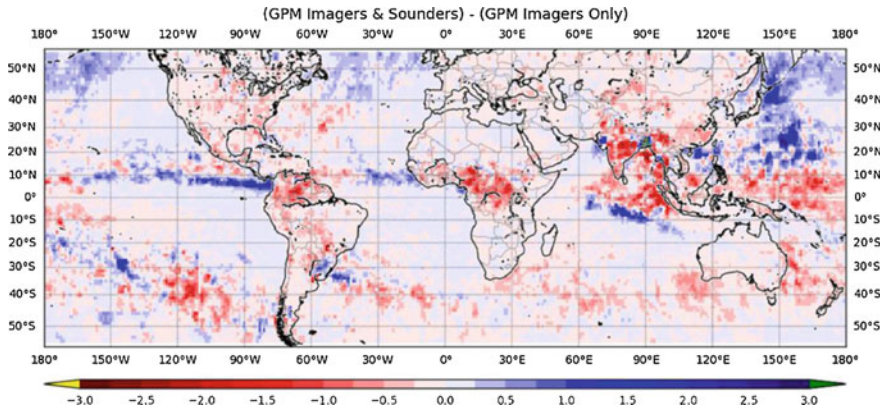
Fig. 24.6 Map of the monthly mean difference between the two runs of GIRAFE with or without the sounders in the constellation (mm day^{-1})

the sounders are incorporated in the estimation. Conversely, over land the integration using only imagers yield systematically larger monthly estimates in the tropics.

As a result, the conditional mean rain amount over land (ocean) is 3.5 mm day^{-1} (3.2) and 3.7 mm day^{-1} (3.6) for imagers only. The precipitation fraction for the baseline run is 55% and 55% over land and ocean respectively while it is 56% and 49% for the imager only integration.

Over the tropical land, the systematic difference therefore arises from the systematic underestimation of the imagers and sounders integration over the 10–20 mm day^{-1} range as indicated by the analysis of the distribution of the daily $1° \times 1°$ accumulation (Fig. 24.7). Over the ocean the situation is slightly more complex with a significant overestimation for the low accumulation (up to 4 mm day^{-1}) and an underestimation for the higher rain accumulation. Such a response is also observed over the tropical Atlantic Ocean characterized by a west-east gradient in the difference between the two configurations of GIRAFE. These preliminary results show the great benefit of adding the sounders in the constellation as well as the challenges of ingesting these together with the imagers retrievals in a consistent way.

24.4.2   Future Evolution

The GIRAFE production is foreseen in 2021 with a first integration ranging from 2002 to 2020. In the upcoming years the GIRAFE developments will first focus on:

- using instantaneous retrievals of precipitation from HOAPS/imager;
- using instantaneous retrievals of precipitation from sounders;
- reaching global coverage and extend to snowfall;
- implementing a time varying uncertainty model.

Fig. 24.7 GPM imagers
and sounders (in blue) and
GPM imagers only (in red)
precipitation volume
distributions over all the
region (top), over land
(middle) and ocean (bottom)
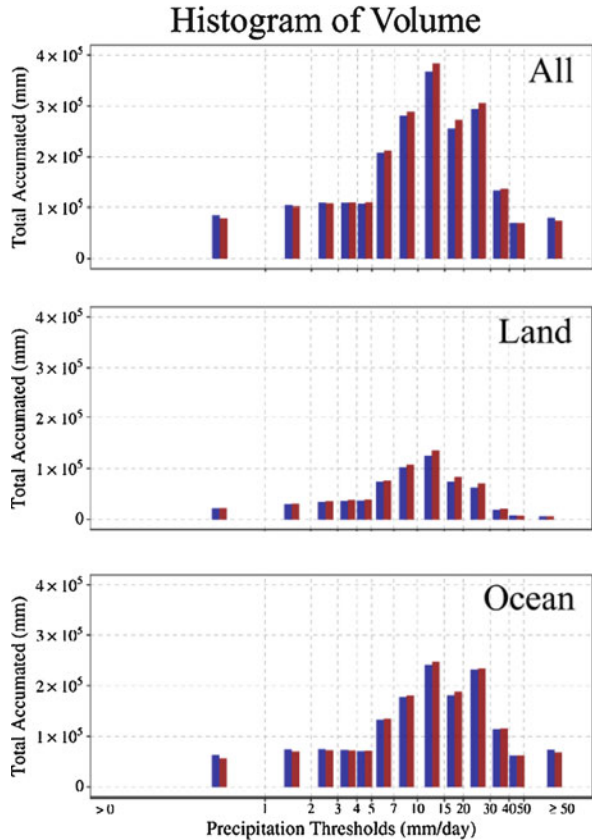
24.4.2.1 The Evolution of the HOAPS Instantaneous Precipitation Rate Estimate

Since the late 1980s, several groups at the Max-Planck Institute for Meteorology (MPI-M) and the University of Hamburg (UHH) have been developing retrievals based on SSM/I microwave observations. The retrieved parameters include precipitation, latent heat flux and various other parameters which were incorporated in a data set, which was named the "Hamburg Ocean- Atmosphere Parameters and Fluxes from Satellite Data" (HOAPS). Since version 3.1, EUMETSAT's Climate Monitoring-Satellite Application Facility (CM-SAF) releases the HOAPS data set, in close cooperation with UHH and MPI-M. The latest version is HOAPS 4 (Andersson et al. 2017) which provides quasi-global coverage over the ice-free ocean surface, i.e., within $\pm 180°$ longitude and $\pm 80°$ latitude. The products are available as both 6-hourly composites and monthly averages on a regular latitude/longitude grid with a spatial resolution of $0.5° \times 0.5°$ degrees. The temporal coverage of HOAPS 4 ranges from July 1987 to December 2014. HOAPS relies entirely on observations from SSM/I and SSMIS (Graw et al. 2017). An exception is the utilization of SST data from AVHRR (Reynolds et al. 2007).

The HOAPS 4 precipitation retrieval is an artificial neural network (Andersson et al. 2010). Currently, CM-SAF is developing a new physical retrieval for precipitation. In a first step, background and first guess profiles are estimated which are then used as input to a 1-dimensional variational scheme (1D-Var) to retrieve precipitation. The background profile that is most consistent with the measured conditions is estimated from the profile data set by constructing a weighted average of selected profiles, similar to the Bayesian approach outlined in Chap. 7. The selection is based on sensor derived data and SST only. The HOAPS 1D-Var retrieval is an implementation of the Numerical Weather Prediction-SAF (NWP-SAF) package containing the merged capabilities of the UK MetOffice and ECMWF 1D-Var schemes (Deblonde et al. 2007), among others, with the extension to handle hydrometeor profiles in precipitating scenes by using a multiple scattering module in the Radiative Transfer model for TIROS Operational Vertical Sounder (RTTOV) as the forward operator (Saunders et al. 2013). The 1D-Var scheme will be further fine-tuned to optimize retrieval quality. Future developments also include an extension of the state vector to allow retrieval applicability also over land areas (Boukabara et al. 2011) and an uncertainty analysis using the uncertainty estimate from the 1D-Var retrieval scheme and results from comparisons with ground-based observations (e.g., from the Ocean Rainfall And Ice-phase precipitation measurement Network, OceanRAIN, Klepp et al. 2018; Chap. 34 of volume 2).

24.4.2.2 Use of Sounders

As exemplified above, the use of sounders is an important aspect of the implementation of GIRAFE for climate monitoring that will benefit from two recent advances on the sounders archive and sounder based retrievals (e.g., Laviola and Levizzani 2011). First on the climate data record aspect, the EUMETSAT CM-SAF is finalizing the AMSU-B FCDR that shows long term stability and homogeneity over the last decade. Second, as exemplified in this chapter, the PRPS instantaneous precipitation retrievals (Kidd 2018) has matured and will be used for the GIRAFE implementation. These advances will make it possibility to benefit from research satellite observations such as SAPHIR data on board the Megha-Tropiques mission (see Chap. 3). Efforts will nevertheless be needed to investigate the consistency among the imagers and sounders retrievals in the RR_{cond} computations as well as on the uncertainty propagation.

24.4.2.3 Extension to the Poles and to Snow

Estimates of daily accumulated precipitation globally requires reaching out to the poles. Poleward of 55°, the geostationary viewing angle and pixel deformation prevents its classical use It is therefore planned to rely on a microwave only estimation of both the conditional rainrates and the rain fraction. Fortunately, the recent growth of the constellation including the sounders yield an impressive number
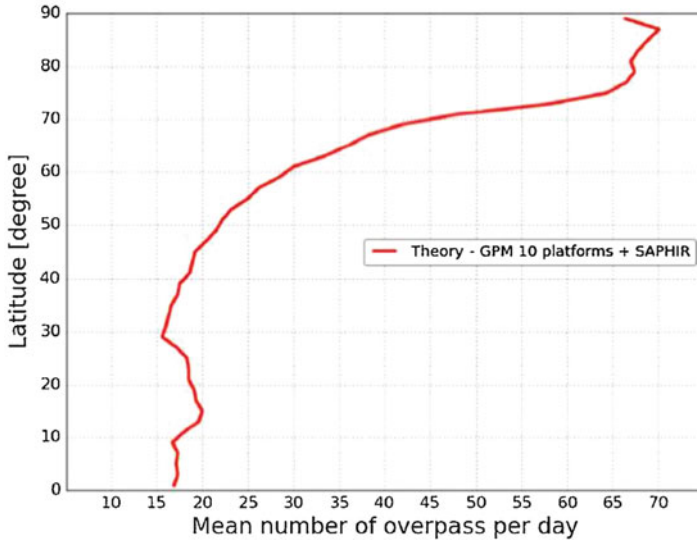
Fig. 24.8 Zonal mean number of overpass of the full-blown microwave constellation including imagers, sounders and SAPHIR. Computations realized using the IXION package. (Capderou 2014)

of microwave data available for that region where more than 50 daily overpasses can be used poleward of 70° (Fig. 24.8). Beyond the 55° and 70° latitude range, the density of observations is characterized by a strong increase that will need to be carefully accounted for.

Extending from the tropics and the TAPEER algorithm to the global GIRAFE products not only requires a change to a microwave-only approach, but also for solid precipitation to be accounted for. The retrieval of precipitation over land and the retrieval of precipitation over polar regions is very challenging but instead of using a surface temperature-based partitioning between rain and snowfall, at this stage, it is envisioned to keep the same philosophy for snowfall as used for rainfall, using dedicated the instantaneous snowfall rate initially developed in the H-SAF (Rysman et al. 2018).

24.4.2.4   The Time Dependent Uncertainty Estimation

While the amount of geostationary data has been steady over the last two decades, the constellation of passive microwave imagers and sounders has changed significantly. Using the strength of the merging technique presented here, data denial experiments (e.g., Roca et al. 2018) will be performed to assess the relative uncertainty in the final products induced by changes in the constellation over time.

24.5 Conclusions

The combination of various passive microwave (imagers and sounders) instantaneous precipitation rate retrievals together with geostationary infrared data have benefited from the recent decades of algorithms improvements. The so-derived accumulation at the daily scale exhibits very good performances that enables their use for various hydrometeorological applications, in particular over un-gauged tropical lands. Similarly, global climate monitoring can also benefit from this progress. Besides efforts to improve existing products, a European Initiative has been formed to generate a new global precipitation product dedicated to climate analysis and climate services. An associated white paper provides details on background, motivation, application areas, scientific methods and validation (Tapiador et al. in preparation).

The accumulated rainfall amount perspective further provides a powerful framework for investigating the uncertainty of the final products and its downstream propagation from the various raw measurements. The uncertainty characterization is a much-needed step before addressing smaller space and time scales where downscaling techniques appear well suited for that endeavor. Similarly, the uncertainty arising from the evolution of the configuration of the constellation of microwave imagers and sounders over the recent decades will be tackled within this framework, offering enhanced climate monitoring performances.

References

Andersson, A., Fennig, K., Klepp, C., Bakan, S., Graßl, H., & Schulz, J. (2010). The Hamburg Ocean Atmosphere Parameters and Fluxes from Satellite Data – HOAPS-3. *Earth System Science Data, 2*, 215–234. https://doi.org/10.5194/essd-2-215-2010.

Andersson, A., Graw, K., Schröder, M., Fennig, K., Liman, J., Bakan, S., Hollmann, R., & Klepp, C. (2017). *Hamburg ocean atmosphere parameters and fluxes from satellite data – HOAPS 4.0*. Offenbach: CM-SAF. https://doi.org/10.5676/EUM_SAF_CM/HOAPS/V002.

Bell, T. L., & Kundu, P. K. (2000). Dependence of satellite sampling error on monthly averaged rain rates: Comparison of simple models and recent studies. *Journal of Climate, 13*, 449–462. https://doi.org/10.1175/1520-0442(2000)013<0449:DOSSEO>2.0.CO;2.

Blackwell, W. J., Braun, S., Bennartz, R., Velden, C., DeMaria, M., Atlas, R., Dunion, J., Marks, F., Rogers, R., Annane, B., & Leslie, R. V. (2018). An overview of the TROPICS NASA Earth venture mission. *Quarterly Journal of the Royal Meteorological Society, 144*(S1), 16–26. https://doi.org/10.1002/qj.3290.

Boukabara, S. A., Garrett, K., Chen, W. C., Iturbide-Sanchez, F., Grassotti, C., Kongoli, C., Chen, R. Y., Liu, Q. H., Yan, B. H., Weng, F. Z., Ferraro, R. R., Kleespies, T. J., & Meng, H. (2011). MiRS: An all-weather 1DVAR satellite data assimilation and retrieval system. *IEEE Transactions on Geoscience and Remote Sensing, 49*(9), 3249–3272. https://doi.org/10.1109/TGRS.2011.2158438.

Brown, P. J., & Kummerow, C. D. (2014). An assessment of atmospheric water budget components over tropical oceans. *Journal of Climate, 27*, 2054–2071. https://doi.org/10.1175/jcli-d-13-00385.1.

Capderou, M. (2014). Satellites of other celestial bodies. In *Handbook of satellite orbits* (pp. 803–882). Cham: Springer. https://doi.org/10.1007/978-3-319-03416-4_16.

Casella, D., Panegrossi, G., Sanò, P., Milani, L., Petracca, M., & Dietrich, S. (2015). A novel algorithm for detection of precipitation in tropical regions using PMW radiometers. *Atmospheric Measurement Techniques, 8*, 1217–1232. https://doi.org/10.5194/amt-8-1217-2015.

Cassé, C., Gosset, M., Peugeot, C., Pedinotti, V., Boone, A., Tanimoun, B. A., & Decharme, B. (2015). Potential of satellite rainfall products to predict Niger River flood events in Niamey. *Atmospheric Research, 163*, 162–176. https://doi.org/10.1016/j.atmosres.2015.01.010.

Cassé, C., Gosset, M., Vischel, T., Quantin, G., & Tanimoun, B. A. (2016). Model-based study of the role of rainfall and land use–land cover in the changes in the occurrence and intensity of Niger red floods in Niamey between 1953 and 2012. *Hydrology and Earth System Sciences, 20*, 2841–2859. https://doi.org/10.5194/hess-20-2841-2016.

Chambon, P., Jobard, I., Roca, R., & Viltard, N. (2012a). An investigation of the error budget of tropical rainfall accumulation derived from merged passive microwave and infrared satellite measurements. *Quarterly Journal of the Royal Meteorological Society, 139*, 879–893. https://doi.org/10.1002/qj.1907.

Chambon, P., Roca, R., Jobard, I., & Aublanc, J. (2012b). The TAPEER-BRAIN product: Algorithm theoretical basis document, level 4. *Megha-Tropiques Technical Memorandum, 4*, 13. Available at http://meghatropiques.ipsl.polytechnique.fr/technical-documentation/?wpdmc=technical. Last accessed 17 Oct 2018.

Chambon, P., Roca, R., Jobard, I., & Capderou, M. (2013). The sensitivity of tropical rainfall estimation from satellite to the configuration of the microwave imager constellation. *IEEE Geoscience and Remote Sensing Letters, 10*, 996–1000. https://doi.org/10.1109/LGRS.2012.2227668.

Deblonde, G., Mahfouf, J.-F., Bilodeau, B., & Anselmo, D. (2007). One-dimensional variational data assimilation of SSM/I observations in rainy atmospheres at MSC. *Monthly Weather Review, 135*, 152–172. https://doi.org/10.1175/MWR3265.1.

Elsaesser, G. S., & Kummerow, C. D. (2015). The sensitivity of rainfall estimation to error assumptions in a Bayesian passive microwave retrieval algorithm. *Journal of Applied Meteorology and Climatology, 54*, 408–422. https://doi.org/10.1175/jamc-d-14-0105.1.

Fleischmann, A., Siqueira, V., Paris, A., Collischonn, W., Paiva, R., Pontes, P., Crétaux, J.-F., Bergé-Nguyen, M., Biancamaria, S., Gosset, M., Calmant, S., & Tanimoun, B. (2018). Modelling hydrologic and hydrodynamic processes in basins with large semi-arid wetlands. *Journal of Hydrology, 561*, 943–959. https://doi.org/10.1016/j.jhydrol.2018.04.041.

Gosset, M., Alcoba, M., Roca, R., Cloché, S., & Urbani, G. (2018). Evaluation of TAPEER daily estimates and other GPM era products against dense gauge networks in West Africa, analyzing ground reference uncertainty. *Quarterly Journal of the Royal Meteorological Society, 144*(S1), 255–269. https://doi.org/10.1002/qj.3335.

Graw, K., Kinzel, J., Schröder, M., Fennig, K., & Andersson, A. (2017). *Algorithm theoretical baseline document HOAPS version 4.0*. Offenbach: CM-SAF, 30 pp. https://doi.org/10.5676/EUM_SAF_CM/HOAPS/V002.

Guilloteau, C., Roca, R., & Gosset, M. (2016). A multiscale evaluation of the detection capabilities of high-resolution satellite precipitation products in West Africa. *Journal of Hydrometeorology, 17*, 2041–2059. https://doi.org/10.1175/jhm-d-15-0148.1.

Guilloteau, C., Foufoula-Georgiu, E., & Kummerow, C. D. (2017). Global multiscale evaluation of satellite passive microwave retrieval of precipitation during the TRMM and GPM eras: Effective resolution and regional diagnostics for future algorithm development. *Journal of Hydrometeorology, 18*, 3051–3070. https://doi.org/10.1175/JHM-D-17-0087.1.

Guilloteau, C., Roca, R., Gosset, M., & Venugopal, V. (2018). Stochastic generation of precipitation fraction at high resolution with a multiscale constraint from satellite observations. *Quarterly Journal of the Royal Meteorological Society, 144*(S1), 176–190. https://doi.org/10.1002/qj.3314.

Hong, G. (2005). Detection of tropical deep convective clouds from AMSU-B water vapor channels measurements. *Journal of Geophysical Research, 110*. https://doi.org/10.1029/2004jd004949.

Huffman, G. J., Adler, R. F., Morrissey, M. M., Bolvin, D. T., Curtis, S., Joyce, R., McGavock, B., & Susskind, J. (2001). Global precipitation at one-degree daily resolution from multisatellite observations. *Journal of Hydrometeorology, 2*, 36–50. https://doi.org/10.1175/1525-7541 (2001)002<0036:GPAODD>2.0.CO;2.

Kacimi, S., Viltard, N., & Kirstetter, P.-E. (2013). A new methodology for rain identification from passive microwave data in the Tropics using neural networks. *Quarterly Journal of the Royal Meteorological Society, 139*, 912–922. https://doi.org/10.1002/qj.2114.

Kidd, C. (2001). Satellite rainfall climatology: A review. *International Journal of Climatology, 21*, 1041–1066. https://doi.org/10.1002/joc.635.

Kidd, C. (2018). *NASA global precipitation measurement (GPM) precipitation retrieval and profiling scheme (PRPS)*. Algorithm Theoretical Basis Document, v. 01-02, 17 pp. Available at https://pps.gsfc.nasa.gov/Documents/20180203_SAPHIR-ATBD.pdf. Last accessed 18 Oct 2018.

Kidd, C., Matsui, T., & Chern, J. (2016a). Global precipitation estimates from cross-track passive microwave observations using a physically based retrieval scheme. *Journal of Hydrometeorology, 17*, 383–400. https://doi.org/10.1175/JHM-D-15-0051.1.

Kidd, C., Matsui, T., Chern, J., Mohr, K., Kummerow, C., & Randel, D. (2016b). Global precipitation estimates from cross-track passive microwave observations using a physically based retrieval scheme. *Journal of Hydrometeorology, 17*, 383–400. https://doi.org/10.1175/JHM-D-15-0051.1.

Kirstetter, P.-E., Viltard, N., & Gosset, M. (2013). An error model for instantaneous satellite rainfall estimates: evaluation of BRAIN-TMI over West Africa. *Quarterly Journal of the Royal Meteorological Society, 139*, 894–911. https://doi.org/10.1002/qj.1964.

Klepp, C., Michel, S., Protat, A., Burdanowitz, J., Albern, N., Kähnert, M., Dahl, A., Louf, V., Bakan, S., & Buehler, S. A. (2018). OceanRAIN, a new in-situ shipboard global ocean surface-reference dataset of all water cycle components. *Scientific Data, 5*, 180122. https://doi.org/10.1038/sdata.2018.122.

Kummerow, C., & Giglio, L. (1995). A method for combining passive microwave and infrared rainfall observations. *Journal of Atmospheric and Oceanic Technology, 12*, 33–45. https://doi.org/10.1175/1520-0426(1995)012<0033:amfcpm>2.0.co;2.

Kummerow, C. D., Randel, D. L., Kulie, M., Wang, N.-Y., Ferraro, R., Munchak, S. J., & Petkovic, V. (2015). The evolution of the Goddard Profiling Algorithm to a fully parametric scheme. *Journal of Atmospheric and Oceanic Technology, 32*, 2265–2280. https://doi.org/10.1175/JTECH-D-15-0039.1.

Laviola, S., & Levizzani, V. (2011). The 183-WSL fast rainrate retrieval algorithm. Part I: retrieval design. *Atmospheric Research, 99*, 443–461. https://doi.org/10.1016/j.atmosres.2010.11.013.

Levizzani, V., Kidd, C., Aonashi, K., Bennartz, R., Ferraro, R. R., Huffman, G. J., Roca, R., Turk, F. J., & Wang, N.-Y. (2018). The activities of the International Precipitation Working Group. *Quarterly Journal of the Royal Meteorological Society, 144*(S1), 3–15. https://doi.org/10.1002/qj.3214.

Reynolds, R. W., Smith, T. M., Liu, C., Chelton, D. B., Casey, K. S., & Schlax, M. G. (2007). Daily high-resolution-blended analyses for sea surface temperature. *Journal of Climate, 20*, 5473–5496. https://doi.org/10.1175/2007JCLI1824.1.

Roca, R., Chambon, P., Jobard, I., Kirstetter, P. E., Gosset, M., & Bergés, J. C. (2010). Comparing satellite and surface rainfall products over West Africa at meteorologically relevant scales during the AMMA campaign using error estimates. *Journal of Applied Meteorology and Climatology, 49*, 715–731. https://doi.org/10.1175/2009JAMC2318.1.

Roca, R., Brogniez, H., Chambon, P., Chomette, O., Cloché, S., Gosset, M. E., Mahfouf, J.-F., Raberanto, P., & Viltard, N. (2015). The Megha-Tropiques mission: A review after three years in orbit. *Frontiers in Earth Science, 3*. https://doi.org/10.3389/feart.2015.00017.

Roca, R., Taburet, N., Lorant, E., Chambon, P., Alcoba, M., Brogniez, H., Cloché, S., Dufour, C., Gosset, M., & Guilloteau, C. (2018). Quantifying the contribution of the Megha-Tropiques

mission to the estimation of daily accumulated rainfall in the Tropics. *Quarterly Journal of the Royal Meteorological Society, 144*(S1), 49–63. https://doi.org/10.1002/qj.3327.

Rodell, M., Beaudoing, H. K., L'Ecuyer, T. S., Olson, W. S., Famiglietti, J. S., Houser, P. R., Adler, R., Bosilovich, M. G., Clayson, C. A., Chambers, D., Clark, E., Fetzer, E. J., Gao, X., Gu, G., Hilburn, K., Huffman, G. J., Lettenmaier, D. P., Liu, W. T., Robertson, F. R., Schlosser, C. A., Sheffield, J., & Wood, E. F. (2015). The observed state of the water cycle in the early twenty-first century. *Journal of Climate, 28*, 8289–8318. https://doi.org/10.1175/JCLI-D-14-00555.1.

Rysman, J. F., Panegrossi, G., Sanò, P., Marra, A. C., Dietrich, S., Milani, L., & Kulie, M. S. (2018). SLALOM: An all-surface snow water path retrieval algorithm for the GPM Microwave Imager. *Remote Sensing, 10*, 1278. https://doi.org/10.3390/rs10081278.

Saunders, R. W., Hocking, J., Rundle, D., Rayer, P. J., Matricardi, M., Geer, A., Lupu, C., Brunel, P., & Vidot, J. (2013). *RTTOV v11 science and validation report*, NWP-SAF, NWPSAF-MO-TV-032, 62 pp. Available at https://nwpsaf.eu/oldsite/deliverables/rtm/docs_rttov11/rttov11_svr.pdf. Last accessed 18 Oct 2018.

Szantai, A., Six, B., Cloché, S., & Sèze, G. (2011). Quality of geostationary satellite images. *Megha-Tropiques Technical Memorandum, 3.* Available at http://meghatropiques.ipsl.polytechnique.fr/megha-tropiques-technical-memorandum/. Last accessed 18 Oct 2018.

Tapiador, F. J., Navarro, A., Levizzani, V., García-Ortega, E., Huffman, G. J., Kidd, C., Kucera, P. A., Kummerow, C. D., Masunaga, H., Petersen, W. A., Roca, R., Sánchez, J.-L., Tao, W.-K., & Turk, F. J. (2017). Global precipitation measurements for validating climate models. *Atmospheric Research, 197*, 1–20. https://doi.org/10.1016/j.atmosres.2017.06.021.

Tapiador, F. J., Roca, R., Del Genio, A., Dewitte, B., Petersen, W., & Zhang, F. (2019). Is precipitation a good metrics for model performance? *Bulletin of the American Meteorological Society, 100*, 223–233. https://doi.org/10.1175/BAMS-D-17-0218.1.

Viltard, N., Burlaud, C., & Kummerow, C. D. (2006). Rain retrieval from TMI brightness temperature measurements using a TRMM PR–based database. *Journal of Applied Meteorology and Climatology, 45*, 455–466. https://doi.org/10.1175/jam2346.1.

Xu, L., Gao, X., Sorooshian, S., Arkin, P. A., & Imam, B. (1999). A microwave infrared threshold technique to improve the GOES Precipitation Index. *Journal of Applied Meteorology, 38*, 569–579. https://doi.org/10.1175/1520-0450(1999)038<0569:amittt>2.0.co;2.

Correction to: TAMSAT

Ross Maidment, Emily Black, Helen Greatrex, and Matthew Young

Correction to:
Chapter 22 in: V. Levizzani et al. (eds.), *Satellite Precipitation Measurement*, Advances in Global Change Research 67,
https://doi.org/10.1007/978-3-030-24568-9_22

Chapter 22, "TAMSAT" was previously published non-open access. It has now been changed to open access under a CC BY 4.0 license and the copyright holder updated to 'The Author(s)'. The book has also been updated with this change.

The updated version of the chapter can be found at
https://doi.org/10.1007/978-3-030-24568-9_22